Oil & Natural Gas Technology

DOE Award No.: DE-FC26-05NT42667

Final Report

Combining Multicomponent Seismic Attributes, New Rock Physics Models, and In Situ Data to Estimate Gas-Hydrate Concentrations in Deep-Water, Near-Seafloor Strata of the Gulf of Mexico

Submitted by:
Bureau of Economic Geology
The University of Texas at Austin
Austin, TX 78713-8924

Prepared for:
United States Department of Energy
National Energy Technology Laboratory

April 30, 2009

Reporting Period: 3/01/2006-4/30/2009

Office of Fossil Energy

Disclaimer

Abstract

The Bureau of Economic Geology was contracted to develop technologies that demonstrate the value of multicomponent seismic technology for evaluating deep-water hydrates across the Green Canyon area of the Gulf of Mexico. This report describes the methodologies that were developed to create compressional (P-P) and converted-shear (P-SV) images of near-seafloor geology from four-component ocean-bottom-cable (4C OBC) seismic data and the procedures used to integrate P-P and P-SV seismic attributes with borehole calibration data to estimate hydrate concentration across two study areas spanning 16 and 25 lease blocks (or 144 and 225 square miles), respectively. Approximately 200 km of two-dimensional 4C OBC profiles were processed and analyzed over the course of the 3-year project.

The strategies we developed to image near-seafloor geology with 4C OBC data are unique, and the paper describing our methodology was peer-recognized with a Best Paper Award by the Society of Exploration Geophysicists in the first year of the project (2006). Among the valuable research findings demonstrated in this report, the demonstrated ability to image deep-water near-seafloor geology with sub-meter resolution using a standard-frequency (10–200 Hz) air gun array on the sea surface and 4C sensors on the seafloor has been the accomplishment that has received the most accolades from professional peers.

Our study found that hydrate is pervasive across the two study areas that were analyzed but exists at low concentrations. Although our joint inversion technique showed that in some limited areas, and in some geologic units across those small areas, hydrates occupied up to 40-percent of the sediment pore space, we found that when hydrate was present, hydrate concentration tended to occupy only 10-percent to 20-percent of the pore volume. We also found that hydrate concentration tended to be greater near the base of the hydrate stability zone than it was within the central part of the stability zone.

CONTENTS

Figures

Tables

Executive Summary

Approximately 200 km of four-component ocean-bottom-cable (4C OBC) seismic data were processed and analyzed across two known hydrate sites in the Green Canyon area of the Gulf of Mexico in order to determine whether multicomponent seismic data offer any advantages over conventional, towed-cable, single-component data for studying deep-water hydrate systems. The principal difference between towed-cable seismic data and 4C data is that only a compressional (P-P) image of sub-seafloor geology can be made with towed-cable data; whereas, two independent images—a P-P image and a converted-shear (P-SV) image—can be made with 4C OBC data.

We found that the P-SV seismic wave component provided by 4C OBC technology is a great advantage for studying deep-water, near-seafloor geology. Specifically we found that with the P-SV mode, we could image near-seafloor geological features (such as bedding and minor fault throws) having dimensions smaller than one meter with standard-frequency (10–200 Hz) air-gun source illumination. In contrast, the spatial resolution of the companion P-P mode was a factor of approximately 50 to 30 times less for geology within the shallowest 100 meters of seafloor strata. This amazing resolution of the P-SV mode (available only with 4C data) is invaluable for studying deep-water hydrate systems. No previous study had demonstrated this important wave physics that comes into play when 4C seismic data are utilized in preference to towed-cable data.

Although the new concepts we developed and published that produce optimal-resolution P-P and P-SV images of near-seafloor geology has received the widest attention among our peers, we consider our technique for estimating hydrate concentration from resistivity log data to also be a seminal research finding. The material in this report shows that the Hashin-Shtrikman Lower Bound must be used to determine the constants that have to be used in the clay-term form of the Archie Equation (or whatever equation is used to describe formation resistivity) in order to obtain correct estimates of hydrate concentration from resistivity measurements made in a high-porosity, unconsolidated medium such as deep-water, near-seafloor sediments. To our knowledge, this important role that the Hashin-Shtrikman Lower Bound plays when inverting resistivity data to predict the magnitude of the hydrate fraction present within deep-water hydrate-bearing strata is also a new, unpublished concept.

We present in this report one detailed rock physics theory that documents how seismic interval velocity can be inverted to obtain an estimate of hydrate concentration and then a second theory that shows how resistivity should be inverted to hydrate concentration for the unique medium associated with high-porosity, unconsolidated seafloor strata. We use these two theories to do joint inversions of resistivity and seismic velocity to estimate hydrate concentrations at calibration wells, and then use the velocity form of these well-calibration inversions to continue the estimation of hydrate along 4C OBC seismic profiles that extend away from calibration wells. The end results are maps of the volume of hydrate across the two selected study areas.

These maps show a few small areas where hydrate concentration reaches a maximum of approximately 40-percent of the pore space in some stratigraphic units near the base of the hydrate stability zone. However, hydrate concentration is small across the majority of the two study areas and for most of the geologic units within the hydrate stability zone. We found hydrate concentration to usually be 10-percent to 15-percent of the available pore space and sometimes to increase to occupy as much as 20-percent to 25-percent of the pore space.

DOE Gas Hydrate Final Report

Chapter 1

Overview of Research Findings

Introduction

The objective of this study was to demonstrate the value of **4-component ocean-bottom-cable** (**4C OBC**) **seismic data** for estimating deep-water hydrate concentrations. In this introductory chapter, we summarize how we used 4-C OBC data to study hydrate systems across two project sites in the Green Canyon area of the Gulf of Mexico (GOM). We use this first chapter to illustrate the high-resolution properties of the P-P and P-SV seismic images produced by our specialized seismic data-processing concepts, demonstrate the features of near-seafloor geology that can be interpreted from 4C OBC data across our project area, summarize how we performed raytrace modeling to create sub-seafloor layer models of **compressional-wave velocity** ($\mathbf{V_P}$) and **shear-wave velocity** ($\mathbf{V_S}$), and show how these interval velocities were used with local resistivity logs to estimate hydrate concentration using a statistical-based joint inversion procedure

Chapters 2 through 10 are the supporting material for this introductory chapter. These following chapters provide details about the methodologies that we used to:

- Create high-resolution P-P and P-SV images from 4C OBC seismic data,
- Develop a rock physics model that relates interval values of seismic-based V_P and V_S velocities to hydrate concentration,
- Develop a rock physics model that relates resistivity log data to estimates of hydrate concentration,
- Perform seismic raytrace analysis to determine interval values of sub-seafloor V_P and V_S velocities to high accuracy (<1 percent) across a series of Earth layers extending from the seafloor to below the **base of the hydrate stability zone** (**BHSZ**), and
- Combine V_P and V_S velocities with well log resistivities in a joint inversion to estimate hydrate concentration.

Study Sites

Our study was done across two sites in the Green Canyon area of the Gulf of Mexico where 2D profiles of 4C OBC seismic data were acquired by WesternGeco, our industry partner. The locations of these sites are defined on the map displayed as Figure 1.1. One study area encompassed Typhoon Field; the second site spanned Genesis Field. There were several reasons for selecting

these study sites. First, profiles of low-frequency (10 – 200 Hz) 4C OBC seismic data and high-frequency (1 – 10 kHz) **autonomous underwater vehicle (AUV)** data traversed each site. The positions of these data profiles, and also the positions of the associated OBC profiles, are defined on the maps displayed as Figure 8.1 and will not be repeated here. These multicomponent and multi-frequency data form the critical remote measurements that we analyzed to determine the advantages of combining P-wave and S-wave data to evaluate deep-water hydrate systems.

Second, geotechnical reports were available describing laboratory measurements of seafloor sediment properties made on seafloor borings at Genesis and Typhoon Fields. These measurements were critical for calibrating sediment properties to seismic attributes. Third, the seafloor across portions of each study site exhibited bright reflectivity, which is proving to be an excellent proxy that can be used to indicate where a hydrate system exists beneath the seafloor (Roberts and others, 1992, 2006). The reflectivities across each study site are displayed on Figures 1.2 with the locations of local OBC and AUV profiles superimposed.

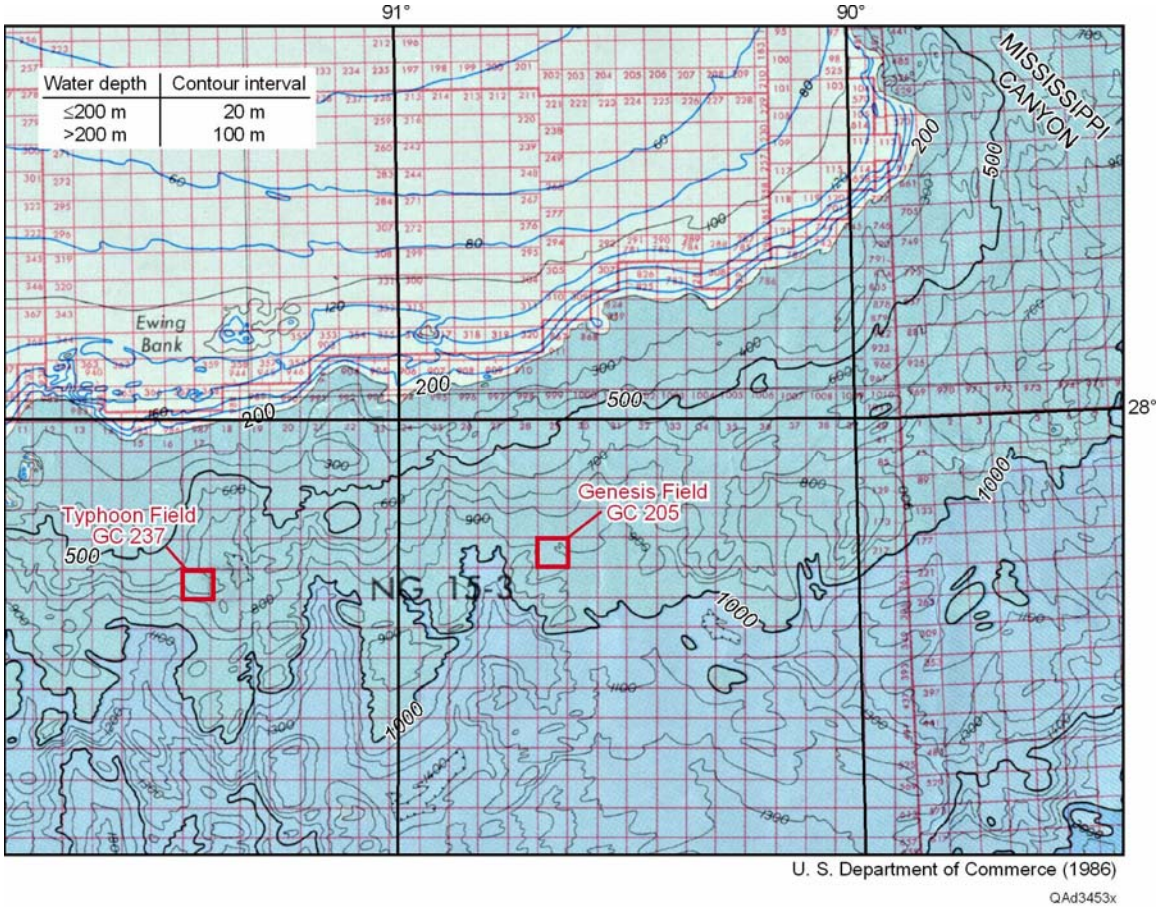

Figure 1.1. Location of project study sites in the Green Canyon area of the Gulf of Mexico.

(a)

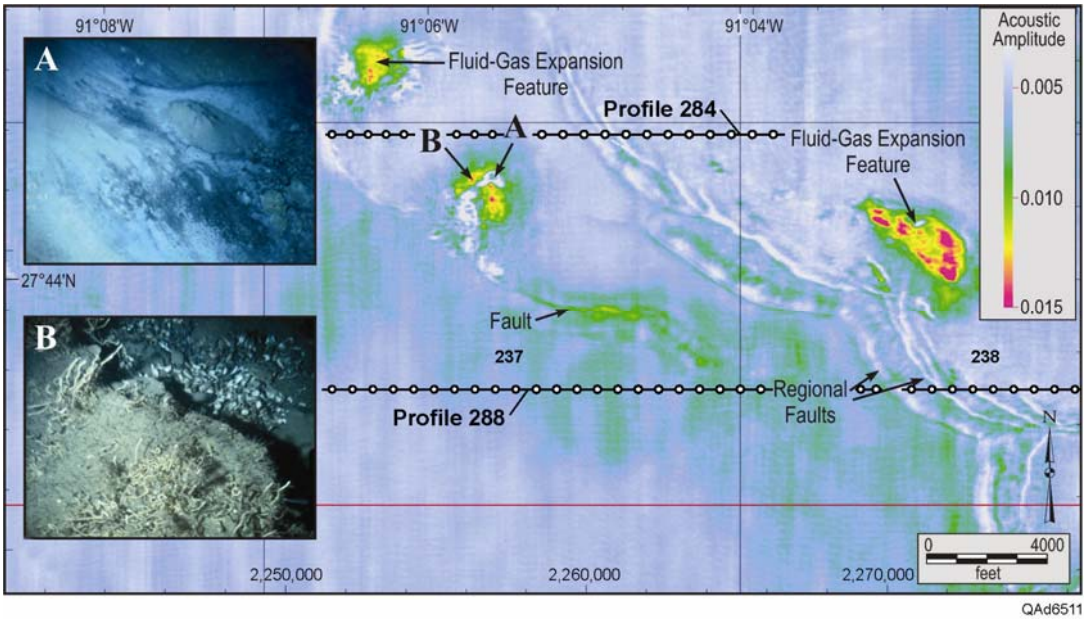

(b)

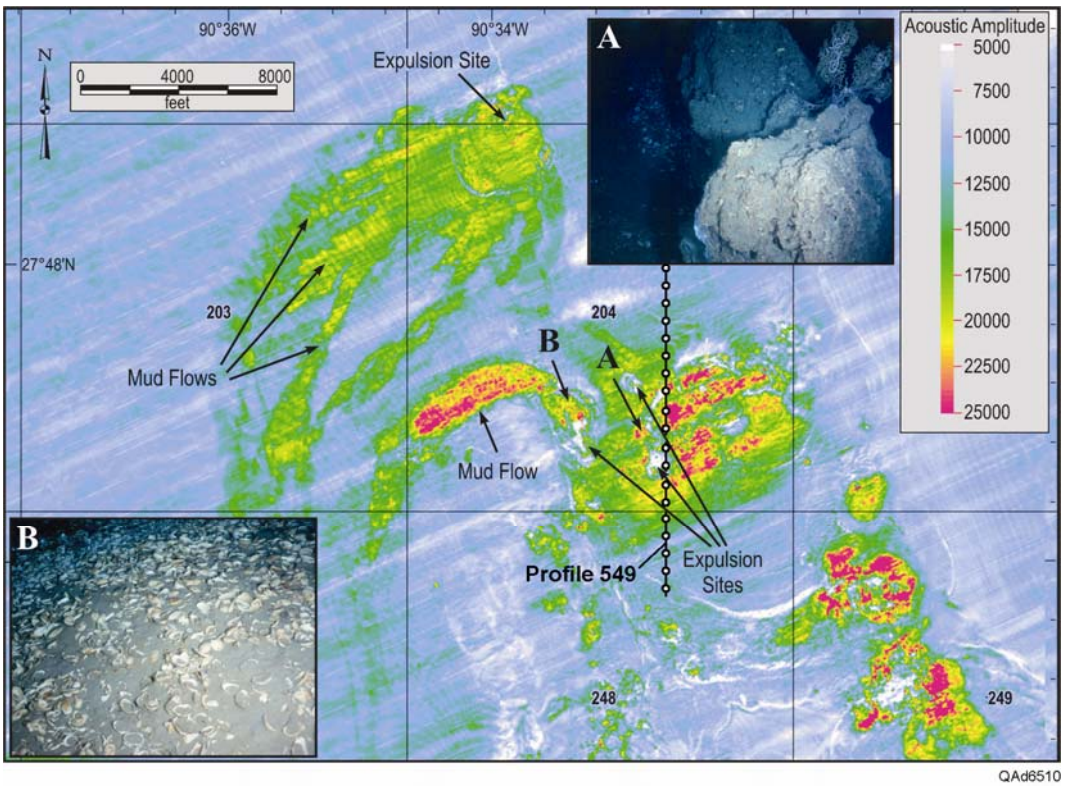

Figure 1.2. Seafloor reflectivity across (a) part of Study Site 1, Typhoon Field, and (b) part of Study Site 2, Genesis Field. The locations of local OBC and AUV profiles are superimposed. Photos **A** and **B** show seafloor biota and hardground at each site. The proliferation of clam and mussel shells and carbonate hardgrounds across each site indicate the presence of methane and sulfate, which are proxies that identify active sub-seafloor hydrate systems. Data and photos courtesy of Harry Roberts, Louisiana State University.

Research Result 1: New Seismic Imaging Concept

We consider the new technology we developed for imaging near-seafloor geology with 4C OBC data to be one of the important research results achieved in this study. This opinion is supported by the fact that our paper that explained the data-processing procedure was named Best Paper in The Leading Edge in 2006 (Backus and others, 2006). The data-processing concept is based on the following calculation steps:

1. Apply operators that cause the hydrophone and geophone elements in each 4C seafloor receiver to have equivalent amplitude and phase spectra.
2. For each receiver station, add hydrophone and vertical geophone responses to create the downgoing P wavefield.
3. At each receiver station, subtract the vertical geophone response from the hydrophone response to create the upgoing P wavefield.
4. At each seafloor receiver, combine the hydrophone data and the horizontal-geophone data to create the upgoing SV wavefield.
5. At each receiver location, divide the upgoing P wavefield by the downgoing P wavefield to produce the P-P reflectivity beneath the seafloor in the vicinity of the receiver position.
6. For each seafloor sensor station, divide the upgoing SV wavefield by the downgoing P wavefield to generate the P-SV sub-seafloor reflectivity in the vicinity of the receiver position.
7. For each receiver coordinate, convert the P-P reflectivity and P-SV reflectivity determined in steps 5 and 6, which are defined in terms of source offset from the seafloor receiver, to functions of depth-point offset from the seafloor receiver in the same manner as an image is produced with a walkaway vertical seismic profile (VSP).

The details of this unique imaging procedure and examples of data produced at each critical data-processing step are provided in Chapter 2.

Research Result 2: High Resolution of P-SV Data

One of the key research findings developed in this study was the documentation that low-frequency (10 – 200 Hz) converted-shear (P-SV) data extracted from 4C OBC seismic data provide amazing resolution (less than 1 meter) of deep-water, near-seafloor geology. We demonstrate the resolution of the P-SV mode here by comparing air-gun-generated P-SV images with high-frequency (1 – 10 kHz) compressional-wave (P-P) images acquired with AUV technology. The unique, seismic data-processing procedures used to create the P-SV image are discussed in Chapter 2. The concept of using autonomous underwater vehicle (AUV) technology to create high-resolution P-P images of the shallowest near-seafloor geology (1 to 40 m below the seafloor) across deep-water hydrate study areas is discussed in Chapter 8 (*Project Database*). In this introductory chapter, we select representative P-P images from the AUV profiles

we utilized (line locations are shown in map view on Figure 8.1) and use these AUV data to illustrate depth-equivalent P-P and P-SV geology extending from 0 to 50 ms of P-P image time below the seafloor. Comparisons of these high-frequency (1 to 10 kHz) AUV P-P images and their corresponding low-frequency (10 to 200 Hz) OBC P-SV images are shown as Figures 1.3 through 1.5.

Four horizons labeled **A**, **B**, **C**, **D** are labeled on the OBC P-SV images (Figs. 1.3c, 1.4c, 1.5c). Their depth-equivalent P-P horizons are labeled on the AUV P-P images (Figs. 1.3d, 1.4d, 1.5d). The shallowest horizon **A** can be seen on only one of the AUV P-P images - the image along OBC profile 276 displayed as Figure 1.5d. Sub-seafloor depths of these shallow horizons were calculated using V_P velocities and vary as tabulated below:

Horizon	Sub-seafloor depth (m)	
	Minimum	Maximum
A	1	2
B	2	7
C	4	14
D	12	24

An important point is that each OBC P-SV image resolves an interface (**A**) that is often within 1 meter of the seafloor; whereas, AUV P-P data along several profiles do not image this horizon. Low-frequency (10-200 Hz) OBC P-SV data thus often resolve some near-seafloor geologic features better than do high-frequency (1-10 kHz) AUV P-P data, which is an important project finding and demonstration. The reason for this superb resolution of OBC P-SV data is that the low values of V_S velocity in the shallowest seafloor strata, coupled with the fundamental equation,

$$(1.1) \quad \lambda_{SV} = V_S/f,$$

that links wavelength (λ), velocity (V), and frequency (f), causes most of the SV wavelengths ($\boldsymbol{\lambda_{SV}}$) to be less than 1 meter. A second equation of importance is,

$$(1.2) \quad V_P/V_S = 2(\Delta T_{PS}/\Delta T_{PP}) - 1,$$

which relates the V_P/V_S velocity ratio across a sub-seafloor layer to the P-SV time thickness (ΔT_{PS}) and P-P time thickness (ΔT_{PP}) measured across that layer. Applying this equation to the depth-equivalent horizons exhibited on Figures 1.3 through 1.5 shows that the V_P/V_S ratios for the shallowest interpretations of near-seafloor layering are,

Interval	V_P/V_S
Seafloor to B	45 to 48
Seafloor to C	38 to 40
C to D	18 to 20

Because the V_P velocity from the seafloor to horizon D varies from 1430 to 1550 m/s, these velocity ratios result in V_S values that range from 30 to 75 m/s across the sub-seafloor interval extending to depth D, 12 to 24 m below the seafloor.

The image comparisons illustrated on Figures 1.3 through 1.5 are typical of the AUV P-P and OBC P-SV image registrations along all of the AUV profiles that were studied in this project. Except for small areas local to some expulsion features, depth-equivalent P-P and P-SV horizons that were interpreted for the AUV P-P and OBC P-SV profiles established the following principles of deep-water, near-seafloor geology across our Green Canyon project area:

- The base of the hemipelagic layer is the horizon labeled **C**. The thickness of this layer ranges from 6 to 20 ms of P-P image time along the AUV profiles that were available for analysis, which positions the base of the interval at sub-seafloor depths of 4 to 14 m across the project area.
- In P-SV image space, the base of the hemipelagic layer is commonly between 200 and 220 ms.
- A P-P image time of 30 ms, which is close to the deepest good-quality reflection seen on most AUV profiles, is depth equivalent to a P-SV image time that is in the range of 400 ms [±50 ms].

These principles apply to AUV data and OBC data acquired at Typhoon Field (Figs. 8.1a, 1.3, 1.4) and at Genesis Field (Figs. 8.1b, 1.5). Because the distance between these two fields is 60 km, these observations span a large area of Green Canyon.

(a)

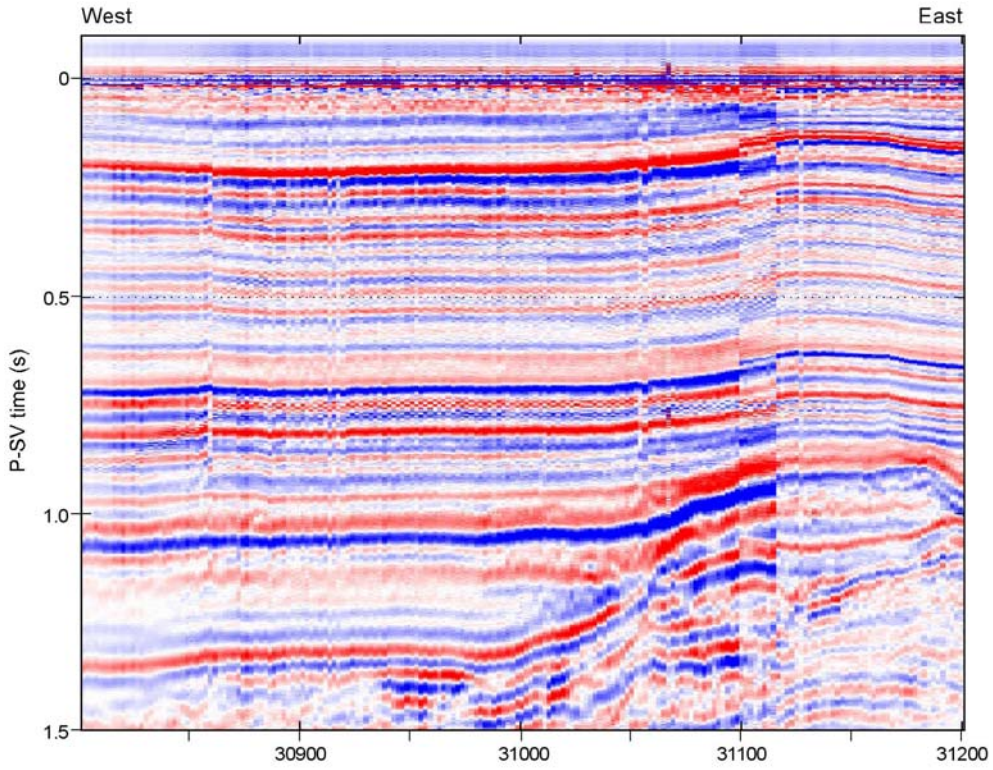

(b)

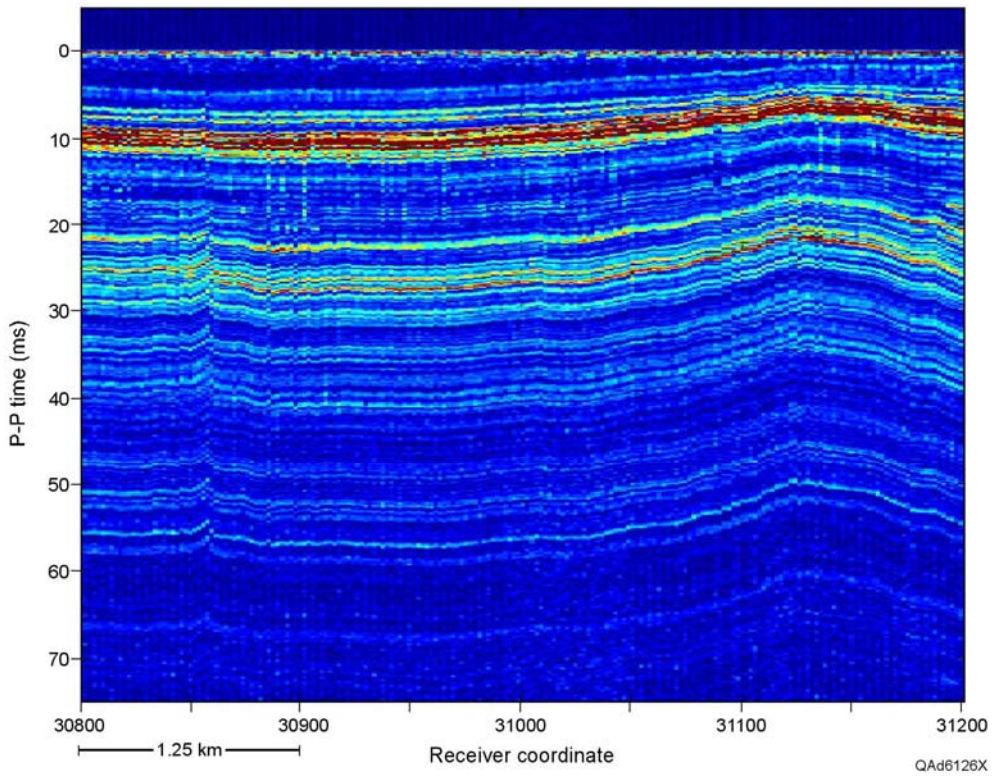

Figure 1.3. Comparison of OBC P-SV image (a) and AUV P-P image (b) along OBC profile 288, Typhoon Field area. These images extend across Block GC237. Refer to Figure 1.2a for the location of profile 288 and Block GC237. Interpreted images follow as (c) and (d) with depth-equivalent horizons labeled. All images are shown relative to a flattened seafloor.

(c)

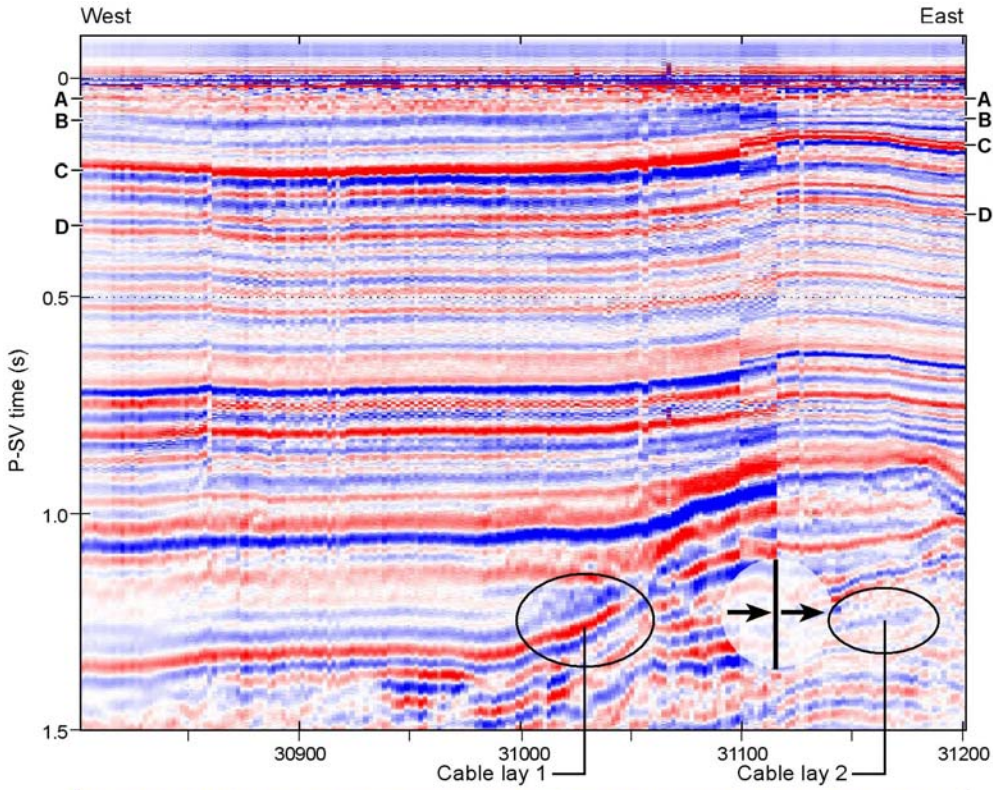

(d)

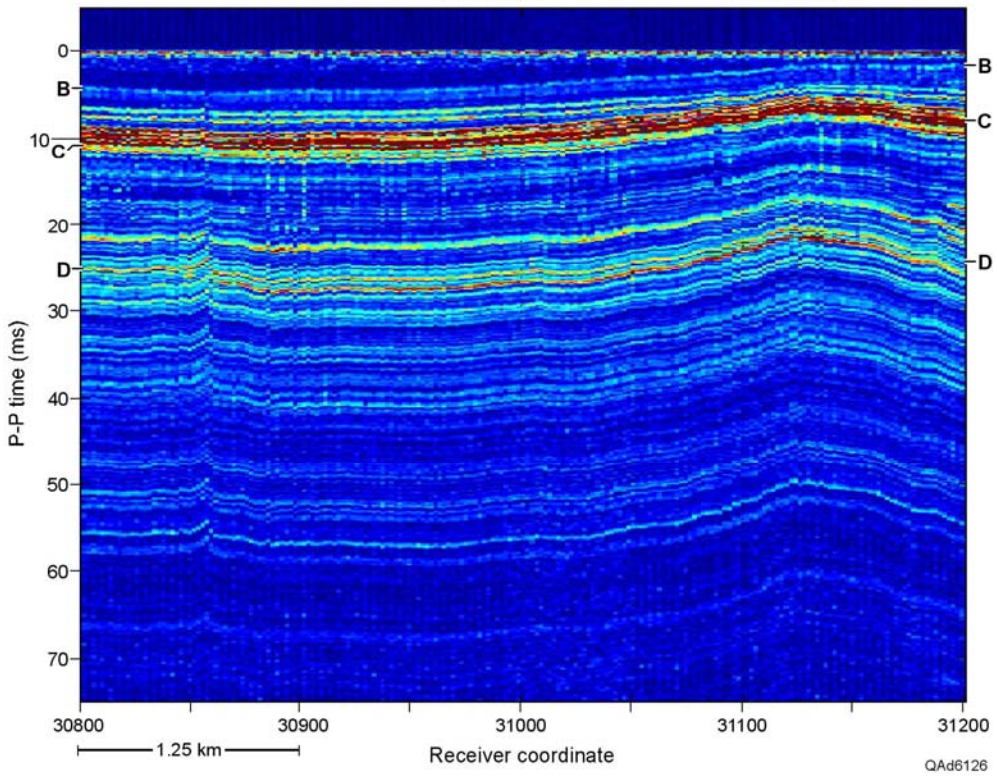

Figure 1.3, cont'd. (c) Interpreted OBC P-SV image. (d) Interpreted AUV P-P image. Depth-equivalent P-SV and P-P reflections are labeled **A** to **D**. Unit **A** is not imaged by the AUV data.

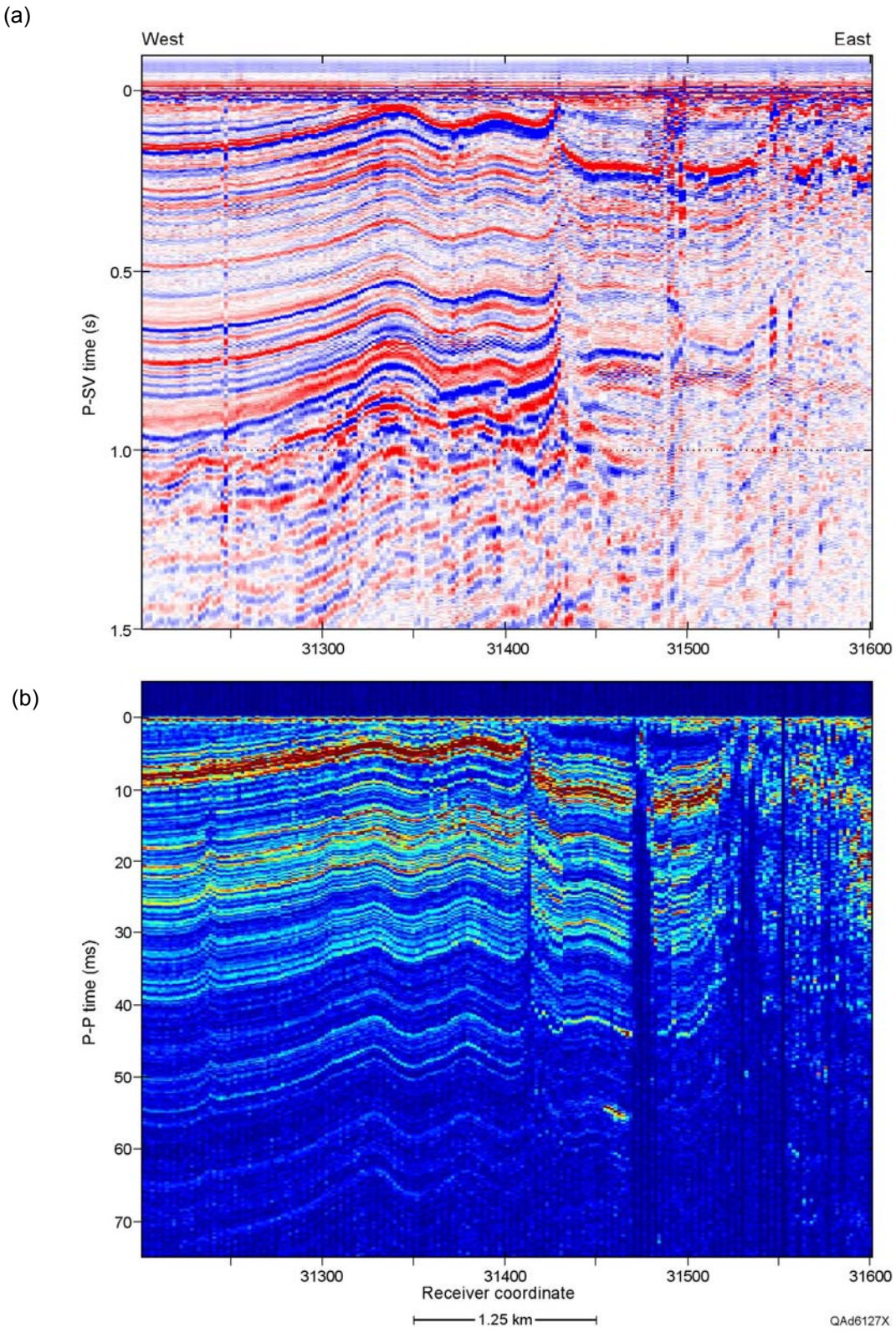

Figure 1.4. Comparison of OBC P-SV image (a) and AUV P-P image (b) along OBC profile 288, Typhoon Field area. These images extend across Block GC238. Refer to Figure 1.2a for the location of profile 288 and Block GC238. Interpreted images follow as (c) and (d) with depth-equivalent horizons labeled. All images are shown relative to a flattened seafloor.

(c)

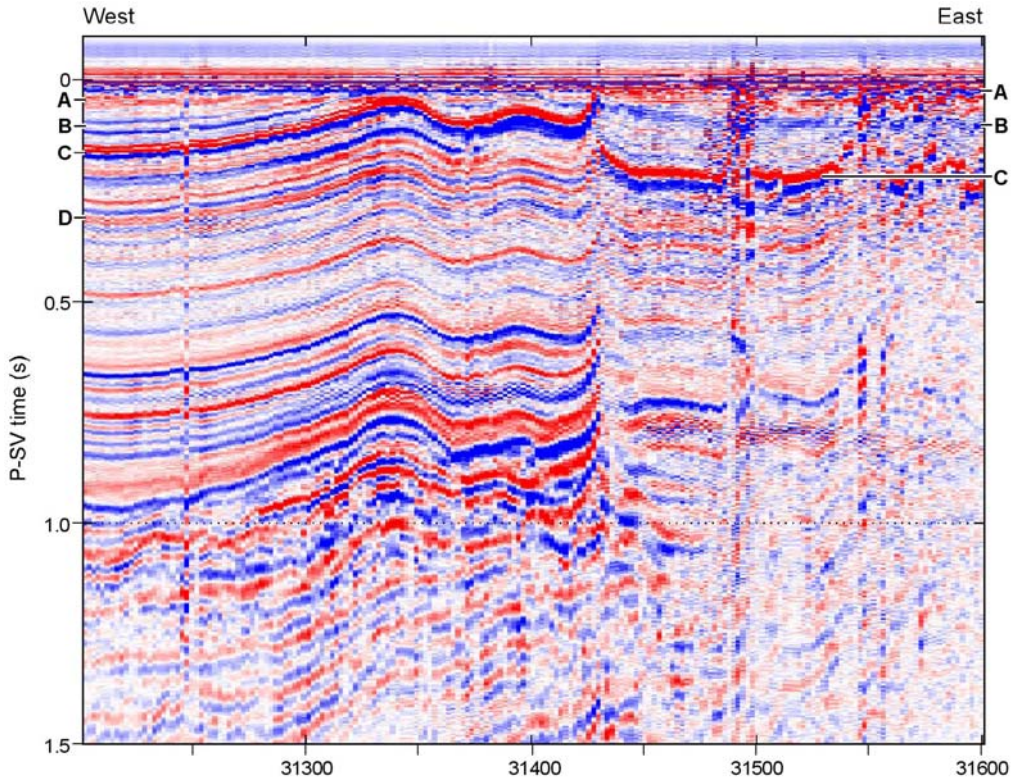

(d)

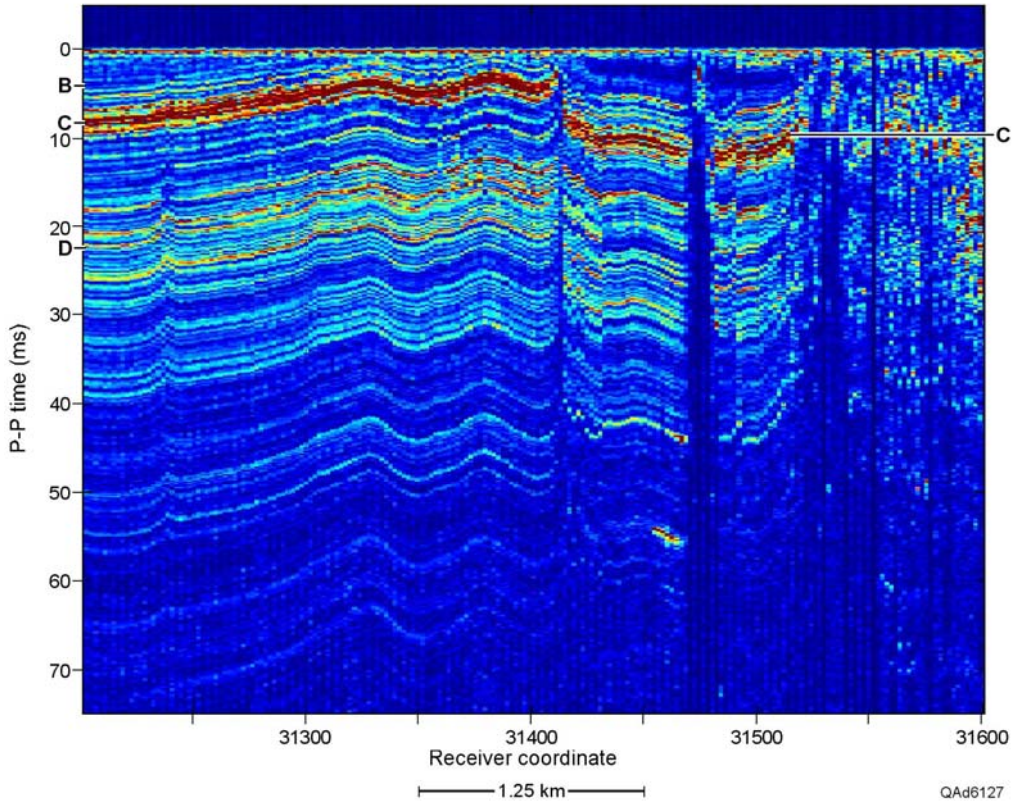

Figure 1.4, cont'd. (c) Interpreted OBC P-SV image. (d) Interpreted AUV P-P image. Depth-equivalent P-SV and P-P reflections are labeled **A** to **D**. Unit **A** is not imaged by the AUV data.

(a)

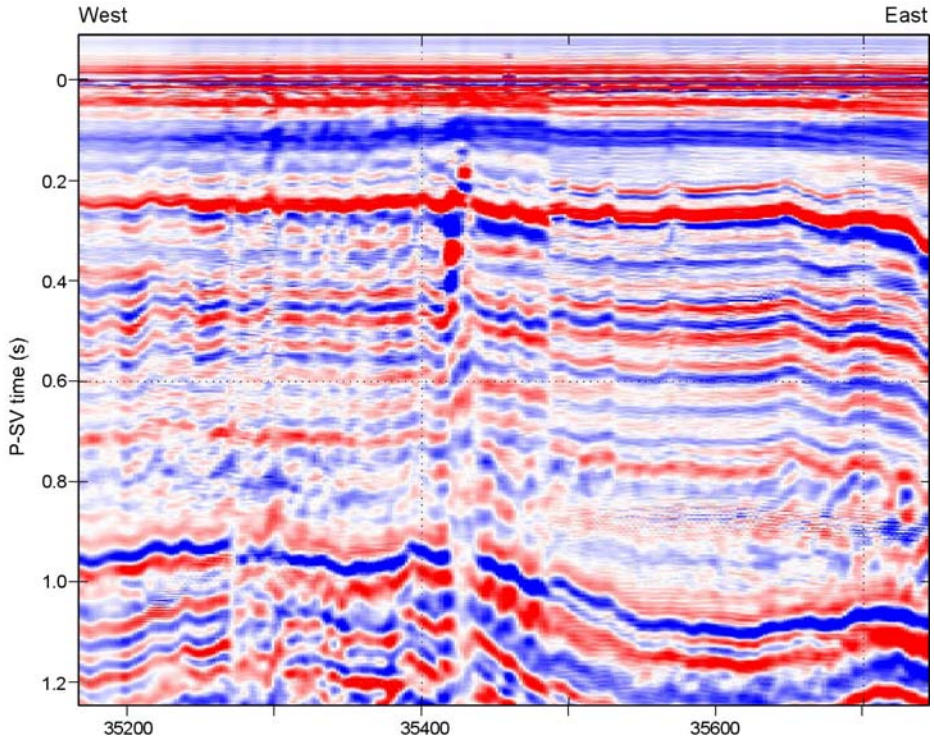

(b)

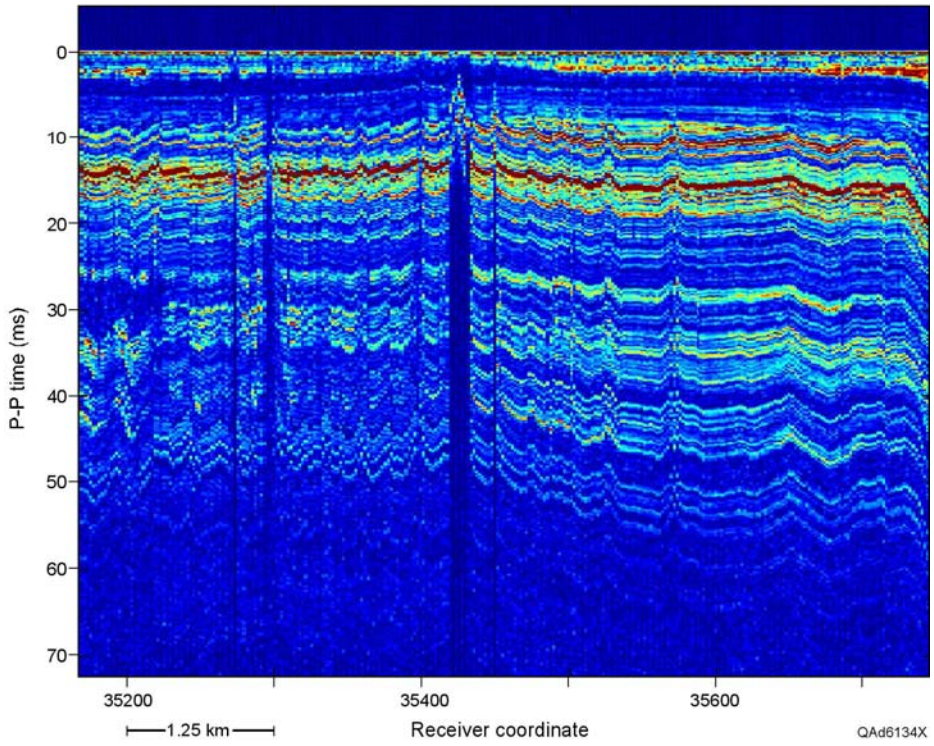

Figure 1.5. Comparison of OBC P-SV image (a) and AUV P-P image (b) along OBC profile 276, Genesis Field area. These images extend across portions of Blocks GC160 and GC161. Refer to Figure 8.1b for the location of profile 276 and Blocks GC160 and GC161. Interpreted images are shown as (c) and (d) with depth-equivalent horizons labeled. All images are shown relative to a flattened seafloor.

(c)

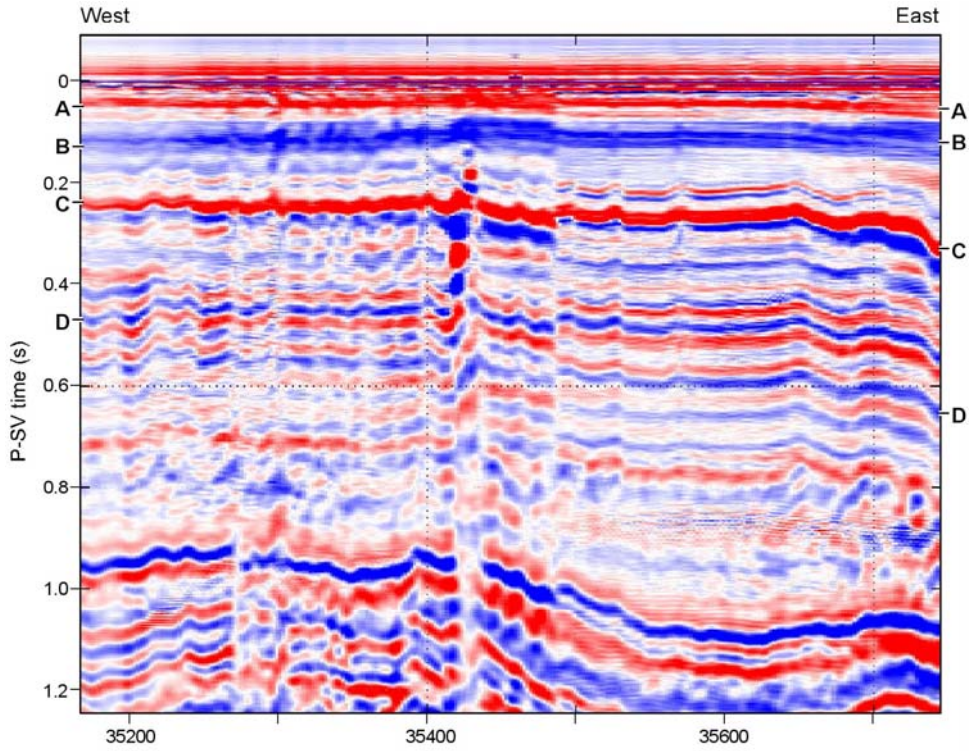

(d)

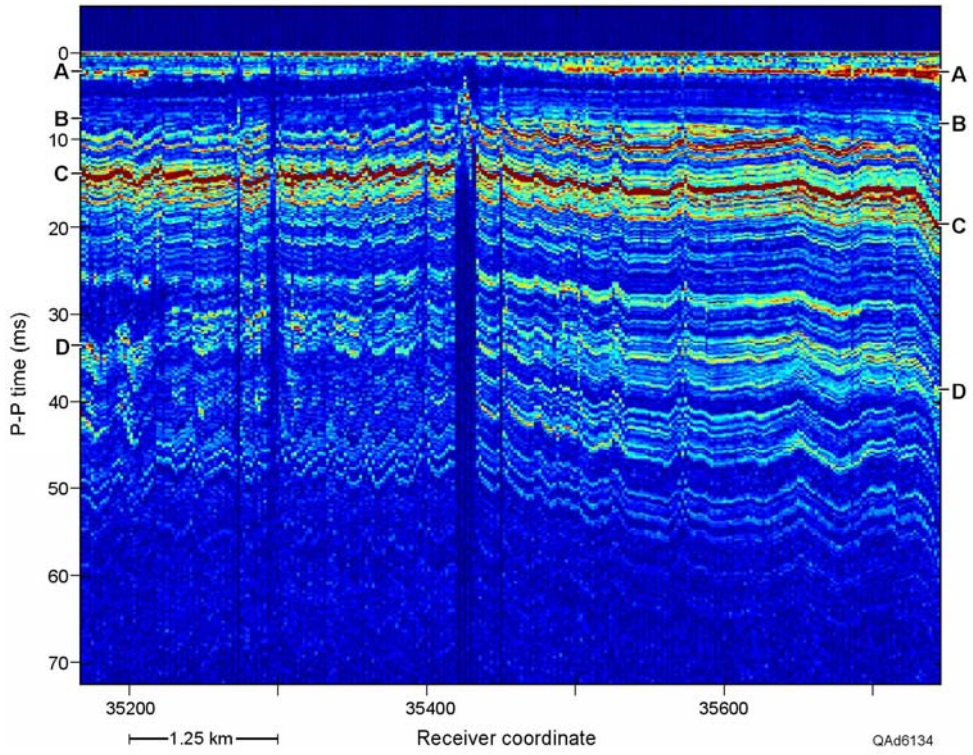

Figure 1.5, cont'd. (c) Interpreted OBC P-SV image. (d) Interpreted AUV P-P image. Depth-equivalent P-SV and P-P reflections are labeled **A** to **D**.

Examples of Interpreted OBC P-P and P-SV Images

In this section we illustrate our interpretations of representative OBC P-P and P-SV images across the project area. The data-processing procedures used to make these images are described in Chapter 2 (*Processing 4C OBC Seismic Data to Image Deep-Water, Near-Seafloor Geology*). The horizons produced in our interpretations define depth-equivalent sub-seafloor layers that are then used in raytrace analyses to create depth-layered values of interval-velocity estimates of V_P and V_S (Chapter 7. *Raytracing and Velocity Analysis*). Two OBC profiles, one across Typhoon Field and one across Genesis Field are included as Figures 1.6 and 1.7 to illustrate depth-equivalent geology in P-P image space and P-SV image space. The P-P and P-SV images along these profiles are shown in both interpreted and uninterpreted formats.

We use OBC profile 288 (Fig. 1.6) at Typhoon Field to illustrate our interpretation of P-P and P-SV images to sub-seafloor depths of approximately 500 m. Shallow horizons **B** through **D** marked on the P-SV image (Fig. 1.6c) are depth equivalent to P-P horizons **B** to **D** labeled on the high-frequency AUV P-P images in Figures 1.3 and 1.4. These shallow horizons are difficult to define on the low-frequency OBC P-P image at the display scale used in Figure 1.6d. In expanded-image views, it is more obvious that the low-frequency OBC P-P data succeed in imaging rather shallow sub-seafloor geology. This image comparison shows that when OBC hydrophone data and vertical-geophone data are adjusted to have equivalent amplitude and phase spectra, the resulting downgoing and upgoing P wavefields that are calculated by adding and subtracting the hydrophone and geophone data (Equations 2.4 and 2.5, Chapter 2) lead to surprising resolution of near-seafloor strata with OBC P-P data (Eq. 2.6). The methodology used to calibrate hydrophone and geophone data that results in this resolution is explained and illustrated in Chapter 2. Deeper horizons **E** to **K** labeled on the P-SV image (Fig. 1.6c) are interpreted to be depth equivalent to P-P horizons **E** to **K** labeled on Figure 1.6d.

OBC profile 264 displayed as Figure 1.7 is used to illustrate depth-equivalent geology in P-P and P-SV image spaces in the area of Genesis Field. This profile is important because it traverses two calibration wells (Well B and Well C) shown on the Genesis Field database map provided as Figure 8.1b. Log data acquired in these wells span part of the hydrate stability zone at each well location. The resistivity-log measurements across these hydrate-stability intervals are key calibration data used in our joint-inversion technique that estimates hydrate concentration by combining resistivity responses with seismic-based velocities.

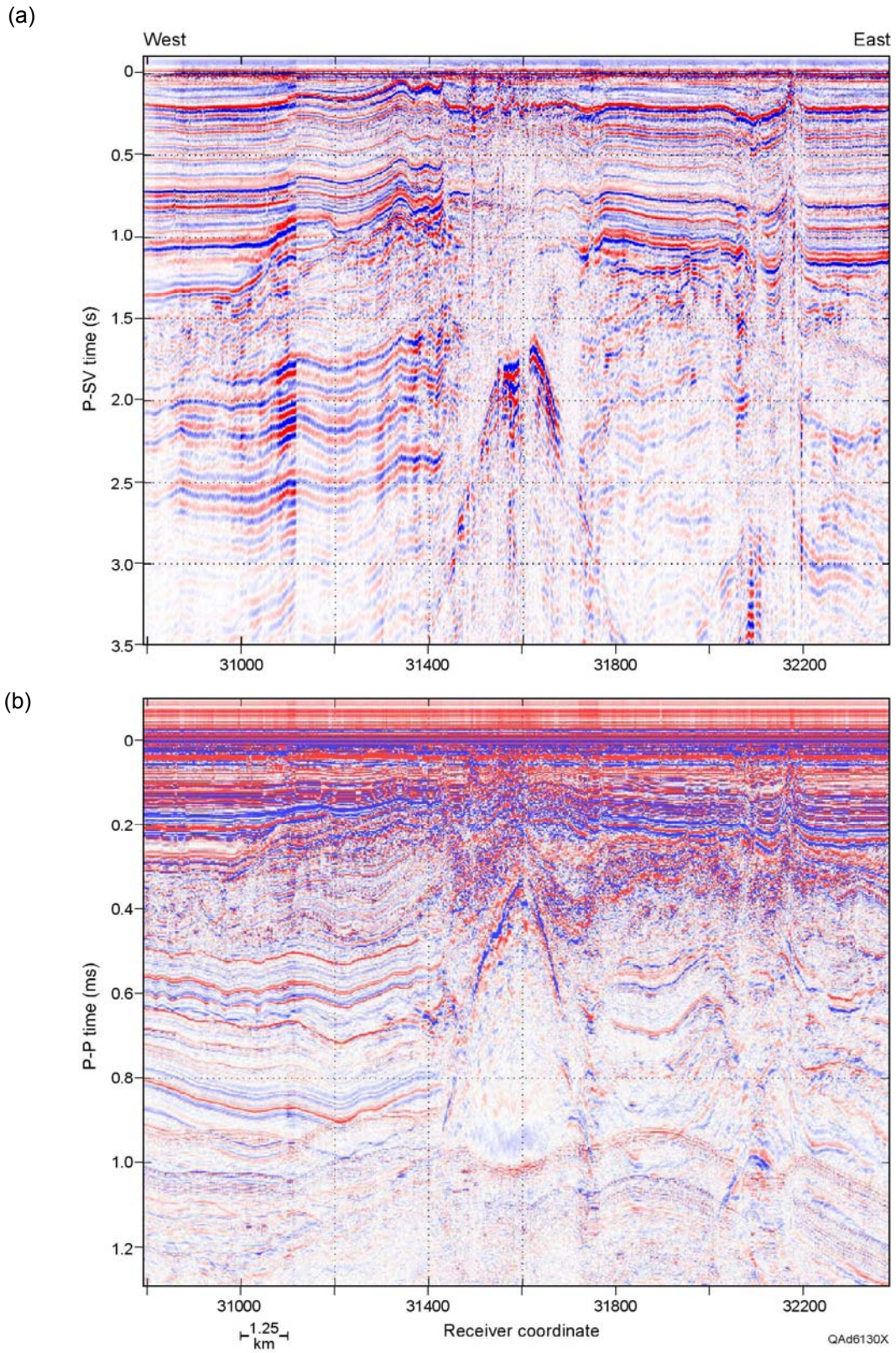

Figure 1.6. Uninterpreted P-SV image (a) and P-P image (b) along OBC profile 288 that crosses the area of Typhoon Field.

(c)

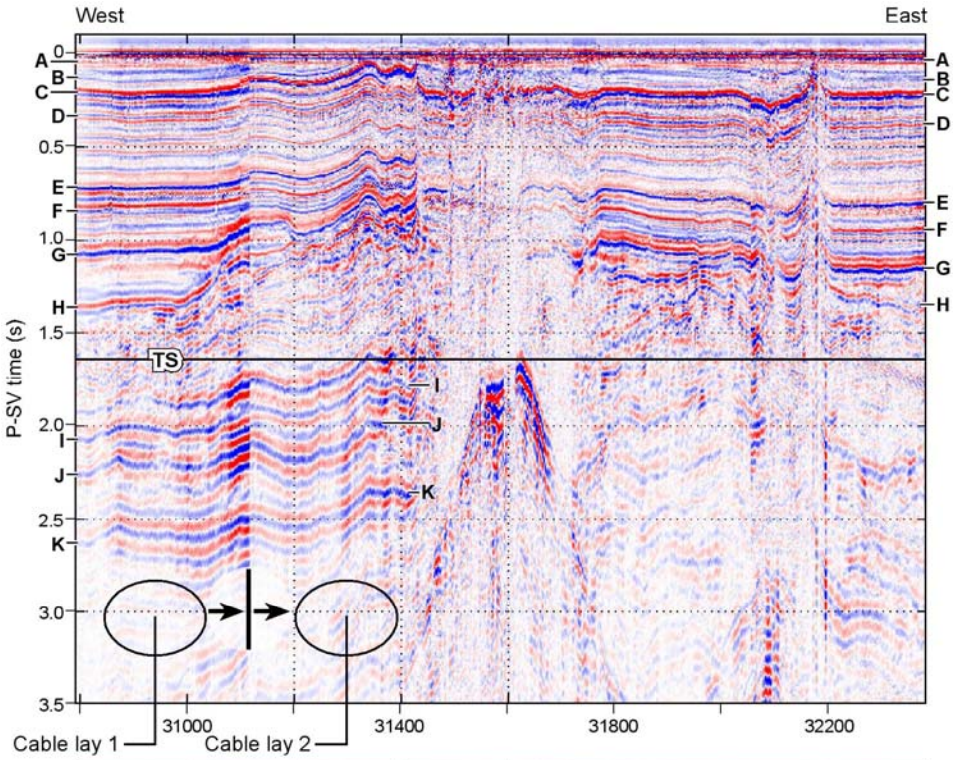

(d)

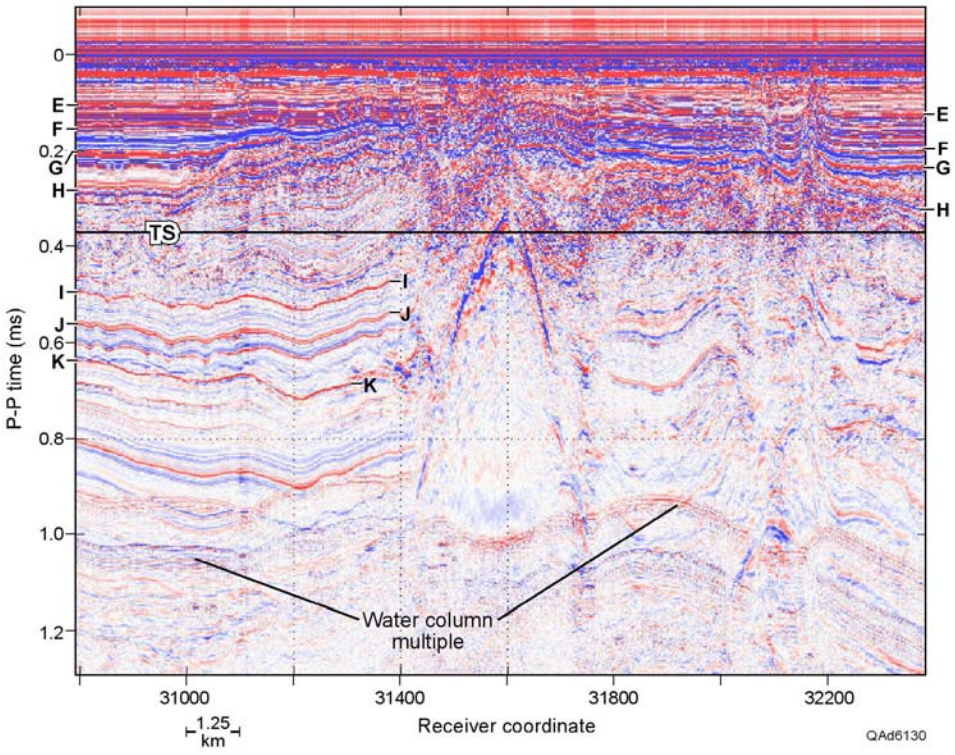

Figure 1.6, cont'd. Interpreted P-SV image (c) and P-P image (d) along OBC profile 288, Typhoon Field area. Depth-equivalent P-P and P-SV reflections are labeled **E** through **K**. P-SV events **A** through **D** are identified on Figures 1.3 and 1.4. Time slice **TS** marks depth-equivalent structure.

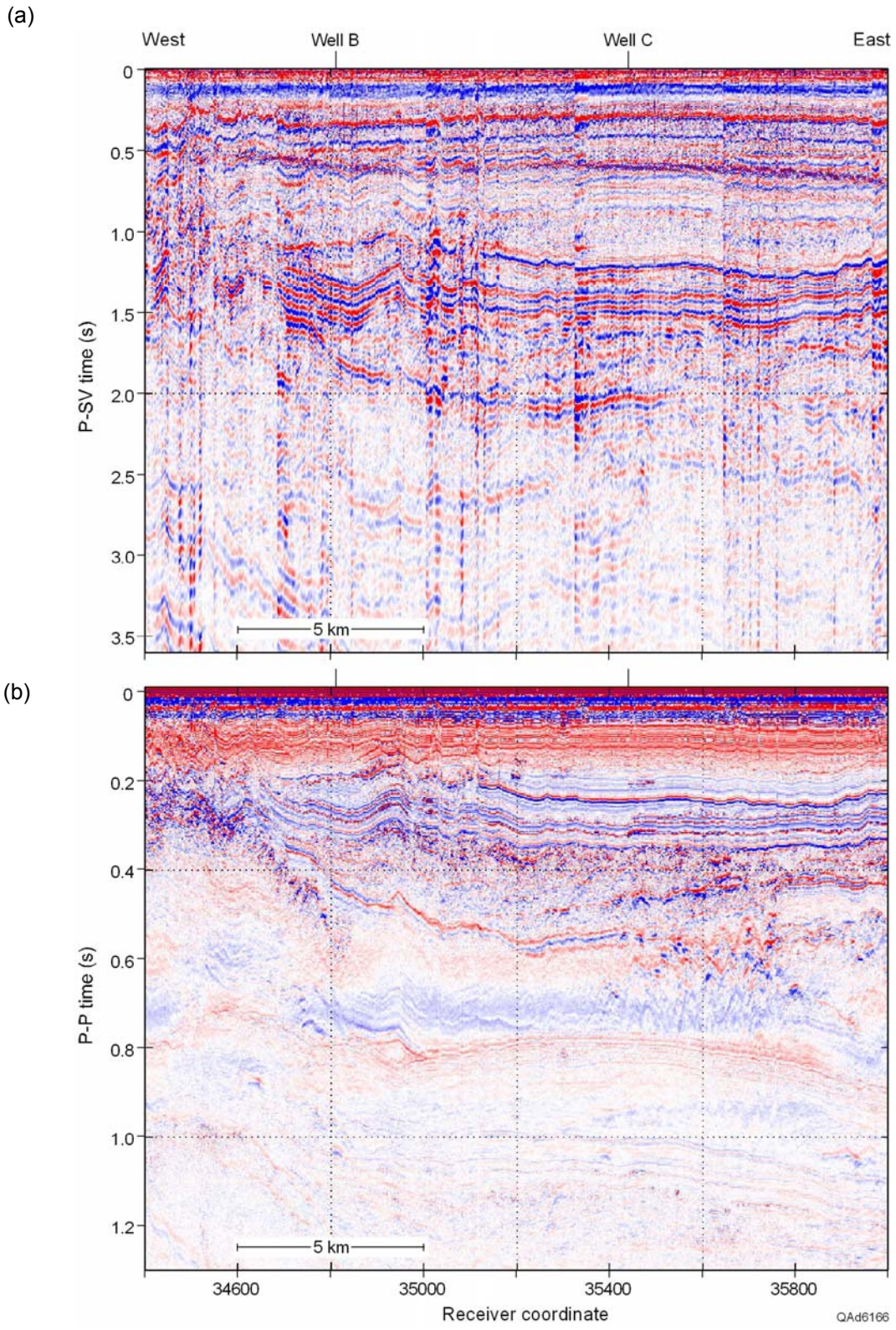

Figure 1.7. Uninterpreted P-SV image (a) and P-P image (b) along OBC profile 264, Genesis Field area.

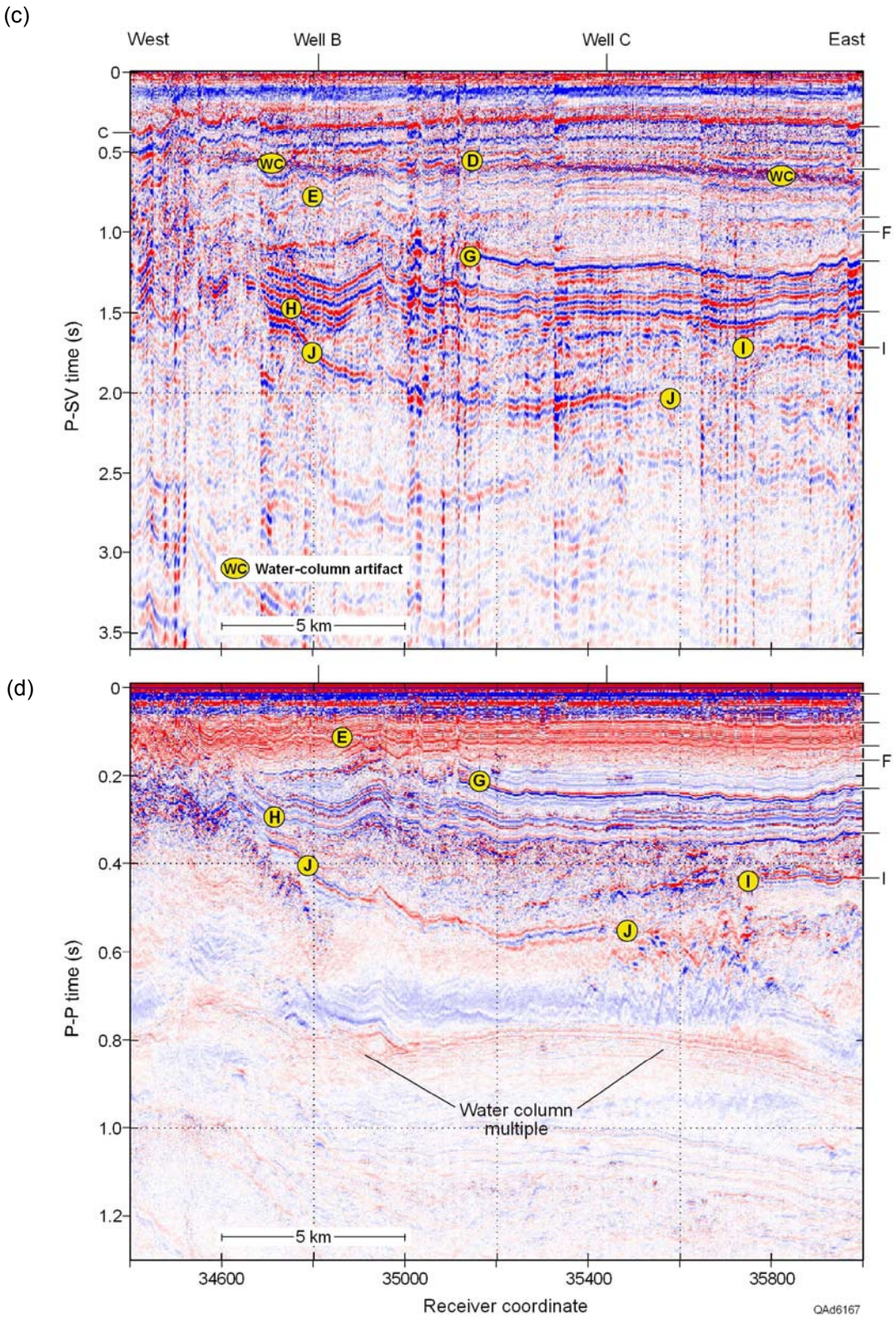

Figure 1.7, cont'd. Interpreted P-SV image (c) and P-P image (d) along OBC profile 264, Genesis Field area. Depth-equivalent reflections are labeled **E** to **J**. P-SV events **C** and **D** are depth equivalent to AUV P-P events **C** and **D** in Figures 1.3 and 1.4.

Research Result 3: Raytracing to Determine Layer Velocities

The objective of our interpretations of P-P and P-SV images along each OBC profile was to define which sub-seafloor P-SV reflection events occurring between the seafloor and the **base of the hydrate stability zone** (**BHSZ**) were depth-equivalent to selected P-P reflections existing across this same sub-seafloor depth interval. The depth-equivalent P-P and P-SV horizons shown on Figures 1.6 and 1.7 were determined by interpretation logic, not by mathematical rigor. We consider interpreted horizons such as those exhibited in these figures to be "tentatively" depth-equivalent. To create seismic interval velocities across sub-seafloor layers that have accuracies sufficient to make reliable estimates of hydrate concentration within these layers, interpreted horizons need to be subjected to a rigorous numerical analysis to determine if each pair of "tentative" depth-equivalent P-P and P-SV reflections is truly depth-equivalent, or whether alternate events need to be selected to establish depth equivalency. A major part of our study was the development and use of a raytracing procedure that:

1. Created a system of sub-seafloor layers with defined thicknesses and with specified V_P and V_S velocities,
2. Calculated traveltimes along P-P and P-SV reflected raypaths through this velocity layering from a large number of sea-level source stations to a defined seafloor receiver station,
3. Compared these calculated raytrace reflection times to actual times of the P-P and P-SV reflections that were interpreted to be depth equivalent at that receiver station, and
4. Adjusted layer thicknesses and V_P and V_S velocities until raytrace times and actual times for each layer interface converged to acceptable agreement.

This Earth-layer construction process was done at selected seafloor receiver stations distributed across the OBC grid of 2D profiles to build a continuous velocity layering along each line of profile. Velocity Layer 1 started at the seafloor and extended to the shallowest interpretable P-P reflection. Velocity Layers 2, 3, and 4 extended to successively deeper seafloor depths until a Velocity Layer N was created that extended deeper than the BHSZ boundary. A detailed explanation of this critical data-analysis procedure is provided as Chapter 7 (*Raytracing and Velocity Analysis*).

Velocity Analysis at Calibration Wells

We will use data at calibration wells B and C on OBC profile 264 that traverses the Genesis Field area to illustrate our joint-inversion technique for estimating hydrate concentration. Positions of these wells are defined on Figure 1.7.

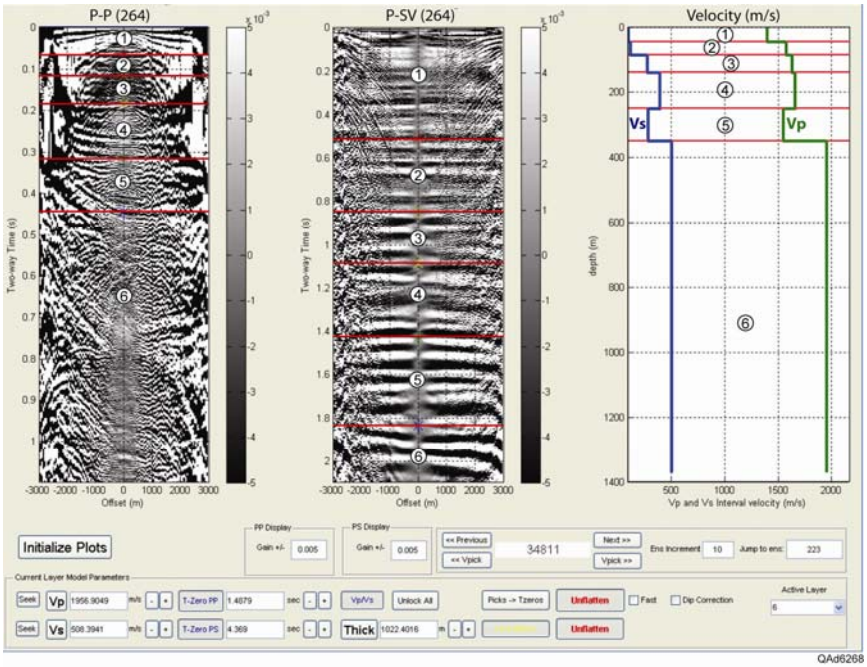

Figure 1.8. Raytrace-based velocity analysis at calibration Well B, OBC profile 264, Genesis Field area. (Right) 6-layer V_P and V_S model at receiver station 34811, the well location. (Center) OBC P-SV receiver gather shows “flatness” of P-SV reflections associated with layer interface horizons when time shifts determined by raytracing are applied to all offset traces. (Left) OBC P-P receiver gather showing reflections associated with interface horizons after raytraced time shifts are applied.

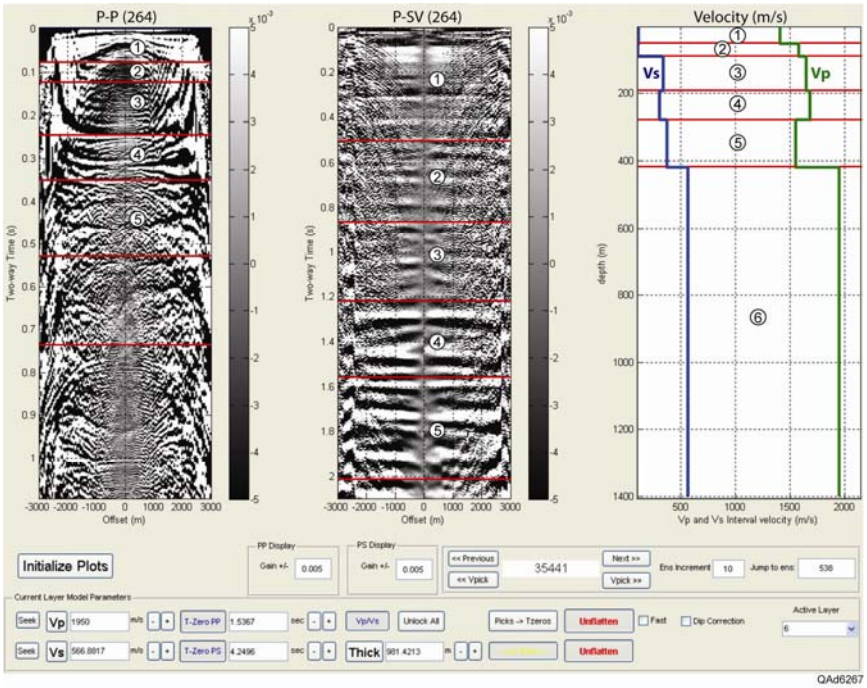

Figure 1.9. Raytrace-based velocity analysis at calibration Well C, OBC profile 264, Genesis Field area. (Right) 6-layer V_P and V_S model at receiver station 35411, the well location. (Center) OBC P-SV receiver gather shows “flatness” of P-SV reflections associated with layer interface horizons when time shifts determined by raytracing are applied to all offset traces. (Left) OBC P-P receiver gather showing reflections associated with interface horizons after raytraced time shifts are applied.

Our raytrace velocity analyses at these two well locations are displayed as Figures 1.8 and 1.9. A 6-layer velocity model spanning the hydrate stability zone was constructed at Well B (Fig. 1.8) and then at Well C (Fig. 1.9).

The horizons positioned atop the P-P and P-SV trace gather displays in Figures 1.8 and 1.9 represent depth-equivalent P-P and P-SV reflection events generated at the base of each interpreted velocity layer. Our raytrace model is based on the assumption that the sub-seafloor layering is flat and horizontal. This assumption is reasonably true at Well C (refer to the P-P and P-SV images in Figure 1.7), thus each reflection event associated with the six interpreted horizons overprinted on the wiggle-trace data is reasonably flat out to significant source-offset distances when each data trace is time shifted by an amount determined by raytracing with the layer model (Fig. 1.9). This “reflection flatness” indicates the velocity-layer model is an appropriate description of the sub-seafloor geology at the receiver station located at the position of Well C.

The assumption of flat, horizontal sub-seafloor layering does not apply to all layer interfaces at Well B. For example, the images in Figure 1.7 show that the deeper strata of the hydrate stability zone, particularly horizon **J**, have considerable dip at the location of Well B. As a result, the reflection from the base of dipping Layer 4 (Fig. 1.8) is a horizontal “S-shaped” event with the raytrace horizon passing through the symmetry point of the horizontal “S”. This intersection of the model horizon with the symmetry point of this S-shaped reflection event confirms that the velocity model is correct down to the depth of this interface when reflector dip is present. This concept is discussed in detail in Chapter 7 (Fig. 7.12).

A principal advantage of this raytrace-based velocity-analysis strategy is that velocity layers are defined as a function of depth below the seafloor. As a result, seismic-based V_P and V_S velocities can be depth correlated with depth-based resistivity logs. These velocity-vs.-resistivity comparisons illustrate one of the challenges of our joint-inversion effort: even though there are calibration wells where there is an extensive portion of the hydrate stability zone over which velocity and resistivity data can be compared (for example Well B, Figure 1.10, next section), at other wells there is only a limited part of the hydrate stability zone over which resistivity and velocity data can be analyzed (Well C, Figure 1.11, next section).

Research Result 4: Integration of Resistivity, Velocity, and Seismic Data

The resistivity and velocity profiles at calibration wells B and C will be used to demonstrate how these Earth properties correlate with P-P and P-SV images and seismic attributes along OBC profile 264. Data comparisons are shown at Well C first because of the geologic implications that result from data interpretations at this well location.

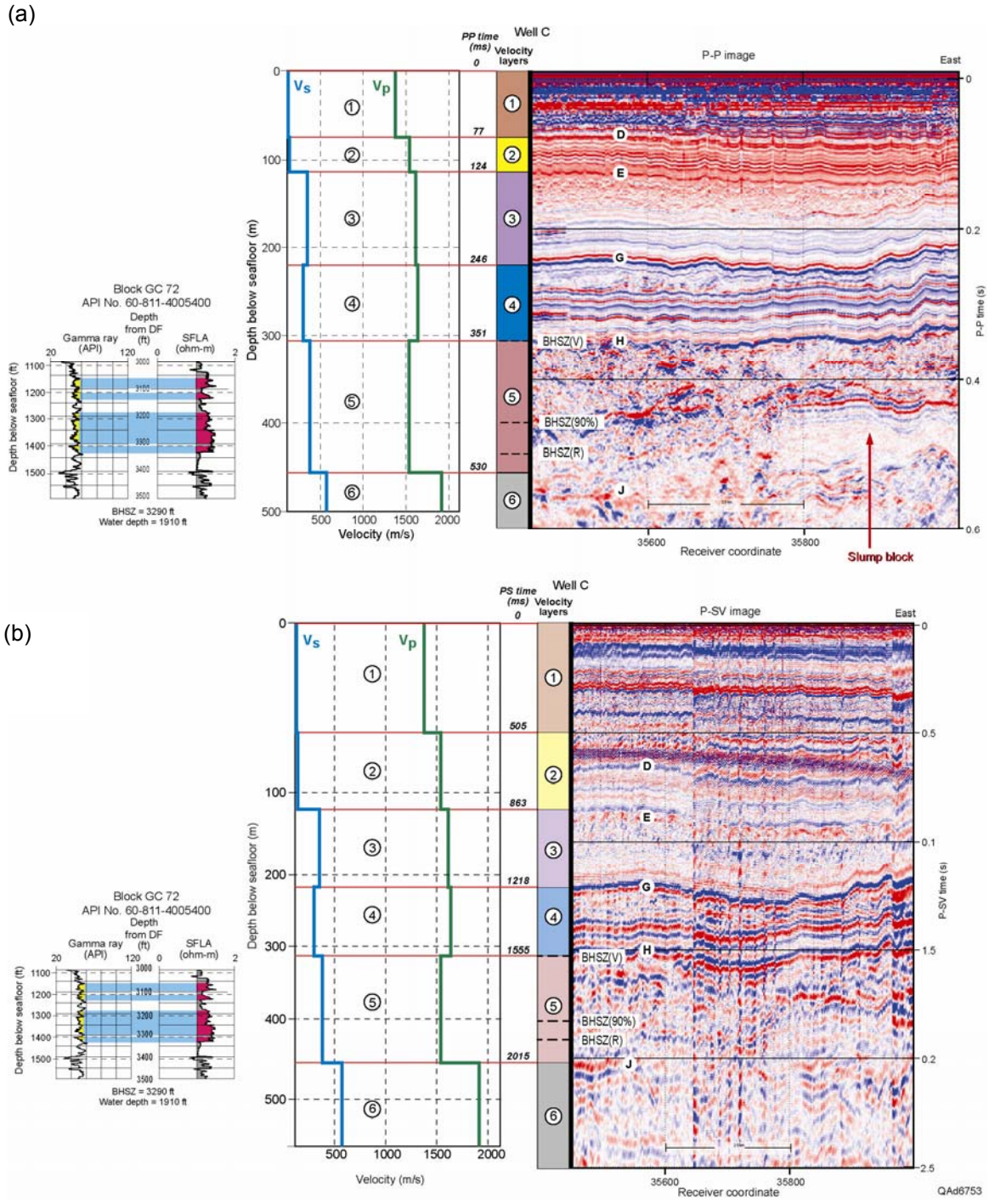

Figure 1.10. Integration of resistivity profile and V_P and V_S velocity analyses at Well C with (a) P-P seismic data along OBC profile 264 (Genesis Field) and (b) P-SV seismic data. Horizon **BHSZ(R)** is the base of the hydrate stability zone interpreted from the resistivity log. Horizon **BHSZ(V)** is the adjusted position of the BHSZ based on V_P velocity behavior.

First, the layer-velocity model built at Well C is adjusted to match the P-P and P-SV image-time axes at the well location, as shown in Figure 1.10. This correlation process allows depth-based data to be compared against time-based seismic

velocities. Inspection of the figure shows that each Earth-velocity layer correlates with a distinct seismic facies unit in both P-P image space and in P-SV image space. The V_P and V_S velocity profiles increase in unison from the seafloor to the base of Layer 3, and then the P and SV velocities change in opposing directions across the lower portion of the hydrate stability zone (Layers 4 and 5).

Three estimates of the base of the hydrate stability zone [labeled **BHSZ(90%)**, **BHSZ(R)**, **BHSZ(V)**] are marked on each seismic profile. These horizons have the following meanings:

- **BHSZ(90%)**: The depth of the base of the hydrate stability zone for a natural gas having 90.4-percent methane as was calculated by Milkov and Sassen (2001) for the hydrate system in Block GC185 and illustrated as depth prediction curves on Figure 4.13.
- **BHSZ(R)**: The depth of a decrease in formation resistivity that is "close to" the depth of horizon BHSZ(90%) and that appears to be a logical choice for the base of the hydrate stability zone when examining resistivity log data acquired in the calibration well.
- **BHSZ(V)**: The depth of a decrease in V_P velocity that is "close to" the depth of horizon BHSZ(90%) and that appears to be a logical choice for the onset of free-gas trapped below the base of stable hydrate, as defined by seismic V_P interval velocities.

It is important to note that the V_P velocity profile at Well C (Fig. 1.10) exhibits an increasing trend in magnitude through Layer 4 and then undergoes a velocity reversal in Layer 5. It is also important to note that horizons BHSZ(90%) and BHSZ(R) at the base of Layer 5 are transferred directly from the interpretation of the resistivity logs displayed on Figure 4.17 and are not interpreted from the V_P and V_S velocity behavior or from any seismic attribute.

The resistivity log from Well C is included in the correlation of the P-P and P-SV images on Figure 1.10. All of the resistivity data associated with the interpreted hydrate stability zone are confined to velocity Layer 5. The position of the BHSZ(R) horizon shown on the figure is "interpreted" as the resistivity break at a depth of 1430 ft below the seafloor. Further detail about the philosophy used to interpret the BHSZ horizon on resistivity logs is given in Chapter 5. A tentative dilemma presented by this data-correlation exercise is that formation resistivity increases in Layer 5, indicating increased hydrate content in that layer; whereas, the P-wave velocity decreases, which indicates decreased (or absent) hydrate content. *We thus have opposing interpretations: resistivity data imply hydrate is present in Layer 5, but velocity data indicate hydrate is absent.*

We now invoke unpublished information provided to our project team that aids in resolving this dilemma. First, a Chevron scientist studying the hydrate system at Genesis Field inspected our Figures 1.10 and 1.11 and stated that Chevron considers the reflection-free P-P facies between 0.4 s and 0.5 s east of receiver coordinate 35800 to be a **slump block**; consequently, we label it as such on the P-P image on this figure. The two distinctive characteristics of slump blocks that are used by Chevron when studying near-seafloor geology across our study area are: (1) P-P reflection-free interval, and (2) straight, vertical sides when the slump is viewed in a cross-section slice. Both characteristics are associated with the labeled

seismic facies on our P-P OBC image along OBC profile 264, assuming the slump moved southward across this east-west profile.

Second, the data correlations on Figure 1.10 were then discussed with a respected consultant who has done numerous seafloor geomechanical analyses across deep-water GOM prospects. He confirmed that the facies labeled “slump block” is a classic depiction of near-seafloor slump features across the GOM, and further added that in his experience, units in which slumping occurs usually have some amount of free gas. The chaotic character of the P-P reflectivity within the unit containing the slump (Layer 5) indicates high levels of bioturbation and associated free gas exist within the unit (Fig. 1.10).

These observations led us to interpret the increased formation resistivity in velocity Layer 5 to be caused by free gas, not by hydrate. This adjusted interpretation of the resistivity log brings the resistivity data and velocity data at calibration well C into agreement because the decrease in V_P velocity in Layer 5 is also consistent with the presence of free gas. From this logic, we readjust the base of hydrate stability at Well C upward to depth BHSZ(V), the base of velocity Layer 4 where the reversal in V_P velocity begins.

The integration of resistivity, velocity, and 4C seismic data at Well B is shown as Figure 1.11, using the information developed at Well C that resistivity-log behavior across velocity Layer 5 is caused by free gas, not by hydrate. Again, depth BHSZ(V), where there is a reversal in the magnitude of the V_P interval velocity, appears to be the proper choice of the base of stable hydrate.

As an added note, from our experience in several multicomponent seismic projects, a basic principle demonstrated by the P-P and P-SV images is that P-SV data often indicate that bedding exists within units where P-P data indicate the geology is chaotic and/or reflection free. This contrasting imaging behavior between P-P and P-SV images occurs throughout Layer 5 exhibited on Figures 1.10 and 1.11 and particularly within the slump-block facies embedded in that layer. We have seen this basic difference between P-P and P-SV data in other marine 4C studies and also in onshore 3C seismic projects.

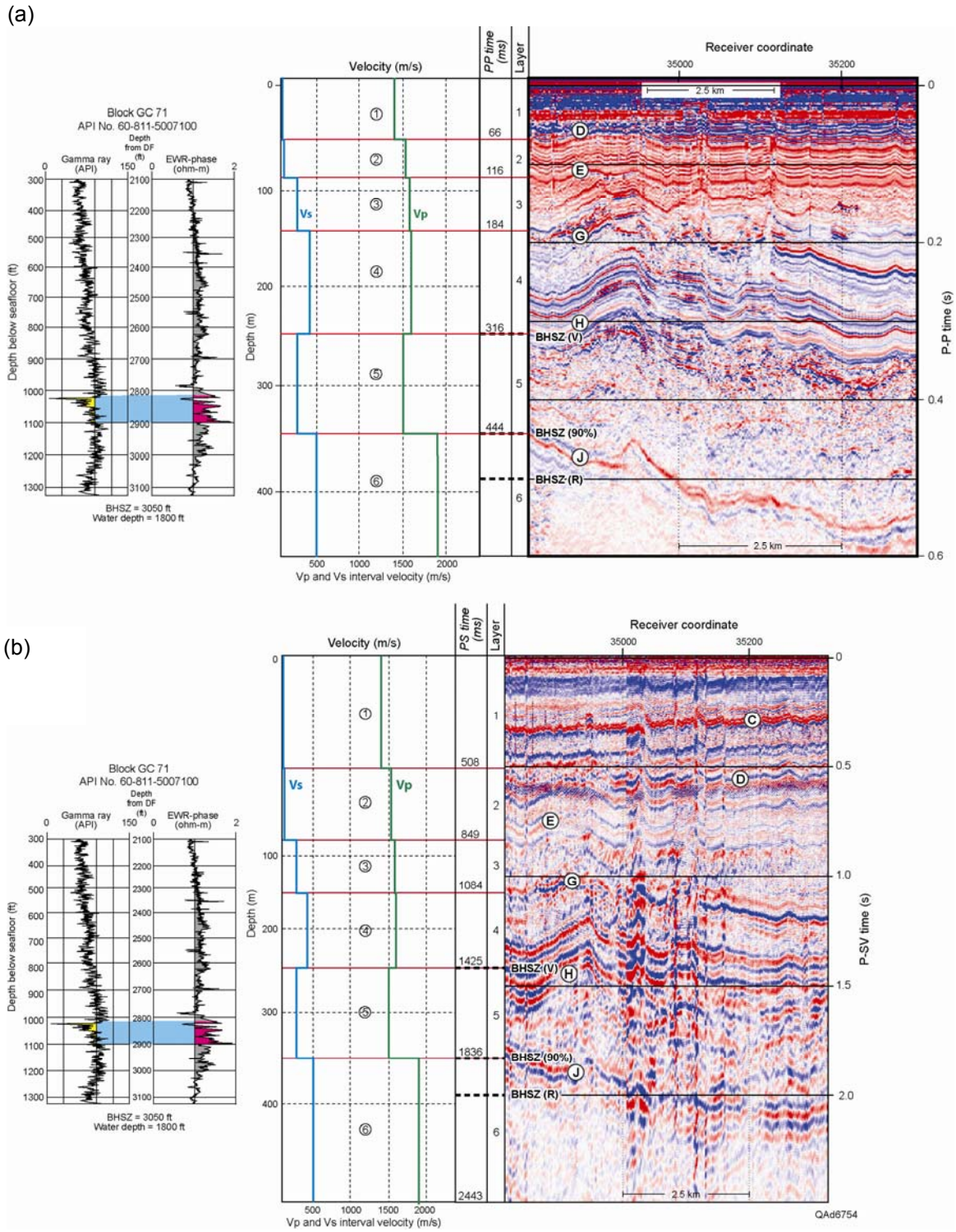

Figure 1.11. Integration of resistivity profile and V_P and V_S velocity analyses at Well B with (a) P-P seismic data along OBC profile 264 (Genesis Field) and (b) P-SV seismic data. Horizon **BHSZ(R)** is the base of the hydrate stability zone interpreted from the resistivity log. Horizon **BHSZ(V)** is the adjusted position of the BHSZ based on V_P velocity behavior.

Research Result 5: Joint Inversion of Resistivity and Velocity

The relation between hydrate concentration and resistivity of strata containing hydrates is non-unique and uncertain, as is any relationship between hydrate concentration and seismic propagation velocity in sediment containing hydrate. By combining different types of hydrate-dependent geophysical information, particularly velocity estimates and formation-resistivity measurements, predictions of hydrate concentration can be constrained, and the uncertainty of predictions can be reduced. To take advantage of this principle, we developed a method for predicting hydrate concentration that is based on stochastic simulations and on a rock-physics theory that relates hydrate concentration to formation resistivity (**R**) and a second theory that relates seismic $\mathbf{V_P}$ and $\mathbf{V_S}$ velocities to hydrate concentration.

To implement a joint-inversion technique, each parameter in our rock-physics elastic modeling and in our formulation of the Archie Equation is expressed as a **probability density function** (**PDF**). The PDFs used in this joint inversion are either Gaussian distributions or uniform distributions. **Gaussian distributions** are used when the expected value for the model parameter is known. The **mean** of the Gaussian function is the **expected value** of the parameter; the **standard deviation** of the function defines the **uncertainty** associated with this expected parameter value. In contrast to a Gaussian distribution, a **uniform distribution** is used when the value of a parameter is not known, but the **range of variability** for the parameter can be defined. A uniform distribution assumes that within the range of variability being considered, any value of the described parameter is **equally probable**.

At each sub-seafloor depth coordinate, we model the joint theoretical relations between **hydrate concentration $\mathbf{c_{gh}}$** (the model parameter we need to calculate) and the resistivity R and seismic propagation velocity (both V_P and V_S) of sub-seafloor strata (which represent the observed parameters). We use a Monte Carlo procedure to draw values for common parameters Φ and V_{cl} from their associated PDFs and then compute the corresponding velocity and resistivity values using Monte Carlo draws from the PDFs for each of the model parameters that are required for calculating hydrate concentration.

In this fashion we obtain many possible realizations of the functions relating hydrate concentration, resistivity, and seismic propagation velocity. This joint relation is non-unique, uncertain, and can be expressed mathematically as a probability density function in three-dimensional (c_{gh}, V_P, R) data space [or in (c_{gh}, V_S, R) data space if preferred]. We emphasize V_P velocities rather than V_S velocities in our inversion because we found that across most of the OBC seismic grid we analyzed, hydrate fills less than 25-percent of the available pore space of the host sediment. For this range of hydrate fraction, there is a quasi-linear relationship between V_P and c_{gh} (Fig. 3.5, Models A and B); whereas, V_S exhibits little sensitivity to changes in c_{gh} when c_{gh} is less than 25-percent (Fig. 3.6, Models A and B).

The joint inversions exhibited on Figures 10.6 through 10.11 established the fundamental calibration points that allowed seismic interval velocities

determined along each OBC seismic profile to be inverted into reliable estimates of hydrate concentration at seismic-profile coordinates that were far removed from any calibration well. In each example, the velocity inversion is simplified by using an average V_P velocity across each velocity-layer interval. As a result, the velocity-dependent hydrate concentration shown on the right panel of these figures is a constant value across each velocity layer. We concluded this simplification was sufficient for a “big picture” view of hydrate concentration.

We must stress that our hydrate estimates involve an inescapable bias that comes into play when we impose a specific hydrate-sediment morphology in order to formulate the inversion algorithms that we used. For example, our resistivity inversion was based on the assumption that hydrate exists in sub-seafloor sediment as a disseminated morphology rather than as a thin-layered morphology (Chapter 4). Thus a disseminated-hydrate bias is ingrained in the selection of parameter values that we use when inverting resistivity log data. Similarly, our velocity inversion assumed that this disseminated hydrate existed as a load-bearing morphology, not as a free-floating morphology or as a thin-layered morphology (Chapter 3). Thus a load-bearing, disseminated-hydrate bias is embedded in our inversion algorithm that relates velocity to hydrate concentration.

Research Result 6: 2D Profiles of Velocity Layering

After performing joint inversions such as those illustrated in Chapter 10 at several calibration wells, we determined an optimal function that could be used to relate hydrate concentration to seismic-based V_P velocity at OBC line coordinates between calibration wells. The input data for this velocity-based hydrate estimation were 2D profiles of V_P layer velocities determined by raytrace analysis of common-receiver gathers (see Figs. 1.12 and 1.13). These raytrace analyses were done at intervals of 10 receiver stations (250 meters) along each OBC profile. Because there were approximately 8,000 receiver stations across the OBC grid we studied, our approach to velocity analysis required that we construct more than 800 models of depth-based layers of V_P and V_S velocities along the approximately 200 km of OBC profiles that we analyzed. This velocity study was laborious and time consuming, but was essential for reliable hydrate estimation. Two examples of the types of 2D velocity layer models that we created are exhibited as Figures 1.12 and 1.13.

We made no attempt to smooth the velocity values displayed on these two figures (or on any of the other velocity profiles) in order to make data displays have a more pleasing cosmetic appearance. If we were constructing a map of hydrate concentration across a small local area, we would probably smooth the velocity data in a gentle fashion. Because this study covers a rather large area, we saw no advantage to smoothing the layer-velocity values. Over an area of the size of our study sites, we believe we produced a large-scale map estimate of hydrate distribution by using unsmoothed velocity data that was similar to the estimate we would have obtained with smoothed velocity data.

Our velocity analyses across the OBC data grid consistently indicated a V_P velocity inversion occurred near the depth of the expected BHSZ boundary. On OBC profiles 549 and 553 (Figs. 1.12 and 1.13), that sequence boundary that marks the BHSZ(V) boundary that is the base of velocity layer 4.

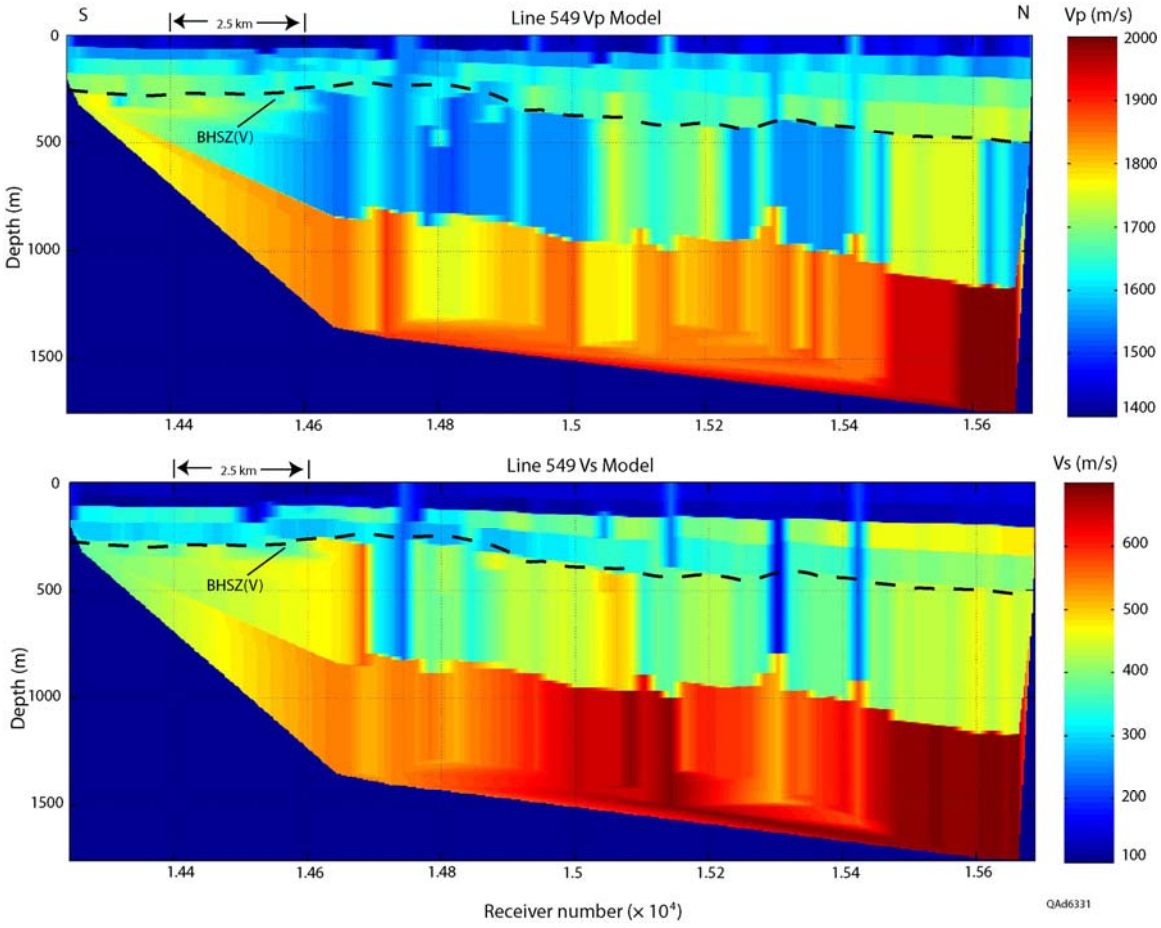

Figure 1.12. 2D layer velocity models along OBC profile 549, Genesis Field. The location of profile 549 is defined on the map shown as Figure 8.1. The BHSZ(V) boundary is the dash line marking the top of the layer where V_P velocity has a reversal in magnitude.

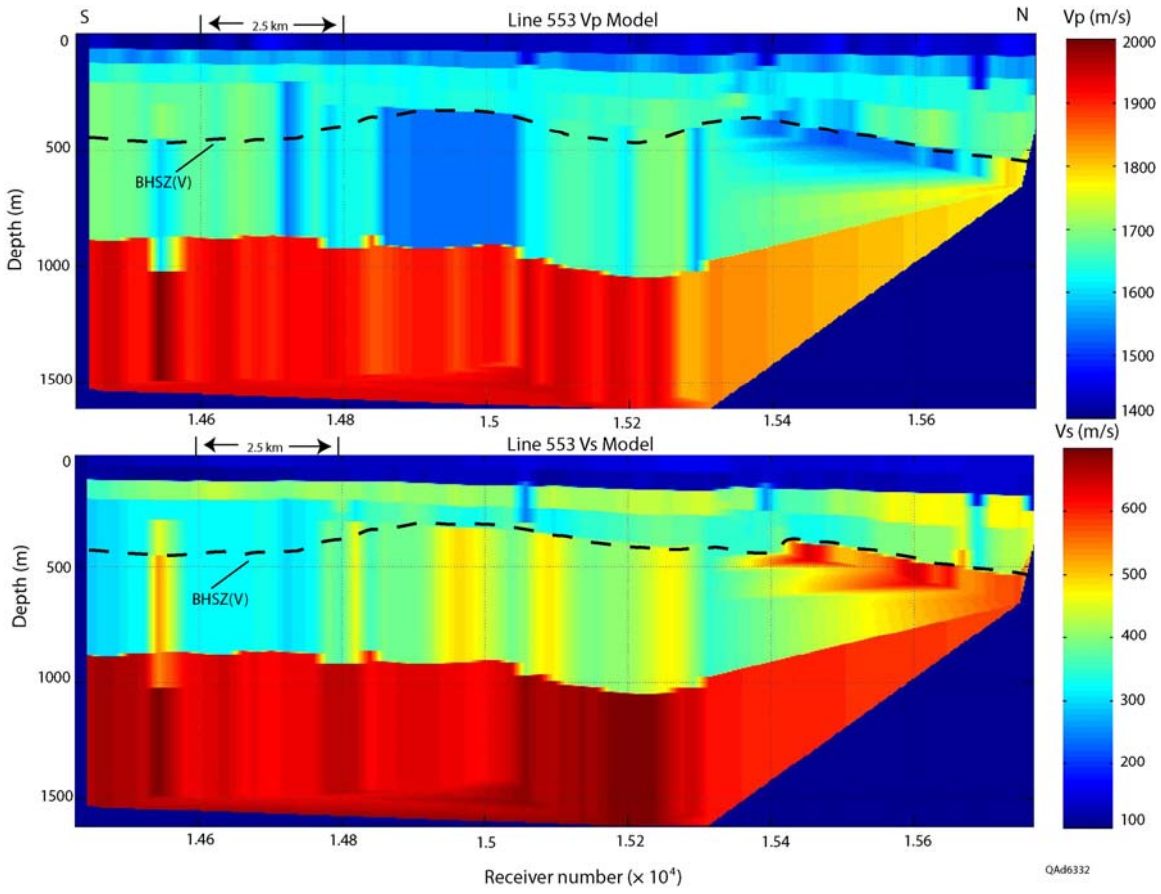

Figure 1.13. 2D layer velocity models along OBC profile 553, Genesis Field. The location of profile 553 is defined on the map shown as Figure 8.1. The BHSZ(V) boundary is the dash line marking the top of the layer where V_P velocity has a reversal in magnitude.

Research Result 7: 2D Profiles of Hydrate Concentration

Relationships between V_P velocity and hydrate concentration developed at calibration wells were applied to the V_P velocity layer models constructed along each OBC profile. The inversion results for the velocity layering along profiles 549 and 553 (Fig. 1.12 and 1.13) are displayed as Figure 1.14. Along the southern half of each profile, the BHSZ boundary was defined as the onset of a reversal in V_P magnitude. Along the northern half of each line, the BHSZ boundary was defined by the water-depth-based thermal constraint for 90-percent methane hydrate (see Chapter 5, Figure 5.5) published by Milkov and Sassen (2001).

(a)

(b)

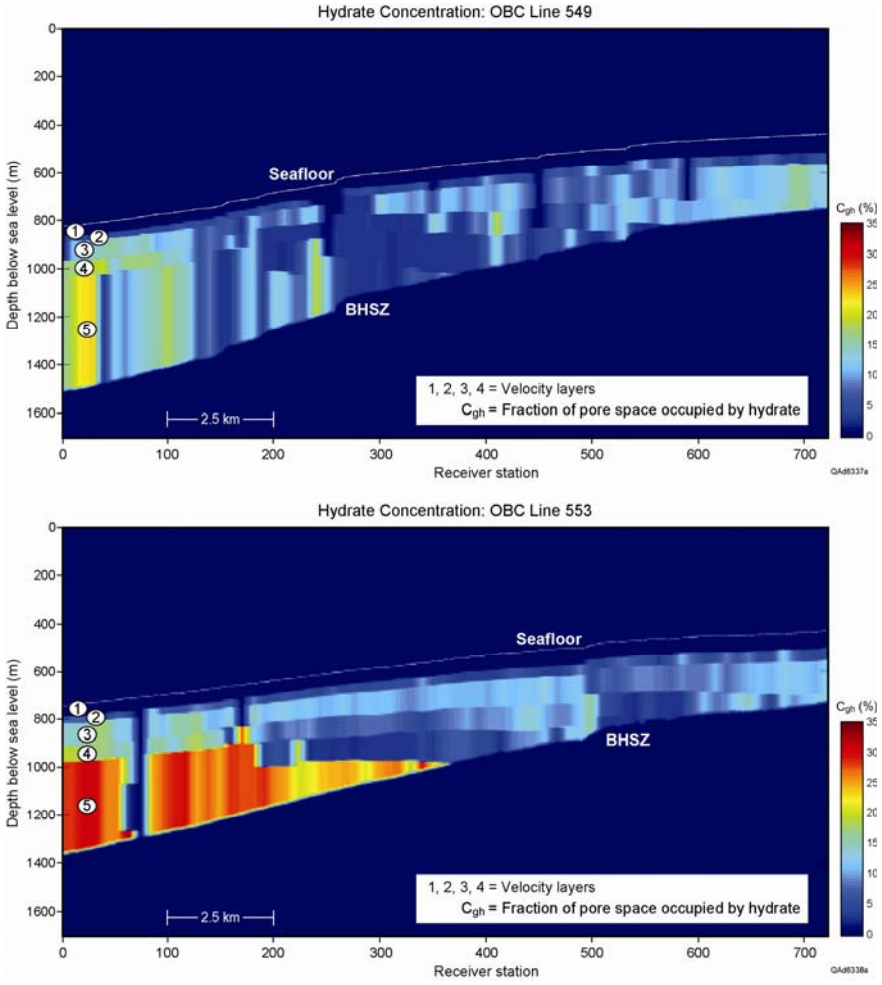

Figure 1.14. Hydrate concentrations estimated along OBC profile 549 (a) and profile 553 (b), Genesis Field. The units are "percent of pore space occupied by hydrate." Hydrate concentration was not estimated for Layer 1 because no log data were available to confirm the trend of the normal compaction curves across this shallowest interval immediately below the seafloor. At the south end of the line, the BHSZ boundary is defined by a reversal of V_P velocity. At the north end, the Milkov and Sassen (2001) thermal constraint for 90-percent methane hydrate is used to define the BHSZ.

Because the normal compaction curve NC discussed in Chapter 9 has such a dynamic depth variation across velocity Layer 1 immediately below the seafloor and no log data were available across this shallowest layer to confirm the effect of compaction on velocity, we assigned a constant, near-zero hydrate concentration to Layer 1 and focused our hydrate estimation on velocity Layer 2 and deeper layers that extend down to the BHSZ horizon. Our velocity analyses did not indicate a velocity magnitude in Layer 1 anywhere across the OBC profile grid that would infer hydrate was present in this shallowest layer.

Our calculated hydrate concentrations exhibit considerable lateral spatial variation within each velocity layer and even greater vertical variability from layer

to layer. The maximum hydrate concentration found along the two particular OBC profiles exhibited as Figure 1.14 were local, limited areas where hydrate occupied a little more than 30-percent of the pore space of the host sediment.

It is challenging to make a single graphic that illustrates the critical data analysis steps that are done along each OBC profile that traversed our study sites and the interpretation of hydrate concentration that resulted from these analyses. The display format illustrated on Figures 1.15a and 1.15b is our attempt to portray the maximum amount of pertinent information for each OBC profile on a single page. The data displayed on each set of our 2-page montages present the following research results along an OBC profile:

1. New imaging technology: Our new data-processing procedure for 4C OBC data that creates high-resolution images of near-seafloor geology is documented across the top row by the P-P and P-SV images that were produced along the profile.
2. Interpretation of depth-equivalent horizons: The depth-equivalent P-P and P-SV horizons that resulted when we used the combination of (1) interpreter logic, and (2) raytracing of reflection events in common-receiver gathers to determine depth equivalency is displayed across the center row. Establishing depth-equivalent horizons in P-P and P-SV images is a critical requirement for interpreting near-seafloor geology with 4C seismic data, and the methodology developed in this study ensures accurate depth-equivalent horizons are created.
3. Layered-velocity model: Our raytrace analysis of common-receiver-gather data yielded accurate estimates of V_P and V_S interval velocities. These velocity analyses were done at intervals of 250 m along each OBC profile to build the continuous-layer velocity model that is shown on the left of the bottom row of the first page of the 2-page montage set for each profile (for example Figure 1.15a). These velocities were not interpolated to create smoothed velocity functions at every image trace along a layer but were left in a blocky format where a discrete velocity value spans a lateral distance of 250 m centered on the receiver station where the velocity analysis was done.
4. Estimate of hydrate concentration: The final objective of our research was to use 4C OBC data to estimate hydrate concentration across each study site. The layer-by-layer estimates of hydrate concentration along each OBC profile are shown on the second page of the 2-page montage for each OBC profile (Figure 1.15b in this example). The data displayed on this second page (Fig. 1.15b) are identical to the data shown on the first page (Fig. 1.15a) except for the lower-right panel where the estimated hydrate concentration is substituted for the V_S velocity panel. This hydrate estimation is the output of (a) our rock physics theories, and (b) our joint inversions of resistivity and velocity at calibration wells, which set the parameters that need to be used for velocity-only inversion along the OBC profiles that extended away from calibration wells. Display formats similar to those exhibited as Figures 1.15a and 1.15b were made for each 4C OBC profile involved in our study and are included as Appendix A.

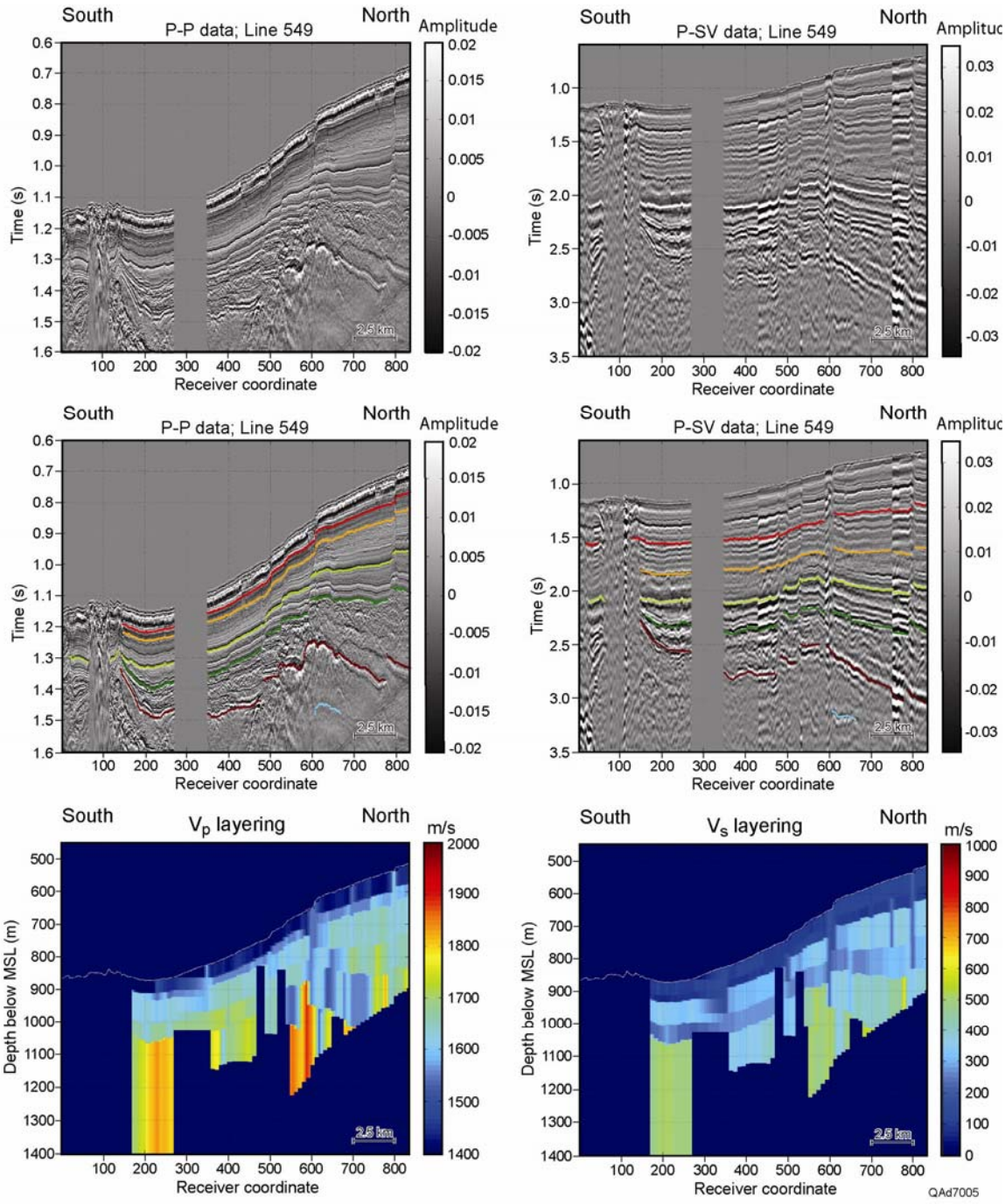

Figure 1.15a. Critical information developed along profile 549, Study Site 2, Genesis Field area (line location shown on Fig. 1.2b). Top row = uninterpreted P-P and P-SV images. Center row = interpreted P-P and P-SV images showing depth-equivalent horizons. Bottom row = V_P layer velocities (left) and V_S velocities (right).

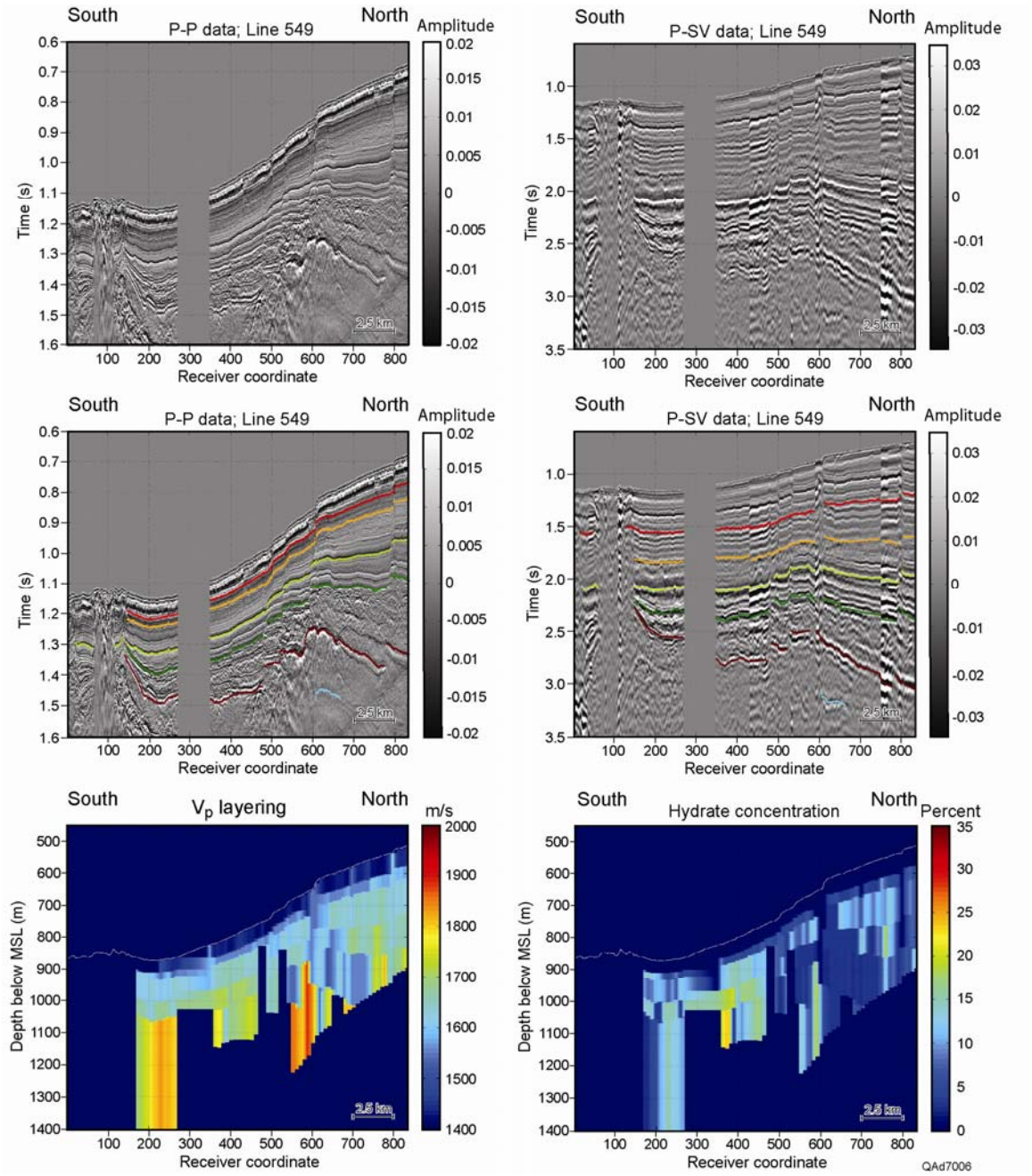

Figure 1.15b. Critical information developed along profile 549, Study Site 2, Genesis Field area (line location shown on Fig. 1.2b). Top row = uninterpreted P-P and P-SV images. Center row = interpreted P-P and P-SV images showing depth-equivalent horizons. Bottom row = V_S layer velocities (left) and estimate of hydrate concentration expressed as "percent of pore occupied by hydrate" (right).

Research Result 8: Mapping the Amount of In Situ Hydrate

To determine the amount of in situ hydrate existing within the interval extending from the seafloor to the BHSZ boundary, we multiplied our seismic-based hydrate concentrations (expressed as the fraction of occupied pore space)

by each layer thickness and layer porosity and summed these products to create an estimate of total in-place hydrate. The resulting maps of in-place hydrate across the study areas are shown as Figure 1.16 and 1.17. Our seismic-based quantification of in situ hydrate indicates the largest accumulation of hydrate exists in Green Canyon Block GC116 north of Genesis Field (Fig. 1.17). At some locations across this trend, the amount of in-place hydrate is estimated to be as much as 2000 to 4000 m^3 beneath 1-m × 250-m rectangular strips centered on receiver stations where V_P interval velocities were determined for estimating hydrate concentration. Other significant accumulations of hydrate are shown by the green to red colors that are shown at several locations across the OBC grid.

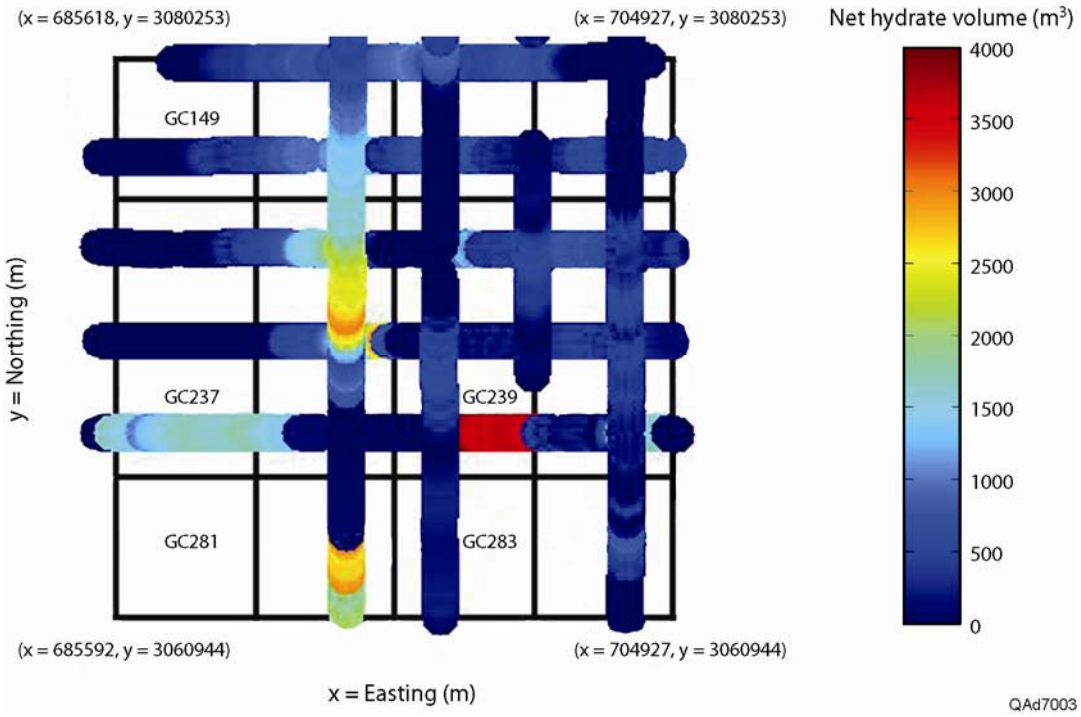

Figure 1.16. Amount of in situ hydrate across Study Site 1, Typhoon Field area. The values plotted on this map are the product: (hydrate concentration) × (layer porosity) × (layer thickness) × (250 m). The 250-m factor is the distance between adjacent velocity analysis points where V_P velocities are calculated. The color bar defines the amount of in-place hydrate (in units of cubic meters) below a 1-m × 250-m strip centered on the sequence of seafloor receiver stations where velocity analyses were done.

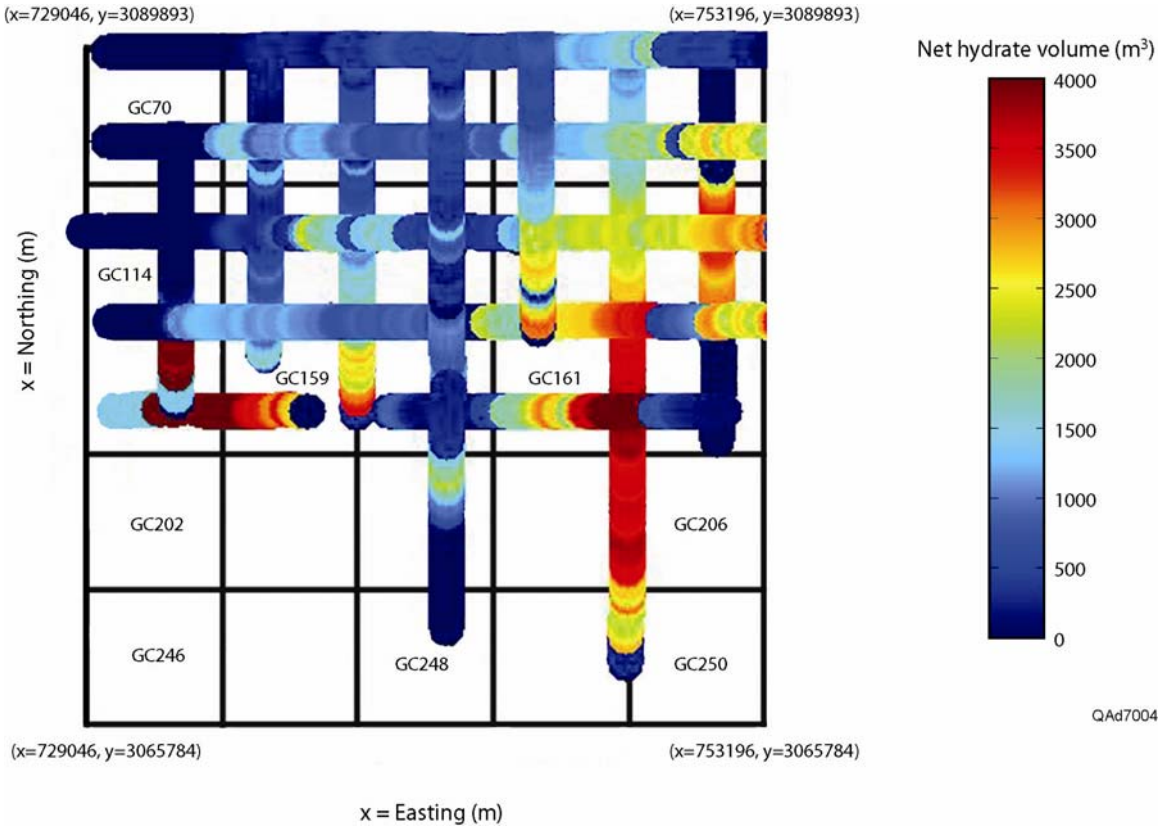

Figure 1.17. Amount of in situ hydrate across Study Site 2, Genesis Field area. The values plotted on this map are the product: (hydrate concentration) × (layer porosity) × (layer thickness). × (250 m). The 250-m factor is the distance between adjacent velocity analysis points where V_P velocities are calculated. The color bar defines the amount of in-place hydrate (in units of cubic meters) below a 1-m × 250-m strip centered on the sequence of seafloor receiver stations where velocity analyses were done.

Comparing Load-Bearing and Free-Floating Hydrate Assumptions

The hydrate distributions displayed as Figures 1.16 and 1.17 were estimated using the assumption that the hydrate granules embedded in the sediment bear a proportionate part of the sediment weight. This assumption leads to the “load-bearing” rock physics theory described as Model A in Chapter 3 (see Figures 3.1 through 3.7). An alternate assumption that has merit is that unit volumes of hydrate float in the pore spaces of the host sediment and are not part of the load-bearing matrix. This assumption leads to the “free-floating” rock physics theory described as Model B in Chapter 3 (Figs. 3.1 - 3.7).

For a given value of V_P within a near-seafloor layer, a free-floating assumption for the hydrate-sediment morphology results in greater hydrate saturation than does a load-bearing assumption. A comparison of the hydrate concentrations predicted by these two hydrate-morphology models along OBC profile 557 is displayed as Figure 1.18. For the range of interval V_P velocities that we found within the hydrate stability zone in the Green Canyon area, our free-floating-hydrate theory causes approximately five more percentage points to be added to the hydrate fraction than what is predicted by our load-bearing-hydrate

theory. If our load-bearing-hydrate calculation at location 1 yielded a hydrate fraction of 16-percent and a fraction of 22-percent at location 2, our free-floating-hydrate theory predicted approximately 21-percent and 27-percent, respectively, at these same two locations. The almost-constant difference of approximately five percentage points of hydrate concentration that results when using these two hydrate-morphology assumptions is illustrated by the profiles displayed as Figure 1.18.

It should be emphasized that the difference of approximately five percentage points of hydrate fraction predicted by these two theories applies only when the V_P interval velocity is in the range of 1550 m/s to 1800 m/s, as can be seen by comparing the suite of curves for Model A on Figure 3.5 with the corresponding suite of curves for Model B in that same figure. For values of V_P greater than 1800 m/s, a free-floating-hydrate morphology will result in an increase of more than five percentage points in the hydrate fraction, sometimes an increase as large as seven or eight percentage points.

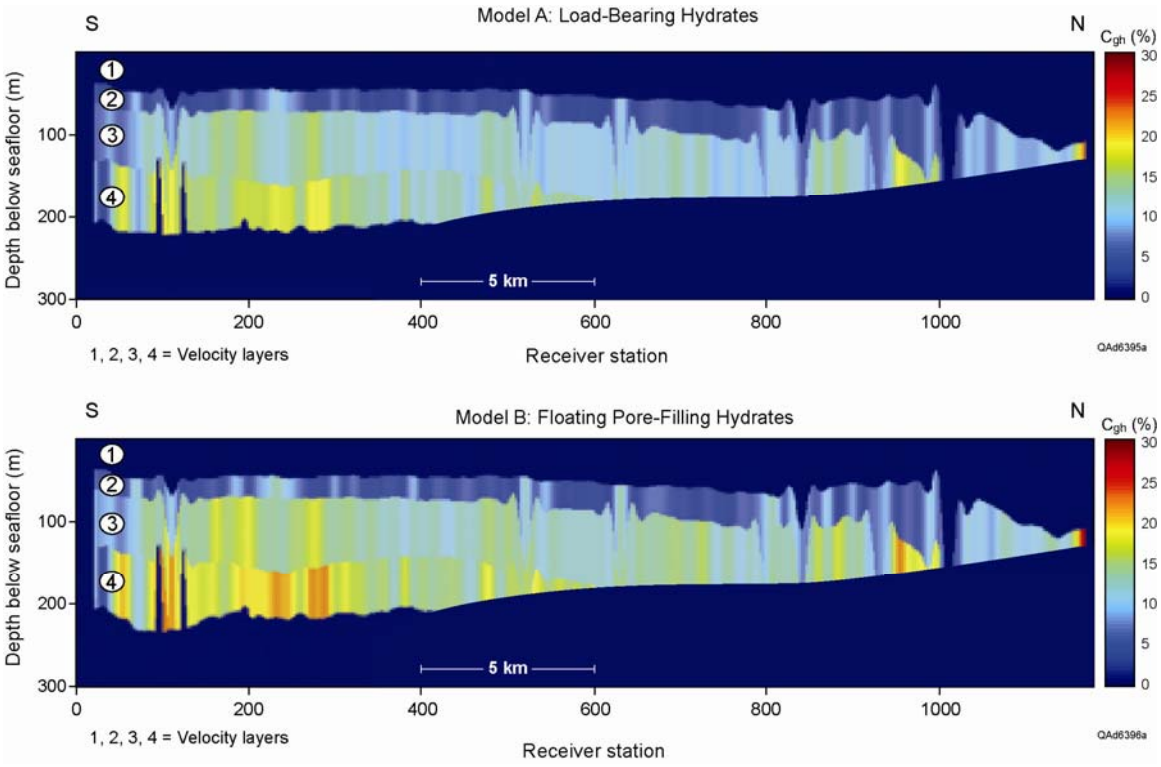

Figure 1.18. Comparison of hydrate concentrations predicted along OBC profile 557 when hydrate is load-bearing (top) or free-floating (bottom). The same color bar is used in each display. For the range of sub-seafloor V_P interval velocities determined along this profile, an assumption of free-floating hydrate (bottom) results in an almost uniform increase of approximately five percentage points in the hydrate fraction along the entire profile.

Examples of Bottom Simulating Reflectors

The Gulf of Mexico (GOM) is noted for not having bottom simulating reflectors (BSRs) beneath many known hydrate systems. We searched for BSR evidence in the P-P and P-SV images we made along each OBC profile. We found no BSR events on any P-SV image. This finding was what we expected to observe because a BSR seems to be a boundary between hydrate (above) and free gas (below), and P-SV data do not respond to a gas boundary unless the gas saturation is high enough to alter formation density within the free-gas interval. We did find evidence of a BSR on two P-P profiles. These P-P images are shown as both uninterpreted and interpreted data on Figures 1.19 and 1.20. A terminology that should probably be used across the GOM is “bottom simulating horizon” or BSH rather than BSR because the base of the hydrate stability zone is more commonly marked by an invisible horizon that connects terminating reflection anomalies as shown on Figure 1.19 rather than by a definitive reflection event.

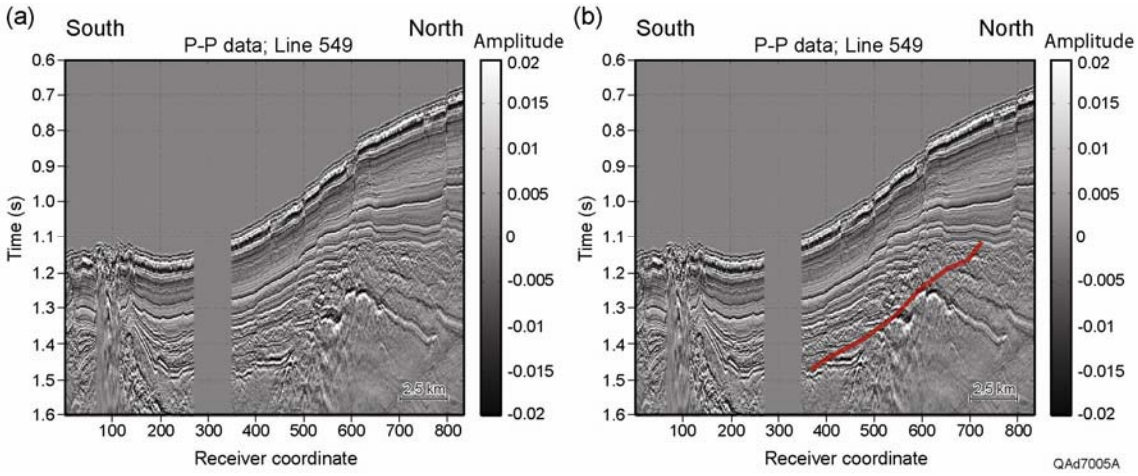

Figure 1.19. Evidence of a bottom-simulating-reflection (BSR) along profile 549, Genesis Field area. (Left) No interpretation. (Right) With interpretation. This BSR is invisible as are most BSRs across the Gulf of Mexico but can be defined by the series of reflections that terminate along the marked horizon.

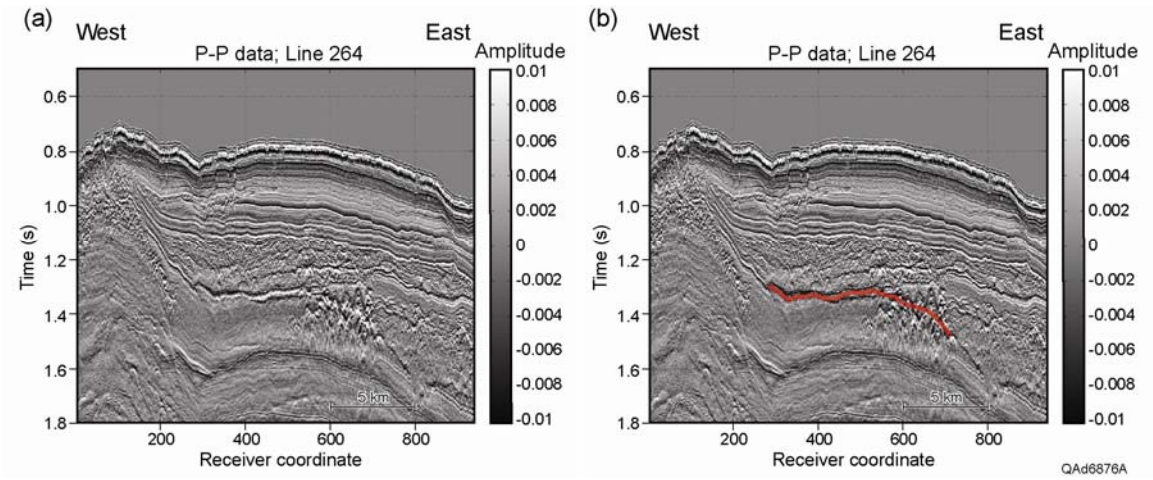

Figure 1.20. Evidence of a bottom-simulating-reflection (BSR) along profile 264, Study Site 2, Genesis Field area. (Left) No interpretation. (Right) With interpretation.

Conclusions

We had to develop several new technologies to estimate hydrate concentrations in strata spanned by the hydrate stability zone that extends across the deep-water area of Green Canyon. Our key technology developments were:

1. Calibration of hydrophone and geophone sensor responses to create optimal estimates of downgoing and upgoing wavefields when adding and subtracting hydrophone and geophone data.
2. A new strategy for processing 4C OBC seismic data that produces high-resolution P-P and P-SV images of near-seafloor geology.
3. A new raytrace procedure that creates a model of sub-seafloor layering of V_P and V_S velocities at selected seafloor-receiver stations.
4. Rock physics models that relate seismic velocities to hydrate concentration for four different sediment-hydrate morphologies.
5. Rock physics concepts based on the theory of the Hashin-Shtrikman lower Bound that relates hydrate concentration to formation resistivity in high-porosity, unconsolidated sediments.
6. The use of probability distribution functions to describe all variables that are used to estimate hydrate concentration.
7. The use of joint inversion of resistivity and velocity to constrain our predictions of hydrate concentration to a range of most-probable expectation.

Using these techniques, we found that hydrate is pervasive across the Green Canyon area. The hydrate concentration was generally less than 15-percent of the available pore space. In a few local areas concentrations increased to more than 40-percent of the pore space of the host sediment.

We determined that a free-gas layer immediately under lays the base of the hydrate stability zone across our study area. This free-gas zone is revealed by a reduction in V_P velocity determined by our high-resolution raytrace modeling technique. The amount of free gas in this zone was not estimated, but we expect the zone has a gas saturation of only a few percentage points. Dominico (1976) has demonstrated that a small amount of free gas can produce a significant reduction in V_P velocity. This free-gas zone was not easily distinguished from a hydrate-bearing zone when examining resistivity logs available across the area. The observed increase in log resistivity related to free gas can be confused with a resistivity increase caused by hydrate. Thus interpreting the thickness of the hydrate stability zone from resistivity logs alone can lead to an overestimation of the thickness of stable hydrate and of the amount of hydrate that is present.

Even though we developed and applied excellent technologies in this study, additional technologies should be considered in future hydrate studies. Foremost among the applications that should be tried would be an inversion of the P-P and P-SV seismic data to create a trace-by-trace, datapoint-by-datapoint estimation of seismic impedance rather than relying on the averaged, layered velocities that we used. The higher spatial resolution of velocity behavior provided by inversion of P-P and P-SV traces should provide more detail about the internal fabric of the hydrate systems than what we have achieved with our larger-scale, interval-velocity approach. Our large-scale velocity approach is adequate for this study and can even be considered to be a preferred approach for a “big-picture” view of hydrate concentration. A more detailed velocity analysis than what we have done would be attractive where a specific site is being analyzed to decide if hydrate exploitation should be attempted.

We conclude, as has Zillmer (2006), that it is important to utilize two or more hydrate-sensitive, real-data measurements to estimate hydrate concentration. Zillmer utilized well-log-measured formation density and seismic-based V_P and V_S velocity data to constrain hydrate estimations. In our case, we relied on well-log-measured resistivity and on seismic-based V_P and V_S velocities. Zillmer (2006) also emphasizes that the input data used to estimate hydrate concentrations must be measured with high accuracy and indicates the uncertainty associated with predictions of hydrate concentrations for various ranges of measurement error of the input data used to calculate a hydrate concentration. We concur with this philosophy and stress: (1) that the V_P and V_S velocities determined by our raytrace analysis can be accurate to ±1 percent (Chapter 7; Figure 7.17), and (2) all of our hydrate predictions have an associated estimation error, the standard deviation of the calculated probability distribution function.

In future studies, we see a need to adjust our seismic data-processing strategy so that water-column multiples are removed from the data. Because water depths ranged from 500 m to 1000 m across the area we studied, water-column multiples begin arriving at delay times ranging from 670 ms (500-m water depth) to 1330 ms (1000-m water depth), assuming a propagation velocity of 1500 m/s in seawater. These delay times placed the multiples near or immediately below the BHSZ in P-P image space and allowed us to use simple

data-processing strategies that involved no demultiple operations. However, water-column multiples did contaminate our P-SV data within the hydrate stability zone and sometimes even contaminated the P-P data near the base of the hydrate stability zone. These multiples sometimes made it difficult to interpret velocity layers at and immediately below the BHSZ boundary where it is important to know if a velocity inversion is present. If similar deep-water hydrate studies are done in the future, it will be wise to remove the water-column multiples on all OBC-sensor data.

Acknowledgment

Funding for this project came in part through the National Energy and Technology Laboratory (NETL) under the Office of Fossil Energy's Oil and Natural Gas Program, which supports research and policy options to ensure clean, reliable, and affordable supplies of oil and natural gas for American consumers.

DOE Gas Hydrate Final Report
Chapter 2

Processing 4C OBC Seismic Data to Image Deep-Water, Near-Seafloor Geology

Introduction

We developed a new seismic data-processing concept that creates the downgoing **compressional** (**P**) wavefield and the upgoing P and **converted-shear** (**SV**) wavefields that are needed to construct P-P and P-SV images of near-seafloor geology. In our data-processing approach, we work with **four-component ocean-bottom-cable** (**4C OBC**) data collected at only one seafloor receiver station, segregate these data into common-receiver gathers for each of the four sensor components, and then use these four common-receiver gathers to create the downgoing P wavefield and the upgoing P and SV wavefields at that seafloor receiver location. With these three wavefields (P-down, P-up, and SV-up), we then proceed to calculate P-P and P-SV reflectivities of near-seafloor strata.

Our data-processing concepts can be applied to 4C OBC data acquired in deep water only. Our data-processing assumptions are invalid when the vertical distance between the source and receiver (i.e. water depth) is of the order of 200 m or less. There is a strong equivalence between our processing of seafloor-based common-receiver gathers and the processing of **walkaway vertical seismic survey** (**VSP**) data. No one in the seismic data-processing industry has utilized this deep-water, 4C OBC data-processing technique before to our knowledge. We consider our development of this new method for creating high-resolution downgoing and upgoing seismic wavefields to be a significant technology advance that will benefit others engaged in deep-water hydrate research or in any deep-water seismic investigation that requires improved seismic imaging of near-seafloor geology.

We show in this chapter how our new approach to OBC seismic data processing allows high-resolution P-P and P-SV images to be made of targets embedded in the unique near-seafloor medium where deep-water hydrates are found, a medium characterized by

- high porosity (40 to 70 percent),
- low effective pressure (literally zero at the seafloor and near zero at shallow depths), and
- minimal grain-to-grain contact.

These physical properties are not those of a typical seismic propagation medium.

Theoretical Concepts

In our seismic imaging approach, 4C OBC seismic data are treated as common-receiver gathers, which is basically the same form in which the data are recorded by an ocean-floor sensor system. The 4C data acquired at one typical

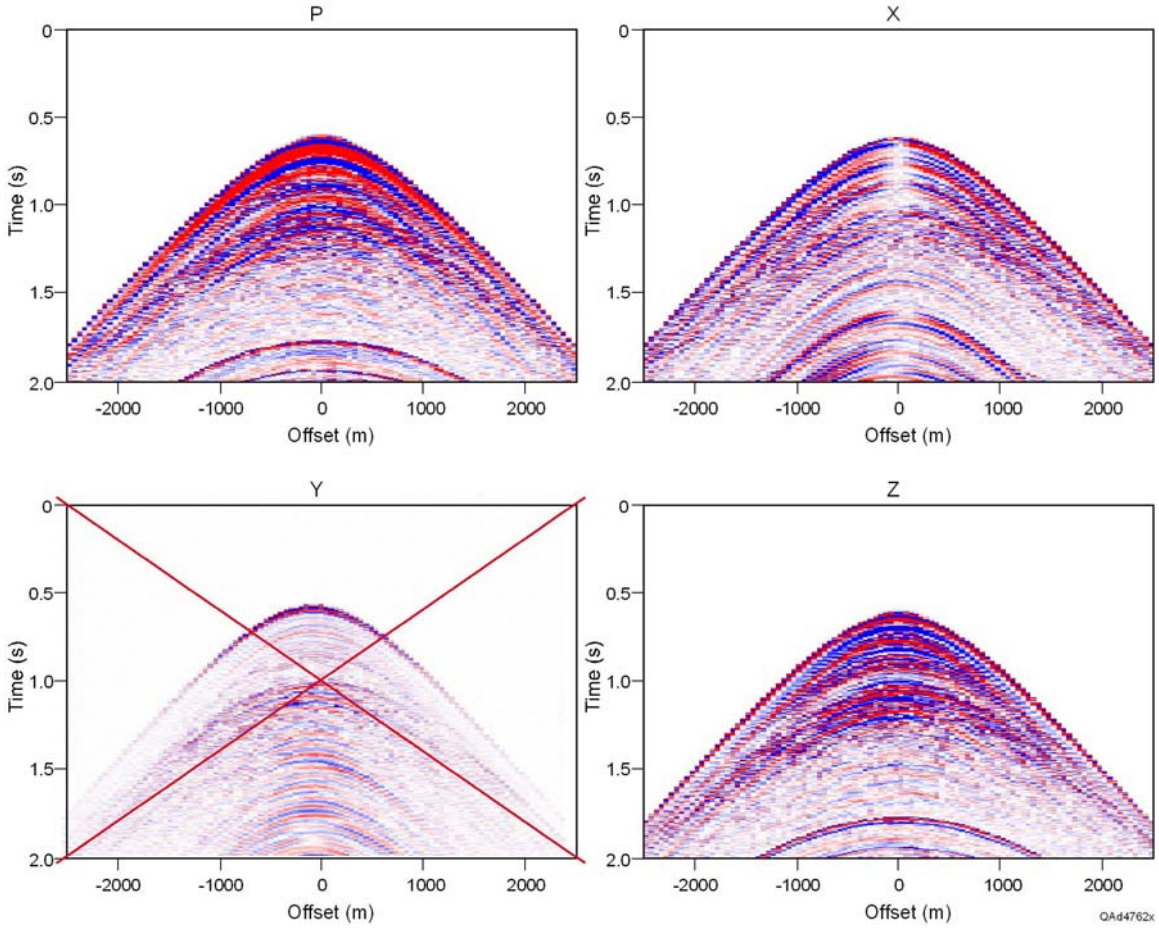

Figure 2.1. 4C OBC data collected at a single deep-water seafloor receiver station in the Green Canyon lease area. Source spacing is 50 m along the horizontal axis that defines the range of source-receiver offset. At this location, a sea-bottom multiple appears at a normal-incidence time of 1.75 seconds. Although this multiple dominates the P-P section when it arrives, we can ignore it because its arrival time is below our hydrate target zone. However, the sea-bottom multiple also appears on the **X** (radial) component data and interferes with P-SV reflections arriving between 1.6 and 2 seconds. These P-SV events are in the range of hydrate interest, 130–200 m below the seafloor. In our 4C OBC data, the crossline **Y** component is low amplitude and can be ignored in our normal data-processing flow. **P** is the hydrophone response; **Z** is the response of the vertical geophone.

seafloor receiver station inside our study area are shown as Figure 2.1. All of our data processing is performed on isolated receiver-station data like the data illustrated in this figure. Receiver stations were spaced at 25-m intervals along all of the OBC profiles that traversed our study area, and the data-processing procedure described here was repeated at each of these receiver stations. Our

project team has produced trace-gather displays like that in Figure 2.1 at **8,640** seafloor stations (216 km of OBC profiles) across our Green Canyon study area, and we have examined the responses of all four sensor elements at each of these receiver stations to determine which trace gathers cannot be used for imaging purposes without some type of data modification. Approximately 10 percent of the receiver gathers needed special handling or some amount of data muting to eliminate problems such as excessive noise, incorrect sensor channel designations, and so forth.

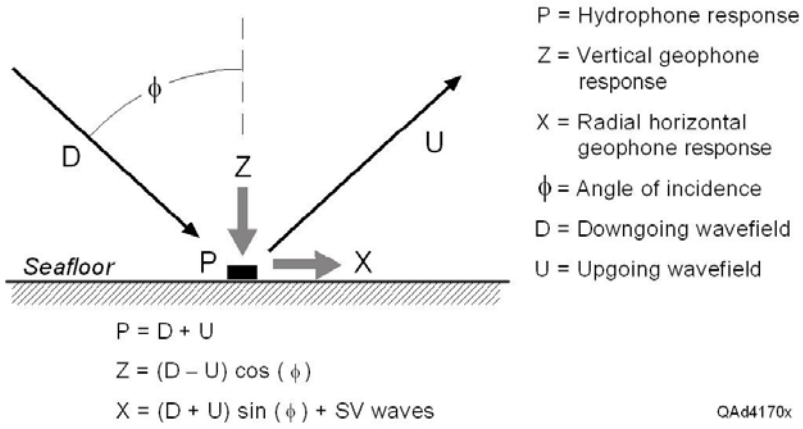

Figure 2.2. Basic responses of 4C ocean-bottom sensors. The three response equations listed here are the keys to our imaging theory. We assume that the response of the **Y** (crossline) horizontal geophone can be ignored. This assumption is correct for the data used in this study but needs to be verified at other study sites. A second assumption is that the V_P/V_S velocity ratio is high, which positions the P-to-SV conversion point almost directly beneath the seafloor receiver station. As a result, the upgoing SV raypath is almost vertical, and essentially all of the SV response is on inline horizontal geophone **X**. The SV wavefield can then be separated from the **X** response by calibrating and weighting the **P** response and subtracting it from **X**. We determine the wavefield to subtract from **X** by calculating a constrained cross-equalization filter that changes **P** to **X**.

P-P Trace Gathers

The fundamental theory of our P-P data-processing strategy is based on analyzing data that have been acquired with a sensor that has a hydrophone and a vertical geophone. The key sensor-response equations involved in OBC data acquisition are illustrated and explained on Figure 2.2. Defining **D** as the downgoing compressional (P) wavefield that reaches a seafloor station and **U** as the upgoing compressional (P) wavefield at that same station, the responses of the hydrophone **P**, vertical geophone **Z**, and inline horizontal geophone **X** are

(2.1) **P = D + U**

(2.2) **Z = (D – U) cos(Φ)**

(2.3) **X = (D + U) sin(Φ) + SV waves**.

Φ is the incident angle at which the downgoing compressional wave arrives at the seafloor (Fig. 2.2). These equations imply that after appropriate calibration, a seafloor hydrophone response (**P**) and a seafloor vertical-geophone response (**Z**) can be combined to create the unknown downgoing (**D**) and upgoing (**U**) P-P wavefields at each receiver station using the following relationships:

(2.4) **D = P + Z/cos(Φ)**

(2.5) **U = P – Z/cos(Φ).**

In Figure 2.3 we show **P**, **Z**, **U**, and **D** waves at a single deep-water seafloor receiver location. To better demonstrate separation of the data into downgoing and upgoing P wavefields, a static time shift has been applied to flatten the direct arrival (and thus the ocean-floor reflection) and to position this flattened event at time T = 0. This data shift is referred to as a **reduced time** display in the geophysical literature. The flat events in the downgoing wavefield appear in all four panels. In the time window that is displayed, we see two of the several air-gun bubble pulses (**B**) that exist in these data. Reflection events (**R**) appear as smiles. The downgoing wavefield panel **D** produced by Equation 2.4 shows almost no sign of the reflection events that appear in the other three panels. The upgoing wavefield **U** (Eq. 2.5) shows the air-gun bubbles that result when the strong seafloor reflection coefficient convolves with the downgoing wavelet. Vertical geophones **Z** tended to provide a better reflection picture than did hydrophones **P**. The difference between these two sensor responses occurs because the downgoing wavelet and the seafloor-reflected wavelet combine constructively on hydrophone data but destructively on geophone data (Equations 2.1 and 2.2). The P-P wavefield separation procedure illustrated in Figure 2.3 was done at all of the 8,640 OBC receiver stations involved in the OBC profiles that traverse our Green Canyon study area.

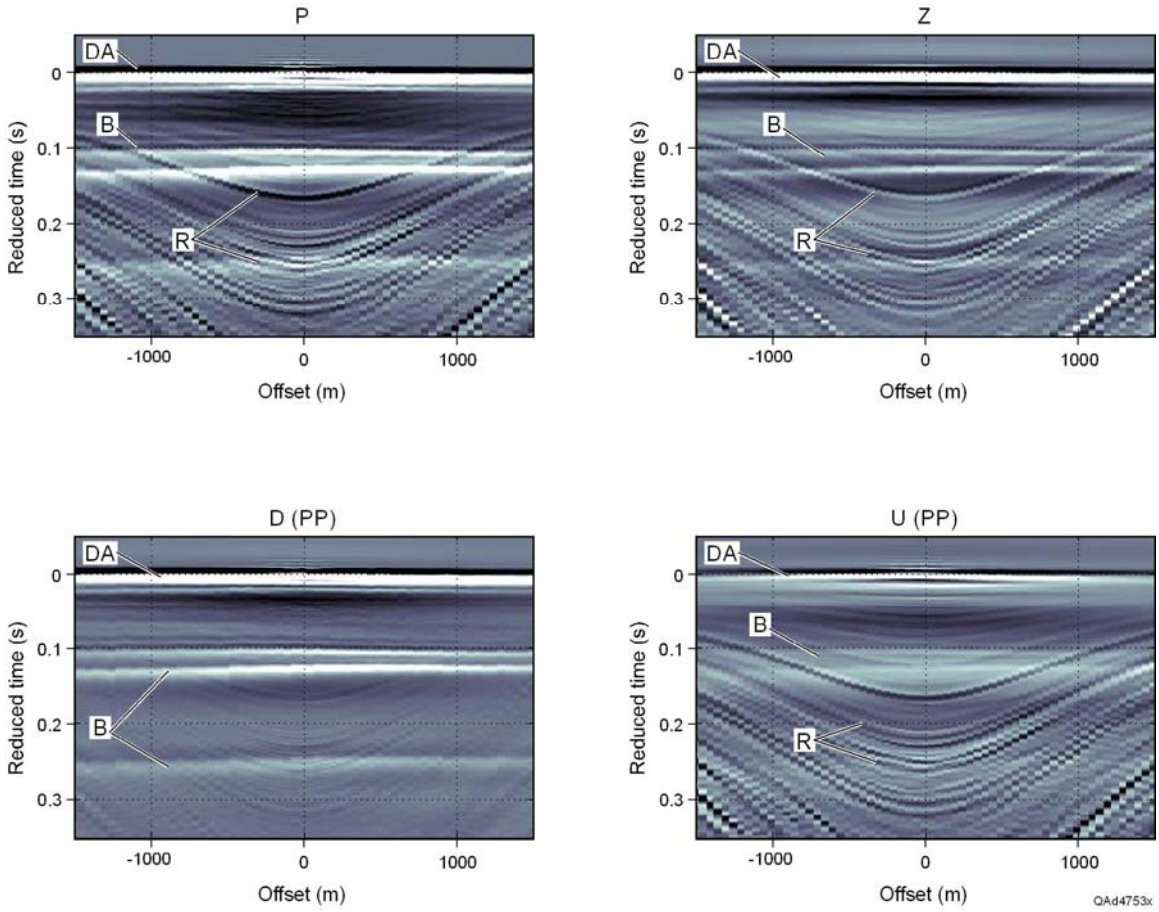

Figure 2.3. Reduced-time display showing **P** (hydrophone), **Z** (vertical geophone), **U** (upgoing P), and **D** (downgoing P) waves extending to 0.35 seconds below the seafloor, which is a time interval of interest in our hydrate study. The separation of up- and down-traveling P waves (bottom two panels) is quite good. By taking the ratio of the up-traveling and the down-traveling P waves, we uncover shallow P-P data that are overprinted by air-gun bubbles without stacking the data. For display, these data have been statically corrected to align the seafloor reflection and the direct arrival at time zero. **DA** is the direct arrival, **B** is an air-gun bubble, and **R** is a P-P reflection.

P-SV Trace Gathers

In Figure 2.4 we show the isolation of the P-SV wavefield, using the formulation defined in Equation 2.3. In this case, calibration of the horizontal geophone **X** with the hydrophone (**P**) is critical to successful P-SV wavefield separation. To accomplish this X-to-P sensor calibration, we first use a single filter that is an average empirical estimate based on P-P reflection data (or on head waves if they exist in the data) to roughly correct the **X** geophone to the hydrophone **P**. We then calculate a cross-equalization filter to change **P** to **X** for each trace. This procedure is discussed in a following section (*Receiver Calibration*). This cross-equalization step must be done judiciously because it is easy to overdo the correction and to eliminate some of the P-SV component—

just as when doing conventional spiking deconvolution one can overdo a correction and attenuate (or eliminate) valid reflections.

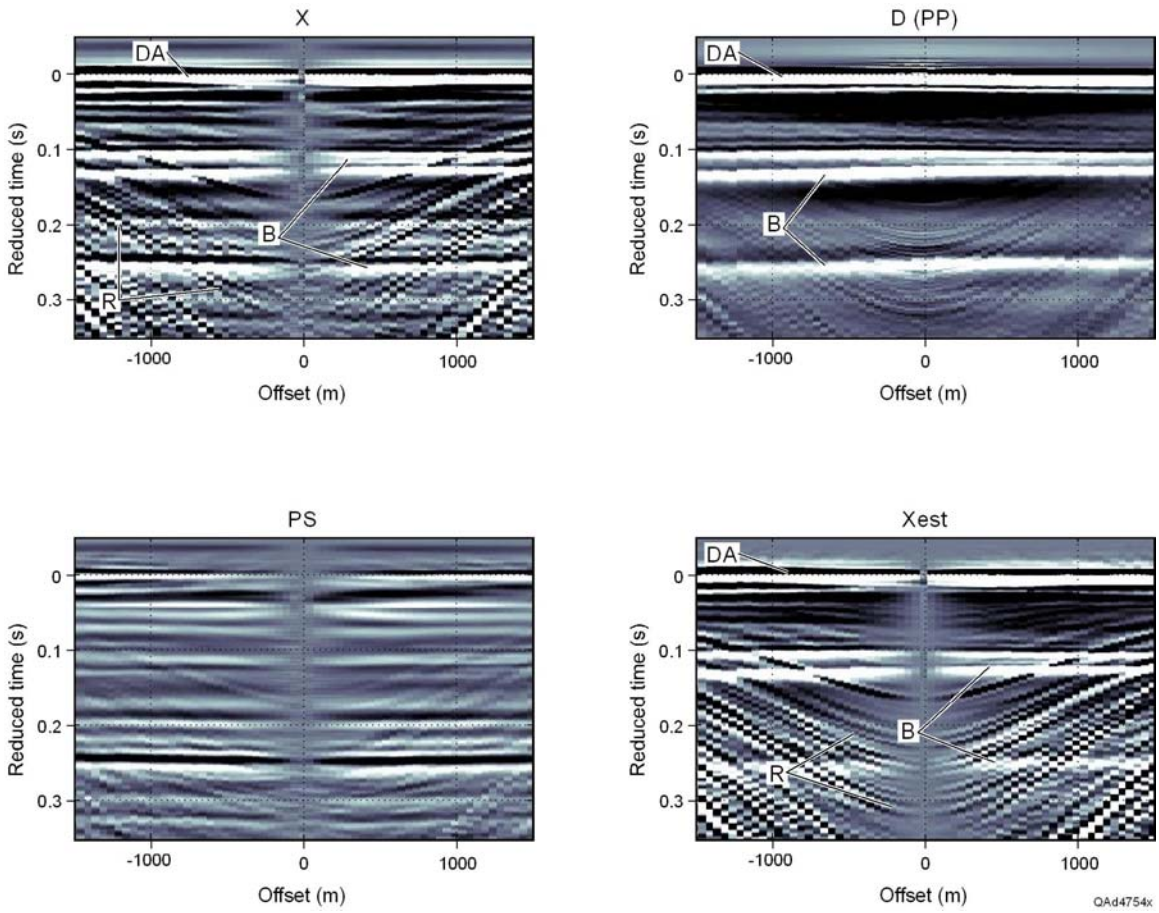

Figure 2.4. Reduced-time display illustrating isolation of the P-SV wave by the combination of **P** (hydrophone) and **X** (horizontal geophone) data. The radial component **X** (upper left) is the superposition of the downgoing P wave (upper right), the upgoing P-P wave (lower right, Fig. 2.3), and upgoing P-SV reflections (Equation 2.3). In the lower right is the result of cross-equalization of **P** to **X**. This wavefield $\mathbf{X}_{est}$ should contain the downgoing P wavefield (flat events) and upgoing P-P waves (smiles labeled "R"). By subtracting the lower-right panel from the upper-left panel, we obtain the lower-left panel that consists of nearly isolated P-SV reflections (flat) and some residual energy.

A separate cross-equalization is calculated to eliminate the seafloor multiple, which arrives at an angle different from that of the direct wave and the shallow P-P reflection data. In Figure 2.4, all data panels have been corrected to flatten the direct arrival. In the upper-right panel, we show the extracted downgoing P wavefield **D** from Figure 2.3 (lower right), which is dominated by air-gun bubbles. The inline **X** component looks like the hydrophone response (Fig. 2.1) because the **X** sensor is dominated by the flattened downgoing wave and by the P-P reflection events that smile. The lower-right panel of Figure 2.4 shows the estimate of the **X** component obtained from the hydrophone response by

cross-equalization. The estimate $\mathbf{X_{est}}$ is indeed a good copy of **X** (upper left, Figure 2.4). When we subtract the lower-right panel from the **X** component, we produce the lower-left panel (labeled PS), which shows the isolated P-SV reflection events. These P-SV events have the same flat appearance as the direct-wave bubbles. The moveout of these P-SV events is negligible because the V_S velocity is quite low for deep-water, near-seafloor strata.

This P-SV trace-gather and wavefield-separation process has been done at all of the 8,640 receiver stations across our Green Canyon study area.

Calculating Reflectivity

By having access to the downgoing (**D**) and upgoing (**U**) P-P wavefields, sub-seafloor P-P reflectivity **R** can be recovered by taking the ratio,

(2.6) $\mathbf{R_{PP} = U_P/D_P,}$

in the frequency domain, **f**. The inverse Fourier transform of $\mathbf{R_{PP}(f)}$ then creates a time-based reflectivity series that starts at the seafloor and extends to a depth below the base of the hydrate stability zone. It is this time-based reflectivity $\mathbf{R_{PP}(t)}$ that we use to create our high-resolution images of deep-water, near-seafloor geology.

Figure 2.5 shows P-P and P-SV reflectivities estimated for a seafloor datum using this wavefield ratio strategy. To obtain these results we first calculate the Fourier transform of the up- and down-traveling P-P waves obtained from the simple combinations of raw **P** and **Z** data that are defined by Equations 2.1 through 2.5. At each offset, we divide the up-traveling P-P wave (lower right of Figure 2.3) by the down-traveling P wave (lower left, Figure 2.3), with a modest damping applied for stability. An inverse Fourier transform then yields the P-P reflectivity result at the upper right in Figure 2.5. The reduction to seafloor datum is automatic in this ratio process.

To determine the reflectivity of the P-SV wave, we follow a similar procedure. We divide the extracted P-SV wave (lower left, Fig. 2.4) by the downgoing P wavefield (lower left, Fig. 2.3) in the frequency domain to produce P-SV reflectivity defined as,

(2.7) $\mathbf{R_{PS} = U_{PS}/D_P}$.

An inverse Fourier transform produces the P-SV reflectivity shown at the lower right of Figure 2.5. Because the direct arrival has already been removed, the effect of this deconvolution is less dramatic for P-SV data than for P-P data.

For both reflectivities (P-P and P-SV), we can follow reflection events out to large source offsets corresponding to local incident angles that exceed 60°. At this stage of data processing, both P-P and P-SV data are suitable for detailed isolation and analysis of individual reflection events.

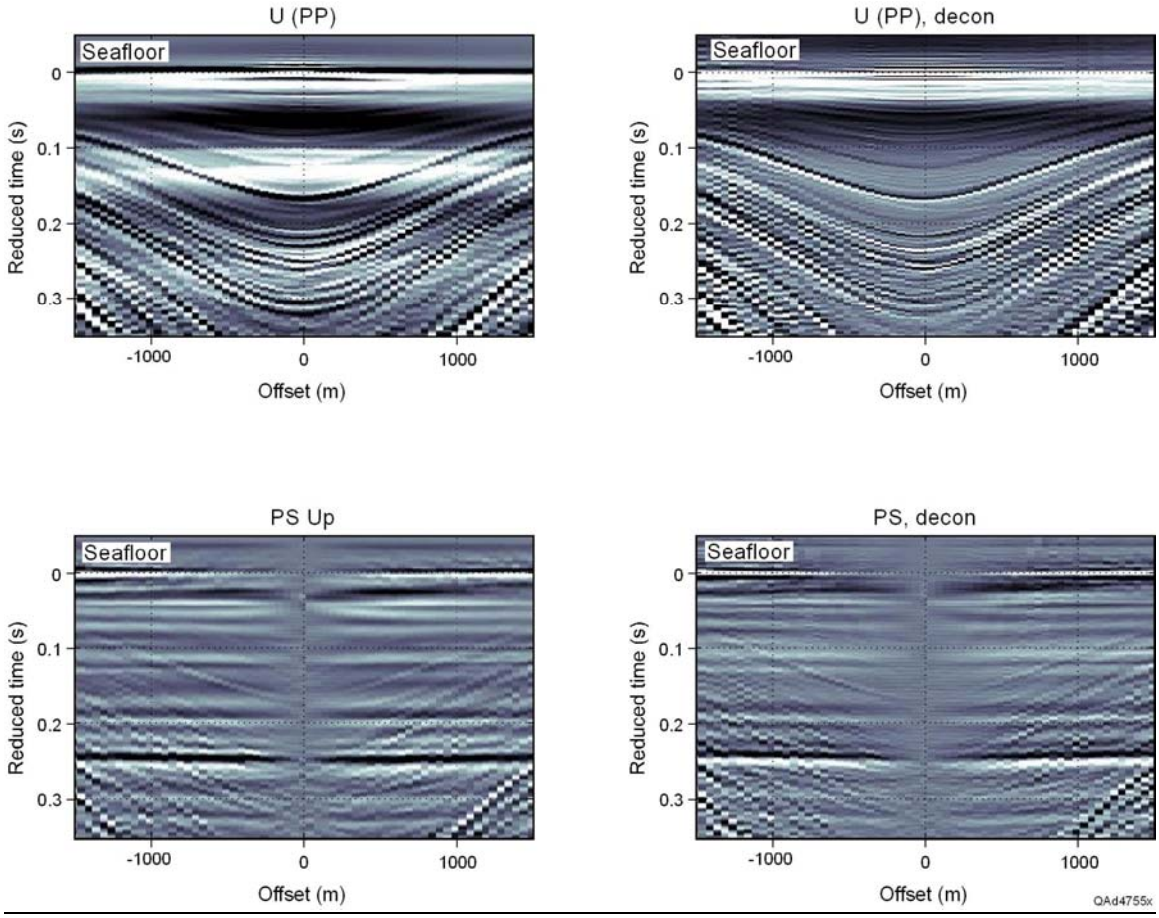

Figure 2.5. Upgoing P-P and P-SV waves are shown on the left. Deconvolution with the downgoing **P** wave produces the reflectivity panels on the right. The upper-right display is the P-P reflectivity; the lower-right display is the P-SV reflectivity.

Creating Local Common-Receiver Images

To create P-P and P-SV images, we apply dynamic corrections to our reflectivity estimates to correct for the moveout on the near-offset traces. On Figure 2.6, we show the deconvolved P-P data (that is, the P-P reflectivity) from Figure 2.5 for a ±2,500-m offset range after applying a time differentiation to enhance the frequency of the data. The data are excellent quality over the full offset range. Raytracing with a layered-velocity model of sub-seafloor geology is then used to calculate curves of source-receiver offset versus time that correspond to reflection depth points that are a fixed offset distance from the receiver location. Examples of raytrace curves calculated for this common-receiver gather are shown as Figure 2.7 for depth-point offsets starting at ±10 m from the receiver station and increasing at 25-m intervals out to ±160 m from the receiver coordinates. Image-trace data can now be recovered by interpolation

along these curves to produce P-P image traces at specified depth-point offsets from the receiver location.

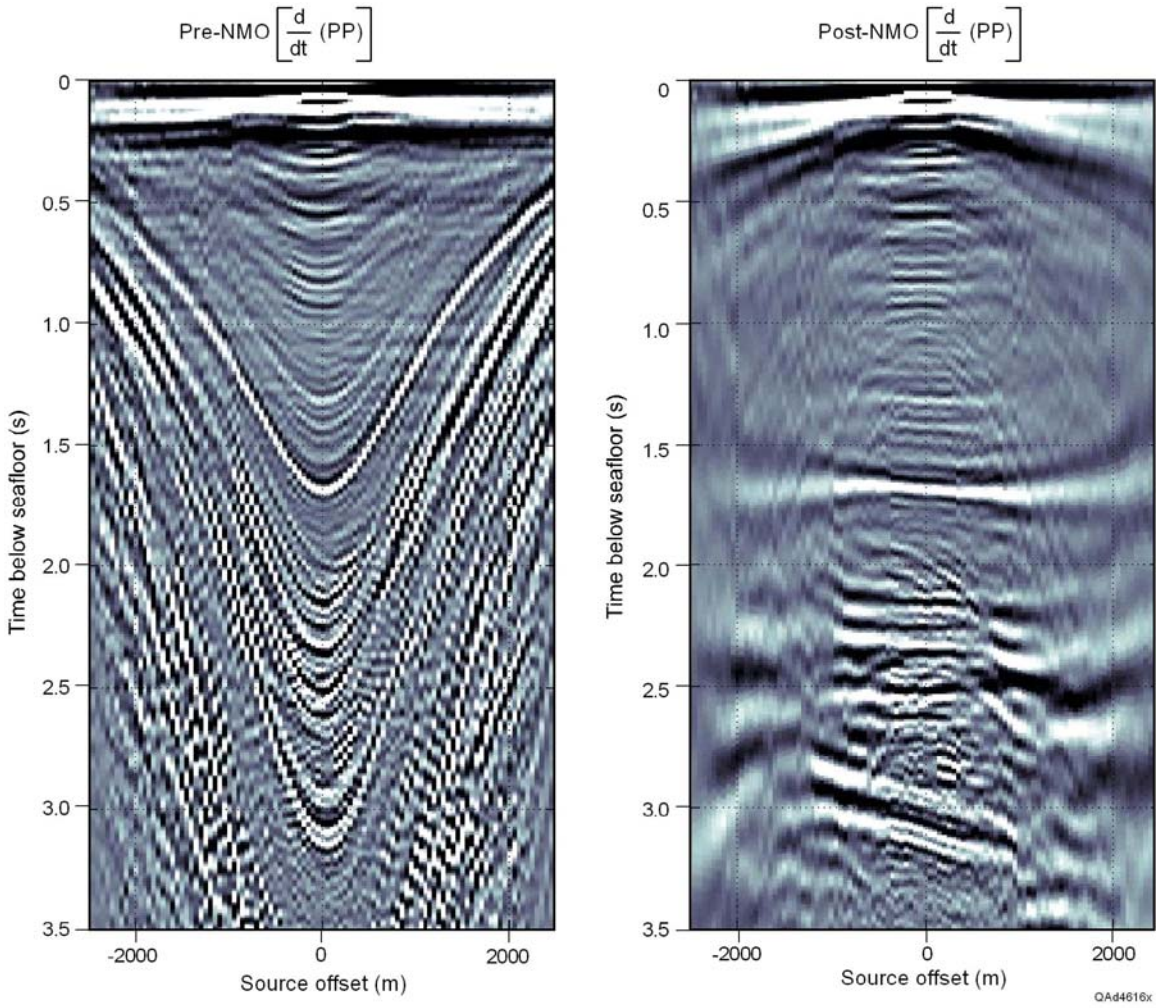

Figure 2.6. After time differentiation to enhance the frequency content of the data, P-P reflectivity for a single common-receiver gather is shown on the left. The data used here are the data displayed as the upper-right panel of Figure 2.5. The same data are shown on the right after dynamic time correction. The extreme moveout stretch at large source offsets is apparent.

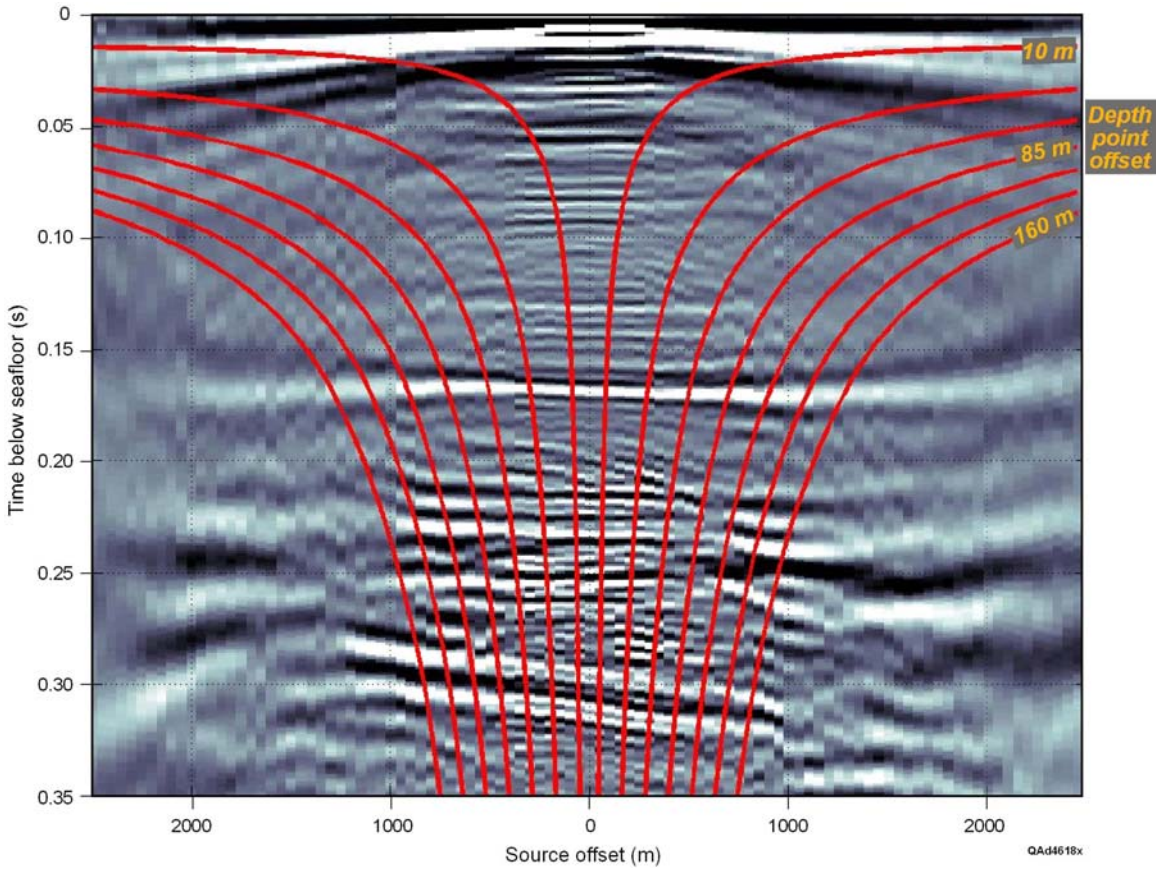

Figure 2.7. P-P reflectivity from Figure 2.5 after application of raytrace-based, dynamic time corrections calculated for a flat-layered Earth model (the same data shown on the right panel of Figure 2.6). Red curved lines define the location of P-P image-trace data at fixed depth-point offsets from the receiver location. Depth-point-offset curves are shown for offsets of ±10 m to ±160 m at 25-m intervals.

On Figure 2.8, we show the deconvolved P-SV common-receiver gather at this same receiver station, before and after dynamic corrections. These data are an enlarged window of the sub-seafloor P-SV reflectivity data shown in the lower-right of Figure 2.5. Note that even before dynamic moveout corrections, the P-SV events are nearly flat, so a limited-range stack before applying a dynamic moveout correction can provide a fairly good P-SV image. Depth-point-offset curves overlain on the P-SV reflectivity show that for our OBC data, which have a high V_P/V_S velocity ratio, any P-SV image trace of near-seafloor geology will extend only 1 or 2 m away from a receiver station.

Creating Continuous Images Along an OBC Profile

When these data-processing steps are followed at all receiver stations along an OBC profile, mini-scale P-P and P-SV images are created at each receiver station. Each mini-image represents the sub-seafloor image across a 25-m distance centered on a receiver station, which is the receiver-station

interval for the OBC data that we used in this study. We then combine these small-scale images to make continuous P-P and P-SV images that extend for several kilometers along each OBC profile. This concept is illustrated on Figure 2.9 for P-P imaging and in Figure 2.10 for P-SV imaging.

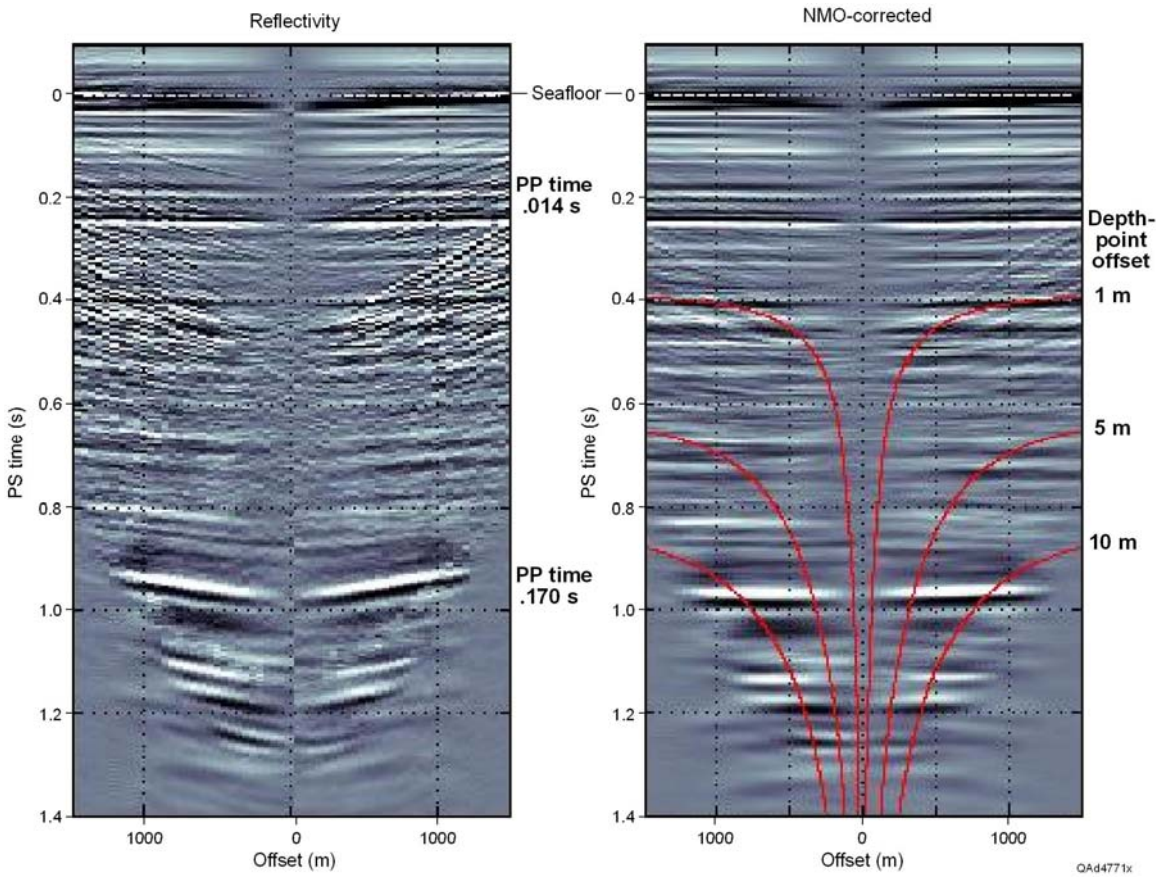

Figure 2.8. An expanded view of the P-SV reflectivity from Figure 2.5 (lower right) before and after dynamic moveout correction. A five-trace mix was applied on the right panel. 1-m, 5-m, and 10-m depth-point offset lines are shown in red on the right. P-P strong reflector times of .014 and .170 seconds are shown at depth-equivalent P-SV times of 0.25 and 0.98 seconds.

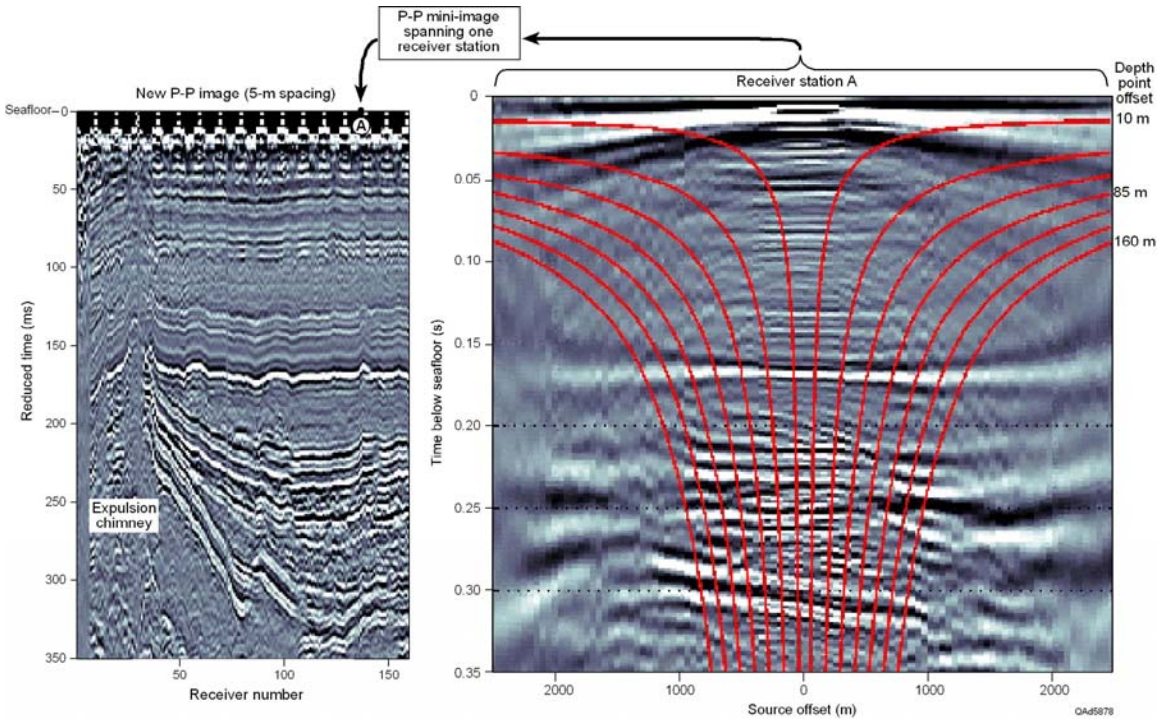

Figure 2.9. (left) A 4-km P-P near-seafloor image traversing Block GC204, Genesis area. (right) The imaging process that creates a local, five-trace, 25-m-wide, P-P image at receiver station A. This common-receiver P-P imaging process was done at 160 consecutive receiver stations along this OBC profile to create the 4-km image on the left.

The 4-km P-P image in Figure 2.9 is a series of small-scale, local P-P images constructed at each seafloor receiver station. Each local image is created by first calculating P-P reflectivity at each receiver station using Equation 2.6. The P-P reflectivity at one arbitrary seafloor station A is shown on the right of the figure. We then determine a sequence of constant-depth-point-offset traces across these P-P reflectivity data, such as a data trace along any of the red curves that overlay the P-P reflectivity. In this project, we arbitrarily decided to interpolate a P-P image trace at depth-point-offset intervals of 5 m. Five of these traces create a 25-m-wide P-P image centered on the receiver station. For the data on Figure 2.9, we created a five-trace, 25-m-wide, local image at 160 consecutive receiver stations to make the 4-km P-P image that is displayed.

This same scenario is repeated in Figure 2.10 for the P-SV reflectivity. The principal difference between P-SV imaging and P-P imaging is that the low V_S velocities in deep-water, near-seafloor strata do not allow constant-offset depth-point image traces to be calculated at distances farther than 1 or 2 m from each seafloor receiver station. As a result, we could not create a 25-m-wide P-SV image with 5-m trace spacing as we did with P-P data. Instead, we created a single, zero-offset P-SV image trace at each receiver coordinate by summing all the traces between the +1 m and -1 m depth-point-offset curves (Fig. 2.10). The

result was a P-SV image along each OBC profile that had a trace spacing of 25 m, the same distance as the receiver-to-receiver interval.

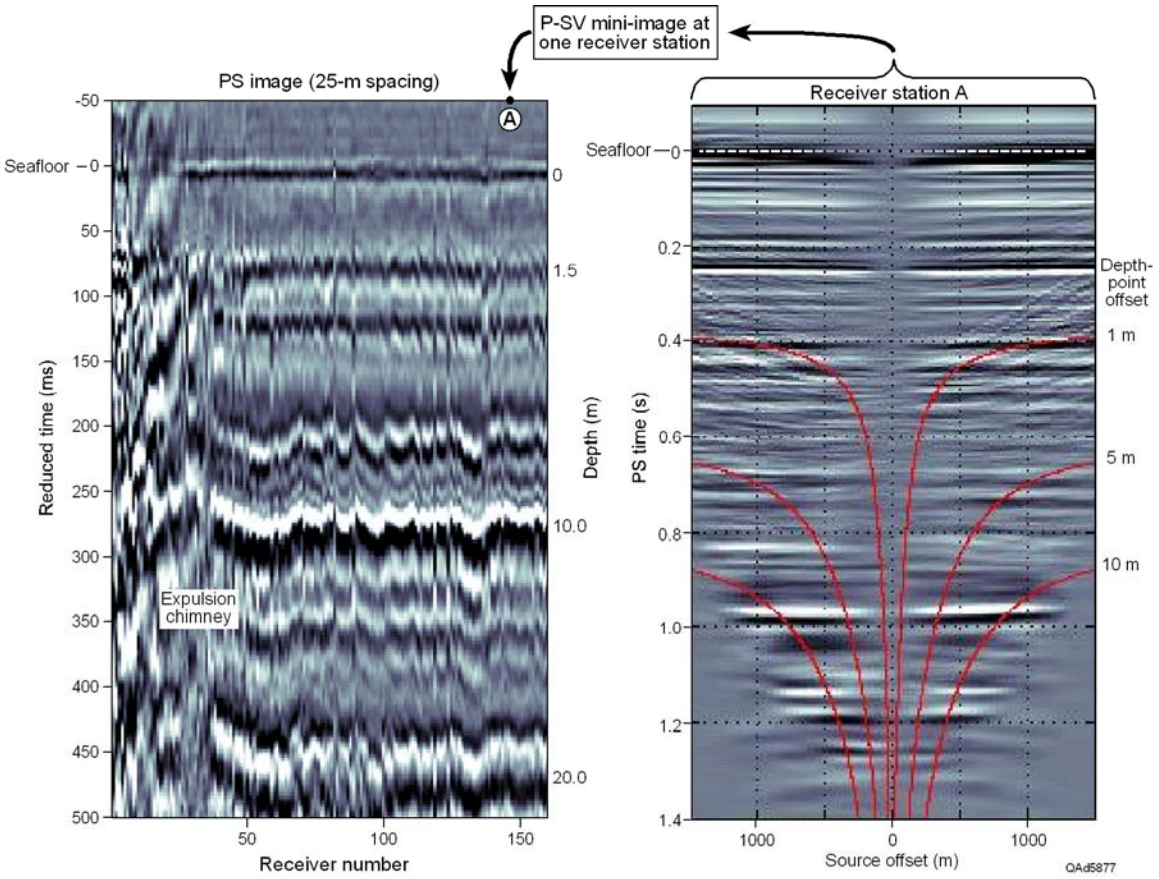

Figure 2.10. (Left) A 4-km P-SV near-seafloor image traversing the same OBC profile as the P-P data in Figure 2.9. Depths below the seafloor are labeled along the right margin. (Right) The imaging process that creates a local, one-trace, zero-offset, P-SV image at receiver station A. This single image trace is the sum of all of the traces between the +1 m and -1 m depth-point-offset curves. This common-receiver P-SV imaging process was done at 160 consecutive receiver stations along this OBC profile to create the 4-km image on the left.

Comparison with State-of-the-Art Imaging

In Figure 2.11 we compare a P-P section produced by state-of-the-art imaging done by a leading seismic contractor (left) with our P-P imaging technique that utilizes common-receiver gathers (right). The data are displayed with a seafloor datum. The ocean-floor multiple arrives at a time greater than the maximum time shown on this P-P section, which allows us to use our data-processing simplifications to produce this excellent quality image. The improvement in detail in our image compared with that of conventional processing is striking. In addition to improved vertical resolution, there is a marked increase in structural detail and horizontal resolution, even though the contractor data have been migrated and our data have not. Of special interest is the comparison on the far left of each image, especially above 100 ms, where

our image shows strata that dip sharply to the left, the same stratigraphic dip observed in the kilohertz-range P-P data that are exhibited in Figure 2.13.

In Figure 2.12 we compare a state-of-the-art P-SV section (produced by the same leading contractor that made the P-P image in Figure 2.11) with our processing approach that is based on common-receiver gathers. We see that our technique provides significant data-quality improvement close to the seafloor. Note the strong P-SV reflection at a shallow depth of 1.5 m that parallels the seafloor. The strong reflection at a sub-seafloor depth of 10 m is at the center of a sedimentary package that is unconformable with the seafloor. Note also an obvious unconformity boundary at 150 ms that is revealed by the simple processing used in our imaging technique.

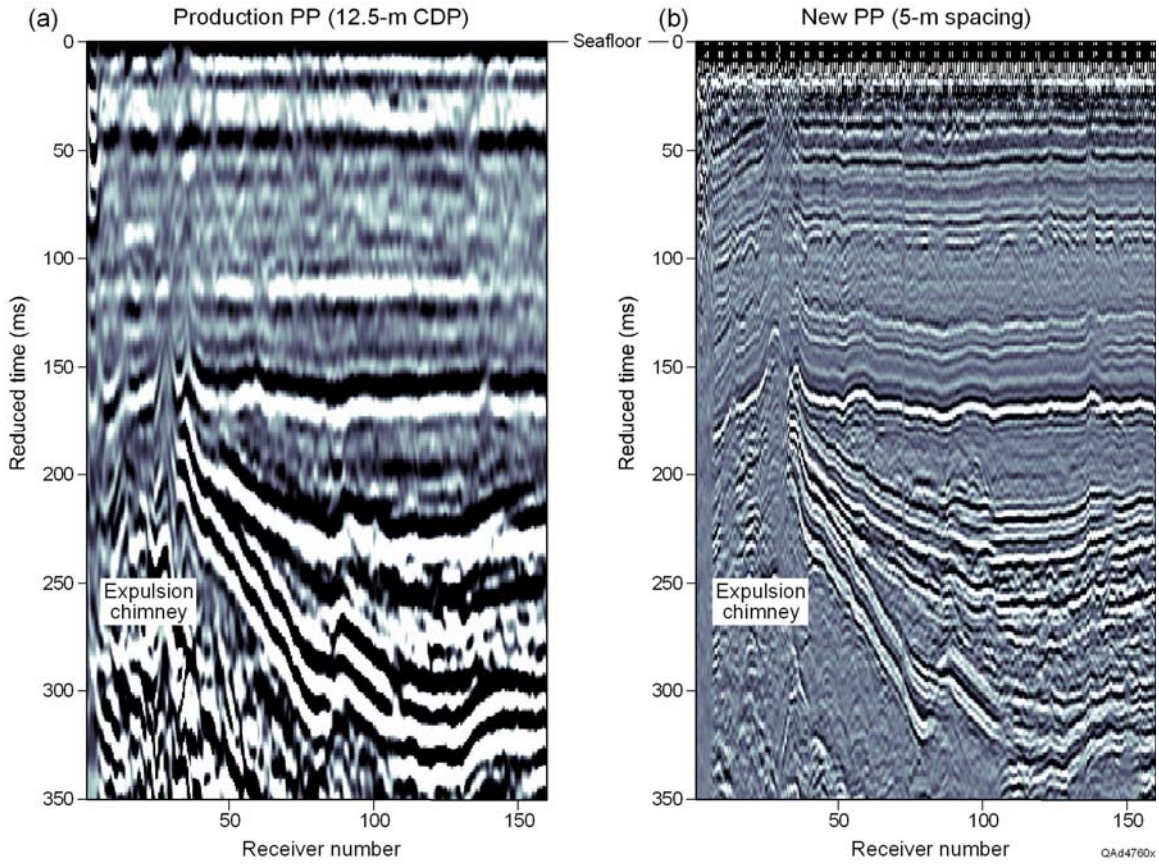

Figure 2.11. (a) Standard P-P production processing of deep-water 4-C OBC seismic data across Block GC204, genesis Field area. (b) Improved P-P resolution of near-seafloor geology using our simplified processing approach. Both images are flattened to the seafloor, and both approximate the time derivative of P-P reflectivity. The expulsion chimney at the left side of each image allows deep, thermally generated gases to migrate upward into near-seafloor strata to form hydrates. Water depths along the profile are approximately 850 m. Note the differences in trace spacing, 12.5 m in (a) and 5 m in (b). For the horizontal scale, an interval of 100 receiver numbers spans 2.5 km.

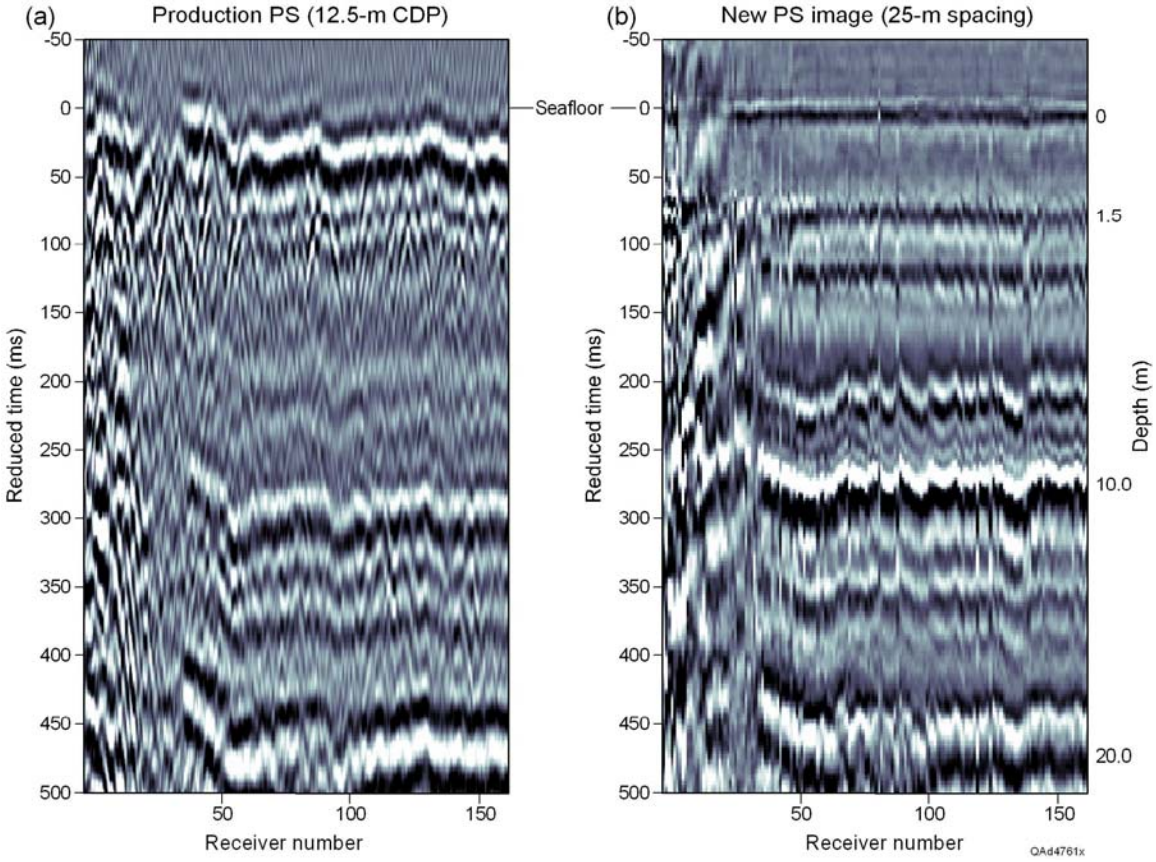

Figure 2.12. (a) Standard P-SV production processing of deep-water 4-C OBC seismic data by a leading contractor. (b) Improved P-SV resolution of near-seafloor geology using our simplified processing approach. Both images are flattened to the seafloor. This figure shows data to a depth of about 20 m below the seafloor, or to about 30 ms below the seafloor in Figure 2.11. An approximate sub-seafloor depth scale is shown on the right. Note the sequence of reflectors parallel to the seafloor extending down to about 150 ms, where an unconformable sequence of reflectors then begins. This unconformity represents the base of the hemipelagic zone (Harry Roberts, Louisiana State University, private communication). This display shows the remarkable vertical resolution available with P-SV data recorded by OBC systems. With the 25-m OBC receiver spacing in this survey, we are limited to 25-m horizontal sampling for the shallow section because of the low shear-wave speed in the upper few tens of meters of sediment. An interval of 100 receiver numbers spans 2.5 km.

What we consider amazing is the resolution of the P-SV images produced by our imaging technique. To illustrate this resolution, we compare, in Figure 2.13, our air-gun-frequency (10–200 Hz) P-SV image with a high-frequency (2–10 kHz) P-P image acquired by deep-water **Autonomous Underwater Vehicle** (**AUV**) technology. Depth-equivalent P-P and P-SV horizons are identified on the images. These images show that the frequency of P-P data has to be increased into the kilohertz range for P-P data to have a spatial resolution that is equal to

that of low-frequency P-SV data. This observation confirms the simple principle that in order for P-P data and P-SV data to have equivalent resolution, they must have equivalent spatial wavelengths. This requirement leads to the simple conclusion that if

(2.8) $\lambda_P = \lambda_S$,

where λ is wavelength and subscripts **p** and **s** refer, respectively, to P-wave and S-wave, then the frequencies (**f**) must be related as,

(2.9) $f_P = (V_P/V_S)f_S$.

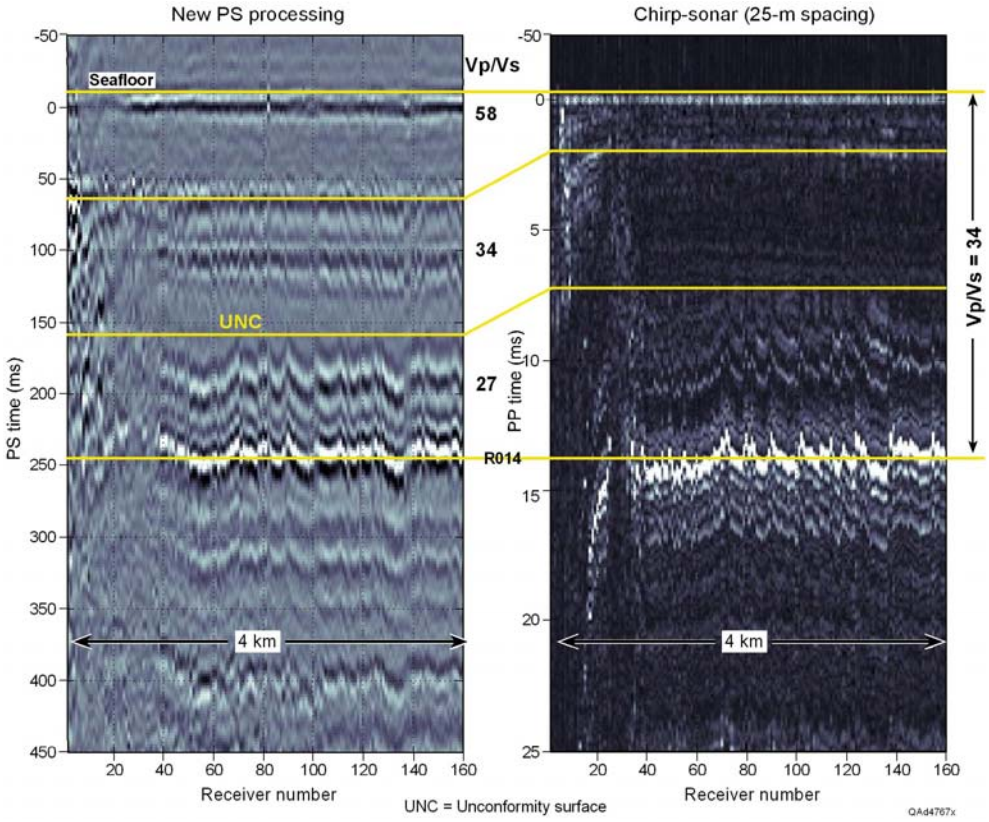

Figure 2.13. Comparison of high-resolution P-P imagery obtained from a near-seafloor chirp-sonar AUV system (right), resampled to 25-m horizontal spacing, with our OBC P-SV image (left), which has 25-m trace spacing. The OBC P-SV data provide vertical resolution comparable to the 2–10 kHz AUV chirp-sonar system over the upper 20 m of sediment. Note that the relative strength of P-P and P-SV events is quite different, but the detailed structural configuration in both images is almost the same. This detailed structural correspondence between P-P and P-SV serves as an excellent basis for depth registering P-P and P-SV sections near the seafloor. At this near-seafloor level, OBC P-P data lack the resolution to make the interpretation of the event labeled R014 that is emphasized in this low-gain AUV display. The Vp/Vs ratio (listed between the images) for the 10-m layer from seafloor to R014 is 34. Internal to this layer, the ratio decreases from 58 to 27, as shown. Horizon **UNC** is an unconformity surface. The AUV horizon at 2 ms is faint at this display gain but is prominent at higher gain.

This wave physics requires P-P frequency to be boosted by an amount equal to V_P/V_S relative to P-SV frequency in order for P-P data to have the same wavelength spectrum as P-SV data. In the near-seafloor strata across our study area, V_P/V_S can exceed 55 (Fig. 2.13, top layer), which requires that P-P frequency be boosted into the kilohertz range to match the resolution that we achieve with 10 to 200 Hz P-SV data using our data-processing strategy. It appears that the significance of this high-resolution imaging is what caused the Society of Explorationists to name our paper that describes this seismic imaging strategy (Backus and others, 2006) as *Best Paper* in *The Leading Edge*.

Comparison with VSP Imaging

Our data processing of a 4C OBC common-receiver gather is similar to the processing of walkaway vertical seismic profile (VSP) data, where high-resolution reflection images are created in the immediate vicinity of the VSP vertical receiver array. In a VSP, we rarely have a hydrophone at the downhole receiver stations. Instead, separation of up- and down-traveling waves is accomplished by processing data acquired with a vertical array of 3C geophones. The use of the down-traveling wave as the wavelet for the VSP deconvolution process is analogous to the approach we use to determine reflectivity (Eqs. 2.6 and 2.7). Our approach to the recovery of a set of image traces at fixed offsets from a seafloor receiver station is also similar to the traditional VSP-to-CDP transform used to image offset VSP sources. In either case (deep-water OBC data or deep-well VSP data), there is a large difference between the lengths of the raypath from source to target and the raypath from target to receiver. For those knowledgeable in VSP data processing, particularly the processing of walkaway VSP data, these comments may be helpful in understanding the OBC data-processing approach we use. Unfortunately, in VSP applications there is not a line of wells at 25-m intervals along a profile like we have with the deep-water seafloor receivers stationed along the OBC profiles that traverse our study area.

Receiver Calibration

Construction of downgoing and upgoing wavefields is a key step in our strategy for making P-P and P-SV images of deep-water, near-seafloor geology. To construct these downgoing and upgoing modes, data acquired by hydrophone and geophone sensors have to be combined, as defined in Equations 2.3 through 2.5. If the responses of the hydrophone, vertical geophone, and horizontal geophones are not calibrated to one another, data recorded by these sensors may not combine to create optimal-quality definitions of downgoing and upgoing wavefields.

We show as Figure 2.14 an example of a common-hydrophone trace gather in which source offsets extend to 8 km. These data are shown in a **reduced-time** format in which the downgoing P-wave first arrival is defined as

time zero for all data traces. Shown on the figure are two data windows labeled "*Early arrivals*" and "*Near-trace stack*". These data windows are used to calculate sensor-to-sensor calibration operators that can be utilized to optimize the quality of the separated downgoing and upgoing wavefields.

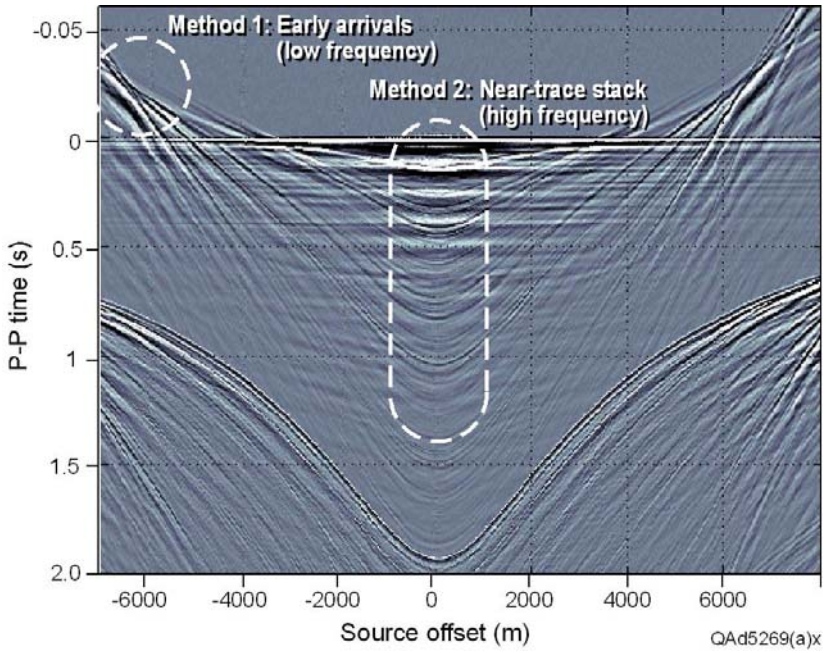

Figure 2.14. The two data windows, *large-offset early arrivals* and *small-offset reflections*, used to calculate sensor-to-sensor calibration operators.

It is important that the long-offset geometry involved in the 4C data acquisition along our OBC study lines produced early-arrival events like those noted in Figure 2.14. These events are combinations of upgoing wide-angle reflections, head waves, and diving waves (Fig. 2.15) that are ideal for calculating sensor-to-sensor calibration operators because they are not contaminated by any downgoing events. In this discussion, we illustrate sensor-to-sensor calibration operators determined from these early-arrival data.

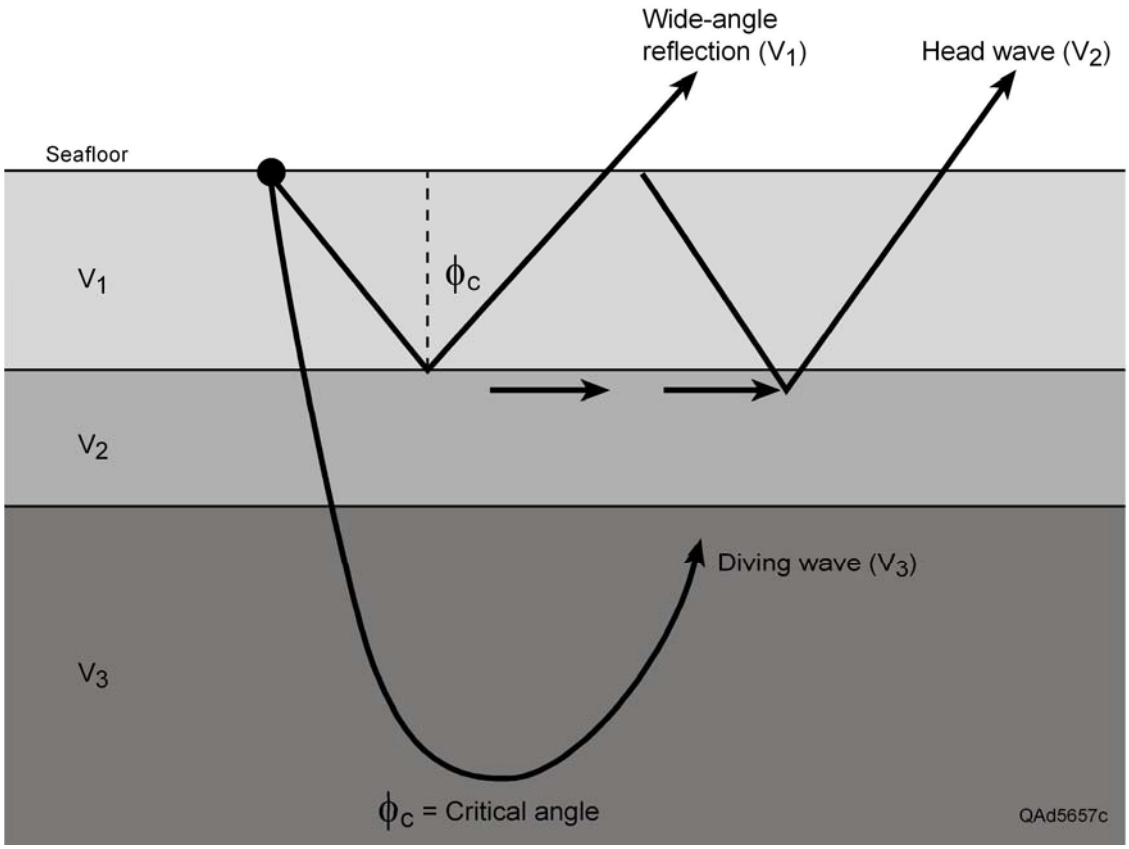

Figure 2.15. The early-arrival events labeled in Figure 2.14 consist of upgoing (1) wide-angle reflections, (2) head waves, and (3) diving waves.

Equalizing Hydrophone and Vertical-Geophone Data

Wide-angle data windows from the common-hydrophone trace gather displayed on Figure 2.14 are shown in the left two panels of Figure 2.16. The top-center panel shows the hydrophone response estimated from the early-arrival wavefield recorded by the vertical geophone (Z) at this seafloor receiver station. The bottom-center panel shows the hydrophone response calculated from the early-arrival wavefield recorded by the inline horizontal-geophone (X). The panels on the right illustrate the difference between the hydrophone data and each of the hydrophone responses estimated from the respective geophone sensor. The differences between the real hydrophone data and each of the estimated hydrophone data are approximately zero (right panels), confirming that sensor-to-sensor calibration operators calculated from full-wavefield early arrivals do a reasonable job of converting one sensor response to its companion-sensor response.

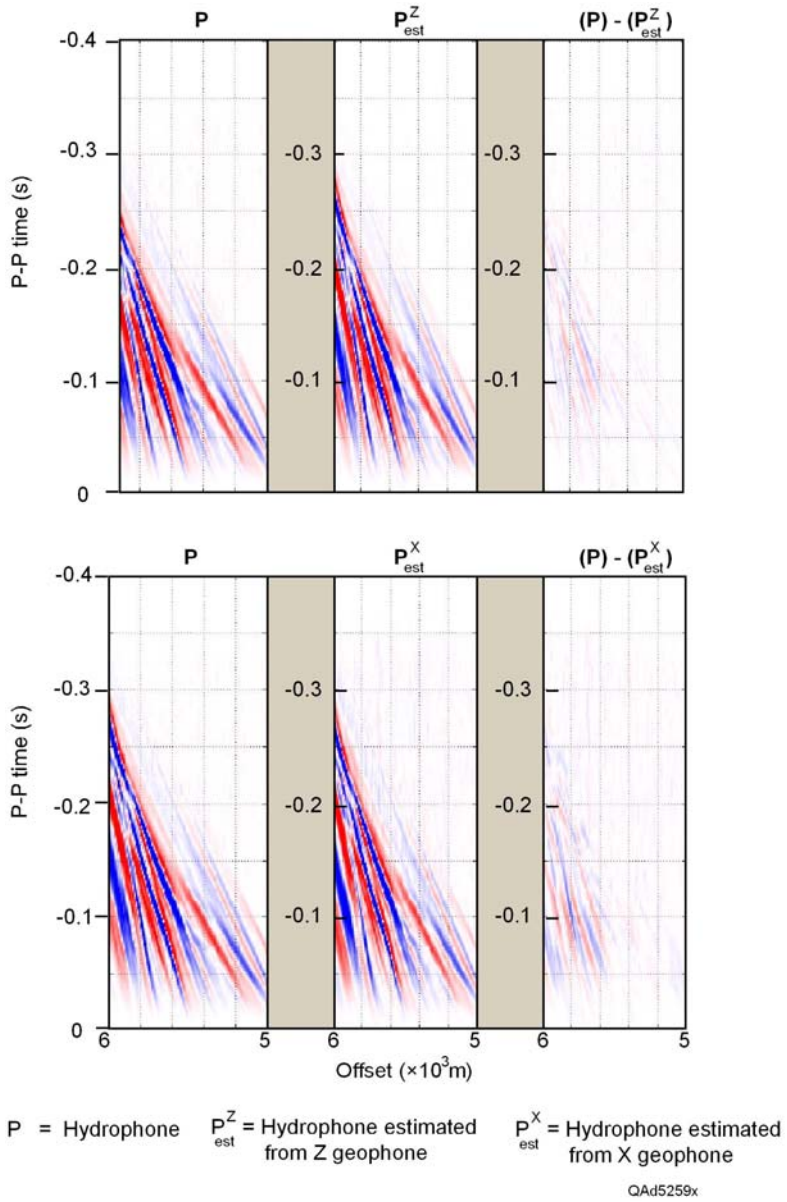

Figure 2.16. (Left) Early-arrival wavefields used to calculate sensor-to-sensor calibration operators. These data windows are the wavefields labeled "*Early-arrival events*" on Figure 2.14 that extend above the T = 0 time datum; hence the time coordinates used here are negative. These displays show that operators determined from these upgoing wavefields can convert either vertical-geophone data (top center) or inline horizontal-geophone data (bottom center) to hydrophone data.

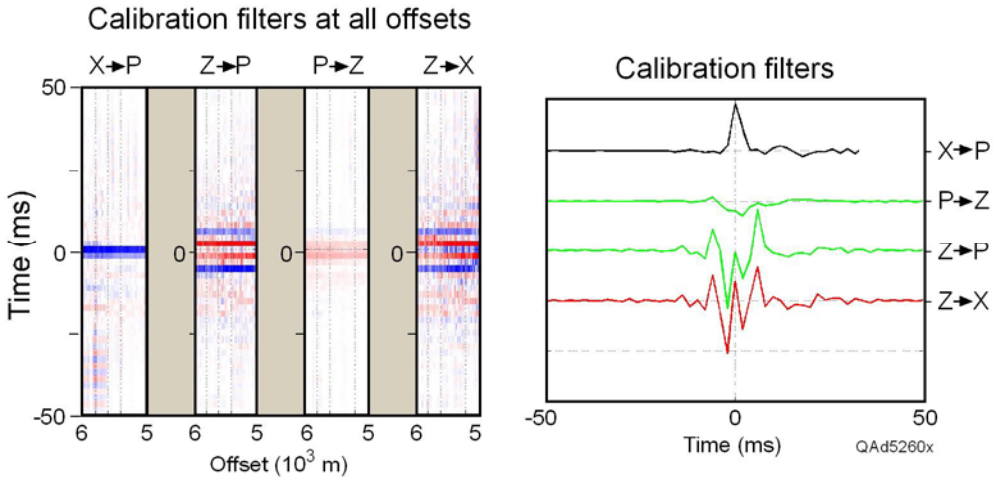

Figure 2.17. Examples of operators determined from early-arrival events that allow hydrophone (P), vertical-geophone (Z), and horizontal inline-geophone (X) data to be transformed from one sensor response to the other. In this notation, the term to the left of an arrow identifies the input-sensor response, and the term to the right of each arrow defines the output-sensor (or estimated) response. (Left) Operators are independent of offset. The offset range used in this display is the same as the offset range displayed in Figure 2.16. (Right) Expanded views of operators calculated at one specific source offset.

Examples of sensor-to-sensor calibration operators calculated at different source-to-receiver offsets for this common-receiver gather are plotted in Figure 2.17. An important finding illustrated on this figure is that these operators are independent of source-to-receiver offset, as demonstrated by the consistency of the operators in the offset-dependent data panels on the left. Consequently, a single sensor-calibration operator can be used for the complete offset range of each common-receiver gather, which simplifies the wavefield separation process.

In Figure 2.18 we show the averaged cross-equalization filters (or sensor calibration operators) that were determined for the hydrophone and vertical geophone along a test OBC line. The top panel shows the impulse responses of the operators. The bottom panel illustrates the frequency responses. The curve labeled "**Coher**" is the product of the two filter functions and represents the frequency response of one sensor (either P or Z) when the data are filtered with the appropriate calibration filter (either a P-to-Z filter or a Z-to-P filter). A value of 1.0 for this "Coher" curve indicates the frequency range over which a reliable sensor-to-sensor calibration should be achieved. In this example, the sensor calibration is limited to approximately 70 Hz because the early-arrival events used in the calibration procedure were deep, lower-frequency events that had minimal signal response above 70 Hz.

We expand the frequency range over which we can produce calibrated-sensor data by calculating additional sensor-calibration filters from isolated high-frequency reflections in the "*Near-trace stack*" data window identified on Figure 2.14. When we repeat this sensor-calibration process using near-trace reflection data, the sensor calibration can be extended to frequencies well above 100 Hz (often to 150 Hz).

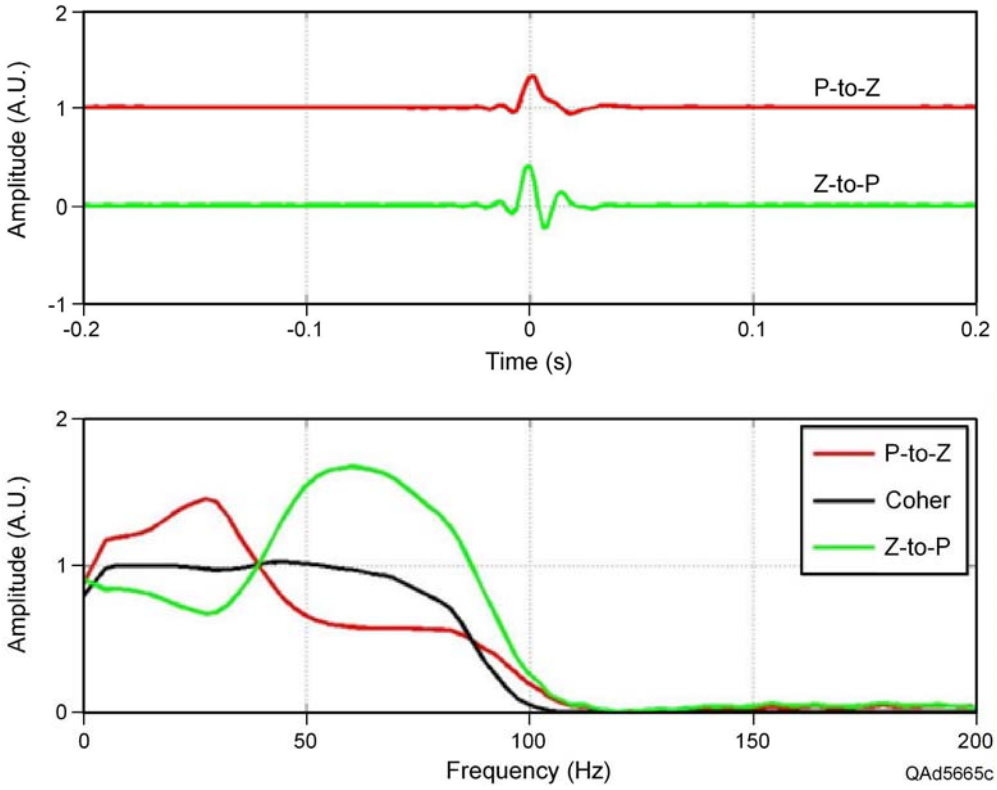

Figure 2.18. Averaged cross-equalization filters (or sensor-calibration operators) determined along a selected OBC line for hydrophones (P) and vertical geophones (Z). The frequency range over which the filters are valid is the portion of curve **Coher** that has a value of 1.0.

Equalizing Hydrophone and Horizontal-Geophone Data

We did this same type of cross-equalization procedure to equalize the responses of the hydrophone and horizontal-geophone data. The averaged cross-equalization filters calculated for this same OBC profile are displayed as Figure 2.19. These X-to-P and P-to-X filters are almost identical and apply smaller adjustments to the data than do the P and Z filters exhibited in Figure 2.18.

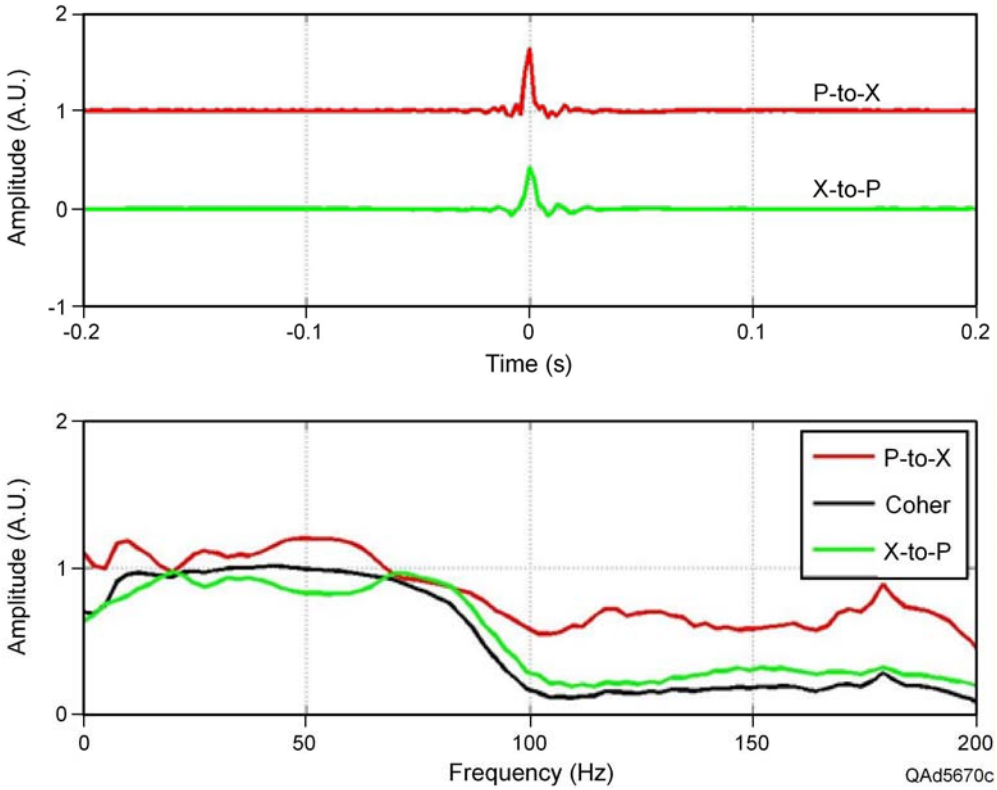

Figure 2.19. Averaged cross-equalization filters determined for the hydrophone (P) data and radial horizontal-geophone (X) data along the same OBC profile analyzed in Figure 2.18. A **Coher** value of 1.0 indicates the frequency range over which valid sensor calibration should occur.

These horizontal-geophone filters are not as effective as the filters determined for the vertical geophone. Our tests to date lead us to the conclusion that the effectiveness of P and X sensor-calibration operators is less than that of P and Z operators by about 6 dB (a factor of 4). The amplitude of the estimation error for P and X calibration filters tends to be about 15 dB (a factor of 32) below the amplitude of the input data, which is not precise estimation. Even so, the quality of the separated SV wavefield produced from Equation 2.3 is improved when we use calibrated P and X sensor data.

Calibrated vs. Uncalibrated Data

How important is it that hydrophone (P), vertical-geophone (Z), and horizontal-geophone (X) sensors be calibrated before P, Z, and X wavefields are combined to create downgoing and upgoing P-P and P-SV wavefields? Many OBC data processors who concentrate on deep geologic targets, not on near-seafloor geology, ignore sensor calibration and simply add and subtract P, Z, and X wavefields using time-invariant scaling factors. When 4C OBC data are acquired with long offsets, as are the data used in this study, P-P and P-SV images can be made with either calibrated-sensor or uncalibrated-sensor data,

which allowed us to determine the value of each imaging strategy. Portions of the P-P image along one OBC test line are illustrated in Figure 2.20. The top displays illustrate geology that extends to only 200 ms below the seafloor. The bottom displays focus on the geology that is between 200 and 500 ms below the seafloor.

These images show that sensor calibration improves P-P imaging only for the shallowest geology that extends to approximately 50 ms below the seafloor. For targets deeper than 50 ms, calibrated-sensor data and uncalibrated-sensor data produce equivalent images. However, we have also found that the improvement in P-P imaging across this shallow window immediately below the seafloor is important for accurate depth registration of P-P and P-SV images in near-seafloor geologic studies. Previously we have had to use high-frequency (2 to 10 kHz) chirp-sonar data acquired with deep-running Autonomous Underwater Vehicle (AUV) technology to achieve P-P imaging of geology within 50 ms of the seafloor (Fig. 2.13). With sensor-calibrated P and Z data, we now achieve some ability to image within this 50-ms interval with P-P images constructed from air-gun-source OBC data. This improvement in the shallowest portion of the P-P image is a major technology advance for studying deep-water hydrate systems.

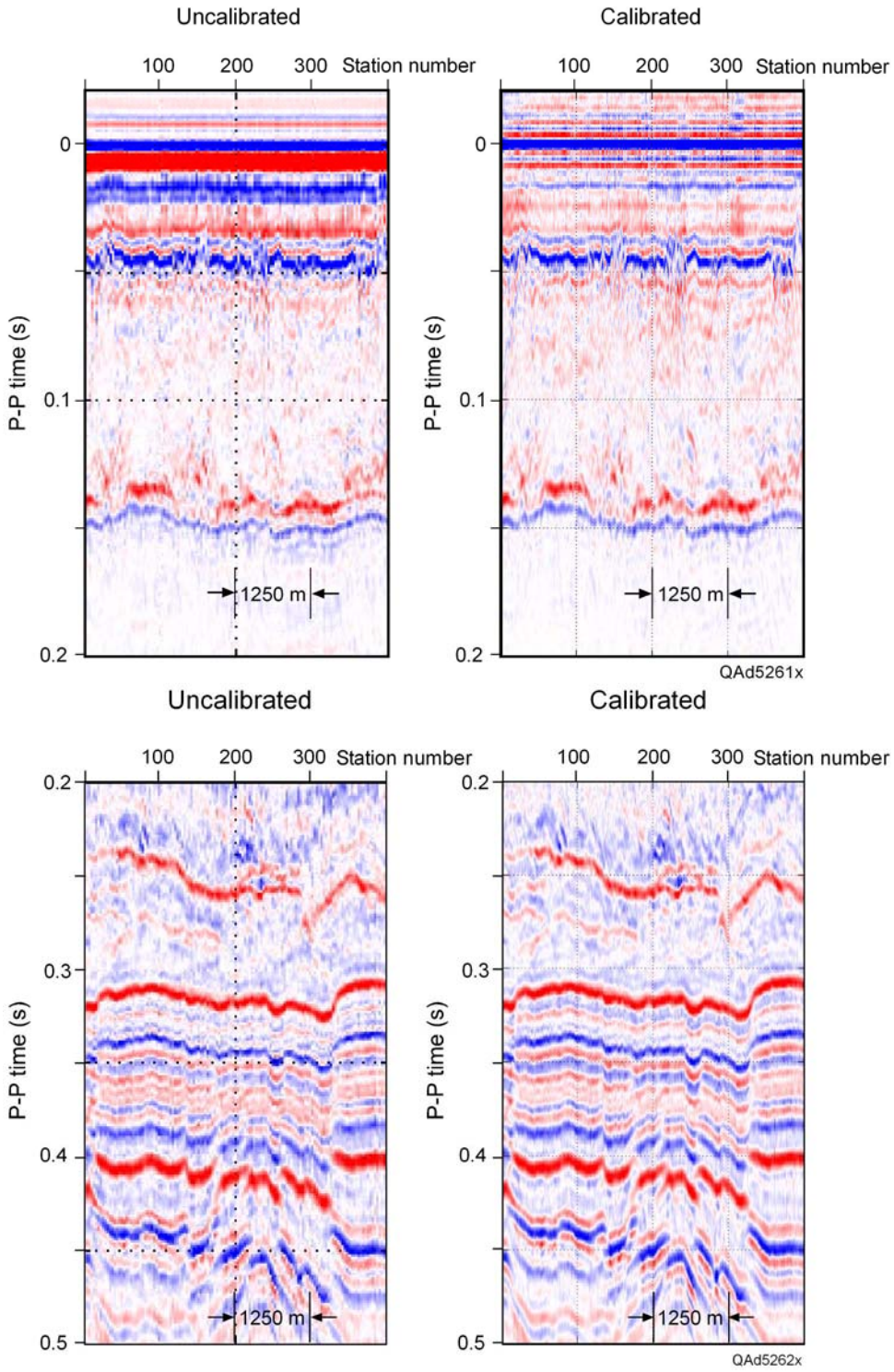

Figure 2.20. Comparisons of P-P images made with (right) and without (left) calibrated P and Z sensors. Calibrated data produce a superior image of the shallowest geology (top 50 ms, upper right). There are no significant differences between the calibrated-sensor and uncalibrated-sensor images at deeper depths (bottom displays). The improved P-P image in the first 50 ms of image space is important for P-P to P-SV image registration when studying geology immediately below the seafloor.

Conclusions

We emphasize that our seismic data-processing methodology is specialized for optimal imaging of deep-water, near-seafloor geology. Because our imaging procedure is to treat a seafloor-receiver trace gather as a walkaway vertical seismic profile (WVSP), there needs to be a significant vertical distance between the surface-based source and the seafloor receiver. We have not applied our data-processing strategy to 4C OBC data acquired in water depths less than 450 meters and do not know the minimum water depth where our data-processing technique begins to produce unacceptable results. As stated in the introduction to this chapter, we arbitrarily set 200 m as the minimum water depth where we think our data-processing procedure should be used. This water depth limitation will not be a factor in applying our data-processing methodology to hydrate systems across the Gulf of Mexico.

We do not champion the use of our data-processing technique for imaging geology at significant depths (≥1000 m) below the seafloor. Although our data-processing concepts should produce acceptable-quality images of geology at sub-seafloor depths of 1000 m and more, our procedure appears to have no advantage for imaging deep geology over that provided by the procedures used across the seismic data-processing industry. The decades-old **common-midpoint** (**CMP**) procedures used in the industry are superb for creating P-P images of deep geology. The **common-conversion-point** (**CCP**) binning/imaging techniques used by commercial seismic data-processing shops for generating P-SV images is also an excellent method for imaging deep geology.

One limitation of our current data-processing method is that we make no attempt to remove water-column multiples from the data. Once these multiples begin to appear in the data, there is often a significant reduction in the signal-to-noise ratio and less-accurate imaging. Because the water depth ranged from 500 m to 1000 m along the OBC profiles that we analyzed, water-column multiples do not appear in the data until the image extends below the base of the hydrate stability zone. We can expand our data-processing procedure to attenuate water-column multiples, but we do not see the need to do so at this time.

We show in this chapter that our data-processing strategy was to create the equivalent of a WVSP P-P image and a WVSP P-SV image at each receiver station and then combine these local VSP-type images to create continuous P-P and P-SV images along each OBC profile. An immense amount of work was involved in this data-processing effort. More than 200 km of OBC data had to be processed. These profiles spanned approximately 8,640 receiver stations (25-m station spacing), meaning that we had to produce 8,640 P-P WVSP images and 8,640 P-SV WVSP images to complete our study. One way to describe the challenge and magnitude of our data-processing effort is to recognize that a major VSP data-processing contractor (say Schlumberger or VSFusion) will make no more than 50 WVSP images in a year. Our data-processing task was thus a 100X greater data-processing effort than that done by any VSP contractor during the project period.

DOE Gas Hydrate Final Report

Chapter 3

Near-Seafloor Sediments and Seismic Velocities

Introduction

Our goal of rock physics modeling of marine hydrate systems was to infer hydrate concentration in seafloor sediment from seismic measurements. Many published relations between hydrate concentration and seismic attributes are empirical (Pearson and others, 1983; Miller and others, 1991; Wood and others, 1994; Holbrook and others, 1996; Lee and others, 1996; Yuan and others, 1996; Collett, 1998; Lu and McMechan, 2002, 2004). Empirical approaches are easy to implement, but they do not have predictive power and should be used only at the specific site where the relationships are derived. An additional shortcoming is that empirical relations do not provide insights into the morphological character of how gas hydrates are distributed within sediments.

There are studies that use physics-based, effective-medium models of hydrate systems to relate hydrate concentration to seismic properties (Helgerud and others, 1999; Ecker and others, 2000; Carcione and Tinivella, 2000; Chand and others, 2004; Winters and others, 2004; Waite and others, 2004; Kleinberg and Dai, 2005; Murray and others, 2006). Some of these effective-medium models are based on Dvorkin and Nur's (1996) model of unconsolidated sediments, which uses Hertz-Mindlin's theory (Mindlin, 1949; Mavko and others, 1998). These models are appropriate for deep marine sediments (>300 mbsf), but they do not explain lab observations and in-situ observations made within the first 200 meters below the seafloor where sediments have small shear strengths, large V_P/V_S ratio, and low effective pressure.

There is a need for improved rock physics models that can characterize seismic velocity behavior in unconsolidated sediments within deep-water, near-seafloor strata where hydrates may be present. Rock physics models are also needed to aid in understanding how hydrates are distributed relative to their host sediments. Numerous questions about hydrate-sediment morphology have to be considered. Are the hydrates disseminated as part of the load-bearing frame? Do the hydrates fill the pores of the sediments without affecting the mineral frame? Are the hydrates present as layered bodies? Do the hydrates occur as nodules and veins? Rock physics properties are different for each of these hydrate-sediment morphologies.

In this chapter, we present rock physics models for unconsolidated sediments in which hydrates are assumed to be present in the following geometrical occurrences: ***a***) disseminated, load-bearing clathrates that are part of the mineral frame of the host sediments; ***b***) pore-filling clathrates that float in

the porous space without changing the dry mineral frame of the host sediments; ***c***) thin horizontal or vertical layers of pure hydrates intercalated with layers of hydrate-free sediments saturated with fluid; and ***d***) thin horizontal layers of disseminated, load-bearing hydrates intercalated with layers of hydrate-free sediments saturated with fluid.

Our objective was to understand the relationships between hydrate concentrations and V_P and V_S seismic velocities for these four scenarios of possible hydrate-sediment morphology. We also simulated the behavior of seismic reflection amplitude as a function of angle of incidence (AVA modeling) for P-P and P-SV reflections at the interface separating the base of the hydrate stability zone and deeper sediments that contain free gas. For aligned vertical layers of pure hydrate (fracture-filling hydrate), we modeled P-P and P-SV amplitude variation with incidence angle and also with azimuth because this type of medium has azimuthal variability in V_P and V_S velocities. We emphasize the importance of analyzing azimuthal variations of P-P and P-SV seismic amplitudes to identify and quantify this type of hydrate distribution (vertical hydrate-filled fractures); however, azimuthal data analysis could not be done with our 4C data because the data were acquired only as 2D profiles.

We found that the geometrical details of how hydrates are distributed within sediments have a significant impact on the relationships between hydrate concentration and seismic velocities. Our research finding shows that to produce estimates of hydrate concentrations from seismic data, we need to understand how hydrates are distributed within their host sediments. Our modeling results for the two, thin-layered, hydrate-sediment morphologies (cases **c** and **d** listed in the preceding paragraph) show significant S-wave anisotropies. These S-wave-splitting effects can be used to infer hydrate distribution and concentration in near-seafloor environments that have alternating thin layers of hydrate-bearing and hydrate-free sediments, aligned either horizontal or vertical, if multicomponent seismic data are acquired. Due to time constraints, we were not able to perform S-wave splitting analysis. This research needs to be done in a follow-up project.

Rock Physics Model for Unconsolidated Sediments

Newly deposited sediments at the bottom of the ocean are in a pseudo-suspension regime and their shear strength is almost zero near the seafloor. The V_P/V_S velocity ratio is large within the first few meters of sediment and tends to infinity at the boundary between ocean-bottom sediments and the water column. Effective pressure is zero at the seafloor and increases slowly with depth. Any rock physics theory used to describe a near-seafloor seismic propagation medium in the GOM must account for these unique physical properties: low shear strength, large V_P/V_S velocity ratios, and near-zero effective pressure.

Most rock physics models for unconsolidated sediments use contact models, such as Hertz-Mindlin's theory (Mindlin, 1949), to describe the elastic properties of granular materials. The porosity at which a granular composite

ceases to be a suspension and becomes grain-supported is called the **critical porosity**. Dvorkin and Nur (1996) assume that at critical porosity the effective elastic moduli of the dry-mineral frame of sediments can be calculated using Hertz-Mindlin's contact theory for elastic particles. For porosity values smaller than critical porosity, the elastic properties of the dry-mineral frame are estimated using the modified **Hashin-Shtrikman Lower Bound** (Hashin and Shtrikman, 1963). For porosity values larger than critical porosity, Dvorkin and others (1999) propose to use a modified **Hashin-Shtrikman Upper Bound** to derive the elastic properties of the dry-mineral frame of granular materials. Gassmann's (1951) theory is then used to derive the elastic properties of the sediments when they are saturated with fluids.

These modeling assumptions have been applied to marine sediments in various areas around the globe (Prasad and Dvorkin, 2001). However, Hertz-Mindlin's theory is not appropriate for sediments within the first 100 or 200 meters below the seafloor where S-wave velocity is quite small, and implicitly the V_P/V_S ratio is large, as in-situ observations from 4C OBC data suggest (Backus and others, 2006; Hardage and others, 2007). For this type of environment, Hertz-Mindlin theory will predict V_S velocities that are too high. S-wave velocities have also been observed in laboratory measurements on unconsolidated sediments (e.g. Zimmer, 2003; Yun and others, 2005) which are significantly lower than V_S values predicted by Hertz-Mindlin's theory. The main reason for the discrepancy between S-wave velocity measurements and Hertz-Mindlin theory is that the Hertz-Mindlin model overestimates the shear modulus for granular composites. Hertz-Mindlin theory assumes infinite friction at grain contacts and does not allow grain rotation nor slip at grain boundaries, which are physical processes that occur between unconsolidated grains, especially at the low effective pressures encountered near a deep-water seafloor. We propose a new model that is based on the initial approach of Dvorkin and Nur (1996) and Dvorkin and others (1999), but we use the distinction that at critical porosity the elastic properties of deep-water, near-seafloor sediments are described by **Walton contact theory** (Walton, 1987), not by Hertz-Mindlin theory. Walton's model allows grain rotation and grain slippage. However, Walton's model, like other contact models (Digby, 1981; Mavko and others, 1998), assumes that the granular material is made up of an aggregate of perfect spheres, which is not an optimal description of clay minerals found in many deep-water near-seafloor strata in the GOM.

Hertz-Mindlin Theory

To illustrate the difference between Hertz-Mindlin and Walton models, we note that the elastic moduli of a granular material derived using Hertz and Mindlin's solutions for the strain displacement of two identical spheres in contact under normal and shear forces are (Mavko and others, 1998):

$$K_{eff} = \frac{C(1-\phi)}{12\pi R} S_n,$$
$$G_{eff} = \frac{C(1-\phi)}{20\pi R}(S_n + 1.5S_\tau). \quad (3.1)$$

K_{eff} and G_{eff} are the effective **bulk** and **shear moduli**, respectively, for the granular material. C is the **coordination number**, which represents the average number of contacts between a grain and its neighboring grains. Φ is the **porosity** of the aggregate of spheres, and R is the **radius** of the identical spheres representing the grains. S_n and S_τ are the **normal** and **tangential stiffnesses**, respectively, of two grains in contact and depend on effective pressure, radius of contact of the two grains, and elastic bulk and shear moduli of the grain mineral. In terms of effective pressure, the standard Hertz-Mindlin's expressions for the effective bulk and shear moduli are:

$$K_{eff} = \sqrt[3]{\frac{C^2(1-\phi)^2 G^2}{18\pi^2(1-\nu)^2} P},$$
$$G_{eff} = \frac{5-4\nu}{5(2-\nu)} \sqrt[3]{\frac{3C^2(1-\phi)^2 G^2}{2\pi^2(1-\nu)^2} P}. \quad (3.2)$$

G and ν are the **shear modulus** and **Poisson's ratio**, respectively, for the mineral grains and P is the **effective pressure**. The basis of the Hertz-Mindlin model is the assumption that the ***friction between grains is infinite***. Although contacting grains distort, they do not move relative their point of contact.

Walton Model

Walton (1987) derived a model that assumes there is no friction between contacting grains, referred to as a "**smooth model**". The physical meaning of this model is that ***grains are allowed to rotate and slip at their contact boundaries***. This assumption reduces the effective shear strength of a granular material in contrast with the Hertz-Mindlin's assumption that there is infinite friction between the grains. Mathematically, Walton's model sets the tangential stiffness (S_τ) between two grains in contact to zero in the standard Hertz-Mindlin's expressions in Equation 3.1, which causes the effective shear modulus (G_{eff}) to be reduced to 60-percent of the bulk modulus. The expressions for the bulk and shear moduli for a random arrangement of dry spheres using Walton's approach are:

$$K_{eff} = \sqrt[3]{\frac{C^2(1-\phi)^2 G^2}{18\pi^2(1-\upsilon)^2} P},$$

(3.3)

$$G_{eff} = \frac{3}{5} K_{eff}.$$

If we compare Equations 3.2 and 3.3, we observe that the effective shear modulus for Walton's smooth model is smaller than that of Hertz-Mindlin's model. The ratio between the two shear moduli is the following simple function of the Poisson's ratio of the grain mineral:

$$G_{eff}^{Walton} = \frac{2-\nu}{5-4\nu} G_{eff}^{Hertz-Mindlin} \quad . \tag{3.4}$$

In the case of quartz grains that have a Poisson's ratio of 0.08 (Mavko and others, 1998), the effective shear modulus given by Walton's expression is only 41 percent of the effective shear modulus predicted by Hertz-Mindlin's theory. Therefore, Walton's model predicts a shear velocity that is approximately 0.64 of the shear velocity predicted by Hertz-Mindlin's model for granular materials with quartz grains.

Walton's model is particularly appropriate for unconsolidated sediments at low effective pressure where grain rotation and slip along grain boundaries are most likely to occur. Walton's model is a better explanation of the low shear strengths and high V_P/V_S ratios observed in 4C OBC seismic data acquired across deep-water, near-seafloor strata, and in laboratory measurements made on unconsolidated sediments, than is the Hertz-Mindlin model.

Methodology

We calculate the elastic properties of unconsolidated deep-water granular materials over a large porosity range using the following five steps:

1. Compute the bulk and shear moduli of the dry mineral frame at *critical porosity* using Walton's theory (Equation 3.3). If the solid grains are a mixed mineralogy, then the bulk modulus and shear modulus (*K* and *G*) of the composite material can be computed from the moduli of the individual mineral constituents using Hill's (1963) average defined as:

$$K = \frac{1}{2}\left[\sum_{i=1}^{m} f_i K_i + \left(\sum_{i=1}^{m} \frac{f_i}{K_i}\right)^{-1}\right],$$

(3.5)

$$G = \frac{1}{2}\left[\sum_{i=1}^{m} f_i G_i + \left(\sum_{i=1}^{m} \frac{f_i}{G_i}\right)^{-1}\right].$$

In this equation, m is the number of mineral constituents for the solid phase, f_i is the volumetric fraction, and K_i and G_i are the bulk and shear moduli, respectively, of the i^{th} constituent.

2. Derive the elastic moduli of the dry frame for porosity values Φ smaller than critical porosity Φ_c, using the modified Hashin-Shtrikman Lower Bound, as follows:

$$K_{dry} = \left(\frac{\phi/\phi_c}{K^{Walton} + \frac{4}{3}G^{Walton}} + \frac{1-\phi/\phi_c}{K + \frac{4}{3}G^{Walton}} \right)^{-1} - \frac{4}{3}G^{Walton}, \tag{3.6}$$

$$G_{dry} = \left(\frac{\phi/\phi_c}{G^{Walton} + Z} + \frac{1-\phi/\phi_c}{G + Z} \right)^{-1} - Z,$$

where

$$Z = \frac{G^{Walton}}{6}\left(\frac{9K^{Walton} + 8G^{Walton}}{K^{Walton} + 2G^{Walton}} \right). \tag{3.7}$$

Moduli K_{dry} and G_{dry} from Equation 3.6 correspond to the weakest possible option for combining the solid phase (which has moduli K and G) and the critical-porosity material [which has moduli given by Walton's theory (K^{Walton} and G^{Walton})].

3. Derive the elastic moduli of the dry frame for porosity values Φ larger than the critical porosity Φ_c using a modified Hashin-Shtrikman Upper Bound by combining the critical-porosity material and the void space, the latter having zero bulk and shear strength:

$$K_{dry} = \left(\frac{(1-\phi)/(1-\phi_c)}{K^{Walton} + \frac{4}{3}G^{Walton}} + \frac{(\phi-\phi_c)/(1-\phi_c)}{\frac{4}{3}G^{Walton}} \right)^{-1} - \frac{4}{3}G^{Walton}, \tag{3.8}$$

$$G_{dry} = \left(\frac{(1-\phi)/(1-\phi_c)}{G^{Walton} + Z} + \frac{(\phi-\phi_c)/(1-\phi_c)}{Z} \right)^{-1} - Z.$$

Moduli K_{dry} and G_{dry} from Equation 3.8 correspond to the stiffest possible combination of critical-porosity material and void space.

4. Compute the elastic moduli for the unconsolidated granular material saturated with fluid using Gassmann's (1951) equation:

(3.9)
$$K_{sat} = K\frac{\phi K_{dry} - (1+\phi)K_{fl}K_{dry}/K + K_{fl}}{(1-\phi)K_{fl} + \phi K - K_{fl}K_{dry}/K},$$
$$G_{sat} = G_{dry}.$$

In Equation 3.9, K_{sat} represents the bulk modulus of the fluid-saturated granular material. G_{sat} is the shear modulus for the fluid-saturated sediment, which is the same as the shear modulus G_{dry} for the dry granular material. K_{fl} is the bulk modulus of the fluid, K_{dry} is the effective bulk modulus of the dry frame, and K is the bulk modulus of the solid grains.

5. Compute the bulk density of the unconsolidated sediments, which is given by:

(3.10)
$$\rho = \phi\rho_{fl} + (1-\phi)\rho_{grain},$$

with

(3.11)
$$\rho_{grain} = \sum_{i=1}^{m} f_t \rho_i .$$

In Equation 3.10, ρ is the bulk density of the fluid-saturated sediments, ρ_{fl} is the density of the saturating fluid, and ρ_{grain} is the density of the solid phase. In a case of mixed mineralogy, the density of the solid phase (ρ_{grain}) is given by the volumetric average of the densities of the individual constituents (Eq. 3.11). In Equation 3.11, m is the number of mineral constituents for the solid phase, and f_i is the volumetric fraction and ρ_i is the density of the i^{th} mineral constituent.

If we assume an isotropic medium, then the bulk modulus and shear modulus (Eq. 3.9) together with density (Eq. 3.10) completely characterize the elastic properties of unconsolidated, fluid-saturated sediments over the full porosity range of deep-water sediments. From these three quantities (K, G, ρ), we derive the P- and S-wave velocities of the unconsolidated sediments. Based on the methodology summarized in steps 1 to 5, we next proceed to develop rock-physics models for unconsolidated sediments in deep-water, near-seafloor strata that contain hydrates.

Rock Physics Models for Hydrate Systems

The effective elastic properties of hydrate systems depend on: 1) the elastic properties of the host sediments, 2) the elastic properties of pure

hydrates, 3) hydrate concentration, and 4) the geometrical details of how the hydrates are distributed within the sediments. We developed four morphological models of hydrate systems that can occur in the low-effective-pressure zone that spans the first 200 or 300 meters of sub-seafloor strata. We based our rock physics modeling of these deep-water hydrate systems on the mathematical development of the elastic properties of unconsolidated sediments presented in the previous section. Specifically, we considered the following four rock physics models can be used to describe GOM hydrate systems (Figure 3.1):

- **Model A** assumes hydrates are uniformly disseminated throughout the sediment and are part of the load-bearing frame of the host sediments.
- **Model B** assumes hydrates are also disseminated throughout the sediment, but they float in the porous space and do not change the dry mineral frame of their host sediments.
- **Model C** assumes an anisotropic, thin-layered medium in which layers of pure gas hydrate are intercalated with layers of hydrate-free sediments saturated with fluid. These thin layers can be horizontal or vertical. Vertical thin layers approximate thin fractures and veins filled with pure hydrate.
- **Model D** is also an anisotropic, thin-layered medium. However, in this model, hydrates are disseminated in thin horizontal layers of sediments in which they occupy 99-percent of the porous space and are part of the load-bearing frame. These thin hydrate-bearing layers are intercalated with thin layers of hydrate-free sediments saturated with fluid.

The key input parameter in all of these models is hydrate concentration. Our goal was to quantitatively relate hydrate concentration to seismic P- and S-wave velocities and to P-P and P-SV amplitude variation with angle of incidence (AVA) for each of these hydrate-sediment morphologies.

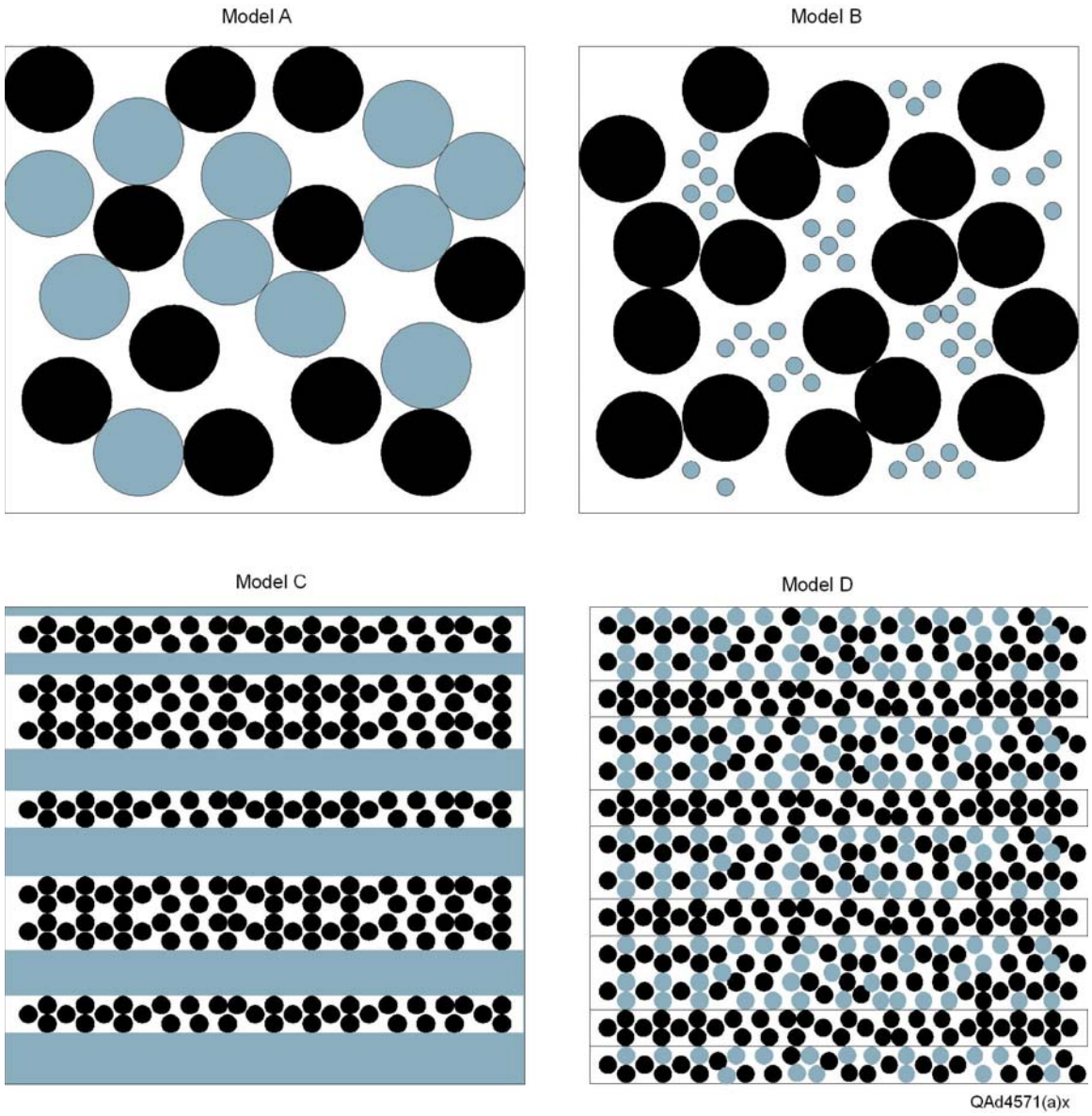

Figure 3.1: Graphical sketches of the four models of marine hydrate systems assumed in this work: load-bearing hydrates (Model A); free-floating hydrates (Model B); thin layers of horizontal or vertical pure hydrate intercalated with unconsolidated hydrate-free sediments (Model C); thin horizontal layers of disseminated, load-bearing hydrates intercalated with unconsolidated, hydrate-free sediments (Model D). Hydrates are represented in light blue and sediment in black.

Model A: Hydrates as a Load-Bearing Component

In this model we assume that hydrates are disseminated throughout the volume of sediments and are a part of the load-bearing frame, a concept proposed by Helgerud and others (1999). We start with the rock physics model for unconsolidated granular materials presented as Equations 3.1 through 3.11. Then we derive the effective elastic properties of sediments containing different concentrations of hydrate by incorporating the hydrate phase into the mineral

frame (Helgerud and others, 1999) and by reducing accordingly the initial porosity of the host sediments. When hydrate is present, the initial porosity Φ of the unconsolidated sediments without hydrates reduces to an effective porosity Φ_{eff} given by:

$$\phi_{eff} = \phi - c_{gh}, \tag{3.12}$$

where c_{gh} represents the volumetric hydrate concentration in the unconsolidated sediment. When we incorporate hydrates into the system, the porosity (Φ) of our base model for unconsolidated sediments without hydrate is replaced in Equations 3.6, 3.8, 3.9 and 3.10 by the effective porosity defined in Equation 3.12.

When hydrate is considered to be part of the mineral frame, its volumetric fraction within the solid phase, f_{gh}, is given as:

$$f_{gh} = \frac{c_{gh}}{1-\phi_{eff}}. \tag{3.13}$$

The volumetric fractions of the other mineral phases change accordingly as,

$$f_i^{eff} = \frac{1-\phi}{1-\phi_{eff}}. \tag{3.14}$$

These new volumetric fractions for the mineral phases (f_i^{eff}) and for the gas hydrates (f_{gh}) replace the original volumetric fractions (f_i) in Equations 3.5 and 3.11 for the model of unconsolidated sediments without gas hydrates. In this way, we compute a new bulk modulus, shear modulus, and density for a dry mineral frame containing hydrates with a concentration of c_{gh}.

Using Equations 3.12, 3.13, and 3.14 together with the model for unconsolidated sediments presented in the previous section, we compute the elastic properties of sediments having disseminated, load-bearing hydrates in different concentrations.

Model B: Hydrates as Free-Floating Clathrates

In this model, we assume that hydrates are distributed in the porous space, but they do not alter the dry mineral-frame of the sediments, (Helgerud and others, 1999). This model implies that the hydrates are floating in the pores, away from the grains, and their effect is to modify only the elastic properties of the material filling the sediment pores without affecting the shear-strength of the host sediments.

We assume small unit volumes of hydrates are suspended in the fluid that saturates the pores. The elastic properties of the pore-filling material (a mixture of hydrate clathrates and fluid) are given by Reuss (1929) averaging, implying

this mixture does not have any shear strength. The bulk modulus of the mixture of hydrate clathrates suspended in fluid is:

$$K_{gh\_fluid} = \left[\frac{f_{gh}}{K_{gh}} + \frac{f_{fluid}}{K_{fluid}} \right]^{-1} . \quad (3.15)$$

In this equation, K_{gh_fluid} is the bulk modulus of the mixture of hydrates and fluid in the porous space, f_{gh} represents the fraction of hydrates that occupies the porous space (which varies from *0* to *1*), and $f_{fluid}=1- f_{gh}$ is the fraction of fluid that occupies the porous space.

The volumetric hydrate concentration, c_{gh}, in the whole volume of sediments is related to the volumetric fraction of hydrates in the pores (f_{gh}) and is given by,

$$c_{gh} = \Phi f_{gh}, \quad (3.16)$$

where Φ is the porosity of the host sediments.

To summarize our model calculations, we start with the rock physics model for unconsolidated sediments presented as Equations 3.1 through 3.11. Initially, these sediments with porosity Φ are saturated with fluid. Next we predict the elastic properties of the sediments with hydrates in the pores using Gassmann's (1951) theory. The bulk modulus of the mixture of hydrates and fluid (K_{gh_fluid}) from Equation 3.15 then replaces the fluid bulk modulus (K_f) used in Equation 3.9 in the original model for unconsolidated sediments without hydrates.

This model predicts that the shear strength of sediments with free-floating hydrates is the same as the shear strength of sediments that are 100-percent saturated with fluid. Therefore, the shear modulus of sediments with free-floating hydrates is the same as the shear modulus of the unconsolidated sediments in Equation 3.9. In contrast, Gassmann (1951) theory predicts the bulk modulus of the sediments with free-floating hydrates will increase as hydrate concentration increases.

The bulk density of the sediment changes when hydrates replace part of the fluid in the porous space because the densities of fluid and hydrates are different. The adjusted bulk density is given by:

$$\rho = \left[f_{gh}\rho_{gh} + (1 - f_{gh})\rho_{fl} \right]\phi + (1-\phi)\rho_{grain} \quad (3.17)$$

In this equation, ρ is the bulk density of the sediments with pore-filling hydrates, ρ_{gh} is the density of the hydrates, f_{gh} is the fraction of hydrates that replaces the fluid in the pores, ρ_{fl} is the density of the fluid, Φ is the porosity of the unconsolidated sediments, and ρ_{grain} is the density of the mixture of mineral grains (Equation 3.11).

Model C: Thin Layers of Pure Hydrate and Sediment

Our third model is represented by a layered medium made up of thin beds of pure hydrates intercalated with unconsolidated hydrate-free sediments. Backus (1962) showed that in the long-wavelength limit, a stratified medium with individual isotropic layers is effectively anisotropic. If the thin layers are horizontal, this type of anisotropy is transversely isotropic with a vertical axis of symmetry (VTI medium). The effective anisotropic elastic properties of such a thin-layered medium depend on the elastic properties of the individual layered materials and their volumetric proportions in the rock (Backus, 1962).

In our case, the stratified medium is composed of two different materials: pure hydrate and unconsolidated marine sediments saturated with fluid. The elastic properties of pure hydrate are known (Sloan, 1998), and the elastic properties of unconsolidated sediments saturated with fluid can be estimated from the rock physics model presented in Equations 3.1 through 3.11. Therefore, using Backus averaging, we predict the elastic stiffness matrix for a layered medium having different hydrate concentrations. The volumetric concentration of hydrate (c_{gh}) for the whole volume of sediments is equal to the volumetric fraction (f_{gh}) of hydrate layers in the stratified medium:

$$c_{gh} = f_{gh}. \tag{3.18}$$

Because this model describes an anisotropic medium, the effective elastic properties vary with direction across the wave-propagation space. In particular, S-waves polarized perpendicular to the layers (slow direction) will propagate with a slower velocity than S-waves polarized parallel to the layers (fast direction). Also, P-waves propagating orthogonal to the layers will have slower velocity than the P-waves propagating along the layers. This fast and slow wave-propagation physics can be applied to either horizontal or vertical alignments of these intercalated layers.

The bulk density of this anisotropic thin-layered model is given by volumetric averaging of the densities of the two constituent materials: hydrate (ρ_{gh}) and unconsolidated sediments saturated with fluid (ρ, from Equation 3.10).

If the layers are vertical instead of horizontal, we can still use Backus averaging to estimate the effective anisotropic elastic properties of such a medium, but we need to apply a rotation to the elastic stiffness matrix to obtain a transversely isotropic medium with a horizontal axis of symmetry (HTI medium). This model of thin vertical layers approximates thin, vertical, aligned fractures/veins or vertical dykes filled with hydrate. The main difference between HTI and VTI media is that an HTI medium generates an azimuthally anisotropic medium, but a VTI medium does not.

Model D: Thin Layers of Disseminated Hydrate

The last model we consider is another thin-layered medium, with horizontal layers of hydrate disseminated in unconsolidated sediments. The hydrate in these layers is assumed to be part of the load-bearing frame and to occupy a certain fraction (f_{gh}) of the porous space of the host sediment. Layers containing hydrates are intercalated with layers of unconsolidated sediments that are 100-percent saturated with fluid. The elastic properties of the layers containing hydrates are estimated using Model A; whereas, the elastic properties of the unconsolidated sediments saturated with fluid are estimated using the rock physics model presented as Equations 3.1 through 3.11. In the assumption that the medium is thin-bedded, we again use Backus (1962) averaging to determine the elastic properties of the layered sediments for different hydrate concentrations. The overall volumetric concentration of hydrate in the rock is given by,

$$c_{gh} = f_{lr} f_{gh} \Phi. \tag{3.19}$$

In this equation, f_{lr} represents the volumetric fraction of layers containing disseminated hydrates, f_{gh} represents the proportion of hydrates occupying the porous space of these layers, and Φ is the porosity of the layers containing hydrates. For this model, we arbitrarily assumed hydrates occupy 99-percent of the porous space ($f_{gh} = 0.99$) when we calculated the velocity properties that are illustrated in this chapter. This model is also anisotropic, and P- and S-wave velocities will vary with direction, as they do for layered model C.

The bulk density of the thinly bedded medium is given by volumetric averaging of the densities of the two constituent materials: the sediments with load-bearing hydrates (see Model A) and the unconsolidated sediments saturated with fluid (Equation 3.11).

Modeling Results

In this section we present P- and S-wave velocities predicted by the four different rock physics models of hydrate systems described in the previous section. These calculations were done for two types of hydrate-host sediments: (1) pure quartz, and (2) mixtures of arbitrary fractions of quartz and clay. The rock-property parameters used in the modeling are summarized in Table 3.1.

Table 3.1. Parameter values used in rock physics models

Constituent	Bulk Modulus	Shear Modulus	Density
quartz	37 GPa	44 GPa	2650 kg/m3
clay	25 GPa	9 GPa	2550 kg/m3
brine	2.29 GPa	0 GPa	1005 kg/m3
gas hydrate	7.14 GPa	2.4 GPa	910 kg/m3

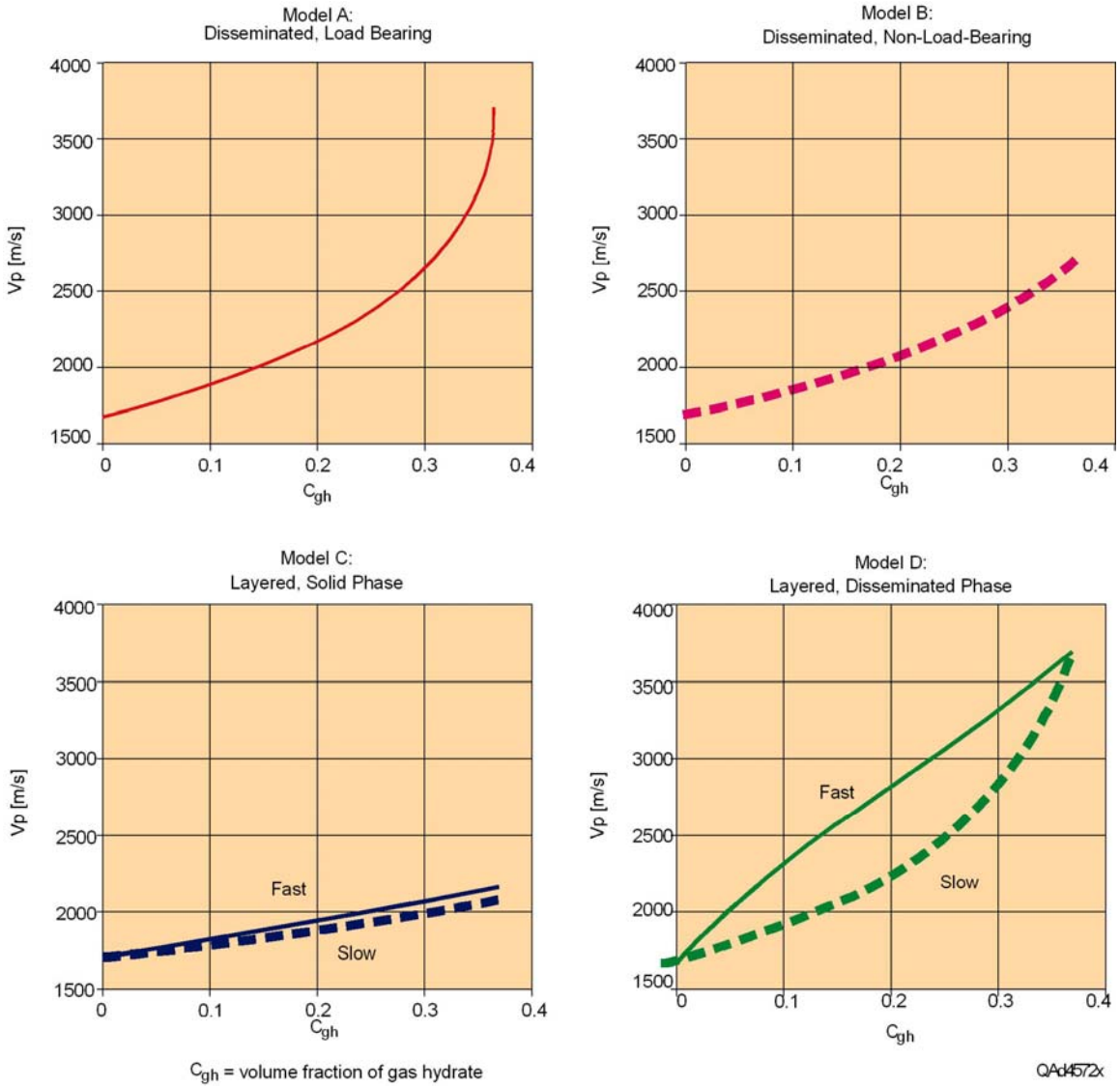

Figure 3.2: P-wave velocity as a function of the volumetric fraction of hydrate (c_{gh}) in pure quartz sediments for the four rock physics models. **Model A**: load-bearing hydrates disseminated in the sediments; **Model B**: free-floating hydrates disseminated in the sediments; **Model C**: horizontal or vertical layers of pure hydrates producing slow P-waves (dotted line) and fast P-waves (solid line); **Model D**: horizontal or vertical layers of disseminated, load-bearing hydrates producing slow P-waves (dotted line) and fast P-waves (solid line). C_{gh} is shown as a fraction of the unit volume. All curves terminate at critical porosity, 0.37. The effective pressure is 0.01 MPa, which simulates a shallow burial depth of 2 m.

Pure-Quartz Host Sediment

In the examples displayed as Figures 3.2, 3.3, and 3.4, we consider the unconsolidated host sediment to be represented by pure quartz grains saturated with brine. The sediments are assumed to be at a critical porosity of 37 percent. The coordination number *C* is considered to be 8, and the effective pressure is set at a low value of 0.01 MPa. This effective pressure corresponds to a depth of approximately 2 meters below the seafloor. This low effective-pressure value can also correspond to deeper strata within overpressured zones, which are sometimes encountered in the Gulf of Mexico.

Figures 3.2, 3.3, and 3.4 present the modeling results for P-wave velocity (V_P), S-wave velocity (V_S), and V_P/V_S ratio, respectively, as a function of hydrate concentration (c_{gh}) for the four rock physics models A, B, C, and D (Fig. 3.1). For the two anisotropic layered models (C and D), we display two curves corresponding to velocities of waves with their particle-displacement vector parallel to the layering (solid line) and to velocities of waves with their particle-displacement vector orthogonal to the layers (dotted lines). From all these figures we observe that P- and S-wave velocities depend on the geometrical details of how hydrates are distributed in their host sediments.

The results presented as Figure 3.2 show that for our four rock physics models, the presence of hydrate increases the P-wave velocity in the sediments. The smallest increase in P-wave velocity with hydrate concentration is obtained for the thin-bedded model with layers of pure hydrates (Model C), while the largest increase in P-wave velocity is obtained for the models having disseminated, load-bearing hydrates (Models A and D). The rate of change of V_P with hydrate concentration is greatest when measured parallel to the thin layers of load-bearing clathrates (Model D, solid curve).

If we consider the two thin-layered models (Models C and D), we see that the fast P-wave velocity propagating parallel to the layers (solid lines) and the slow P-wave velocity propagating orthogonal to the layers (dotted lines) are different for these two morphologies (Figure 3.2). For example, at a 0.3 volumetric concentration of hydrate, fast P-wave velocity can range from 2100 m/s for layers of pure hydrates (Model C, solid line) to 3300 m/s for layers of disseminated, load-bearing hydrates (Model D, solid line). This large difference in V_P is caused partly because the elastic moduli of layers having load-bearing hydrates are larger than the elastic moduli of pure hydrates. In addition, the volumetric fraction of layers having disseminated hydrates is 2.73 $[(0.99\Phi)^{-1}]$ times larger than the corresponding fraction of layers of pure hydrates for the same volumetric hydrate concentration in the two layered media. This value of 2.73 is obtained by comparing Equations 3.17 and 3.18, and setting Φ, the porosity of the unconsolidated sediments, to a value of 0.37, a common value for the critical porosity of round, uniform-size grains. When the volumetric fraction for the layers of disseminated hydrates in the thin-bedded medium is 1, the rock becomes isotropic, and the end points of the two curves for Model D coincide with the end point of the curve for Model A (Figure 3.2).

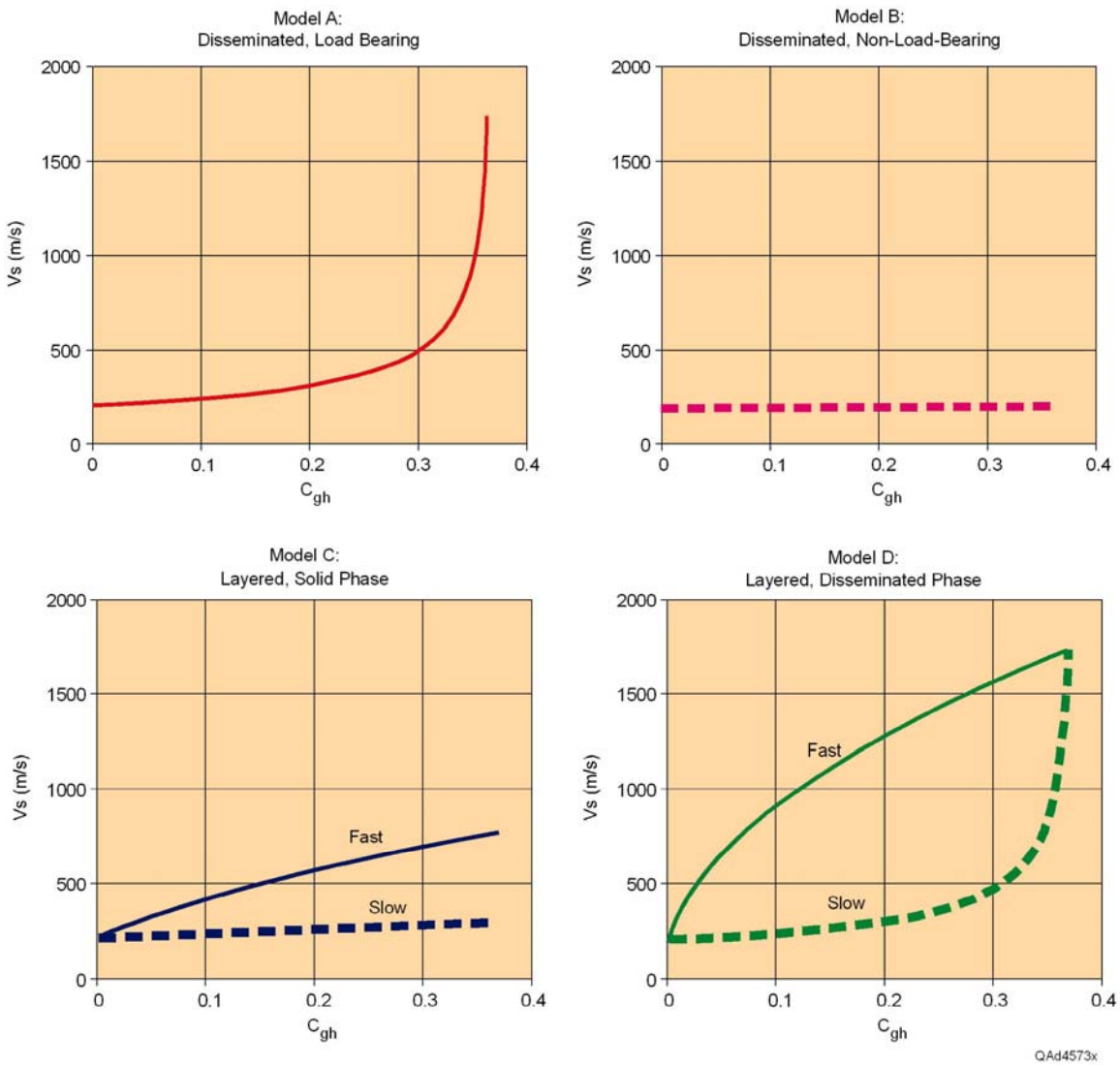

Figure 3.3: S-wave velocity as a function of the volumetric fraction of hydrate (c_{gh}) in pure quartz sediments for the four rock-physics models. **Model A**: load-bearing hydrates disseminated in the sediments; **Model B**: free-floating hydrates disseminated in the sediments; **Model C**: horizontal or vertical layers of pure hydrates producing S-waves with slow polarization (dotted line) and fast polarization (solid line); **Model D**: horizontal or vertical layers of disseminated, load-bearing hydrates producing S-waves with slow polarization (dotted line) and fast polarization (solid line). C_{gh} is shown as a fraction of the unit volume. All curves terminate at critical porosity, 0.37. The effective pressure is 0.01 MPa, which simulates a shallow burial depth of 2 m.

From Figure 3.3 we observe that S-wave velocity also increases with hydrate concentration for three of the rock physics models (A, C, D), but for the model in which the hydrate floats in the porous space without contributing to the load-bearing frame of the host sediments (Model B), the increase in S-wave velocity is insignificant. In Model B, the hydrates are not connected to the mineral frame, and even though the hydrate unit volumes are solid, they do not support any shear load. Gassmann's (1951) theory used for this model predicts that the

shear modulus of the sediments does not change with hydrate concentration, and because there is only a minor difference in the densities of brine and hydrate, there is also only a small increase in V_S when hydrate replaces brine in the pores.

The results presented in Figure 3.3 show a large increase in S-wave velocity occurs when the waves are polarized parallel to the layers of a medium having horizontal thin beds of disseminated, load-bearing hydrates (Model D, solid line). In this particular type of hydrate-sediment morphology, the velocity of S-waves propagating with their displacement vector polarized parallel to the layering (fast direction) increases significantly for small hydrate concentrations. This behavior suggests that for disseminated, load-bearing hydrates occurring in thin beds, we may be able to detect small hydrate concentrations using anisotropic S-wave information. The S-wave anisotropy for this model is large. There is a large difference between S-wave velocities polarized parallel (Model D, solid line) and orthogonal (Model D, dotted line) to layers of disseminated, load-bearing hydrates.

S-wave anisotropy for a system of layers of pure hydrates (Model C) is large as well. Therefore, if hydrates occur in thin vertical layers (fractures) or horizontal layers within near-seafloor strata, we should expect significant shear-wave anisotropy, and this anisotropy may be used with other seismic information to estimate hydrate concentrations. If the medium exhibits thin vertical layers of pure hydrate (approximating aligned, vertical thin fractures/veins filled with hydrates), we should expect not only shear-wave splitting, but also azimuthal variations in both wave velocities and reflectivities. These anisotropic seismic attributes can be excellent indicators for quantifying hydrate distribution and concentration.

For Model A, S-wave velocity increases little at small hydrate concentrations, then increases abruptly at hydrate concentrations larger than 0.3 (i.e. when load-bearing clathrates occupy more than 80-percent of the pore volume). Because of this behavior it will be more challenging to determine small hydrate concentrations using S-wave information when load-bearing clathrates are uniformly disseminated within the sediments. Note again that the end points of the curves for Model A and Model D coincide, as they should.

Figure 3.4 presents the V_P/V_S ratio for the four rock-physics models. This velocity ratio decreases with hydrate concentration for all models except Model B, which assumes free-floating hydrates. This anomalous behavior for Model B occurs because P-wave velocity increases with hydrate concentration (Figure 3.2) while S-wave velocity remains practically constant (Figure 3.3). As a result, the V_P/V_S velocity ratio for Model B increases with hydrate concentration.

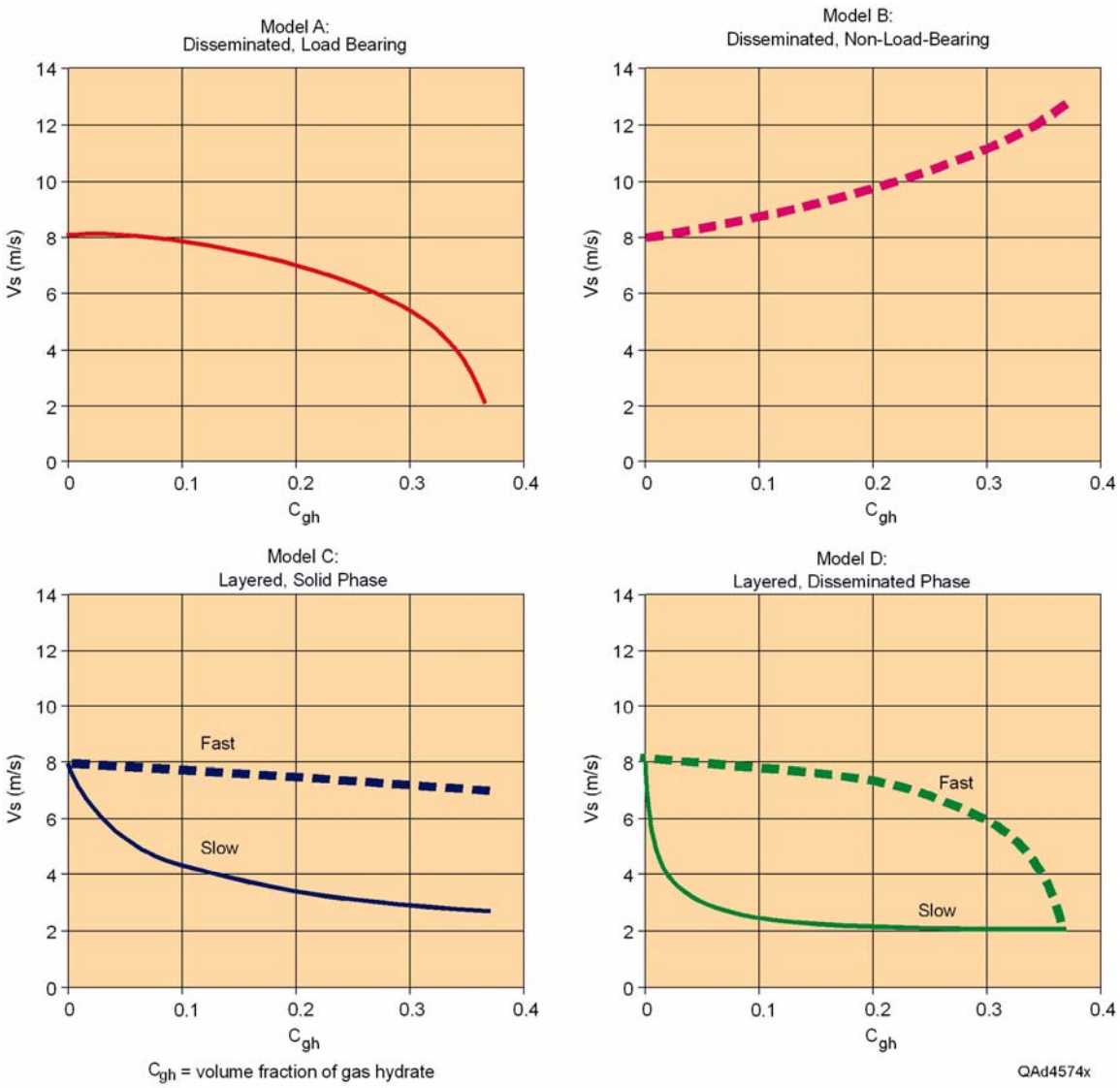

Figure 3.4: Vp/Vs ratio as a function of the volumetric fraction of hydrate (c_{gh}) in pure quartz sediments. **Model A**: load-bearing hydrates disseminated in the sediments; **Model B**: free-floating hydrates disseminated in the sediments; **Model C**: horizontal or vertical layers of pure hydrates producing slow waves (dotted line) and fast waves (solid line); **Model D**: horizontal or vertical layers of disseminated, load-bearing hydrates producing slow waves (dotted line) and fast waves (solid line). C_{gh} is shown as a fraction of the unit volume. All curves terminate at critical porosity, 0.37. The effective pressure is 0.01 MPa, which simulates a shallow burial depth of 2 m.

From Figure 3.4 we observe that the V_P/V_S velocity ratio for slow P and S-waves polarized orthogonal to layers of disseminated, load-bearing gas hydrates (Model D, dotted line) is similar to the V_P/V_S ratio when load-bearing hydrates are uniformly disseminated in the sediments (Model A). For these two models, the velocity ratio decreases slightly at small hydrate concentrations and more abruptly for larger hydrate concentrations. This behavior suggests it will be challenging to estimate small hydrate concentrations using V_P/V_S ratios in media represented by either of these two sediment-hydrate morphologies for certain

wave polarizations. In contrast, for anisotropic Models C and D, there is a significant decrease in the V_P/V_S ratio at low hydrate concentration for waves with particle-displacement vectors parallel to the layers (fast direction, solid curve). This modeling result suggests that for layered hydrate morphologies, we may be able to use V_P/V_S ratios, selected fast-wave polarizations, and anisotropy information to detect small hydrate concentrations in sediments.

Mixed-Mineralogy Host Sediment

The theory presented in the preceding sections allows mixed mineralogy and different saturating fluids to be included in the wave-propagation media that we modeled. Examples of this expanded modeling capability are shown as Figures 3.5, 3.6, and 3.7, which are similar to Figures 3.2, 3.3, and 3.4, respectively, except that the curves displayed in each panel correspond to different clay and sand mixtures. The clay content in the sediments varies from 0 to 100 percent at a 25-percent increment. Some parameters used in the modeling, such as critical porosity and coordination number, vary with mineralogy (Murphy, 1982). For clean quartz grains (0 percent clay content), the critical porosity is assumed to be 37 percent, and the coordination number *C* is considered to be 8. For pure clay minerals (100-percent clay content), we use a larger critical porosity of 67 percent and a smaller coordination number of 4, as many geotechnical data suggest (Murphy, 1982). For each mixture of quartz and clay minerals, we derive the values for critical porosity and coordination number by doing a linear interpolation between the corresponding values for the two end members of pure quartz and pure clay. Also, at sub-seafloor depths where hydrates are stable, the porosity of clay-rich sediments is larger than the porosity of pure quartz grains. Therefore, we compute V_P and V_S as a function of hydrate concentration for sediments with different porosity values: 37 percent for pure quartz and 50 percent for pure clay minerals. For each mixture of quartz and clay, we use again a linear interpolation between the values for the two end members of pure quartz and pure clay. The effective pressure we use in these calculations is equal to 0.5 MPa, which corresponds to a depth below seafloor of approximately 60 m.

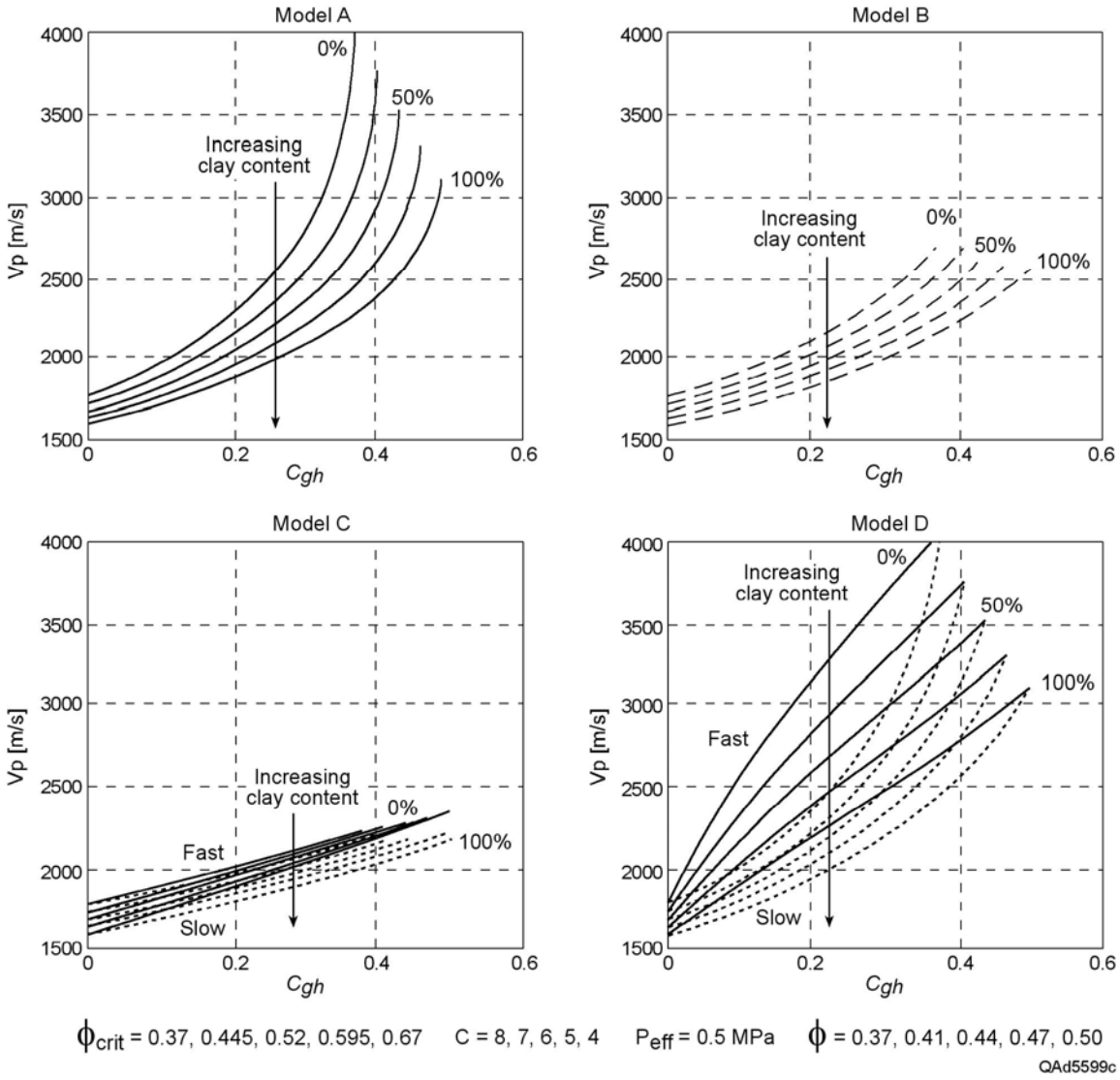

Figure 3.5: P-wave velocity as a function of the volumetric fraction of hydrate (c_{gh}) in a sediment mixture with variable clay content and an effective pressure of 0.5 MPa, which simulates a sub-seafloor depth of approximately 60 m. **Model A**: load-bearing hydrates disseminated in the sediments; **Model B**: free-floating hydrates disseminated in the sediments; **Model C**: horizontal or vertical layers of pure hydrates producing slow P-waves (dotted lines) and fast P-waves (solid lines); **Model D**: horizontal or vertical layers of disseminated, load-bearing hydrates producing slow P-waves (dotted lines) and fast P-waves (solid lines). Each curve corresponds to a different clay content (ranging from 0 to 100 percent at a 25-percent increment), different critical porosity values, and different coordination numbers. The curves are computed at increasing porosity values as the clay content increases. The arrows indicate increasing clay content.

As expected, the P- and S-wave velocities decrease with increasing clay content (and implicitly with increasing porosity), as we observe from each panel of Figures 3.5 and 3.6. For Model A (load-bearing hydrates), as porosity and clay content of the sediments increase, it becomes more challenging to estimate small hydrate concentrations, especially using S-wave velocity data (Fig. 3.6). For layered model D, we observe that both P- and S-wave anisotropy decreases

with increasing clay content because the elastic properties of clay minerals are closer to those of hydrates than are the elastic properties of quartz minerals (Table 3.1). This modeling shows that we should expect larger anisotropy in P- and S-wave velocities if hydrate layers are intercalated with clean sands than with clay-rich sediments. Models C and D take into account only the anisotropy due to thin layers and consider the clay-rich sediments to be isotropic. This assumption may hold for sediments immediately below seafloor. However, as depth increases, the stress-induced anisotropy of clays will increase. At large depths, Models C and D with clay-rich sediments should be adjusted to account for the additional anisotropy caused by the anisotropy of clay minerals.

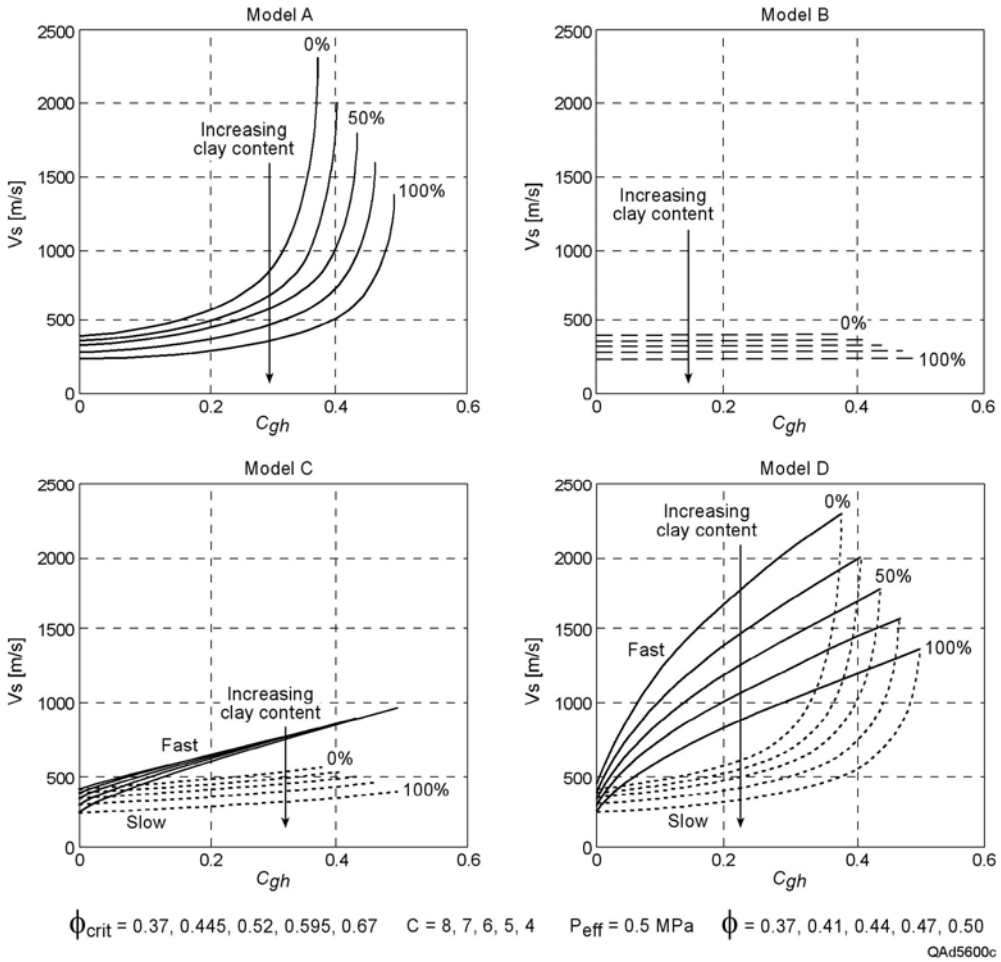

Figure 3.6: S-wave velocity as a function of the volumetric fraction of hydrate (c_{gh}) in a sediment mixture with variable clay content and an effective pressure of 0.5 MPa, which simulates a sub-seafloor depth of approximately 60 m. **Model A**: load-bearing hydrates disseminated in the sediments; **Model B**: free-floating hydrates disseminated in the sediments; **Model C**: horizontal or vertical layers of pure hydrates producing slow S-waves (dotted lines) and fast S-waves (solid lines); **Model D**: horizontal or vertical layers of disseminated, load-bearing hydrates producing slow S-waves (dotted lines) and fast S-waves (solid lines). Different curves correspond to different clay content (from 0 to 100 percent with a 25-percent increment), different critical porosity values, and different coordination numbers. The curves are computed at increasing porosity values as clay content increases. The arrows indicate increasing clay content.

Figure 3.7 presents the V_P/V_S ratio for the four rock physics models when the clay content is varied. This velocity ratio decreases with hydrate concentration for all models except Model B, which assumes hydrates float in the pores and do not support the shear load. As expected, the V_P/V_S ratio increases with increasing clay content for this hydrate-sediment morphology.

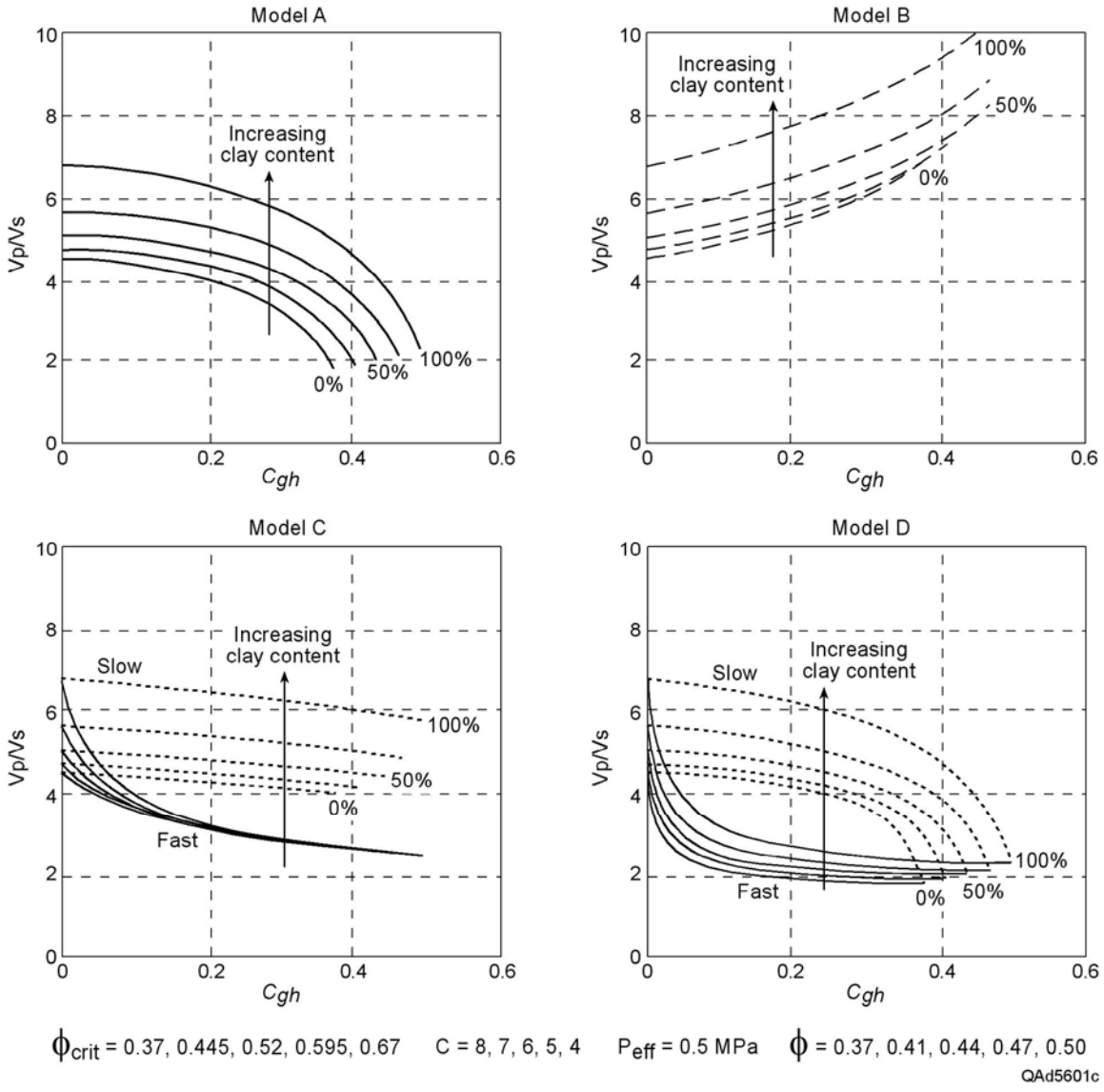

Figure 3.7: V_P/V_S velocity ratio as a function of the volumetric fraction of hydrate (c_{gh}) in sediment mixtures with variable clay content and an effective pressure of 0.5 MPa, which simulates a sub-seafloor depth of approximately 60 m. **Model A**: load-bearing hydrates disseminated in the sediments; **Model B**: free-floating hydrates disseminated in the sediments; **Model C**: horizontal or vertical layers of pure hydrates producing slow waves (dotted lines) and fast waves (solid lines); **Model D**: horizontal or vertical layers of disseminated, load-bearing hydrates producing slow waves (dotted lines) and fast waves (solid lines). Different curves correspond to different clay content (from 0 to 100 percent with a 25-percent increment), different critical porosity values, and different coordination numbers. The curves are computed at increasing porosity values as the clay content increases. The arrows indicate increasing clay content.

The different behaviors of the V_P/V_S ratio for the different rock physics models (Figures 3.4 and 3.7) suggest that **amplitude vs. incidence angle** (**AVA**) analyses of P-waves and converted-S waves may provide valuable insights into hydrate morphologies and concentrations, a topic considered in the following section.

P-P and P-SV AVA Modeling: Base of Hydrate Stability Zone

To evaluate the potential value of amplitude-vs-angle (AVA) technology for studying hydrate systems, we simulate the AVA response for P-P and P-SV reflections at an interface between the base of the hydrate stability zone and sediments immediately below that interface that contain free gas (Figure 3.8). We arbitrarily define the host sediment in Layer 1 and Layer 2 of the Earth model to be clean sand. For brevity, the hydrate systems considered in this AVA modeling are represented by isotropic rock physics Model A and Model B only (Figure 3.1), which have hydrates disseminated in the host sediments and no layered hydrate. In Model A, the hydrates are part of the load-bearing frame of the sediments, while in Model B the hydrates fill the pores and do not change the elastic properties of the dry mineral frame. The sediments below the hydrate stability zone are assumed to contain free gas. The elastic properties of this lower layer are estimated from the rock physics model for unconsolidated sediments presented as Equations 3.1 through 3.11.

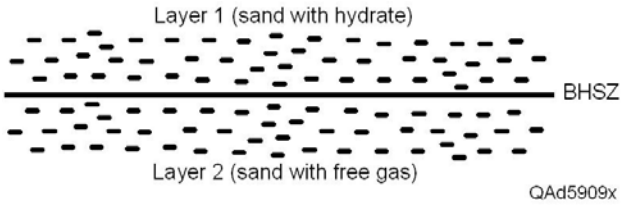

Figure 3.8: Earth model assumed for base of hydrate stability zone (BHSZ). Porosity is set at 0.37 for both layers.

First we consider the pores of Layer 2 to be 80-percent saturated with free gas, and the remaining pore space to be occupied by brine. In a second AVA analysis that follows, we lower the gas saturation to 10 percent. We use Reuss (1929) averaging to derive the bulk modulus of the mixture of gas and liquid. We then use Zoeppritz's (1919) equations to derive P-P and P-SV reflectivity as a function of incidence angle.

Figure 3.9 presents the results for AVA modeling of P-P (left panel) and P-SV (right panel) reflectivity as a function of incidence angle for the model with load-bearing hydrates (Model A). Each curve corresponds to a different hydrate concentration in the upper layer. The arrow indicates increasing hydrate

concentration in the pores, which ranges from 0 to 99 percent at increments of 10 percentage points.

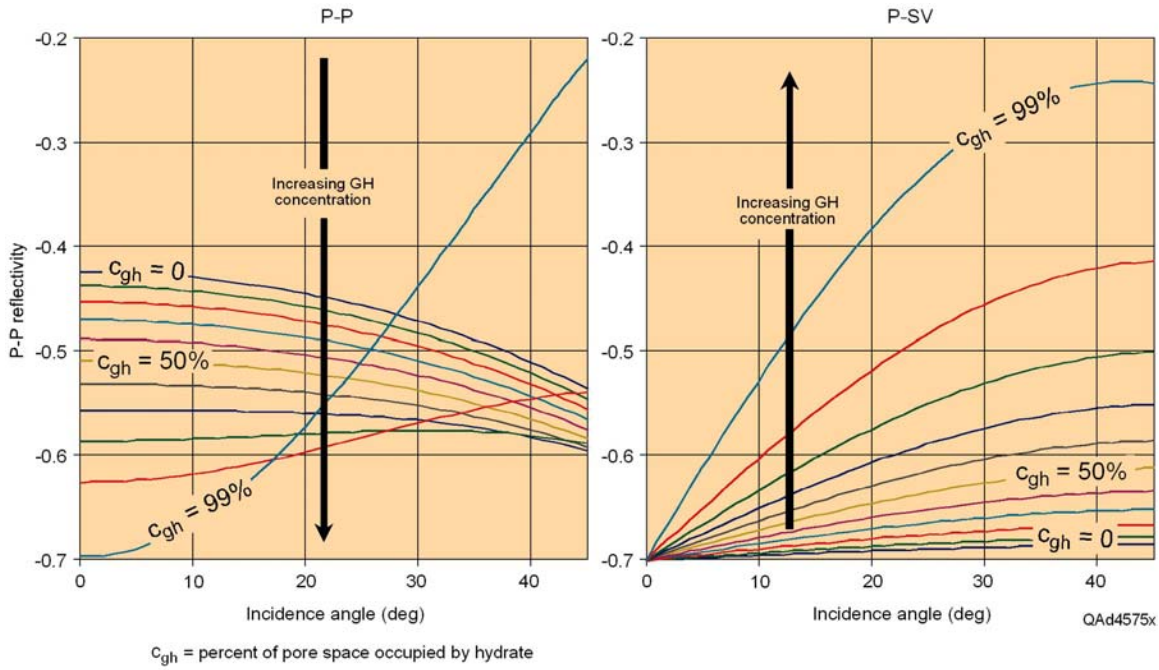

Figure 3.9: Results of AVA **Model A** showing P-P (left panel) and P-SV (right panel) reflectivity as a function of incidence angle at the interface between the base of the hydrate stability zone and sediments below that contain 80-percent free gas. Each curve corresponds to a different hydrate concentration ($\mathbf{c_{gh}}$) in the hydrate stability zone. In this model, hydrates are disseminated in Layer 1 (Fig. 3.8) and are part of the load-bearing frame of the host sediments.

The magnitude of the normal-incidence P-P reflectivity increases with increasing hydrate concentration because the difference between the elastic properties of the hydrate system and the free-gas sediments (lower layer) increases with hydrate concentration. For this model we observe that P-P reflectivity at small incidence angles (near offsets) can better differentiate variations in hydrate concentrations than can P-P reflectivity at larger angles of incidence (far offsets) where the reflectivity curves converge. For small angles, the increase in P-P reflectivity as hydrate concentration increases from 0 to 99-percent is a little more than 60 percent (from -0.43 to -0.69), which should be measurable with good quality seismic data. However, P-P amplitudes increase by only 12 percent when hydrate concentration changes from 0 to 40 percent (from -0.43 to -0.48), which would be difficult to detect even with excellent-quality seismic data.

In contrast to P-P reflectivity, if multicomponent seismic data are acquired so that P-SV reflectivity can be measured at incident angles of 30° or more, P-SV amplitudes increase by a factor of about 3 as hydrate concentration increases from 0 to 40 percent, and by a factor of more than 30 if hydrate concentration

changes from 0 to 99 percent. These amplitude variations should be measurable even when the quality of multicomponent seismic data is not optimal.

For hydrate concentrations between 0 and 0.7, the P-P reflectivity curves in Figure 3.9 are the type associated with **Class 3** AVA reservoirs in the Gulf of Mexico, reservoirs for which the reflectivity at zero offset is negative and the AVA gradient is also negative (Roden and others, 2005; Ruger, 2002; Rutherford and Williams, 1989). As hydrate concentration increases beyond 0.7, the P-P AVA behavior shifts to a **Class 4** AVA reservoir response; reservoirs for which the reflectivity at zero offset is again negative, but for which there is a positive AVA gradient. The hydrate concentration range that produces these Class 4 reservoir responses corresponds to the hydrate concentration range in Figure 3.3 (upper left) where there is a significant increase in V_S in the layer above the free-gas reservoir. This type of V_S behavior in Layer 1 above the reflecting interface is required for a Class 4 P-P AVA response (Castagna and Backus, 1993).

Figure 3.10 shows the results for AVA modeling of P-P (left panel) and P-SV (right panel) reflectivity as a function of incidence angle when using the hypothesis of free-floating hydrates (Model B) in Layer 1. Again, each curve corresponds to a different hydrate concentration in the upper layer of the Earth model (Fig. 3.8). The arrow indicates the direction of increasing hydrate concentration in the pores, which ranges from 0 to 99 percent at increments of 10 percentage points.

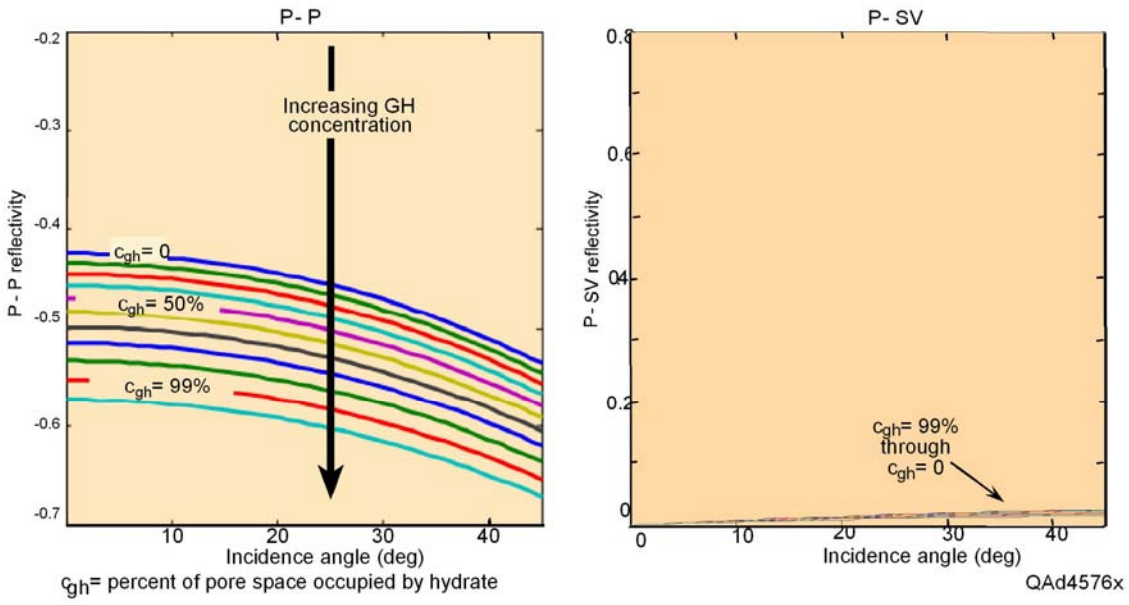

Figure 3.10: Results of AVA **Model B** showing P-P (left) and P-SV (right) reflectivity as a function of incidence angle at the interface between the base of the hydrate stability zone and sediments below that have a gas saturation of 80 percent. Each curve corresponds to a different hydrate concentration ($\mathbf{c_{gh}}$) in the upper layer. In this model, hydrates fill the porous space without changing the dry mineral frame of the host sediments.

In the hypothesis of free-floating hydrates, only P-P reflectivity exhibits any sensitivity to hydrate concentration. All P-P AVA reflectivity curves in Figure 3.10

are Class 3 AVA responses. It will be challenging to identify hydrate concentrations with P-P AVA attributes for this type of hydrate morphology because P-P reflection amplitude increases by less than 10 percent when hydrate concentration increases from 0 to 40 percent, and by only a little more than 30 percent if concentration varies from 0 to 99 percent. For this rock physics model, the shear strengths of the sediments containing hydrates do not change with hydrate concentration. Moreover, S-wave velocities in sediments containing pore-filling hydrates and in sediments containing free gas are similar. The only change in V_S is caused by a small density effect. For this hydrate-sediment morphology (Model B), all P-SV reflections are weak and vary little as hydrate concentration increases.

The modeling results presented in Figures 3.9 and 3.10 show that P-P reflectivity cannot differentiate between the two hypotheses of hydrate occurrence (load-bearing and free-floating). The P-P reflectivity curves in Figure 3.9 (load-bearing assumption) have the same magnitude and offset dependence as do the curves in Figure 3.10 (free-floating assumption). However, P-SV reflectivity for load-bearing hydrates (Model A, Fig. 3.9) is much different than it is for free-floating hydrates (Model B, Fig. 3.10). This distinctive difference in P-SV reflectivity for these two hydrate-sediment morphologies is a key rock physics principle that indicates 4C seismic data should be used to analyze marine hydrate systems whenever possible.

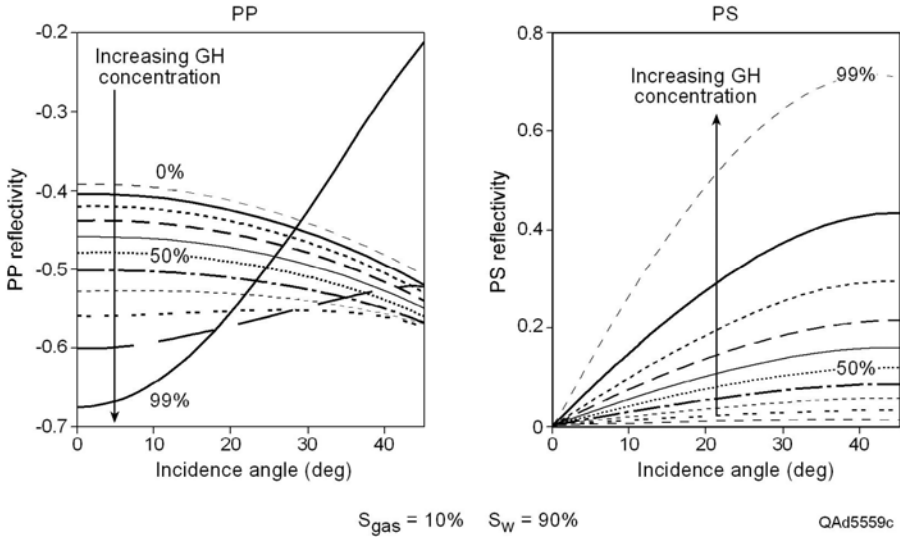

Figure 3.11: Results of AVA **Model A** showing P-P (left) and P-SV (right) reflectivity as a function of incidence angle at the interface between the base of hydrate stability zone and sediments below that have a free-gas saturation of 10 percent. Each curve corresponds to a different hydrate concentration ($\mathbf{c_{gh}}$) in the upper layer. In this model, hydrates are disseminated and are part of the load-bearing frame of the host sediments.

In the AVA reflectivity curves exhibited on Figures 3.11 and 3.12, the free-gas saturation below the **base hydrate stability zone** (**BHSZ**) is 10 percent, rather than 80 percent. The presence of residual gas at a concentration of 10 percent may be a more plausible scenario for most GOM hydrate systems than is a well-developed gas reservoir immediately below the BHSZ. As expected, the AVA responses for 10-percent free gas below the BHSZ (Figs. 3.11 and 3.12) are similar to the AVA responses for 80-percent free gas (Figs. 3.9 and 3.10). The explanation is that small amounts of free gas have the same effect on seismic velocities as do economical gas saturations. Therefore, it will be challenging to use seismic reflectivity to estimate free-gas saturation below the hydrate stability zone.

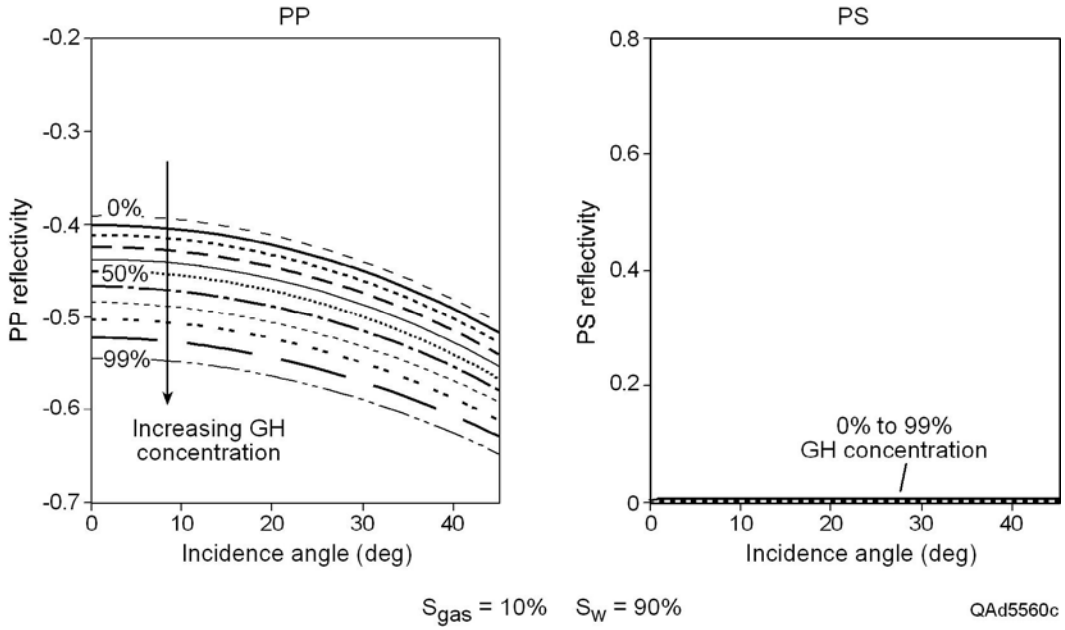

Figure 3.12: Results of AVA **Model B** showing P-P (left) and P-SV (right) reflectivity as a function of incidence angle at the interface between the base of gas-hydrate stability zone and sediments below that have a free-gas saturation of 10 percent. Each curve corresponds to a different hydrate concentration in the upper layer. In this model, hydrates fill the porous space without changing the dry mineral frame of the host sediments.

This modeling shows that multicomponent seismic technology, and the use of P-SV AVA behavior in particular, can be a powerful tool to understand how hydrates are distributed in relation to their host sediments (load-bearing vs. pore-filling). Using combinations of V_P/V_S ratios and AVA analyses of P-waves and converted PS-waves should improve estimates of deep-water hydrate concentrations.

Next we analyzed the behavior of seismic reflection amplitude not only as a function of incidence angle, but also as a function of azimuth, at a hypothetical **base of a hydrate stability zone** (**BHSZ**) where hydrate in Earth Layer 1 (Fig. 3.8) is deposited in vertical and aligned fractures/veins (Model C or D with vertical layers). A generalization of this hydrate/sediment morphology in Layer 1 is represented as Figure 3.13. This model creates a transversely isotropic medium with a horizontal axis of symmetry (HTI medium).

In this calculation, we considered the sediments above and below the BHSZ(Layers 1 and 2 in Figure 3.8)to be clay minerals. For vertical layers of pure hydrate (Model C), the velocity behaviors are identical to those exhibited by the 100%-clay curves exhibited on Figures 3.5 through 3.7 if “fast velocity” is defined as the velocity associated with a propagation direction that results in the particle-displacement vector of the seismic wavefield being parallel to the vertical layering, and “slow velocity” is the velocity when the propagation direction causes the particle-displacement vector to be perpendicular to layering.

A more interesting velocity behavior occurs for vertical layers of disseminated hydrate (Model D). In our first example to illustrate the wave physics associated with this hydrate/sediment morphology, we assumed there was a free-gas residual saturation of 5 percent (Figures 3.14 and 3.15) occurs below the BHSZ. In the second example, we assume no free gas is present below the BHSZ (Figure 3.16). The porosity of the sediments is 40%. The coordination number is 6, and the effective pressure is assumed to be 1 MPa, which corresponds to a sub-seafloor depth of approximately 120 m.

To model the variation in seismic amplitude at this interface, we used Ruger’s (2002) equations for PP and PS reflectivity in two different reflection planes: the isotropy plane and the symmetry-axis plane. The isotropy plane is the plane parallel to the thin vertical hydrate layers; the symmetry-axis plane is orthogonal to the hydrate layers.

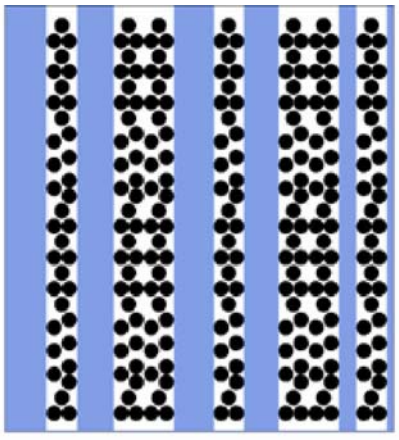

Figure 3.13: Model C with vertical layers of pure hydrate (blue) interspersed with vertical layers of hydrate-free sediment. This model creates a transversely isotropic medium with a horizontal axis of symmetry (HTI medium). This type of medium is azimuthally anisotropic.

Figure 3.14 presents the P-P and P-SV reflectivity modes. The different curves correspond to different hydrate concentrations in the sediments. The amount of hydrate in the vertical layers varies from 0 to 30 percent of a unit volume of the composite material. The arrows indicate the direction of increasing hydrate concentration. The red curves represent the reflectivity responses as a function of incidence angle in the isotropy plane (parallel to the vertical hydrate layers), and the blue curves represent the reflectivity curves as a function of incidence angle in the symmetry axis plane (orthogonal to the vertical hydrate layers).

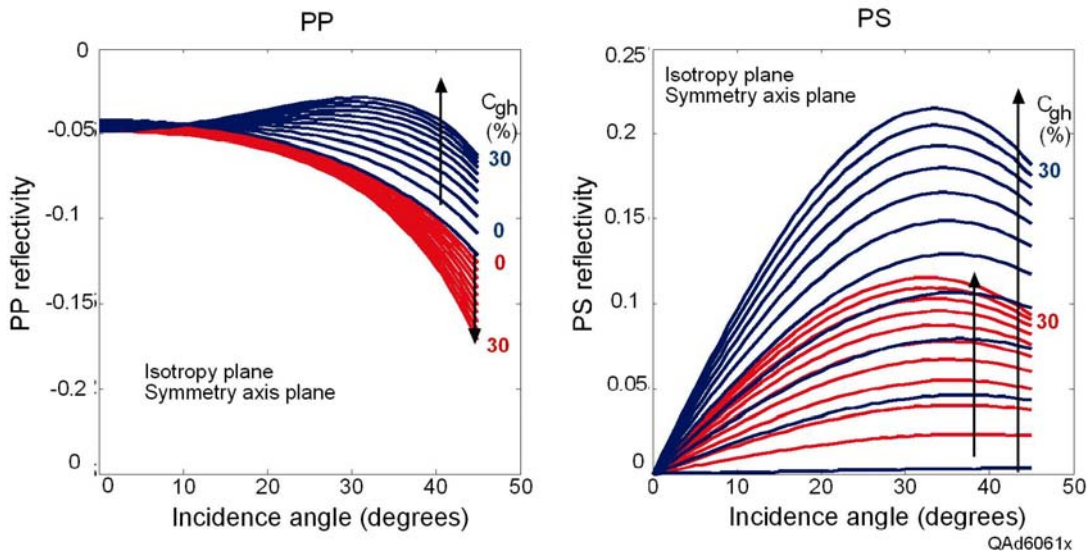

Figure 3.14. P-P (left) and P-SV (right) reflectivity from the base of the GHSZ for Model C with vertical layers of pure hydrate. Red curves show reflectivity for particle-displacement vectors oriented in the isotropy plane (parallel to layering). Blue curves show the reflectivity for particle-displacement vectors oriented in the symmetry-axis plane (perpendicular to layering). The different curves correspond to different hydrate concentrations in the sediments, which vary from 0 to 30 percent of the unit volume (hydrate + sediment). The arrows indicate the direction of increasing hydrate concentration. We assume 5-percent free gas below the HSZ. The effective pressure is 1 MPa, corresponding to a sub-seafloor depth of approximately 120 m.

From Figure 3.14 we can see that P-P and P-SV reflectivities depend on the azimuth in which a wavefield is propagating relative to aligned fractures. The reflectivities in the isotropy plane are different from the reflectivities in the symmetry axis plane. Also, we observe that as hydrate concentration increases, the P-SV response becomes stronger than the P-P response. This behavior is appealing because the P-SV mode provides better resolution of near-seafloor geology than does the P-P mode (Chapter 2).

Figure 3.15 presents the full azimuthal variation of P-P reflectivity from the BHSZ interface when the hydrate concentration is 20 percent. On the left panel we display P-P reflectivity as a function of incidence angle ranging from 0 to 45 degrees and for all azimuths (from 0 to 360 degrees). On the right panel we represent P-P reflectivity as a function of azimuth for incidence angles of 20 and

45 degrees. As we can see in both Figures 3.14 and 3.15, the azimuthal variation in P-P (and P-SV) increases with incidence angle.

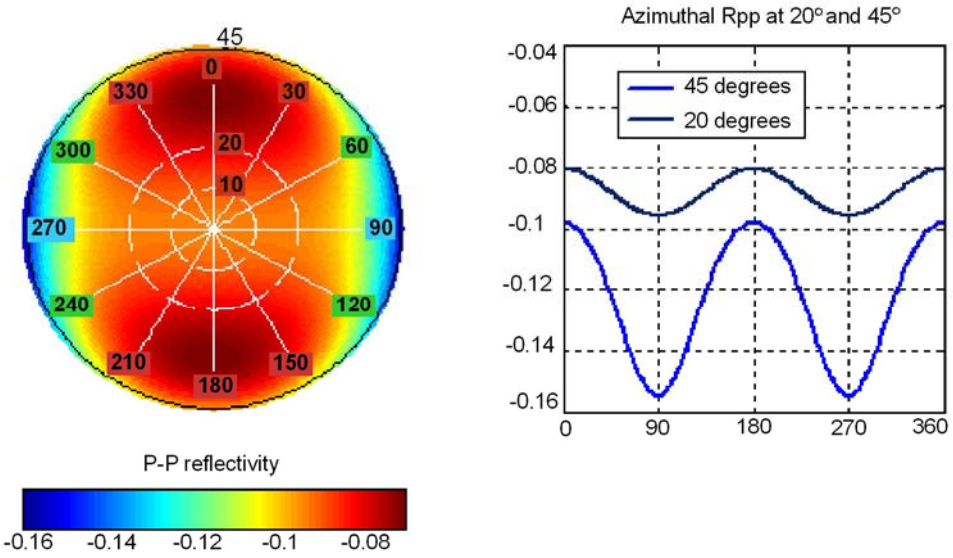

QAd6062

Figure 3.15: (Left) P-P reflectivity as a function of incidence angle from 0 to 45 degrees and azimuth (from 0 to 360 degrees) when the hydrate concentration in vertical fractures in Earth Layer 1 (Fig. 3.8) is 20 percent of the unit volume. (Right) R_{PP} amplitude variation with azimuth for incidence angles of 20 and 45 degrees. Azimuth 0 is perpendicular to the fracture plane. Vertical thin layers of pure hydrate are oriented at an azimuth angle 90 degrees.

Figure 3.16 is similar to Figure 3.14 except there is no free gas below the HSZ. By comparing the right-hand panels in Figures 3.14 and 3.16 we observe that the P-SV response is the same when free gas is below the BHSZ and when it is not. Therefore, we can use the P-SV mode to quantify hydrate concentration whether free gas is present or absent below the BHSZ.

In contrast, P-wave data are sensitive to changes in pore fluid. Therefore, the P-P reflectivity response presented in Figure 3.16, for which there is no free gas below the BHSZ, differs from the behavior presented in Figure 3.14 for which there is some residual gas below the BHSZ. The important fact to observe in Figure 3.16 is that the P-P reflections in the isotropy plane (red curves) and the P-P reflections in the symmetry axis plane (blue curves) are more or less symmetric about the reflectivity axis. This behavior suggests that if we acquire 3D seismic data and stack the P-P mode over all azimuths, we will get weak (perhaps no) reflections from the BHSZ interface because negative-reflectivity data will cancel positive-reflectivity data. In contrast, on specific 2D seismic lines oriented close to the azimuth of the isotropy plane or to the azimuth of the symmetry axis, we may be able to observe a relatively strong P-P AVO effect (Figure 3.16, left panel).

Our modeling suggests that P-SV reflections from the BHSZ, especially in the symmetry-axis plane, are strong, independent of the presence of free gas, and will be the preferred seismic mode for estimating hydrate concentration using AVA technology. We conclude that multiazimuth and multicomponent seismic data are essential for understanding hydrate distribution and concentration.

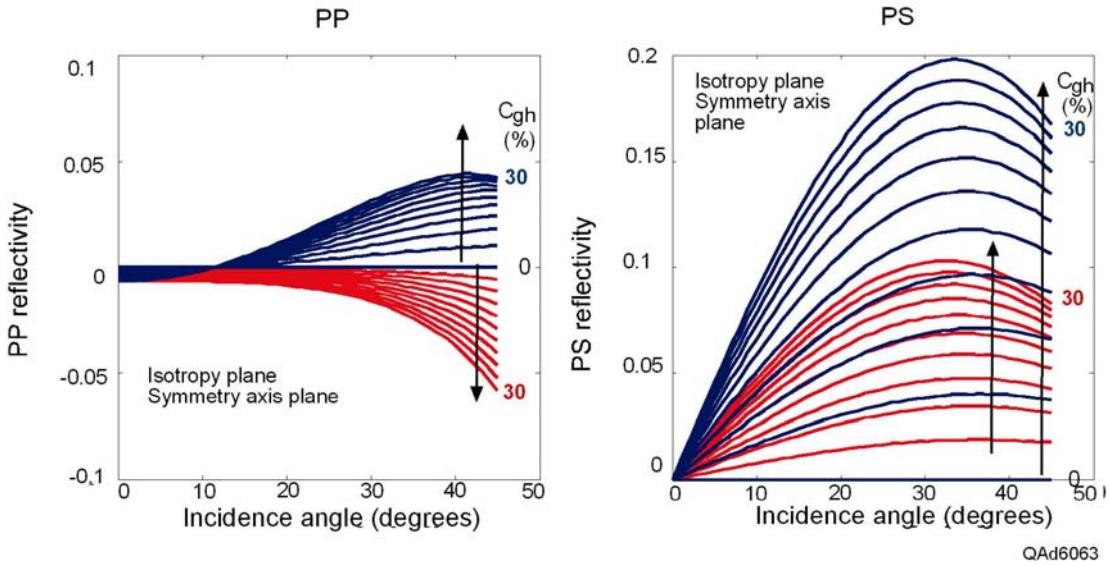

Figure 3.16: P-P (left) and P-SV (right) reflectivity from the base of the HSZ for Model C with vertical layers of pure hydrate in Layer 1 above the interface (Fig. 3.8). Red curves show reflectivity when the particle-displacement vector is oriented in the isotropy plane (parallel to layering). Blue curves show reflectivity when particle-displacements vectors are oriented in the symmetry-axis plane (perpendicular to layering). The different curves correspond to different hydrate concentration (0 to 30 percent of the unit volume) in the sediments. The arrows indicate the direction of increasing hydrate concentration. In this model, there is no free gas below the BHSZ. The effective pressure is 1 MPa, corresponding to a sub-seafloor depth of approximately 120 m.

Comparing Modeling Results with Laboratory Measurements

We have compared our rock physics modeling results for Model A with laboratory measurements on synthetic gas hydrates formed in unconsolidated fine sands. Yun and others (2005) performed laboratory measurements on sediments containing synthetic gas hydrates in concentrations ranging from 0 to 100-percent of the porous space. For hydrate concentration smaller than 100 percent, the remaining pore space was occupied by brine. The porosity of the sand samples was 0.37. The laboratory measurements were performed at low effective pressure, smaller than 0.01 MPa, which corresponds to a shallow burial depth of 2 m or less.

In Figures 3.17 and 3.18 we compare their laboratory measurements for P- and S-wave velocity as a function of hydrate concentration with our results for rock physics Model A (load-bearing hydrates). The left panels in these figures show the lab measurements and the right panels show our rock physics modeling results. The unconsolidated sediments in the rock physics model are represented by quartz grains at critical porosity, assumed to be 0.37, the same value as the porosity of the sand samples used in the laboratory measurements.

Figure 3.17 shows that P-wave velocity increases with hydrate concentration for both lab measurements and for our rock physics model of load-bearing hydrates. The increase in P-wave velocity is non-linear and is larger when hydrate concentrations in the pores exceed 50 percent. For hydrate concentrations smaller than 50 percent, the increase in P-wave velocity due to the presence of hydrates is small. We observe a good agreement between the laboratory measurements of P-wave velocity as a function of hydrate concentration and our rock physics modeling results.

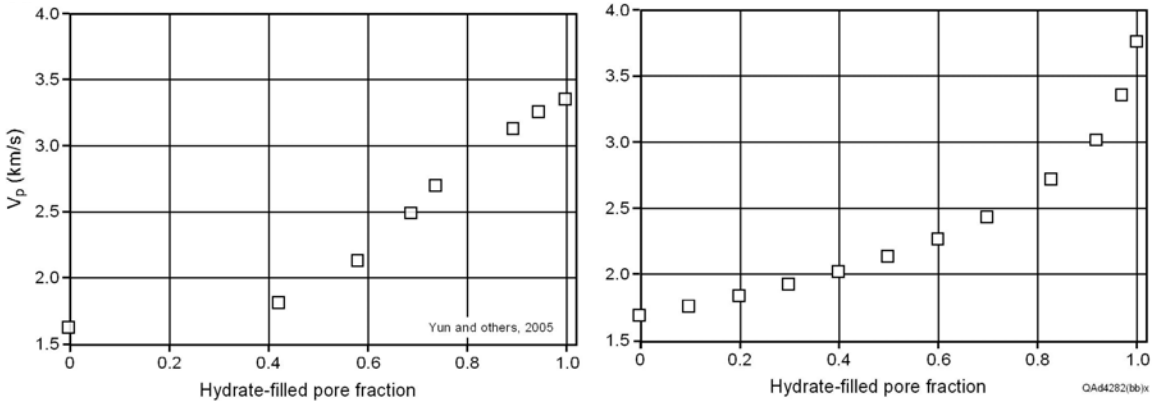

Figure 3.17: Comparison of laboratory measurements and **Model A** results for P-wave velocities as a function of hydrate concentration. *Left panel*: Yun and others (2005) lab results using tetrahydrofuran (THF) as a hydrate proxy. *Right panel*: Our rock physics modeling results when hydrates are assumed to be part of the load-bearing dry frame of the sediments. Effective pressure is 0.01 MPa, corresponding to a sub-seafloor depth of approximately 2 m.

Figure 3.18 shows how S-wave velocity increases with hydrate concentration for the Yun and others (2005) lab measurements and for our rock physics model of load-bearing hydrates. The increase in S-wave velocity is large when the hydrate concentration in the pores exceeds 50 percent. For hydrate concentrations smaller than 50 percent, the increase in S-wave velocity due to the presence of hydrates is small. We observe a relatively good agreement between the laboratory measurements of S-wave velocity as a function of hydrate concentration and our rock physics modeling results.

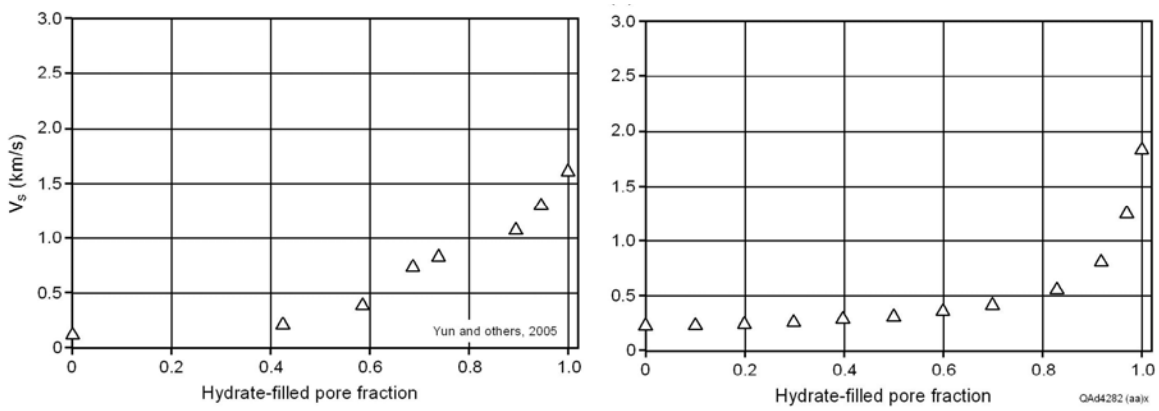

Figure 3.18: Comparison of laboratory measurements and **Model A** results for S-wave velocities as a function of hydrate concentration. *Left panel*: Yun and others (2005) lab results using tetrahydrofuran (THF) as a hydrate proxy. *Right panel*: Our rock physics modeling results when hydrates are assumed to be part of the load-bearing dry frame of the sediments. Effective pressure is 0.01 MPa, corresponding to a sub-seafloor depth of approximately 2 m.

Based on the agreement between these lab data and our rock physics modeling results, we concluded our rock physics theory was sound and could be a valuable diagnostic tool as we proceeded to determine interval seismic-based values of V_P and V_S near the seafloor across our study areas.

As an additional comment on the validity of using our Model A to interpret hydrate concentrations in hydrate-sediment mixtures, we note that Winters and others (2004) studied samples containing natural gas hydrates from the Mallik 2L-38 well, Mackenzie Delta, and found that these naturally formed hydrates were part of the load-bearing frame of their host sediments also. However, they then performed measurements on Ottawa sands containing synthetic methane hydrate formed in the laboratory, and these lab measurements suggested that hydrates cement their host sediments. A cementation hypothesis implies a large increase in P- and S-wave velocities for small hydrate concentrations (Dvorkin and others, 1994; Ecker and others, 1998). This type of velocity behavior is not usually observed in published field data acquired across hydrate zones. This laboratory study by Winters and others (2004) presents an apparent contradiction between the hydrate-sediment morphology associated with naturally-forming hydrates, which appeared to be part of the load-bearing frame and did not cement the grains, and laboratory-formed hydrates, which appeared to cement the grains of the host sediments.

Based on our rock physics results using Model A, we observe that the laboratory measurements by Yun and others (2005) done on synthetic gas hydrates (Figures 3.17 and 3.18, left panels) are in qualitative agreement with the laboratory observations by Winters and others (2004) performed on natural, in situ hydrates. Both studies suggest that a load-bearing hypothesis is appropriate for hydrates that are uniformly distributed throughout their host sediments.

More laboratory and field measurements are needed to understand the complex mechanisms of hydrate formation and distribution in sediments.

Probably different hydrate/sediment morphologies apply in different natural settings.

Conclusions

We developed rock physics models for unconsolidated sediments that host hydrates in deep-water, near-seafloor strata and that are characterized by large V_P/V_S ratios. We have described four possible rock physics models for such hydrate systems in which we assume various morphologies for the hydrates and their host sediments. Modeling results show that the elastic properties, and hence the seismic velocities, of hydrate-bearing units depend on the geometry of the hydrate distribution within the sediments.

We find good agreement between our theoretical predictions for P- and S-wave velocities in a medium of load-bearing hydrate (our Model A) and laboratory measurements on synthetic gas hydrates (tetrahydrofuran [THF]) formed in unconsolidated sands. We conclude that, in some natural environments, hydrates are a part of the dry mineral frame of their host sediments. However, more laboratory and field studies are needed to understand the mechanisms of hydrate formation in sediments. These mechanisms may require that different hydrate/sediment morphologies be used from site to site, depending on specific in-situ conditions.

In some deep-water environments there may be layered types of sediment/hydrate morphologies. Our modeling shows that in such media, the effective elastic properties of stratified near-seafloor sediments containing hydrates are anisotropic, and in such cases, the acquisition of fast and slow components of multicomponent seismic data has great value. If the hydrate layering is vertical, approximating steeply dipping and aligned fractures filled with hydrates, the effective elastic properties will be azimuthally anisotropic.

AVA modeling indicates multicomponent seismic technology can be important for understanding how hydrates are distributed in relation to their host sediments and for estimating hydrate concentrations. Using combinations of P-P and P-SV AVA reflectivity, P- and S-wave interval velocities, and V_P/V_S ratios should improve our understanding of deep-water hydrate systems. When hydrates form in steeply dipping and aligned fractures, our modeling suggests that multiazimuth and multicomponent 3-D seismic data are essential for understanding and quantifying hydrate distributions.

We emphasize throughout this report that we use **probability distribution functions** (**PDFs**) of petrophysical parameters to calculate hydrate concentration from rock-physics relationships (Chapters 1 and 5). As a result, our estimations of hydrate concentration are also PDFs in which the **mean value** of the PDF defines the **expected hydrate concentration**, and the **standard deviation** of the PDF defines the **uncertainty** associated with the estimate.

Specific examples of some PDFs that have been used in some analyses are displayed as Figures 5.5 and 5.6. The numerical ranges of these PDFs are significant and make major contributions to the uncertainty associated with our

estimations of hydrate concentrations. However, the wide variation in velocity behavior associated with the four hydrate-sediment morphology Models A to D described in this chapter introduce even greater uncertainty into seismic-based estimates of hydrate concentration than do the uncertainties associated with the PDFs we assigned to the variables used in our rock physics calculations. This large uncertainty introduced by the lack of knowledge of the appropriate hydrate morphology that should be assumed cannot be overlooked as our hydrate estimates are analyzed. We will use morphology Model A (load-bearing hydrate) and Model C (thin layers of pure hydrate), which are probably the most likely morphologies to be found in hydrate systems, to illustrate this morphology-based uncertainty. If the measured value of V_P is 2000 m/s, examination of Figure 3.5 shows that when the host sediment is a 50-50 mix of quartz and clay, the estimated hydrate concentration can be 18 percent (Model A), 24 percent (Model C, fast mode), or 32 percent (Model C, slow mode). These three predictions span a great range, and that morphology-induced error range is usually greater than the range of uncertainty introduced by the PDF assigned to any single petrophysical parameter or combination of parameters. We conclude that seismic-based estimates of hydrate concentration can always be questioned if there is insufficient knowledge of the specific sediment-hydrate morphology that is being embedded in the hydrate system that is being analyzed.

The fundamental rock physics theory of shearing action in unconsolidated sediment does not seem to be adequately developed in the literature. We think the popular Hertz-Mindlin theory that many investigators use is not appropriate for unconsolidated sediments because that theory assumes there is infinite friction at grain-to-grain contacts, which does not allow grains to slip or rotate relative to each other. We conclude that Walton's grain-contact model, which allows grains to rotate and slip at their contacts, is more appropriate for the high-porosity, unconsolidated sediments that exist in deep-water hydrate systems, and we incorporate Walton's theory into our rock physics description of V_S velocity.

DOE Gas Hydrate Final Report

Chapter 4

Formulating the Archie Equation for Deep-Water Hydrate Systems

Introduction

An important aspect of the work done during this project is our interpretation of the resistivity-log response of high-porosity mixtures of sediment, hydrate, and brine. We developed evidence and logic that the **Hashin-Shtrikman Lower Bound** should dictate the functional behavior for the resistivity of a high-porosity mixture of sediment, hydrate, and conductive brine. In our terminology, "**high porosity**" means that the porosity of the mixture equals or exceeds **critical porosity**, which is the porosity condition across the shallower portions of the hydrate stability interval at our study sites. We are not aware of any other hydrate project that concludes that the resistivity behavior of high-porosity, deep-water hydrate systems should converge to the functional trend of the Hashin-Shtrikman Lower Bound.

In this chapter, we present evidence that the classical Archie Equation that is used to interpret hydrocarbon concentration from resistivity logs in consolidated media may also be used to predict hydrate concentration in high-porosity, unconsolidated, deep-water sediments **if** appropriate constants are used to adjust the equation response to the resistivity predicted by the Hashin-Shtrikman Lower Bound for that medium. We present further evidence that the Hashin-Shtrikman Lower Bound is important for defining the response of any function that is used to estimate hydrate concentration from deep-water resistivity logs. Neither the Archie Equation nor the Hashin-Shtrikman Lower Bound should be used to interpret hydrate concentration when thin layers of pure hydrate are intercalated with sediment layers (either as horizontal layers or as vertical sheets). An additional restriction is that the Hashin-Shtrikman Lower Bound should be used to estimate hydrate concentration only when hydrate is uniformly dispersed throughout the sediment and each sediment grain and each clathrate cluster is surrounded by brine. In our methodology, we use the Hashin-Shtrikman Lower Bound to determine the constants in the Archie Equation and then apply this calibrated Archie Equation to resistivity logs acquired across the Green Canyon area to illustrate that thick intervals of hydrate are present at several locations and that some zones within these intervals have hydrate concentrations that exceed 50 percent of the pore space.

Resistivity Models of Sediment-Hydrate Systems

Log data across our Green Canyon hydrate study areas were acquired by petroleum companies who were interested in deep oil and gas targets, not in near-seafloor gas hydrate systems. Consequently, these companies acquired minimal lithofacies-sensitive log data consisting of only gamma-ray and resistivity measurements across shallow, near-seafloor intervals where hydrates occur. All other logs acquired across hydrate-bearing zones were measurements such as temperature and rate of penetration, which provide limited lithofacies information. For this reason, any log-based evidence of sub-seafloor hydrates across Green Canyon lease blocks has to be inferred from resistivity logs.

We developed two Earth models to describe the resistivity properties of deep-water hydrate systems. The first model, illustrated as Figure 4.1, assumes that hydrate is uniformly dispersed throughout the sediment. This model is appropriate for resistivity analyses of hydrate-sediment mixtures whether the hydrate is load-bearing or pore-filling. The only requirement is that each clathrate cluster and each mineral grain be surrounded by fluid except at their points of contact with neighboring hydrate clusters and mineral grains. This dispersed-hydrate model will be used as the principal Earth-resistivity model for our Green Canyon study sites.

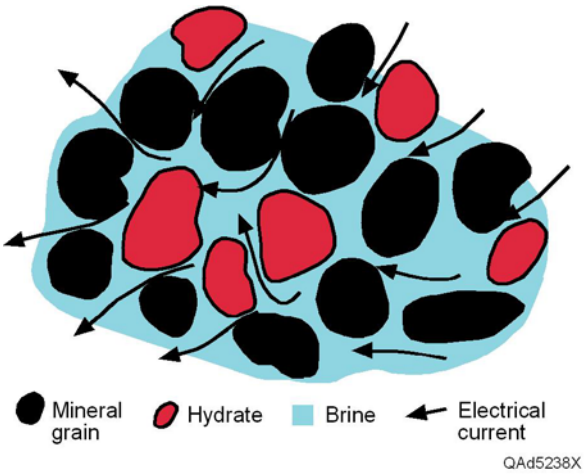

Figure 4.1. Resistivity model for a hydrate system in which hydrate is uniformly distributed throughout its host sediment. A fundamental assumption is that each mineral grain (black) and each clathrate cluster (red) is surrounded by conductive brine (blue), which creates a medium with many pathways for electrical current flow (arrows).

Our second model, illustrated as Figure 4.2, assumes that the hydrate is layered. This model allows pure-hydrate layers to be either horizontal (Fig. 4.2a) or vertical (Fig. 4.2b). Although this layered-hydrate model will not be utilized in this report, recent deep-water cores of near-seafloor strata from offshore India and Korea have demonstrated that it is a resistivity model that applies to some deep-water hydrate systems. In several zones in the logs that will be shown Chapter 5, hydrate appears to be present as horizontal layered strata that have

high hydrate concentration (Fig. 4.18, Well E; Fig. 4.20a; Fig. 4.21a). A layered-hydrate model is intriguing in that it illustrates that a layered-hydrate system can have a high resistivity, similar to that of resistors connected in series, if the layering is perpendicular to the direction in which resistivity is measured (Fig. 4.2a), but a low resistivity, like that of resistors connected in parallel, if the layering is parallel to the direction of the resistivity measurement (Fig. 4.2b). In both situations, the layer geometries have the same amount of hydrate in a unit Earth volume, but different resistivities are measured. The arrow drawn beside each layered system on Figure 4.2 shows the direction in which the sonde measures Earth resistivity. The terms “perpendicular layering” and “parallel layering” are defined relative to this indicated measurement direction of the sonde.

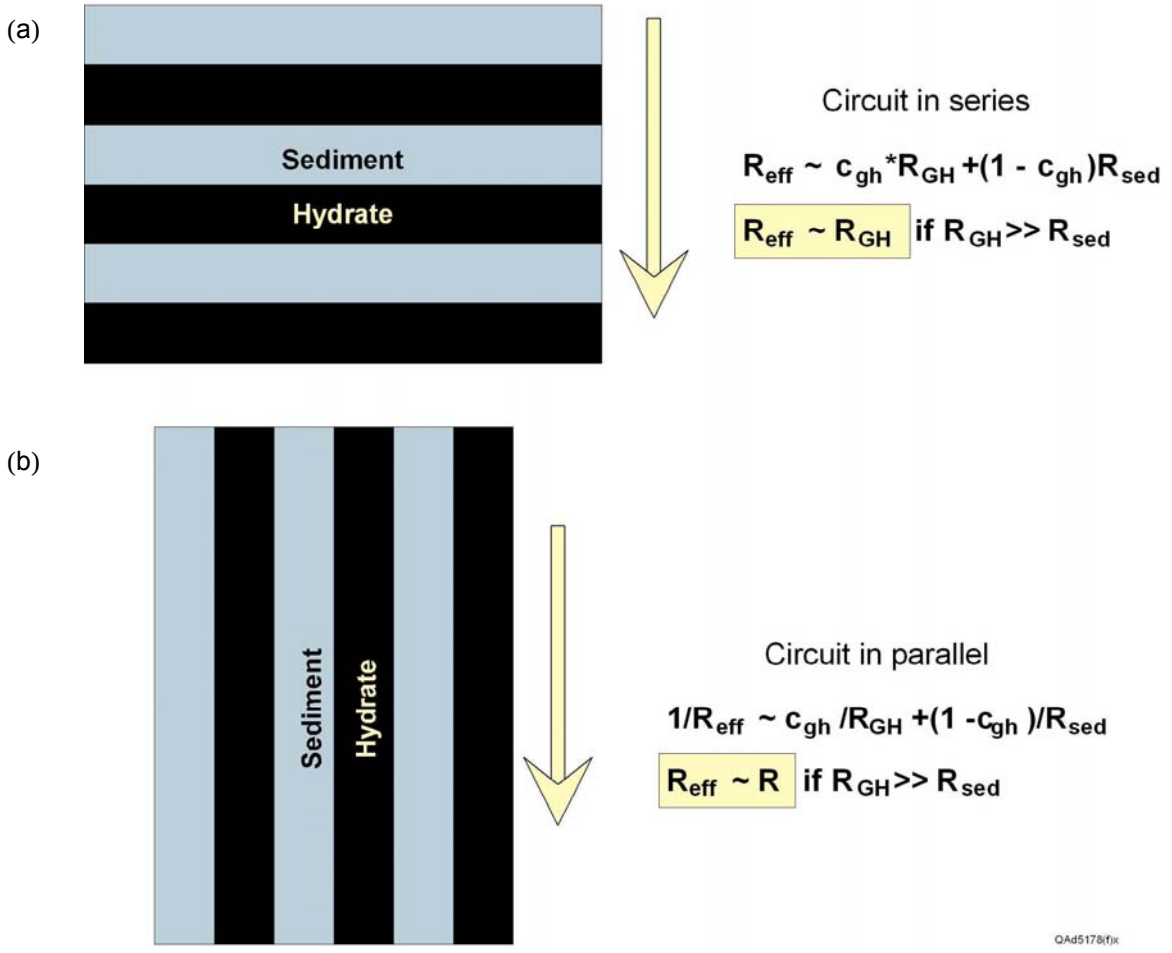

Figure 4.2. Resistivity model for a hydrate system in which hydrate is not disseminated throughout the host medium but occurs as thin layers of pure-hydrate that are intercalated with layers of sediment. This model can be used for horizontal layering (a) or for vertical dikes and fractures (b). C_{gh} is the fraction of hydrate in the Earth volume for which an effective resistivity R_{eff} is measured. Arrows show the direction in which resistivity is measured. R_{GH} is the resistivity of pure hydrate; R_{sed} is the resistivity of the sediment.

The possibility that hydrate may occur as vertical dikes in fine-grained sediments (Fig. 4.2b) is gaining favor with some deep-water hydrate researchers. This vertical-layer concept is sometimes based on the principle of **polygonal faults** and **polygonal fractures**, which are now recognized in many basins (Cartwright and others, 2003). A photograph of sand-filled polygonal fractures in a lithified dolomitic mud is shown as Figure 4.3. Larger-scale polygonal fault features that can be seen in 3D seismic time slices are displayed in Figure 4.4. These phenomena, whether at a fracture scale (cm) or at a fault scale (km), are assumed to be caused by (1) **syneresis**, the spontaneous volumetric contraction of a gel without evaporation, or by (2) **density inversion**, a situation where denser (heavier) sediment is deposited atop a fine-grained layer, or by (3) a **gravity sliding** of a weak, fine-grained interval (Cartwright and others, 2003). Deep-water, fine-grained sediments that form the host medium for many GOM hydrates are an ideal “gel” material in which any of these mechanisms, particularly syneresis, can occur.

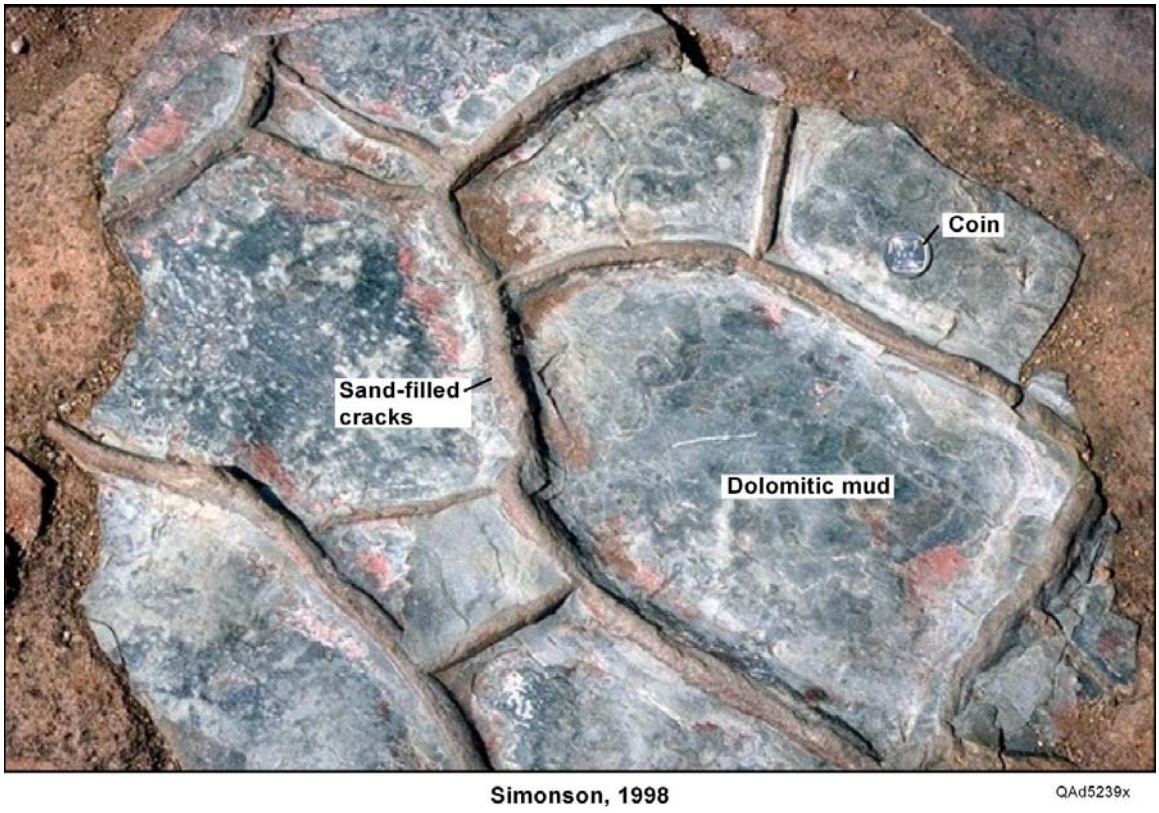

Figure 4.3. An outcrop of lithified dolomitic mud having a grid of sand-filled polygonal fractures. Photograph taken near Bourke’s Luck, South Africa, by Bruce M. Simonson, Department of Geology, Oberlin College.

To date, polygonal faults have not been described in published works related to the GOM. However, polygonal faults were not noticed in other basins

(for example the North Sea) until the 1980's, so the recognition of these features seems to require that a deliberate search has to be done to reveal their presence. Polygonal fractures, which are below the scale of seismic resolution, could be abundant across the GOM, yet difficult to recognize.

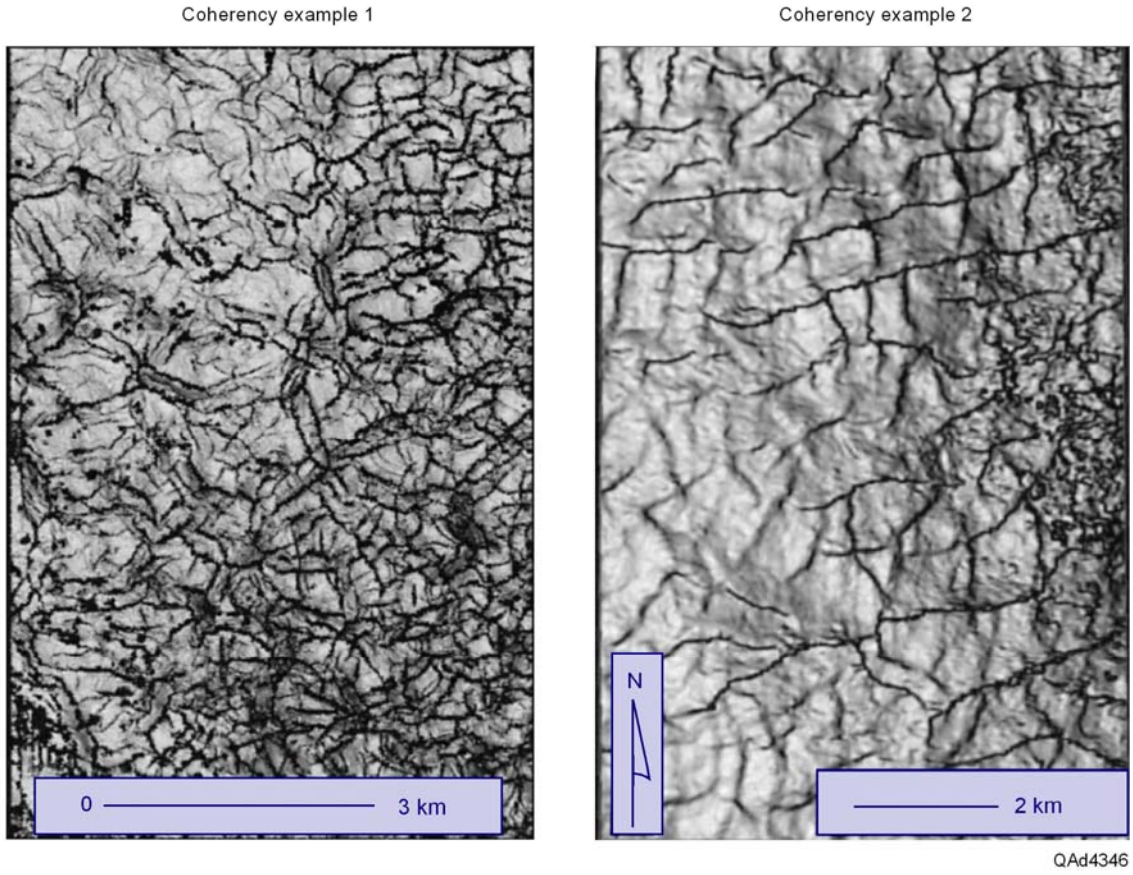

Figure 4.4. Time slices through 3D seismic coherency volumes showing polygonal faults extending through a fine-grained interval (Cartwright and others, 2003)

Archie Equation

The Archie Equation has been used to analyze resistivity responses of fluid-filled porous rocks for more than six decades (Archie, 1942). The clay-free form of this equation with which we begin our analysis can be written as

$$(4.1) \quad R = (aR_W\Phi^{-m})(S_W)^{-n},$$

where

- R = resistivity of the logged interval (ohm-m),
- a = dimensionless parameter related to the grain shape,

- R_W = resistivity of the pore fluid (ohm-m),
- Φ = porosity (dimensionless fraction),
- m = dimensionless parameter related to the cementation of the grains,
- S_W = water saturation (dimensionless fraction), and
- n = saturation exponent (a dimensionless parameter).

In Chapter 6, we will utilize a corrected form of this equation that includes the effect of clay minerals on sediment resistivity (Eq. 6.1). Because the Archie Equation is an empirical model, when it is applied to a specific rock matrix and a specific type of pore fluid, parameters a, m, and n must be derived and adjusted to create optimal agreement between resistivity readings and independent knowledge of R_W, Φ, and S_W for that rock-fluid system. In typical oil and gas reservoir applications, a is ~1.0, n = 2, and m ranges from 2.0 to 2.5.

There is limited experience in applying the Archie Equation to high-porosity mixtures of sediment, brine, and hydrate. In their analysis of Blake Ridge resistivity data, Collett and Ladd (2000) used the following values for their formulation of the Archie Equation: a = 1.05, m = 2.56, n = 2, and R_W = 0.23 ohm-m. We cannot find the exact value of R_W that was used in their Blake Ridge study. We know only that the pore fluid salinity was assumed to be 32,000 ppm. If the hydrate formation temperature is assumed to be 65ºF, then this salinity leads to R_W = 0.23 ohm-m. Given our application of the Hashin-Shtrikman bounds that will be discussed in the following sections, we conclude that the parameter values used for the Archie Equation at Blake Ridge are not optimal for high-porosity unconsolidated sediments found in deep water. In our formulation of the Archie Equation, we alter the values to be probability distribution functions in which the expected values of the parameters are: a = 1.0, m = 1.2, n = 2, and R_W = 0.17 ohm-m. A value of m = 1.2 for unconsolidated sediments has been suggested by other researchers (Archie, 1942; Sen and others, 1981; Mendelson and Cohen, 1982). Our reasoning for our parameter choices will be further explained as we discuss our second analytical resistivity model, the Hashin-Shtrikman Lower Bound.

Hashin-Shtrikman Bounds

Calculation of Hashin-Shtrikman bounds is a valuable analysis technique for defining the maximum and minimum values that can be observed for magnetic, electrical, and thermal properties of rock systems that are mixtures of several distinct minerals and fluids (Hashin and Shtrikman, 1962). In Chapter 3, we used Hashin-Shtrikman bounds to guide our logic as we developed rock-physics models that describe P-wave velocity (V_P) and S-wave velocity (V_S) behavior in deep-water hydrate systems that are mixtures of quartz, clay, hydrate, and brine. We have found Hashin-Shtrikman theory to be invaluable for understanding the elastic properties, and thus the V_P and V_S behavior, of these complex mixtures (Hashin and Shtrikman, 1963). We now expand our application of Hashin-Shtrikman bounds to the analysis of the resistivity behavior of sediment-hydrate-brine mixtures.

We use the Earth model illustrated in Figure 4.1 (disseminated hydrate) to describe the sediment-hydrate-brine mixture that needs to be analyzed. For this medium, the Hashin-Shtrikman Upper Bound (**HS+**) for resistivity is given by (Hashin and Shtrikman, 1962):

$$(4.2) \quad R_{HS+}^{-1} = \sigma_{HS-} = \sigma_{\min} + \frac{A\_}{1-\alpha\_A\_}$$

where subscript HS- indicates the Hashin-Shtrikman Lower Bound, and

$$(4.3) \quad A\_ = \sum_{i=2}^{N} \frac{f_i}{(\sigma_i - \sigma_{\min})^{-1} + \alpha\_}$$

$$(4.4) \quad \alpha\_ = \frac{1}{3\sigma_{\min}}$$

In this notation, σ_i is the conductivity and f_i is the volume fraction of constituent component **i** of the 4-element mixture (quartz, clay, hydrate, brine), σ_1 is the minimum conductivity, and σ_N is the maximum conductivity of the individual components that form the mixture. The Hashin-Shtrikman Lower Bound (**HS-**) for resistivity is given by

$$(4.5) \quad R_{HS-}^{-1} = \sigma_{HS+} = \sigma_{\max} + \frac{A_+}{1-\alpha_+ A_+},$$

where

$$(4.6) \quad A_+ = \sum_{i=1}^{N-1} \frac{f_i}{(\sigma_i - \sigma_{\max})^{-1} + \alpha_+}$$

$$(4.7) \quad \alpha_+ = \frac{1}{3\sigma_{\max}}.$$

Using subscripts Q for quartz, cl for clay, w for brine, and gh for gas hydrate, we defined the following values as the conductivities of the constituent components of the deep-water medium:

(4.8) $\sigma_1 = \sigma_Q = 10^{-14}$ S/m,

(4.9) $\sigma_2 = \sigma_{gh} = 10^{-6}$ S/m,

(4.10) $\sigma_3 = \sigma_{cl} = 10^{-3}$ S/m, and

(4.11) $\sigma_4 = \sigma_W = 3$ S/m.

The subscript order of this conductivity sequence is important because it is the "minimum-to-maximum" order of parameters that are required in the Hashin-Shtrikman theory. The order conforms to the subscripting notation used in Equations 4.3 and 4.6.

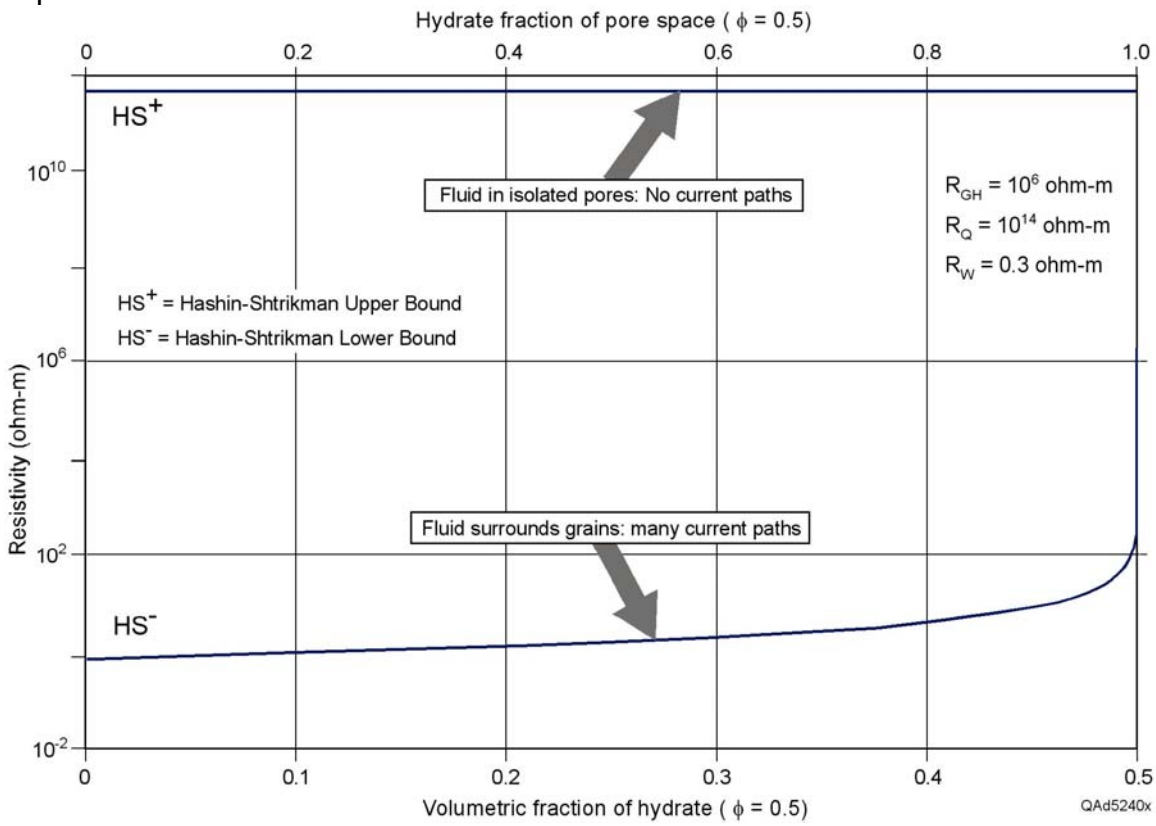

Figure 4.5. Hashin-Shtrikman Upper Bound (HS+) and Lower Bound (HS-) calculated for a mixture of quartz grains, hydrate, and brine. Porosity is assumed to be 0.5. The calculation is based on the dispersed-hydrate model illustrated in Figure 4.1.

We used these conductivity values and the dispersed-hydrate model illustrated in Figure 4.1 to calculate the Hashin-Shtrikman bounds for a pure quartz-grain host medium. Graphical representations of the upper and lower resistivity bounds are illustrated on Figure 4.5, assuming that the porosity of the medium is 0.5. The range between upper and lower bounds is huge—approximately 10^{12} ohm-m. The upper bound is shown only for completeness of the analysis because this bound represents the hypothetical, but physically unrealistic, case in which conductive brine resides in isolated, unconnected pores and does not form any continuous conductive paths through the material. This assumption is invalid for most rocks and certainly is incorrect for deep-water, near-seafloor, high-porosity, hydrate-bearing sediments.

In contrast, the Hashin-Shtrikman Lower Bound represents resistivity behavior that results when brine surrounds each matrix grain and each hydrate

clathrate cluster and creates a huge number of interconnected brine-filled paths for electrical current to pass through the sediment-brine-hydrate system. These current paths are shown by arrows in the dispersed-hydrate model depicted as Figure 4.1. Conditions associated with the Hashin-Shtrikman Lower Bound are a good description of the hydrate-sediment-brine mixture that exists in deep-water hydrate systems.

Hashin-Shtrikman Lower Bound

An analysis by Wempe (2000) was particularly germane to our study of the resistivity response of hydrate dispersed throughout unconsolidated, high-porosity, near-seafloor sediments. A key graphic of Wempe's study is reproduced as Figure 4.6a. Our modification of this graphic is shown as Figure 4.6b. In these figures, the horizontal axis is porosity and the vertical axis is normalized resistivity $\mathbf{R/R_W}$, where R is the resistivity measured across a medium of porosity $\mathbf{\Phi}$ and R_W is the resistivity of the fluid that fills the pores. The shaded interval labeled $\mathbf{\Phi_C}$ defines the range of **critical porosity**, which is porosity where the grains of a high-porosity medium convert from a suspended state to a load-bearing condition in which each grain touches at least one other grain. Critical porosity varies from about 0.3 for round, uniform-size grains, to around 0.4 for well-sorted rounded grains of variable size, to about 0.6 for highly oblate (flat) grains.

The data plotted in Figure 4.6 are comprehensive and include laboratory measurements and field data gleaned from 11 studies referenced by Wempe (2000). A key concept demonstrated by these data (Fig. 4.6b) is that the resistivity behavior of all porous media converge to the Hashin-Shtrikman Lower Bound (HS-) when the porosity of the medium equals or exceeds critical porosity. Because the porosity of the deep-water, near-seafloor sediments that span the hydrate stability zone in the Green Canyon area equals or exceeds critical Porosity for many tens of meters (sometimes even a few hundred meters) below the seafloor, we are led to an important conclusion: ***the Hashin-Shtrikman Lower Bound is an ideal function for describing the resistivity of deep-water hydrate systems.***

The Hashin-Shtrikman Lower Bound that we calculated in Figure 4.5 is replotted in Figure 4.7 to better illustrate how the resistivity of deep-water sediment varies as a function of hydrate concentration. As hydrate concentration increases from 0 to 60 percent of the pore space, resistivity increases from ~0.6 ohm-m to only 2 ohm-m. The implication is that with 60 percent of the pore space occupied by hydrate, a large number of connected paths of conductive brine continue to wend through the mixture (Fig. 4.1).

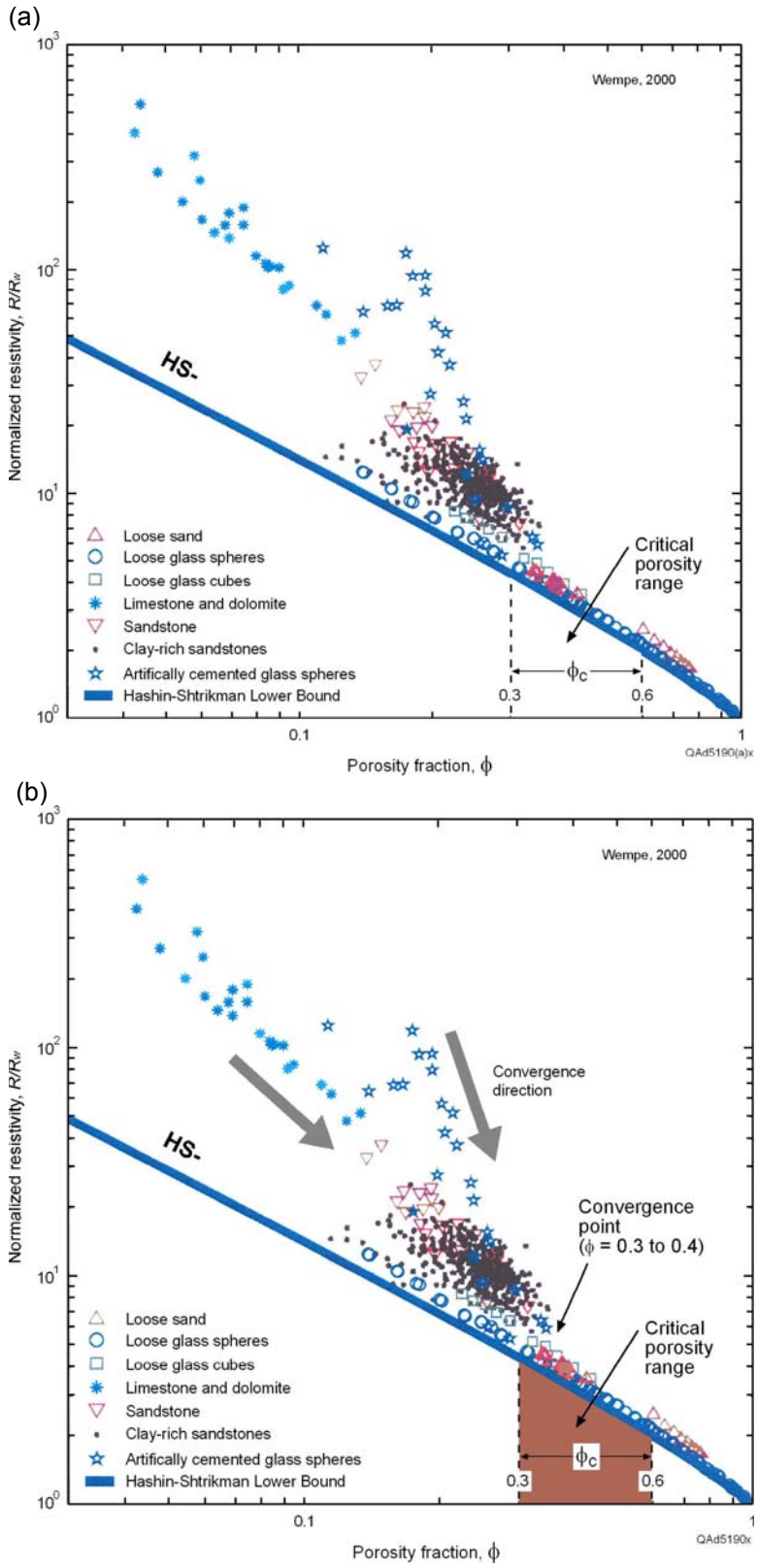

Figure 4.6.
(a) Crossplot of normalized resistivity (R/R_W) and porosity for a large number of laboratory tests and field-data observations that involve a wide range of conductive media (Wempe, 2000).
(b) Our modification of the crossplot to emphasize principles important for deep-water hydrate systems. R is measured resistivity; R_W is the resistivity of the pore-filling fluid. The shaded interval Φ_C is the range of critical porosity for grains of different geometrical shapes. Note that all data converge to the Hashin-Shtrikman Lower Bound as porosity increases and enters the critical-porosity range.

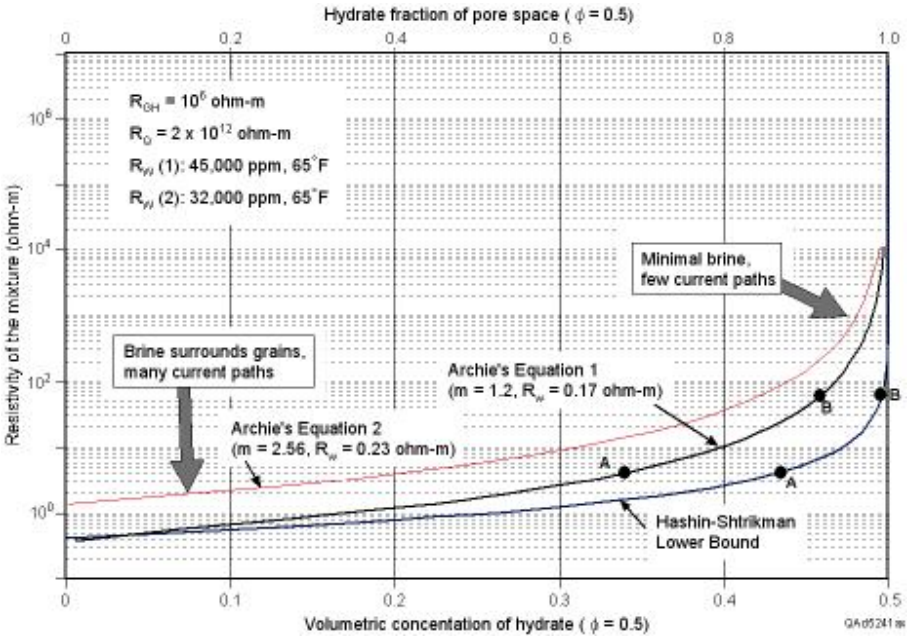

Figure 4.7. The Hashin-Shtrikman Lower Bound (HS-) and two formulations of the clay-free form of the Archie Equation (Eq. 4.1) displayed as functions of resistivity and hydrate fraction. Hydrate fraction is defined in terms of the pore volume (top axis) or the unit volume (bottom axis). Archie Equation 1 is our formulation for deep-water hydrate systems. Archie Equation 2 was proposed by Collett and Ladd (2000) at Blake Ridge. We stress this fundamental principle: at low hydrate concentrations where porosity is a maximum, deep-water mixtures of sediment and dispersed hydrate must have resistivities that agree with, or approximate, the Hashin-Shtrikman Lower Bound.

Even when hydrate fills 80 percent of the pore space, there are enough electrical current flow paths so that the resistivity increases to only 4 ohm-m. One factor that keeps the resistivity of this sediment-brine-hydrate mixture at a low value, even though the hydrate concentration is high, is that as hydrate grows, it expels salt into the surrounding brine and makes the brine more conductive. If some of this expelled salt stays local to its point of expulsion (a point of contention among hydrate researchers), the increased salinity will result in low resistivity even at high hydrate concentrations. In terms of electrical conductivity, a smaller number of electrical-current flow paths through a higher-salinity brine are equivalent to a larger number of flow paths through a reduced-salinity brine. In our analysis, however, we do not decrease pore-fluid resistivity as hydrate concentration increases. Using this constraint of a constant pore-fluid resistivity, the Hashin-Shtrikman Lower Bound implies that a significant increase in resistivity does not occur until hydrate concentration exceeds 90 percent of the pore space and the number of connected brine-filled paths is severely reduced.

Included in Figure 4.7 is a curve labeled **Archie Equation 1** that describes the resistivity behavior of the clay-free form of the Archie Equation (Eq. 4.1) that we think is appropriate for hydrate systems across Green Canyon that are embedded in clean-sand host sediment. Also included is a curve (**Archie Equation 2**) that describes how the Archie Equation developed by Collett and

Ladd (2000) at Blake Ridge would appear. The difference between the responses of these two Archie Equations is created by different choices for **m** and $\mathbf{R_W}$. Specifically, the parameter values used in these two formulations of the Archie Equation are shown in the following table.

Parameter	Collett and Ladd	Our Choice
a	1.05	1.0
m	2.56	1.2
n	2.0	2.0
Rw	0.23 ohm-m	0.17 ohm-m

We present the following arguments to support our parameter choices for the clay-free form of the Archie Equation:

1. A major contributor to the difference between the two Archie Equations is the different values (2.56 versus 1.2) for the cementation exponent, m. Studies by Sen and others (1981) and by Mendelson and Cohen (1982) show that m should be reduced to approximately 1.2 for unconsolidated sediments. Cementation exponent values of approximately 2.5 are appropriate for consolidated rocks but appear to be inappropriate for unconsolidated sediments.

2. The valuable study by Wempe (2000) summarized in Figure 4.6 forces us to conclude that any resistivity equation that is used to analyze deep-water hydrate systems when porosities are equal to or greater than critical porosity must have a functional behavior that approximates the Hashin-Shtrikman Lower Bound. With the above parameters, our version of the Archie Equation is a close approximation of the Hashin-Shtrikman Lower Bound at low hydrate concentrations where porosities exceed the critical porosity value (Fig. 4.7). We think that an Archie Equation that uses a large value of m deviates too far from the Hashin-Shtrikman Lower Bound and does not represent true resistivity conditions of a deep-water hydrate-sediment-brine mixture.

3. We use a value of 0.17 ohm-m for R_W because we assume that the pore fluid has a salinity of 45,000 ppm rather than 32,000 ppm, as was assumed by Collett and Ladd (2000) in their analysis of Blake Ridge resistivity logs. Pore fluid across a hydrate interval should have increased salinity because in converting local brine into clathrate cages, the hydrate-forming process expels NaCl and retains H_2O. The magnitude of salinity increase is unknown. We found one resistivity log in our study area to which the logging contractor added the comment that pore fluid salinity was 45,000 ppm. We decided to use that salinity value when we calculated Archie Equation 1 displayed in Figure 4.7.

Laboratory Confirmation of Resistivity Behavior

The resistivity behaviors of the Hashin-Shtrikman Lower Bound and Archie Equation that we use for estimating hydrate concentrations are crucial and need to be confirmed by laboratory experiments, core analyses, and actual hydrate production tests to determine the limitations and validity of these predictive models. We know of only one laboratory test that has measured the electrical conductivity of a simulated high-porosity hydrate-sediment mixture. The experimental data are shown as Figure 4.8. These tests were done by Professor Santamarina and his colleagues and students at Georgia Tech. Results were presented as a poster at the AAPG Hedberg Hydrate Conference in 2004.

In this experiment, measurements of electrical conductivity were made for clay and sand sediments that had a porosity of 0.37 and three different magnitudes of associated hydrate concentrations: 0, 50, and 100 percent of the available pore space. Test data (Fig. 4.8) show that electrical conductivity decreases by a factor of approximately 2 as hydrate concentration increases from 0 to 50 percent, which would cause resistivity to increase by a factor of approximately 2, just as indicated by the Hashin-Shtrikman Lower Bound (curve shown on Figure 4.7). Test data further indicate that conductivity decreases by 3 orders of magnitude (or resistivity increases by 3 orders of magnitude) as hydrate concentration increases from 50 to 100 percent of the pore space. However, the lab data do not define whether this large resistivity change is a linear or nonlinear function of hydrate concentration over this latter test range.

The Hashin-Shtrikman Lower Bound plotted on Figure 4.7 indicates that the resistivity of a high-porosity mixture of mineral grains, hydrate clathrate clusters, and brine increases by about 3 orders of magnitude as the hydrate fraction grows from 50 to 100 percent of the pore space, in good agreement with the laboratory data. Our predictive equations further specify that the rate of change of resistivity in this mixture is nonlinear with respect to hydrate concentration, with most of the resistivity change occurring when the hydrate concentration exceeds 90 percent of the pore volume.

(a)

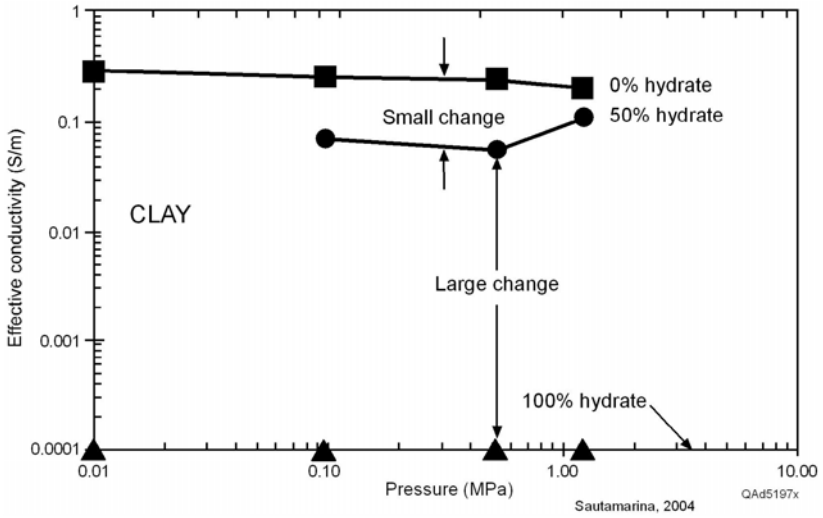

(b)

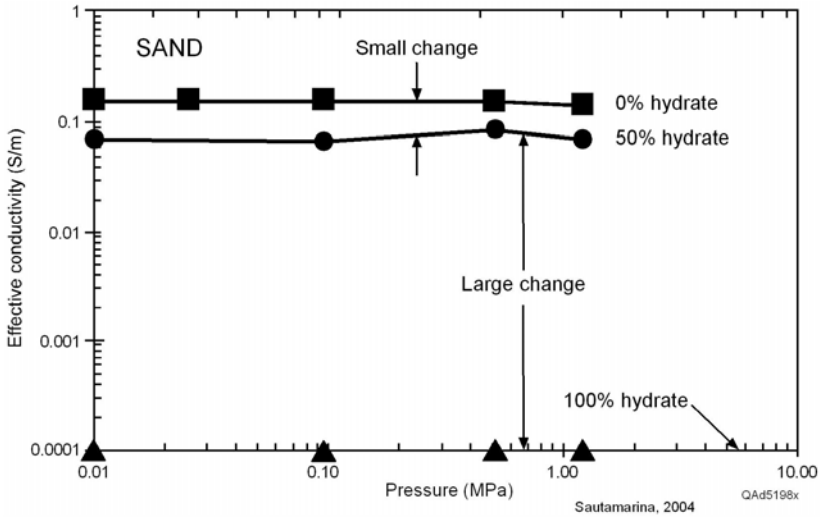

Figure 4.8. Laboratory measurements of the conductivity of homogeneous mixtures of quartz grains and simulated hydrate (Santamarina and others, 2004).

DOE Gas Hydrate Final Report

Chapter 5

Well Log Profiles

Introduction

The well logs illustrated in this report are replicas of hardcopy logs that we amassed across the Green Canyon area. We did not acquire digital log data for this study. The only log data that we could locate that measured properties of the hydrate stability zone were gamma-ray, resistivity, conductivity, temperature, and rate-of-penetration data. Strangely, no log suites across near-seafloor strata in the Green Canyon area included hole-caliper data. In some wells there were several resistivity curves, each one specifying resistivity at a different depth of investigation or presenting the resistivity data at a different display scale. We created a consistent petrophysical definition of the hydrate-bearing interval at each well by extracting only two log curves from each log suite: (1) the gamma-ray response, and (2) a consistent depth-of-investigation resistivity curve, with this latter curve displayed by a linear scale ranging from 0 to 2 ohm-m.

The most valuable data came from wells in which **logging-while-drilling** (**LWD**) technology was used to measure the resistivity of the hydrate stability zone. In some wells logged with LWD technology, there were short bursts of incorrect gamma-ray and resistivity responses that repeated at intervals of 90 ft (or at some multiple of 90 ft) when a new 90-ft section of drill pipe was added to the drill string. In these instances, the LWD system exhibited some type of temporary instability when a new 90-ft section of pipe was inserted into the data-communication link to the downhole sonde. These erroneous gamma-ray and resistivity responses typically spanned only 10 to 20 ft (3 to 6 m) and were easily recognized. We identify some of these noise bursts on some of the data displays in this chapter.

We interpreted the gamma-ray and resistivity curves on our hardcopy log plots, marked key intervals and important log features, and then passed our work to skilled drafting people. Our drafting section used a digital scanner to make digital images of these marked hardcopies, traced the gamma-ray and resistivity curves, and replicated our interpretations of the data. Each drafted copy was then reviewed for accuracy. In each report figure that displays log data, we have added labels that identify the lease block number and API number of the well where the data were acquired. These labels allow readers to locate the same log data and check the validity of our reproduced log curves if they wish to do so.

Well Log Data: Typhoon Field Area

Green Canyon lease blocks surrounding Typhoon Field (Block GC237) are outlined in Figure 5.1. Unfortunately, many wells in the Typhoon Field area were drilled without the use of LWD technology, with the result that:

1. The acquisition of log data often started at depths below the base of the hydrate stability zone, or
2. The hydrate interval was not logged until several days after the interval was drilled and some hydrate had dissociated near the well, or
3. The resistivity sonde sometimes exhibited unacceptably poor sensitivity across intervals of near-seafloor sediment.

Superimposed on this map as lettered red triangles are the locations of five wells (A, B, C, D, E) where log data were acquired that could be used to estimate hydrate concentration. Wells in the Typhoon area where near-seafloor log data were examined and found to not be useful for hydrate calibration are defined on the map displayed as Figure 5.2.

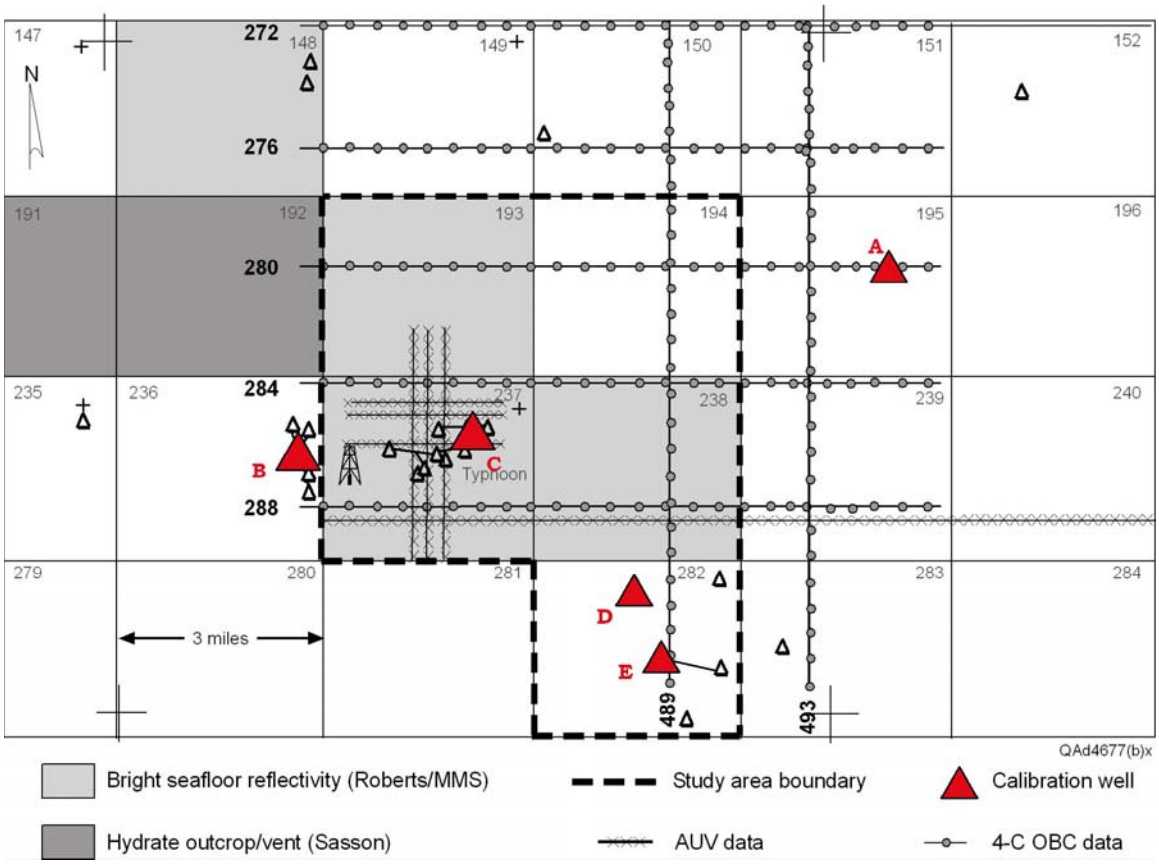

Figure 5.1. Area surrounding Typhoon Field (Block GC237) showing wells (marked with lettered red triangles) where log data exist that can be used for hydrate analysis.

Well log cross sections along the profiles of Typhoon-area calibration wells B, C, A and wells B, D, E are displayed as Figures 5.3 and 5.4, respectively. Because these log data were acquired using LWD technology within a few minutes of the bit penetrating each logged depth, the data should define in situ resistivity before any significant hydrate dissociation has occurred. The **base of the hydrate stability zone** labeled [**BHSZ(90%)**] drawn on each profile was determined using the model that Milkov and Sassen (2001) developed for a natural gas having 90.4% methane (Fig. 5.5). This Milkov/Sassen model is based on the chemistry of gases found in nearby Block GC185 and on geothermal gradients local to our study area. Also noted on the log cross-sections is a second estimate, labeled **BHSZ(R)**, of the depth of the BHSZ. BHSZ(R) marks a decrease in formation resistivity that: (1) can be interpreted as the BHSZ, and (2) is "close to" the depth BHSZ(90%) predicted by the Milkov and Sassen model.

The Milkov/Sassen estimation of the sub-seafloor thickness of the hydrate stability zone is shown by the three solid-line curves on Figure 5.5. These curves show that the BHSZ boundary moves deeper as the amount of methane decreases in the local natural gases and is replaced by a greater percentage of heavier gases (ethane, butane, propane). We have added a fourth dash-line curve to this Milkov/Sassen model to represent (approximately) a natural gas that has 85-percent methane, a gas chemistry suggested as appropriate for this area by scientists at the Minerals Management Service (private communication).

On Figures 5.3 and 5.4, the upper boundary of the BHSZ labeled **BHDZ** represents the inferred **base of the hydrate depletion zone**. Above this horizon, hydrate is absent through chemical interactions with sulfates migrating down from the seawater, or by thermally induced dissociation caused by spin-off eddies from the warm Loop Current, or because of other biological, chemical, and physical processes.

With resistivity behavior defined by the Hashin-Shtrikman Lower Bound and our Archie Equation 1 (Fig. 4.7) as guides, resistivity values less than 1 ohm-m represent low hydrate concentrations, typically less than 20 percent. Zones on the resistivity logs that have resistivities greater than 1 ohm-m are shaded gray on the well log cross-section profiles to define intervals that have increased hydrate concentration. Several intervals where the gamma-ray response implies the grain size increases are shaded yellow on the gamma-ray curves and indicate possible reservoir-quality lithofacies. Blue-shaded layers define units where increased resistivity (shaded red) indicates a possible increase in hydrate concentration internal to these larger-grain facies.

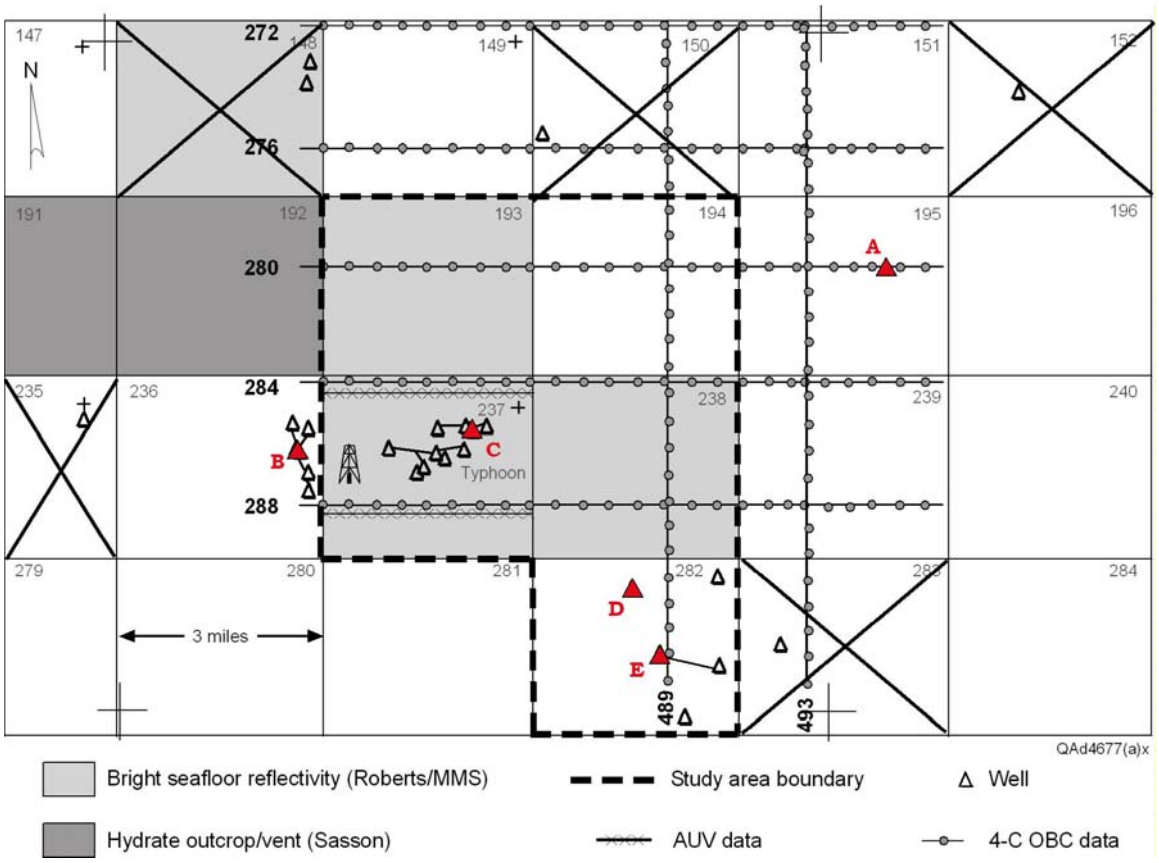

BLOCK	COMMENT
148	Logs start below hydrate zone
150	Logs start below hydrate zone
152	Poor-quality logs (1985 vintage)
235	Logs start below hydrate zone
283	No resistivity log

Figure 5.2. Wells local to the Typhoon Field area where near-seafloor log data were not appropriate for hydrate analysis. Blocks where unacceptable log data occur are marked with an X.

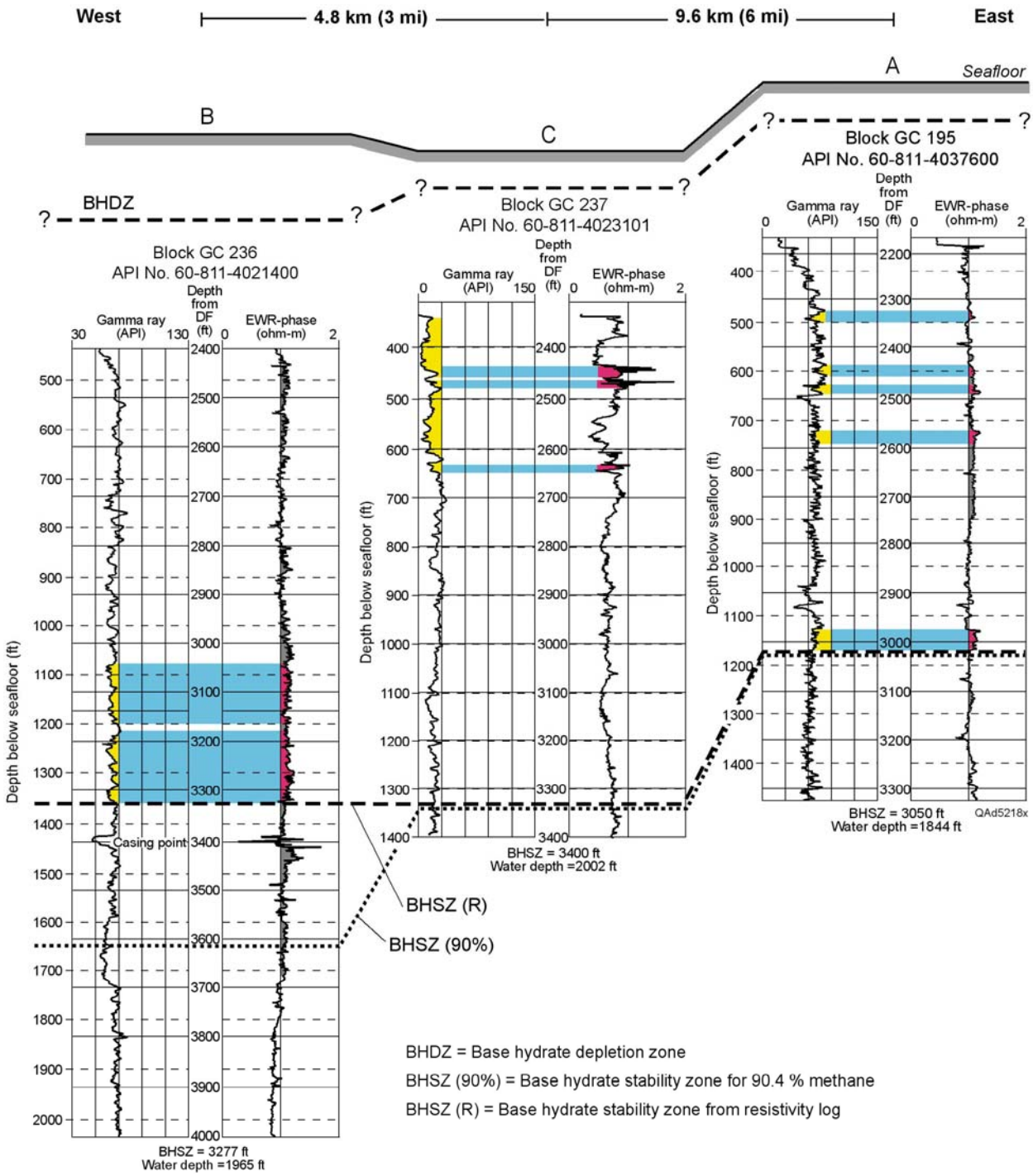

Figure 5.3. Well log cross section across calibration wells **B**, **C**, **A**, Typhoon Field area. There is a low concentration of hydrate along this profile. Well locations defined on Figure 5.1. The BHSZ(90%) depth labeled below each log suite is the depth of the base of the hydrate stability zone associated with the 90.4 percent methane curve from Figure 5.5. At each well, the BHSZ(R) horizon is drawn at a resistivity anomaly that is “close to” the depth coordinate suggested by the 90.4 percent methane curve. Gray zones emphasize intervals where resistivity exceeds 1 ohm-m. Yellow zones indicate possible larger-grain facies. Red identifies units that have both increased grain size and increased resistivity.

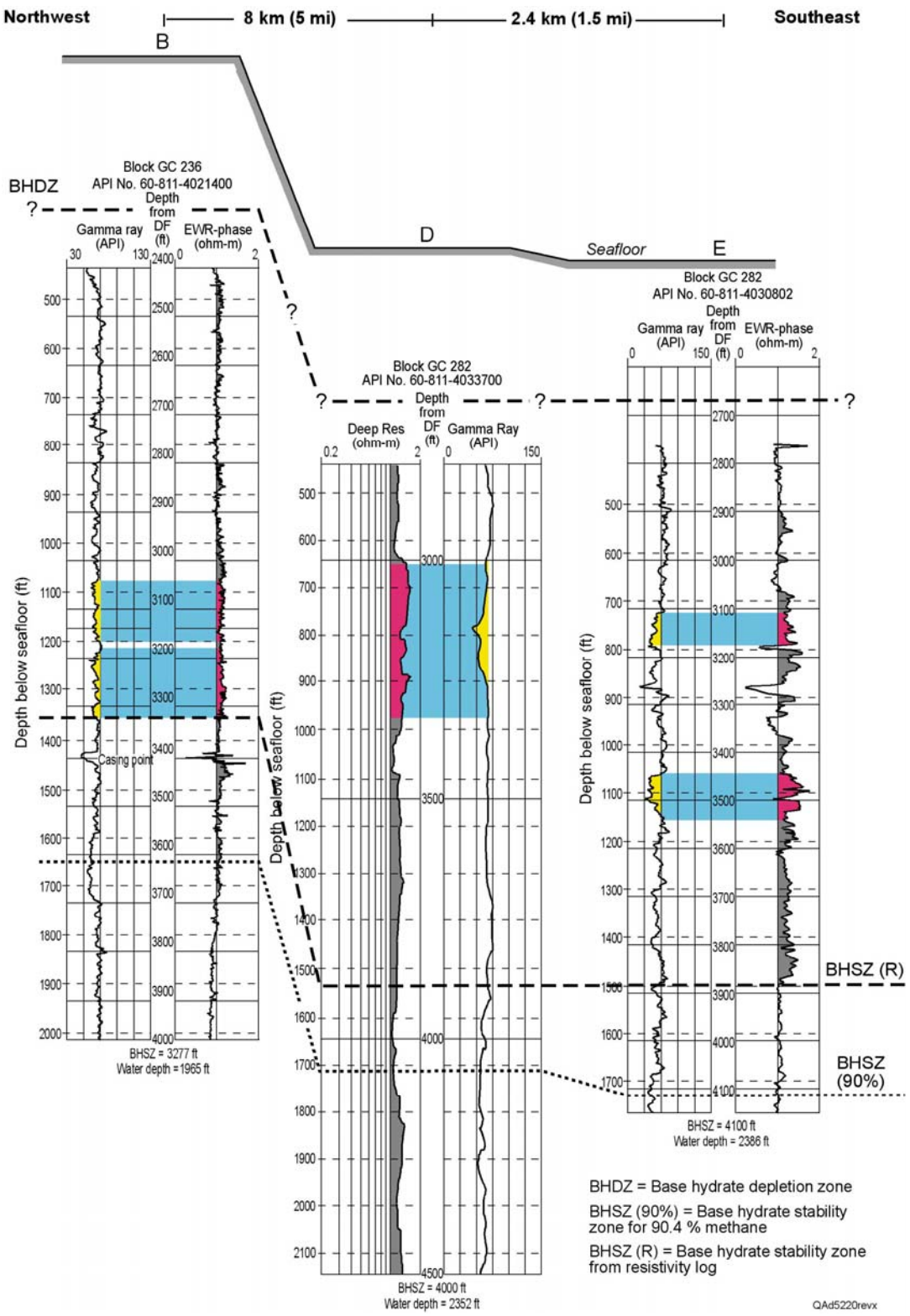

Figure 5.4. Well log cross section along the profile of calibration wells **B**, **D**, **E**, Typhoon Field area. Well locations defined in Figure 5.1. Hydrate concentration increases along the southeast part of this profile. Horizons BHSZ(90%) and BHSZ(R), colors, and shadings are explained in the caption of Figure 5.3.

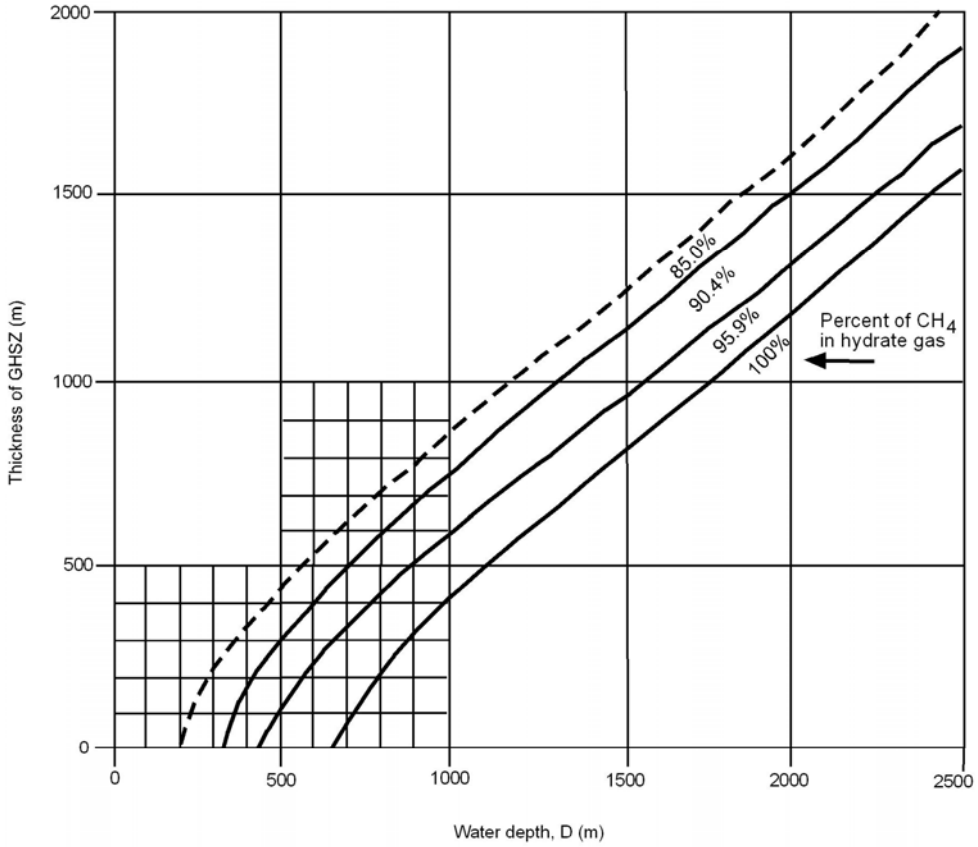

Modified from Milkov and Sassen, 2001

QAd4674(a)

Figure 5.5. Thicknesses of hydrate stability zones for various water depths and gas chemistries. The three solid-line curves were developed by Milkov and Sassen (2001) and are based on gas chemistry from Block GC185 and on geothermal gradients local to our Green Canyon study area. The dash-line curve is our approximation of the behavior of the thickness of the stability zone for a natural gas that has 85-percent methane, a gas chemistry favored by some scientists at the Minerals Management Service. We added a detailed coordinate grid that covers the range of water depths encountered across our research area.

These blue/red zones are candidates for hydrate production tests because they are not only a preferred reservoir facies but also represent a local increase in the concentration of hydrate. Some observations that can be made upon examining the resistivity data shown on Figures 5.3 are:

1. The hydrate-bearing interval beneath the Typhoon Field area spans a depth interval of approximately 460 m (~1,500 ft).
2. The resistivity relationships defined in Figure 4.7 imply the hydrate concentration within the zone of hydrate stability ranges from about 20 to 40 percent of the available pore space.

Well Log Data: Genesis Field Area

Lease blocks around Genesis Field (Blocks GC205 and GC161) are outlined in Figure 5.6. The red triangles define wells where log data exist that are appropriate for determining hydrate concentration. There are more hydrate-calibration wells (13) in the vicinity of Genesis Field than near Typhoon Field (5) because more wells were drilled in the area of Genesis Field after the early 1990's when LWD logging technology was widely used by GOM operators. We document in Figure 5.7 those lease blocks local to Genesis Field where log data were examined but were not found to be useful for hydrate calibration.

These numerous calibration wells allow a variety of well-log cross-section profiles to be made across the Genesis Field area. We show west-to-east profiles traversing wells A, B, C as Figure 5.8, along wells D, E, F, G as Figure 5.9, and along wells H, I, L, J as Figure 5.10. The BHSZ(90%) horizons drawn on these profiles were defined in the same manner as was done at Typhoon Field using the Milkov and Sassen (2001) model defined in Figure 5.4. Depths BHSZ(R) again indicate decreases in formation resistivity that: (1) may indicate the base of stable hydrate, and (2) are "close to" the BHSZ(90%) prediction of the BHSZ boundary provided by the Milkov and Sassen (2001) model. In interpreting these resistivity profiles, we used the following guidelines dictated by our Archie Equation 1 and the Hashin-Shtrikman Lower Bound plotted on Figure 4.7:

1. A resistivity value ≤1 ohm-m indicates a hydrate concentration of less than 20 percent.
2. Resistivities greater than 1 ohm-m indicate hydrate concentrations in excess of 20 percent, with a resistivity of 2 ohm-m representing a hydrate concentration of almost 60 percent.
3. Reduced gamma-ray readings indicate larger-grain sediment (shaded yellow), and within some of these larger-grain intervals are units (shaded blue/red) with relatively high hydrate concentration.

These log data imply that a more robust hydrate system exists in the vicinity of Genesis Field than what was found across the Typhoon area. Specifically the data indicate that:

- The hydrate interval varies from a thickness of about 365 m (~1,200 ft) at wells A and B (Fig. 5.8) to about 760 m (~2,500 ft) at well I (Fig. 5.10). Well D (Fig. 5.9) is unusual in that the resistivity response indicates that no hydrate is present.
- Hydrate occupies 20 to 40 percent of the pore volume over most of the interval between the boundaries marked BSRZ and BHSZ.

Numerous depositional units, some as thick as approximately 50 ft (~15 m), appear to have hydrate concentrations that exceed 0 percent.

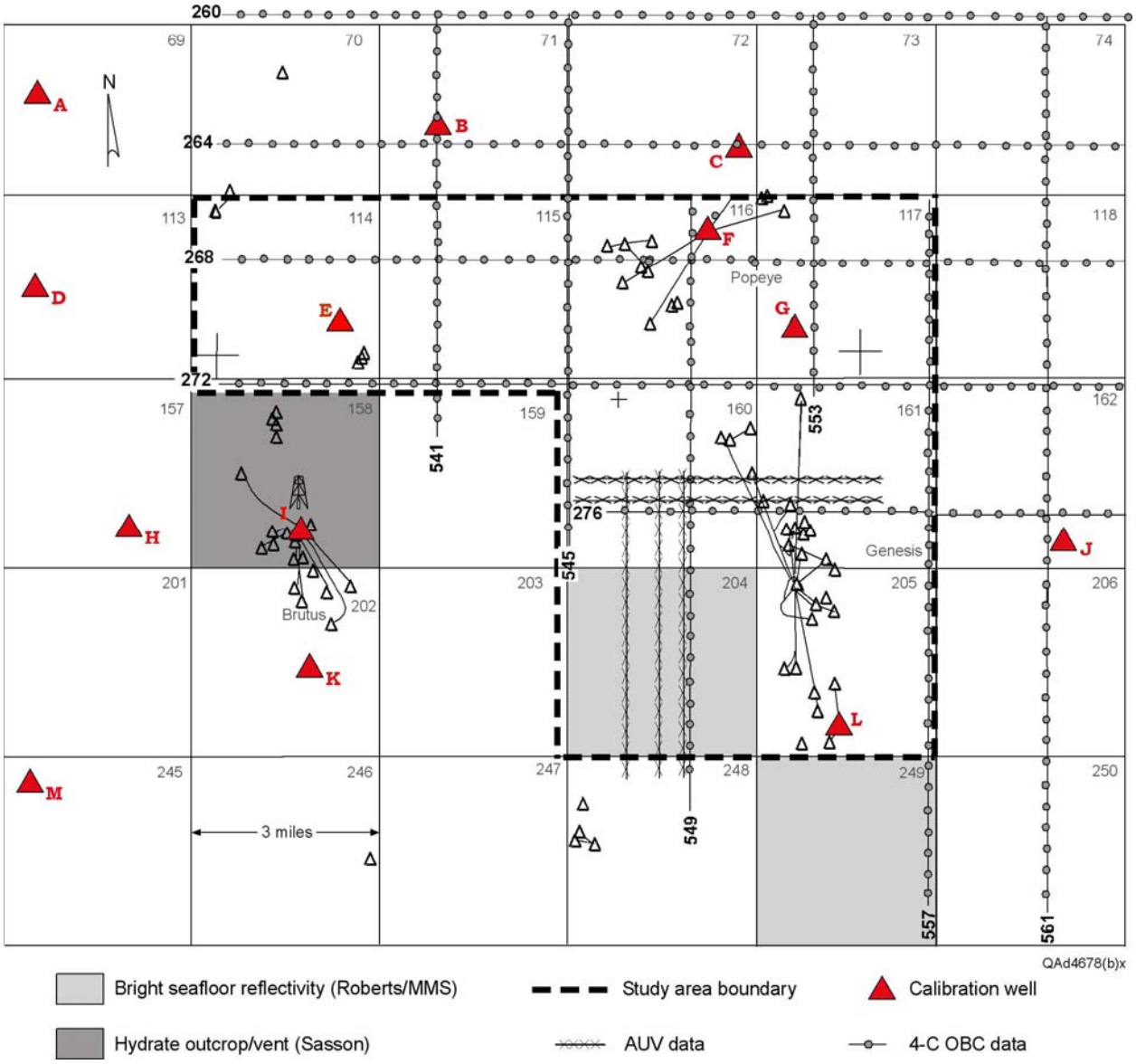

Figure 5.6. Map of Genesis Field area showing wells where log data (marked as lettered red triangles) exist that can be used for hydrate analysis.

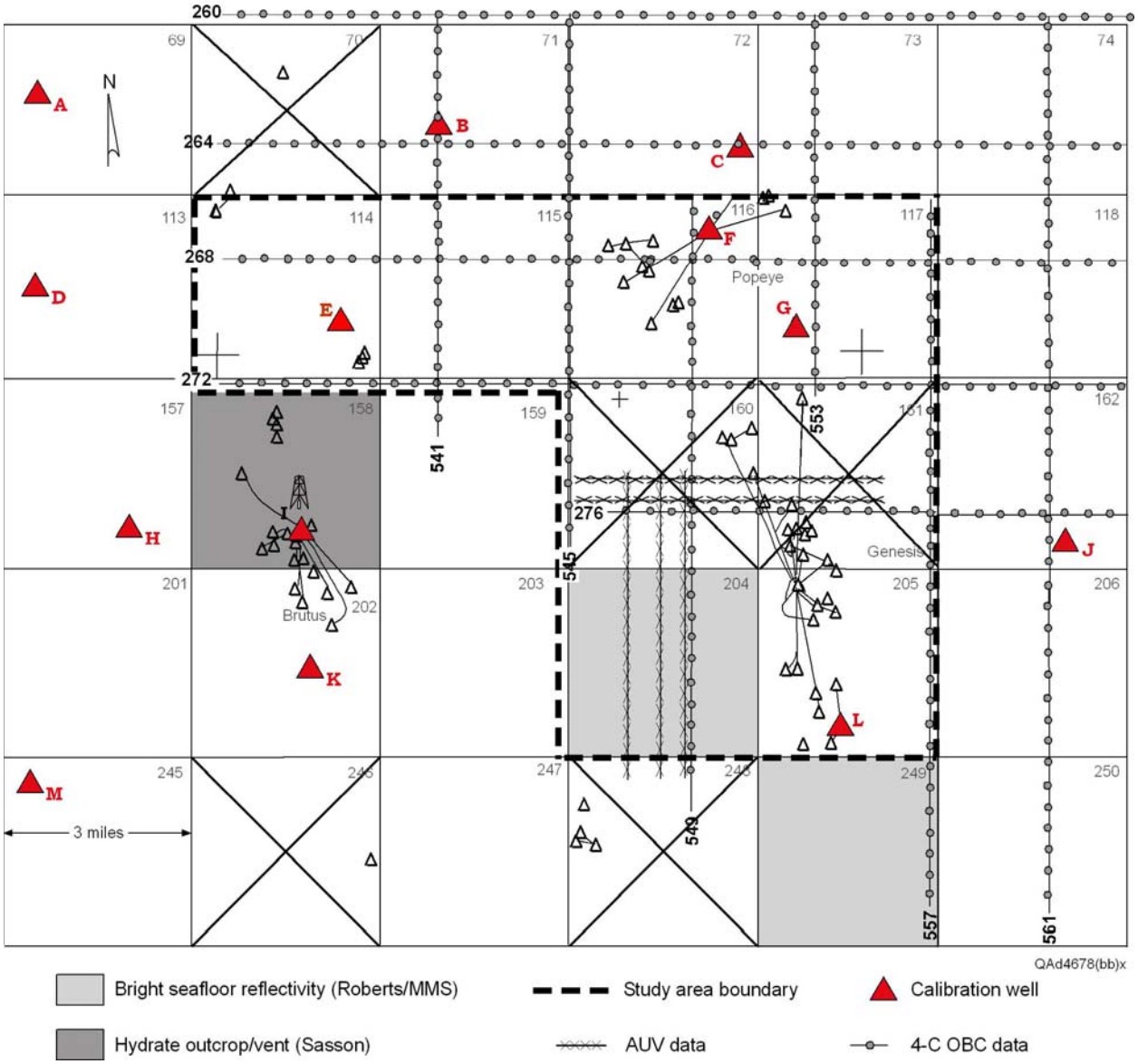

BLOCK	COMMENT
70	Poor-quality logs (1984 vintage)
160	Drilled from Block 205
161	Drilled from Block 205
246	Cannot find logs
248	Cannot find logs

Figure 5.7. Wells local to Genesis Field where near-seafloor log data could not be used for hydrate analysis. Blocks where unacceptable log data occur are marked with an X.

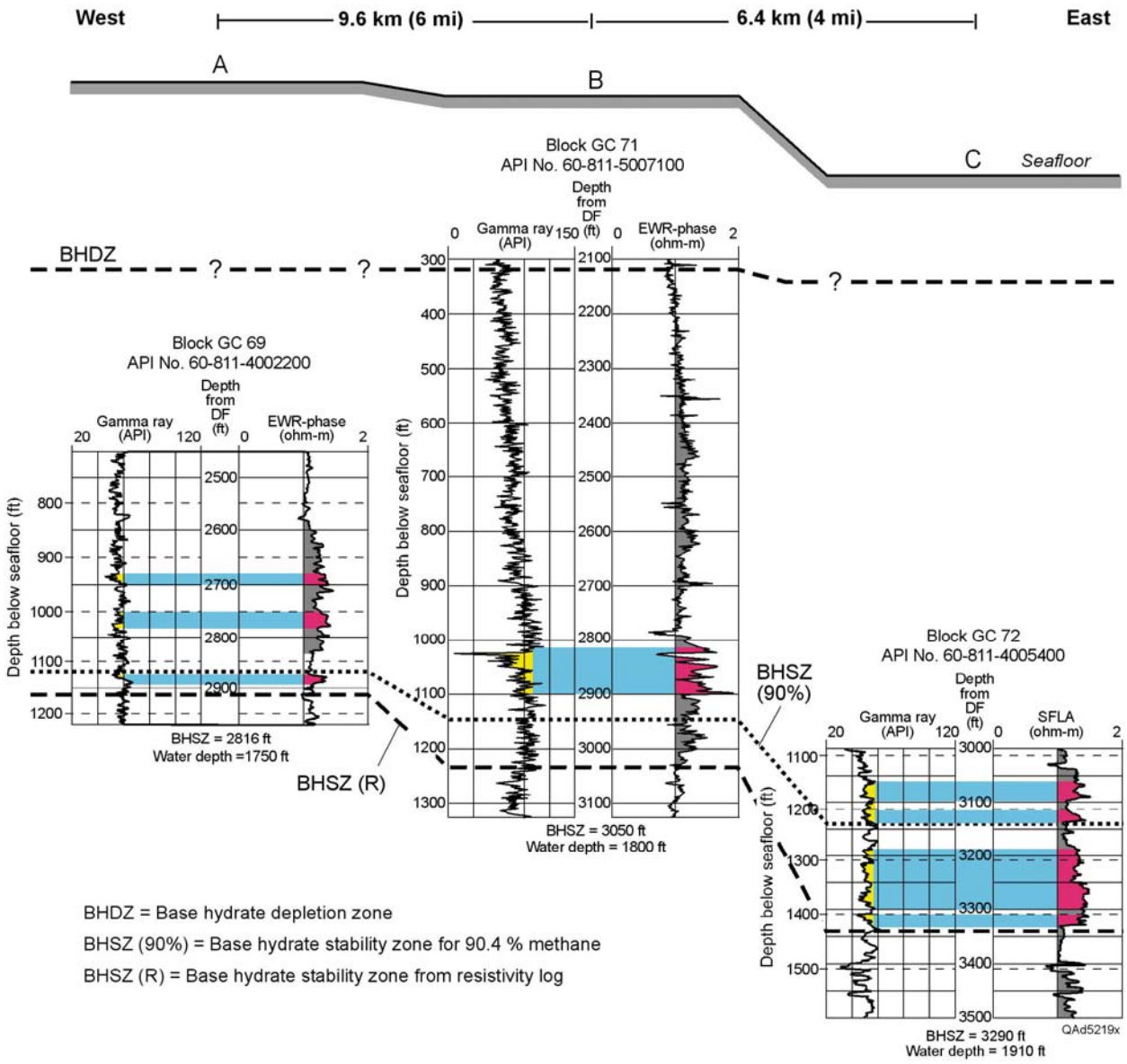

Figure 5.8. Well log cross section along the profile of calibration wells **A**, **B**, **C**, Genesis Field. There is a robust hydrate system along this profile. Well locations are defined on Figure 5.6. The BHSZ(90%) depth labeled below each log suite is the depth of the base of the hydrate stability zone associated with the 90.4 percent methane curve from Figure 5.4. At each well, the BHSZ(R) horizon is drawn at a resistivity change that is “close to” the depth coordinate suggested by the 90.4 percent methane curve. Gray zones emphasize intervals where resistivity exceeds 1 ohm-m. Yellow zones indicate possible larger-grain facies. Red identifies units that have both increased grain size and increased resistivity.

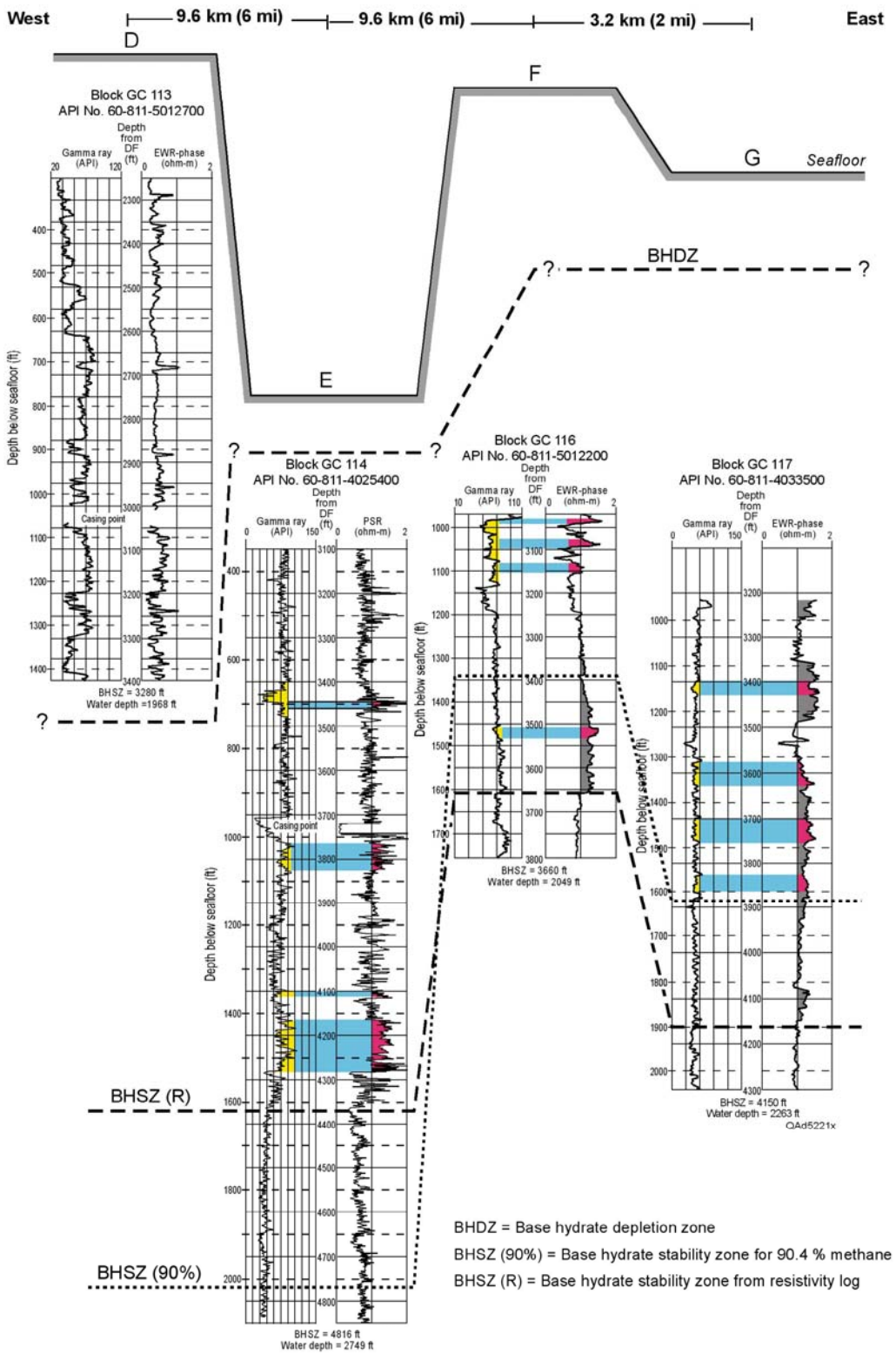

Figure 5.9. Well log cross section along the profile of calibration wells **D**, **E**, **F**, **G**, Genesis Field. This profile shows that there is no hydrate at well D but identifies several hydrate intervals that enlarge to the east. Well locations are defined on Figure 5.6. Horizons BHSZ(90%) and BHSZ(R), colors, and shadings are explained in the caption of Figure 5.8.

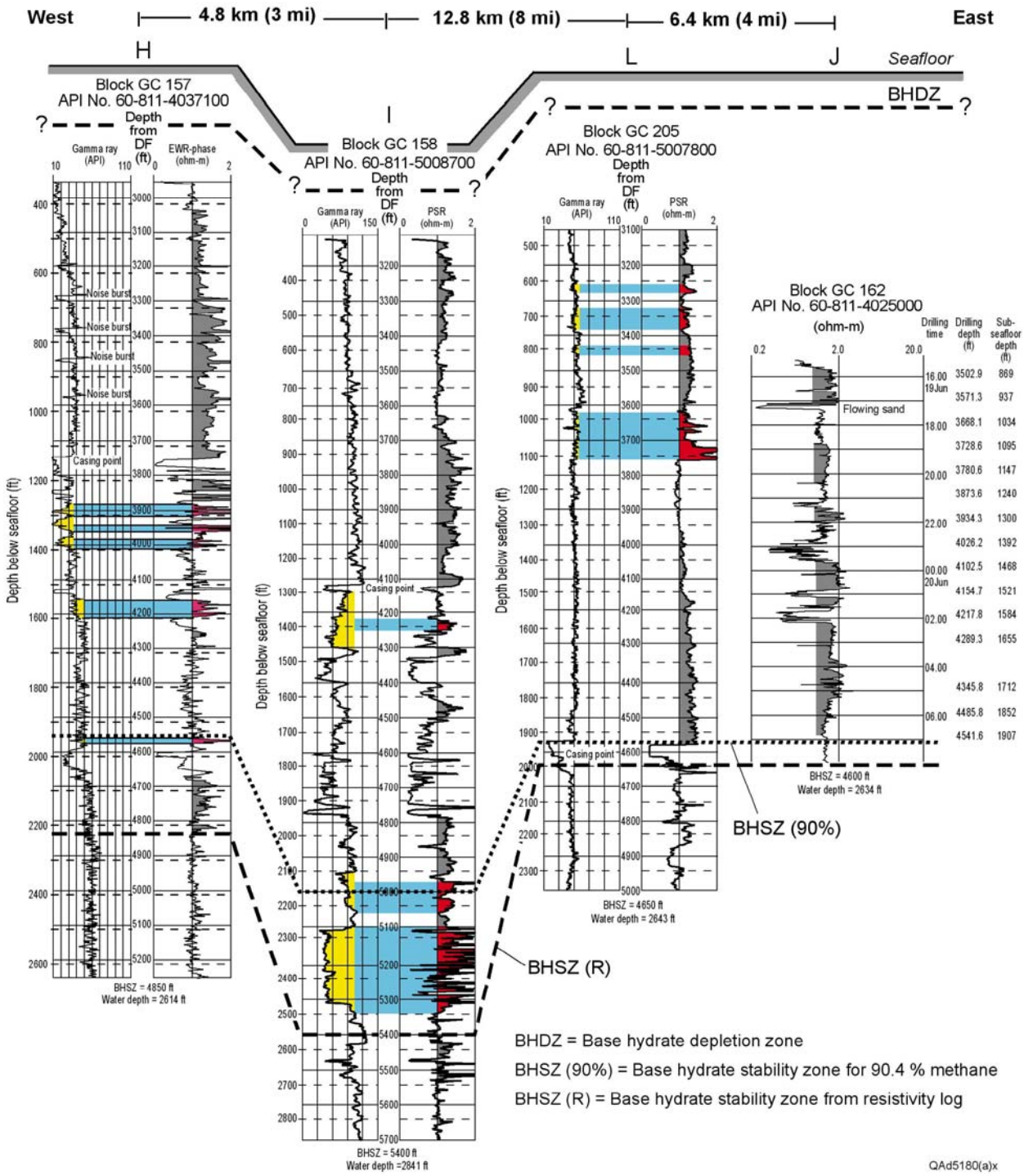

Figure 5.10. Well log cross section along the profile of calibration wells **H**, **I**, **L**, **J**, Genesis Field. This profile traverses thick hydrate sections. Well locations are defined on Figure 5.6. Horizons BHSZ(90%) and BHSZ(R), colors, and shadings are explained in the caption of Figure 5.8.

Maps of Generalized Properties of Hydrate Systems

The log-based cross sections shown from Figures 5.2 through 5.10 indicate that the hydrate systems across the Green Canyon area are complex. The distances between adjacent control wells on these cross sections are too great to construct a detailed stratigraphic model of the hydrate-bearing interval. However, upon examining the general appearance of each cross section, we can conclude that stratigraphy, sediment type, and hydrate concentration vary rapidly in both the vertical and lateral directions across the hydrate stability zone.

We have found it helpful to make the following qualitative inferences about the hydrate system defined at each control well displayed on the well log cross sections:

1. The accumulated thickness over which resistivity exceeds 1 ohm-m is either “thin” or “thick,” where “thin” and “thick” are arbitrary judgments, not quantitative measurements. At Typhoon Field, an example of a “thin” hydrate system at occurs at well C (Fig. 5.2); an example of a “thick” system is the geology described by well D (Fig. 5.3).
2. The hydrate concentration is either “high” or “low” in a “significant number” of individual hydrate-system units, where “high,” “low,” and “significant number” are again arbitrary judgments that differ from person to person. At Genesis Field, examples of what we consider to be “low” hydrate concentrations are shown by wells D and E (Fig. 5.9); an example of a “high” concentration is the resistivity behavior at well I (Fig. 5.10).

These generalized descriptors of the hydrate systems in the vicinity of Typhoon and Genesis Fields are best assessed in map views. Maps displaying the areal extents of these system properties are shown as Figures 5.11 and 5.12, respectively. The hydrate system at each site is divided into two domains identified as **A** and **B**. Domain **B** is a more robust hydrate system than the system across domain **A**.

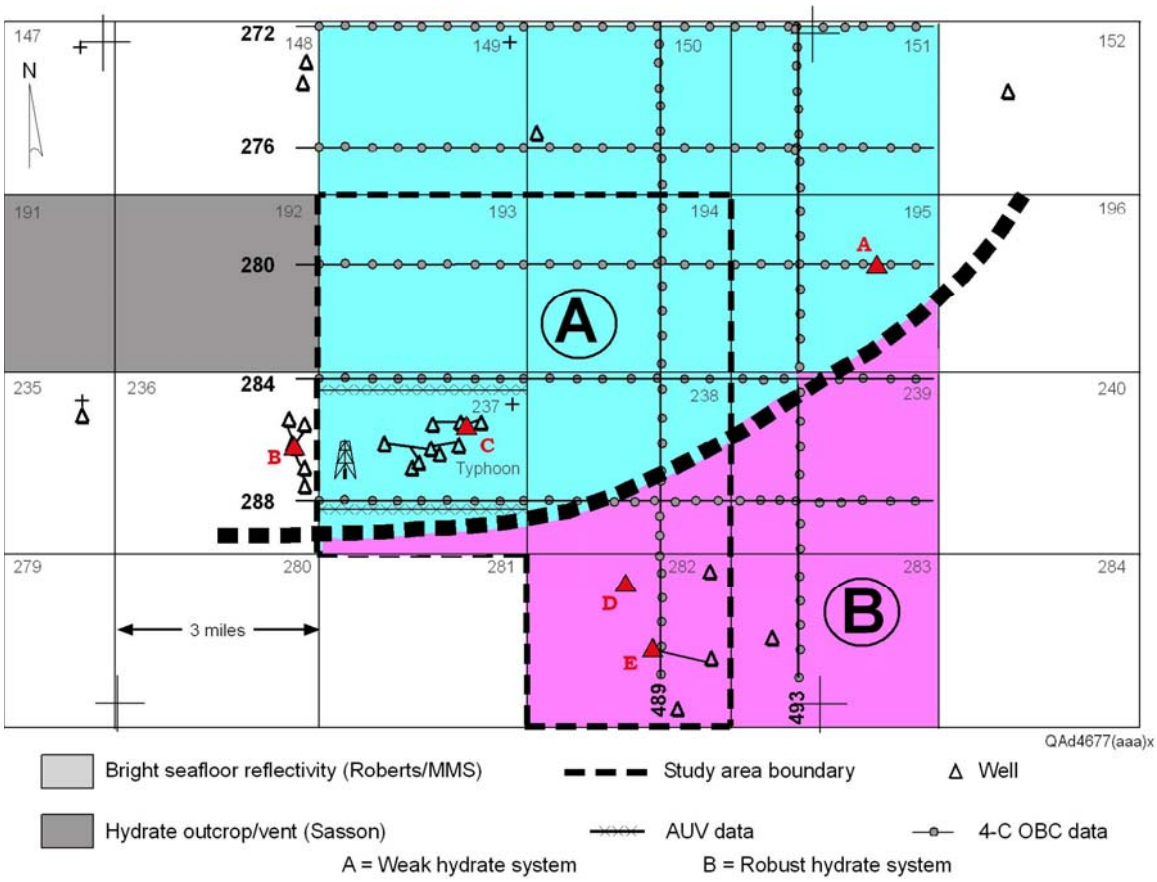

Figure 5.11. Generalized properties of the hydrate system across the Typhoon Field area. The system can be segregated into two domains, **A** and **B**. Domain **A** has thin hydrate intervals and/or low hydrate concentration, as illustrated along well profile BCA (Fig. 5.2). Domain **B** has thick hydrate intervals and numerous units with high hydrate concentrations, as shown by well profile BDE (Fig. 5.3).

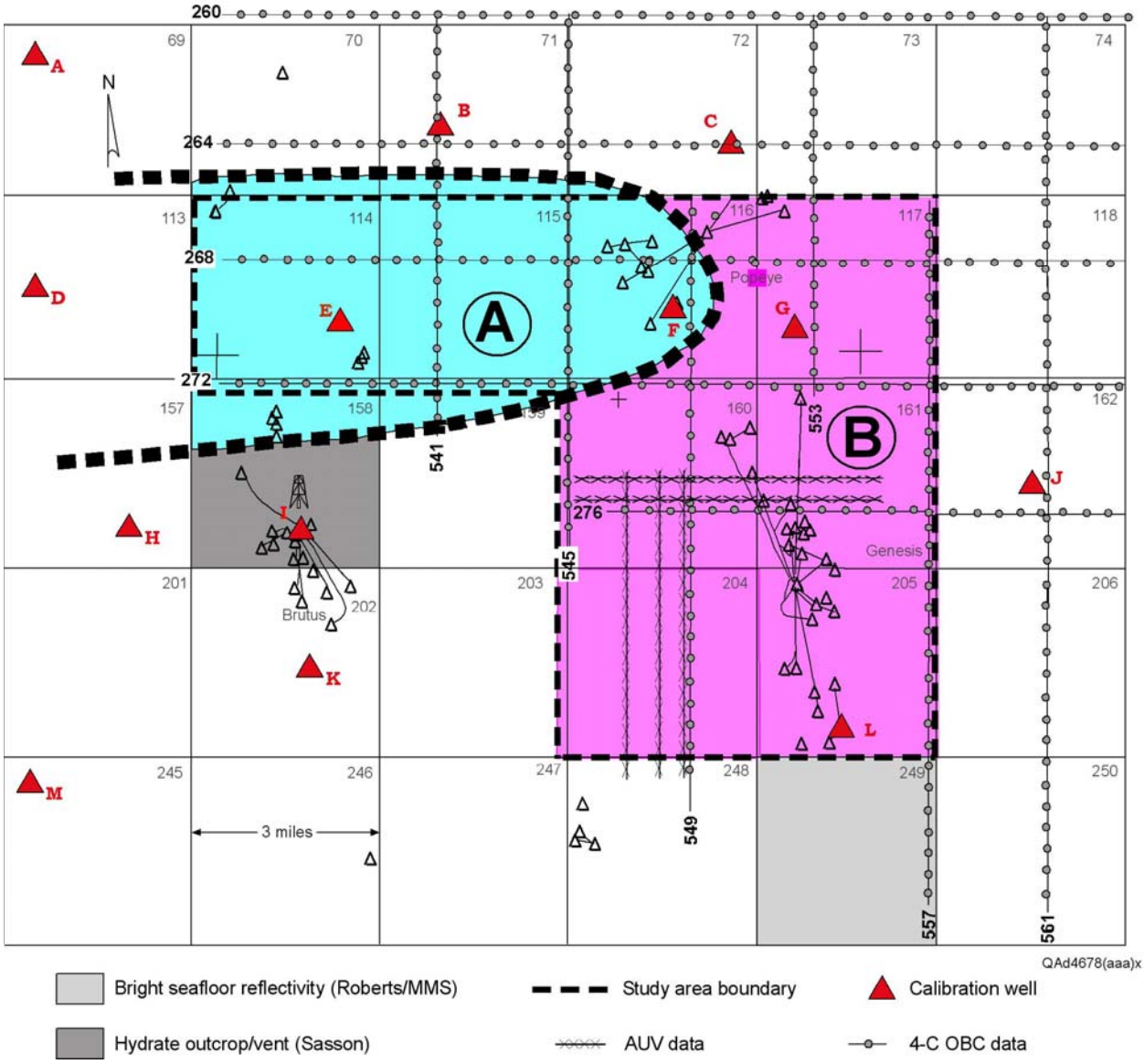

Figure 5.12. Generalized properties of the hydrate system across the Genesis Field area. The system can be segregated into two domains, **A** and **B**. Domain **A** has thin hydrate intervals and/or low hydrate concentration, with examples being wells D and E in Figure 5.9. Domain **B** has thick hydrate intervals and numerous units with high hydrate concentrations, as illustrated by well profiles in Figures 5.9 and 5.10.

Conclusions

The fact that we do not know the exact hydrate-sediment morphology that is penetrated by the logged wells exhibited in this chapter, and the inherent uncertainty that this lack of knowledge introduces into the application of formation resistivity to the estimation of hydrate saturation, cannot be overemphasized. An

inescapable enigma is that the resistivity-log responses shown here lead to different conclusions about hydrate concentration depending on whether the hydrate is disseminated throughout its host sediment (Fig. 4.1) or is embedded in the sediment as thin vertical or horizontal layers of pure hydrate (Fig. 4.2). For the present, we will assume that a disseminated-hydrate model is appropriate for hydrate systems across the Green Canyon area. This assumption is the basis of the resistivity-to-hydrate inversion that is discussed in Chapter 6. If a layered-hydrate model is more appropriate than is our disseminated-hydrate model, the estimates of hydrate concentration that have been produced in this study are incorrect, and a different resistivity-log response equation other than the Archie Equation has to be developed and applied to the log data that are exhibited here.

We must emphasize that there has been no attempt in the data analyses presented in this chapter to distinguish between the resistivity responses of hydrate and free gas. Any increase in resistivity occurring shallower than the inferred base of the hydrate stability zone is assumed to be caused by hydrate, even though free gas can also cause an increase in resistivity readings. We are able to distinguish between hydrate and free gas when we integrate V_P velocity behavior into our interpretation (as emphasized in Chapter 1) because V_P increases when hydrate is present but decreases when free gas is present.

DOE Gas Hydrate Final Report

Chapter 6

Estimating Hydrate Concentrations from Resistivity Logs

Introduction

When calculating hydrate concentration from resistivity logs, we emphasize that each parameter that is used in the Archie Equation should be described in terms of a realistic **probability distribution function** (**pdf**), not as a single numerical value. This approach allows uncertainty associated with each parameter to be incorporated into our estimates of hydrate concentration. Using this philosophy, we express our estimates of hydrate concentrations as probability distribution functions. The **mean value** of each pdf represents the "**best estimate**" of the hydrate concentration across the interval being analyzed, and the **standard deviation** of the pdf represents the "**uncertainty**" that should be assigned to the estimation.

Our implementation of the Archie Equation shows that measured formation resistivities between 1 ohm-m and 2 ohm-m in the clay-quartz sediment mixtures found across our study sites often indicate hydrate saturations that occupy approximately 50-percent of the pore space. Numerous thick, near-seafloor stratigraphic intervals across the Green Canyon have resistivities greater than 1 ohm-m, and many zones within these intervals have resistivities of 2 ohm-m or more. This resistivity behavior is fundamental evidence that leads us to conclude that several hydrate systems across the Green Canyon have significant hydrate accumulations.

We emphasize that our estimations of hydrate concentration from resistivity logs are based on the assumption that hydrate is distributed throughout the sediment as clusters of the fundamental clathrate unit volumes by which hydrate deposits grow. These unit volumes vary in size from 6 linked clathrates (Structure H) to 24 linked clathrates (Structure II) and were illustrated and described by Hardage and Roberts (2006). In our disseminated-hydrate resistivity model (Fig. 4.1), these basic volumetric building blocks of hydrate can be either load-bearing components of the sediment matrix, or they can be free-floating objects in the spaces between sediment grains. This resistivity model allows hydrate concentrations up to 50-percent of the pore space to be present across intervals where there are low resistivity log readings because there is so much conductive brine remaining in the pore space. We note that if the hydrate morphology within a low-resistivity interval can be described as vertical sheets of pure hydrate, as has been found in deep-water, fine-grained cores from offshore India and Korea, then our results underestimate hydrate concentration. Until information becomes available indicating that a different hydrate morphology

exists across the Green Canyon area, we will continue to base our resistivity-based estimations of hydrate concentration on the disseminated-hydrate model we have illustrated as Figure 4.1.

Archie Equation Corrected for Clay

The Archie Equation (Eq. 4.1) is an empirical law that was developed to determine water saturation in clean sands from measurements of resistivity and porosity across a sand-fluid mixture. The principal assumption of this empirical law is that electrical current travels only through the brine phase of fluid-saturated sediments because quartz minerals and hydrocarbon fluids are great electrical insulators. However, when clay minerals are present in the host sediments, the original form of the Archie Equation (Eq. 4.1) is no longer accurate. Clay minerals have lower resistivity than clean sands and can have a large impact on the resistivity of a rock formation. If the presence of clay minerals is ignored and the simple form of the Archie Equation is applied to clay-rich sands, water saturation is overestimated at all porosity values. As a result, the saturation of any nonconductive phase that may be in the pores (for example hydrates) will be underestimated.

Schlumberger Wireline Services (1998) proposed a modification to the Archie Equation that takes into account the presence of clay. This modified Archie Equation is valid for several types of clay distribution (clay can be disseminated, structured, or layered). Key parameters required for implementing this modified equation are the volume of clay (V_{cl}) present in the sediments and the resistivity (R_{cl}) of the clay minerals. Volume of clay can be estimated from gamma-ray log data, and the resistivity of clay minerals can be measured in the laboratory. If no core samples are available for lab testing, we must use resistivity data measured across pure-clay intervals from nearby geology or rely on published resistivity measurements of clays. Published information sources confirm that R_{cl} spans a large resistivity range extending from 1 to 1,000 ohm-m (Rider, 1991).

The modified Archie Equation proposed by Schlumberger (1998) is

$$\frac{1}{R} = \frac{\phi^m}{aR_w(1-V_{cl})} S_w^n + \frac{V_{cl}}{R_{cl}} S_w^{n-1}, \tag{6.1}$$

where in our deep-water applications,

- R is the measured resistivity of sediments containing gas hydrates,
- R_w is the resistivity of the brine in these hydrate-bearing sediments,
- ϕ is the porosity of the sediments,
- a is the geometric factor (a ~1.08),
- m is the cementation factor (m = 1.2 to 1.7 for unconsolidated sediments),
- V_{cl} is the volume of clay estimated from gamma-ray log data,
- R_{cl} is the resistivity of clay mineral (R_{cl} = 1 to 1,000 ohm-m),

- S_w is the water saturation, and
- n is the saturation exponent ($1.7 \le n \le 2.2$).

This form of the Archie Equation should be compared with Equation 4.1, the form of the equation for clean sands. If $V_{cl} = 0$, Equation 6.1 reduces to Equation 4.1, the classical form of Archie's Equation.

If we consider the **saturation exponent n** to be 2, as most published papers suggest, then Equation 6.1 is quadratic in S_w, and its positive root is

$$(6.2) \quad S_w = \frac{1}{2} a \phi^{-m} R_w (1 - V_{cl}) \left[\sqrt{\left(\frac{V_{cl}}{R_{cl}} \right)^2 + 4 \frac{\phi^m}{a R R_w (1 - V_{cl})}} - \frac{V_{cl}}{R_{cl}} \right].$$

This expression for S_w estimates water saturation when the Archie Equation is modified for clay content. By definition, the concentration (c_{gh}) of hydrate in the sediments is ($1-S_w$), or

$$(6.3) \quad c_{gh} = 1 - \frac{1}{2} a \phi^{-m} R_w (1 - V_{cl}) \left[\sqrt{\left(\frac{V_{cl}}{R_{cl}} \right)^2 + 4 \frac{\phi^m}{a R R_w (1 - V_{cl})}} - \frac{V_{cl}}{R_{cl}} \right].$$

If $n \neq 2$, the square root term in these equations is replaced with the nth-root equivalent. Figure 6.1 illustrates the difference between hydrate concentration calculated using this modified clay-volume Archie Equation and hydrate concentration derived using the Archie Equation for clean sands. The difference between the two estimates represents the magnitude of the underestimation of hydrate concentration that will occur in porous seafloor sediment when we ignore the presence of clay. The same input parameters were used in the calculations for both forms of the Archie Equation. In these calculations, the porosity of the sediment was assumed to be 50 percent—a typical porosity value for sediment within the hydrate stability zone provided by lab measurements of water content of core samples that we found documented in engineering reports across our study area (Figs. 8.2 and 8.3). Resistivity of the brine was set at $R_W = 0.17$ ohm-m. This resistivity corresponds to a pore-water salinity of 45,000 ppm and a temperature of 65ºF. The cementation exponent **m** was allowed to vary from 1.2 (for highly unconsolidated sediments) to 2.1 (better consolidated sediments). The geometric parameter **a** was fixed at 1.0. The resistivity of clay had a constant value of 100 ohm-m. We assumed that the targeted hydrate interval had an observed logged value of formation resistivity equal to 2 ohm-m, a resistivity value exhibited by numerous logs illustrated in this report (Chapter 5).

Using these values, we computed the hydrate concentration on the basis of the two Archie Equations, using Equation 4.1 for clean sands and Equation 6.1 for shaly sands. The difference between the two estimates shown in Figure 6.1 is due only to the presence of clay. Each curve on the figure represents a different value for the cementation exponent. Results show that the error in estimating hydrate concentration increases as the cementation exponent increases. This behavior occurs because small values of cementation exponent imply a highly unconsolidated medium for which the electrical current travels freely through the conductive brine phase. In such a medium, the conductivity of the clay-quartz matrix plays a minor role. When the cementation exponent **m** increases, the pathways for current through the brine are more obstructed, and the clay in the matrix plays a larger role in conducting electrical current.

For larger values of m, ignoring clay in the sediments induces large errors in the estimation of hydrate concentration in the pores. Even for small values of cementation exponent, which is the parameter range for the high-porosity unconsolidated sediments across our study area, errors in hydrate concentration that result from ignoring clay content are significant. For example, if the volume of clay is 70 percent and the cementation exponent is 1.2, then the difference between the hydrate concentration derived by ignoring the clay content is 20 percentage points less than the value derived by accounting for clay volume.

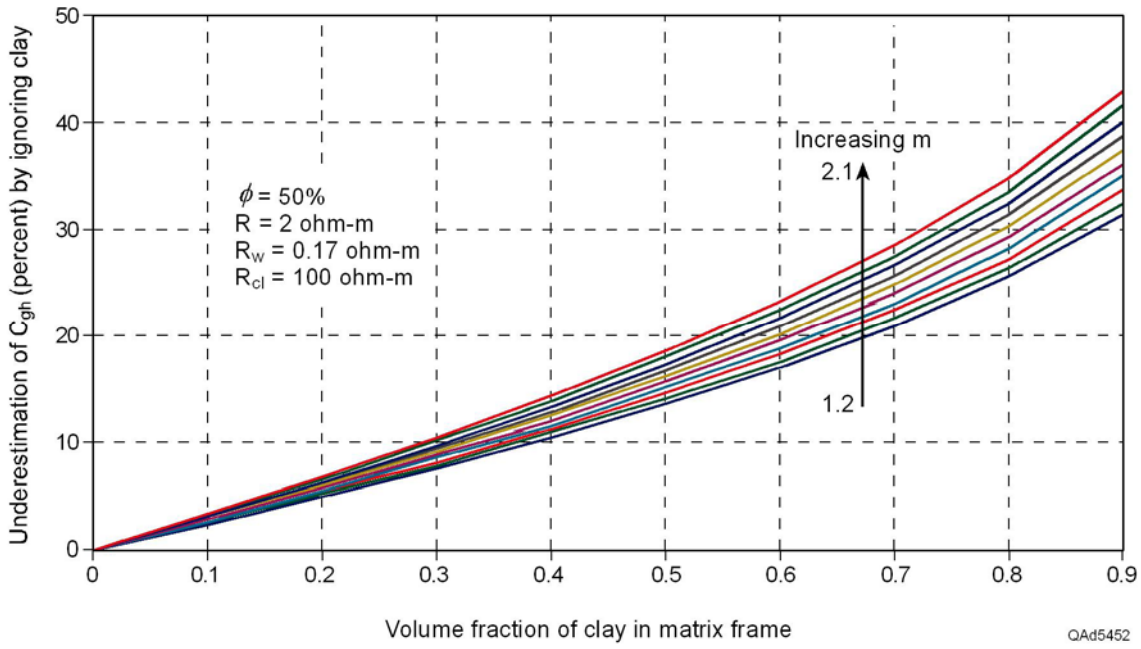

Figure 6.1. The difference between hydrate concentration determined from the Archie Equation modified for clay content and hydrate concentration derived using the Archie Equation for clean sands. The curves correspond to different values of cementation exponent **m**. The arrow indicates the direction in which **m** increases from 1.2 to 2.1 in increments of 0.1. The figure shows the underestimation of hydrate concentration that occurs when clay content is ignored. The sediment has a porosity of 50 percent and a log-measured resistivity of 2 ohm-m.

Figure 6.2 illustrates the same calculations when the cementation exponent **m** is kept constant at 1.2 (for unconsolidated sediments), but different clay resistivities are assumed. The arrow indicates the direction of increasing clay resistivity in a log-scale format that varies from 1 to 100 ohm-m. As expected, the error in hydrate concentration that results when the presence of clay is ignored decreases as the resistivity of clay increases. This finding implies that the lower the resistivity of the clay, the larger the impact of the clay on the overall resistivity of the sediments and the greater the error in hydrate concentration caused by ignoring the presence of clay.

However, if the resistivity of the clay is significantly higher (two orders of magnitude) than the brine resistivity, then the error produced by ignoring clay content is only weakly dependent on resistivity of the clay. This principle is illustrated in Figure 6.3. Also, hydrate concentration, when estimated by the Archie Equation modified for volume of clay, is not sensitive to resistivity of the clay if R_{cl} is more than two orders of magnitude larger than the brine resistivity (Figure 6.4). This is an important observation because the resistivity values of clay minerals will not be available in many hydrate study areas.

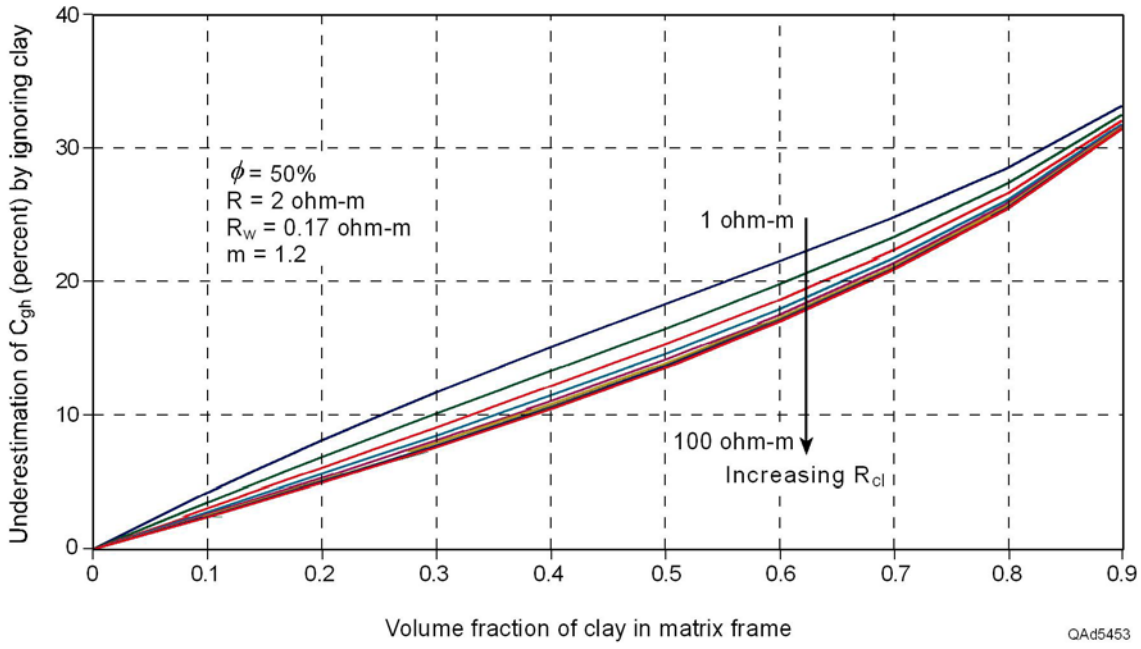

Figure 6.2. The difference between hydrate concentration calculated from the Archie Equation modified for clay content and hydrate concentration derived using the Archie Equation for clean sands. The curves correspond to different values for assumed resistivity of clays when clay resistivity is low. The arrow indicates the direction in which clay resistivity increases (R_{cl} is in log-scale units ranging from 1 to 100 ohm-m). The figure shows the underestimation of hydrate concentration that occurs when clay content is ignored. The sediment has a porosity of 50 percent and a log-measured resistivity of 2 ohm-m.

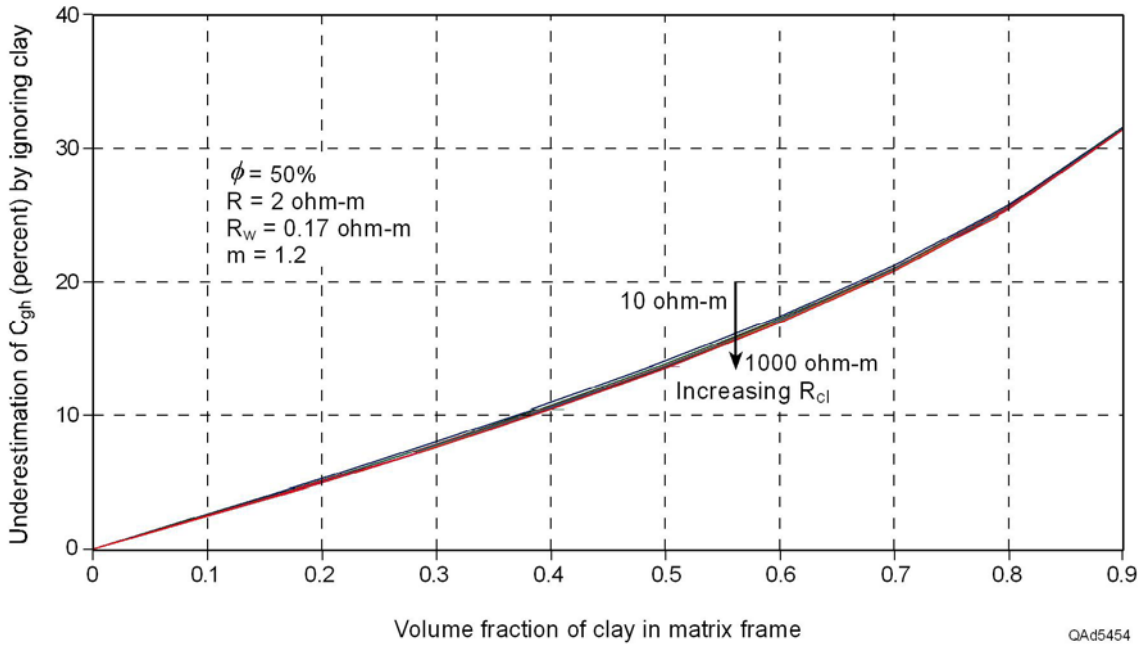

Figure 6.3. The difference between hydrate concentration using the Archie Equation modified for clay content and hydrate concentration derived using the Archie Equation for clean sands. The curves correspond to different values for resistivity of clays when clay resistivity is high. The arrow indicates the direction of increasing clay resistivity in a log-scale format that ranges from 10 to 1,000 ohm-m. The figure shows the underestimation of hydrate concentration when clay content is ignored. The sediment has a porosity of 50 percent and a log-measured resistivity of 2 ohm-m.

Motivation for Quantifying Uncertainty

Archie's original resistivity equation (Eq. 4.1) and its modified version for clay content (Eq. 6.1) are empirical, deterministic laws that are used to compute water saturation of porous media. In this study, we adjusted the ranges of the parameters used in these Archie Equations so that the equations could be used to estimate the concentration of hydrate in deep-water sediments. As stated in the preceding section, the parameters required to evaluate the Archie Equation are

- resistivity of the formation (R) ,
- resistivity of the brine saturating the pores (R_w),
- porosity of the sediments (Φ),
- geometrical parameter (a),
- cementation exponent (m),
- saturation exponent (n),
- volume of the clay minerals present in the sediments (V_{cl}), and
- resistivity of the clay minerals present in the sediments (R_{cl}).

Most of these input parameters vary over a wide range and can be challenging to estimate. Resistivity of the formation can be obtained from electrical wireline logging. However, like any physical measurement, an uncertainty is associated

with the observed values of wireline resistivity because of instrument drift, calibration errors, and improper operational techniques. Sediment porosity is usually obtained from well log data also. For the shallow part of the marine sediments within the hydrate stability zone (HSZ) across our study areas; however, the only available logs were resistivity and gamma-ray data obtained using logging-while-drilling technology. Neutron-porosity or density-porosity logs have not yet been recorded across hydrate-stability zones in logging operations across the Green Canyon area. Sometimes engineering data, such as water content, were available from which porosities for near-seafloor strata could be derived (Chapter 8). In this study, we extrapolated porosity information from these lab-measured water-content data to well locations where resistivity and gamma-ray logs were acquired. Detailed porosity information therefore has a degree of uncertainty across our targeted stratigraphic intervals.

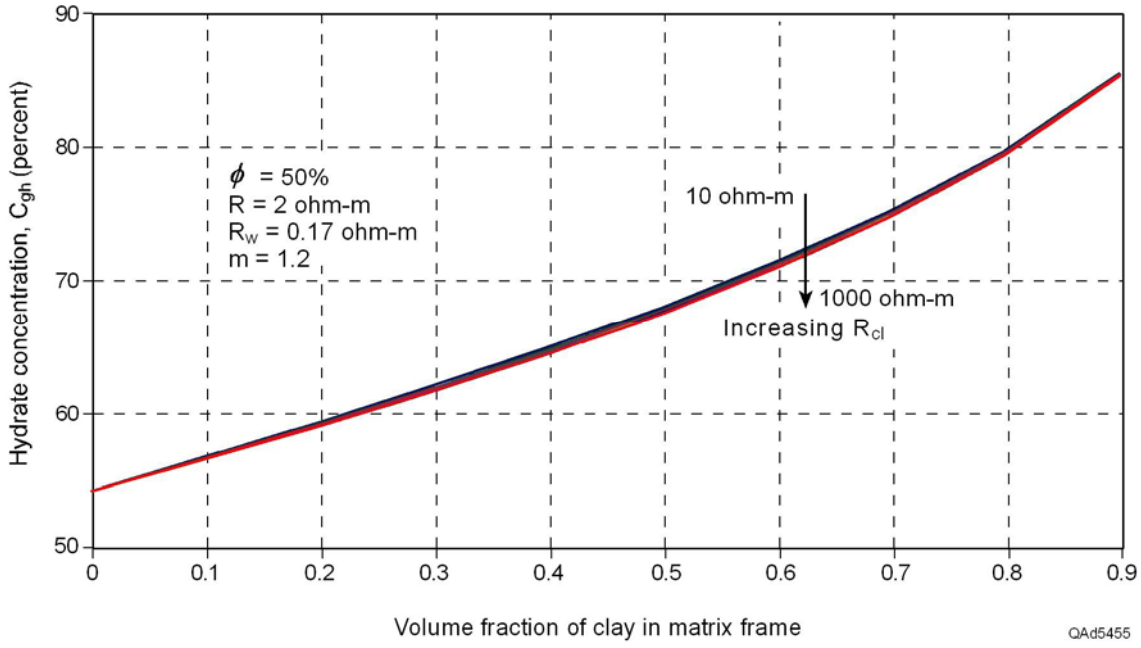

Figure 6.4. The estimated hydrate concentration in clay/quartz sediments when the Archie Equation is modified to accommodate clay volume. The curves represent different values for resistivity of clay minerals (R_{cl} is shown in a log-scale format ranging from 10 to 1,000 ohm-m). Log-measured resistivity of the sediments is 2 ohm-m, and porosity is 50 percent. Hydrate concentration C_{gh} is expressed as fractions of the available pore space (Φ = 50 percent).

Other empirical factors utilized in the Archie Equation, such as the geometrical parameter and the cementation exponent, vary over large ranges, and uncertainty is associated with these parameters as well. The volume of clay over intervals of interest was determined from gamma-ray log data, using the following equation:

$$V_{cl} = \frac{GR - \min(GR)}{\max(GR) - \min(GR)}, \tag{6.4}$$

where V_{cl} is the estimated volume of clay, GR is the value on the gamma-ray log, and min(GR) and max(GR) represent, respectively, minimum and maximum readings on the gamma-ray log. Because this calculation is not a direct measurement of the volume of clay, uncertainty is also associated with the V_{cl} estimates that we use.

Resistivity of clays is a difficult parameter to obtain as well. Although clay resistivity can be measured on cores in a laboratory, these measurements are not cost effective and are not performed on a regular basis. Therefore, we, like many researchers, rely on published lab measurements of resistivity of clay minerals from environments similar to those in the areas where we do our investigations.

Most hydrate concentrations that are predicted from resistivity logs using the Archie Equation are represented in the literature by a single number, without any measure of the uncertainty associated with the calculation. Some of these single-number estimates of hydrate concentration are not accurate because values of the input parameters used in the analyses are not optimal choices (such as large cementation-exponent values being used for unconsolidated sediments).

For all of these reasons, well-log-based estimates of hydrate concentration should be based on a careful analysis of the possible range of variability of each input parameter, and these estimates should always be accompanied by a measure of the uncertainty associated with the parameters and the final calculation.

Uncertainty in Estimating Hydrate Concentration

Our approach to estimating the uncertainty in hydrate concentration calculated from resistivity logs is based on stochastic simulations. We represent input parameters used in the deterministic Archie's Law and in its modified version for clay content by various probability distribution functions (PDFs) that express mathematically the variation and uncertainty of these parameter values. These probability distribution functions are either: (1) uniform distributions over the possible range of variability for each input parameters, or (2) Gaussian distributions. A uniform distribution assumes that any value for an input parameter is equally likely over the range of variability that is allowed. A Gaussian distribution suggests that the most likely value for the parameter is the mean of its associated Gaussian distribution and that the variance of its distribution function is a measure of the uncertainty of the parameter value about the mean.

Therefore, we represent each input parameter in the Archie Equation not by a single number, but by a probability distribution function that allows us to incorporate the inherent uncertainty about that input parameter into the calculation of hydrate concentration. These distribution functions permit us to use

constraints on each parameter that are based on measurements or on knowledge acquired over similar environments. After we assign a probability distribution function to each input parameter, we then run Monte Carlo simulations over these distributions. We randomly draw a set of values of R, R_w, Φ, a, m, V_{cl}, and R_{cl} from their respective PDF's and compute the hydrate concentration using the modified Archie Equation (Eq. 6.1). Then we draw again, randomly and independently, another set of values for these input parameters and obtain another possible realization of the hydrate concentration using the same Archie Law Equation. We repeat this procedure many times (N = 5,000 or more), and we end up with many possible realizations for hydrate concentration at a certain sub-seafloor coordinate. From these many realizations of the possible hydrate concentration at a certain location, we derive a probability distribution function of the estimated hydrate concentration, which mathematically represents the uncertainty of our prediction of hydrate concentration at that target point. From this distribution of hydrate concentration we derive our best estimate of the hydrate concentration, which we express as the expected concentration value (defined as the mean value of the PDF) and the uncertainty of the estimate (the standard deviation of the PDF).

This procedure allows us to incorporate the inherent uncertainty of all of the input parameters into our final calculation result and to estimate the impact of all these uncertainties on our final estimate of hydrate concentration. Another advantage of our approach is that it allows us to understand the sensitivity of hydrate concentration to each of the individual input parameters. In this way we can decide which parameters are the most critical for reducing the inherent uncertainty associated with our predictions of hydrate concentration.

Our definitions of the probability distribution function (PDF) associated with each parameter used in the modified Archie Equation (Eq. 6.1) at one analysis site are illustrated in Figure 6.5. These distribution functions form the basis of the Monte-Carlo-based random and independent "draws" of parameter values that we used to calculate hydrate concentration at that location. In addition to the uncertainties associated with the parameters used in the hydrate estimations, we also assign an uncertainty to the resistivity log readings that we use in the Archie Equation calculations. For example, the PDF used for a log reading of 2 ohm-m is shown in Figure 6.6.

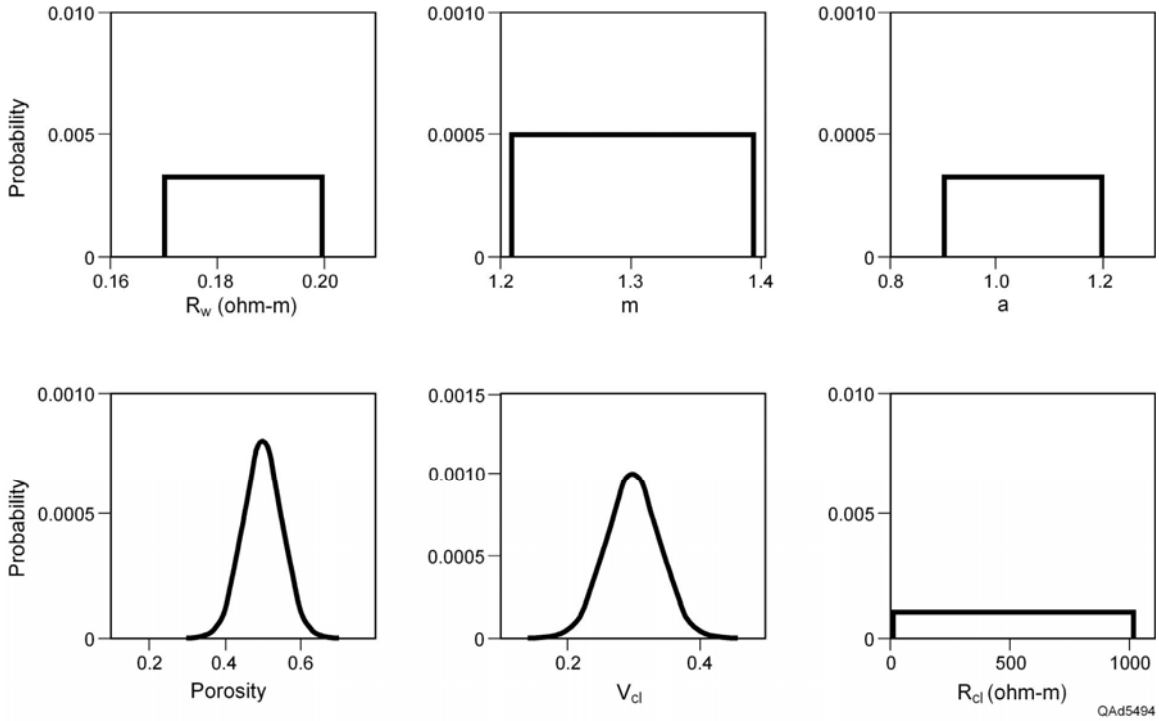

Figure 6.5. Distribution functions used to define the uncertainty of each parameter involved in the modified Archie Equation across one depth interval at one calibration well.

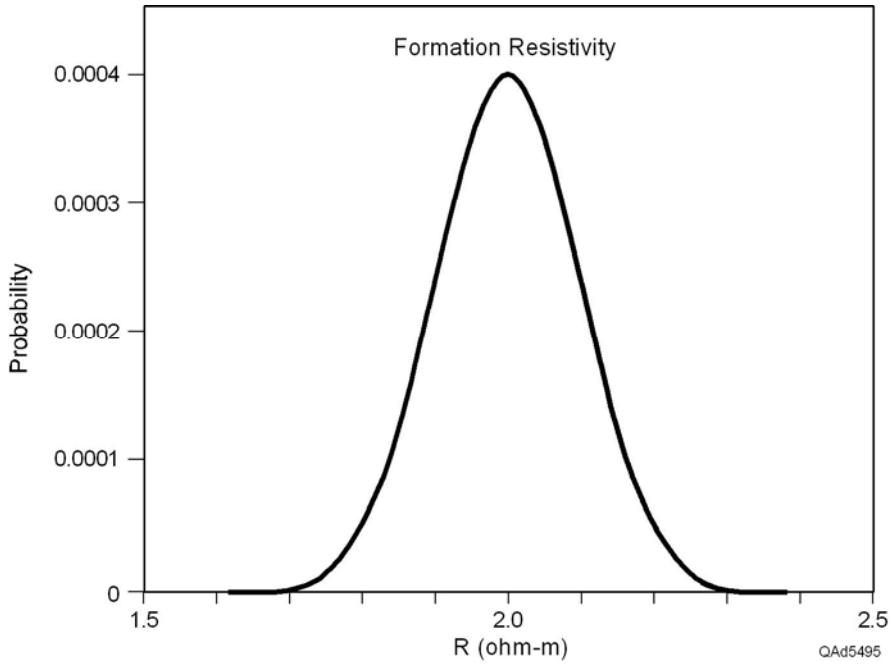

Figure 6.6. Example of a Gaussian distribution function used to describe the uncertainty of a resistivity log measurement. In this example, the log reading is 2 ohm-m.

We now illustrate our statistical approach to estimating hydrate concentration from resistivity logs across selected intervals of the hydrate systems that span our study area. We choose a target interval from five logged wells across the project area in which the mean value of the resistivity log response is, respectively, 2.0, 1.75, 1.5, 1.3, and 0.35 ohm-m. These choices of resistivity readings span the range of resistivity values observed vertically and laterally across our study sites and allow us to demonstrate the magnitudes of hydrate concentrations that occur throughout the area without resorting to excessive graphical displays.

Gamma-ray and resistivity logs across these targeted intervals are displayed on Figures 6.7 through 6.11. In each figure, the specific interval over which hydrate concentration was estimated is indicated by the bracket drawn along the right edge of the resistivity curve. Two estimates of hydrate concentration were calculated for each interval. One estimate used the clay-free form of the Archie Equation (Eq. 4.1), and the other used the clay-dependent form (Eq. 6.1). The PDF of hydrate concentration produced by each form of the Archie Equation is identified on each figure.

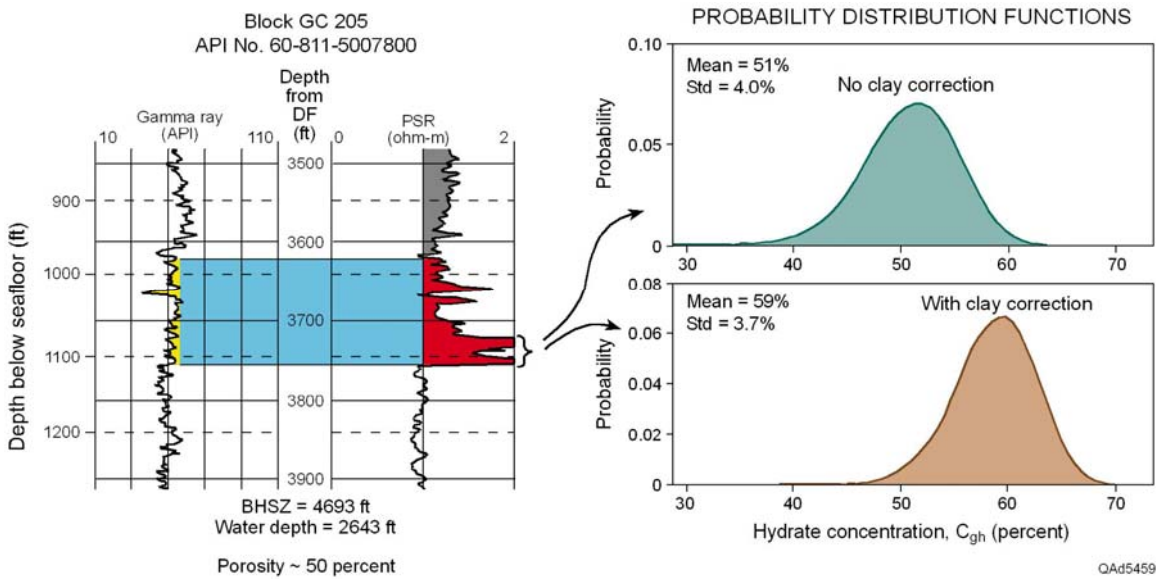

Figure 6.7. Hydrate concentration calculated in example well L, Genesis area (Fig. 8.1b), across depth interval 3,720 to 3,760 ft. The upper PDF results when the clay-free form of the Archie Equation (Eq. 4.1) is used. The lower PDF results when the clay-dependent form (Eq. 6.1) is used. The value for much of the resistivity log across this interval is 2 ohm-m. The average porosity is ~ 50 percent.

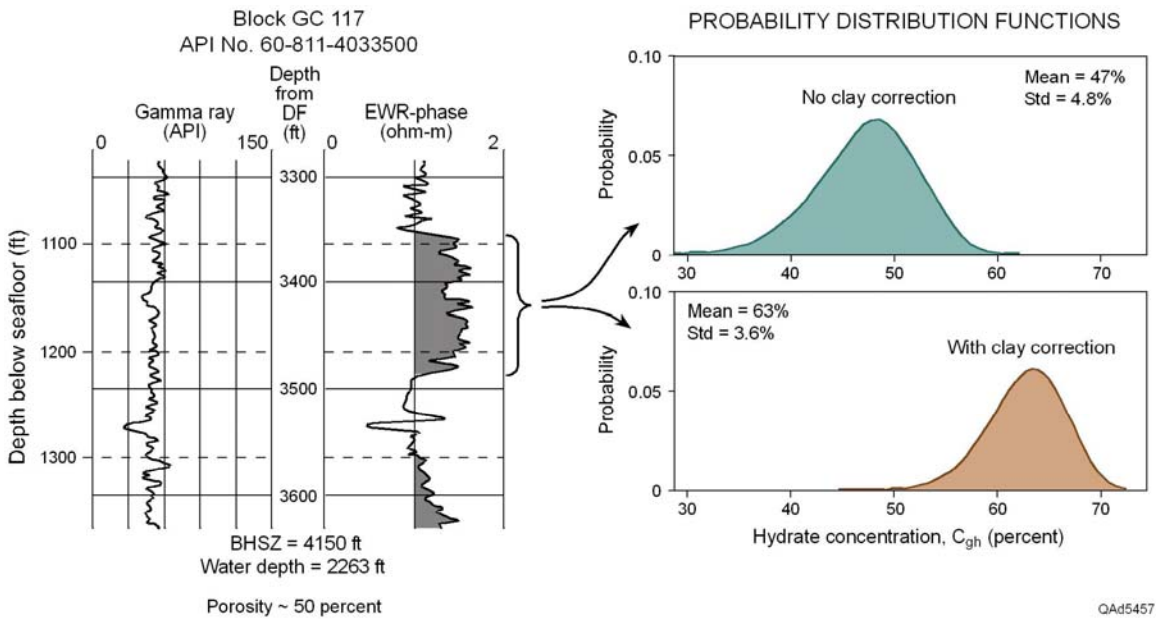

Figure 6.8. Hydrate concentration calculated in example well G, Genesis area (Fig. 8.1b), across depth interval 3,370 to 3,500 ft. The upper PDF results when the clay-free form of the Archie Equation (Eq. 4.1) is used. The lower PDF results when the clay-dependent form (Eq.6.1) is used. The value of the resistivity log across some of the interval is 1.75 ohm-m. The average porosity is ~50 percent.

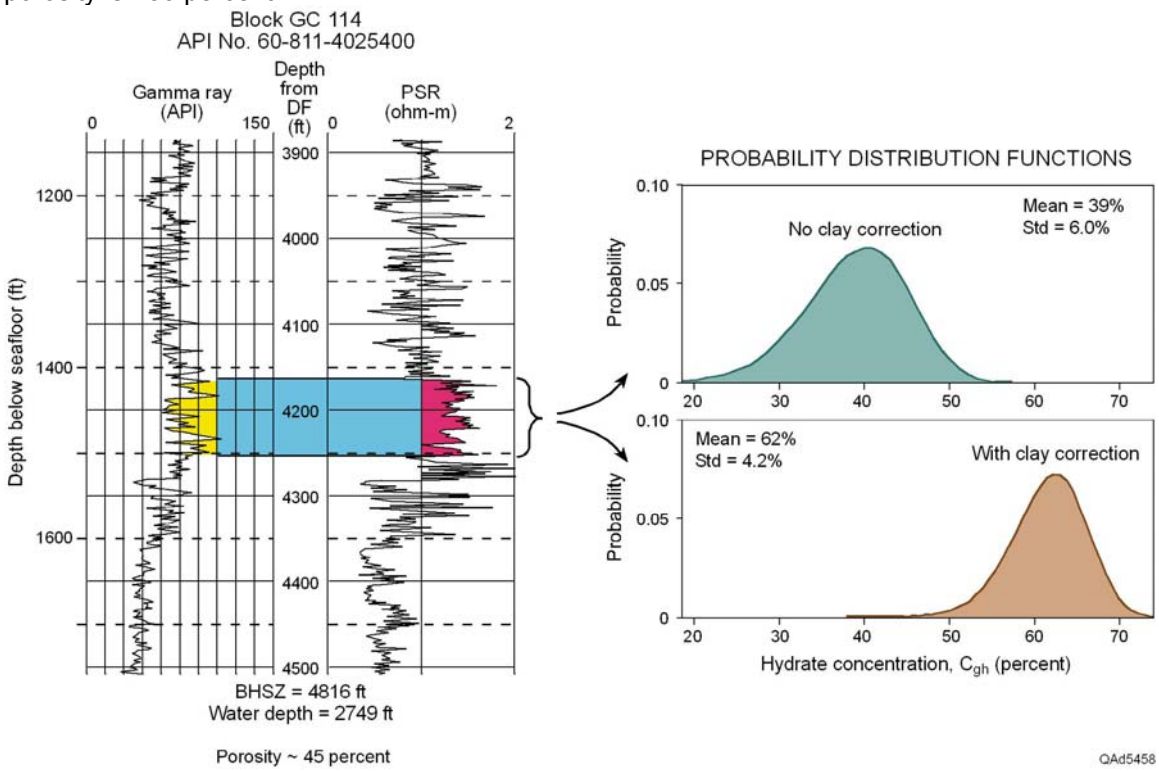

Figure 6.9. Hydrate concentration calculated in example well E, Genesis area (Fig. 8.1b), across depth interval 4,170 to 4,270 ft. The upper PDF results when the clay-free form of the Archie Equation (Eq. 4.1) is used. The lower PDF results when the clay-dependent form (Eq.6.1) is used. The mean resistivity log reading across the interval is 1.5 ohm-m. The average porosity is ~45 percent.

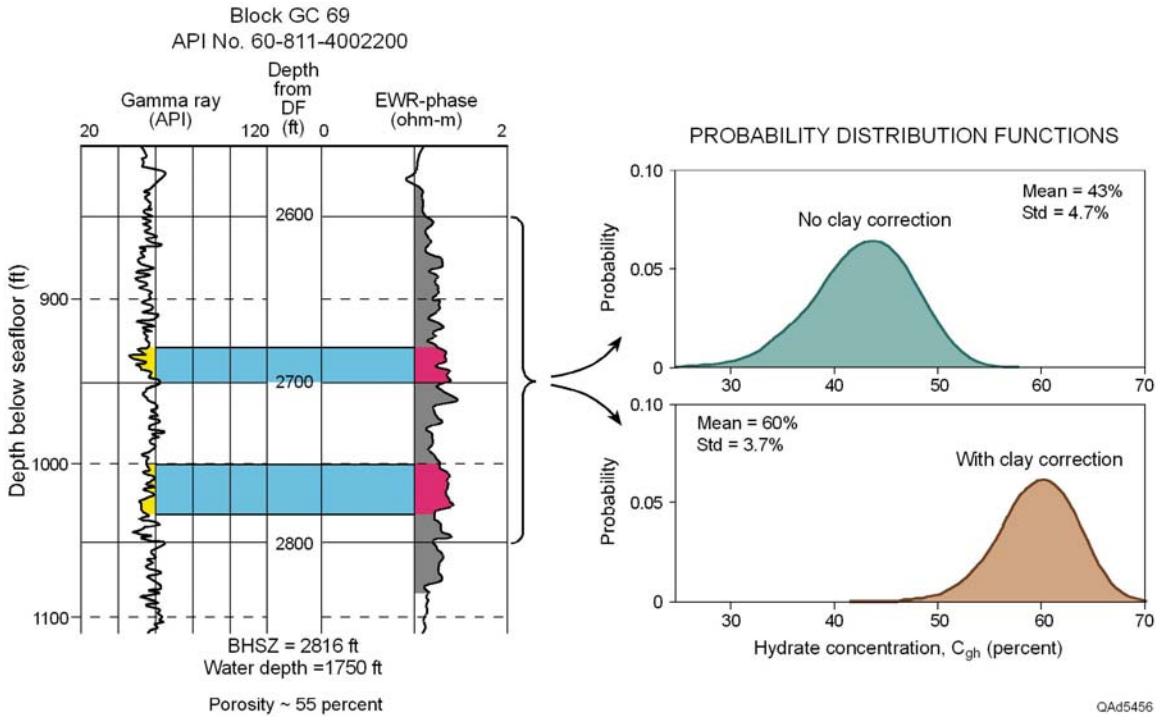

Figure 6.10. Hydrate concentration calculated in example well A, Genesis area (Fig. 8.1b), across depth interval 2,600 to 2,800 ft. The upper PDF results when the clay-free form of the Archie Equation (Eq. 4.1) is used. The lower PDF results when the clay-dependent form (Eq. 6.1) is used. The mean of the resistivity log readings across the interval is 1.3 ohm-m. The average porosity is ~55 percent.

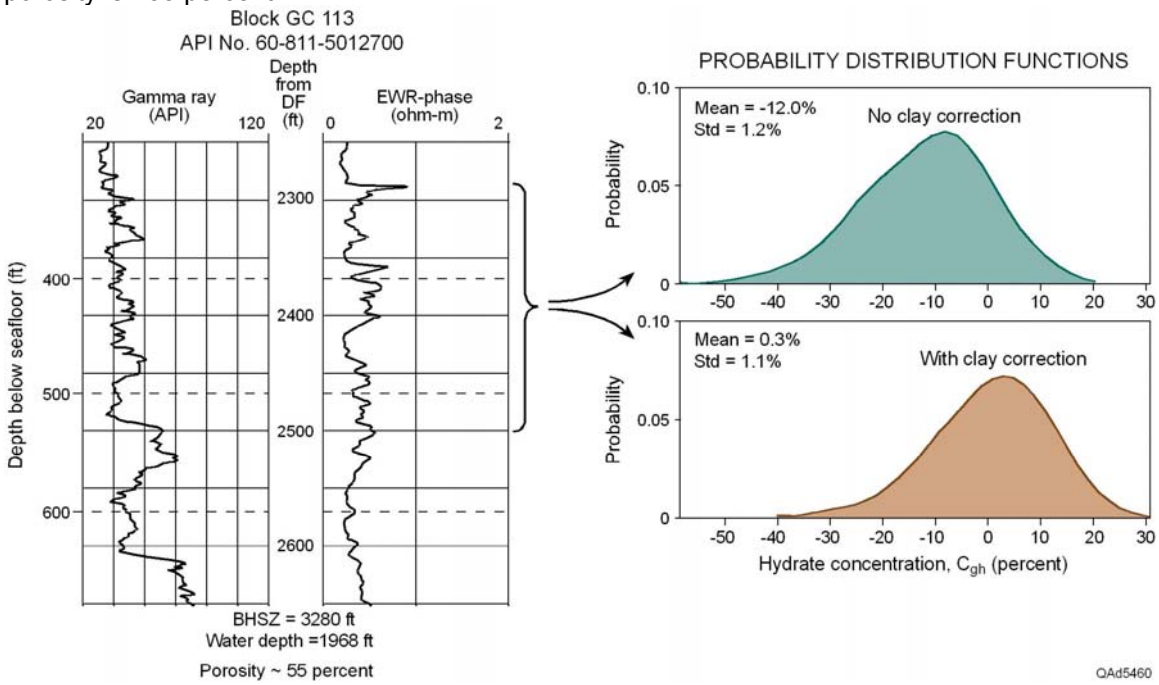

Figure 6.11. Hydrate concentration calculated in example well D, Genesis area (fig. 8.1b), across depth interval 2,270 to 2,500 ft. The upper PDF results when the clay-free form of the Archie Equation (Eq. 4.1) is used. The lower PDF results when the clay-dependent form (Eq. 6.1) is used. The mean of the resistivity log readings across the interval is 0.35 ohm-m. The average porosity is ~55 percent.

The clay-dependent form of the Archie Equation always yields a higher estimation of hydrate concentration (greater mean value of the PDF) than does the clay-free form of the equation, and there is always less uncertainty associated with its estimation (smaller standard deviation of the PDF). When clay content is high within an interval, the difference between the two estimations of hydrate concentration is large (Fig. 6.9). Note that in the sequence of Figures 6.7 through 6.10 that even though formation resistivity drops from about 2 ohm-m (Fig. 6.7) to approximately 1.3 ohm-m (Fig. 6.10), the clay-dependent form of the Archie Equation predicts a consistent hydrate concentration of about 60 percent, meaning hydrate occupies about 0.6 of the space available between sediment grains. In contrast, the clay-free form of the Archie Equation produces a wide range of hydrate estimations varying from a concentration of around 39 percent (Fig. 6.9) to a concentration of about 51 percent (Fig. 6.7). In Figure 6.11, where the formation resistivity is much less than 1 ohm-m, the clay-free form of the Archie Equation yields a ridiculous estimate of -12 percent for the hydrate concentration. In contrast, the clay-dependent form of the equation predicts a realistic value of less than 1 percent concentration.

Our calculation procedure allows us to present our estimations of hydrate concentration in a depth-based log-curve format in which the calculated hydrate fraction is displayed at each depth point across a targeted interval. Examples of such displays are shown as Figures 6.12 through 6.16. The intervals portrayed in these figures are the same intervals that are illustrated in Figures 6.7 through 6.11. The clay-fraction curves shown in this latter set of figures were calculated using Equation 6.4. Either data display option (Figures 6.7 to 6.11 or Figures 6.12 to 6.16) is valuable, depending on the application needed for the data.

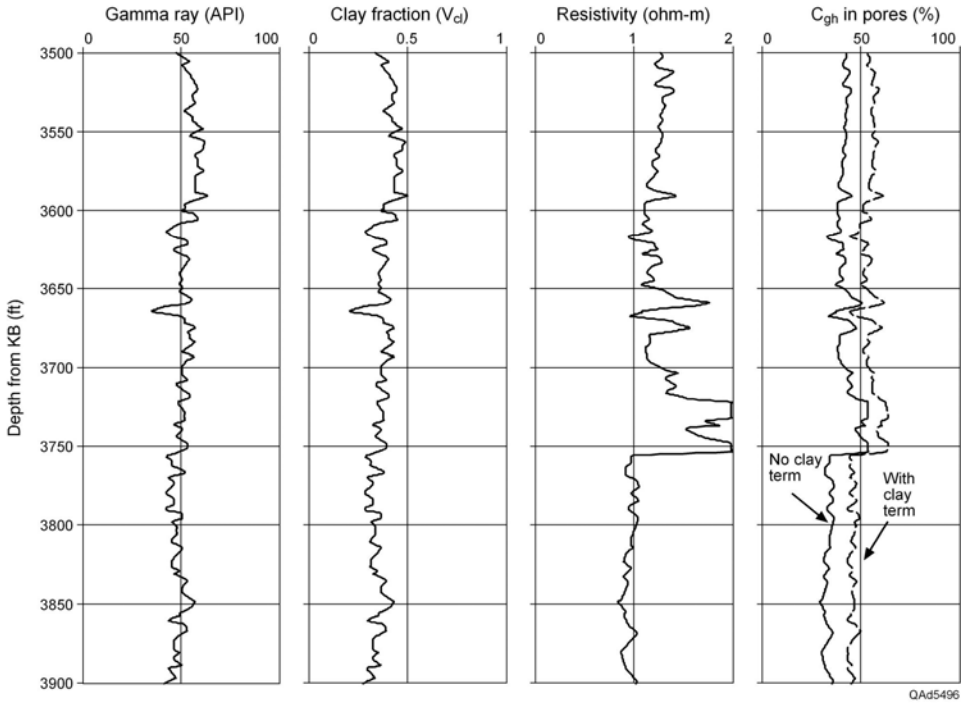

Figure 6.12. Clay fraction (V_{cl}) and hydrate concentration (C_{gh}) expressed as depth-based log curves across a target interval of example well L, Genesis area. Compare with Figure 6.7.

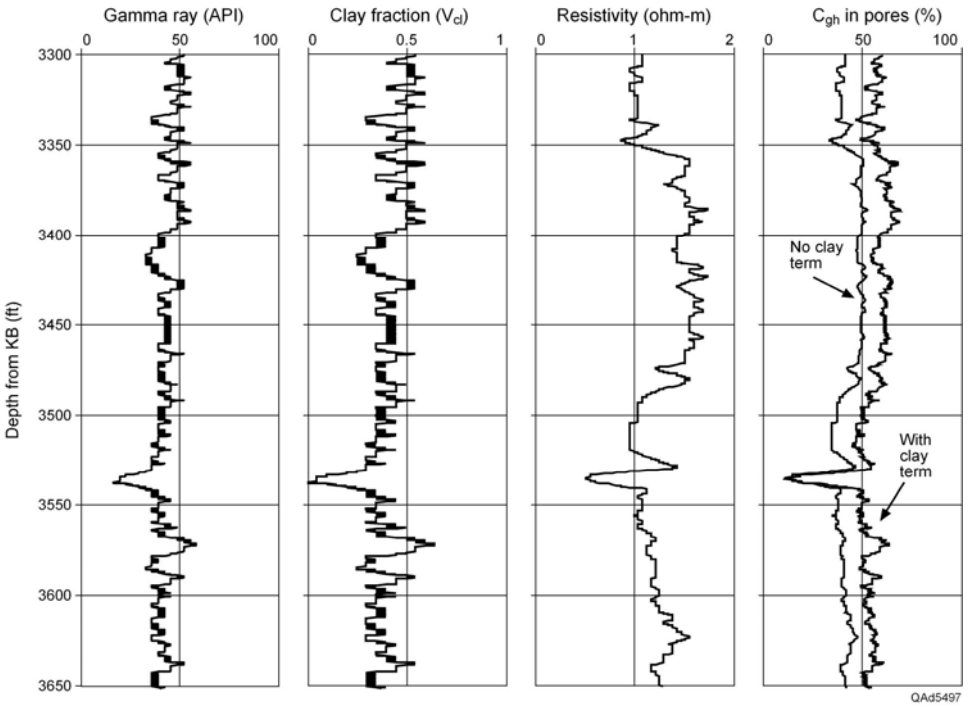

Figure 6.13. Clay fraction (V_{cl}) and hydrate concentration (C_{gh}) expressed as depth-based log curves across a target interval of example well G, Genesis area. Compare with Figure 6.8.

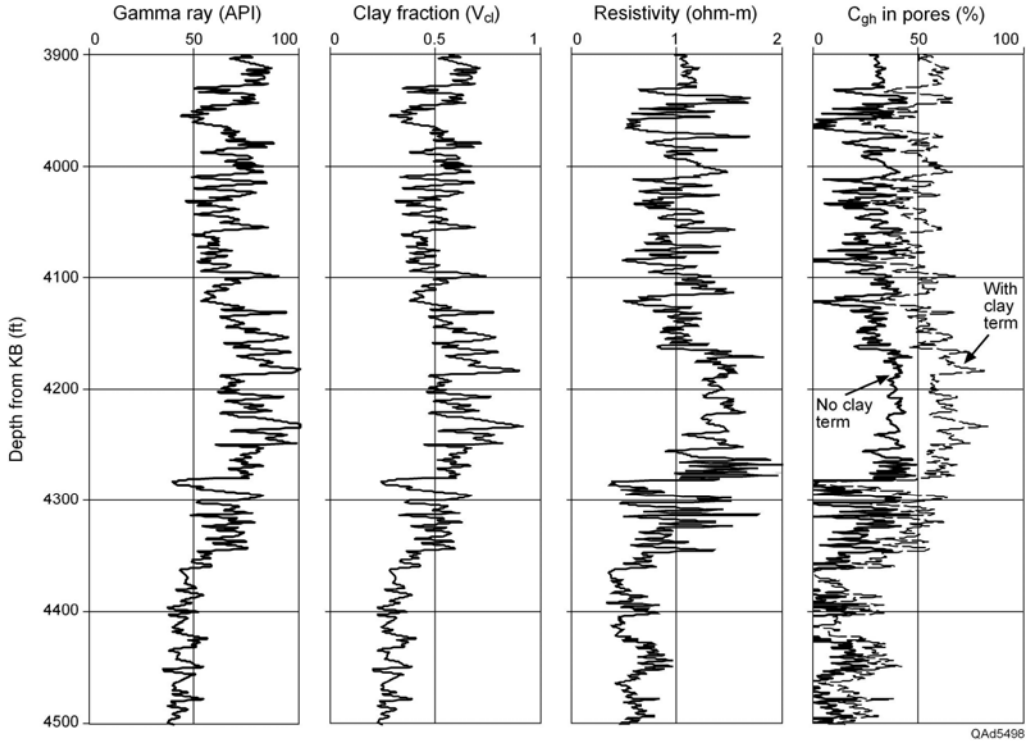

Figure 6.14. Clay fraction (V_{cl}) and hydrate concentration (C_{gh}) expressed as depth-based log curves across a target interval of example well E, Genesis area. Compare with Figure 6.9.

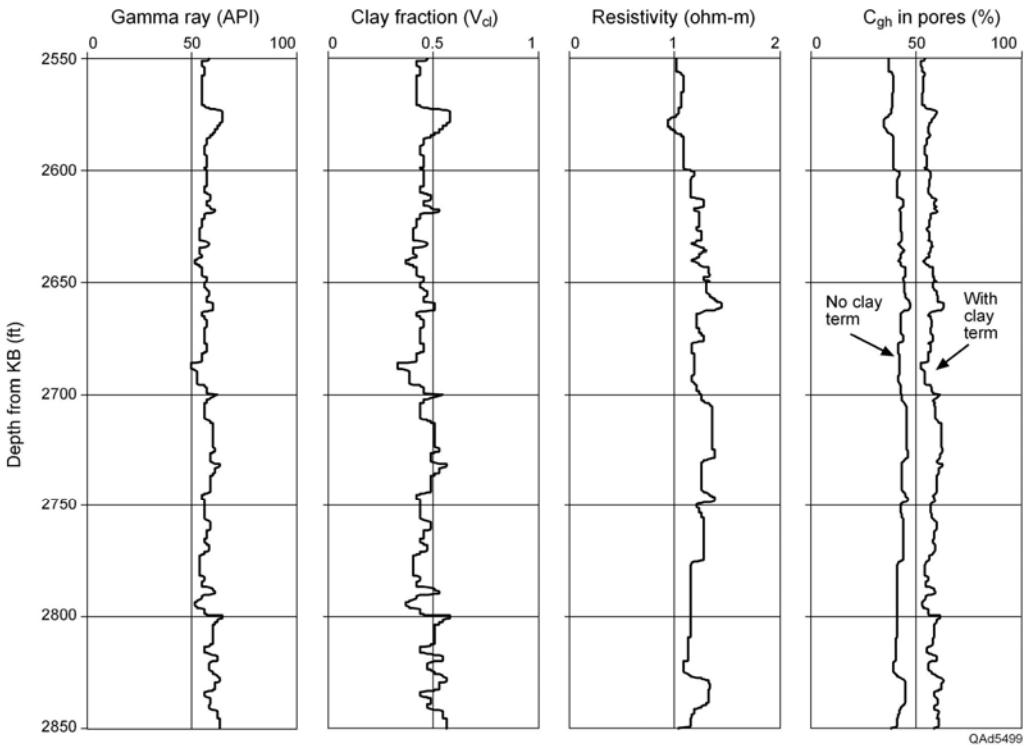

Figure 6.15. Clay fraction (V_{cl}) and hydrate concentration (C_{gh}) expressed as depth-based log curves across a target interval of example well A, Genesis area. Compare with Figure 6.10.

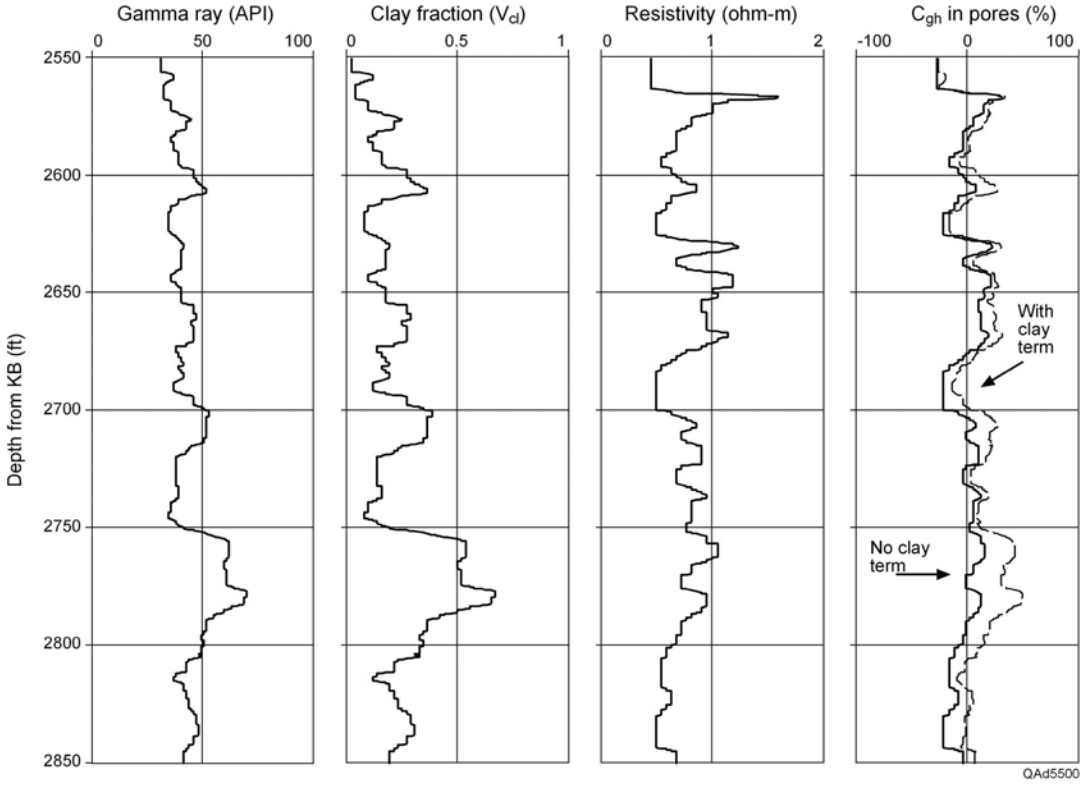

Figure 6.16. Clay fraction (V_{cl}) and hydrate concentration (C_{gh}) expressed as depth-based log curves across a target interval of example well D, Genesis area. Compare with Figure 6.11.

Conclusions

To implement the clay-dependent form of the Archie Equation (Eq. 6.1), we must estimate the clay fraction V_{cl} for each analyzed depth interval from the gamma-ray log (Eq. 6.4). Because the gamma-ray logs shown in Chapter 5 rarely traverse a 100-percent sand interval, a point open for debate is what value of V_{cl} should be assigned as the **baseline** drawn on each gamma-ray curve in order to set the value of V_{cl} for the min(GR) term used in Equation 6.4. We use experience and logic to decide what value of V_{cl} to assign to each baseline of the gamma-ray curve being used in a resistivity-to-hydrate inversion at each calibration well. If our thinking is incorrect, error is introduced into our estimates of hydrate concentration.

We repeat again that a possible source of significant error in our analysis of resistivity logs across the Green Canyon area: the assumption that the hydrate is disseminated uniformly throughout the sediment. This assumption allows the clay-dependent form of the Archie Equation to be utilized. If hydrate is present as thin horizontal layers of pure hydrate or as vertical hydrate-filled fractures, some resistivity-response equation other than the Archie Equation should be used.

An additional issue that needs to be considered is the question, “In a high-resistivity interval, is the resistivity log responding to a resistive hydrate phase or to a resistive free-gas phase?”. A resistivity log, by itself, cannot distinguish between these two resistive phases. However, V_P velocity data can distinguish between a hydrate-bearing interval and a free-gas interval because V_P decreases significantly when free gas is present. As discussed in Chapter 1, we found that a joint inversion approach in which hydrate concentration was estimated from both V_P and resistivity data was invaluable for avoiding the pitfall of interpreting a high-resistivity interval as being hydrate bearing when it actually was an interval having free gas.

DOE Gas Hydrate Final Report

Chapter 7

Raytracing and Velocity Analysis

Introduction

In the earliest phases of this study, we found that 2D OBC data could be processed in the common-receiver-gather domain to create P-P and P-SV images of near-seafloor geology that have better bandwidth and higher resolution than do images created by conventional common-midpoint and common-conversion-point data-processing techniques (Backus and others, 2005, 2006). In our first imaging effort, the limited amount of OBC data provided by our industry cost-sharing partner, WesternGeco, extended only 2 seconds below the seafloor at all offsets, and we used high-resolution P-P chirp-sonar data to correlate near-seafloor P-P and P-SV reflections so we could construct a simple, 3-layer velocity model along a test profile (Backus and others, 2006).

We later received data from WesternGeco that have longer record lengths. These data allowed us to: (1) extend our velocity-layer analysis methodology so that we needed only OBC-derived P-P and P-S images for depth registration (no AUV data), and (2) implement an interactive raytracing analysis that builds spatially varying velocity models of near-seafloor geology. Our current methodology allows us to iterate stratigraphic interpretation of an OBC profile with a velocity analysis along the same profile to build a sub-seafloor velocity-layer model that converges to interpreted depth-equivalent P-P and P-SV horizons data in a physically consistent manner.

The grid of OBC profiles along which velocity-layer models were constructed are shown in map views on Figure 8.1 and will not be repeated here. These OBC data were acquired using 4C seafloor sensors spaced at intervals of 25 m. The source was an air gun array towed 6 m below sea level directly atop each linear profile of seafloor sensors. Source station spacing was 50 m. Because these data were acquired for purposes of imaging deep geology, record lengths were 18.432 s, the sampling interval was 2 ms, and source-receiver offsets varied from 0 to 12,000 m at increments of 50 m. For our study, we limited the data to 3000-m offsets and used record lengths that allowed data to be analyzed to sub-seafloor depths that extended only short distances below the base of the hydrate stability zone.

Interpretation of OBC Profiles

The objective of our interpretation of P-P and P-SV images along each OBC line was to define which sub-seafloor P-SV reflection events were depth-equivalent to selected P-P reflections and to calculate V_P/V_S velocity ratios within the stratigraphic intervals bounded by these depth-equivalent P-P and P-SV horizons. We limited our interpretation to reflection events that extended only a

short distance below the base of the hydrate stability zone (BHSZ), such as the horizons shown on the profiles exhibited as Figure 7.1. We estimated the sub-seafloor depth of the BHSZ from the prediction guidelines developed by Milkov and Sassen (2001) for the Green Canyon area, which are exhibited as Figure 5.5. Once the depth position of the BHSZ was estimated from these Milkov and Sassen calibration curves, we then used logical velocity assumptions to interpret a pair of depth-equivalent P-P and P-SV horizons positioned below that estimated depth. These horizons were the deepest interfaces that we used in our seismic velocity analysis.

We found that the geology within the hydrate stability zone contained few geometric features (unique structural shapes) or stratigraphic terminations that could be used to define depth-equivalent P-P and P-SV reflections. We tried to use faults (when present) for depth registering P-P and P-SV images; however, faults were so steep when they approached the seafloor that any effort to use faults for P-P and P-SV depth registration led to ambiguous conclusions. Seismic facies variations (amplitude, phase, and frequency) between P-P and P-SV data presented additional obstacles for an interpreter to overcome when attempting to define depth-equivalent intervals between the P-P and P-SV seismic modes. For example, across one depth-equivalent interval, both P-P and P-SV data might show strong, bold reflections. Across a second depth-equivalent interval, P-P data might show bold reflections, and P-SV data would should weak reflections. Across a third interval, P-P reflections could be weak, and P-SV reflections would be strong and bold. These distinctive combinations of P-P and P-SV seismic attribute behavior are no doubt a rich source of rock, fluid, and hydrate information, but they complicate the interpretation of depth-equivalent P-P and P-SV reflections. More well log and core data need to be calibrated against OBC data to make definitive conclusions about how P-P and P-SV seismic facies relate to physical properties of hydrate systems.

Because of these interpretational barriers, we concluded that determining depth-equivalent sub-seafloor units and making reliable velocity estimates within near-seafloor layers required that a rigorous numerical raytracing analysis be done to determine if each pair of tentatively interpreted P-P and P-SV reflections were truly depth-equivalent, or whether different events needed to be selected to establish depth equivalency. The following section illustrates how this raytracing procedure was performed at receiver station 550 on OBC profile 264; the position indicated by the vertical line extending across the P-P and P-SV images displayed on Figure 7.1.

Raytracing

If we accept the premise that we can identify depth-equivalent P-P and P-SV reflection horizons on P-P and P-SV stacked images, as exhibited on Figure 7.1, we should be able to locate the reflection events associated with these horizons on common-receiver gathers. Given the large difference in elevation between source and receiver in deep-water OBC data acquisition, normal hyperbolic moveout of reflection events does not apply to deep-water OBC data.

However, we can numerically calculate the arrival times of reflections using a raytracing approach to perform velocity analysis on common-receiver gathers.

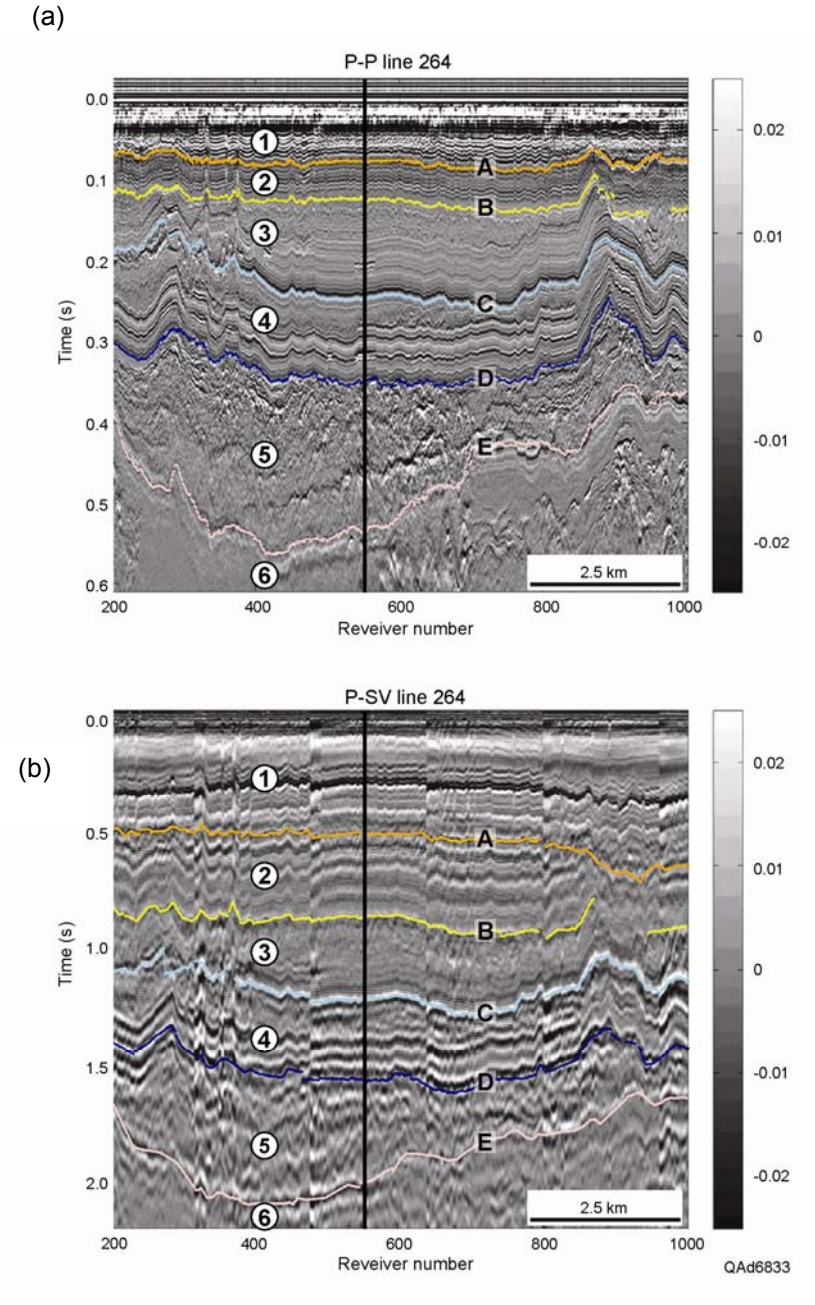

Figure 7.1. Interpretation of (a) P-P image and (b) P-SV image created from limited-offset (<3000 m) stacks of common-receiver gathers. Labeled horizons A through E are an initial interpretation of depth-equivalent geology in P-P and P-SV image spaces. Horizon D is interpreted to be “near” the base of the hydrate stability zone. The next data-analysis step is to verify the depth equivalency of these horizons by raytracing at numerous locations along the profile. Both images are flattened relative to the seafloor. The following figures show the raytracing procedure performed at receiver coordinate 550 marked by the vertical line.

The concept of the raytracing method we implemented is illustrated by the diagram on Figure 7.2. At intervals of 10 seafloor receiver stations (250 m) along each OBC profile, a common-receiver gather was constructed using data generated at 120 source stations centered on the receiver position (-3000 m to +3000 m source offsets). When the P-P and P-SV images showed geology along a profile to be laterally uniform, the distance between consecutive raytrace analysis points was sometimes extended to span 20 receiver stations (500 m).

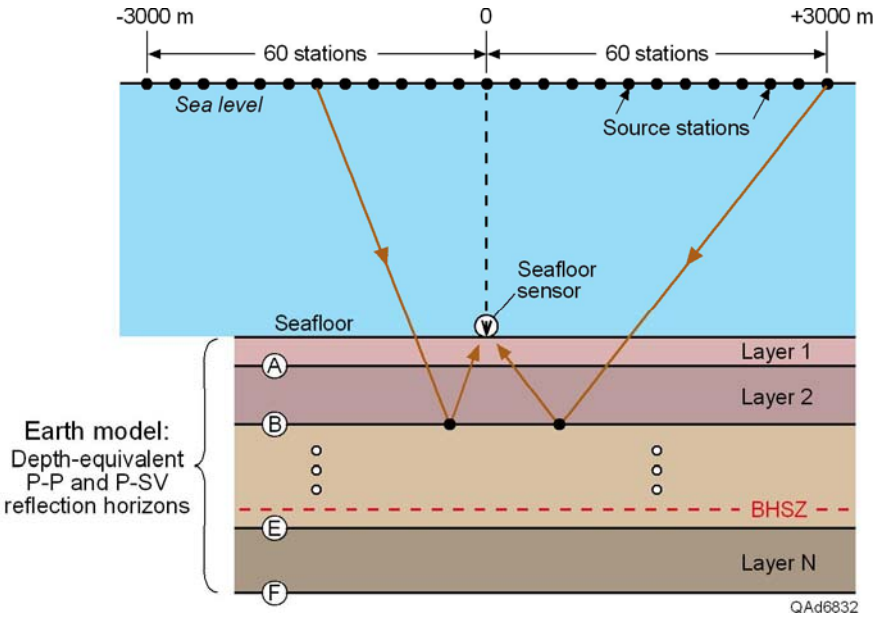

Figure 7.2 Raytracing procedure implemented to construct velocity-layer models of near-seafloor geology spanning the hydrate stability zone. The data used in the raytrace analysis were common-receiver versions of P-P and P-SV reflectivity. Both P-P and P-SV raypaths were constructed that extended from each source station, to a targeted horizon, and then to the seafloor receiver station. BHSZ is the base of the hydrate stability zone. This diagram is simplified. In our real-Earth raytracing, the water layer is much thicker, and raypaths are refracted at interfaces.

An example of a typical common-receiver trace gather of 4C OBC data is exhibited as Figure 2.1, and a second example does not need to be repeated here. These common-receiver data were processed to create common-receiver-gather versions of P-P reflectivity and P-SV common-receiver reflectivity as explained in Chapter 2. Examples of typical P-P and P-SV reflectivities are exhibited as Figures 2.7 and 2.8, respectively. The raytracing procedure that was used to construct velocity-layer models along an OBC profile will be illustrated using common-receiver data acquired at receiver coordinate 550 defined on Figure 7.1.

Once depth-equivalent horizons are interpreted on stacked P-P and P-SV data, as has been done on the P-P and P-SV images along OBC profile 264 on

Figure 7.1, V_P/V_S velocity ratios can be calculated between any two horizon pairs using the equation,

$$(7.1) \quad V_P/V_S = 2(\Delta T_{PS}/\Delta T_{PP}) - 1,$$

where ΔT_{PS} is the interval time between the two P-SV horizons that bound the interval on the stacked P-SV image, and ΔT_{PP} is the interval time between the two corresponding P-P depth-equivalent horizons on the stacked P-P image. The accuracies of the V_P/V_S values determined in this manner depend on the skill of the interpreter in recognizing depth-equivalent P-P and P-SV reflectivity behavior.

Our raytracing methodology uses these interpreter-defined V_P/V_S velocity ratios as a fixed Earth property. As the raytracing progresses from the first sub-seafloor layer to the last layer that extends below the base of the hydrate stability zone, the philosophy of our raytracing approach to building an Earth model of sub-seafloor velocity layers is: (1) assume the V_P/V_S ratios determined by interpreting depth-equivalent P-P and P-SV reflections across each sub-seafloor interval are correct for all intervals, (2) use each raytrace-based interval value of V_P (or V_S) together with the fixed V_P/V_S velocity ratio across the interval to determine the corresponding interval value of V_S (or V_P), and (3) define the picked reflection time of the imaged horizon at the receiver-station coordinates where the velocity analysis is done as the zero-offset time that must be associated with the proper reflection event in the common-receiver gather. Using these concepts, we raytrace down from each sea-level source to the target horizon and then up from that horizon to the seafloor receiver and adjust the velocity model until raytrace-calculated arrival times converge to the observed reflection arrival times of the proper event in the P-P and P-SV common-receiver gathers. The concept is depicted graphically on Figure 7.3.

Because 1D raytracing is not computationally intensive, we can iterate the arrival-time calculation using different layer thicknesses and layer velocities and perform each velocity analysis interactively. The option shown on Figure 7.3 of re-interpreting the stack data to refine the definition of depth-equivalent P-P and P-SV reflections is important for accurate velocity analysis because the parameters T_0(PP), T_0(PS), and V_P/V_S associated with these depth-equivalent events are the critical constraints used in the raytracing analysis. Stack data were sometimes re-interpreted 8 or 10 times to achieve raytrace convergence of V_P and V_S across a layer at some receiver stations.

In practice, we can overlay raytrace-based travel-time curves on the common-receiver gathers, or we can apply raytrace-based time shifts to each trace of the gather to flatten a targeted reflection that is being analyzed. We found the latter approach (time shifting and reflection flattening) to be simpler and more accurate. It is important to note that flattening an event by static shifts is not equivalent to applying dynamic moveout corrections to the data. The flattening

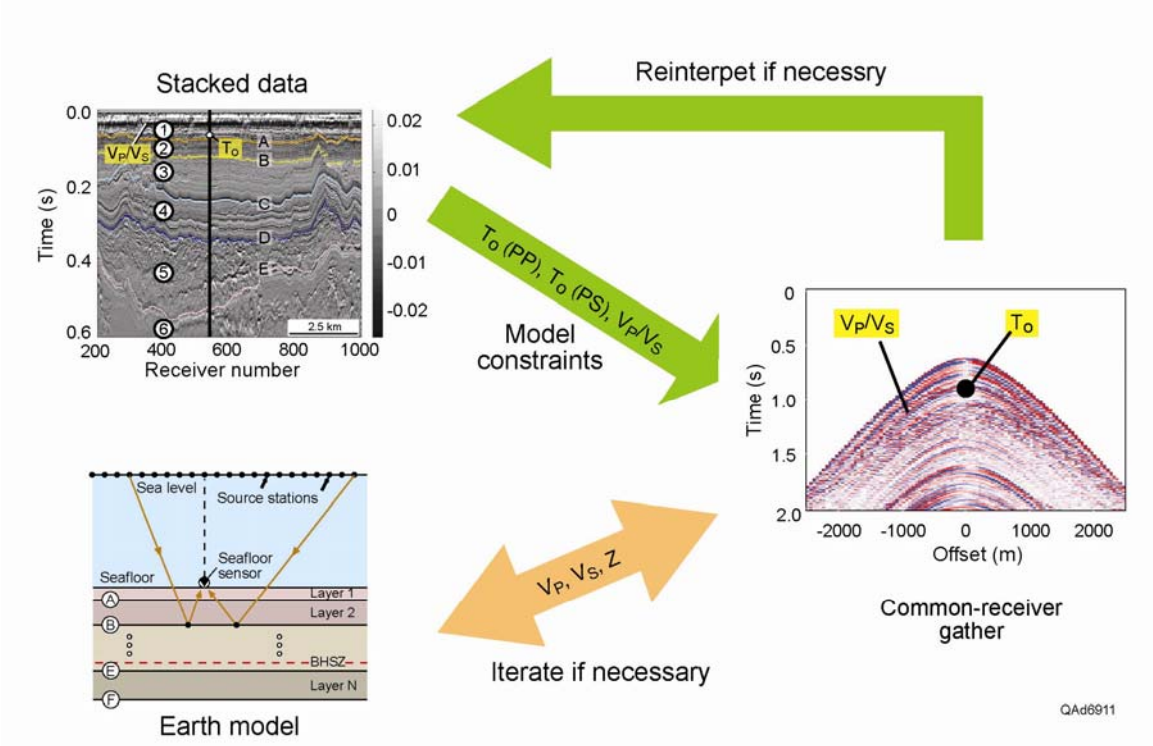

Figure 7.3. Our philosophy of raytrace-based velocity analysis consist of the following steps. Step 1: Interpret P-P and P-SV images (top left) to determine depth-equivalent P-P and P-SV reflections. This interpretation defines zero-offset times T_0(PP) and T_0(PS) at a selected seafloor receiver station and the velocity ratio V_P/V_S between adjacent pairs of depth-equivalent horizons at that station. These three parameters (T_0(PP), T_0(PS), V_P/V_S)serve as constraints on the raytrace analysis. Step 2: Examine the common-receiver-gather data at that receiver station (right) to find a P-P reflection with zero-offset time T_0(PP) and a P-SV reflection with zero-offset time T_0(PS). Determine what value of V_P flattens the P-P event at all offsets. Knowing V_P/V_S and V_P, calculate V_S and check if this value of V_S flattens the P-SV event. Re-interpret the stack data to define different depth-equivalent events if necessary; iterate the raytrace analysis if necessary. Once V_P and V_S converge to stable values, calculate the thickness of the layer bounded by the depth-equivalent events (lower left).

process simply shifts each data trace by a calculated time, thereby eliminating wavelet-stretch artifacts and allowing us to use much longer source-receiver offsets to constrain velocities than can be done in a time-variant moveout-based approach as described in Chapter 2 (Figs. 2.7 and 2.8). An additional benefit of a raytracing approach is that it is not susceptible to limitations of non-hyperbolic moveout associated with low velocities, large offset/depth ratios, and differences in source and receiver elevations. All three of these conditions were present in the deep-water OBC data used in this study.

A principal advantage of our velocity analysis strategy is that velocity layers are defined as a function of depth below the seafloor. As a result, V_P and V_S velocities derived by an analysis can be correlated with depth-based resistivity logs, and both resistivity and velocity data can be used to identify the BHSZ boundary in P-P and P-SV image spaces. This Earth-layer construction process was applied at approximately 800 seafloor receiver stations across the grid of 2D

OBC lines to build a continuous velocity model along each 2D OBC profile. Velocity layer 1 started at the seafloor and extended to the shallowest interpretable P-P reflection. Velocity layers 2, 3, and 4 extended to successively greater depths until a velocity layer N was created that extended deeper than the BHSZ boundary (Fig. 7.2).

An example velocity analysis performed at seafloor receiver station 550 on OBC profile 264 (Fig. 7.1) is shown as Figures 7.4 through 7.11. The analysis was done in the reduced-time domain in which the time origin T = 0 at each source-offset coordinate is the direct-arrival time of the downgoing P-wave.

Water Column Analysis

Because the first layer of the Earth model was the water column, the first event that was raytraced and adjusted to reduced time was the seafloor reflection at the base of the water column. The raytracing result at receiver station 550 is exhibited as Figure 7.4. As noted on the figure, the water-column conditions that result in a flat P-P and P-SV seafloor reflection event are: V_P = 1502 m/s, V_S = 0, and thickness = 577 m. The reflections corresponding to sub-seafloor horizons A and B on the stacked P-P and P-SV images (Fig. 7.1) are the “smiling” events labeled on the common-receiver reflectivities. The zero-offset times for these reflections are the same as the image times of the A and B horizons at receiver station 550 on Figure 7.1.

The raytrace-determined velocity for the water column (1502 m/s) is tentatively assigned to the full extent of the sub-seafloor interval, resulting in the vertical line labeled V_P on the right-most data panel The V_P/V_S velocity function determined by applying Equation 7.1 to the stacked P-P and P-SV data is critical for creating an initial estimate of the layer values of V_S velocities and individual layer thicknesses. At receiver station 550, the V_S velocities displayed on Figure 7.4 are the result of dividing the raytraced V_P function (a constant value of 1502 m/s) by the V_P/V_S velocity ratio calculated for horizons A through E on Figure 7.1. Both the values of V_S and the thickness of each sub-seafloor layer were updated as the raytracing proceeded to Layers 1, 2, 3, . . ., N that extended to successively deeper depths below the seafloor and more velocity detail was created.

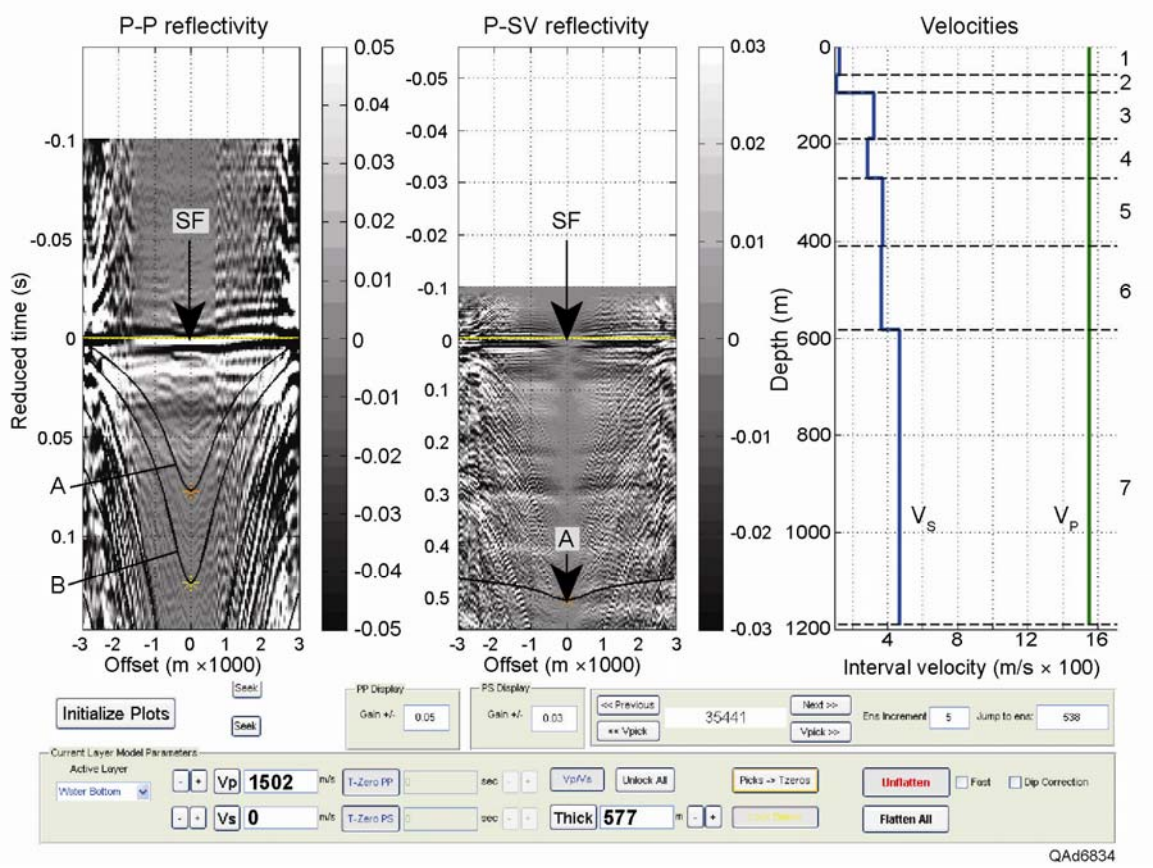

Figure 7.4. Velocity analysis at the seafloor. The seafloor arrival (SF) is flattened at T=0. Reflections A and B correspond to horizons A and B identified on the images displayed as Figure 7.1. Note that the zero-offset times of A and B are the same as the image times on horizons A and B at receiver coordinates 550 on Figure 7.1. Raytracing show the parameters for the water column are V_P = 1502 m/s, V_S = 0, and thickness = 577 m. The vertical line labeled V_P is the raytrace value of 1502 m/s that flattens the seafloor reflection. The V_S velocity function is the result of dividing the constant V_P value by the V_P/V_S velocity ratio calculated by applying Equation 7.1 to the horizons on Figure 7.1.

Layer 1 Analysis

In our notation, Earth Layer 1 is the first velocity layer below the seafloor. The base of this layer is horizon A (Fig. 7.1). To determine the thickness and interval V_P and V_S velocities for the layer, raytracing was done to determine the velocity and thickness parameters that resulted in offset-dependent time shifts that, when applied to the common-receiver reflectivities, made both P-P reflection A and P-SV reflection A optimally flat. The raytracing result is displayed as Figure 7.5, showing acceptable flattening of reflection A on both receiver gathers. The reduced-time where the P-P and P-SV flattened reflections are positioned are the zero-offset times of the reflections on Figure 7.4, the same time coordinates where horizon A appears at receiver coordinate 550 on the respective P-P and P-SV images on Figure 7.1.

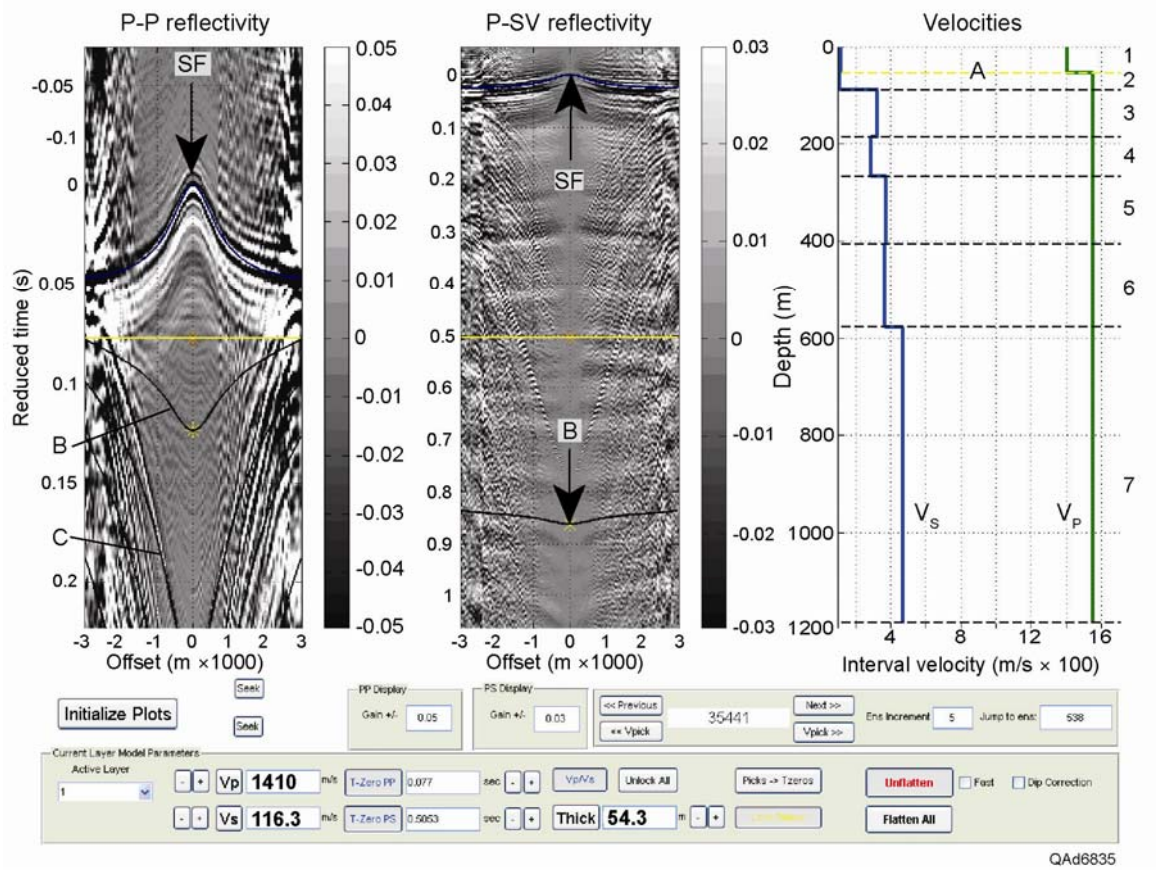

Figure 7.5. Velocity analysis for sub-seafloor Layer 1 bounded at its base by horizon A (Fig. 7.1). V_P and V_S velocities and the thickness for Layer 1 are adjusted until raytrace-based time shifts cause reflection A to be optimally flat in the P-P and P-SV reflectivity gathers above. The raytracing analysis shows the parameters for Layer 1 to be: V_P = 1410 m/s, V_S = 116 m/s, and thickness = 54.3 m. Note the V_P velocity (1410 m/s) is less than the velocity in the water column (1502 m/s), a behavior found at the majority of velocity-analysis points in this study. Flattened reflection A is positioned at 0.077 s on the P-P gather and at 0.505 s on the P-SV gather, the same time coordinates where horizon A is positioned at receiver station 550 on the stacked data shown on Figure 7.1.

The parameters determined for Layer 1 by raytracing were: V_P = 1410 m/s, V_S = 116 m/s, and thickness = 54.3 m. We found that the V_P velocity across Layer 1 at most velocity-analysis locations was less than water velocity (1502 m/s), as it was at this receiver station. A possible explanation for the lower value of the P-wave velocity in Layer 1 is the presence of gas-filled forams in the first several meters of sediment. Samples of foram-bearing sediments have been acquired at numerous locations across the Green Canyon area by Harry Roberts of Louisiana State University through his piston-core studies of shallow hydrate systems. Dr. Roberts shared his insights into the effects of hollow foram tests on sediment properties with us as we conducted these velocity analyses, increasing our confidence in the reduced V_P velocities we consistently found in Layer 1 across our study area. The percentage of the near-seafloor foram population that has gas trapped in tests is uncertain; neither is the chemistry of the entrapped

gas known. Because much of Layer 1 is in the sulfate reduction zone, the sulfate reduction of methane,

$$(7.2)\quad CH_4 + SO_4 \longrightarrow HCO_3 + HS + H_2O,$$

may result in hydrogen sulfide being the principal gas that is entrapped within local foram tests.

Analyses for Layers 2 Through 7

The raytracing solutions for reflections B, C, D, E, F, and G, the respective bottom interfaces of sub-seafloor Layers 2, 3, 4, 5, 6, and 7, are shown in sequence as Figures 7.6 through 7.11. Extensive comments are provided in the caption of each figure to explain the raytracing analysis performed across each sub-seafloor layer.

The behavior of the P-wave velocity demonstrated in this sequence of figures is important in defining the base of the hydrate stability zone along the OBC profiles that spanned our two study areas. At receiver station 550, the V_P velocity increases in a consistent manner from Layer 2 through Layer 4 (Figs. 7.6 through 7.8), decreases in Layer 5 (Fig. 7.9), and then resumes to consistently increase in Layers 6 and 7 (Figs. 7.10 and 7.11). The decrease in V_P velocity in Layer 5 is interpreted as an indication of the presence of free gas, which in turn, defines the base of the hydrate stability zone. At the majority of the receiver stations where we did velocity analyses, we found, as in this example, that a reversal in V_P velocity occurred in a sub-seafloor layer that was within the depth range where the base of hydrate stability would be expected, and that V_P velocity then continued to increase with depth in a normal fashion below that layer, as we show on Figures 7.10 and 7.11.

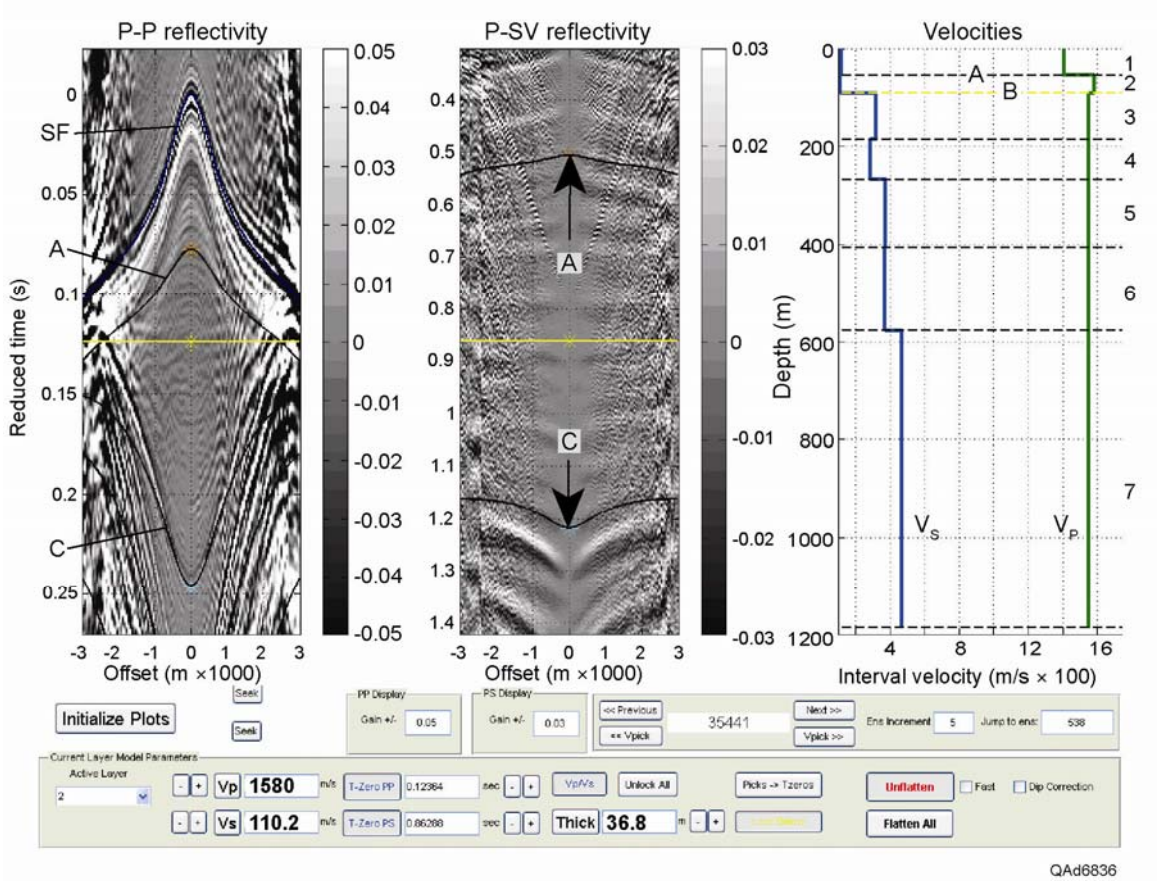

Figure 7.6. Velocity analysis for Layer 2 bounded at its base by horizon B (Fig. 7.1). V_P and V_S velocities and the thickness for Layer 2 are adjusted until raytrace-based time shifts cause reflection B to be optimally flat in the P-P and P-SV reflectivity gathers. The raytracing analysis shows the parameters for Layer 1 to be: V_P = 1580 m/s, V_S = 110 m/s, and thickness = 36.8 m. Flattened reflection B is positioned at 0.124 s on the P-P gather and at 0.863 on the P-SV gather, the same time coordinates where horizon B is positioned at receiver coordinate 550 on the stacked data shown on Figure 7.1. The V_P and V_S velocity profiles are now updated (right).

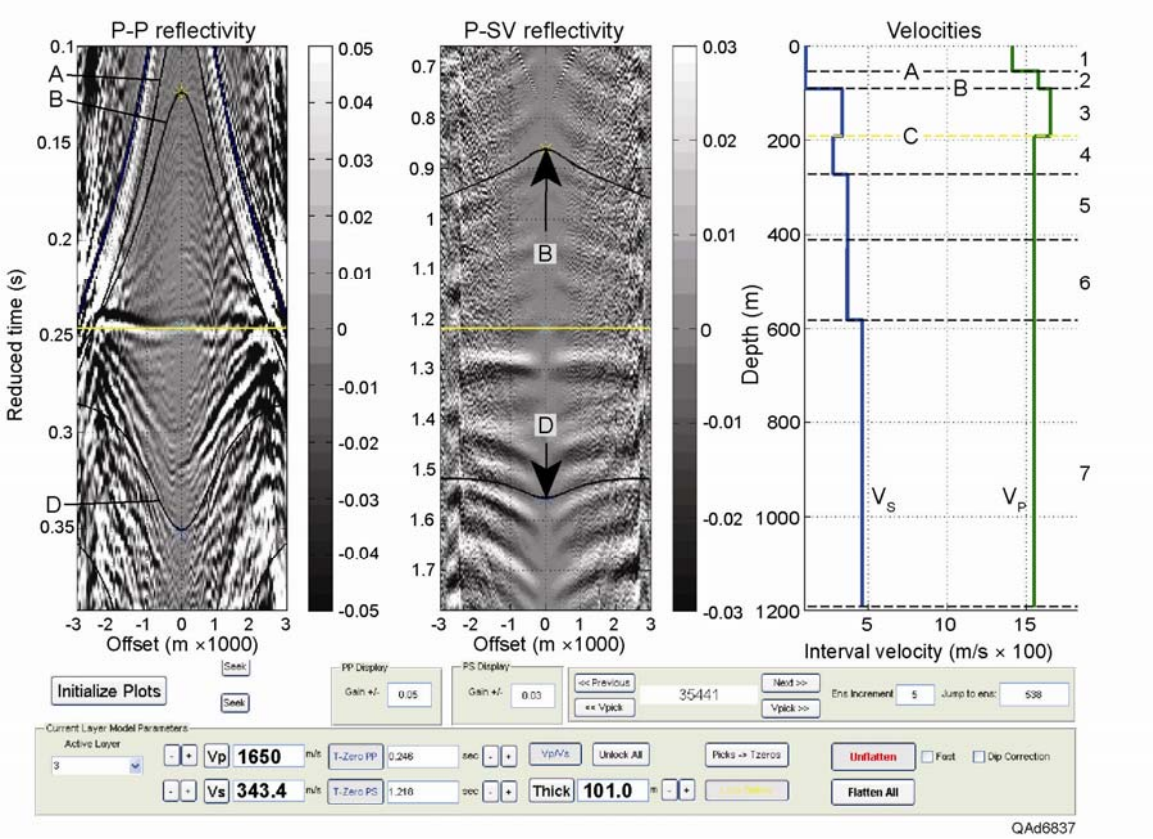

Figure 7.7. Velocity analysis for Layer 3 bounded at its base by horizon C (Fig. 7.1). V_P and V_S velocities and the thickness for Layer 3 are adjusted until raytrace-based time shifts cause reflection C to be optimally flat in the P-P and P-SV reflectivity gathers. The raytracing analysis shows the parameters for Layer 3 to be: V_P = 1650 m/s, V_S = 343 m/s, and thickness = 101 m. Flattened reflection C is positioned at 0.246 s on the P-P gather and at 1.218 s on the P-SV gather, the same time coordinates where horizon C occurs at receiver station 550 on the stacked data shown on Figure 7.1. The V_P and V_S velocities continue to be updated (right).

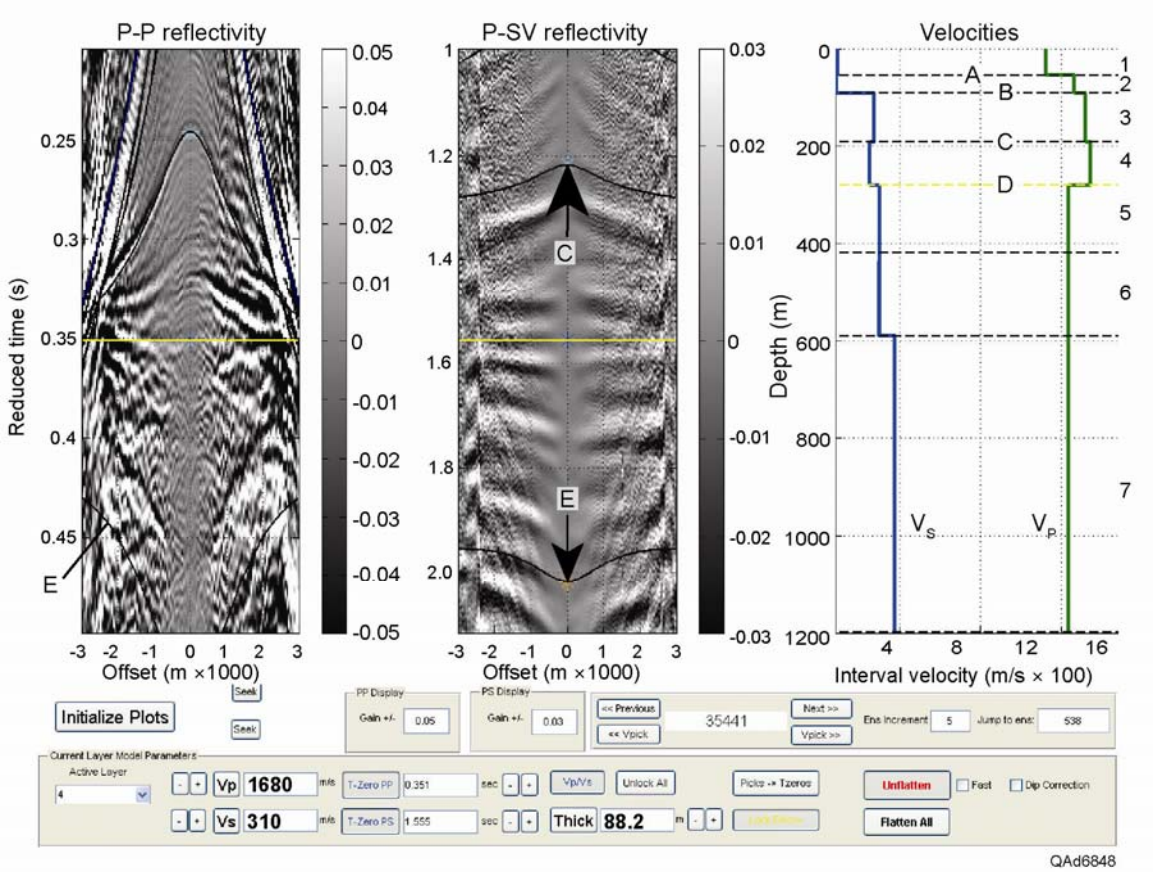

Figure 7.8. Velocity analysis for Layer 4 bounded at its base by horizon D (Fig. 7.1). V_P and V_S velocities and the thickness of Layer 4 are adjusted until raytrace-based time shifts cause reflection D to be optimally flat in the P-P and P-SV reflectivity gathers. The raytracing analysis shows the parameters for Layer 4 to be: V_P = 1680 m/s, V_S = 310 m/s, and thickness = 88.2 m. Flattened reflection D is positioned at 0.351 s on the P-P gather and at 1.555 s on the P-SV gather, the same time coordinates where horizon D occurs at receiver station 550 on the stacked data displayed on Figure 7.1. The V_P velocity continues to increase with depth (right). V_S velocity exhibits a minor decrease in Layer 4, which is assumed to be caused by a modest reduction in shear modulus across the layer.

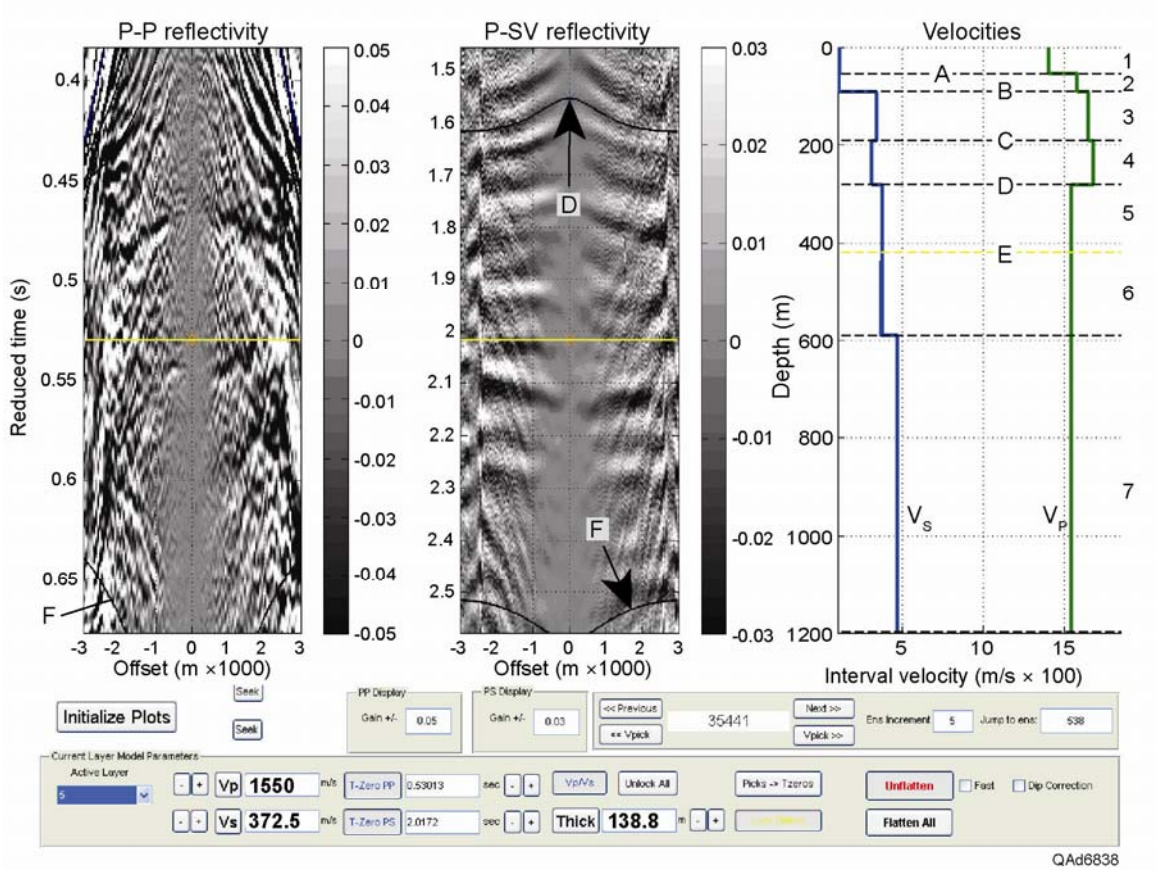

Figure 7.9. Velocity analysis for Layer 5 bounded at its base by horizon E (Fig. 7.1). V_P and V_S velocities and the thickness for Layer 5 are adjusted until raytrace-based time shifts cause reflection E to be optimally flat in the P-P and P-SV reflectivity gathers. The raytracing analysis shows the parameters for Layer 5 to be: V_P = 1550 m/s, V_S = 372.5 m/s, and thickness = 138.8 m. Flattened reflection E occurs at 0.530 s on the P-P gather and at 2.017 s on the P-SV gather, the same time coordinates where horizon E is positioned at receiver station 550 on the stacked data shown on Figure 7.1. V_P velocity reduces significantly in Layer 5; the cause interpreted as the presence of free gas in the layer. V_S does not react to the free gas, as expected. This free-gas-induced reduction in V_P velocity indicates the base of the hydrate stability zone is positioned at the top of Layer 5.

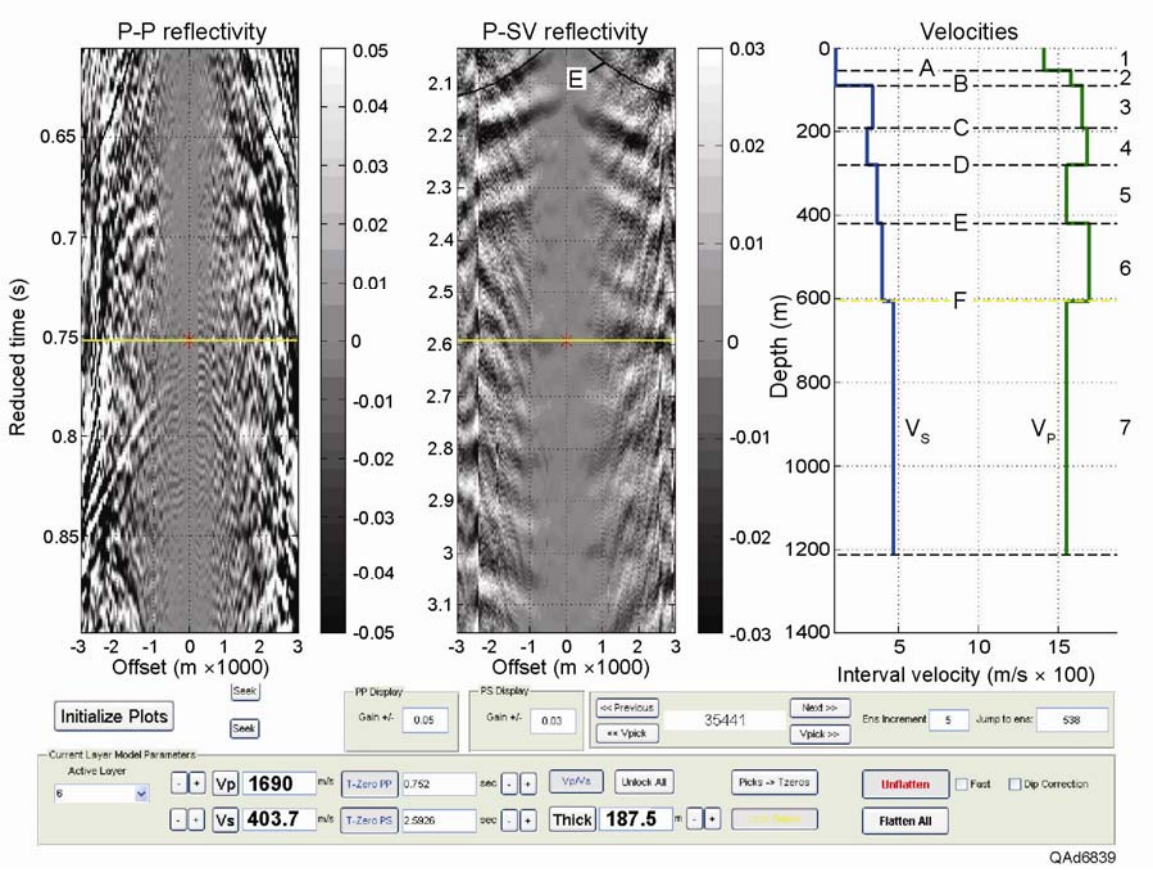

Figure 7.10. Velocity analysis for Layer 6 bounded at its base by horizon F (Fig. 7.1). V_P and V_S velocities and the thickness for Layer 6 are adjusted until raytrace-based time shifts cause reflection F to be optimally flat in the P-P and P-SV reflectivity gathers. The raytracing analysis shows the parameters for Layer 6 to be: V_P = 1690 m/s, V_S = 403.7 m/s, and thickness = 187.5 m. Flattened reflection F is positioned at 0.752 s on the P-P gather and at 2.593 s on the P-SV gather, the same time coordinates where horizon F occurs at receiver station 550 on the stacked data shown as Figure 7.1. V_P velocity now returns to its normal behavior of increasing with increasing burial depth, further emphasizing the character of the reduced V_P velocity in Layer 5.

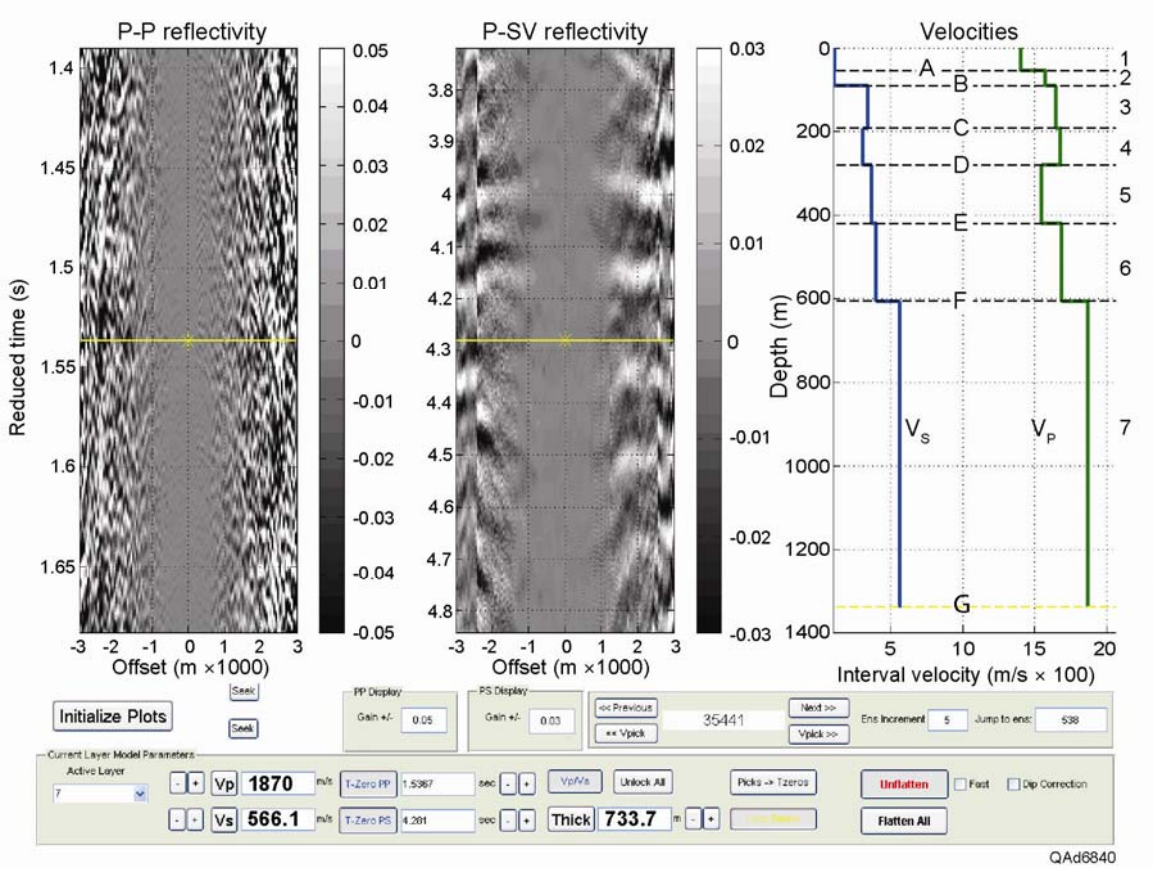

Figure 7.11. Velocity analysis for Layer 7 bounded at its base by horizon G (not shown on Figure 7.1). V_P and V_S velocities and the thickness for Layer 7 are adjusted until raytrace-based time shifts cause reflection G to be optimally flat in the P-P and P-SV reflectivity gathers. The raytracing analysis shows the parameters for Layer 7 to be: V_P = 1870 m/s, V_S = 566.1 m/s, and thickness = 733.7 m. V_P velocity continues to increase with depth, confirming that the velocity behavior calculated across Layers 4, 5, and 6 are correct and not a numerical oscillation created by the raytracing analysis. The construction of velocity layers now stops because interval velocities have been calculated across the hydrate stability zone.

Reflection Interference

An important observation from this work was that, in some cases, a reflection event that was easily identifiable on the stacked images was not apparent on the common-receiver gathers during velocity analysis. Some P-P events interfere destructively with each other at far offsets (Fig. 7.12). Even though the reflection might be seen at short source-receiver offsets, as in this example, there was less confidence in using the event to estimate travel time curvature and the V_P velocity associated with the event. In such cases, it was possible to identify the depth-equivalent P-SV event and to use the raytracing velocity analysis to estimate both P-wave and SV-wave travel times for the converted-shear event. Because V_P/V_S ratios and zero-offset intercept times were constrained in the stacked-data interpretation phase, separate from the

raytracing phase, we could calculate V_P even in these instances. We thus had redundant options for calculating V_P: (1) raytrace the targeted P-P reflection event (the preferred option), or (2) raytrace the depth-equivalent P-SV event which involves V_P on the downgoing leg of the raypath (the option used when reflection interference prevented the implementation of option 1). The availability of P-SV reflections that permitted option 2 to be implemented is one strong appeal of using 4C seismic data to evaluate deep-water hydrate systems.

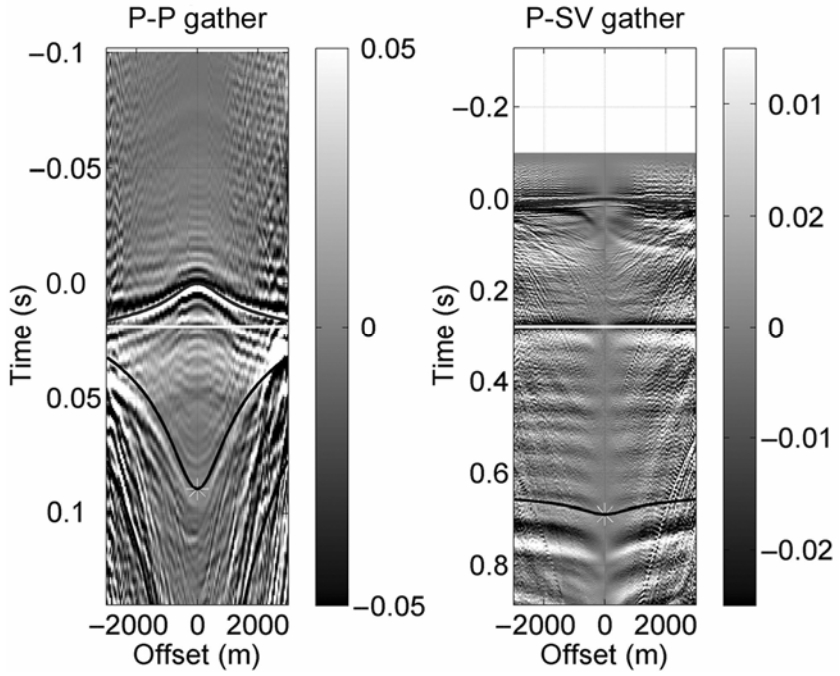

Figure 7.12. Example of a P-P reflection (left) that cannot be seen over the full offset range because of destructive interference with neighboring reflection events. In such instances, the depth-equivalent P-SV reflection (right) can be seen at all offsets and used to estimate V_P velocity along the downgoing leg of the P-SV raypath.

Dipping Interfaces

In areas of moderate dip, the 1D assumption of our raytracing (which implies a flat-layer Earth model at each location), did not allow us to flatten all P-P reflection events. An example of a P-P reflection from a dipping interface is displayed as Figure 7.13. There is evidence that a correct value of V_P was determined in this instance because the P-P event has opposing symmetry in the positive and negative offset domains and the inferred horizon cuts the event at its point of symmetry. However, we elected to not rely totally on such judgments to conclude that a correct V_P value had been determined when we had to do velocity analyses at dipping interfaces but to use the depth-equivalent P-SV event to determine the V_P and V_S for the dipping layer.

The option of reverting to the P-SV common-receiver data for a V_P velocity estimation is logical because V_P/V_S ratios were large (>4) near the seafloor across our study area. As a result, the area of P-SV illumination on a dipping interface is much smaller than the area of P-P illumination (Fig. 7.14). Therefore, the time dip of a P-SV reflection event from a dipping interface is much less than the time dip of a P-P event from the same interface at all source-receiver offsets. As a result, a P-SV reflection from a dipping interface can be flattened in a common-receiver reflectivity display in the same way as can a P-SV reflection from a horizontal interface. When we encountered dipping horizons in our near-seafloor velocity analyses that made it difficult to estimate V_P from P-P data, we estimated both V_P and V_S from velocity analyses of the P-SV reflectivity, using the downgoing leg of the raypath to define V_P and the upgoing leg to define V_S.

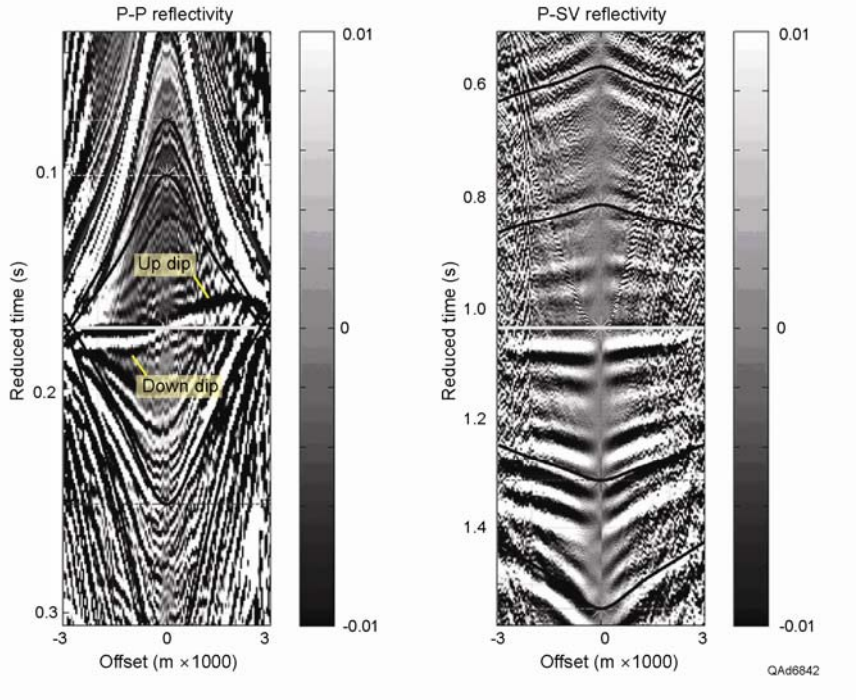

Figure 7.13. Examples of P-P and P-SV reflection behavior from a dipping interface. The P-P event from a dipping interface cannot be flattened to verify that a correct interval value of V_P has been determined. The P-SV event can be flattened (with only minimal deviation from a flat trend) even when the dip of the interface is appreciable, as in this case.

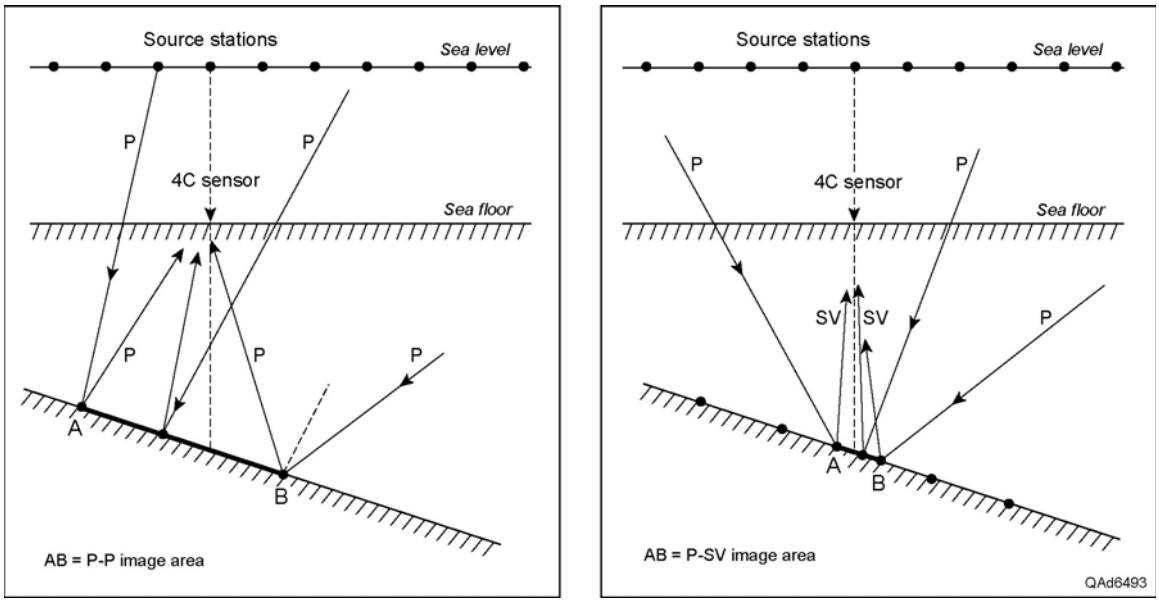

Figure 7.14. Comparison of the area illuminated on a dipping interface by a P-P wave mode and by a P-SV wave mode. P-P reflection points spread across a wide area and cause reflections from updip source stations to arrive earlier than they would from a horizontal interface and reflections from downdip sources to arrive later. In contrast, P-SV conversion points cluster in a small area, and there are minimal differences in arrival times from downdip and updip source stations for dipping and horizontal interfaces. These models are over-simplified cartoons. In our real-Earth models, the water layer is much thicker than any sub-seafloor layer, and raypaths are refracted at interfaces.

The availability of P-SV reflection data to do velocity analysis at dipping interfaces is a second reason why 4C data should be used in deep-water hydrate studies. The V_P/V_S ratio obtained from interpreting the stacked P-P and P-SV data was an invaluable constraint on velocity estimations done at dipping interfaces when we had to abandon a P-P reflection and rely on the depth-equivalent P-SV reflection.

We performed velocity analysis at every 10 receiver stations along each OBC profile, and sometimes at intervals of 20 stations, depending on the lateral consistency of the geology. We then interpolated these velocity models to create continuous velocity profiles of V_P and V_S as shown in Figure 7.15. Although this velocity analysis process seems to be labor intensive, it requires similar time and effort to do traditional velocity analysis techniques.

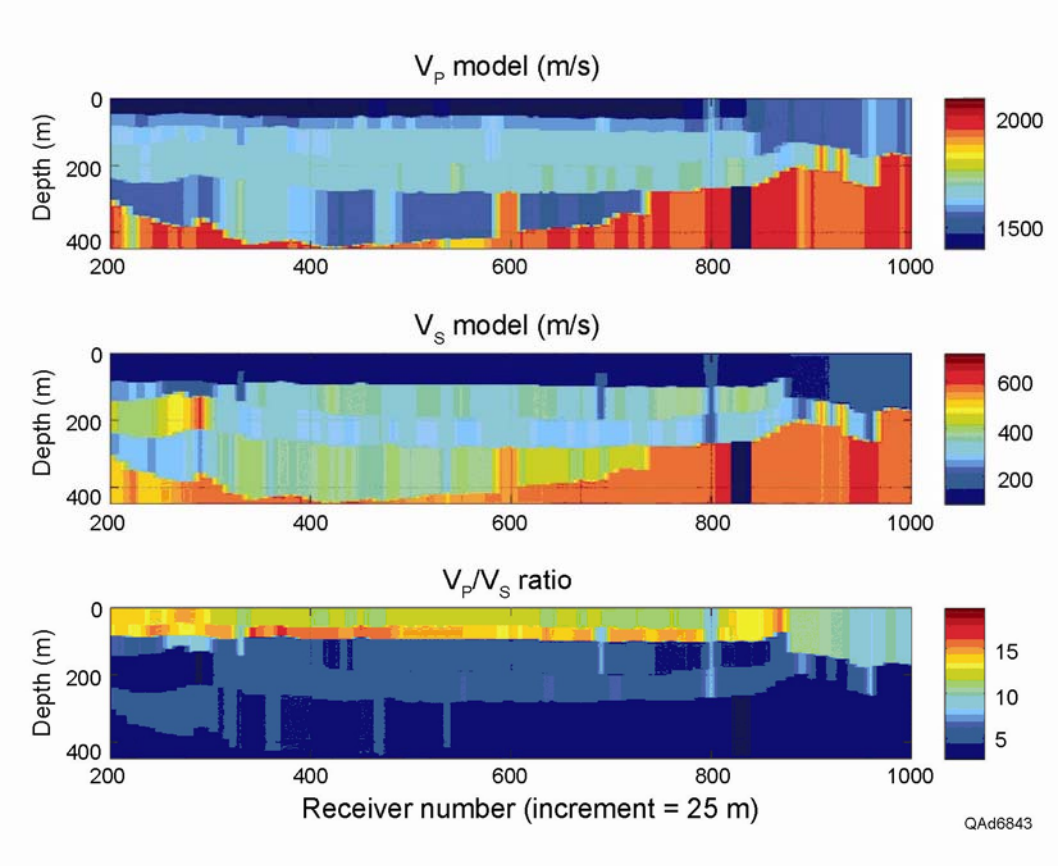

Figure 7.15. Continuous profiles of V_P, V_S, and their ratio along OBC seismic line 264. These profiles were constructed by interpolating between velocity analysis points spaced at intervals of 250 m along the seismic line.

Accuracy of Velocity Estimates

Our raytracing approach to building a sub-seafloor layer model of V_P and V_S velocities produced estimates of interval velocities that were quite accurate. An example of this accuracy is illustrated as Figures 7.16 through 7.18. The simple 2-layer velocity model (water layer + one sub-seafloor layer) used in this analysis is displayed on the left side of Figure 7.16. The center panel shows the raytraced P-P and P-SV reflection events from the base of Layer 1. The actual P-P reflection from the base of Layer 1 is displayed as Figure 7.17 where the data are shown in a reduced-time format in which the interface reflection is positioned at time T = 0 for a zero-offset source station. Each data panel in this figure shows the reflection event after raytrace-calculated time shifts are applied to each source-offset trace. In making these time shifts, the V_P values used for Layer 1 ranged from 1530 m/s to 1580 m/s in velocity steps of 10 m/s, as labeled atop each data panel.

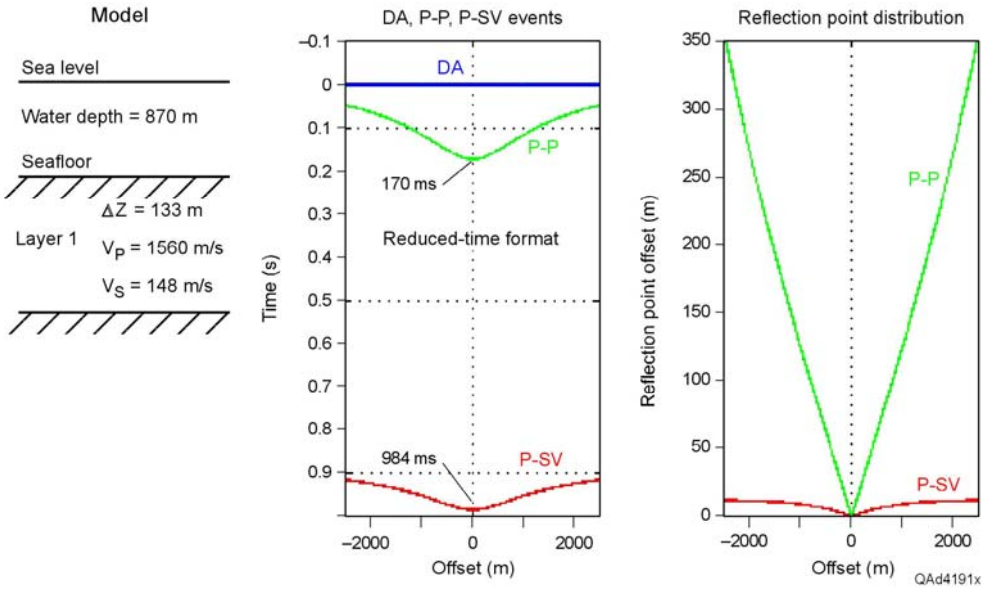

Figure 7.16. Example of the type of velocity-layer analysis used in this project. (left) Earth model of velocity layers. (Center) Raytraced P-P and P-SV reflections from the base of Layer 1. (Right) Raytrace calculations of the lateral distances away from the seafloor receiver that the P-P and P-SV reflections image. Note P-P reflection points extend large distances from the receiver station, but P-SV reflection points cluster near the receiver position, as illustrated by Figure 7.14.

The correct choice for V_P is that value that produces an optimal flattening of the reflection across the full offset range. In this example (Fig. 7.17), optimal flattening occurs when V_P = 1560 m/s. The accuracy of this velocity estimate is ±10 m/s, the velocity step used in the analysis. This estimation error (±10 m/s) is less than 1 percent of the true interval velocity (1560 m/s), verifying our claim that our raytrace-based estimates of interval velocity can be quite accurate. Coupling this velocity value with the 2-way P-P time for the reflection event (170 ms) leads to a thickness for Layer 1 of 133 meters as labeled on Figure 7.16.

The extension of the velocity analysis to the estimation of V_S layer velocity is illustrated on Figure 7.18. If the P-SV reflection observed at 984 ms is depth equivalent to the P-P reflection at 170 ms, as assumed, then the V_S velocity across Layer 1 is

(7.3) V_S = (133 m)/(0.899 s) = 148 m/s,

as indicated on Figure 7.16. The time 0.899 s used in this calculation is the traveltime for the upgoing SV event, which is the difference between the observed P-SV reflection time (0.984 s) and the traveltime of the downgoing illuminating P wave (0.5 X 170 ms). When this V_S velocity is used in the raytracing, the result is an optimally flat P-SV reflection event at a reduced time of 981 ms (Fig. 7.18). The value of V_S determined for Layer 1 should have an estimation error that is approximately the same percentage range as the error bar for V_P (≤1 percent).

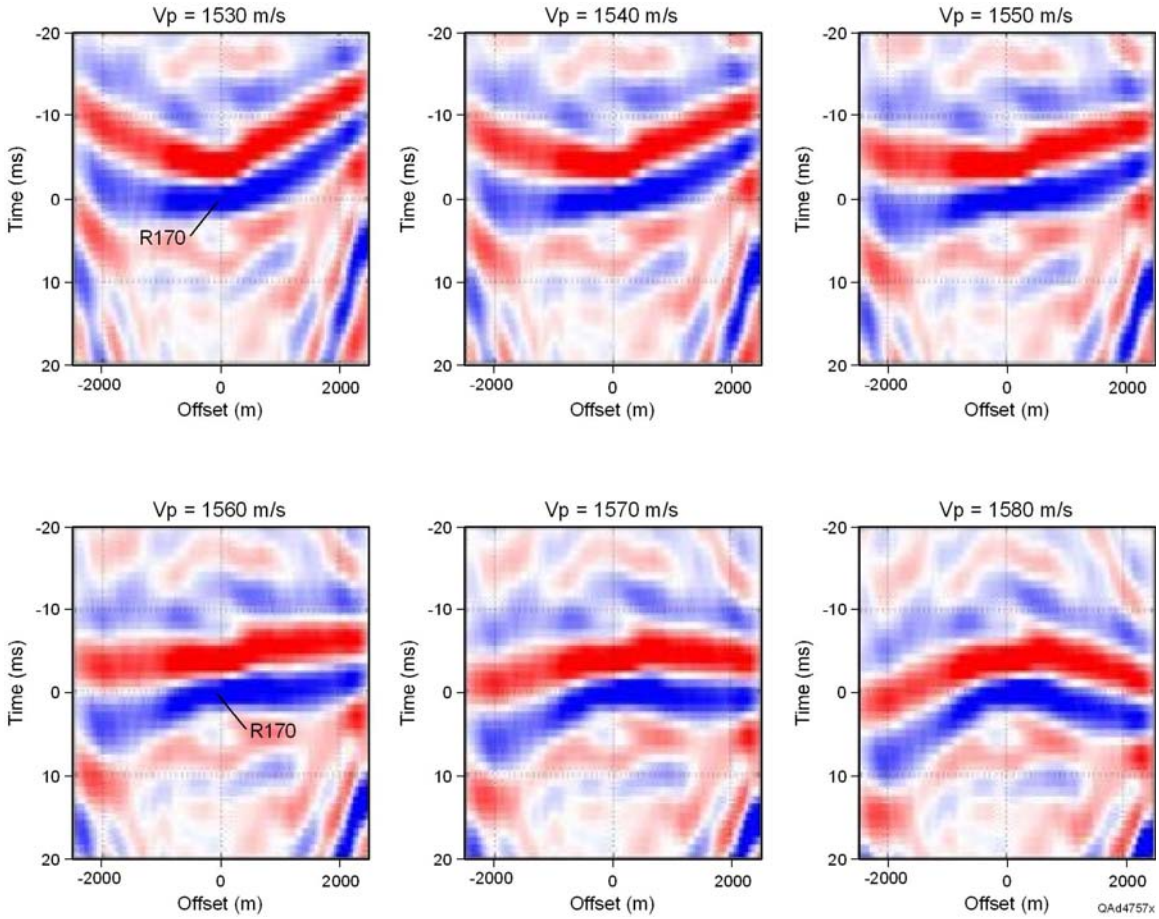

Figure 7.17. Sensitivity of V_P velocities to raytrace analysis. This particular P-P reflection occurred 170 ms below the seafloor, hence the label “R170”.The optimal choice of V_P for Layer 1 is the velocity that creates an optimal flatness of the reflection event (arbitrarily positioned at reduced-time T = 0). Optimal flatness occurs for V_P = 1560 m/s (lower left panel). This velocity analysis technique is sensitive to velocity variations of ±10 m/s, which is an accuracy of less than 1 percent.

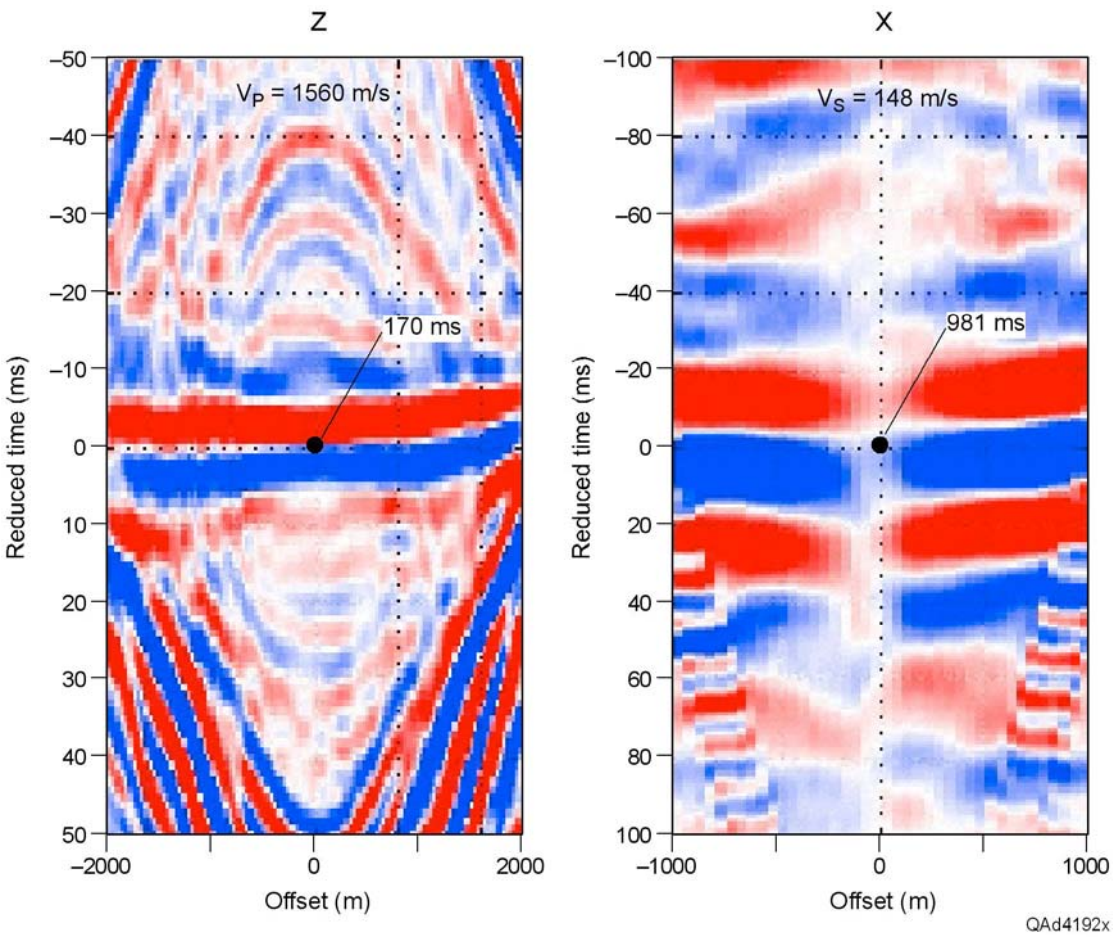

Figure 7.18. Verification that the V_s velocity (148 m/s) assigned to Layer 1 is correct because that velocity produces a flattened P-SV reflection (right panel) from raytraced source stations positioned over an offset range of ±1000 m from the seafloor receiver station. The accuracy of this V_S estimate is less than 1 percent. The left panel shows the depth-equivalent P-P reflection at 170 ms after it is flattened using the V_P value of 1560 m/s determined for Layer 1 in Figure 7.17.

Conclusions

We implemented several new techniques to characterize near-seafloor sediments across our study areas of Green Canyon. This chapter emphasizes the unique interactive raytracing procedure we used to constrain multicomponent P-P and P-SV image interpretations and to create an interval velocity model of near-seafloor strata along each 2D line profile. The raytracing software used in our velocity analyses is unique to our research laboratory and is not commercial code that can be purchased. A considerable amount of sweat equity went into developing and testing this code and then in applying it at approximately 800 receiver stations across our OBC seismic grid during this study. For example, at some receiver stations, the P-P and P-SV stack data were interpreted as many as 8 or 10 times to define depth-equivalent P-P and P-SV events before the raytrace analysis yielded V_P and V_S velocities that satisfied the constraints of the interpreted depth-equivalent reflection events

We found that multicomponent interpretation, combined with raytrace-based velocity analysis, was critical to creating robust velocity models over large areas. Under certain circumstances (P-P events with moderate dip or with reflections from far offsets obscured), the use of P-SV data provided the information needed to construct the V_P velocity model. We believe this use of P-SV data to determine V_P velocities when P-P data cannot be used to provide velocity information is an important research finding developed in this study that should be extended to other uses of multicomponent data beyond our near-seafloor applications.

Future studies should utilize a velocity inversion procedure to create a trace-by-trace, datapoint-by-datapoint velocity estimation of near-seafloor sediments rather than relying on the layered, interpolated-velocity approach we used. The higher spatial resolution of velocity behavior provided by analyzing every common-receiver gather, rather than every tenth or twentieth receiver gather, should also provide additional detail about the internal fabric of the near-seafloor sediments. For this reason, we intend to further automate our raytracing software to allow us to do even closer spaced velocity analyses than what we did in this study. However, our large-scale velocity approach is adequate for this study and can even be considered to be a preferred approach for reconnaissance studies of hydrate concentration. In addition, we see a need to adjust our seismic data-processing strategy to remove water-column multiples from the data so that these multiples are not confused with primary reflections from interfaces near and below the BHSZ boundary.

DOE Gas Hydrate Final Report

Chapter 8

Project Database

Introduction

Constructing a database to describe deep-water, near-seafloor strata across the GOM is challenging because conventional cores and complete well log suites are not acquired by oil and gas companies over the first several hundred meters of stratigraphic section immediately below the mud line. Fortunately, limited well log information starting as shallow as the base of surface casing has been acquired in many GOM wells since operators began using measurement-while-drilling (MWD) logging technology in the early 1990's. Between the base of surface casing (typically about 80 meters below mud line) and the base of the hydrate stability zone, these MWD log data tend to consist of only resistivity profiles and gamma-ray measurements. Thus for deep-water hydrate studies, a database has to be built that allows data other than sonic, porosity-sensitive, and mineralogy-sensitive well logs to be the principal well bore information.

With this observation in mind, this chapter describes how data such as seafloor borings and Autonomous Underwater Vehicle (AUV) technology complement conventional well log data and 4C OBC seismic data and provide critical information needed to correlate sediment/hydrate properties with multicomponent seismic attributes. We amassed the following data as we pursued our project objectives:

1. Seafloor borings. Geomechanical analyses of sub-seafloor samples acquired with seafloor borings provided critical information for this study. Laboratory tests of boring samples defined depth profiles of mineralogy and porosity that we needed for rock physics calculations, identified shear-strength layering that was needed for interpretation and depth registration of P-SV seismic data, and provided evidence of hydrate accumulations at specific depth coordinates. We were able to acquire seafloor boring analyses at Typhoon Field (Block GC237) and at Genesis Field (Block GC205).

2. AUV profiles. Autonomous Underwater Vehicle (AUV) technology has become invaluable for studying deep-water seafloor properties. An AUV system uses inertial guidance to steer an unmanned, self-propelled vehicle along a preselected path at a height of about 50 meters above the seafloor. Navigation accuracy is precise, with deviations from a preprogrammed profile being on the order of 1 or 2 meters over a traverse

of one lease block (4,800 meters [3 miles]). AUV data consist of side-scan sonar, multibeam bathymetry, and chirp-sonar profiles. Chirp-sonar data were important in this study because they provided

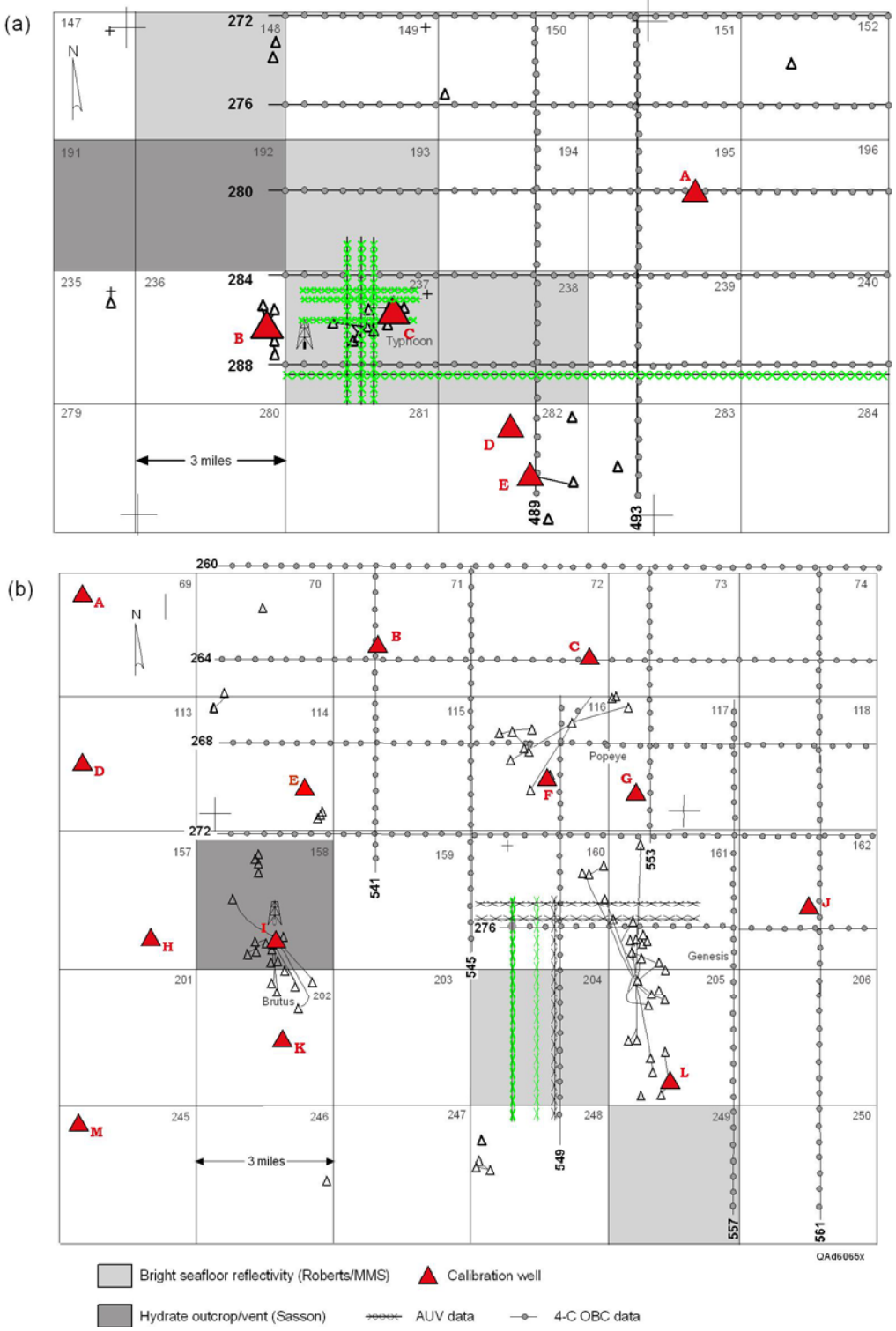

Figure 8.1. Locations of AUV and OBC profiles used in the project. (a) Typhoon Field area. (b) Genesis Field area. AUV data were provided by Dr. Harry Roberts of Louisiana State University.

high-resolution P-P images of seafloor strata to sub-seafloor depths of approximately 50 meters. Approximately 80 km of AUV data were amassed for this study. The locations of these AUV profiles are shown on Figure 8.1.

3. Well log data. Numerous exploration and production wells exist within the boundaries of the 4C OBC seismic survey used in this project. Resistivity and gamma-ray data were acquired across a portion of the hydrate stability zone in several of these wells (Chapter 5). The project team obtained copies of all of these near-seafloor well logs that we could locate within the project boundaries.

4. 4C OBC seismic data. The most critical part of the project database is 4C OBC seismic data. These data were acquired as north-south and east-west 2D profiles spaced at intervals of 2 mi (3.2 km) across the seismic survey area defined on Figure 6.1. We integrated approximately 200 km of 4C OBC seismic data into the project database.

Database Contribution 1: Seafloor Borings

Copies of geotechnical reports were obtained that summarized analyses of seafloor borings across Typhoon Field (Block GC237) and Genesis Field (Block GC205). Laboratory testing of sub-seafloor sediment samples acquired at each location was done by Fugro. The objectives of Fugro's tests were to determine sediment properties needed to design pile foundations for production platforms, not to characterize sub-seafloor stratigraphy, to analyze hydrate concentrations, or to define properties of the near-seafloor seismic propagation medium. However, it was possible to reformat some geotechnical test data to define rock properties needed for this investigation and to gain insights into sub-seafloor layering that helped calibrate P-P and P-SV images. The key information we extracted from these geotechnical reports are described in the remainder of this section of the report.

Porosity Profiles

To do rock physics modeling that allows hydrate concentration to be estimated from seismic velocity attributes, it is necessary to know how the matrix porosity of the host sediment varies with depth below the seafloor. Direct measurements of matrix porosity were not found in any geotechnical reports. However, porosity information across the interval penetrated by seafloor borings was determined from two common geotechnical measurements that were done to describe the load-bearing capability of seafloor sediments: (1) **water content** of the sediment, and (2) **submerged unit weight** of the sediment.

Porosity from Water-Content Data

In geotechnical reports that oil companies generate to improve their understanding of deep-water seafloor geomechanical properties, water content of cored sediment is often measured to aid the engineering design of pile foundations that secure production platforms. Depth-dependent porosity functions that are needed for the rock physics calculations that have to be done in our hydrate study can be calculated from these water-content data. Water content **W** determined in laboratory geotechnical testing is defined as

$$W = \frac{\text{Mass of water in unit volume of sediment}}{\text{Mass of solid matrix in unit volume of sediment}}, \tag{8.1}$$

or

$$W = \frac{\rho_w \Phi S_w}{\rho_g (1-\Phi)}. \tag{8.2}$$

In this expression, Φ is porosity, S_W is water saturation, ρ_W is water density, and ρ_g is grain density of the host sediment. Sediment porosity is then related to **W** by the equation

$$\Phi = \frac{\rho_g W}{\rho_w S_w + \rho_g W}. \tag{8.3}$$

An example of a water-content profile determined by laboratory analysis of seafloor borings acquired in Block GC237 is shown in Figure 8.2a. Using Equation 8.3, this water-content profile is transformed to the porosity profile shown in Figure 8.2b. In this application of Equation 8.3, parameters ρ_W, S_W, and ρ_g were set to 1.025 gm/cm^3, 100%, and 2.55 gm/cm^3 (clay mineralogy), respectively. This porosity profile is critical for defining a depth-dependent porosity function to use in our rock physics calculations of V_P and V_S across the shallowest sub-seafloor strata in Block GC237.

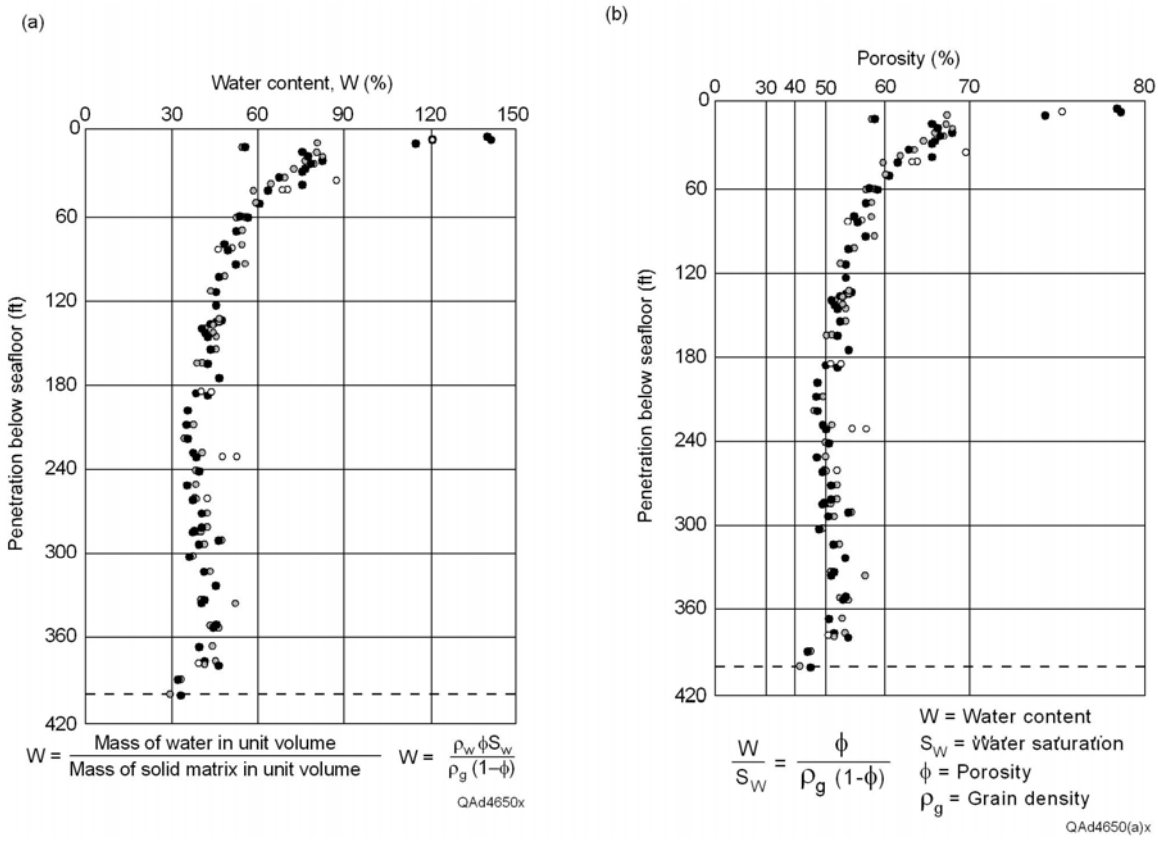

Figure 8.2. (a) Water-content data measured from a seafloor boring in Lease Block GC237. Data were extracted and reformatted from a geotechnical report prepared by Fugro for Chevron, the operator of Typhoon Field in Block GC237 at the time of the geotechnical study. (b) Porosity profile calculated from the water-content data by the project team, assuming S_W = 100%, ρ_w = 1.025 gm/cm^2, and ρ_g = 2.55 gm/cm^3 in Equation 8.3.

Porosity from Measurements of Submerged Unit Weight

A second measurement made in most geotechnical studies of deep-water sediment properties is **submerged unit weight** (**SUW**). This term is defined as

(8.4) $SUW = \delta_{sat} - \delta_w$,

where δ_{sat} is the saturated unit weight of the sediment (in units of lb/ ft^3), and δ_w is the unit weight of the pore fluid (in units of lb/ft^3). This equation can be rewritten as

(8.5) $SUW = 62.4\{[\rho_g(1-\Phi) + \rho_w\Phi] - \rho_w\}$.

In this form, Φ is porosity, ρ_g is grain density of the host sediment (in units of gm/cm^3), ρ_w is pore-fluid density (in units of gm/cm^3), and the constant 62.4

converts lb/ft^3 to gm/cm^3. This equation now allows laboratory measurements of SUW to be translated into measurements of matrix porosity.

An example of a submerged-unit-weight measurement from Genesis Field is shown as Figure 8.3a. The project team converted these SUW data to porosity data in Figure 8.3 b, using values of 2.55 gm/cm^3 and 1.025 gm/cm^3, respectively, for the quantities ρ_g and ρ_w in Equation 8.5. This depth-dependent porosity function has been invaluable for defining porosity conditions to use in rock physics modeling across the shallowest seafloor strata of Block GC205.

The importance of these porosity-defining functions (Figs. 8.2b, 8.3b) cannot be overstated. They are essential to our investigation because:

1. They define porosity across hydrate-bearing intervals where no well log data exist. MWD well logs do not begin until the bit drills out of surface casing that is set to depths of approximately 80 meters below the mudline, and
2. They describe the dynamic behavior of porosity across the subseafloor interval where porosity reduces from ~80 percent to ~45 percent. We must know the depth-dependent dynamics of sediment porosity across this rapid-transition interval in order to apply proper petrophysical constraints to our model and to our data interpretation.

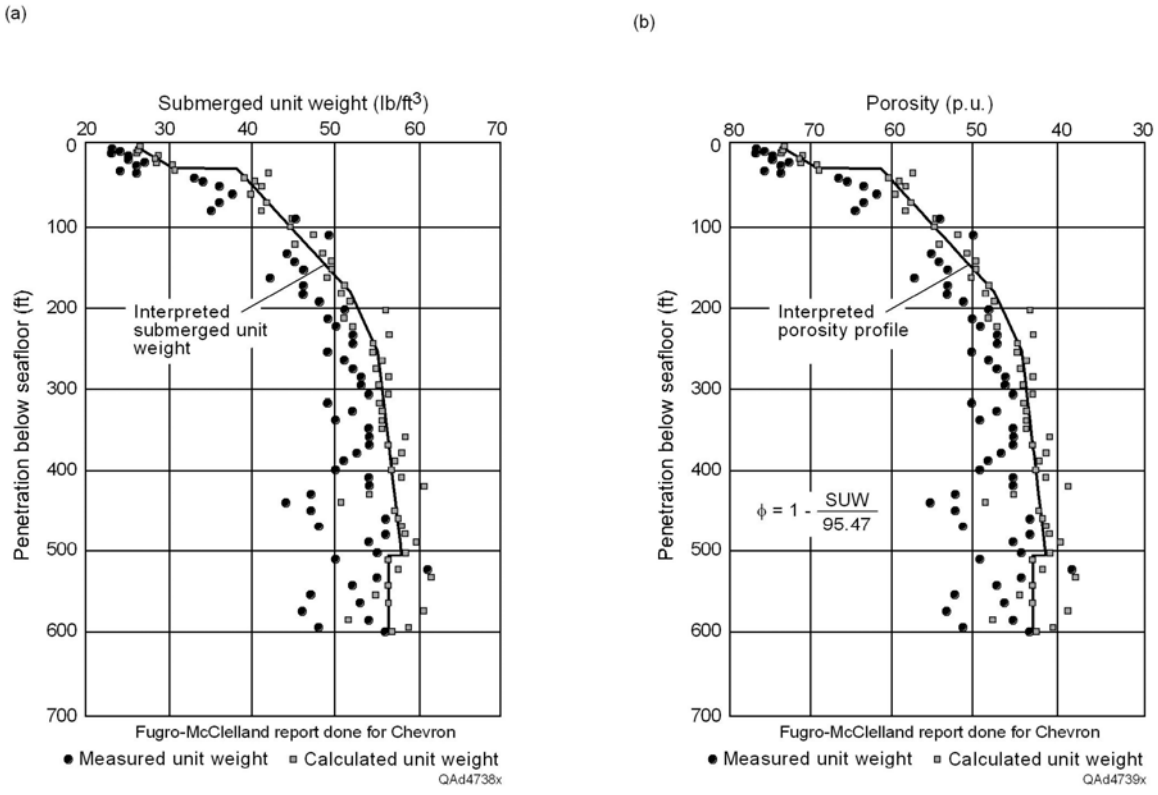

Figure 8.3. (a) Submerged unit weight measurements from Block GC205. (b) Porosity profile derived from these submerged unit weight measurements for this hydrate study.

Shear Modulus

The principal objective of seafloor borings is to determine geomechanical properties of the seafloor where deep-water production platforms will be constructed. Shear strength of deep-water sediment is perhaps the most critical elastic modulus that has to be known before platform design can be finalized. Knowledge of shear moduli is also critical in this hydrate study because interval values of shear modulus provide constraints and calibration points for seismic-derived interval values of S-wave velocity V_S. Examples of shear-strength analyses of near-seafloor strata in Block GC237 and in Block GC205 are displayed as Figure 8.4.

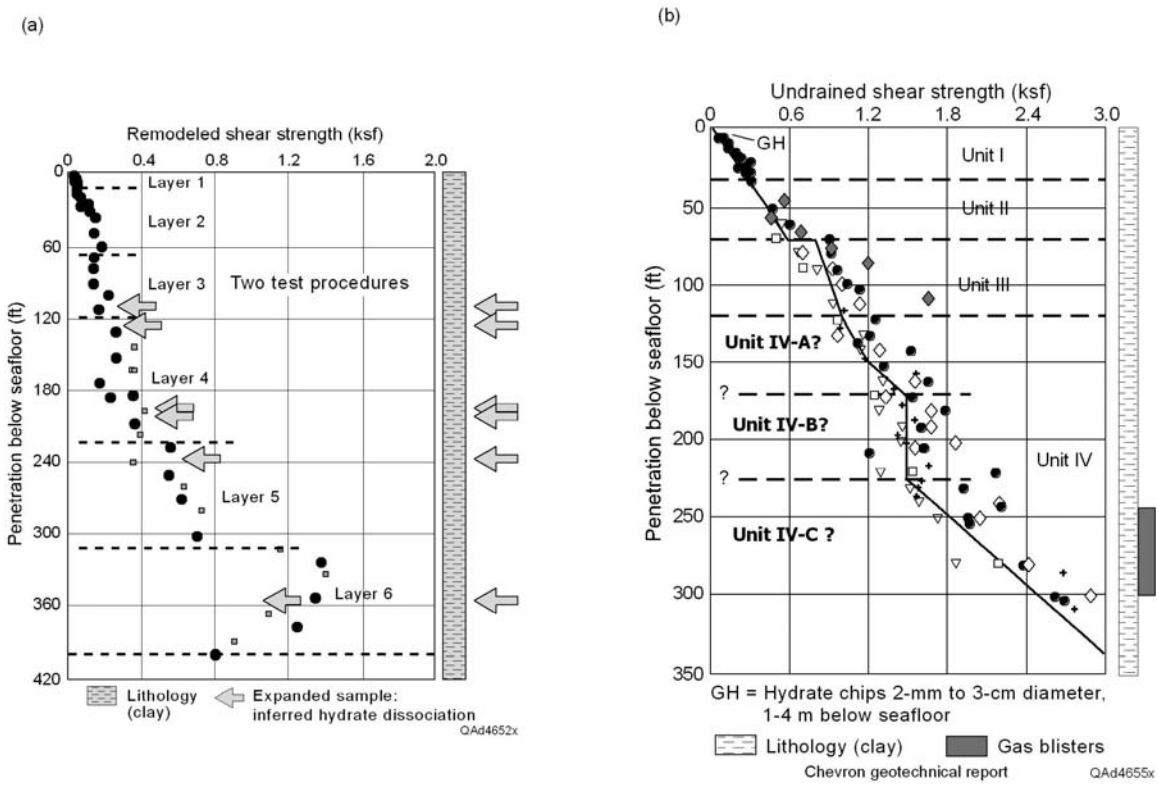

Figure 8.4. Shear-strength profile for (a) Block GC237 and (b) Block GC205. Each type of data-point symbol indicates a different laboratory test procedure. Data were extracted from two Fugro geotechnical reports prepared for Chevron for Typhoon Field (Block GC237) and Genesis Field (Block GC205) and reformatted for this study. The profiles define sub-seafloor lithology and shear-strength-based stratigraphic layering at each study site and document gas-hydrate evidence encountered in seafloor borings [arrows in (a) and the shaded bar in (b)].

These shear-strength profiles are excellent examples of the importance of seafloor borings to this project. Not only do the cored samples allow a depth profile of shear strength to be constructed for calibrating the P-SV seismic

images that we create from 4C OBC seismic data, but they also provide the following critical information about sub-seafloor geology:

1. Lithology profile. In this study, it is essential to know the mineralogy of deep-water sediment across a targeted subsea depth interval in order to use correct grain density and elastic moduli values in the rock physics calculations of P and S velocity attributes for that interval. In both cored intervals shown in Figure 8.4, the mineralogy is clay. Thus we have a valuable lithofacies calibration constraint for the topmost section of the hydrate system underlying both Block GC237 and Block GC205.

2. Hydrate evidence. Cores from seafloor borings are not maintained at in situ temperature and pressure conditions as they are transferred to a surface ship and onshore laboratories or as they are analyzed in various laboratory tests. Thus hydrate in sediment samples obtained from seafloor borings dissociates as the samples are retrieved and tested. It is rare to find hydrate in cores retrieved from seafloor borings that are done strictly for geotechnical purposes. Instead, evidence of hydrate is documented by the presence of expanded, vented sections of core that are created by escaping dissociated hydrate gases. Six of these expanded-sample intervals were observed in the 420-ft core from Block GC237 (arrows in Fig. 8.4a). Collectively, these gas blisters span the sub-seafloor depth interval from 110 feet (33 meters) to the base of the cored interval at 420 feet (128 meters), verifying the presence of a hydrate system. The geotechnical report prepared by Fugro for Chevron' s Genesis Field platform in Block GC205 indicated that gas blisters were observed in core samples from 246 to 300 feet (75 to 91 meters) below the seafloor (black bar in Fig. 8.4b). The report also cited a DOE-funded study (Brooks and Bryant, 1985) in which those researchers observed hydrate chips up to 3 centimeters in diameter over an interval extending from 1 to 4 meters below the seafloor in an earlier study of this lease block. This latter direct evidence of hydrate nodules in Block GC205 is documented by the label **GH** positioned near the seafloor in Figure 8.4b.

3. Stratigraphic layering. Significant variations in the gradient trends of depth profiles of core-measured shear strength imply stratigraphic layering that should be observed with S-wave seismic data. These shear-strength layers may or may not be observed with P-wave seismic data or in depth profiles of bulk moduli. We interpreted and labeled six intervals across the cored interval of Block GC237 (Fig. 8.4a). This stratigraphic layering interpretation will be useful as calibration data for depth registering P-SV images across Block GC237. Five different laboratory techniques, each shown by a different data-point symbol in Figure 8.4b, were used by Fugro to determine shear-strength behavior across Block GC205. The use of different laboratory procedures contributed to the

data scatter exhibited in the plot, but Fugro engineers nevertheless drew an average trend line and interpreted four shear-strength layers that they labeled as Unit I through Unit IV as shown on the figure. Tentatively, we accepted their stratigraphic interpretation and further considered subdividing Unit IV into three sublayers, that are labeled Unit IV-A through IV-C on Figure 8.4b.

Vertical Effective Pressure

Additional core analyses done during geotechnical studies in Blocks GC237 and GC205 were laboratory tests that indicated the magnitudes of overburden pressure experienced by cored samples. Among our research team, we use the term ***effective pressure*** for this pressure quantity. Knowledge of depth profiles of effective pressure is essential for accurate rock physics modeling. Geotechnical engineers refer to data generated by these measurements as ***effective vertical pressure***. Vertical-effective-pressure data measured from cores obtained in Blocks GC237 and GC205 are shown in Figure 8.5. The implication of these data is that a zone of underconsolidation begins about 125 feet (38 m) below the seafloor at both study sites. This depth coincides with the tops of Layer 4 and Unit IV, respectively, defined on the shear-strength profiles (Fig. 8.4a, b). The evidence of underconsolidation is rather definite across Block GC205 (Fig. 8.5b) but is more tenuous at Block GC237 (Fig. 8.5 a). This evidence of

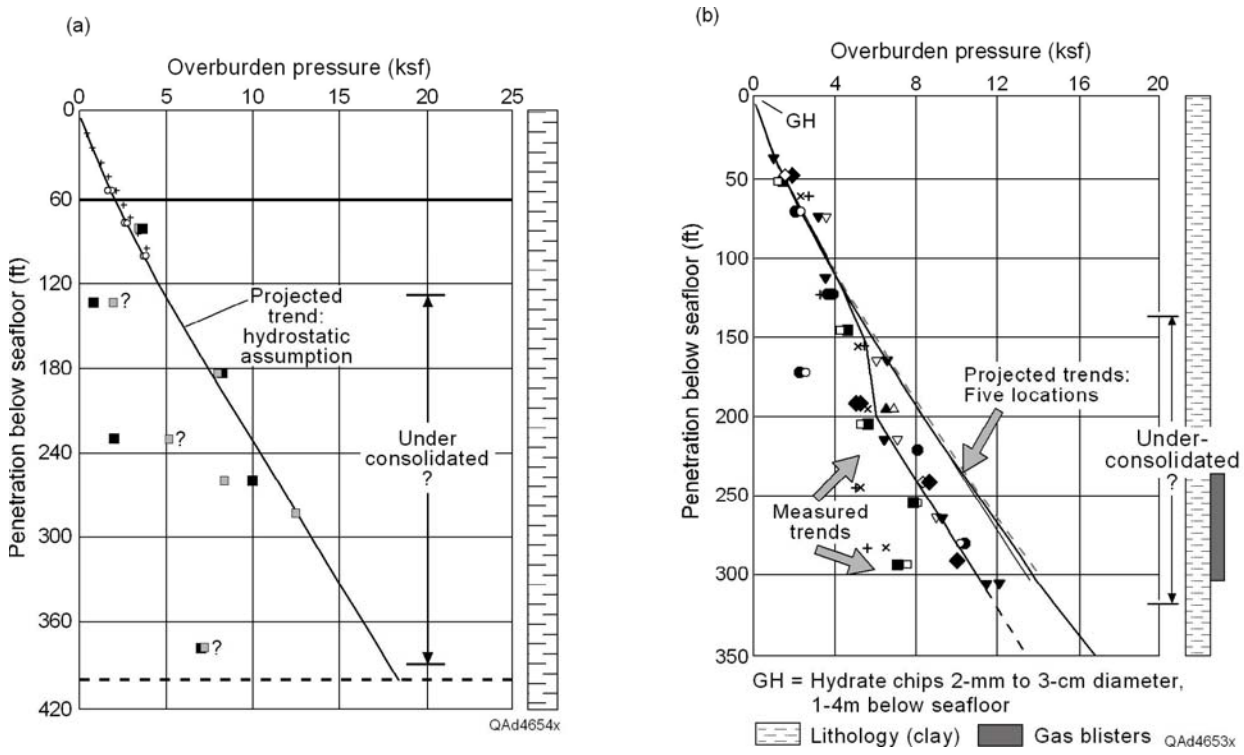

Figure 8.5. Vertical effective pressure data for (a) Block GC237, and (b) Block GC205. At each site, there is evidence of under-compaction starting about 125 feet below the seafloor.

undercompaction will be an important control on depth-dependent porosity and effective-pressure functions used in rock physics calculations across both study areas. It is also important to note that the first appearance of dissociated hydrate gas in the borings taken in Block GC237 (Fig. 8.4a) coincides with the onset of this undercompaction.

Database Contribution 2: AUV Data

The principle of deep-water AUV profiling is illustrated as Figure 8.6. The underwater vehicle is unmanned and self-propelled, not towed by surface ship. An AUV system travels close to the seafloor, usually at a height of about 50 meters above the water-sediment interface, and uses inertial guidance to follow a preprogrammed path with great accuracy. Navigation precision is claimed to be approximately 1 meter over a traverse of 5,000 meters. Three types of data are acquired along an AUV profile: (1) side-scan sonar, (2) multibeam bathymetry, and (3) chirp-sonar reflections. Side-scan sonar and multibeam bathymetry data image seafloor features with great detail but provide no sub-seafloor information. In contrast, chirp-sonar profiling images sub-seafloor strata with chirp pulses having frequency spectra of 2 to 10 kHz. These high-frequency signals image only 50 to 60 meters (approximately) into sub-seafloor strata,

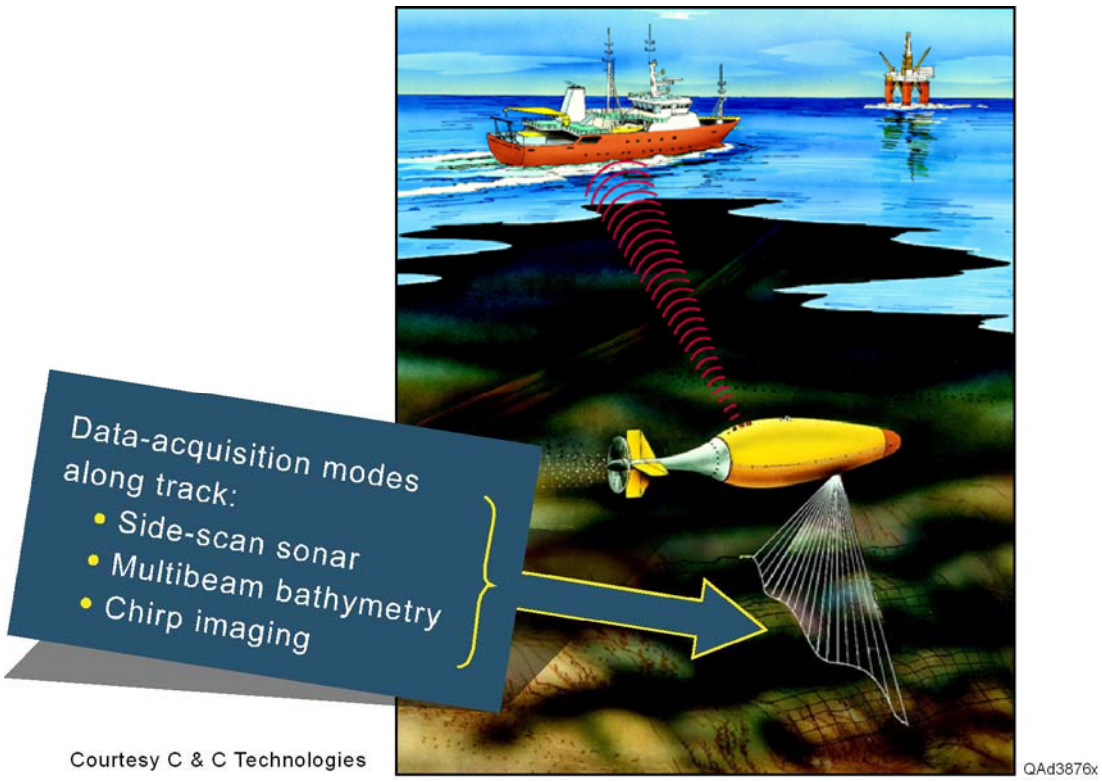

Figure 8.6. An AUV system operating in deep water.

but these images resolve bedding as thin as 1 meter and show faults with vertical throws as small as 1 meter. Chirp-sonar images are created from P-P wavefields and have no P-SV component.

The AUV data used in this study (profiles shown on Figure 8.1) were provided to the project team by Louisiana State University (LSU). Dr. Harry Roberts of LSU acquired the AUV profiles for an LSU/MMS project and allowed our project to have copies of the data. Each AUV profile was positioned to follow the track of an OBC line that was used in this study.

Part of a chirp-sonar profile across Block GC204 is displayed in Figure 8.7. Profile coordinates along this north-south line are defined as northing distances in meters. Software was written by the project team to transform AUV image coordinates to the CDP image coordinates used in OBC seismic profiles so that AUV data and 4C OBC seismic data could be compared in the same coordinate space.

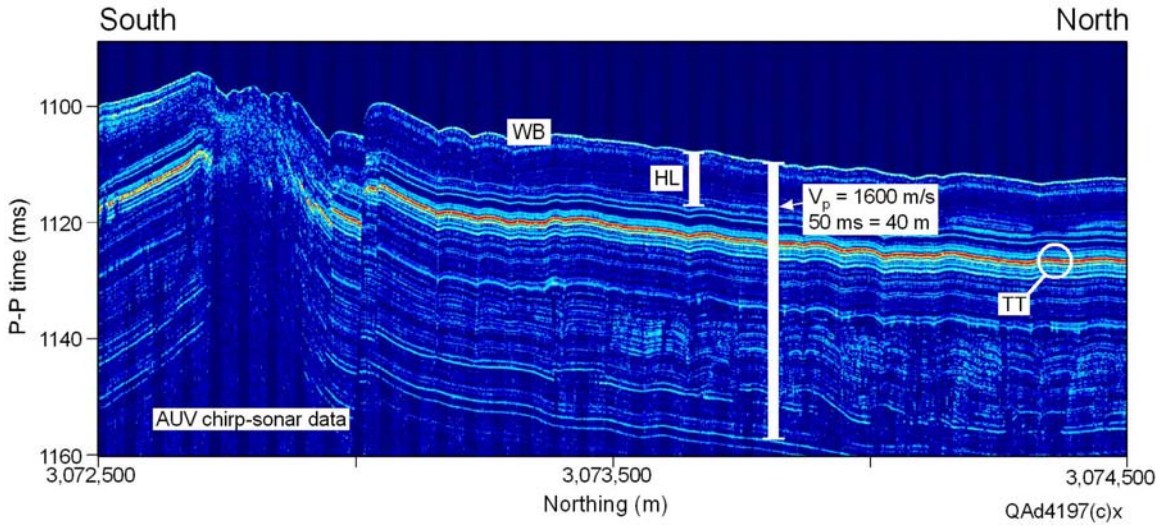

Figure 8.7. AUV chirp-sonar data acquired across a part of Block GC204. **WB** is the water bottom. **HL** is a regional hemipelagic layer ranging in thickness from 6 to 8 meters across this area, and **TT** is a layer of thin heterolithic turbidites that extend across a wide area of the northern shelf of the Gulf of Mexico (Harry Roberts, Louisiana State University, private communication). The base of the P-P image is about 50 ms below the seafloor, which corresponds to a sub-seafloor depth of about 40 meters.

These AUV data are of great value to this hydrate study because they provide a P-P image that resolves stratigraphic and structural features as small as 1 meter within the first 50 meters of seafloor sediment. This resolution is approximately 100 times better than the resolution of conventional P-P seismic data used in oil and gas exploration. Such high-resolution P-P data are essential for demonstrating the high-resolution character of P-SV images that we created from 4C OBC seismic data and for calibrating P-P and P-SV data across the shallowest part of the deep-water hydrate systems.

Database Contribution 3: Well Log Data

The only well log data known to exist across the deep-water, near-seafloor strata where hydrate occurs are resistivity and gamma-ray (GR) curves. Examples of log data acquired across parts of sub-seafloor intervals where pressure and temperature conditions are appropriate for hydrate stability are displayed in Chapter 5.

Logs from approximately 50 wells across the study area were available through the commercial Offshore Well Log (OWL) database. The identification and location of the control wells that we amassed across the study area are defined in Table 8.1 and are shown in map view on Figure 8.1.

Table 8.1: Itemized research database.

Seafloor Borings and Geotechnical Reports

- Typhoon Field: Block GC237, 1 platform location
- Genesis Field: Block GC205, 1 platform location

AUV Data

- 80 km

4C OBC Seismic Data

- 216 km

Well Logs (By lease block and ID number)

Block Well Block Well Block Well

GC112 4024500 GC112 4024501 GC113 5012100
GC113 5012700 GC113 5012701 GC113 5013100
GC114 4025400 GC114 5011700 GC116 5012200
GC117 4033100 GC117 4033500 GC155 4022800
GC155 4022801 GC155 4031100 GC157 4037100
GC158 4026200 GC158 4026201 GC158 4026601
GC158 4026700 GC158 5008770 GC165 4027800
GC165 4028700 GC195 4037600 GC199 4036600
GC200 4020500 GC200 4021600 GC200 4021800
GC200 4021900 GC201 4027500 GC202 4026800
GC202 4026900 GC202 4035100 GC202 5012300
GC205 5007800 GC212 4023200 GC236 4021400
GC237 4023100 GC237 4024100 GC237 4024700
GC243 4027601 GC243 4034000 GC244 4021700
GC245 4032900 GC245 5008900 GC248 0155652
GC248 0155653 GC254 5008300 GC282 4030800
GC282 4033700 GC283 4029900 GC297 4027900
GC326 4022700 GC338 5012600

One point needs to be emphasized about the locations of the well log data specified in Table 8.1. The OWL database has logs from several wells that are drilled from the same platform. For example, the five wells listed as being located in Block GC158 were drilled from one platform (Brutus platform, Fig. 8.1b). Although the bottom-hole locations of these wells are separated by several kilometers, those parts of the wells that penetrate to the base of the hydrate stability zone are vertical and directly beneath the production platform. Consequently, all of the holes drilled from a single platform are laterally separated by only a few meters across the shallow, hydrate-stability interval that we wish to study. Thus, logs from several wells drilled from one platform provide little more information about the hydrate interval than do the logs from a single well. It is somewhat misleading to list the number of logged wells that were amassed without adding this qualification about the redundant nature of some of the log data. It is correct to say that we amassed a reasonable catalog of modern

resistivity and gamma-ray logs from several production platforms across our study area. The map in Figure 8.1 is probably a better indication of the well log coverage of our current database than is the tabular list of wells.

The sub-seafloor depth of the base of the hydrate-stability zone is calculated from the model proposed by Milkov and Sassen (2001), previously illustrated as Figure 5.5. These researchers used GOM seafloor temperature data and GOM sub-seafloor temperature gradient data to reach conclusions about the thickness of a hydrate stability zone for various water depths across the Green Canyon area. The key result of their geothermal modeling is shown in Figure 5.5. Hydrate-stability curves were determined for three specific gases, 100% CH_4, 95.9% CH_4, and 90.4% CH_4, on the basis of geochemical analyses of hydrate gases venting into the water column in Block GC185, the famous Bush Hill site that has been studied by several researchers. Some researchers question the validity of this Milkov/Sassen model for great water depths (various private communications), but most hydrate investigators accept its predictions for water depths in the range of 500 to 1000 meters where our study is concentrated. For the time being, the hydrate stability thicknesses predicted by Milkov and Sassen (2001) will be used as a guideline in our study.

Database Contribution 4: 4C OBC Seismic Data

This research study is structured around an analysis of 4C OBC seismic data that traverse known deep-water gas hydrate systems. The positions of the 4C OBC profiles that were used in this study are illustrated in Figure 8.1.

An important point about the 4C OBC data used in this study is their excellent signal-to-noise ratio. The data often look more like synthetic model data than actual seismic field data (Fig. 2.1). This exceptional data quality was encouraging throughout the study.

Conclusions

Two terms describe the database used in this study: **diverse** and **immense**. Data diversity ranged from lab-based geotechnical measurements made on seafloor borings, to conventional well log data, to seismic data acquired with both AUV and OBC technologies. These data described rock, fluid, and hydrate properties over a wide range of scales and presented numerous challenges in the research area of **data scaling**.

The immensity of the database is largely due to the 200-plus km of 4C OBC seismic data that had to be analyzed. These OBC data involved approximately 16 million input data traces that required 0.6 terabytes of rapid-access storage. Our data-processing for these 4C data required that we build common-receiver gathers of upgoing and downgoing P-P and P-SV wavefields at 8,164 receiver stations, and that we resample 2-ms data to 1-ms data. These data-processing steps raised the data storage requirements to almost 3 terabytes.

DOE Gas Hydrate Final Report

Chapter 9

Velocity and Resistivity Properties of Sediment Due to Normal Compaction

Introduction

In order to recognize hydrate-dependent effects in depth profiles of V_P and V_S velocities and formation resistivity across near-seafloor strata, it is necessary to first establish baseline curves that define how these seafloor sediment properties vary with depth due only to the effects of normal compaction. Positive deviations from these baseline trends at depths above the base of the hydrate stability zone are good indications of the presence of hydrate, because hydrate causes increases in seismic propagation velocity and formation resistivity. This chapter describes how we calculated normal-compaction baseline curves for formation resistivity and for V_P and V_S velocities across our deep-water study area in the Green Canyon area of the Gulf of Mexico.

In our analysis of V_P and V_S velocities, we modeled the elastic properties of the host sediments of deep-water hydrates using the approach proposed by Dvorkin and Nur (1996). However, we made the distinction that the elastic properties of sediments at critical porosity (Nur and others, 1998) should be described by Walton's smooth model (Walton, 1987) rather than by the Hertz-Mindlin model (Mindlin, 1949; Mavko and others, 1998) that Dvorkin and Nur used. We preferred Walton's theory for our analysis because it allows grains to rotate and slip relative to each other, which seems to be a more appropriate assumption for unconsolidated sediments at the low effective pressures that exist near deep-water seafloors. Thus a key assumption in our velocity modeling was that at critical porosity, the effective elastic moduli of the dry-mineral frame of near-seafloor sediments should be calculated using Walton's smooth contact model for elastic particles (Walton, 1987).

In our analysis of formation resistivity, we were attracted to the analysis done by Wimpe (2000) who showed that the resistivity of a mixture of arbitrary volume fractions of mineral grains and brine converges to the resistivity specified by the Hashin-Shtrikman Lower Bound when the porosity of the mixture approaches critical porosity. Critical-porosity conditions were what we observed in the deep-water, near-seafloor sediments spanning the hydrate stability zone across our study sites. We also concluded that any calculation of formation resistivity had to account for the presence of high clay content in the sediments that host hydrates because seafloor borings local to our study area showed clay minerals were more than 90-percent of the sediment volume. The clay-dependent form of the Archie Equation that we elected to use to describe formation resistivity is discussed in Chapter 6 (Eqs. 6.1 through 6.3).

Porosity Profile

One of the most important sediment properties that affect seismic propagation velocity and formation resistivity is porosity. We amassed porosity information for near-seafloor strata across our study area by examining geotechnical reports that analyzed seafloor borings where offshore operators installed production facilities. The methods that we used to convert geotechnical measurements of **water content** and **submerged unit weight** into porosity data are described in Chapter 8. Figure 9.1 presents the porosity information we calculated from Fugro's laboratory measurements of these two geotechnical parameters at our two study sites. The curve superimposed on the data is a non-linear, least-squares fit of the form:

(9.1) $\Phi(z) = \Phi_0 \exp[-k \log(z)]$.

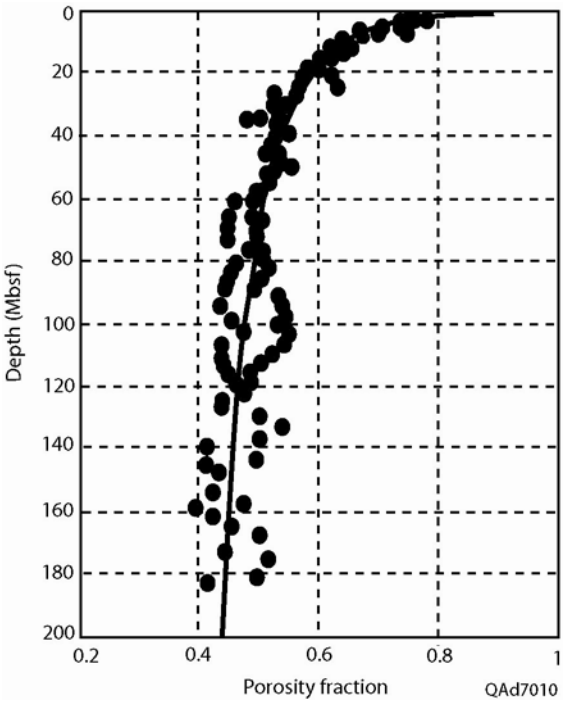

Figure 9.1. Porosity fraction of sediments calculated from geotechnical measurements of water content and submerged unit weight made on seafloor core samples by Fugro across a significant interval of the hydrate stability zone. Refer to Figures 8.2 and 8.3 for the calculation procedures. The data were compiled for Chevron at Genesis and Typhoon Fields, Green Canyon, Gulf of Mexico. The superimposed curve is our non-linear, least-squares fit to Fugro's laboratory measurements of porosity. Over the depth range shown here, the porosity is at, or near, critical porosity.

In Equation 9.1, $\boldsymbol{\Phi}$ represents the porosity of seafloor sediments as a function of depth, and **z** is depth in meters below the seafloor. The empirical parameters are $\boldsymbol{\Phi_0}$, the porosity of sediments 1 m below the seafloor, and ***k***, the decay rate of porosity with the logarithm of depth. For this data set, we used a

non-linear, least-squares method to obtain a value of 0.887 for Φ_0 and a value of 0.1343 for the decay constant *k*. The relations for porosity variation with depth due to compaction of seafloor sediments published in previous studies (Rubey and Hubbert, 1959; Allen and Allen, 1990; Ramm and Bjoerlykke, 1994) do not include a logarithmic dependence on depth as does our Equation 9.1. However, none of the empirical relations proposed by earlier researchers fit the geotechnical-data measurements that Fugro collected across the deep-water, near-seafloor strata of our study area. Evidently, the compaction regime of near-seafloor sediments within our study area has a more dynamic variation with depth than do the compaction regimes of deeper intervals where these previously published models appear to be reliable. We thus have developed a unique empirical equation that has not yet appeared in the literature that is a better description of the depth-dependency of porosity across the first 200 m of deep-water, near-seafloor strata found in the northern Gulf of Mexico than what can be described using popular published models. The key observation to make about the porosity values exhibited on Figure 9.1 is that near-seafloor sediments are at, or near, **critical porosity** across much of the hydrate stability zone.

Coordination Number

Our rock physics models for elastic moduli (Chapter 3) involve a parameter **C** (coordination number), that defines the average number of grains that are in physical contact with another grain at any sub-seafloor depth. This coordination number increases with depth because of increasing effective pressure and decreasing porosity. Murphy (1982) derived an empirical relation between coordination number C and the porosity (Φ) of sediments as follows:

$$C = 20 - 34\Phi + 14\Phi^2. \quad (9.2)$$

This relationship is assumed to be the upper bound for the coordination number. When effective pressure is low, as it is near the seafloor, the average number of effective grain contacts will not increase significantly when porosity decreases. Therefore, in our study we chose to relate the coordination number to effective pressure (or depth) in a linear fashion rather than to use the Murphy (1982) porosity relationship (Eq. 9.2) that applies to regimes that have appreciable effective pressure. In our model, the coordination number is 1 at the seafloor and increases linearly with depth so that at 600 m below the seafloor, it has a value of 6.7.

Elastic and Fluid Parameters

For porosity values smaller than critical porosity, the elastic properties of the dry-mineral frame were estimated using the modified Hashin-Shtrikman Lower Bound (Hashin and Shtrikman, 1963; Dvorkin and Nur, 1996). For porosity values larger than critical porosity, we used a modified Hashin-Shtrikman Upper

Bound (Hashin and Shtrikman, 1963) to derive the elastic properties of the dry-mineral frame of granular materials (Dvorkin and others, 1999). Gassmann's theory (1951) was then used to derive the density and the bulk and shear moduli of the sediments when they were saturated with various fluids.

We assumed that the grain density and elastic moduli for the mineral grains across our study area were those corresponding to Gulf of Mexico clays (Mavko and others, 1998) because geotechnical borings indicate clays are the dominant minerals (Figures 8.4 and 8.5). The density and bulk modulus of the saturating brine were derived as a function of pressure and temperature using empirical relations published by Batzle and Wang (1992). The effective pressure as a function of depth was derived assuming hydrostatic pore pressure.

Normal Compaction and P-Wave Velocity

Using the models and assumptions discussed in the preceding sections, we derived baseline curves that described the behaviors of V_P and V_S velocities in brine-saturated sediments as a function of depth. These baseline curves were assumed to be the normal compaction curves for these sediment properties across our study area. Presented as the left column of graphs on Figure 9.3 are seismic P-wave interval velocities determined from raytrace-based velocity analysis of 4C OBC common-receiver gathers (Chapter 7) at three well locations. Superimposed on these seismic layer velocities is the computed baseline for P-wave velocity behavior as a function of sub-seafloor depth for sediments saturated with brine. Intervals having P-wave velocities greater than the baseline trend exist within the hydrate stability zone at all three well locations. These high-velocity intervals are assumed to be hydrate-bearing. In each of the examples on Figure 9.3, there is an interval with P-wave velocity less than the baseline velocity positioned immediately below the higher-velocity layers. This reduced-velocity layer is interpreted to be free gas below the hydrate stability zone.

Normal Compaction and S-Wave Velocity

V_S interval velocities calculated from the same 4C OBC trace gathers as the P-P interval velocities are displayed as the right column of graphs on Figure 9.3. Because V_S velocity does not react to the presence of low saturations of gas; whereas V_P velocity does, these V_S velocity curves do not always show a

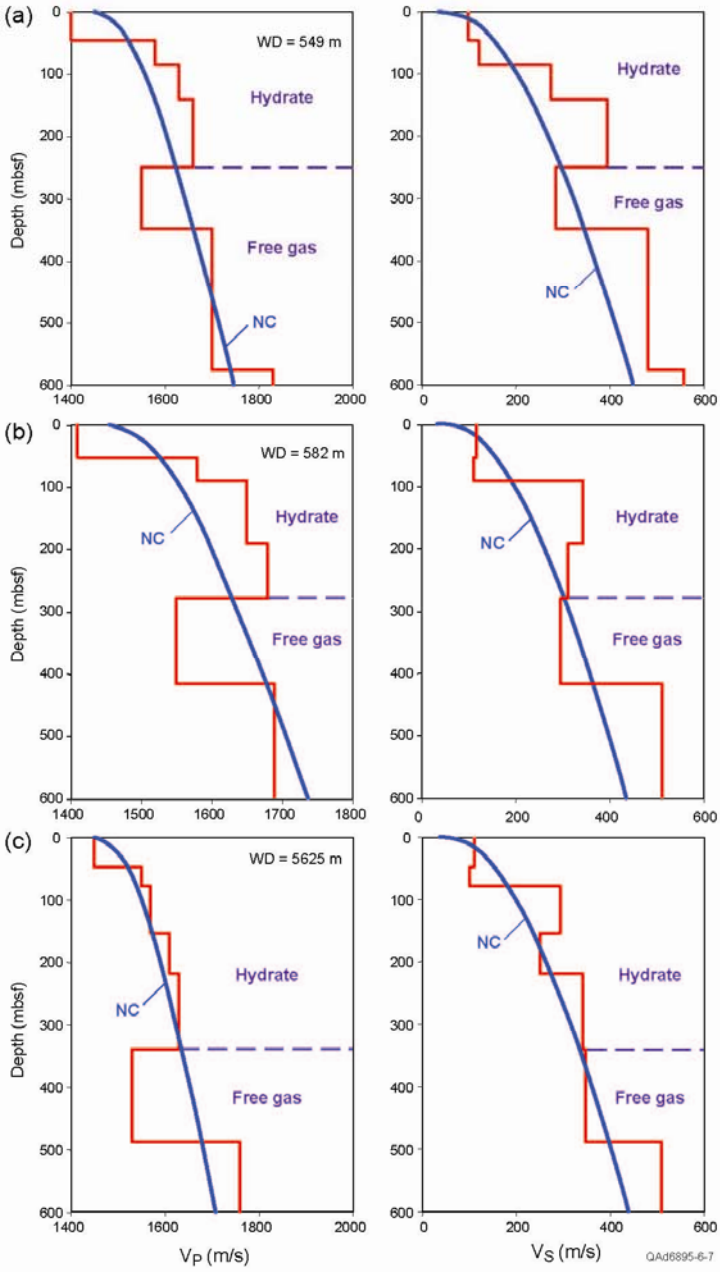

Figure 9.2. Sub-seafloor V_P interval velocities (left) and V_S interval velocities (right) calculated by raytrace analysis of common-receiver-gather data at three calibration wells. **WD** is water depth. Our raytrace-based procedure of velocity analysis is described in Chapter 7. Superimposed on these layer velocities are baseline velocity curves that define the depth-dependent variation in P-wave and S-wave velocity caused by normal compaction. In calculating the V_P and V_S baselines for hydrate-free sediment, we assumed that the sediments were saturated with brine and were composed of 95-percent clay minerals and 5-percent quartz.

reduced-velocity layer at the base of the hydrate stability zone as do the V_P curves on the left side of the figure. However, V_S velocity exceeds the hydrate-free baseline V_S behavior in most of the layers within the hydrate stability zone, adding credibility to our assumption that these layers are hydrate-bearing sediments.

Our velocity analyses at the calibration wells distributed across our study area showed that V_S velocity almost always exceeded hydrate-free V_S behavior in layers where V_P velocity also exceeded hydrate-free V_P velocity behavior. However, layer-to-layer changes in V_S velocities did not always track changes in V_P velocity. That is, sometimes V_S velocity might decrease (increase) in a layer where V_P increased (decreased). In some layers where V_P exceeded the normal-compaction baseline, V_S might even be less than the S-wave velocity baseline.

Some of these differences in V_S and V_P velocity trends are assumed to be caused by the fact that layer-to-layer variations in shear modulus (which dictates V_S behavior) are not the same magnitudes or directions (either increasing or decreasing) as are the layer-to-layer variations in bulk modulus (which dominates V_P velocity). Probably the most important thing that needs to be noted is that when the hydrate saturation is less than 30-percent, which was the situation at almost all analysis points along the OBC profiles that we analyzed, there is a quasi-linear relationship between V_P velocity and hydrate concentration (Fig. 3.5; Model A), but there is an "almost flat" response of V_S velocity to variations in hydrate fraction (Fig. 3.6; Model A). Thus we do not expect V_S velocity to react to hydrate concentration in a consistent, linear fashion as does V_P velocity. The different reactions of P-wave and S-wave velocities to hydrate concentration are well exhibited on Figure 9.2.

Resistivity

To identify hydrate presence and to estimate hydrate concentration in marine sediments from electrical resistivity measurements, we had to build a baseline curve that defined the resistivity of 100-percent brine-saturated sediments as a function of normal compaction with depth below the seafloor. We derived the electrical resistivity of marine sediments fully saturated with brine using the clay-term form of the Archie Equation (Eq. 6.1) with the constraint that $S_w = 1$. The critical parameters in the Archie Equation (porosity $\boldsymbol{\Phi}$, brine resistivity $\boldsymbol{R_w}$, cementation exponent $\boldsymbol{m}$, and internal geometric parameter $\boldsymbol{a}$) all vary with depth. The principles we used to define the depth variations of these parameters are summarized in the following sections.

Porosity

As previously stated, porosity information for near-seafloor sediments was available from geotechnical measurements of submerged unit weight (Fig. 8.3) and water content (Figure 8.2). Figure 9.1 presents the porosity values computed from these geotechnical data as a function of depth below the seafloor. Our new

functional form for porosity variation with depth developed from this data trend (Equation 9.1) was used for the resistivity analysis of hydrate systems across our study area.

Cementation Exponent, m

The cementation exponent ***m*** increases with depth because of increasing consolidation and compaction. Even though porosity decreases significantly within the first few tens of meters of sub-seafloor sediment, the depth variation of the cementation exponent is not a logarithmic behavior as is the depth dependence of porosity. A study by Wempe (2000) shows that for sediments close to the suspension regime (sediments that have low effective pressure and porosities greater than 40-percent), the variation in electrical resistivity when porosity decreases from 80-percent to 40-percent is quite small. The electrical resistivity of such sediments can be described by the Hashin-Shtrikman Lower Bound (1962). In our analysis, we assumed the cementation exponent increased with depth and normal effective pressure, but that its increase is a linear function of depth as opposed to the observed non-linear variation that porosity exhibits with depth (Fig. 9.1). The approximate linear depth-dependence behavior of the cementation exponent was determined at each calibration well. From these analyses, we determined the cementation exponent increased from a value of 1 at the seafloor (by calibration with Hashin-Shtrikman Lower Bound) to a value of approximately 1.7 at a depth of 600 mbsf.

Internal Geometric Parameter, a

The internal geometric parameter ***a*** used in the Archie Equation also increases with depth. For this parameter we used the following equation,

$$a = \frac{3-\phi}{2} \quad , \tag{9.3}$$

which shows the dependence of the internal geometric parameter on porosity. This relationship applies when sediment porosity is close to the suspension regime defined by the Hashin-Shtrikman Lower Bound. The porosity value used to calculate **a** is defined by Equation 9.1.

Brine Resistivity, R_W

The resistivity of brine ($\mathbf{R_W}$) decreases with depth because temperature increases, as dictated by the normal geothermal gradient. Salinity strongly impacts brine resistivity, and geotechnical data often provide important information on brine salinity. Based on notes made by a MWD logging engineer who acquired near-seafloor logs in one of the calibration wells used in our study, a salinity of 45,000 ppm was assigned to the pore-filling brine across our study

area. Using this salinity value and the assumption of a normal geothermal gradient of X^0 per 100 meters, we calculated the variation of brine resistivity with depth.

Saturation Exponent, n

The saturation exponent ***n*** does not enter into the computation of the normal compaction baseline of brine-saturated sediments because S_w=1.

Resistivity Behavior Caused by Normal Compaction

Figure 9.3 shows electrical resistivity logs from three wells in the Green Canyon area of the Gulf of Mexico. These resistivity data were acquired while drilling. On each panel we superimpose the normal-compaction baseline curve for the resistivity of sediments that are fully saturated with brine which we computed using the form of the Archie Equation defined by Equation 6.1 and the depth variations of the Archie-Equation parameters described above.

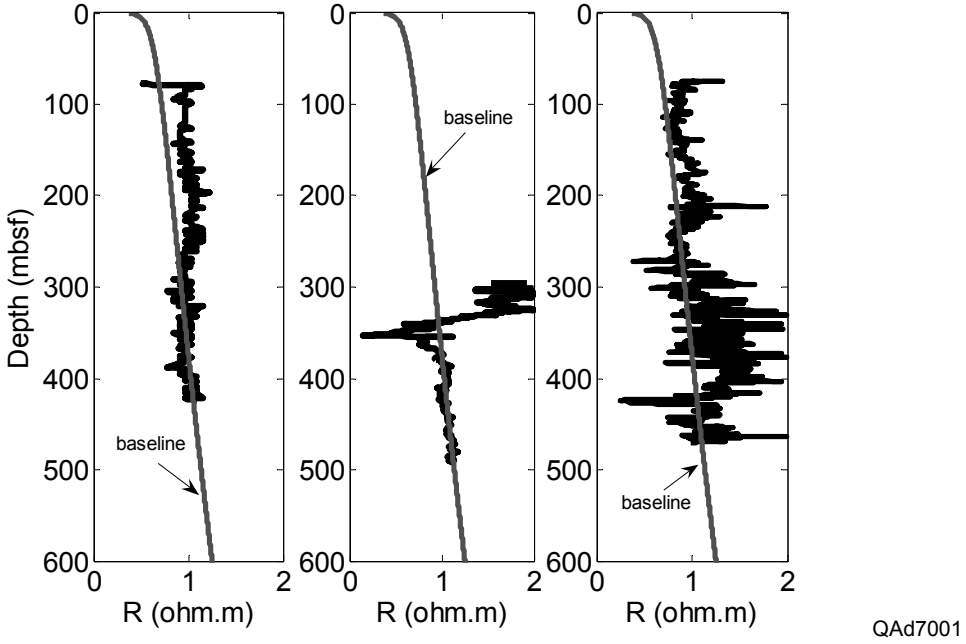

Figure 9.3. Resistivity (R) log data for three calibration wells across our study area of the Green Canyon, GOM. The red curve on the resistivity logs represents the baseline (normal compaction) resistivity behavior as a function of depth for sediments saturated with brine. The cementation exponent m varies from 1 at the seafloor to 1.7 at 600 m below the seafloor. The geometrical factor *a* increases with decreasing porosity (Equation 9.3).

From this figure we observe that our normal-compaction baseline resistivity curve is a good description of the background resistivity trend in these calibration

wells. However, this baseline can vary from location to location due to natural variability of sediment porosity, water salinity, and well bore temperature. A careful analysis must be performed at each calibration well to establish the appropriate normal-compaction baseline for the electrical resistivity of brine-saturated sediments that should be used local to that well location.

Conclusions

To illustrate hydrate concentrations in seafloor sediments, a fundamental calculation that needs to be done is to determine how resistivity, P-wave velocity, and S-wave velocity increase with depth below the seafloor as a result of the normal compaction of sediments. Once the normal-compaction baseline trends for these variables are known, a positive deviation of any one of these hydrate-sensitive variables from its baseline trend is one of the more reliable indications that hydrate is present. The magnitude of the deviation can be used to estimate hydrate concentration.

In order to calculate normal-compaction baseline trends for resistivity and velocity, it is essential to know how porosity varies with depth below the seafloor. Laboratory measurements made on seafloor core samples provided geotechnical data that we were able to convert into sub-seafloor depth profiles of sediment porosity, starting immediately at the seafloor. These lab-generated data showed that sediment porosity was at, or near, critical porosity across much of the hydrate stability interval. With this knowledge, we established the proper theory and physics that were needed to define the behavior of resistivity and elastic moduli as a function of normal compaction (burial depth below the seafloor).

The principle theory that describes the elastic and resistivity properties of mixtures of mineral grains and brine that have porosities near critical porosity is the Hashin-Shtrikman Lower Bound. The constraints of the Hashin-Shtrikman Lower Bound guided our development of the normal-compaction baseline curves that describe how resistivity, V_P velocity, and V_S velocity increase as the result of normal compaction of seafloor sediments. When our calculations of normal-compaction baselines for resistivity, V_P velocity, and V_S velocity were compared to real data examples of these hydrate-sensitive parameters, the baselines were excellent descriptions of the general trend of each variable when the sediments were brine saturated (hydrate free). We concluded that positive deviations of resistivity, V_P velocity, and V_S velocity away from their respective baseline trends at depths above the base of the hydrate stability zone were valid indications that hydrate was present. This assumption is fundamental to the estimates of hydrate concentrations that we present in this report.

A further assumption is that within the hydrate stability zone, the magnitudes of the positive deviations of resistivity and velocity away from their baseline trends are indications of the magnitude of hydrate concentration. This latter assumption forms the basis of our joint inversion methodology that is discussed in Chapter 10.

DOE Gas Hydrate Final Report

Chapter 10

Joint Inversion of Resistivity and Velocity

Introduction

The relation between hydrate concentration and resistivity of strata containing hydrates is **non-unique** and **uncertain**. Similarly, any relationship between hydrate concentration and seismic propagation velocity in sediment containing hydrate is also uncertain and non-unique. Sources of these uncertainties are related to data-measurement errors, inability to define accurate mineral fractions that exist in the sediments that host hydrate, poor understanding of whether hydrate is distributed among sediment grains as a disseminated material or as a layered material (either vertical or horizontal layering), unexpected spatial variations in porosity, and inadequate knowledge of numerous other physical conditions and processes associated with hydrate systems.

By combining different types of hydrate-dependent geophysical information, particularly velocity estimates and formation-resistivity measurements, predictions of hydrate concentration can be constrained, and the uncertainty of predictions can be reduced. To take advantage of this principle, we developed a method for predicting hydrate concentration that is based on stochastic simulations and two rock-physics theories. One theory relates hydrate concentration to formation resistivity (**R**) and is explained in Chapters 4 and 6. The second theory relates seismic $\mathbf{V_P}$ and $\mathbf{V_S}$ velocities to hydrate concentration and is discussed in Chapter 3. In applying our joint-inversion methodology, we account for the uncertainty of every parameter that enters into the calculation of hydrate concentration in our analytical-model formulations of these two theories.

Theory

Our approach to predicting hydrate concentration is based on the concept that all of the parameters used in our rock physics elastic modeling (velocity estimation) and in our applications of the Archie Equation (resistivity estimation) are uncertain. Probability theory enables us to quantify this uncertainty and to combine various types of information, particularly velocity data and resistivity data, into a joint inversion for hydrate concentration. The attraction of a joint inversion approach to estimating hydrate concentration is that joint inversion reduces the uncertainty of the estimation that is made, as illustrated by Figure 10.1.

To implement a joint-inversion technique, each parameter in our rock-physics elastic modeling and in our formulation of the Archie Equation is expressed as a **probability density function** (**PDF**). The PDFs used in this joint

inversion are either Gaussian distributions or uniform distributions. **Gaussian distributions** are used when the expected value for the model parameter is known. The **mean** of the Gaussian function is the **expected value** of the parameter; the **standard deviation** of the function defines the **uncertainty** associated with this expected parameter value. Gaussian PDFs are used in numerous research fields to express measurement uncertainty in data. In our methodology, we use Gaussian PDFs to describe data provided by porosity logs, resistivity logs, gamma-ray logs, sonic and dipole-sonic logs, and seismic-based velocities.

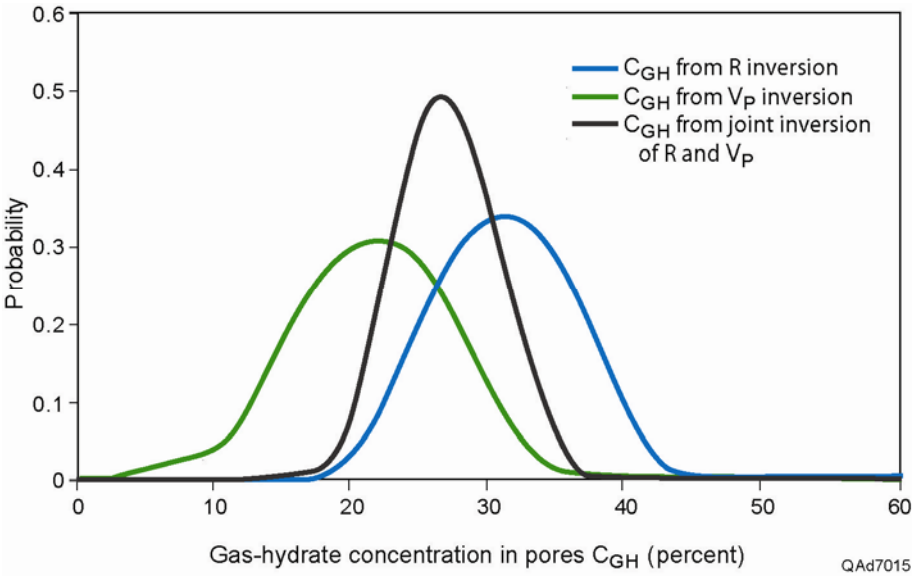

Figure 10.1. Idealized posterior PDF of hydrate concentration at a sub-seafloor depth location based on the inversion of seismic V_P velocity (black curve), inversion of formation resistivity R (blue curve), and joint inversion of both V_P and R (red curve). Joint inversion constrains the hydrate estimate and reduces the uncertainty of the estimate.

In contrast to a Gaussian distribution, a **uniform distribution** is used when the value of a parameter is not known, but the **range of variability** for the parameter can be defined. A uniform distribution assumes that within the range of variability being considered, any value of the described parameter is **equally probable**.

The parameters we used in our joint inversion were assigned the following PDFs:

- Gaussian distribution: porosity (Φ); clay fraction (V_{cl}); bulk and shear moduli for quartz, clay, and brine (K_q, K_{cl}, K_w, G_q, G_{cl}); density of brine, quartz, and clay (ρ_w, ρ_q, ρ_{cl}); effective pressure (P_{eff}); coordination number (C); cementation exponent (m); geometrical factor (a); and pore-fluid resistivity (R_w).
- Uniform distribution: hydrate concentration (c_{gh}); bulk and shear moduli of hydrate (K_{gh}, G_{gh}); hydrate density (ρ_{gh}); critical porosity (Φ_c); saturation exponent (n); and resistivity of clay mineral (R_{cl}).

The parameters listed here encompass all of the variables involved in predicting hydrate concentration for: (1) resistivity-log measurements, and (2) interval-velocity behavior. The manner in which these parameters were segregated between these two data-inversion domains (resistivity and velocity) is shown graphically as Figures 10.2 and 10.3.

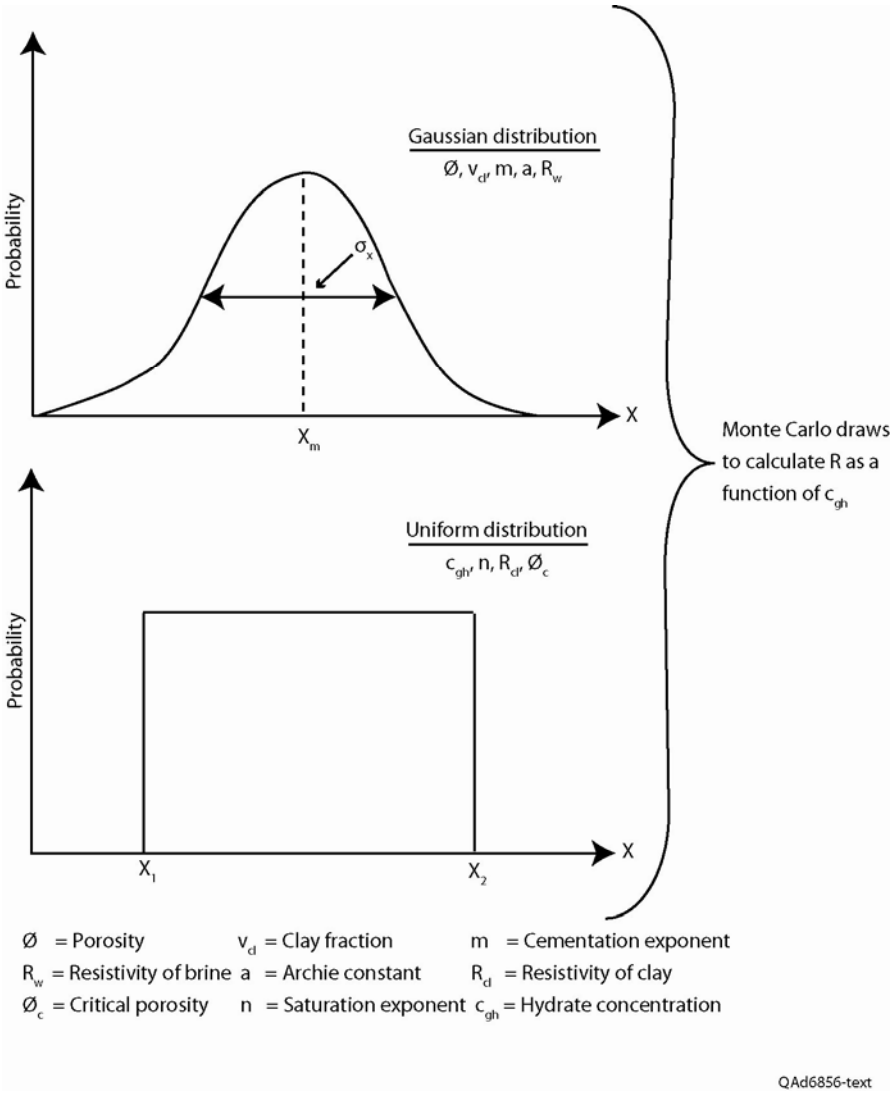

Figure 10.2. The types of PDFs used to describe the parameters needed to invert resistivity data to hydrate concentration. (Top) X_m = mean of Gaussian distribution; σ_x = standard deviation. (Bottom) X_1 to X_2 = range of uniform distribution.

Our probabilistic approach to estimating hydrate concentration is based on the concept that all parameters used in a joint inversion can be described by PDFs that account for the natural variability in the elastic properties of the mineral, hydrate, and fluid constituents of seafloor sediments, as well as for the variability in brine resistivity, cementation exponent, clay mineral resistivity, and other petrophysical parameters involved in a joint inversion of resistivity and seismic velocity to hydrate concentration.

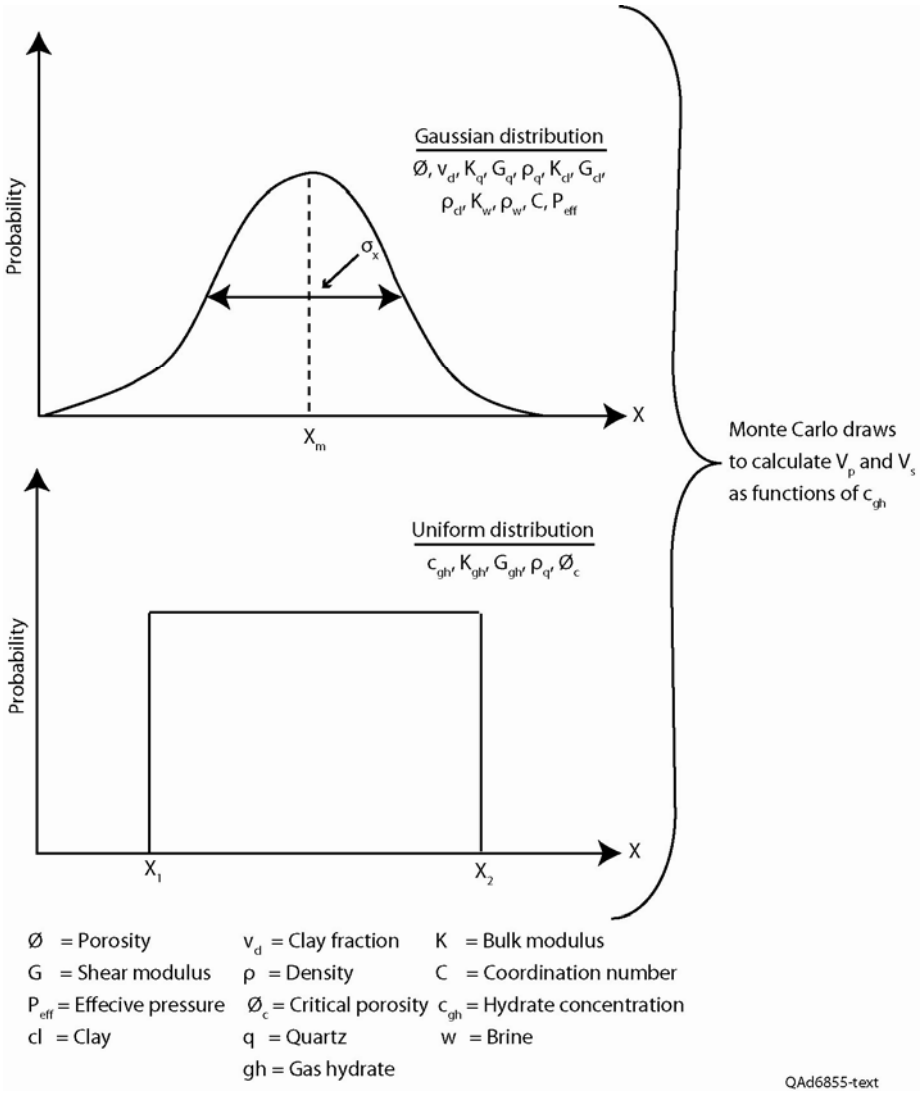

Figure 10.3. The types of PDFs used to describe the parameters needed to invert velocity data to hydrate concentration. (Top) X_m = mean of Gaussian distribution; σ_x = standard deviation. (Bottom) X_1 to X_2 = range of uniform distribution.

It is important to note that probability density functions describing porosity, effective pressure, mineralogy, coordination number, cementation exponent, geometric factor, resistivity of brine, and most other sediment variables needed in an inversion for hydrate concentration vary with depth (Fig. 10.4). In our method, we update the PDFs for these parameters at each depth coordinate, with these updates based on depth variations of parameters observed from geotechnical borings at Typhoon and Genesis Fields and on parameter behavior determined **a priori** (reasoning based on theoretical deduction, not on observation).

At each depth coordinate we model the joint theoretical relations between **hydrate concentration c_{gh}** (the model parameter we need to calculate) and the resistivity R and seismic propagation velocity (both V_P and V_S) of sub-seafloor

strata (which represent the observed parameters). We refer to the parameters involved in both our rock physics elastic modeling and in our Archie Equation (which must be corrected for clay content) as **common parameters**. As shown on Figure 10.5, there are three of these common parameters in our two inversion algorithms: porosity (Φ), hydrate concentration (c_{gh}), and volume fraction of clay (V_{cl}). Clay fraction is estimated from local gamma-ray logs (Eq. 6.4). We use a Monte Carlo procedure to draw values for common parameters Φ and V_{cl} from their associated PDFs and then compute the corresponding velocity and resistivity values using Monte Carlo draws from the PDFs for each of the model parameters that are required for calculating hydrate concentration (Fig. 10.5). The parameters needed in our hydrate-velocity relationship are explained in Chapter 3. Our hydrate-resistivity algorithm and its required parameters are described in Chapter 6.

In this fashion we obtain many possible realizations of the functions relating hydrate concentration, resistivity, and seismic propagation velocity. This joint relation is non-unique, uncertain, and can be expressed mathematically as a probability density function in three-dimensional (c_{gh}, V_P, R) data space [or in (c_{gh}, V_S, R) data space if preferred]. This 3D joint-theoretical PDF, which we will denote as $\boldsymbol{\xi(c_{gh}, V_P, R)}$, changes with depth and defines the correlation (and the inherent uncertainty) between hydrate concentration and the velocity and resistivity properties of hydrate-bearing sediments (Fig. 10.5). We emphasize V_P velocities rather than V_S velocities in our inversion because we found that across most of the OBC seismic grid we analyzed, hydrate fills less than 25-percent of the available pore space of the host sediment. For this range of hydrate fraction, there is a quasi-linear relationship between V_P and c_{gh} (Fig. 3.5, Models A and B); whereas, V_S exhibits little sensitivity to changes in c_{gh} when c_{gh} is less than 25-percent (Fig. 3.6, Models A and B).

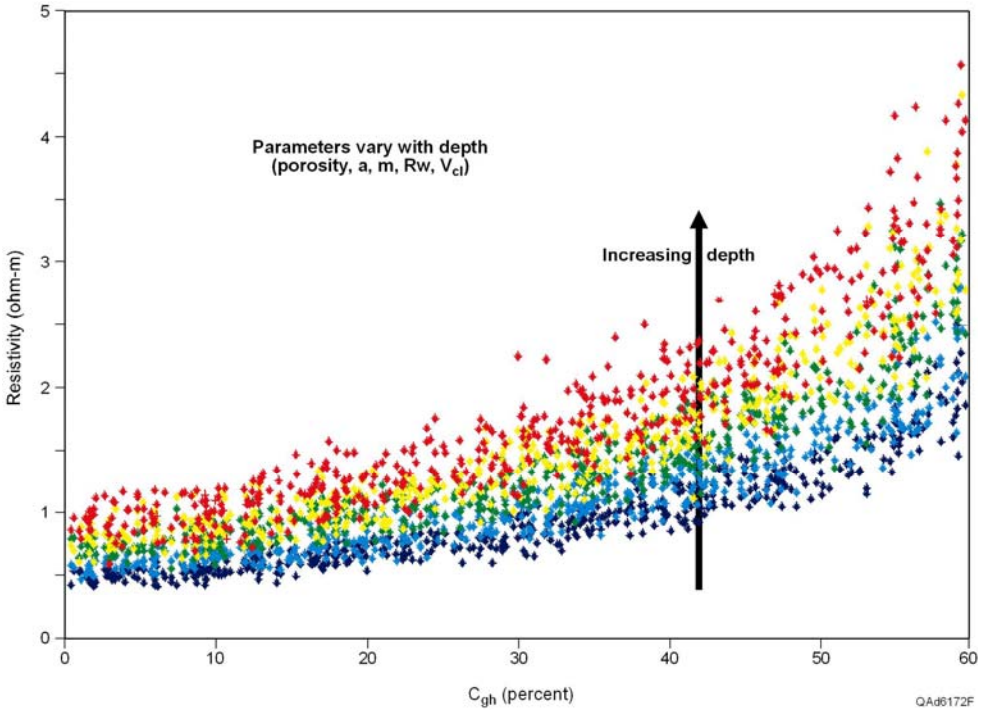

Figure 10.4. Illustration of the concept that petrophysical properties used to estimate hydrate concentration depends on depth below the seafloor. In this example, the depth-dependent petrophysical property is formation resistivity read from near-seafloor well logs.

To estimate hydrate concentration using seismic and resistivity data, we implement a Bayesian approach formulated in the context of an inverse problem, as proposed by Tarantola (1987). First, we express our prior information about hydrate concentration (information obtained before analyzing any seismic data or resistivity data) as a PDF. We denote this **prior PDF** as $\boldsymbol{\Lambda_M(c_{gh})}$, where subscript M stands for "model" parameter. In our study, this prior PDF is assumed to be a uniform distribution over all physically possible values for the hydrate pore-space fraction, meaning we allow this uniform distribution to range from 0 to 100-percent.

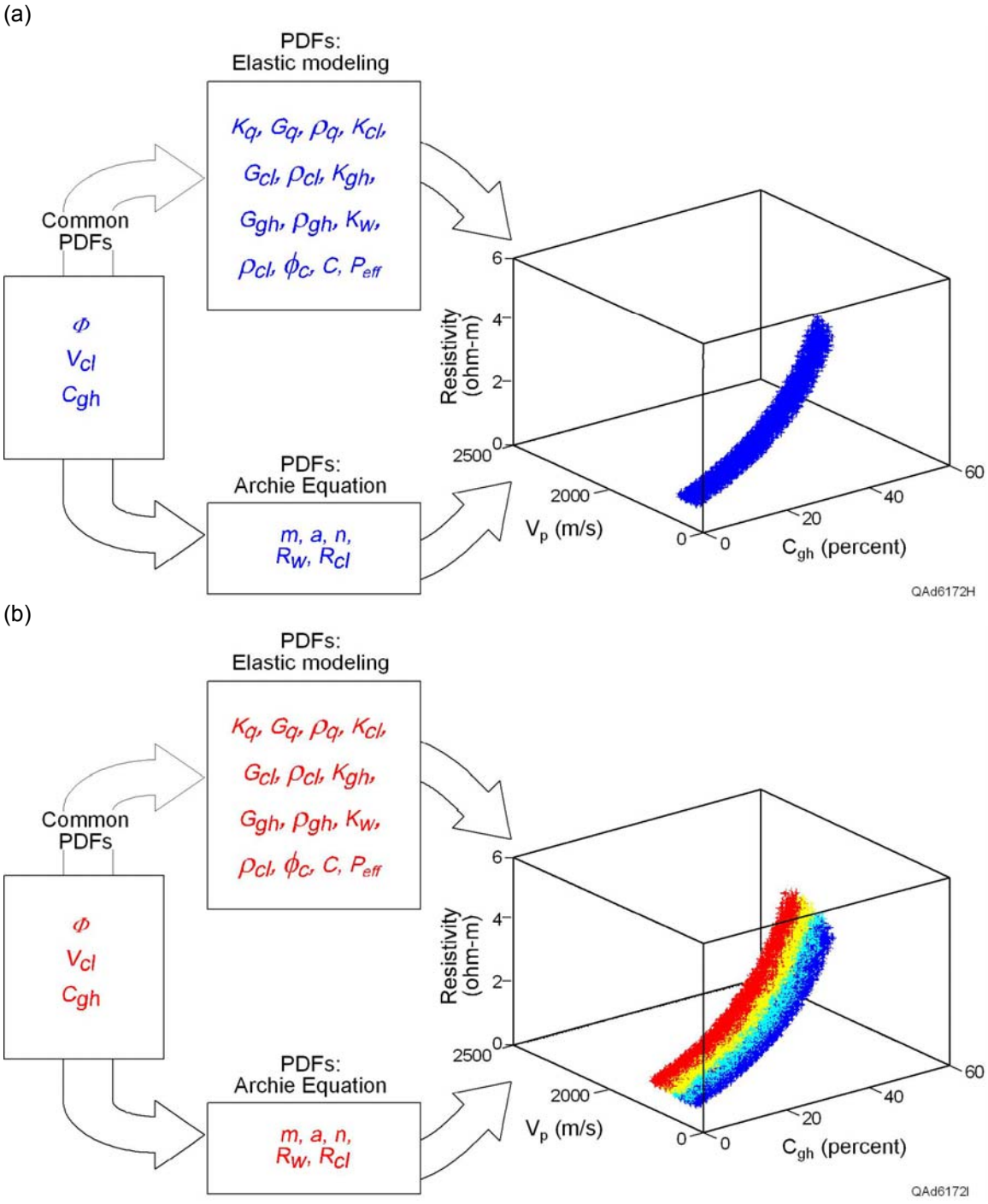

Figure 10.5. Joint inversion of V_P and R to estimate hydrate concentration, $C_{gh.}$ The parameter PDFs [a total of 21 inputs and one output (c_{gh})] involved in the inversion are listed in the boxes. (a) Joint inversion at a shallow sub-seafloor depth. (b) Joint inversion at a deeper depth.

Second, we combine this prior PDF of hydrate concentration, $\mathbf{\Lambda_M(c_{gh})}$, with information provided by seismic and resistivity measurements at calibration wells to create a 3-dimensional PDF spanning c_{gh}, V_P, and R parameter space. Our prior information and any information obtained from seismic and resistivity data are assumed to be statistically independent. This assumption allows the prior joint PDF that combines hydrate concentration and data, $\mathbf{\Lambda(c_{gh},V_P,R)}$, to be written as,

$$(10.1) \qquad \Lambda(c_{gh},V_P,R) = \Lambda_M(c_{gh}).\ \Lambda_D(V_P).\ \Lambda_D(R).$$

In this equation, subscript **D** stands for data, and $\mathbf{\Lambda_D(V_P)}$ and $\mathbf{\Lambda_D(R)}$ are Gaussian PDFs that account, respectively, for measurement uncertainties in the seismic P-wave velocity data and resistivity log data we use in our hydrate inversion. Our assumption of statistical independence between seismic and resistivity measurements is logical because velocity and resistivity data are obtained at different calendar times and with different field procedures and equipment.

Third, we use Tarantola's (1987) strategy that states that the **posterior PDF** combining hydrate concentration and data, $\mathbf{\Psi(c_{gh},V_P, R)}$, is proportional to the **prior joint PDF** for hydrate concentration and data, $\mathbf{\Lambda(c_{gh}, V_P, R)}$, multiplied by the **joint theoretical PDF**, $\mathbf{\xi(c_{gh}, V_P, R)}$, which we derive using stochastic rock physics modeling (Chapters 3, 4, and 6). Therefore, we can write:

$$(10.2) \qquad \Psi(c_{gh},V_P, R) = \Lambda(c_{gh}, V_P,R)\ .\ \xi(c_{gh}, V_P, R).$$

From this posterior joint PDF, $\mathbf{\Psi(c_{gh},V_P, R)}$, we derive the **marginal distribution** of hydrate concentration, $\mathbf{\Psi_M(c_{gh})}$, by integrating the posterior joint PDF over velocity and resistivity data space. This marginal distribution, $\mathbf{\Psi_M(c_{gh})}$, represents the posterior PDF for hydrate concentration in the pore space of the host sediment, and the mean of this distribution is the parameter that we display along our OBC profiles to represent the amount of in-place hydrate.

At each calibration well, we apply this Bayesian inversion procedure to estimate the posterior PDF of hydrate concentration, using both local seismic velocity values and local resistivity-log data in the inversion. This estimation utilizes the theoretical joint PDF, $\mathbf{\xi(c_{gh}, V_P, R)}$, that we derive using the rock-physics stochastic modeling discussed in Chapter 3 (V_P) and Chapter 6 (resistivity, R). When we leave a calibration well and calculate hydrate concentration along an OBC profile, our hydrate estimate is expressed at each depth location along the OBC line as a posterior PDF that involves **only V_P velocities**. We define the mean value of this posterior PDF as the expected value for hydrate concentration at each OBC line coordinate. In addition we produce a measure of the uncertainty associated with this estimate of hydrate concentration, which is the standard deviation of the posterior PDF.

Joint Inversion Examples

The hydrate prediction concepts described in the preceding section were applied to create joint-inversion estimates of hydrate concentration at calibration wells inside our study area. The locations of these calibration wells are shown on the maps displayed as Figures 5.1 and 8.1a (Typhoon area) and Figures 5.6 and 8.1b (Genesis area). The input data for these inversions are the resistivity log acquired in the calibration well and seismic-based V_P and V_S interval velocities determined from raytrace modeling local to each well. We use the theory described in Chapter 6 to relate resistivity to hydrate concentration, and we assume Model A (load-bearing hydrate) discussed in Chapter 3 (Fig. 3.1) is the correct description of the rock physics that relates hydrate concentration and seismic velocity.

The estimation of hydrate concentration at Well B, Genesis Field, is illustrated on Figure 10.6. The function labeled **NC** on the data panels of this figure defines the effect of **normal compaction** on the rock property that is illustrated in each panel. The method used to calculate these normal compaction curves is described in Chapter 9.

Intervals above the base of the hydrate stability zone boundary where both velocity and resistivity have values greater than those associated with normal compaction are assumed to be zones of hydrate concentration. Using this normal-compaction behavior as one constraint for our joint inversion, the mean value of the probability distribution function (PDF) in Figure 10.6b indicates that hydrate occupies more than 14-percent of the pore space in the local vicinity of Well B.

Similar joint inversions of resistivity and velocity data were done to estimate hydrate concentrations at calibration wells across the Genesis Field and Typhoon Field areas. The maps on Figures 5.6 and 8.1b define 13 wells (labeled A through M) within the Genesis Field study area where resistivity logs were found that traversed a portion of the hydrate stability zone. However, only five of these wells (wells B, C, F, G, and J) are positioned close enough to an OBC seismic line to allow seismic-derived interval velocities to be incorporated into a joint resistivity-velocity inversion of hydrate concentration. The joint inversion analyses at these five wells are displayed as Figures 10.6 through 10.10.

The maps displayed on Figures 5.1 and 8.1a identify five wells across the Typhoon Field area where resistivity logs span some portion of the hydrate stability zone. Only one of these wells (well A) is positioned on an OBC profile where seismic interval velocities can be calculated and used for joint inversion. Although wells D and E at Typhoon are near OBC profile 489, they are too close to the end of the seismic profile to allow reliable interval velocities to be determined from common-receiver gathers. The joint inversion of resistivity and velocity data at Typhoon well A is displayed as Figure 10.11.

(a)

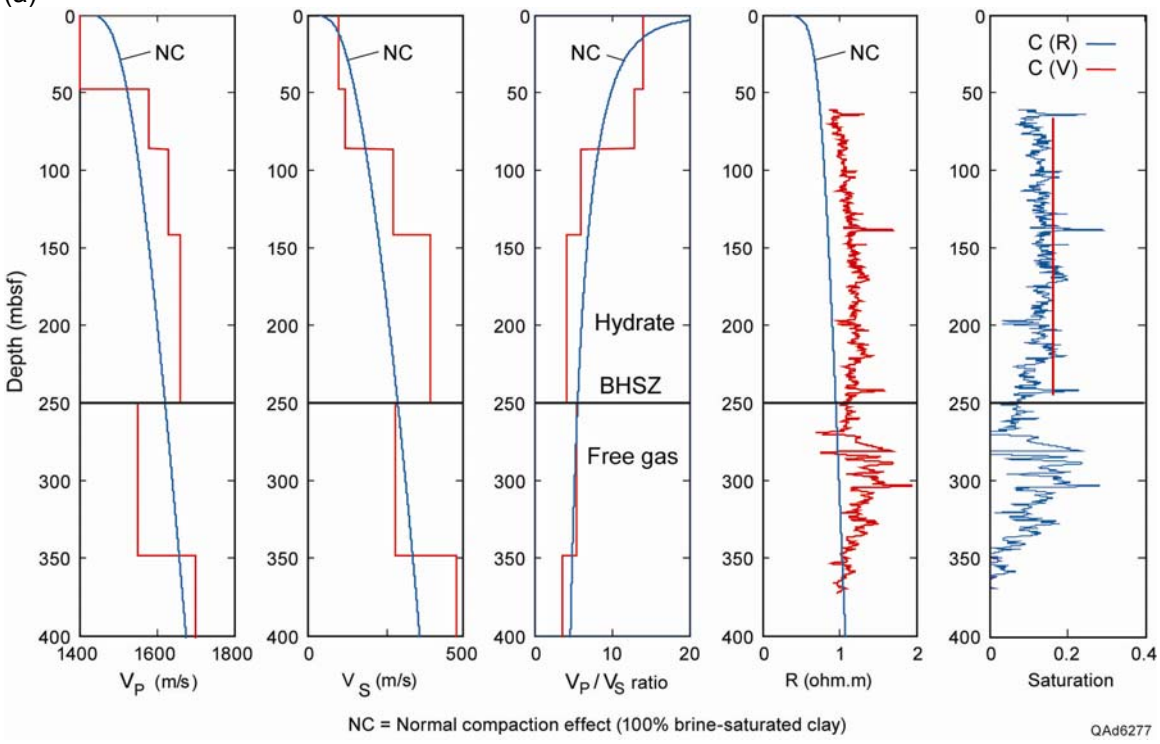

(b)

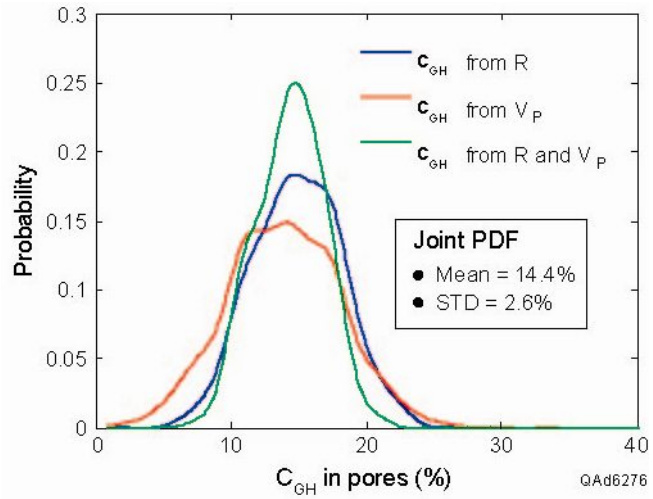

Figure 10.6. (a) Seismic-based V_P and V_S interval velocities, resistivity log, and their respective estimates of hydrate concentration at Well B, Genesis Field. See Figures 5.6 and 8.1b for location of well B. The BHSZ boundary is defined as the top of the layer where V_P velocity exhibits a reversal in magnitude. The increase in resistivity below the BHSZ boundary is caused by free gas. (b) Joint inversion of resistivity and V_P velocity indicates hydrate occupies 14.4 percent of the pore space (mean value of the PDF). The estimation error is ±2.6 percent (standard deviation of the PDF).

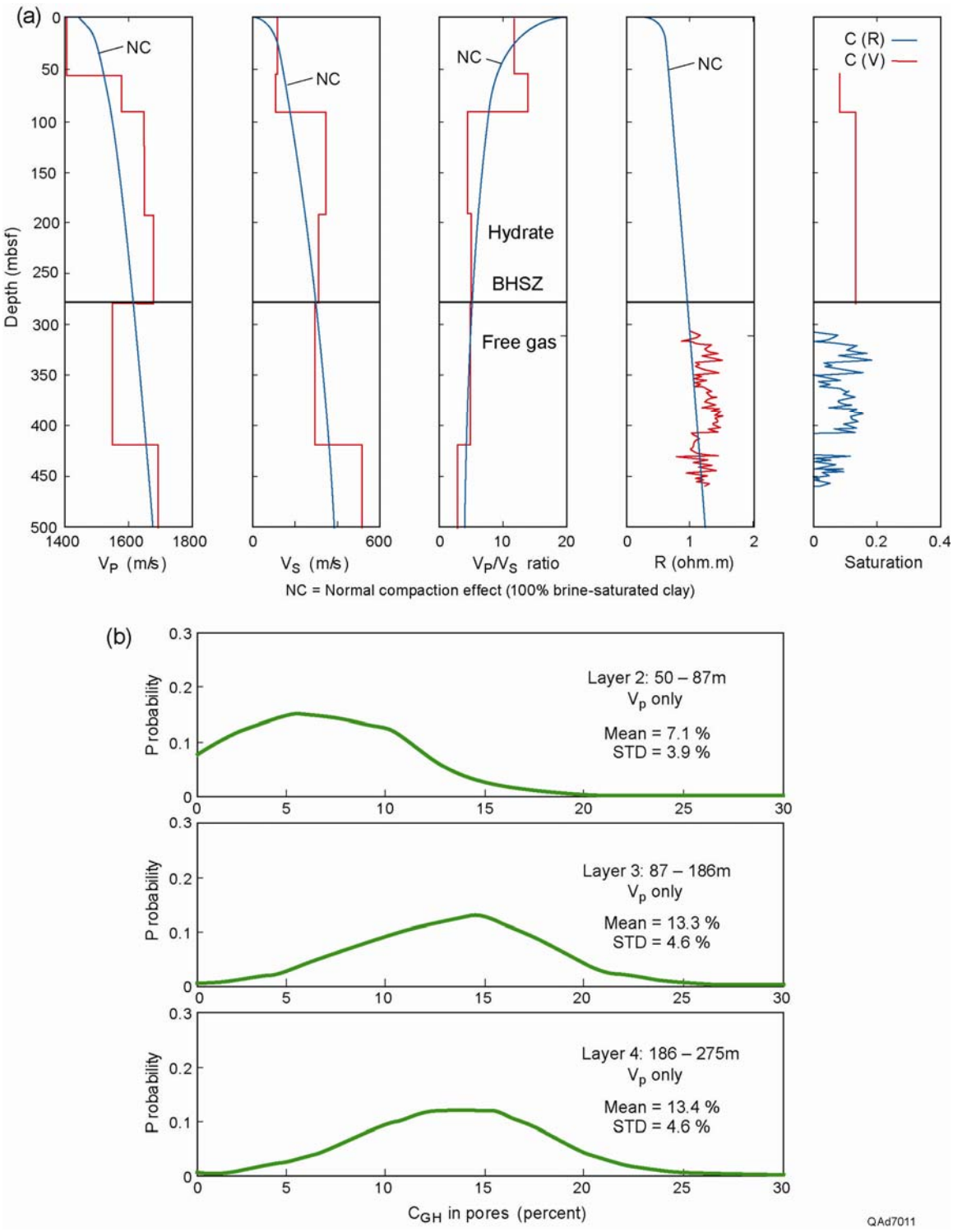

Figure 10.7. (a) Seismic-based V_P and V_S interval velocities, resistivity log, and their respective estimates of hydrate concentration at Well C, Genesis Field. See Figures 5.6 and 8.1b for location of well C. The BHSZ boundary is defined as the top of the layer where V_P velocity exhibits a reversal in magnitude. The increase in resistivity below the BHSZ boundary is caused by free gas. (b) Only V_P velocity can be used for inversion. Inversion results are shown for velocity layers 2, 3, and 4.

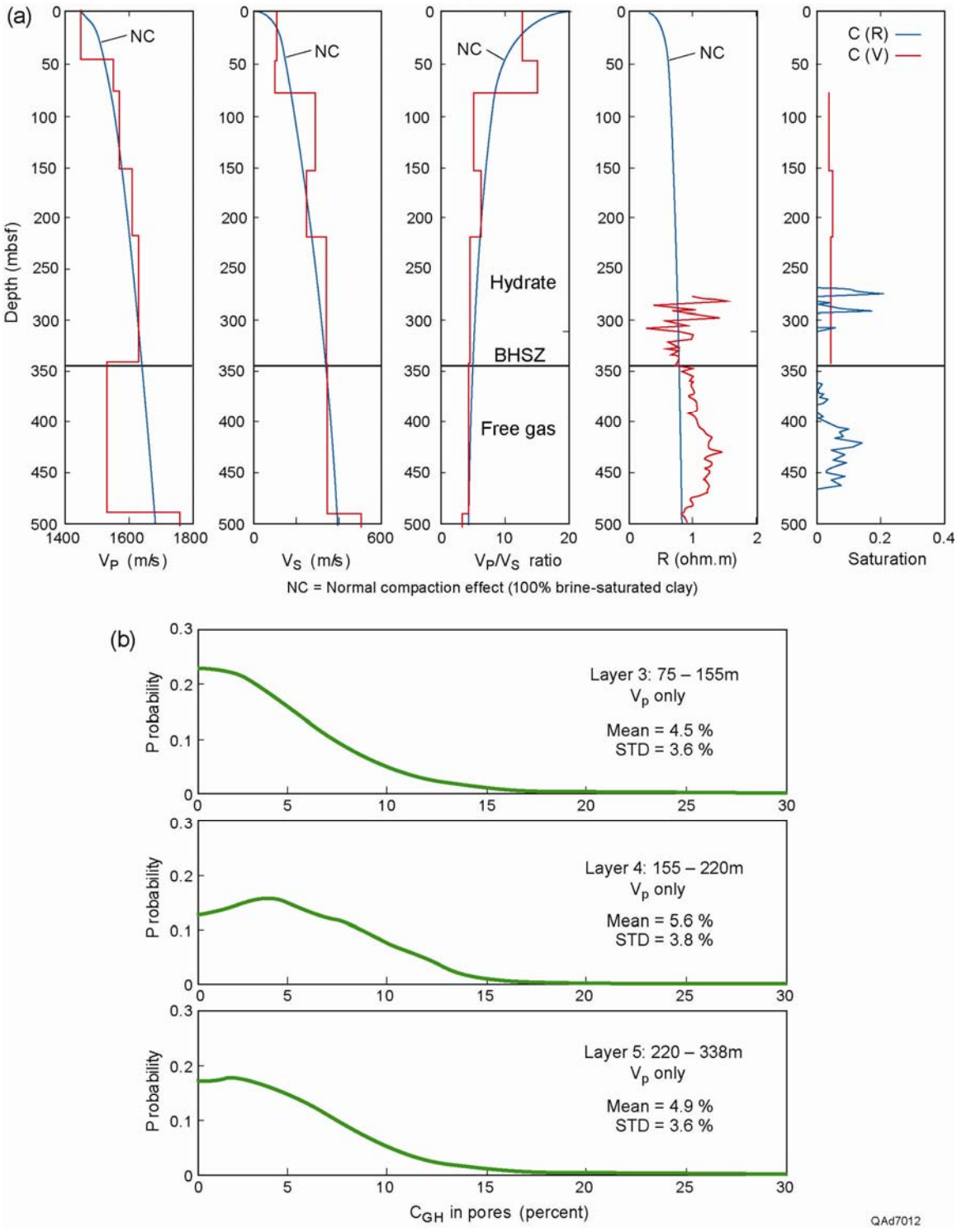

Figure 10.8. (a) Seismic-based V_P and V_S interval velocities, resistivity log, and their respective estimates of hydrate concentration at Well F, Genesis Field. See Figures 5.6 and 8.1b for location of well F. The BHSZ boundary is defined as the top of the layer where V_P velocity exhibits a reversal in magnitude. The increase in resistivity below the BHSZ boundary is caused by free gas. (b) Only V_P velocity can be used for inversion. Inversion results are shown for velocity layers 3, 4, and 5.

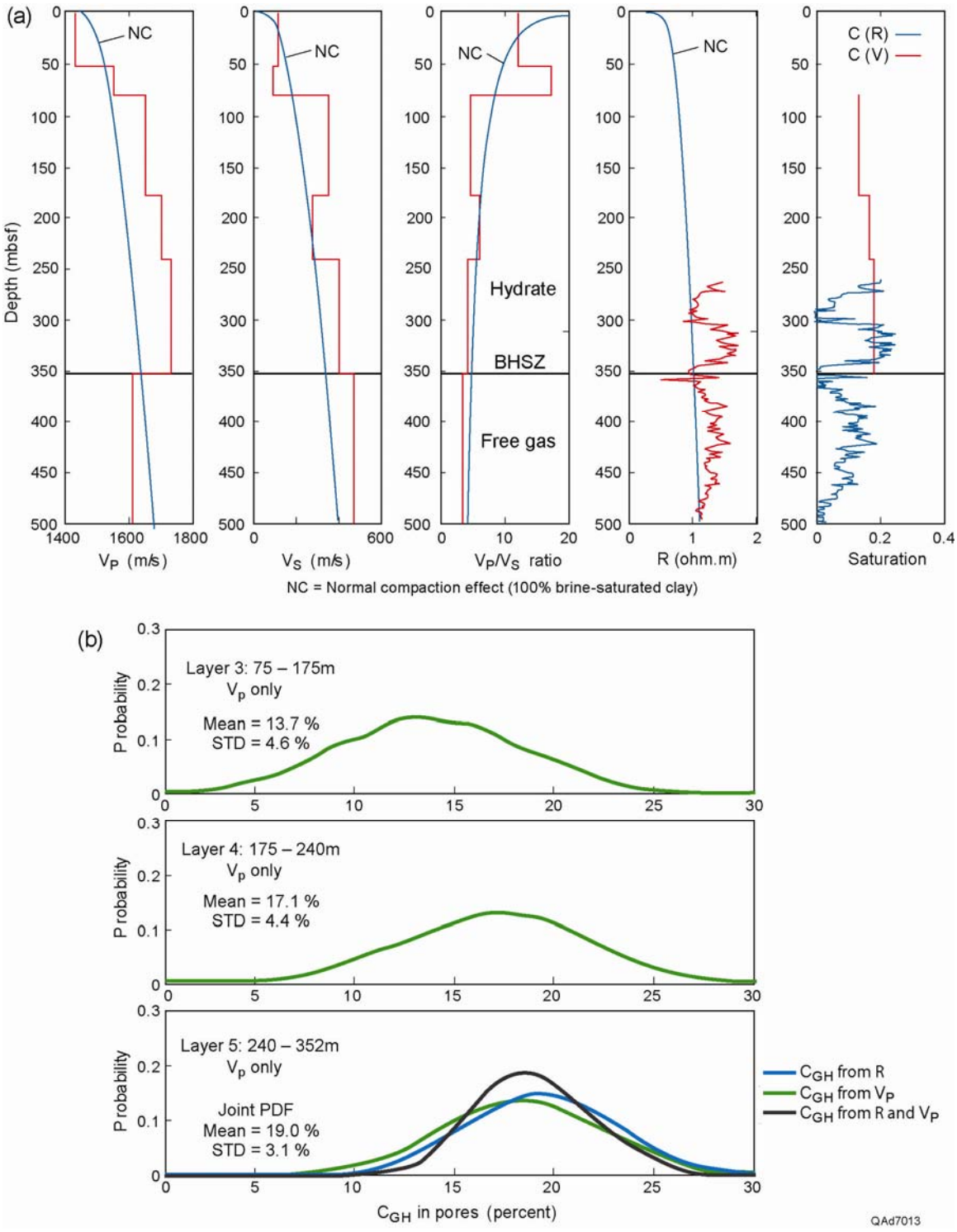

Figure 10.9. (a) Seismic-based V_P and V_S interval velocities, resistivity log, and their respective estimates of hydrate concentration at Well G, Genesis Field. See Figures 5.6 and 8.1b for location of well G. The BHSZ boundary is defined as the top of the layer where V_P velocity exhibits a reversal in magnitude. The increase in resistivity below the BHSZ boundary is caused by free gas. (b) Only V_P velocity can be used for inversion above layer 5. Results are shown for velocity layers 3 and 4. Joint inversion of resistivity and V_P velocity is shown for layer 5.

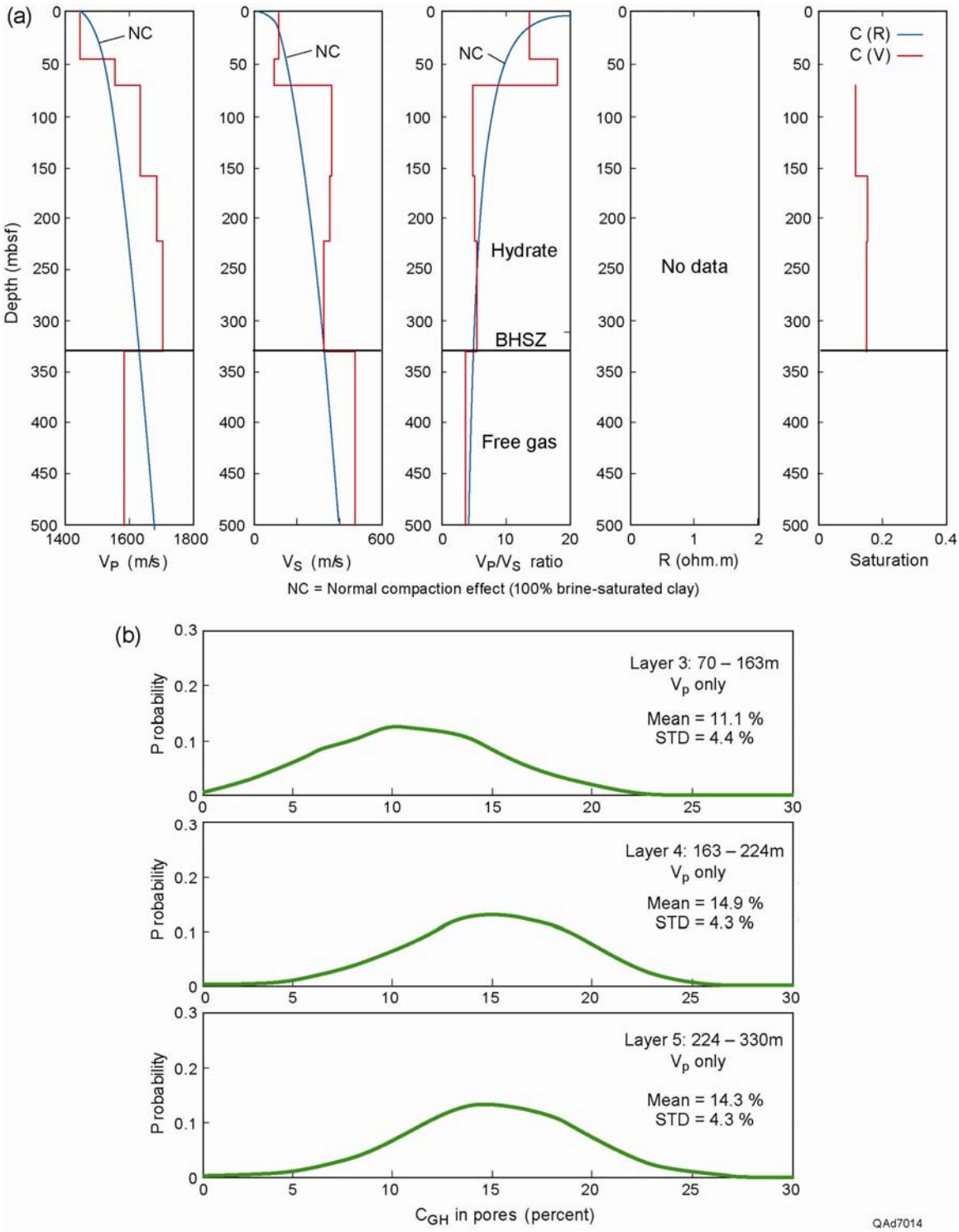

Figure 10.10. (a) Seismic-based V_P and V_S interval velocities, resistivity log, and their respective estimates of hydrate concentration at Well J, Genesis Field. See Figures 5.6 and 8.1b for location of well J. The BHSZ boundary is defined as the top of the layer where V_P velocity exhibits a reversal in magnitude. (b) Only V_P velocity can be used for inversion. Inversion results are shown for velocity layers 3, 4, and 5.

(a)

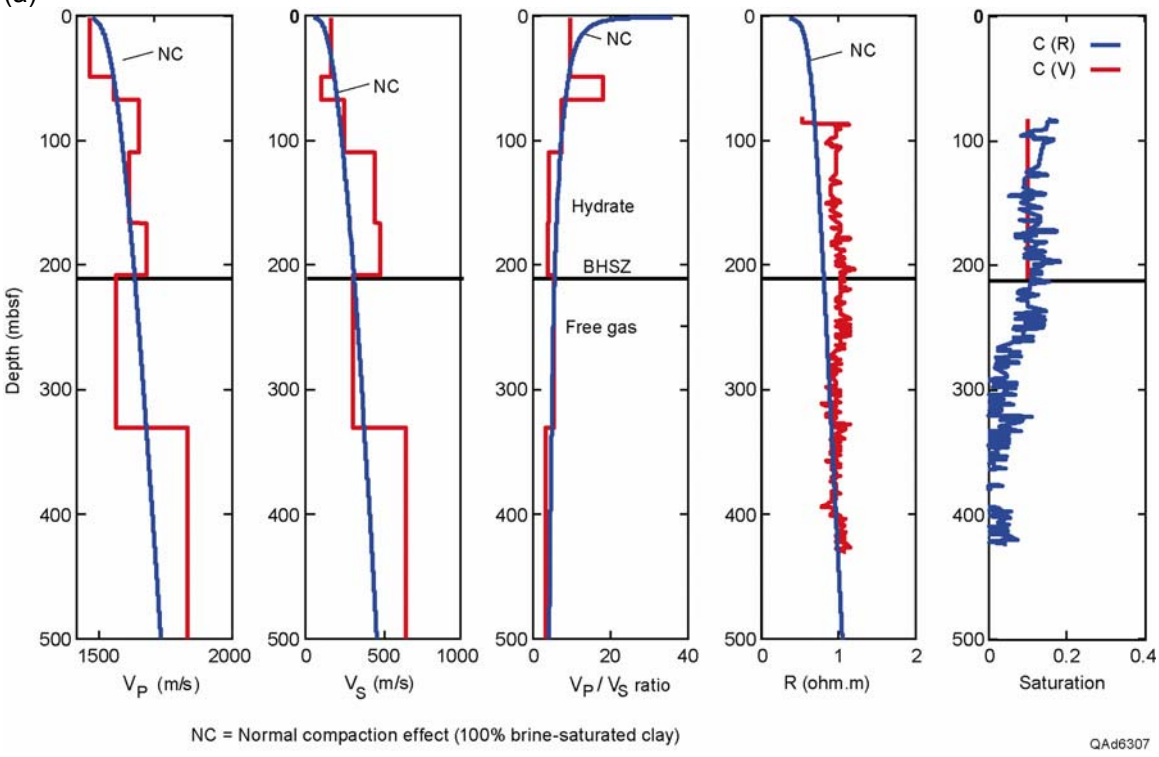

(b)

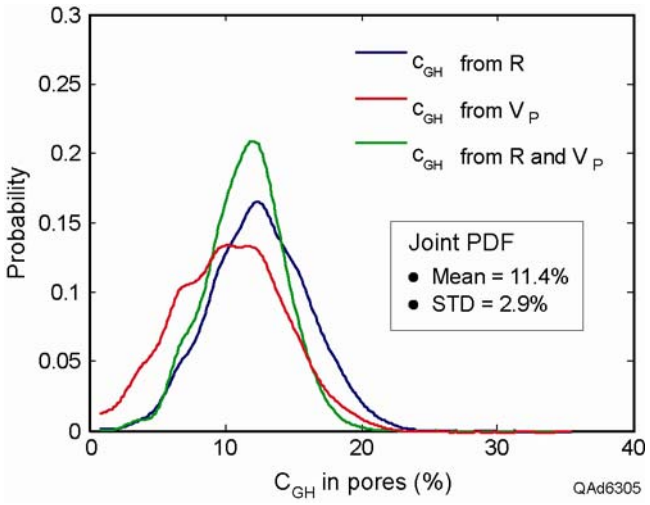

Figure 10.11. (a) Seismic-based V_P and V_S interval velocities, resistivity log, and their respective estimates of hydrate concentration at Well A, Typhoon Field. See Figures 5.1 and 8.1a for location of well. The BHSZ boundary is defined as the top of the layer where V_P velocity exhibits a reversal in magnitude. The increase in resistivity below the BHSZ boundary is caused by free gas. (b) Joint inversion of resistivity and V_P velocity indicates hydrate occupies 11.4 percent of the pore space (mean value of the PDF). The estimation error is ±2.9 percent (standard deviation of the PDF).

The joint inversions exhibited on Figures 10.6 through 10.11 established the fundamental calibration points that allowed seismic interval velocities determined along each OBC seismic profile to be inverted into reliable estimates of hydrate concentration at seismic-profile coordinates that were far removed from any calibration well.

Conclusions

The hydrate inversion results exhibited in this chapter show remarkable agreements between hydrate concentrations predicted from resistivity log data acquired in calibration wells and from seismic interval velocities calculated local to these wells [calibration wells B and G (Genesis area) and calibration well A (Typhoon area)]. The tight overlap of the resistivity-predicted hydrate PDF and the V_P-predicted hydrate PDF documented at each of these calibration wells implies that the rock physics theories and parameters used in our estimations of hydrate concentration are based on sound science and valid calibration data. As a result, we concluded that the extension of our velocity-based inversion methodology to OBC receiver stations positioned considerable distances from a calibration well produced reliable hydrate estimates along each OBC seismic profile.

We must stress that our hydrate estimates involve an inescapable bias that comes into play when we impose a specific hydrate-sediment morphology in order to formulate the inversion algorithms that we used. For example, our resistivity inversion was based on the assumption that hydrate exists in sub-seafloor sediment as a disseminated morphology rather than as a thin-layered morphology (Chapter 4). Thus a disseminated-hydrate bias is ingrained in the selection of parameter values that we use when inverting resistivity log data. Similarly, our velocity inversion assumed that this disseminated hydrate existed as a load-bearing morphology, not as a free-floating morphology or as a thin-layered morphology (Chapter 3). Thus a load-bearing, disseminated-hydrate bias is embedded in our inversion algorithm that relates velocity to hydrate concentration.

If seafloor cores were collected and analyzed to determine the true nature of the hydrate morphology across our study area, a morphology-driven bias would still have to be incorporated into our inversion results. However, that bias would be based on hard evidence, not on assumptions.

DOE Gas Hydrate Final Report

Chapter 11

Project Benefits and Impacts

This 3-year study has demonstrated that 4C seismic data have greater value for evaluating deep-water hydrate systems than do single-component, towed-cable seismic data. The 4C data used in this study were acquired with ocean-bottom-cable (OBC) technology constructed such that the safe operating water depth for the cable was 1000 m. Across the Gulf of Mexico, the most attractive hydrate systems occur at water depths greater than 1000 m. Although 4C sensor cables exist that can operate to water depths of 2000 m, seismic contractors prefer to use robust modular packaging of 4C seafloor sensors when water depths exceed 1000 m. These modular packages have to be deployed as individual, stand-alone, seafloor stations, and there is no interconnecting cable between these seafloor receiver stations. Modular style 4C sensors that function in water depths of 3000 m or more are available from at least three seismic contractors. Thus equipment is available that allows 4C seismic data to be used to evaluate hydrate systems at essentially any water depth.

The present constraint in applying 4C seismic technology to hydrate studies in water depths of more than 1000 m is cost, not technology. The pricing of seismic services is so dynamic that it is not possible to cite specific cost numbers for 4C seismic data acquisition. In general, one can assume it will cost 10 to 20 times more to acquire 4C data across a study area than it will to acquire towed-cable data.

Given this cost difference, the 4C technology developed in this project will probably not be used to explore for hydrates. Instead, broad area searches for evidence of deep-water hydrates should continue to be done using affordable towed-cable seismic data. However, when promising hydrate sites are identified with single-component, towed-cable data, then the technologies developed in this project should be seriously considered as the optimal methodology for characterizing the hydrate-bearing interval, quantifying the amount of in-place hydrate, and specifying the geomechanical stability of the geological units that confine the hydrates.

Specific Benefits

The research findings associated with this project present several benefits to the hydrate research community. The principal benefits are the following:

1. Increased seismic resolution of deep-water hydrate systems – Our strategy of creating P-P and P-SV images of near-seafloor geology by processing common-receiver data in the same way that walkaway VSP

data are processed is a new, never-before-documented concept and yields a spatial resolution of near-seafloor geological features that towed-cable seismic data cannot begin to match. If hydrate distribution within a hydrate-bearing interval is affected by meter-scale depositional and structural features, then the procedures documented in this study provide hydrate investigators their first capability to see such features with standard-frequency air gun arrays towed at the sea surface.

2. Determination of geomechanical properties of hydrate-bearing strata – Of all the elastic constants that need to be known to understand the mechanical strength (or weakness) of a targeted near-seafloor geological unit, the most critical elastic coefficient is the shear modulus. Dynamic estimates of shear modulus are based on the shear-wave velocity V_S. The raytracing methodology we describe for determining interval values of V_P and V_S yields highly accurate velocity values. Thus the techniques described in this report allow V_S to be determine both vertically and transversely across a hydrate-bearing site, which can produce the most accurate mapping of shear moduli associated with seafloor strata that can be achieved with remote measurements. This deterministic quantification of interval values of V_S could not be done with the availability of 4C data, and more specifically, could not be done without a rigorous, accurate methodology similar to that which we demonstrate.
3. Improved inversion of resistivity log data – We believe that previous attempts to invert resistivity log data to estimates of hydrate concentration in deep-water, near-seafloor strata have yielded erroneous results because inappropriate constants were used in the inversion equation, which is typically some formulation of the Archie Equation (Archie, 1942). Our research shows that the Hashin-Shtrikman Lower Bound (HSLB) [Hashin and Shtrikman, 1962] is the rigorous way to define the resistivity that any inversion equation must predict in high-porosity, low-hydrate-saturation, unconsolidated sediment such as exist near the seafloor. Our research documented in this report explains this logic and shows how to implement HSLB strategies to achieve optimal estimates of hydrate concentration.
4. New rock physics concepts – Our research provides hydrate investigators two valuable rock physics theories – one that relates V_P and V_S velocities to hydrate saturation and one that relates formation resistivity measurements to hydrate concentration. Our resistivity model is unique because it is based on the Hashin-Shtrikman Lower Bound as discussed above. Our velocity model has some similarities to previously published work, but it also becomes a unique theory in that we show logical arguments that Walton's theory (Walton, 1987) should be used for describing V_S dependence on hydrate concentration rather than the usually accepted approach of Hertz-Mindlin theory (Mindlin, 1949). Also our velocity-based rock physics theory places equal weight on both V_P and V_S velocities; whereas, studies that have to deal with only single-

component seismic data ignore V_S because P-wave data provide no direct S-wave information.

5. Quantifying the uncertainty of hydrate estimations – Most published studies that present an estimate of the amount of hydrate present at a site fail to couch that estimate in terms of the uncertainty associated with the estimate. We demonstrate how Monte Carlo and Bayesian methodologies can be used to develop a probability distribution function (PDF) that describes an estimate of hydrate concentration as the mean of the PDF and the uncertainty of that estimate as the standard deviation of the PDF. In this methodology, every parameter that enters into the joint inversion of resistivity and velocity to hydrate concentration is described as a PDF, with a PDF created to specify the expected value of each velocity and resistivity parameter (the mean of the specific PDF) and the associated uncertainty of that expected parameter value (the standard deviation of the specific PDF). We produced a total of 21 PDFs to describe the parameters used in our joint inversions of resistivity and velocity data. From our example, hydrate researchers should begin to describe the uncertainty associated with their predictions of the volume of in-place hydrate at study sites.

Specific Impacts

We know our 4C seismic imaging developments have impacted the geophysical community because of:

- The Best Paper Award bestowed by the Society of Exploration Geophysicists when our methodology was published,
- Repeated requests to describe the imaging procedure at luncheons of professional groups and at internal seminars held by seismic contractors and oil companies, and
- Numerous requests for reprints of the award-winning paper.

We wish to stress that our seismic imaging research has received wide international attention and reaction, with notable examples of international responses being:

- A sponsored trip to the Research Institute for Petroleum Exploration and Production (RIPED) in Beijing, China to assist Chinese geophysicists in implementing our 4C imaging technology,
- A program sponsored by the country of Colombia to evaluate deep-water hydrates along both their Caribbean and Pacific coasts, with our seismic imaging strategy being the central basis for the collaborative study, and
- An emerging program to work with the Central American Commission (an alliance of Panama, Nicaragua, Costa Rica, Guatemala, Honduras, Belize, and El Salvador) to identify and evaluate deep-water hydrates across both the Caribbean and Pacific coasts of central America, with our imaging expertise again being the reason for these countries approaching us with this request to do research across their offshore territories similar to that described in this report.

The huge impact of the seismic-imaging component of this project, as documented above, is due in part to the fact that the research that lead to this imaging strategy was an early development that let us publish our research progress in 2006. Now, three years later, at the conclusion of the project, there has been a good length of time in which to see the impact of that seismic-imaging development. Equally important research findings, at least in our mind, are just now being publicized. We cannot predict the future, but we expect our rock physics theories, our emphasis on using the Hashin-Sthrikman Lower Bound to calibrate parameters needed for inverting resistivity to hydrate concentration, and our techniques for quantifying the uncertainty associated with hydrate predictions to also impact the thought processes and operational practices of the worldwide hydrate research community.

References

Allen, P., and Allen, J., 1990, Basin Analysis: Principles and applications, Blackwell, 257 pages.

Archie, G. E., 1942, The electric resistivity log as an aid in determining some reservoir characteristics: AIME Transactions, 46, p. 54.

Backus, G., 1962, Long-wave elastic anisotropy produced by horizontal layering: J. Geophys. Res., 76, 4427-4440.

Backus, M. M., Murray, P. E., Hardage, B. A., and Graebner J., 2006, High-resolution multicomponent seismic imaging of deepwater gas-hydrate systems: The Leading Edge, 25, 578-596.

Batzle, M., and Wang, Z., 1992, Seismic properties of pore fluids, Geophysics, v. 57, no. 11, 1396-1408

Brooks, J. M., and Bryant, W. R., 1985, Geological and geochemical implications of gas hydrates in the Gulf of Mexico: Final report, Department of Energy, Morgantown Energy Technology Center, 131 p.

Carcione, J. M. and Tinivella, U., 2000, Bottom-simulating reflectors: Seismic velocities and AVO effects: Geophysics, 65, 54-67.

Cartwright, J., James, D., and Bolton, A., 2003, The genesis of polygonal fault systems—a review, *in* Van Rensbergen, P., Hillis, R. R., Maltman, A. J., and Morley, C. K., eds., Subsurface Sediment Mobilization: The Geological Society, London, p. 223-243.

Castagna, J. P. and Backus, M. M., 1993, Offset-dependent reflectivity - theory and practice of AVO analysis: Society of Exploration Geophysicists, 348 p.

Chand, S., Minshull, T. A., Gei, D., and Carcione, J. M., 2004, Elastic velocity models for gas-hydrate-bearing sediments-a comparison: Geophys. J. Int., 159, 573-590.

Collett, T. S., 1998, Well log evaluation of gas hydrate saturations: Transactions of the Society of Professional Well Log Analysts 39th Annual Logging Symposium, Paper MM.

Collett, T. S., and Ladd, J., 2000, Detection of gas hydrate with downhole logs and assessment of gas hydrate concentrations (saturations) gas volumes on the Blake Ridge with electrical resistivity log data: *in* Paull, C. K., Matsumoto, R., Wallace, P. J., and Dillon, W. P., eds., Proceedings of the Ocean Drilling Program, scientific results, 164, p. 179-191.

Digby, P. J., 1981, The effective elastic moduli of porous granular rocks. J. Appl. Mech., 48, 803-808.

Domenico, S. N., 1976, Effect of brine-gas mixture on velocity in an unconsolidated sand reservoir: Geophysics, 41, 882-894.

Dvorkin, J., and Nur, A. 1996, Elasticity of high-porosity sandstones - theory for two North Sea data sets: Geophysics, 61, 1363-1370.

Dvorkin, J., Nur, A., and Yin, H., 1994, Effective properties of cemented granular material: Mechanics of Materials, 18, 351-366.

Dvorkin, J., Prasad, M., Sakai, A., and Lavoie, D., 1999, Elasticity of marine sediments: Geophys. Research Lett., 26, 1781-1784.

Ecker, C., Dvorkin, J., and Nur, A., 1998, Sediments with gas hydrates: Internal structure from seismic AVO: Geophysics, 63, 1659-1669.
Ecker, C., Dvorkin, J., and Nur, A., 2000, Estimating the amount of gas hydrate and free gas from marine seismic data: Geophysics, 62, 565-573.
Gassmann, F., 1951, On the elasticity of porous media: Vier. Der Natur. Gesllschft in Zurich, 96, 1-23.
Hardage, B. A., and Roberts, H. H., 2006, Gas hydrate in the Gulf of Mexico - what and where is the seismic target?: The Leading Edge, 25, p. 566-571.
Hardage, B. A., Roberts, H. H., Murray, P. E., Remington, R., Sava, D. C., Shedd W., Hunt, J., Jr., 2007, Multicomponent seismic technology assessment of fluid-gas expulsion geology, Gulf of Mexico: *in* Collett, T., Johnson, A., Knapp, C., and Bosswell, R., eds., Natural Gas Hydrates: Energy Resource Potential and Associated Geologic Hazards: AAPG Special Publication (page numbers not yet assigned).
Hashin, Z., and Shtrikman, S., 1962, A variational approach to the theory of the effective magnetic permeability of multiphase materials: Journal of Applied Physics, 33, no. 10, p. 3125-3131.
Hashin, Z., and Shtrikman, S., 1963, A variational approach to the elastic behavior of multiphase materials: J. Mech. Phys. Solids, 11, 127-140.
Helgerud, M. B., Dvorkin, J., and Nur, A., Sakai, A., and Collett, T., 1999, Elastic-wave velocity in marine sediments with gas hydrates—effective medium modeling: Geophys. Res. Lett., 26, 2021-2024.
Hill, R. 1963, Elastic properties of reinforced solids—some theoretical principles: J. Mech. Phys. Solids, 11, 357-372.
Holbrook, W. S., H. Hoskins, W. T. Wood, R. A. Stephen, D. Lizarralde, and Leg 164 Scientific Party, 1996, Methane hydrate and free gas on the Blake Ridge from vertical seismic profiling: Science, 273, 1840-1843.
Kleinberg, R. L. and Dai, J., 2005, Estimation of the mechanical properties of natural gas hydrate deposits from petrophysical measurement: OTC 17205, Offshore Technology Conference, Houston, TX, 2-5 May 2005.
Lee, M. W., Hutchinson, D. R., Collett, T. S., and Dillon, W. P., 1996, Seismic velocities for hydrate bearing sediments using weighted equation: J. Geophys. Res., 101, 20, 347-358.
Lu, S. and McMechan, G. A., 2002, Estimation of gas hydrate and free gas saturation, concentration, and distribution from seismic data: Geophysics, 67, 582-593.
Lu, S. and McMechan, G. A., 2004, Elastic impedance inversion of multichannel seismic data from unconsolidated sediments containing gas hydrate and free gas: Geophysics, 69, 164-179.
Mavko G., Mukerji, T., and Dvorkin, J., 1998, The rock physics handbook: Cambridge University Press, 329 pages.
Mendelson, K. S., and Cohen, M. H., 1982, The effect of grain anisotropy on the electrical properties of sedimentary rocks: Geophysics, 47, p. 257-263.
Milkov, A. V., and Sassen, R., 2001, Estimate of gas hydrate resource, northwestern Gulf of Mexico continental slope: Marine Geology, 179, 71-83.

Miller, J. J., Lee, M. W., and von Huene, R., 1991, An analysis of seismic reflection from the base of a gas hydrate zone, offshore Peru: AAPG Bulletin, 75, 910-924.
Mindlin, R. D., 1949, Compliance of elastic bodies in contact: J. Appl. Mech., 16, 259-268.
Murphy, W. F., 1982, Effects of microstructure and pore fluids on the acoustic properties of granular sedimentary materials: Ph. D. dissertation, Stanford University.
Murray, D. R., Kleinberg, R. L., Sinha, B. K., Fukuhara, M., Osawa, O., Endo, T. and Namikawa, T., 2006, Saturation, acoustic properties, growth habit, and state of stress of a gas hydrate reservoir from well logs: Petrophysics, 47, 129-137.
Pearson, C. F., Hallek, P. M., McGuire, P. L., Hermes, R., and Mathews, M., 1983, Natural gas hydrate deposits—a review of in-situ properties: J. of Phys. Chem., 87, 4180-4185.
Prasad, M., and Dvorkin, J., 2001, Velocity to porosity transform in marine sediments: Petrophysics, 42, 429-437.
Ramm, M., and Bjoerlykke K., 1994, Porosity/depth trends in reservoir sandstones: assessing the quantitative effects of varying pore-pressure , temperature history and mineralogy, Norwegian Shelf Data; Clay minerals, 29, 475-490.
Reuss, A., 1929, Berechunung der fliessgrense von mischkristallen auf grund der plastizitatsbedinggung fur einkristalle: Zeitschrift fur Angewandte Mathematik and Mechanik, 9, 49-58.
Rider, M. H., 1991, The Geologic Interpretation of Well Logs, revised edition: Cathness, Scotland, Whittles Publishing.
Roberts, H.H., Hardage, B.A., Shedd, W.W. and Hunt, J., Jr., 2006, Seafloor reflectivity – An important seismic property for interpreting fluid/gas expulsion geology and the presence of gas hydrate: The Leading Edge, Society of Exploration Geophysicists, 25, 620-628.
Roberts, H.H., Cook, D.J. and Sheedlo, M.K., 1992a, Hydrocarbon seeps of the Louisiana continental slope: Seismic amplitude signature and sea floor response: Transactions 42nd Annual Gulf Coast Association of Geological Societies Convention, p. 349-362.
Roden, R., Forrest, M., and Holeywell, R., 2005, The impact of seismic amplitudes on prospect risk analysis: The Leading Edge, 24, 706-711.
Rubey, W., and Hubbert, M. K., 1959, Role of fluid pressure in mechanics of overthrust faulting, II, Geol. Soc. Amer. Bull., 70, 167-206.
Ruger, A., 2002, Reflection coefficients and azimuthal AVO analysis in anisotropic media: Geophysical Monograph Series No. 10, Society of Exploration Geophysicists, Tulsa, OK, 189 pages.
Rutherford, S.R., and Williams, R.H., 1989, Amplitude-versus-offset in gas sands: Geophysics, 54, 680-688.
Santamarina, J. C., Francisca, F., Yun, T. S., Lee, J. Y., Martin, A. I., and Ruppel, C., 2004, Mechanical, thermal, and electrical properties of hydrate-

bearing sediments: AAPG Hedberg Conference on Hydrates, Victoria, B.C., Canada, poster presentation.
Schlumberger Wireline Services, 1998, Log interpretation principles/applications: Schlumberger Educational Services, Houston, TX.
Sen, P. N., Scala, C., and Cohen, M. H., 1981, A self similar model of sedimentary rocks with application to the dielectric constant of fused glass beads: Geophysics, 46, 781-796.
Sloan, E. D., 1998, Clathrate hydrate of natural gas, 2nd ed.: Marcel Dekker.
Tarantola, A., 1987, Inverse problem theory: Elsevier Science B. V.
Waite, W. F., Winters, W. J., and Mason, D. H., 2004, Methane hydrate formation in partially water-saturated Ottawa sand: American Mineralogist, 89, 1202-1207.
Walton, K., 1987, The effective elastic moduli of a random packing of spheres: J. Mech. Phys. Solids, 35, 213-226.
Wempe, W., 2000, Predicting flow properties using geophysical data—improving aquifer characterization: Stanford University, Ph.D. dissertation.
Winters, W. J., Pecher, I. A., Waite, W. F., and Mason, D. H., 2004, Physical properties and rock-physics models of sediment containing natural and laboratory-formed methane gas hydrate: American Mineralogist, 89, 1221-1227.
Wood, W. T., Stoffa, P. L., and Shipley, T. H., 1994, Quantitative detection of methane hydrate through high-resolution seismic velocity analysis: J. Geophys. Res., 99, 9681-9695.
Yuan, T. S., Hyndman, G. D., Spence, G. D., and Desmons, B., 1996, Seismic velocity increase and deep-sea gas hydrate concentration above a bottom-simulating reflector on the northern Cascadia continental slope: J. Geophys. Res., 101, 13655-13671.
Yun, T. S., Francisca, F. M., Santamarina, J. C., and Ruppel, C., 2005, Compressional and shear wave velocities in uncemented sediment containing gas hydrate: Geophys. Res. Lett., 32, L10609-L10613.
Zillmer, M., 2006, A method for determining gas-hydrate or free-gas saturation of porous media from seismic measurements: Geophysics, 71, N21-N32, 10.1190/1.2192910.
Zimmer, M. A., 2003, Controls on the seismic velocities of unconsolidated sands: Measurements of pressure, porosity and compaction effects, Ph.D. Thesis, Stanford University.
Zoeppritz, K., 1919, Erdbebenwellen VIIIB, On the reflection and propagation of seismic waves: Gottinger Nachrichten, I, 66-84.

Acronyms and Abbreviations

4C: four component
AVA: amplitude versus angle
c_{gh}: hydrate concentration
BHSZ: base hydrate stability zone
CDP: common depth point
f: (1) volume fraction, or (2) frequency
G: shear modulus
GR: gamma ray
K: bulk modulus
LSU: Louisiana State University
MMS: Minerals Management Service
MWD: measurement while drilling
OBC: ocean bottom cable
OWL: Offshore Well Logs (a commercial database)
P-P: seismic mode involving downgoing and upgoing P waves
P-SV: seismic mode involving a downgoing P wave and an upgoing SV wave
SV: converted shear wave
V_P: P-wave velocity
V_S: S-wave velocity
VSP: vertical seismic profile
X: horizontal inline geophone
Y: horizontal crossline geophone
Z: vertical geophone
Φ: porosity
ρ: density

Appendix A

Seismic Analyses, Study Site 1, Typhoon Field Area

This appendix documents the results of our research analyses along the OBC profiles that traversed the study area spanning Typhoon Field. The location and line numbers of the OBC profiles involved in this study site are defined on the map included as Figure A1.

The graphical format used to display the research findings is discussed in the text associated with Figure 1.15 in Chapter 1 and will not be repeated here. In each figure, the data are presented as a 2-page montage. The first page (part **a** of each figure) shows the P-P and P-SV images side-by-side for ease of comparison, followed by illustrations of the interpreted depth-equivalent horizons in P-P image space and P-SV image space, and the V_P and V_S interval velocities determined along the profile. The second page (part **b** of each figure) is a repeat of the first page with the exception that the V_S velocity panel (lower right on the bottom row) is replaced with a display of the estimated hydrate concentration along the profile.

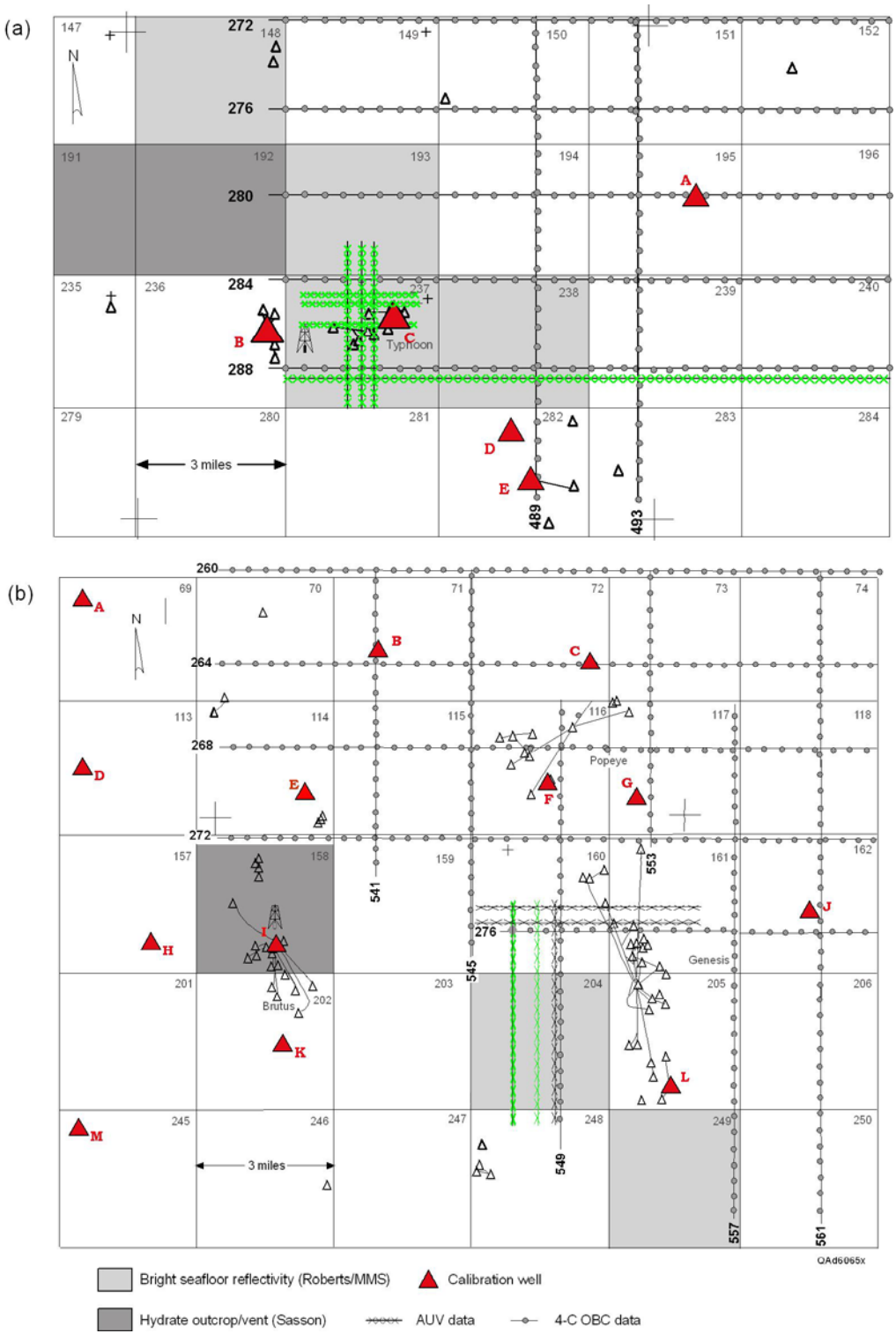

Figure A1. Map showing the locations and line numbers of 4C OBC seismic profiles that traverse (a) Study Site 1, Typhoon Field area, and (b) Study Site 2 that includes the Genesis Field area.

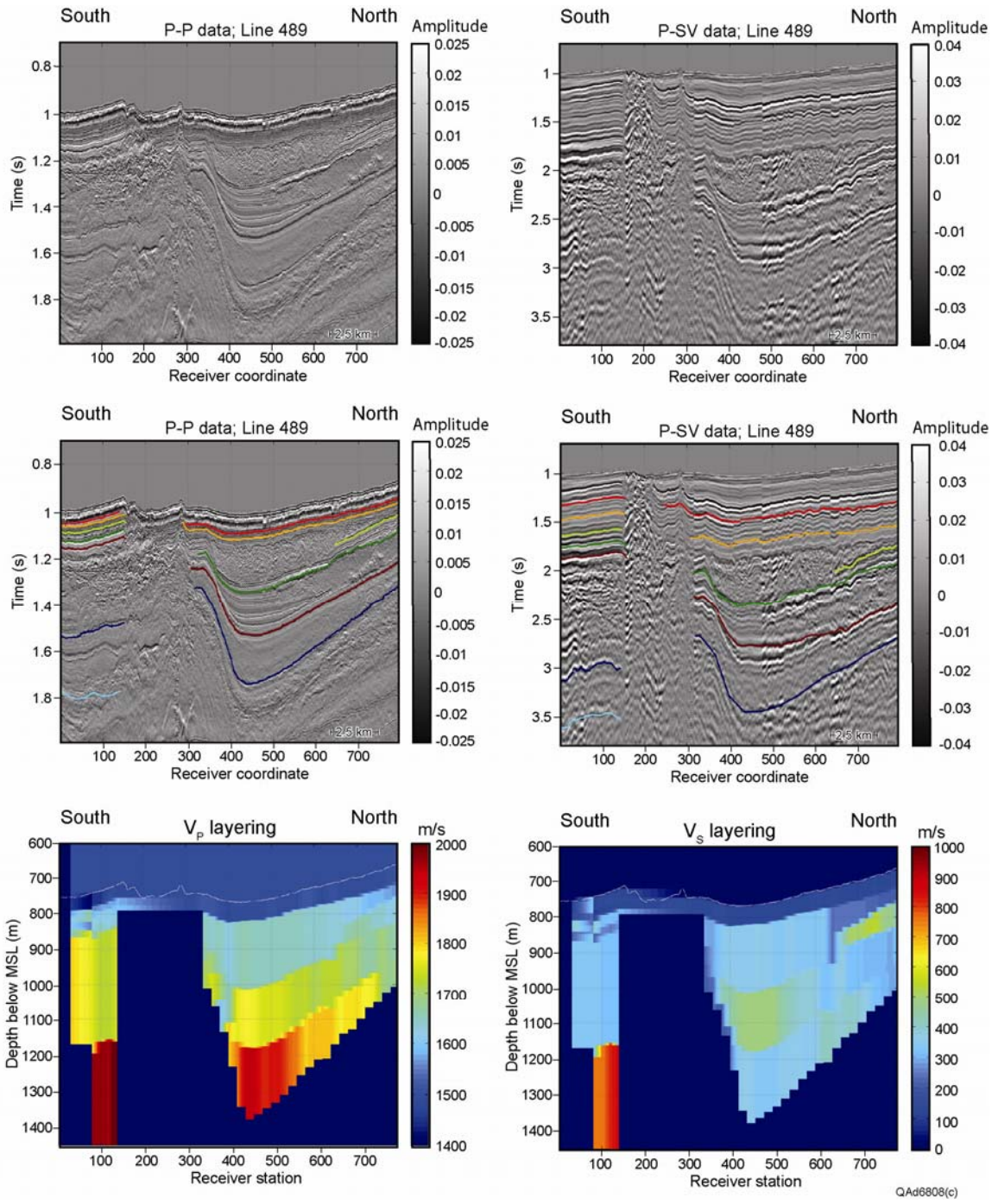

Figure A2a. Research results along profile 489, Study Site 1, Typhoon Field area.

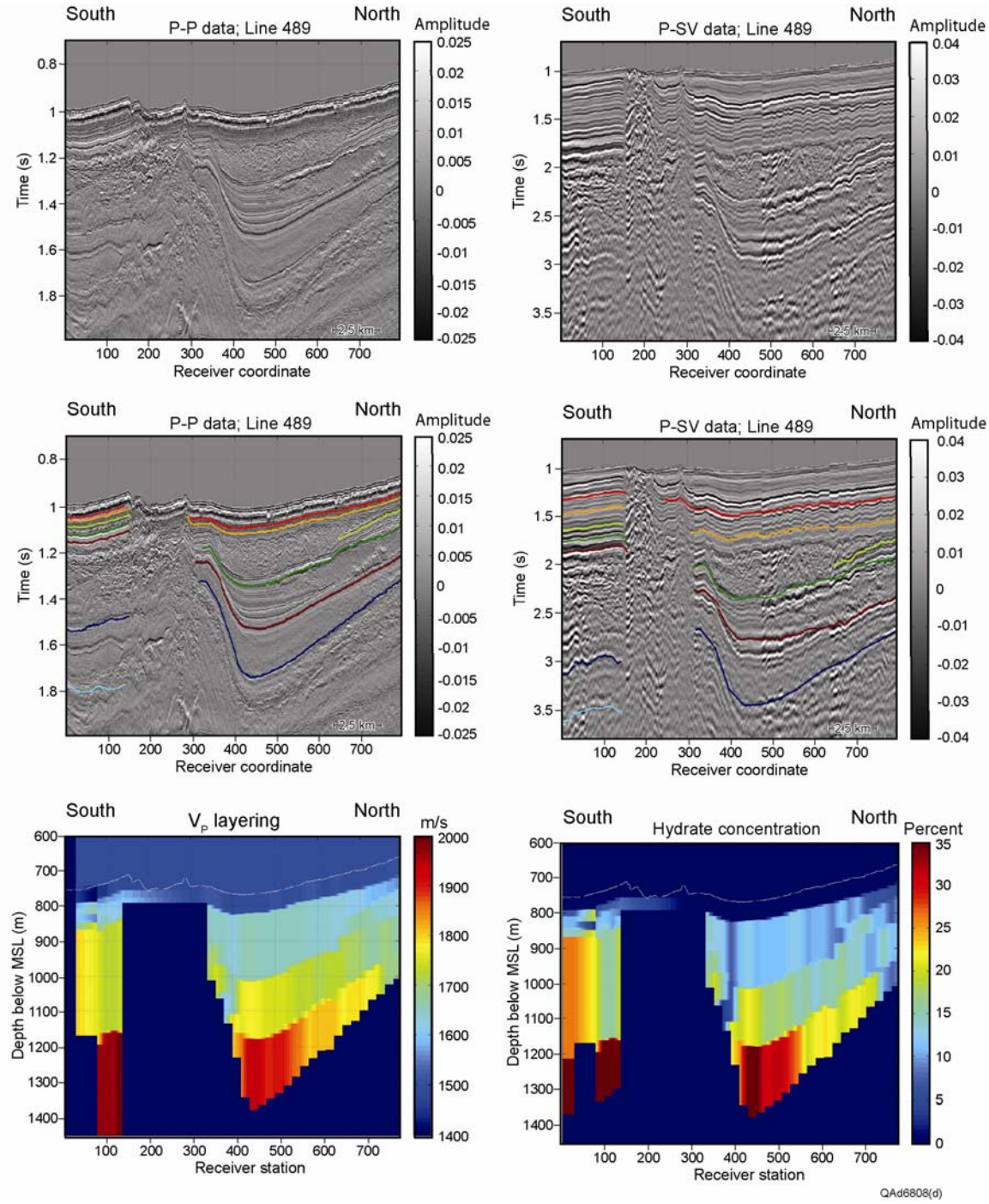

Figure A2b. Research results along profile 489, Study Site 1, Typhoon Field area.

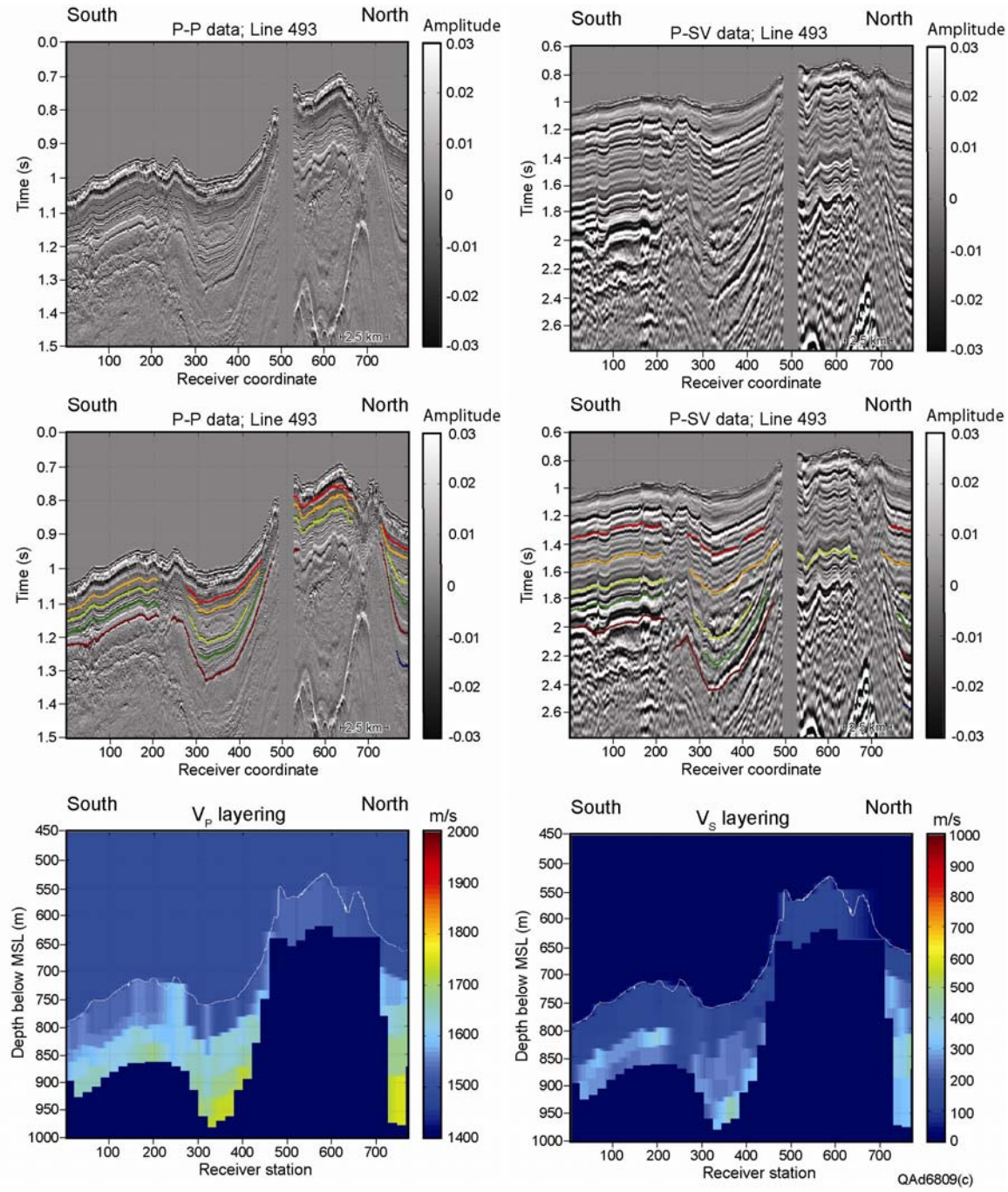

Figure A3a. Research results along profile 493, Study Site 1, Typhoon Field area.

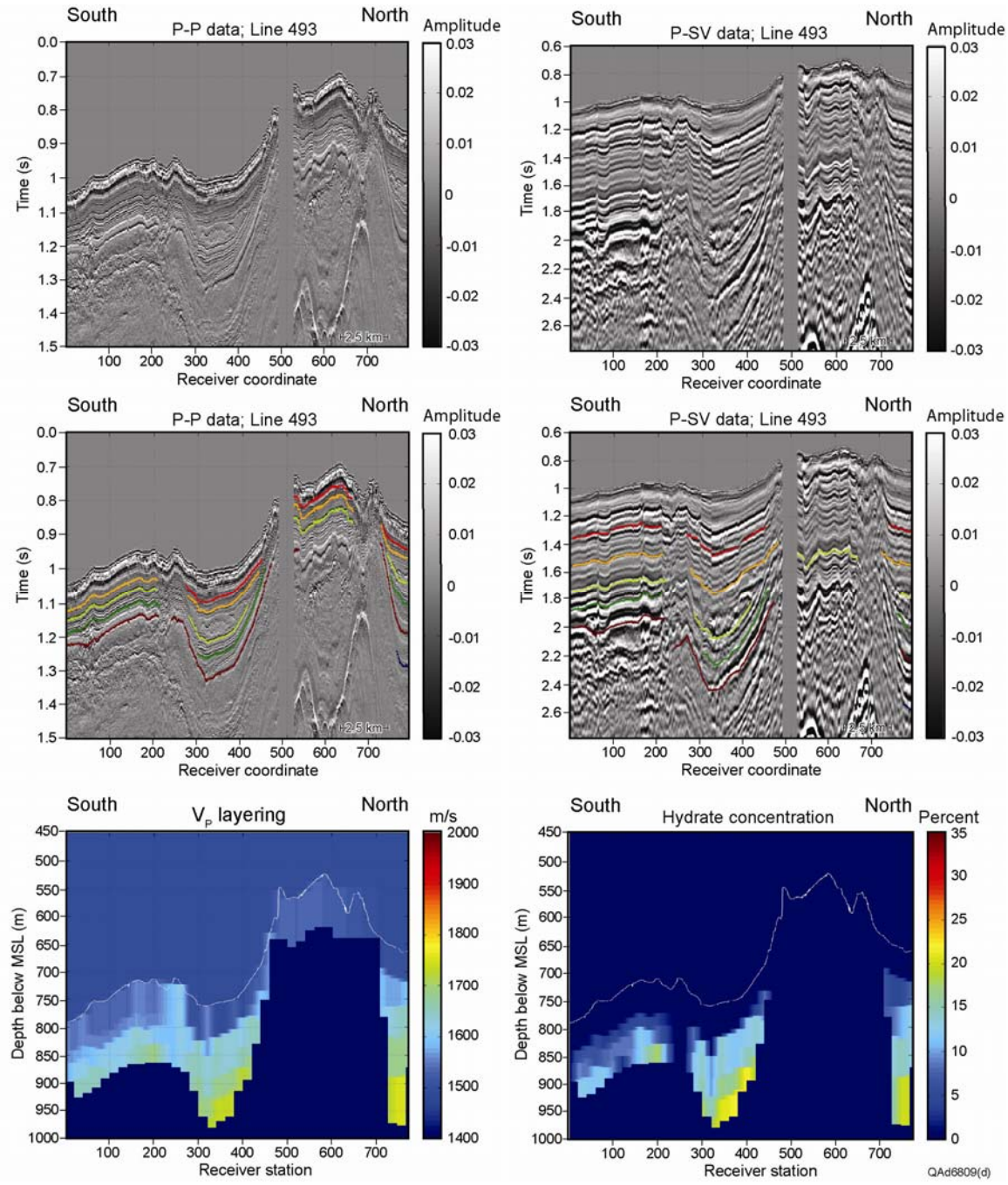

Figure A3b. Research results along profile 493, Study Site 1, Typhoon Field area.

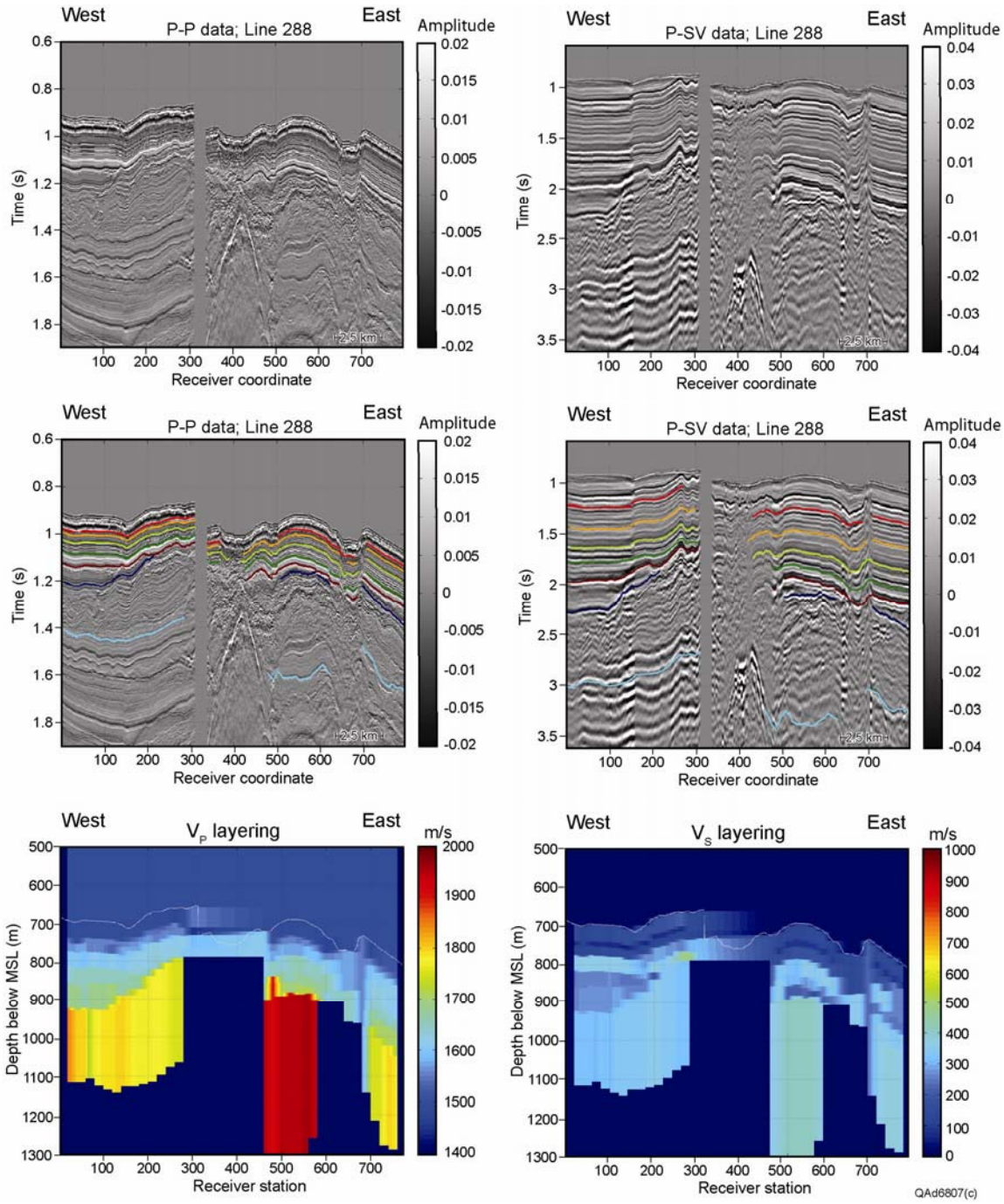

Figure A4a. Research results along profile 288, Study Site 1, Typhoon Field area.

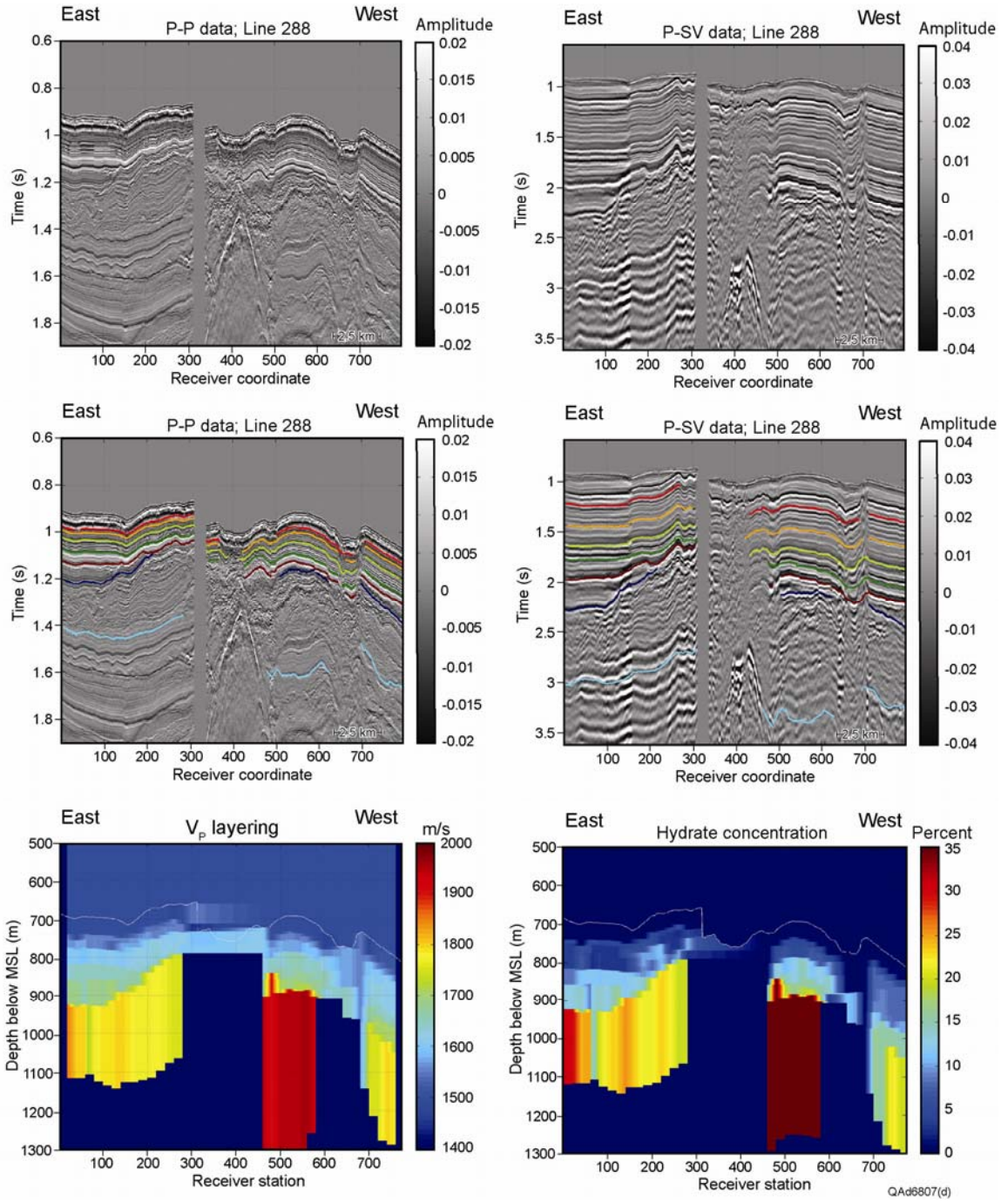

Figure A4b. Research results along profile 288, Study Site 1, Typhoon Field area.

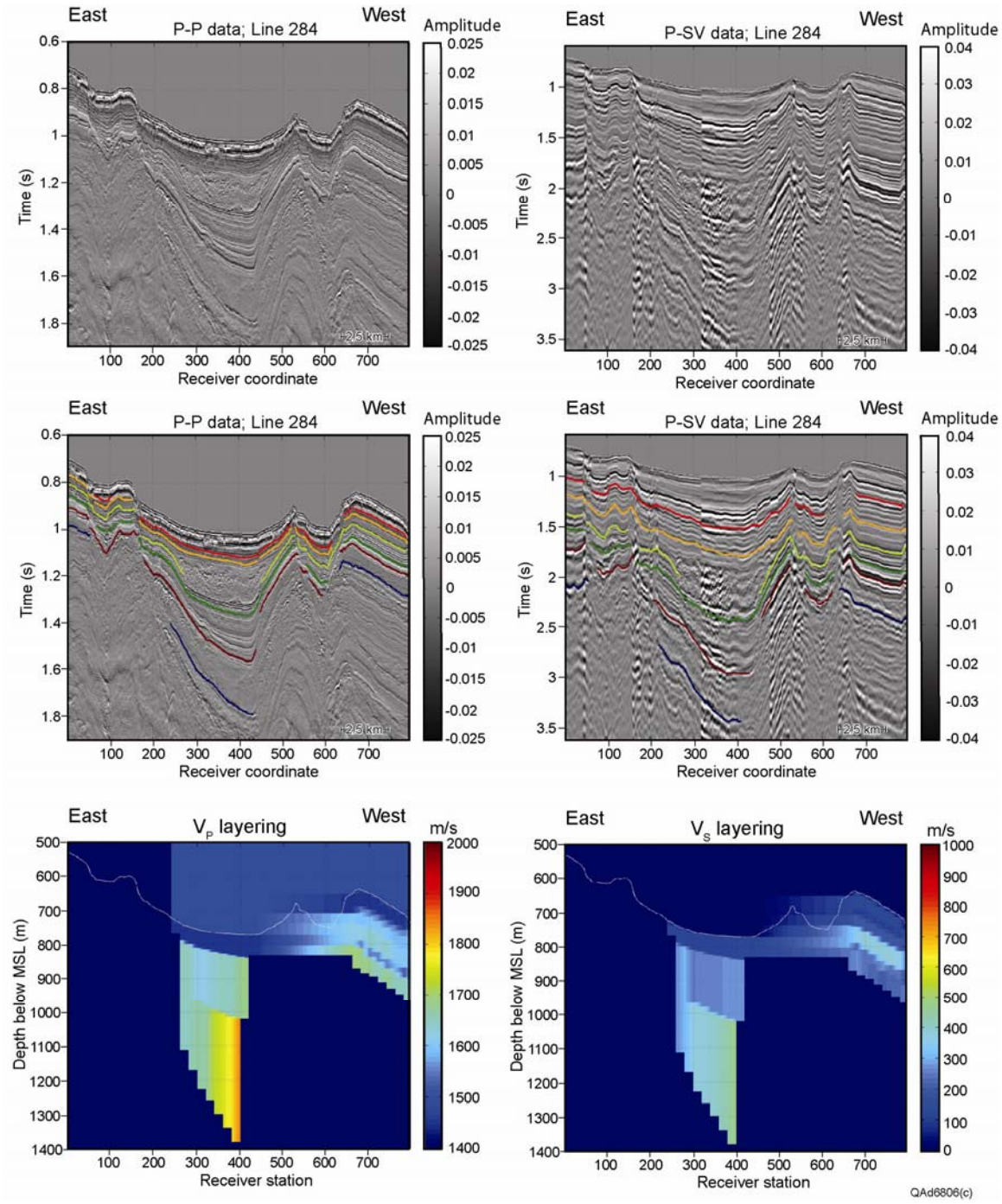

Figure A5a. Research results along profile 284, Study Site 1, Typhoon Field area.

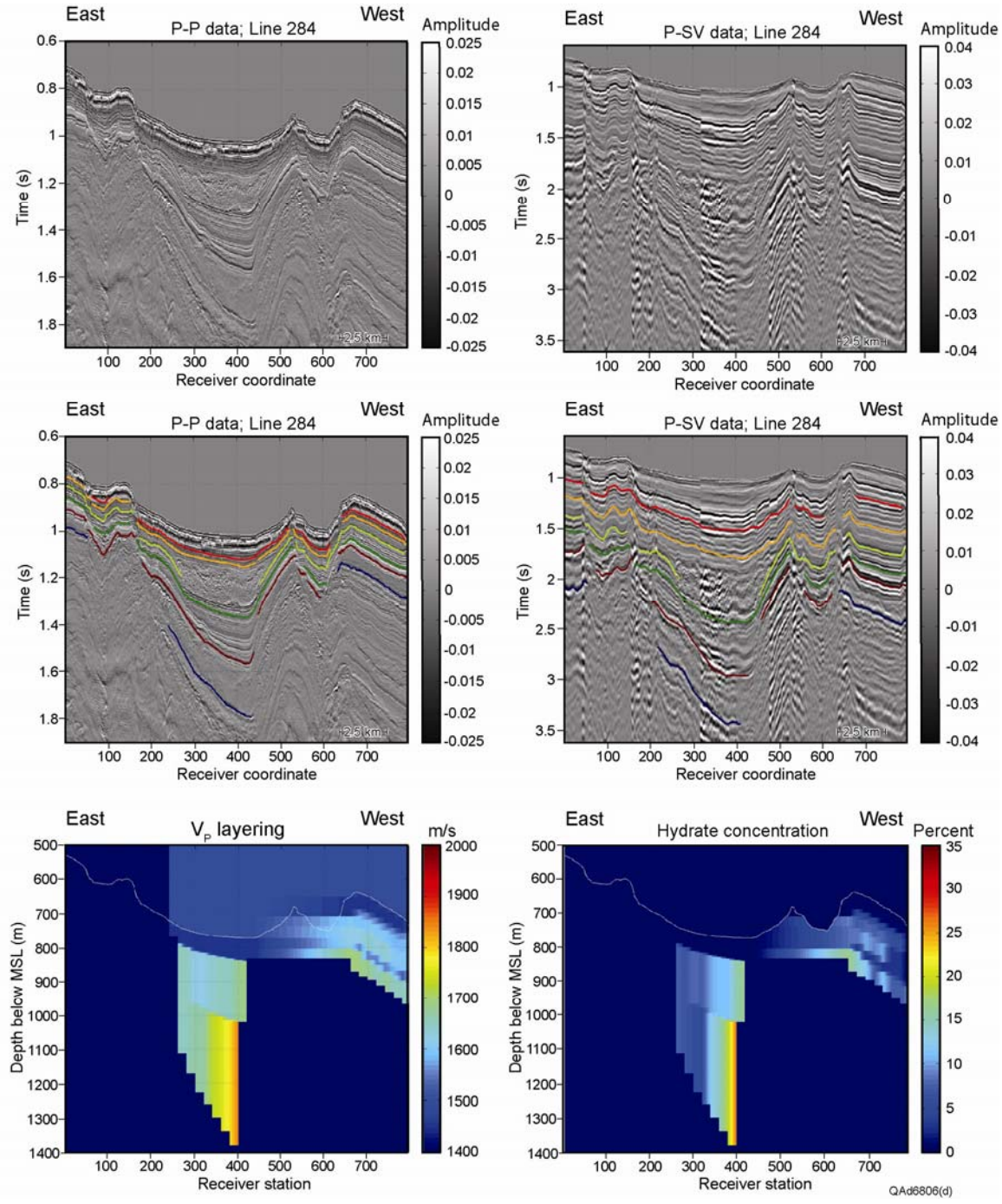

Figure A5b. Research results along profile 284, Study Site 1, Typhoon Field area.

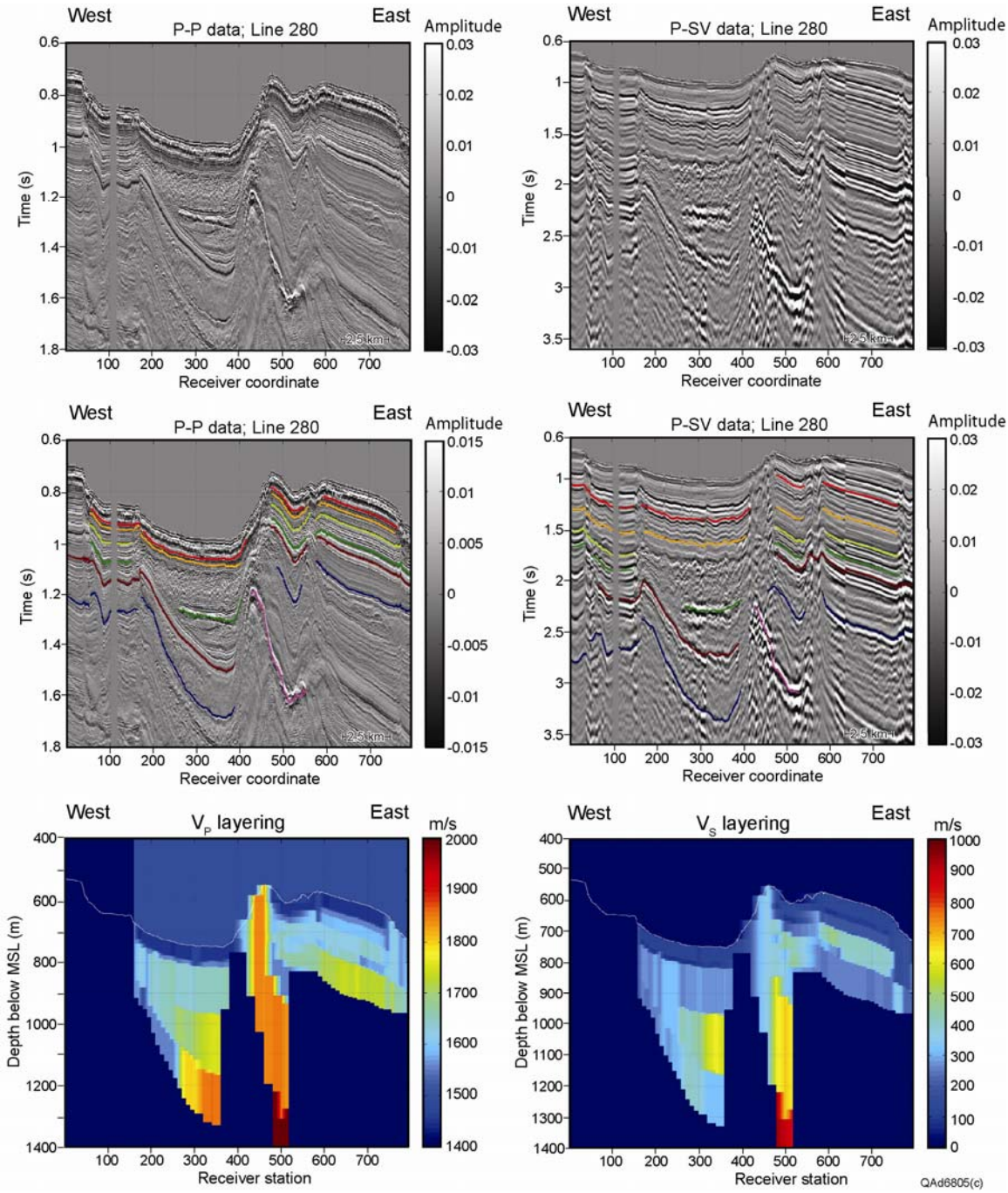

Figure A6a. Research results along profile 280, Study Site 1, Typhoon Field area.

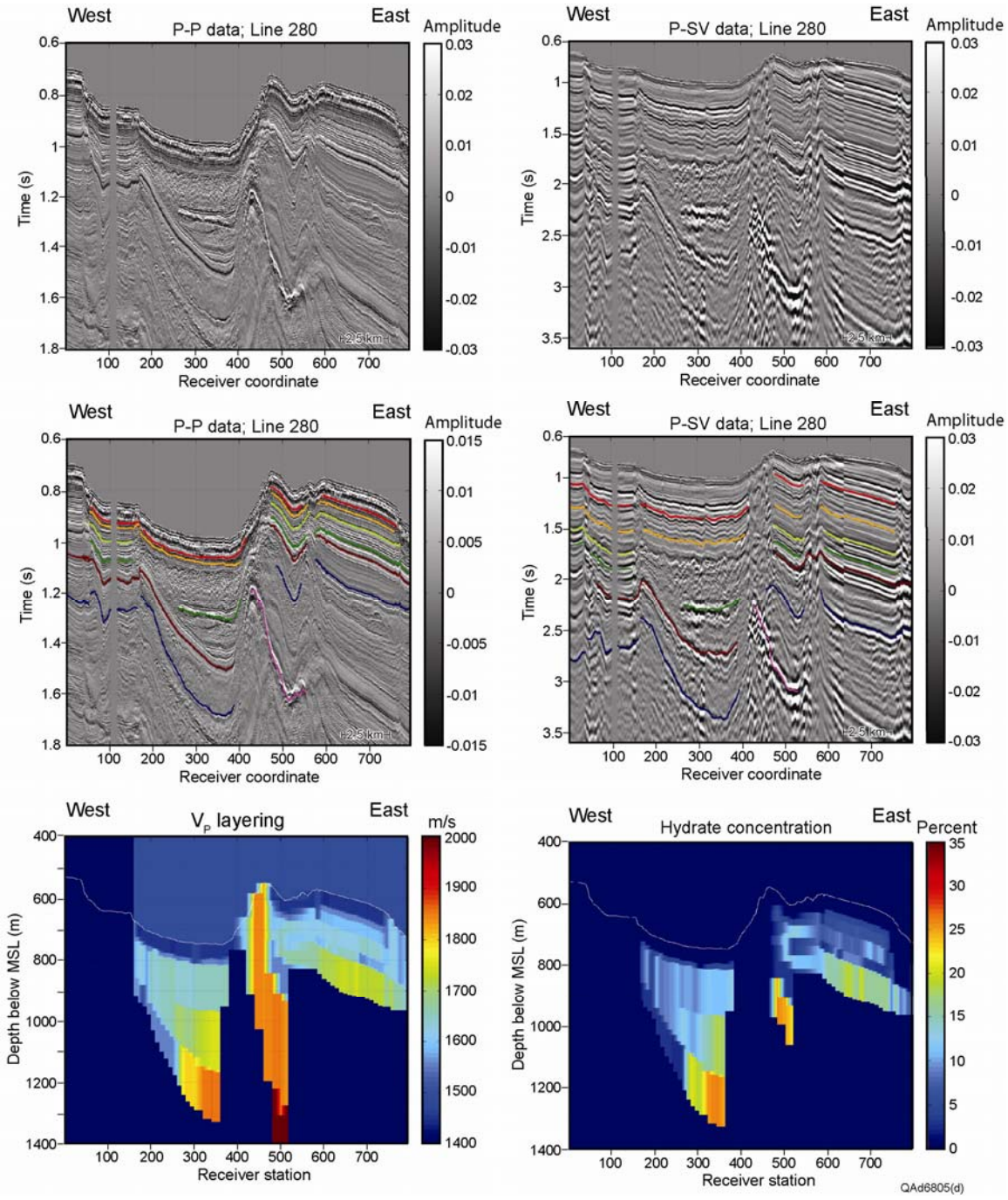

Figure A6b. Research results along profile 280, Study Site 1, Typhoon Field area.

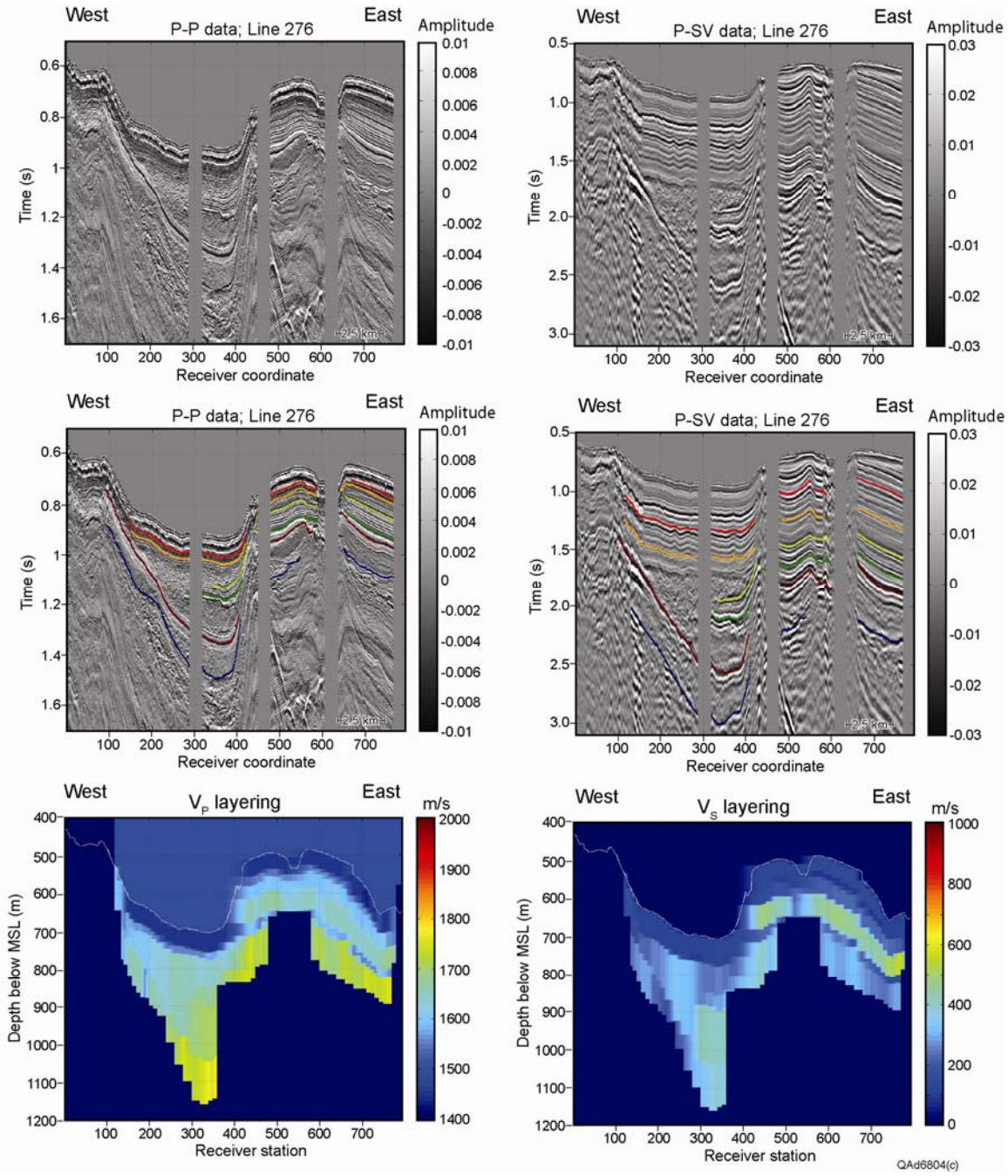

Figure A7a. Research results along profile 276, Study Site 1, Typhoon Field area.

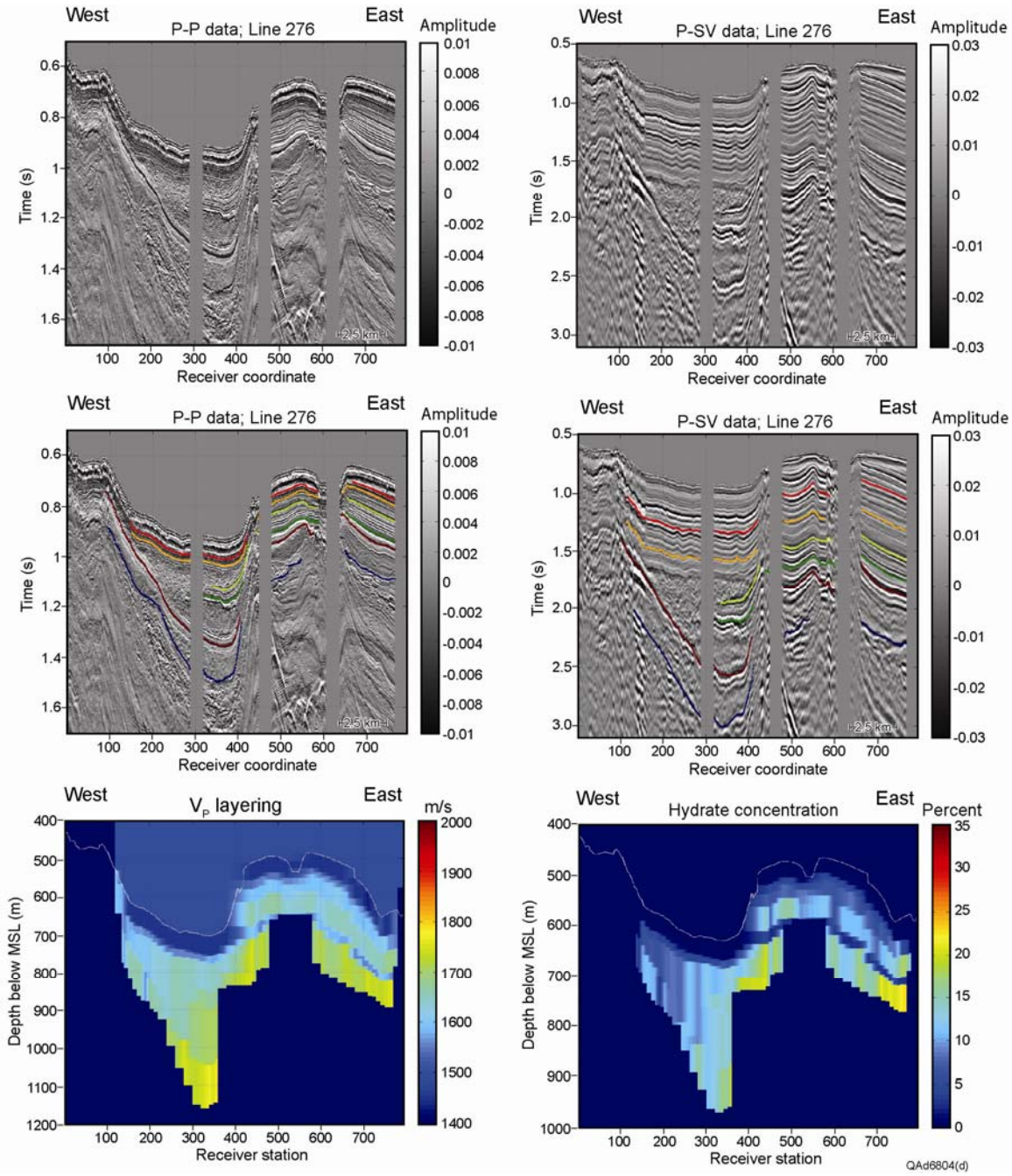

Figure A7b. Research results along profile 276, Study Site 1, Typhoon Field area.

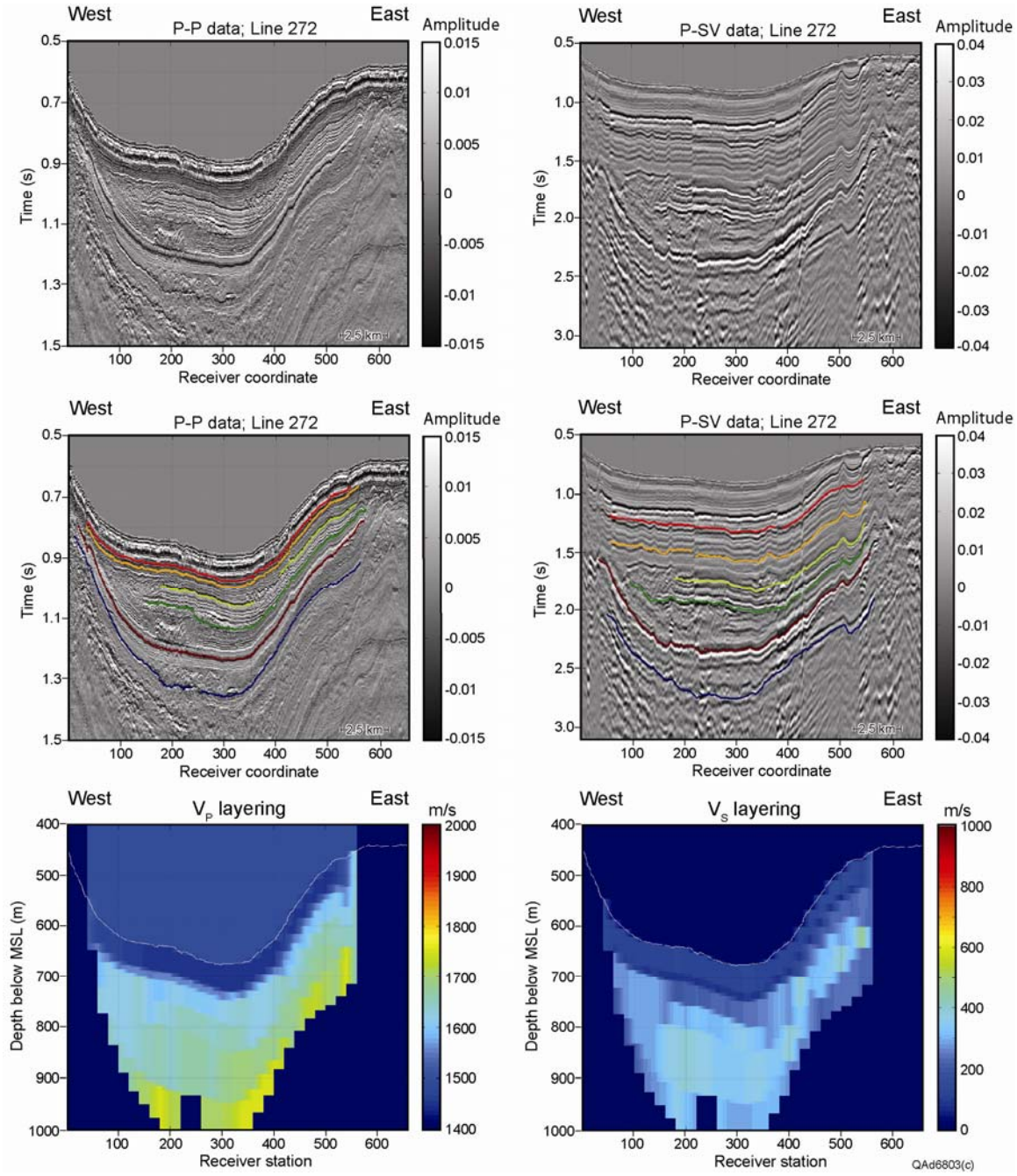

Figure A8a. Research results along profile 272, Study Site 1, Typhoon Field area.

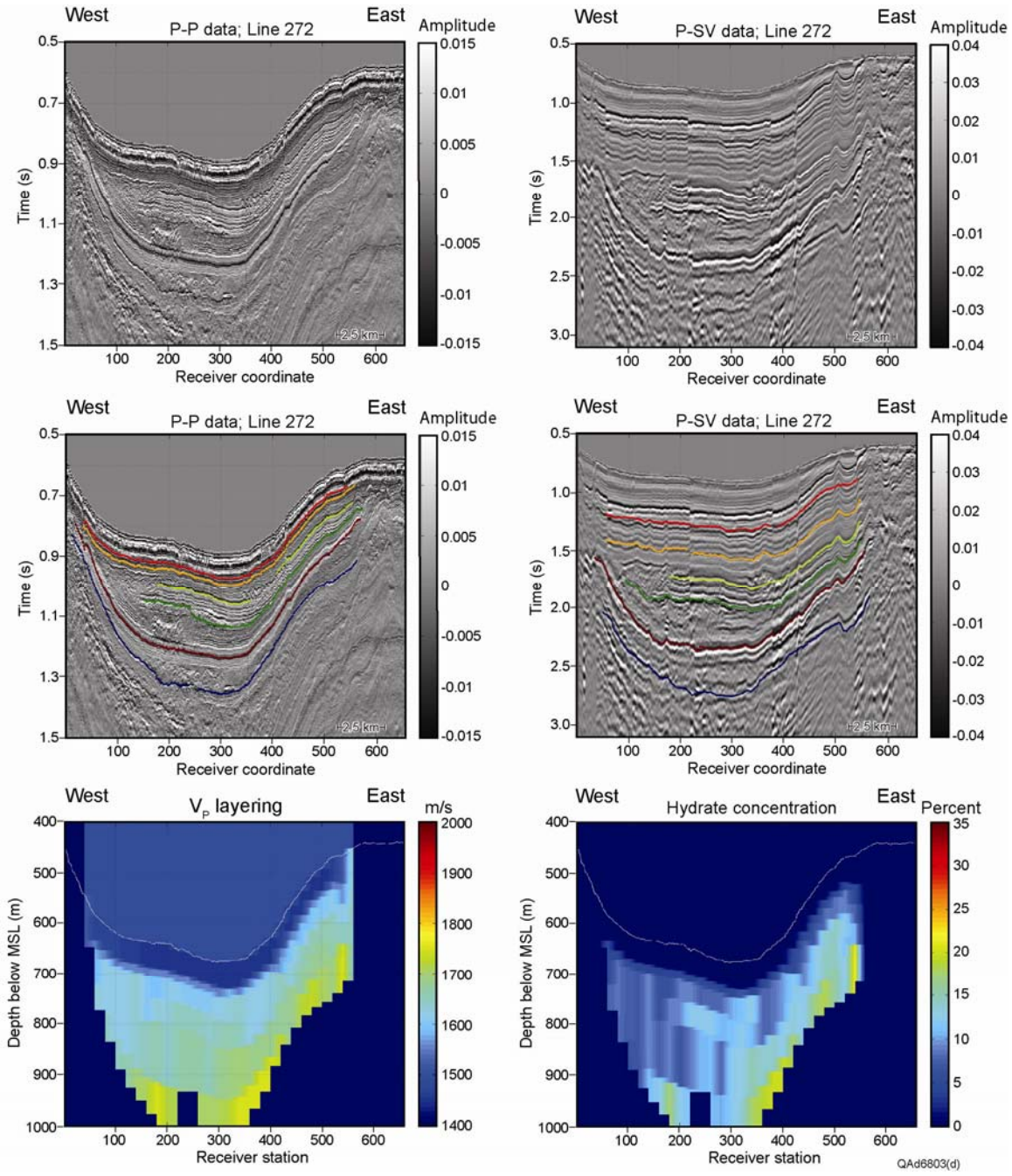

Figure A8b. Research results along profile 272, Study Site 1, Typhoon Field area.

Appendix B

Seismic Analyses, Study Site 2, Genesis Field Area

This appendix documents the results of our research analyses along the OBC profiles that traversed the study area spanning Genesis Field. The location and line numbers of the OBC profiles involved in this study site are defined on the map included as Figure A1 in Appendix A.

The graphical format used to display the research findings is discussed in the text associated with Figure 1.15 in Chapter 1 and will not be repeated here. In each figure, the data are presented as a 2-page montage. The first page (part **a** of each figure) shows the P-P and P-SV images side-by-side for ease of comparison, followed by illustrations of the interpreted depth-equivalent horizons in P-P image space and P-SV image space, and the V_P and V_S interval velocities determined along the profile. The second page (part **b** of each figure) is a repeat of the first page with the exception that the V_S velocity panel (lower right on the bottom row) is replaced with a display of the estimated hydrate concentration along the profile.

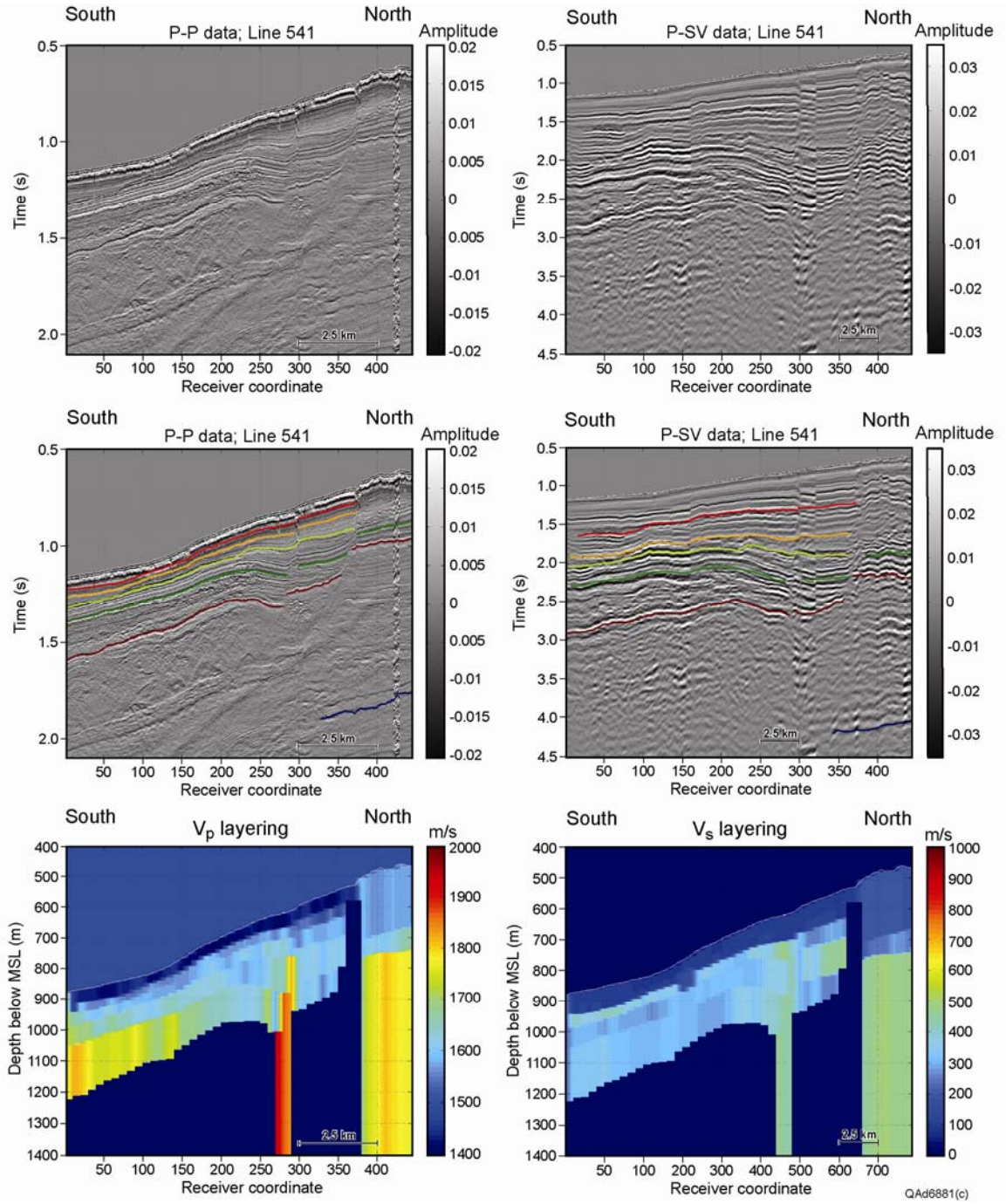

Figure B1a. Research results along profile 541, Study Site 2, Genesis Field area.

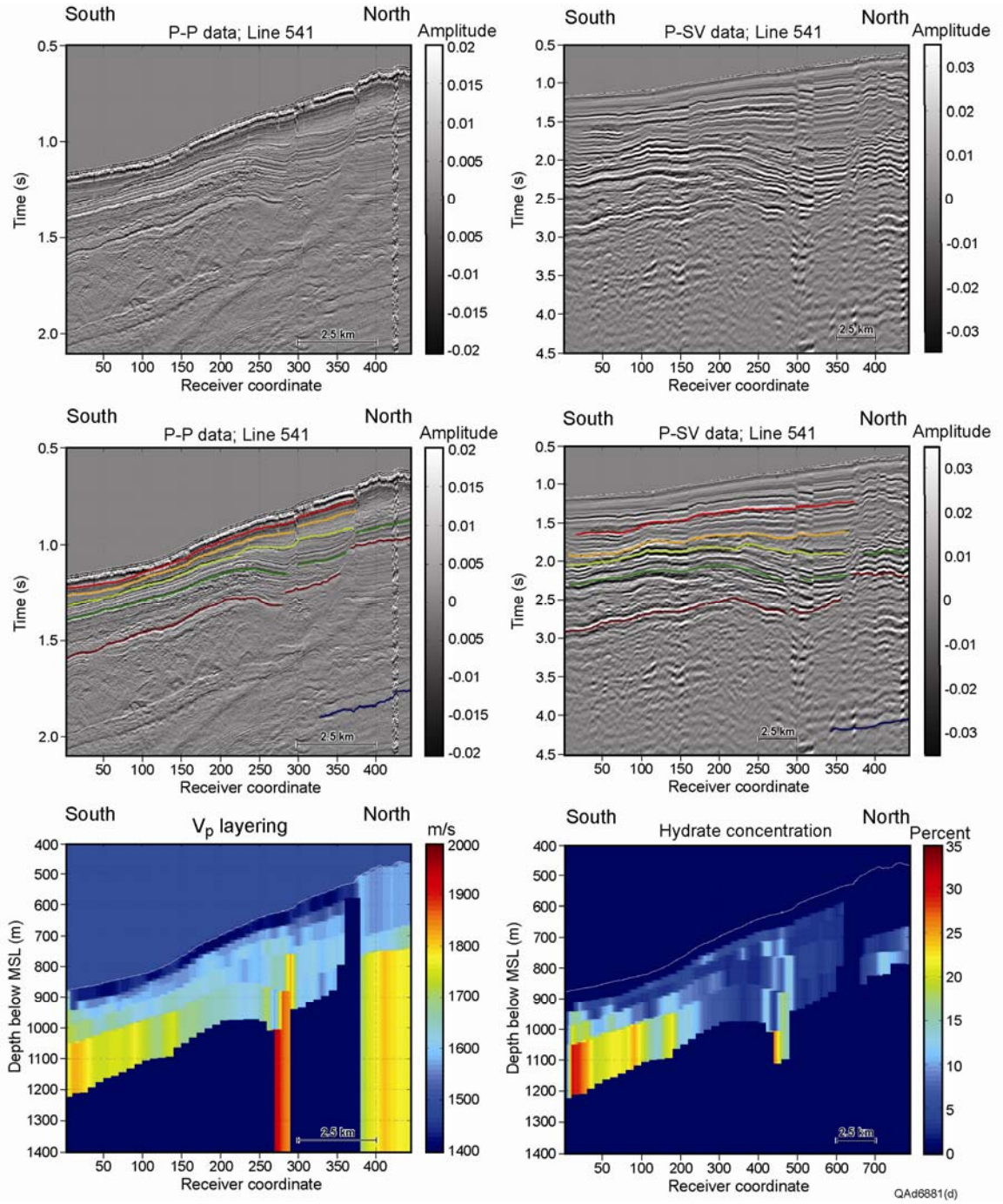

Figure B1b. Research results along profile 541, Study Site 2, Genesis Field area.

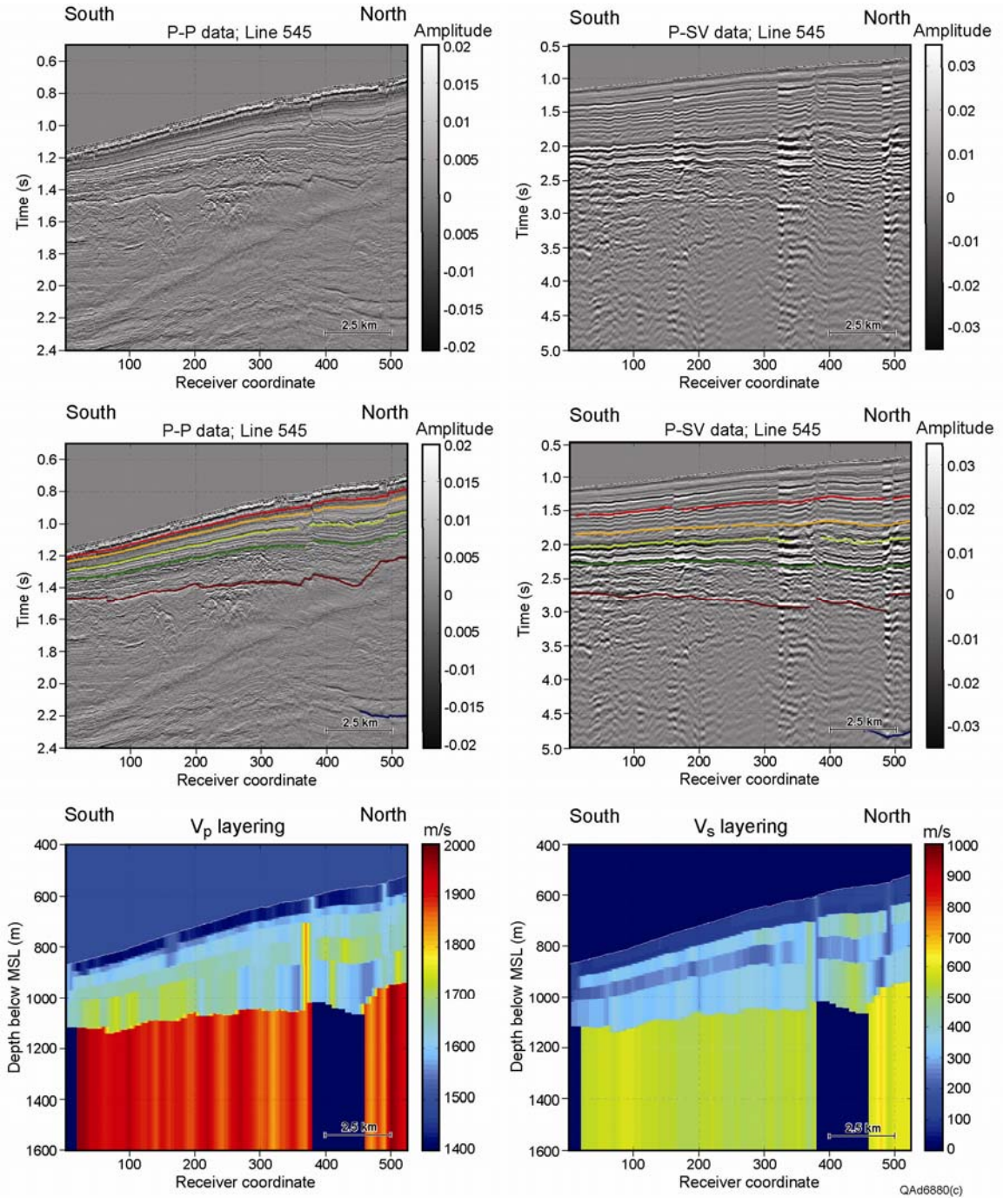

Figure B2a. Research results along profile 545, Study Site 2, Genesis Field area.

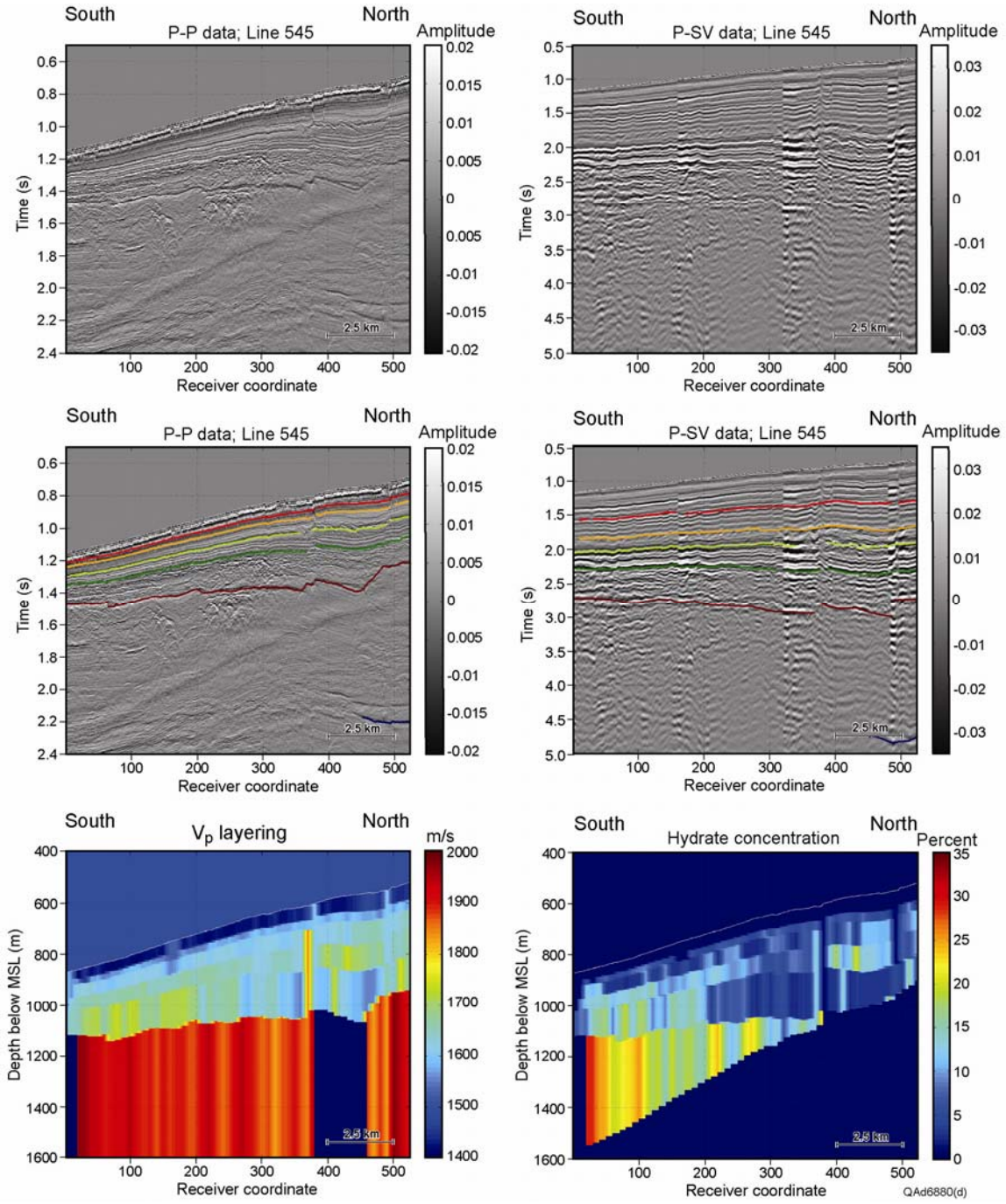

Figure B2b. Research results along profile 545, Study Site 2, Genesis Field area.

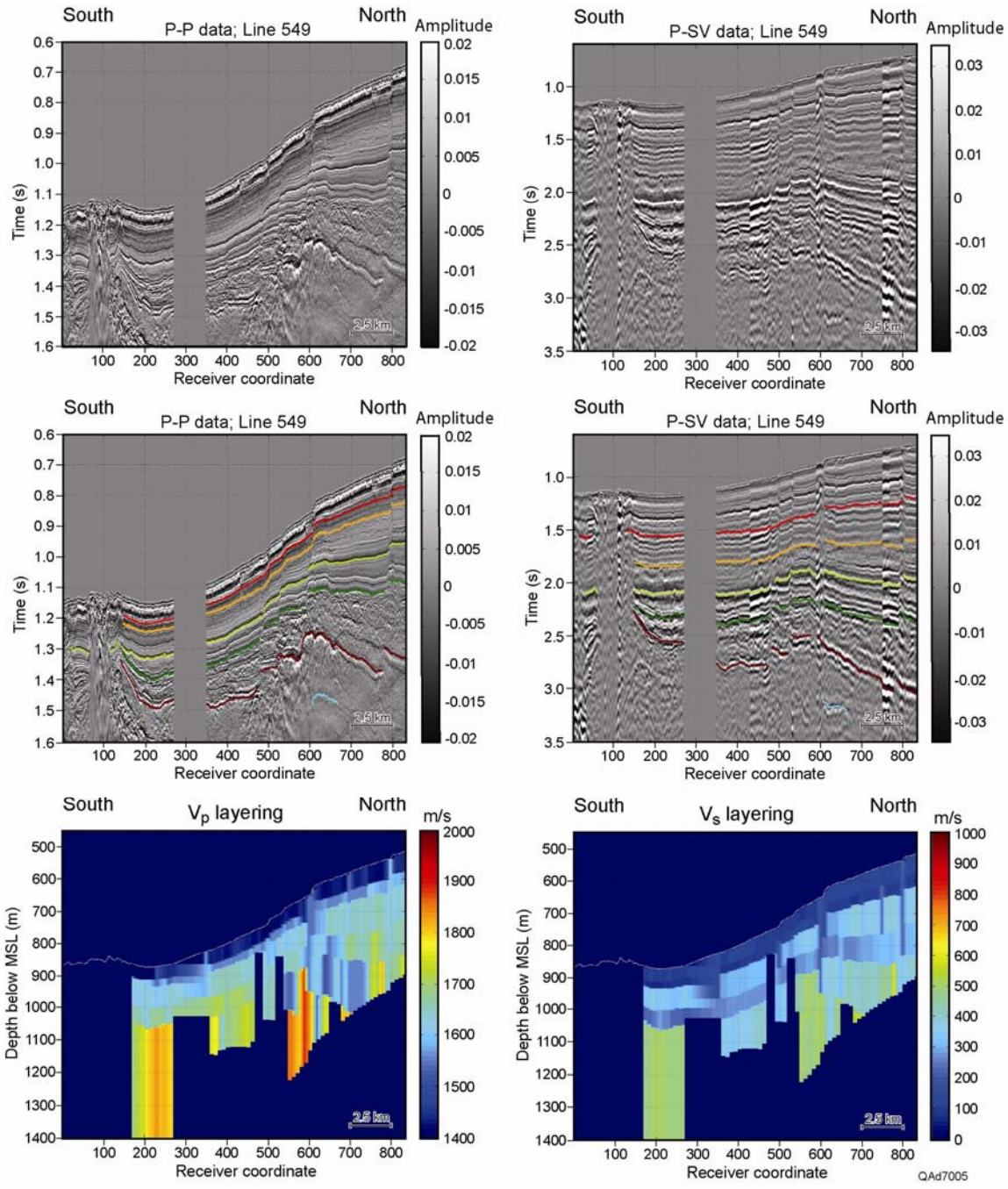

Figure B3a. Research results along profile 549, Study Site 2, Genesis Field area.

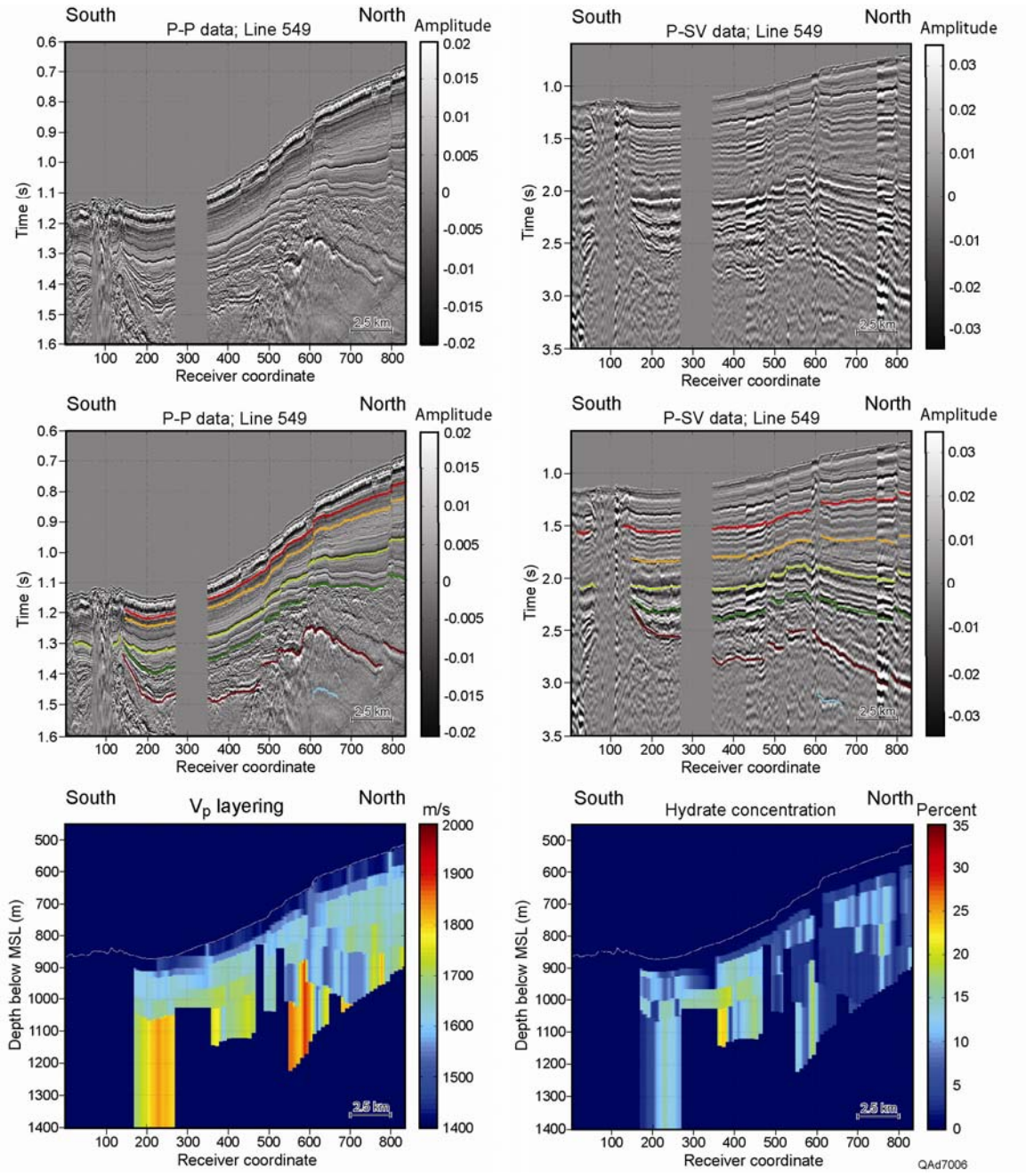

Figure B3b. Research results along profile 549, Study Site 2, Genesis Field area.

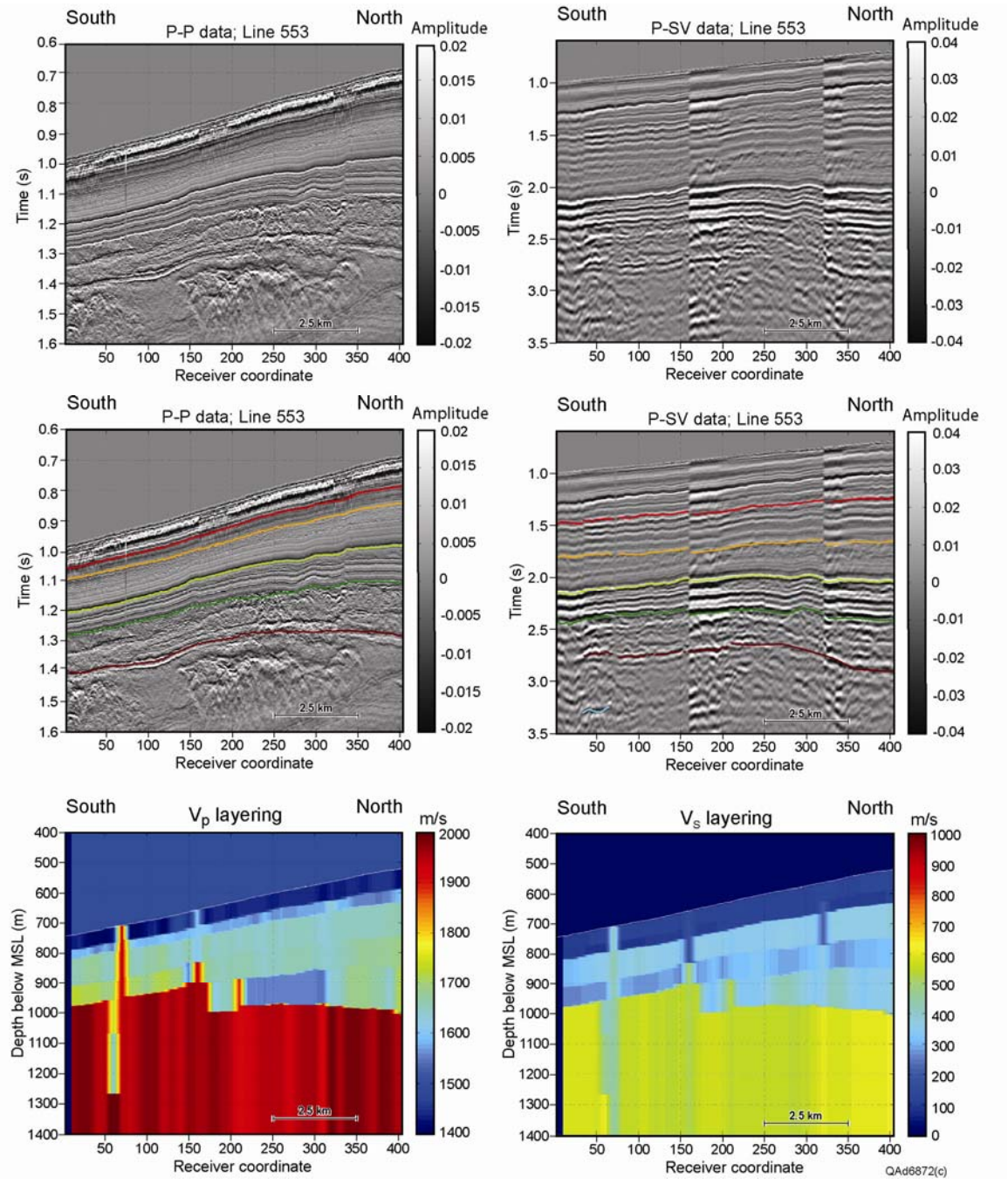

Figure B4a. Research results along profile 553, Study Site 2, Genesis Field area.

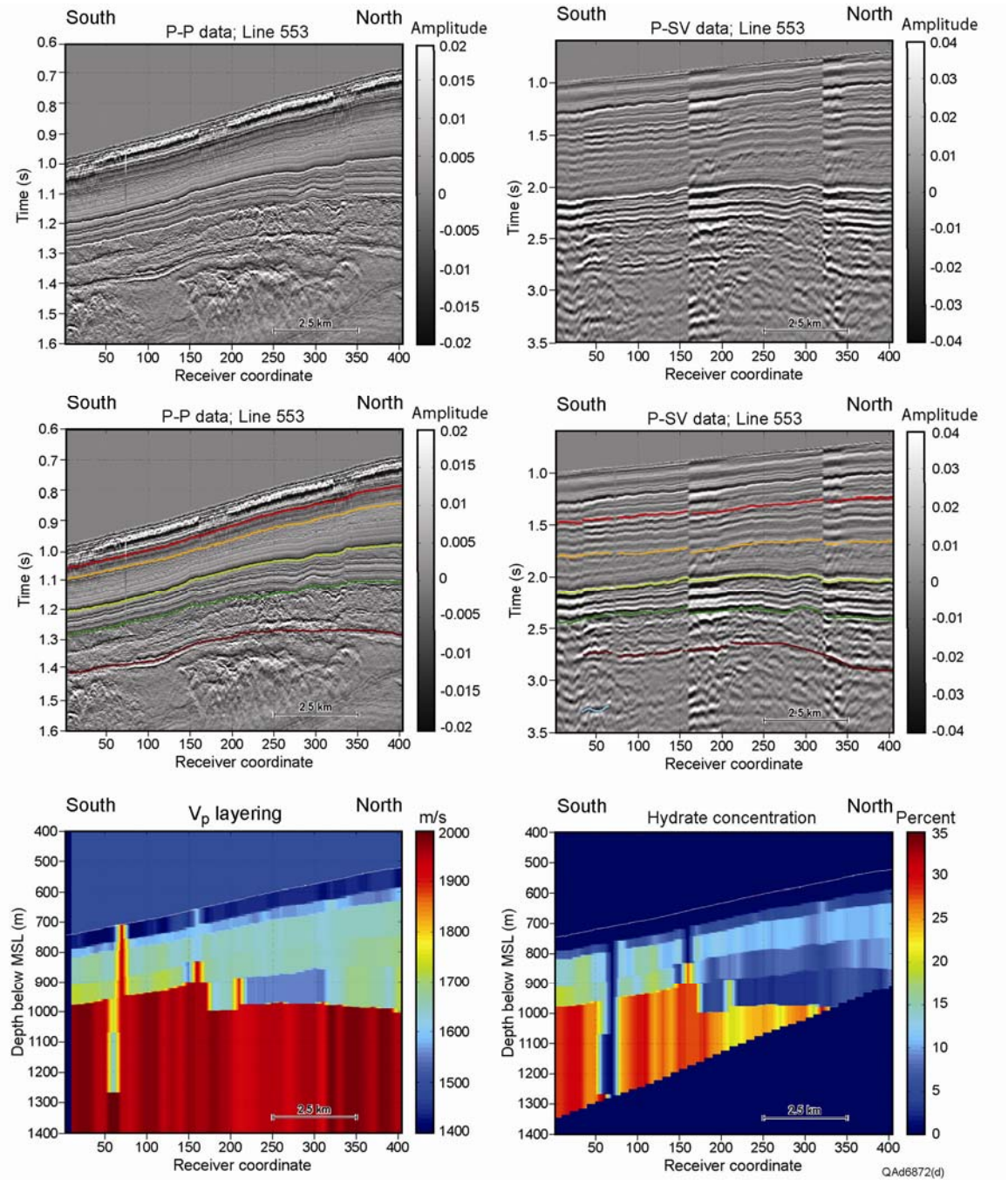

Figure B4b. Research results along profile 553, Study Site 2, Genesis Field area.

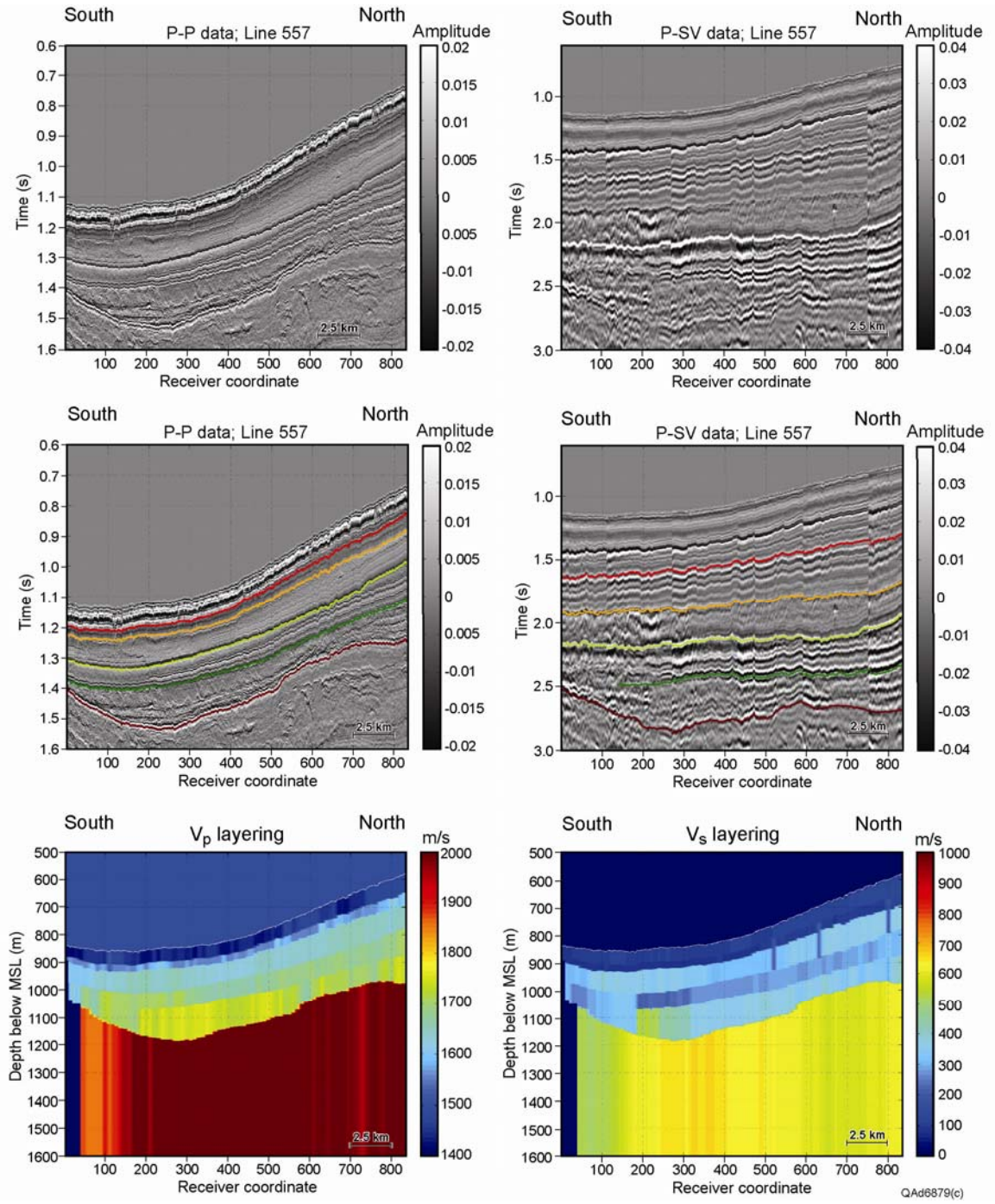

Figure B5a. Research results along profile 557, Study Site 2, Genesis Field area.

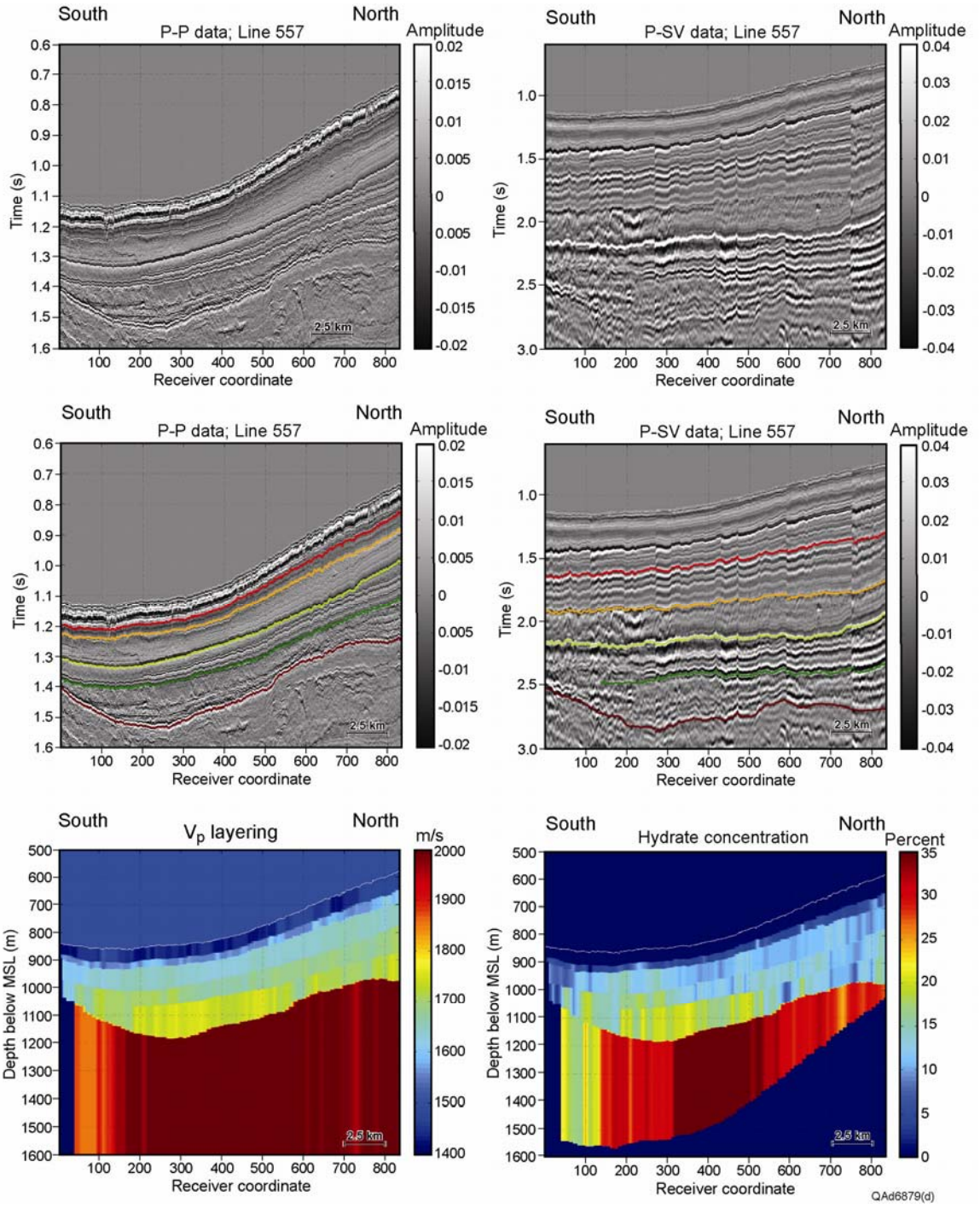

Figure B5b. Research results along profile 557, Study Site 2, Genesis Field area.

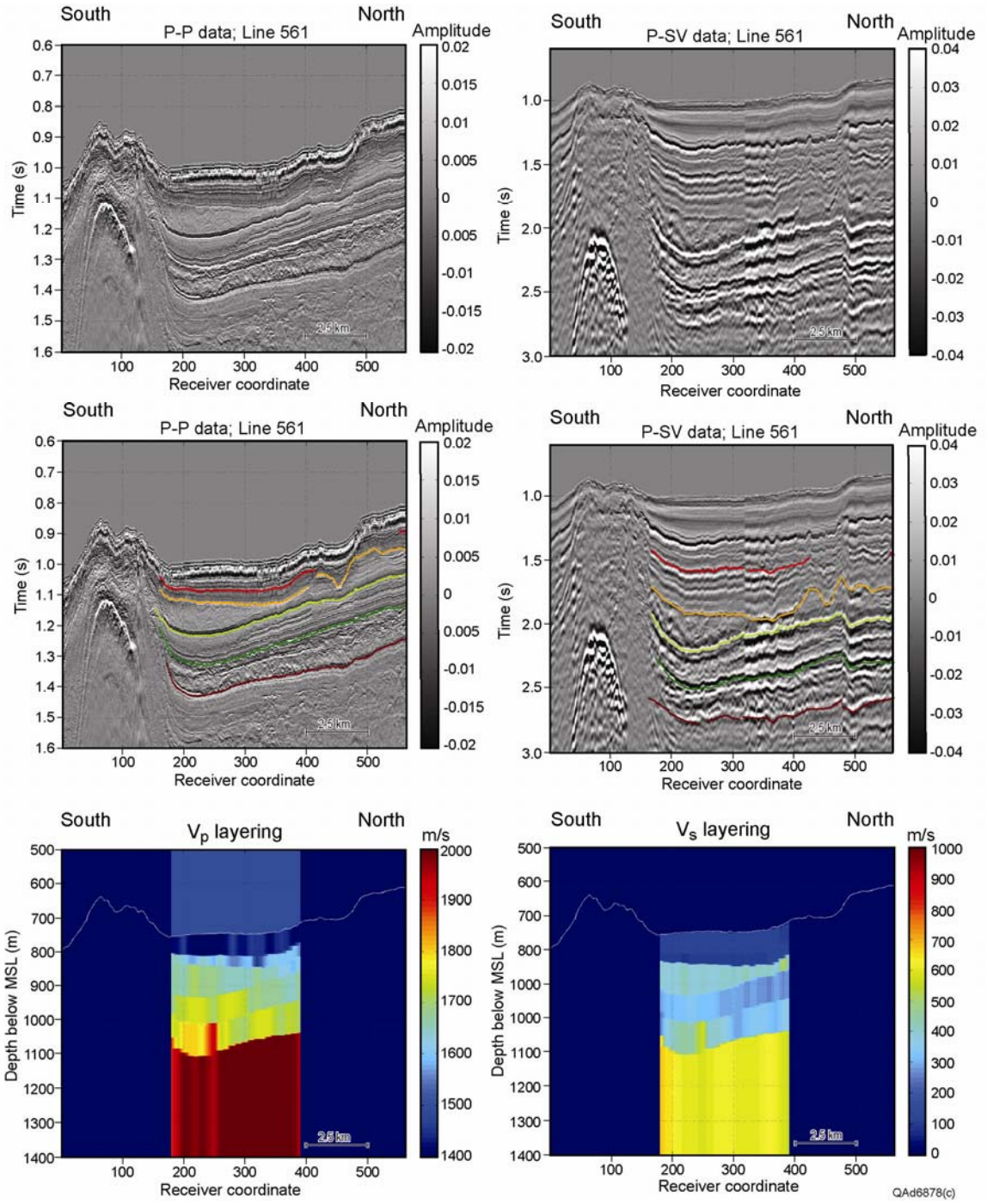

Figure B6a. Research results along profile 561, Study Site 2, Genesis Field area.

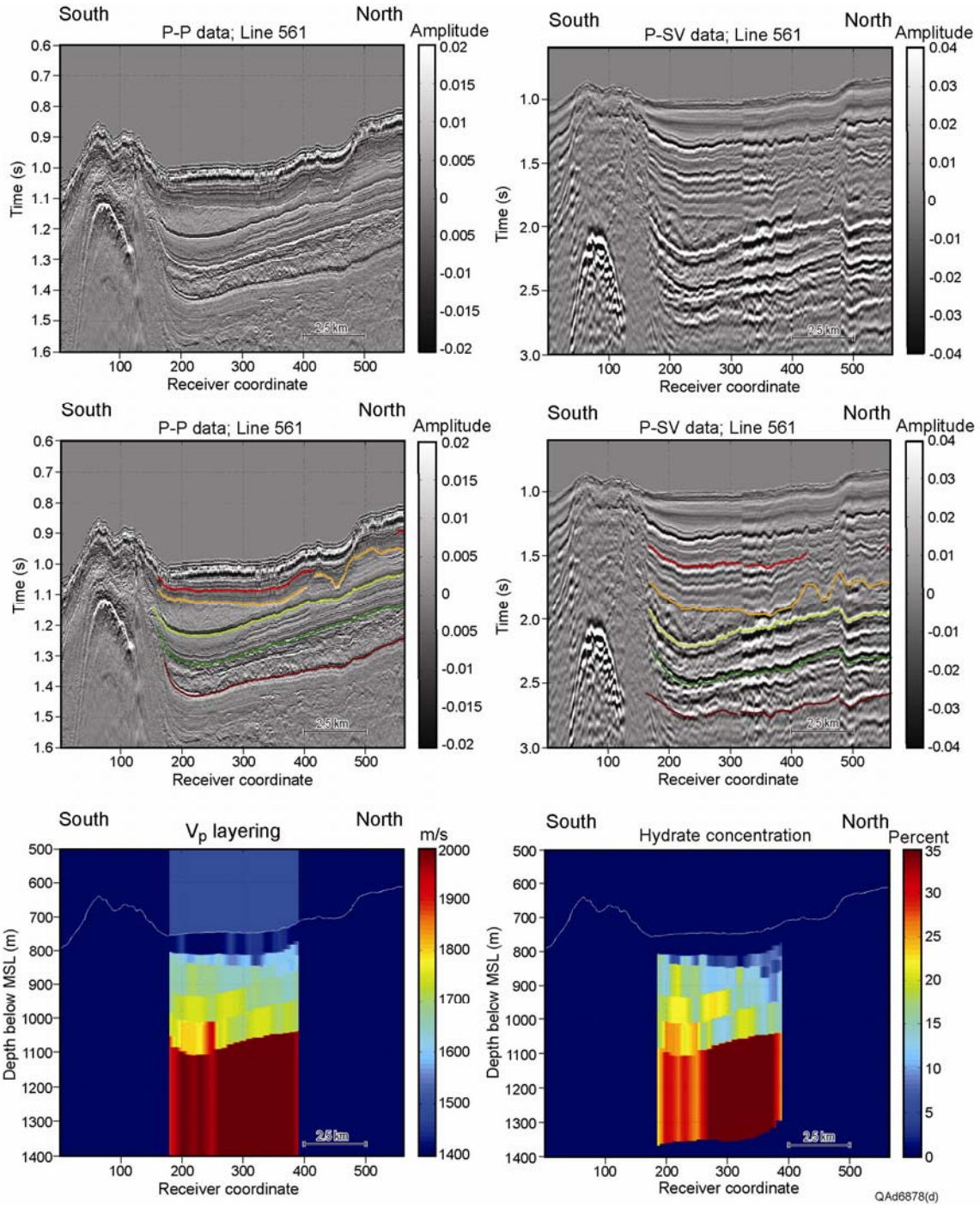

Figure B6b. Research results along profile 561, Study Site 2, Genesis Field area.

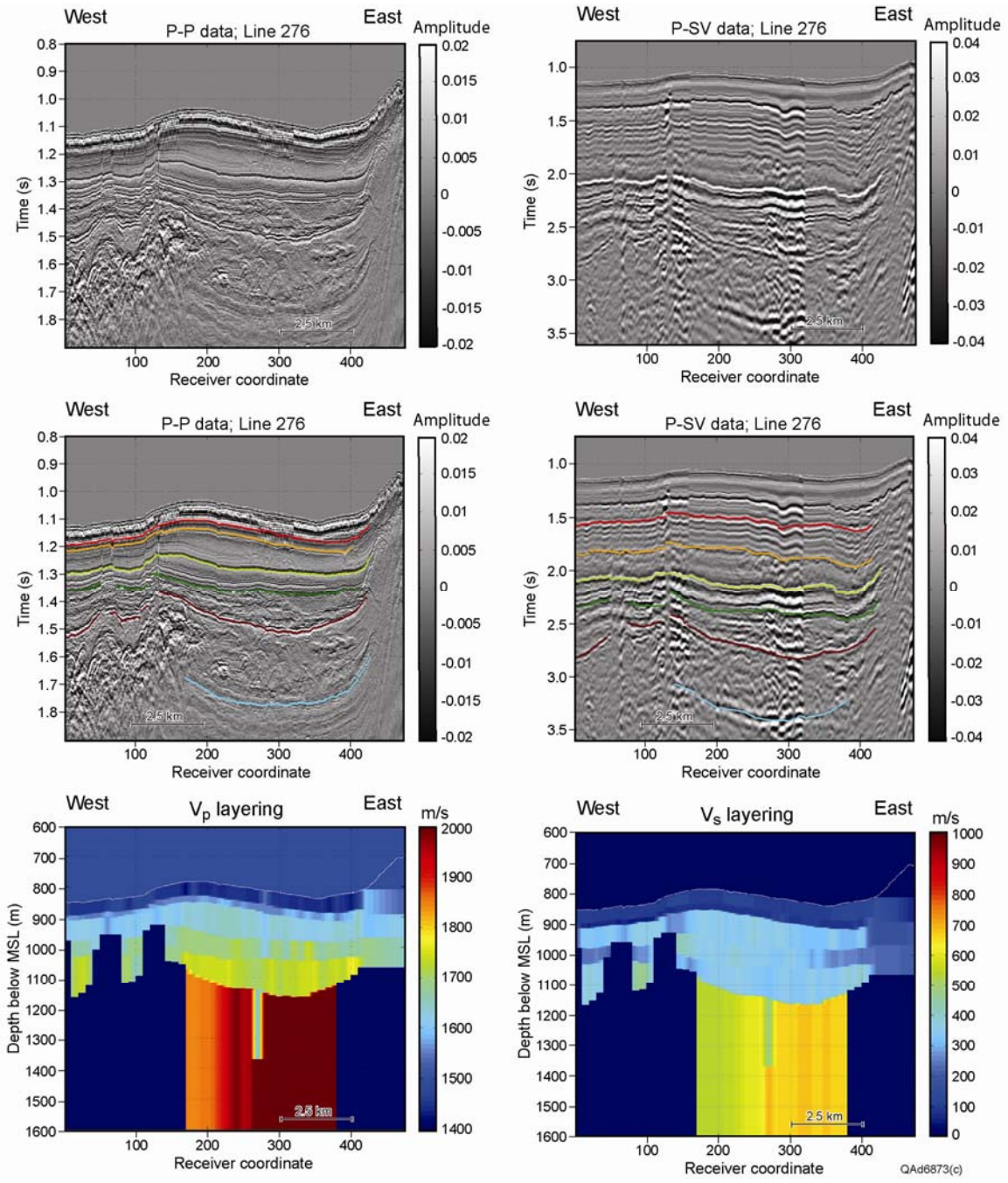

Figure B7a. Research results along profile 276, Study Site 2, Genesis Field area.

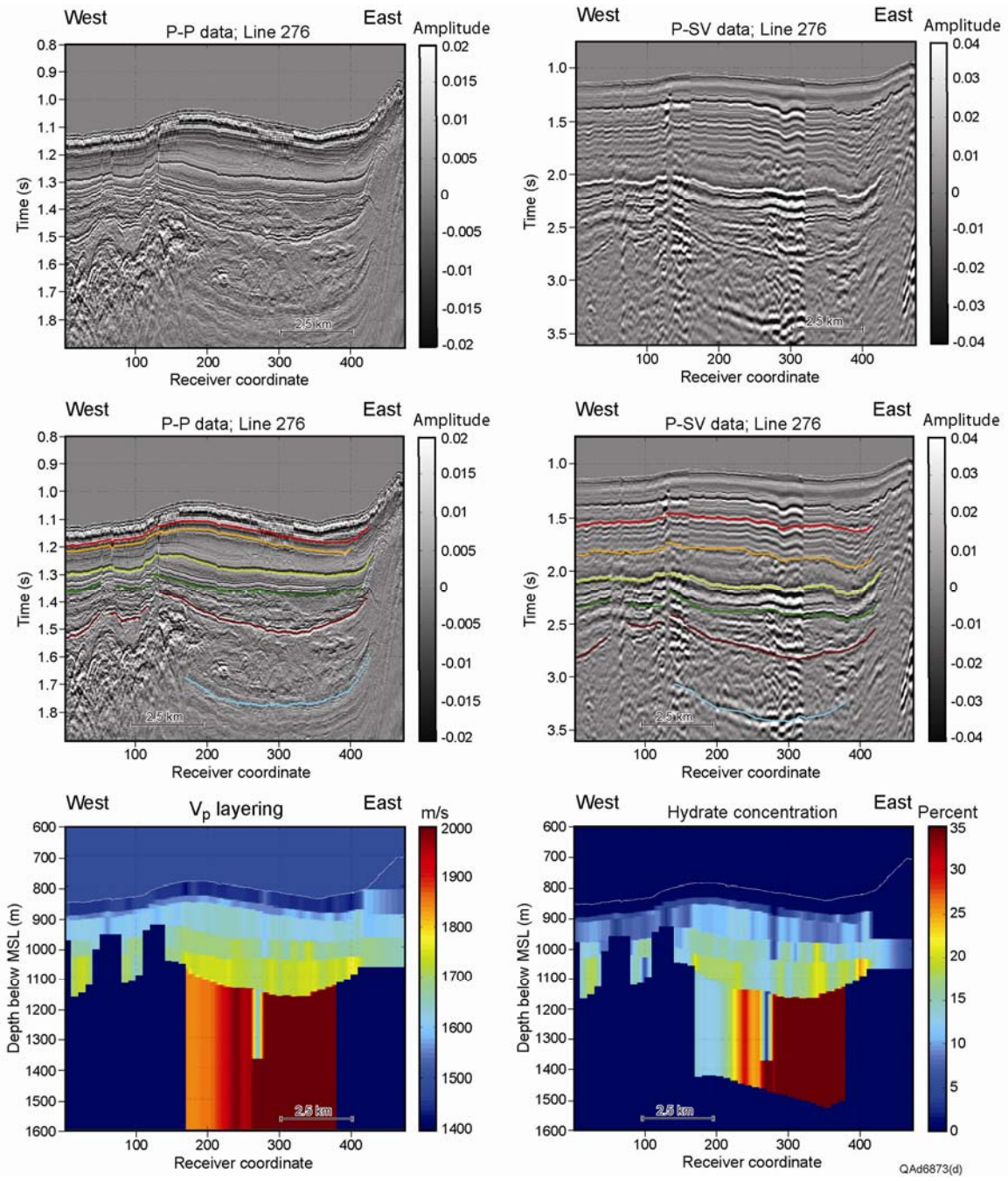

Figure B7b. Research results along profile 276, Study Site 2, Genesis Field area.

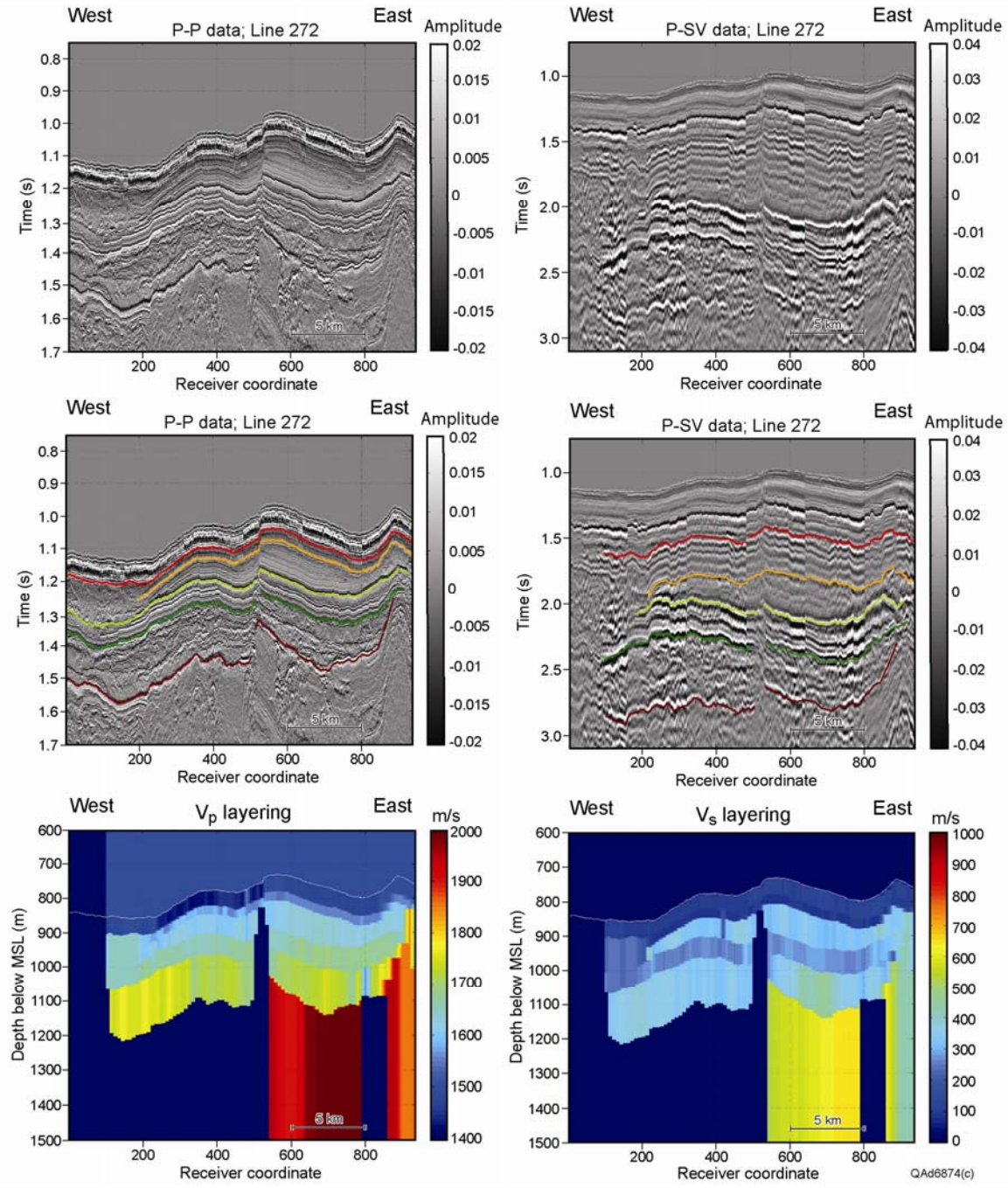

Figure B8a. Research results along profile 272, Study Site 2, Genesis Field area.

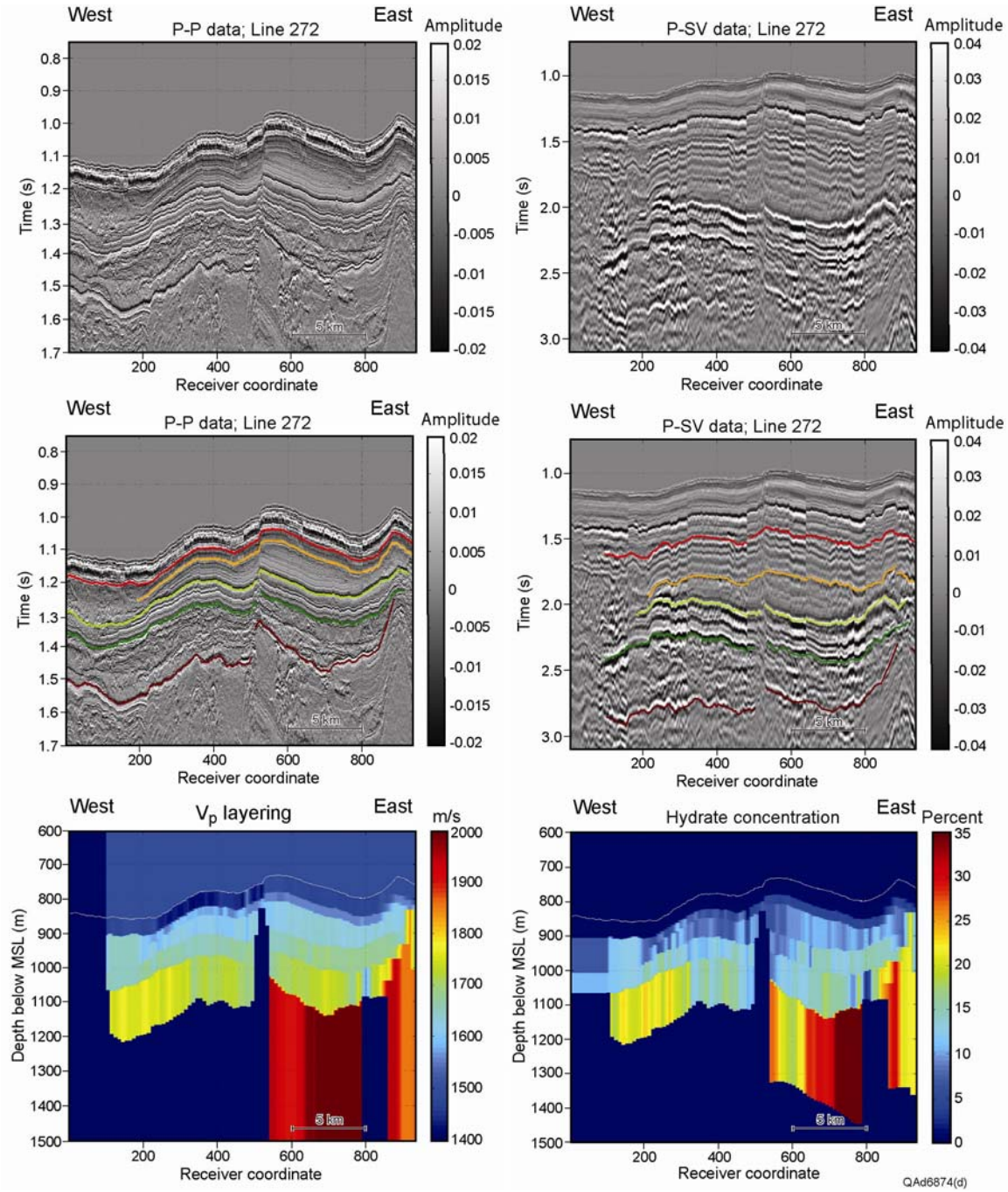

Figure B8b. Research results along profile 272, Study Site 2, Genesis Field area.

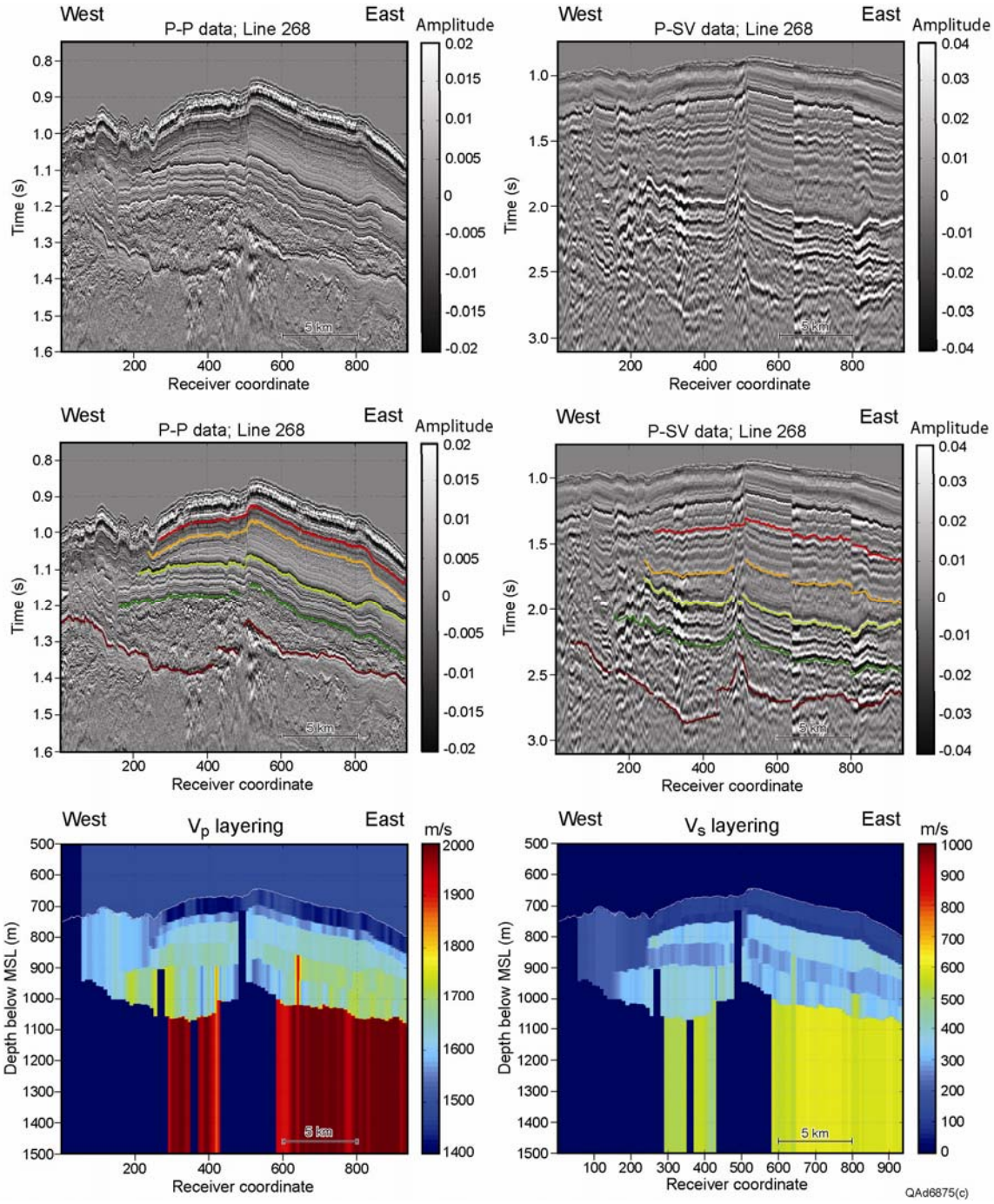

Figure B9a. Research results along profile 268, Study Site 2, Genesis Field area.

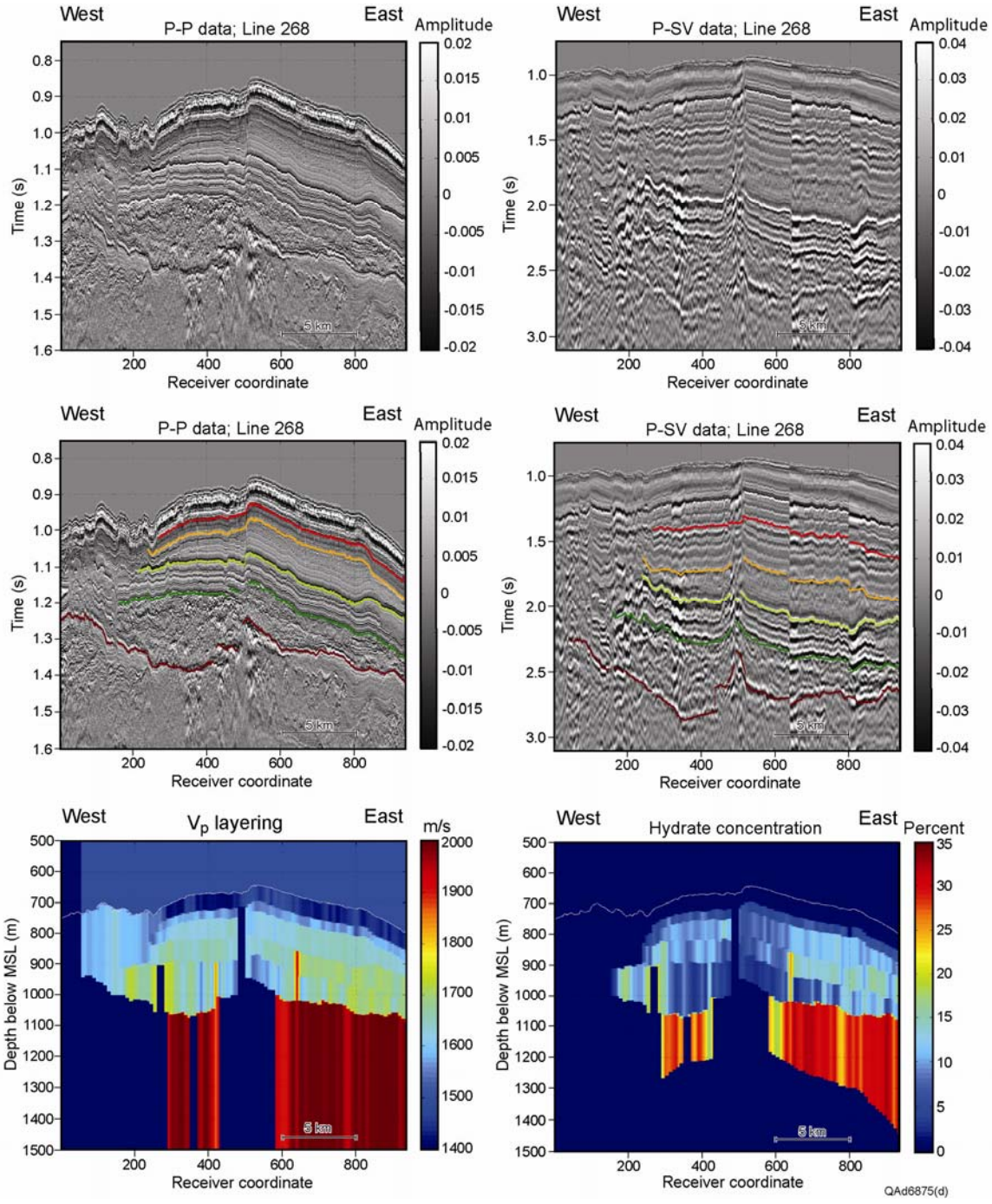

Figure B9b. Research results along profile 268, Study Site 2, Genesis Field area.

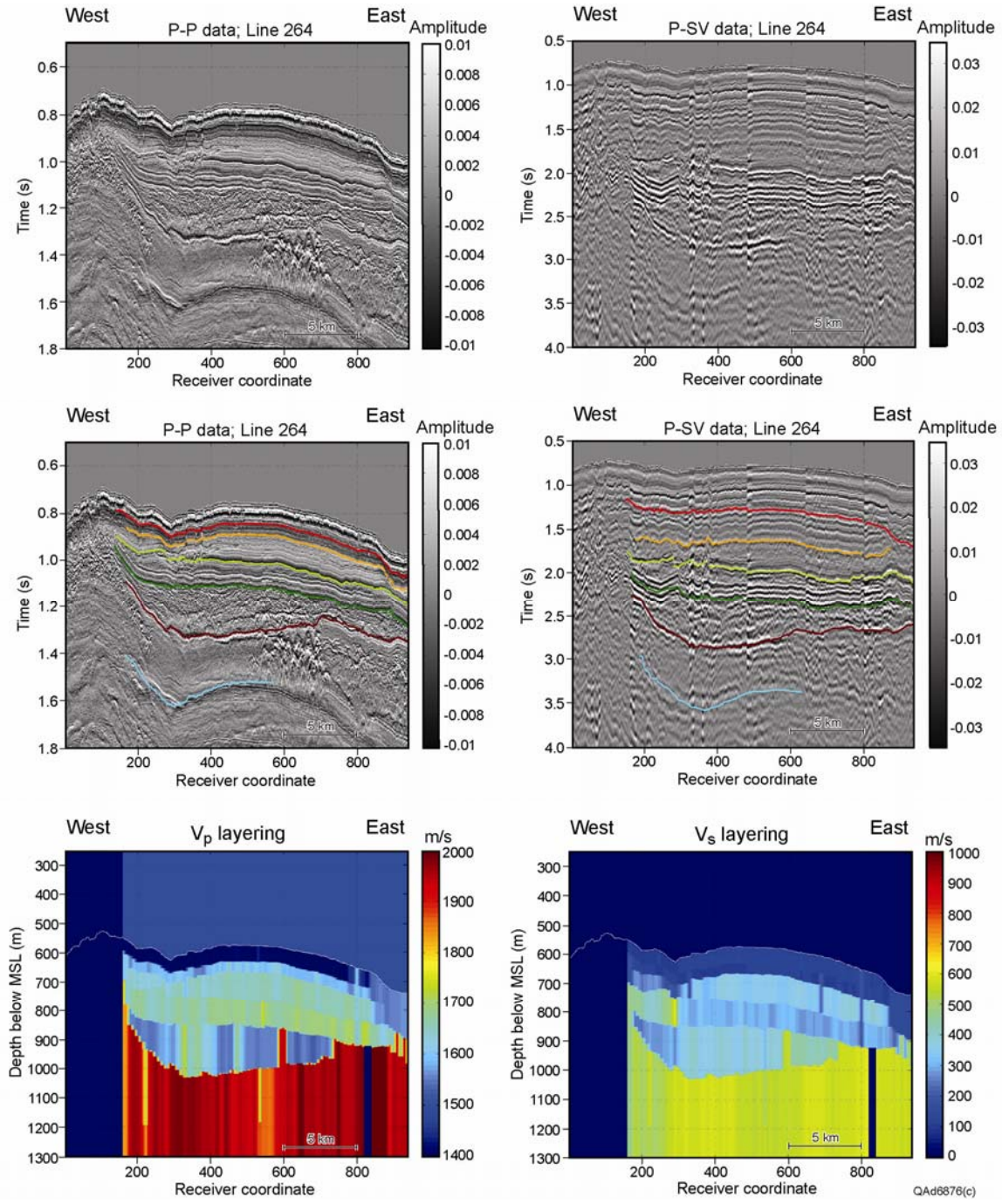

Figure B10a. Research results along profile 264, Study Site 2, Genesis Field area.

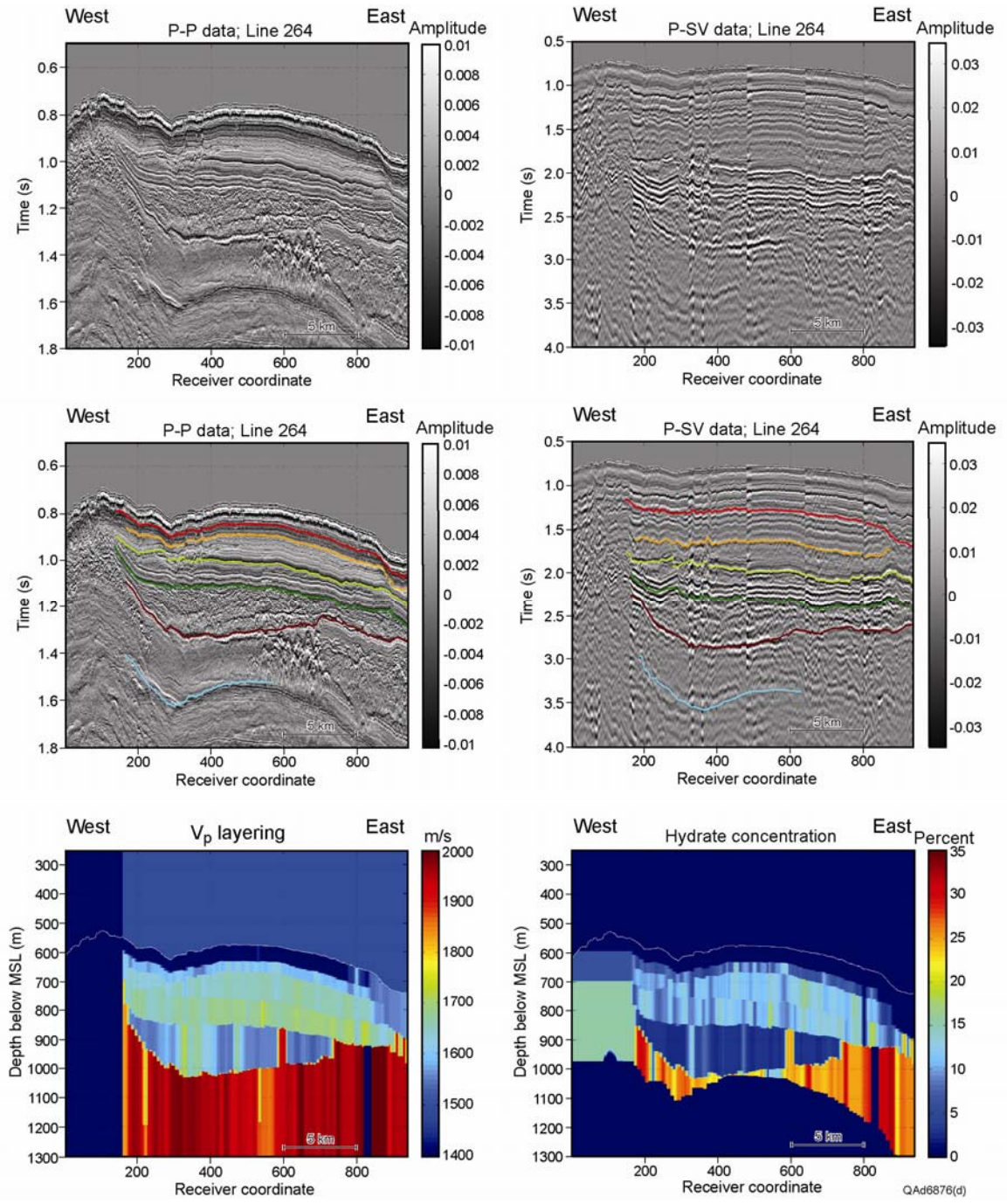

Figure B10b. Research results along profile 264, Study Site 2, Genesis Field area.

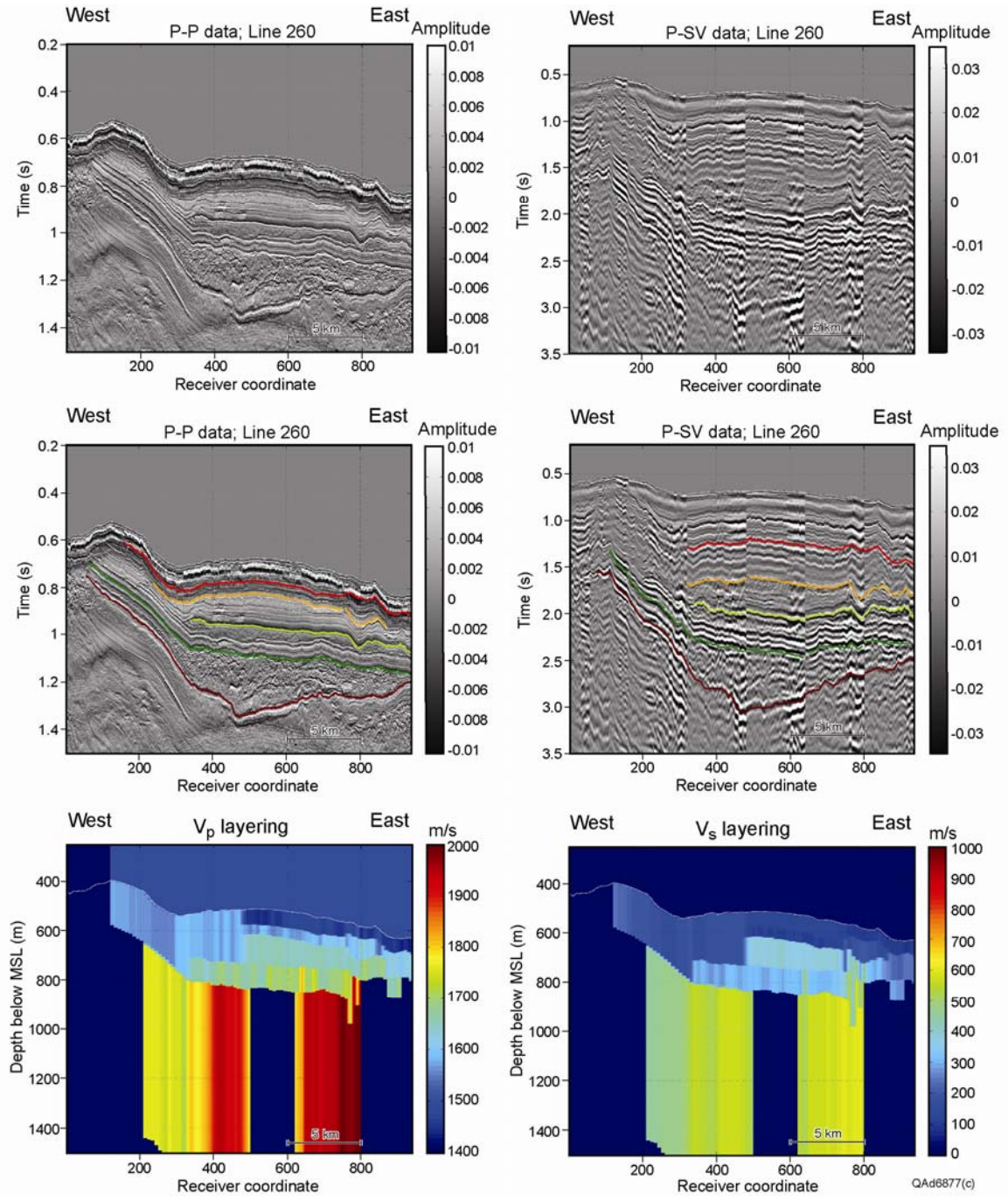

Figure B11a. Research results along profile 260 Study Site 2, Genesis Field area.

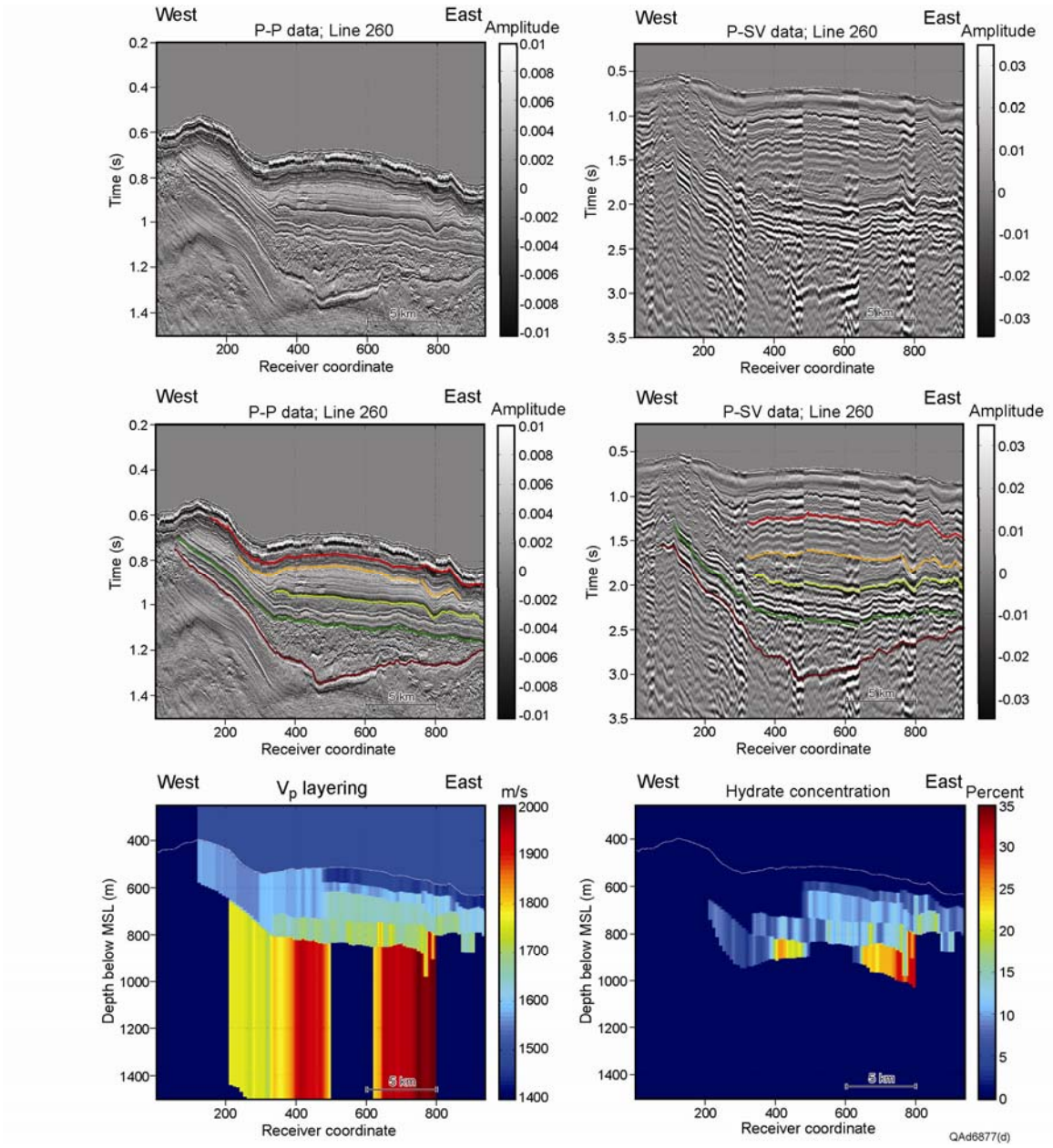

Figure B11b. Research results along profile 260, Study Site 2, Genesis Field area.

National Energy Technology Laboratory

626 Cochrans Mill Road
P.O. Box 10940
Pittsburgh, PA 15236-0940

3610 Collins Ferry Road
P.O. Box 880
Morgantown, WV 26507-0880

1450 Queen Avenue SW
Albany, OR 97321-2198

539 Duckering Bldg./UAF Campus
P.O. Box 750172
Fairbanks, AK 99775-0172

Visit the NETL website at:
www.netl.doe.gov

Customer Service:
1-800-553-7681